De l’adsorption du cobalt et du zinc sur l’hectorite et le quartz à la nucléation hétérogène de phyllosilicates

Michel Schlegel

To cite this version:

Michel Schlegel. De l’adsorption du cobalt et du zinc sur l’hectorite et le quartz à la nucléation hétérogène de phyllosilicates. Géochimie. Université Joseph-Fourier - Grenoble I, 2000. Français. NNT : . tel-00718598

HAL Id: tel-00718598
https://theses.hal.science/tel-00718598

Submitted on 17 Jul 2012

OBSERVATOIRE DE GRENOBLE
et
LABORATOIRE DE GEOPHYSIQUE INTERNE ET TECTONOPHYSIQUE

THESE

présentée par

Michel Schlegel

pour obtenir le titre de
Docteur de l'Université Joseph Fourier - Grenoble I

Spécialité : Géophysique - Géochimie - Géomécanique

De l'adsorption du cobalt et du zinc sur l'hectorite et le quartz, à la nucléation hétérogène de phyllosilicates

Date de soutenance : 3 février 2000

Composition du jury :

Jean Cases	Président	Directeur de recherche, CNRS, Nancy
Alain Decarreau	Rapporteur	Professeur, Université de Poitiers
Pierre Toulhoat	Rapporteur	Directeur CEA, Saclay
Laurent Charlet	Examinateur	Professeur, Université Grenoble1, Grenoble
Alain Manceau	Examinateur	Directeur de recherche, CNRS, Grenoble
Denis Raoux	Examinateur	Directeur de recherche, CNRS, Grenoble
André Scheidegger	Examinateur	Paul Scherrer Institut, Zürich

OBSERVATOIRE DE GRENOBLE
et
LABORATOIRE DE GEOPHYSIQUE INTERNE ET TECTONOPHYSIQUE

THESE

présentée par

Michel Schlegel

pour obtenir le titre de
Docteur de l'Université Joseph Fourier - Grenoble I

Spécialité : Géophysique - Géochimie - Géomécanique

De l'adsorption du cobalt et du zinc sur l'hectorite et le quartz, à la nucléation hétérogène de phyllosilicates

Date de soutenance : 3 février 2000

Composition du jury :

Jean Cases	Président	Directeur de recherche, CNRS, Nancy
Alain Decarreau	Rapporteur	Professeur, Université de Poitiers
Pierre Toulhoat	Rapporteur	Directeur CEA, Saclay
Laurent Charlet	Examinateur	Professeur, Université Grenoble1, Grenoble
Alain Manceau	Examinateur	Directeur de recherche, CNRS, Grenoble
Denis Raoux	Examinateur	Directeur de recherche, CNRS, Grenoble
André Scheidegger	Examinateur	Paul Scherrer Institut, Zürich

Résumé

Les approches macroscopiques (cinétique chimique) et microscopiques (spectroscopie EXAFS polarisée) ont été couplées dans le but de caractériser les mécanismes moléculaires de fixation de cations divalents (Co, Zn) sur l'hectorite, une smectite magnésienne, et sur le quartz.

À pH = 6,5, haute force ionique, et pour un rapport Zn/hectorite de ~ 50 µmol/g, une adsorption spécifique de Co et Zn a lieu. Cette adsorption n'atteint pas l'équilibre avant plusieurs heures, et coïncide avec une libération initiale accrue de protons et de Mg en solution, puis une inhibition à long terme ($t \geq 48$ h) de la cinétique de dissolution de l'hectorite. Co et Zn adsorbés forment des complexes de surface mononucléaires en continuité structurale de la couche octaédrique des feuillets d'hectorite. À basse force ionique, Co et Zn sont initialement adsorbés par échange cationique. Cette réaction atteint l'équilibre en moins de 5 min. Ces cations forment initialement des complexes de sphère externe sur les sites d'échange, puis ils migrent progressivement vers les sites de bordure des feuillets, où ils forment des complexes de surface similaires à ceux formés à haute force ionique.

Le mécanisme et l'amplitude de l'adsorption de Zn sur l'hectorite à pH 7,3, à haute force ionique et pour un rapport Zn/hectorite de 1480 µmol/g, dépend de la concentration en silice dissoute, [Si]. La quantité de Zn adsorbé est limitée pour [Si] ≈ 30-60 µmol/L, et Zn forme des polymères de petite taille (2-3 octaèdres) en continuité structurale de la couche octaédrique de l'hectorite. La quantité de Zn adsorbé est beaucoup plus importante pour [Si] ≈ 540 µmol/L; cette adsorption est corrélée à une adsorption de Si, et correspond à la nucléation de phyllosilicates TOT zincifères en épitaxie dans le plan ab des feuillets.

Une analyse approfondie de spectres EXAFS de Co adsorbé sur le quartz révèle que cet élément polymérise sous forme de couches d'octaèdres liées à des couches de tétraèdres de Si, pour former des phyllosilicates cobaltifères. Le mécanisme de cette néoformation est discuté.

Mots clefs : hectorite, quartz, cobalt, zinc, EXAFS, cinétique, adsorption, échange cationique, épitaxie, phyllosilicate

Abstract

The sorption mechanism and the crystallochemical environment of divalent Co and Zn on hectorite, a magnesian smectite, and quartz are investigated by combined kinetics chemical studies and polarized-EXAFS (P-EXAFS) spectroscopy. At high ionic strength (0.3 M $NaNO_3$), pH 6.5, and a sorbate/hectorite ratio of ~50 µmol/g, Zn and Co adsorb via a pH-dependent mechanism. This sorption process coincides with an initial excess release of protons and Mg in the supernatant, and with a long term inhibition of hectorite dissolution. Sorbate cations form mononuclear surface complexes in the continuity of the magnesian octahedral sheet of the clay structure. At low ionic strength, Zn and Co initially sorb rapidly by cation exchange, and form outer-sphere surface complexes. Following this fast sorption process, sorbed ions are progressively transferred from interlayer exchange sites to layer edges sites, where they form inner-sphere surface complexes. Cation exchange sites thus act as transient cationic buffer.

At pH 7.3, high ionic strength and sorbate/hectorite ratio (1480 µmol/g), the amplitude and kinetics of Zn sorption depend on the concentration of dissolved Si, [Si]. At [Si] ≈ 30-60 µmol/L, Zn forms small polynuclear complexes of 2-3 atoms located in structural continuity of hectorite octahedral sheets. At [Si] ≈ 540 µmol/L, heteronucleation and growth of a Zn-rich phyllosilicate occurs in structural continuity of hectorite layers.

EXAFS spectra of Co-sorbed quartz first indicate formation of large Co octahedral sheets. However, close examination of atomic contributions revealed that these sheets are connected to Si tetrahedral sheets, meaning that the sorption of Co on quartz leads to the neoformation of phyllosilicate. The mechanism of this neoformation is discussed.

Remerciements

Voici déjà venu le temps de faire mes valises et de quitter cette ville pour d'autres horizons. C'est aussi pour moi le moment de me retourner sur les cinq années que j'ai passé à Grenoble (en comptant le DEA et le service militaire), et de remercier tous ceux qui ont enrichi ces années de leur chaleur et de leur générosité.

Je voudrais d'abord exprimer ma gratitude envers mes deux directeurs de thèse, Laurent Charlet et Alain Manceau, pour avoir su me guider dans ce travail où leurs qualités se sont admirablement complétées. Merci à Alain pour son engagement passionné, sa volonté, son exigence intellectuelle, pour sa rigueur dans la composition de figures et de documents rédigés tant en anglais qu'en français. Merci également à Laurent pour son enthousiasme et son foisonnement intellectuel, qui m'ont permis de tourner mon regard vers d'autres horizons que le monde pourtant vaste des argiles.

Monsieur Jean Cases a bien voulu être le président de mon jury de thèse. Qu'il trouve ici l'expression de ma gratitude, laquelle s'adresse également à Alain Decarreau et Pierre Toulhoat, pour avoir accepté d'examiner en un temps record cet épais manuscrit, ainsi qu'à Denis Raoux, pour avoir accepté de siéger au sein du jury.

Je voudrais remercier ici tout particulièrement André Scheidegger, d'abord pour la qualité des échanges scientifiques que nous avons pu avoir, ensuite pour tout l'intérêt qu'il a manifesté pour mon travail de thèse, acceptant de siéger à mon jury de thèse. Pour moi, ce fut toujours un réel plaisir de tourner ma pensé du côté de Zürich, et j'espère qu'il en sera encore longtemps ainsi.

Merci à Bruno et Lorenzo pour avoir su me recevoir et discuter avec moi à maintes reprises. Je voudrais tout particulièrement souligner l'extraordinaire patience de Bruno dans les innombrables fois où j'ai tordu et dispersé son matériel dans les endroits qui n'étaient pas vraiment prévus à cet effet.

Martine a tenu avec fermeté son poste central au sein du laboratoire, avec énormément de bonne humeur, et sachant me rappeler à l'ordre avec beaucoup de justesse. Encore pardon, Martine, pour cette synthèse de goethites substituées qui a laissé le labo dans un état que tu as su décrire avec des mots si justes...

À coté de cette fameuse endurance, Laurent, Jean-Bernard et Christophe se sont succédés assez rapidement au poste d'ingénieur, et Delphine est arrivée ; tous avec une égale bonne volonté. Je les salue ici chaleureusement.

Merci aux étudiants qui m'ont accueilli au laboratoire à mon arrivée, pour avoir su m'initier aux bases de méthodes physiques et chimiques : Jean-Claude, Manue, Céline, Géraldine. Maintenant que je pars, je laisse derrière moi une belle et solide équipe animée par la bonne humeur de Francis, l'accent de Marie-Pierre, la gentillesse d'Alix, d'Anne-Claire, et de Virginie, et la sérénité d'Ahmad. Géraldine, fidèle au poste, s'est à présent muée en cadre permanent, mais ça ne change (presque) rien : c'est dans cette atmosphère vivante, chaleureuse, que j'ai pu rédiger ma thèse, et si le rush final s'est bien passé, c'est en grande partie grâce à vous tous.

Merci à l'équipe de la ligne de CRG-IF de l'ESRF, notamment à Jean-Louis, pour nous avoir supporté avec gentillesse, même quand on l'a appelé à des horaires qui se disent pas, et nous avoir préparé un spectromètre toujours plus efficace, à tous les Oliviers (j'en ai perdu le compte), à Yvonne et Jean-Jacques, pour leur accueil chaleureux.

Beaucoup de personnes se sont intéressés de près ou de loin à ce travail, et m'ont fait part d'observations et de remarques qui m'ont toujours beaucoup appris. Je pense notamment à Philippe Van Cappellen, et ses notes extrêmement pertinentes sur la forme et le contenu du deuxième article, et à Vala Ragnarsdottir. I also want to thank Kathryn Nagy for many fuitful discusions about heterogeneous nucleation and crystal growth. Special thanks to Will Gates, to whom I owe most of my skills in clay purification and thin film preparation. And I don't want to forget Victoria Von Hagen.

Merci à tous ceux qui ont choisi de partager les moments de détentes de cette thèse, Edgar, Hélène, Bruno, Chaton (pardon, Christophe), Marie-Agnès M., Pétro et son millenium hollandais, Florent et ses cristaux d'hydrogène, Sandra, et le groupe du Sappey au grand complet.

Enfin, je voudrais remercier ici du fond du cœur mon père et ma mère, pour m'avoir soutenu sans réserve et jusqu'au bout de mes études. J'ai plus qu'une tendre pensée pour Mélanie, qui m'a souvent écouté, conseillé, conforté et calmé dans les moments de doute et de stress. À vous trois, je dédie le résultat de ces quatre années de travail : cette thèse.

Terminons par Luna, petite chatte dont la litière en bentonite peut fournir un véritable sujet de thèse, si, si...

Sommaire

Introduction générale

> À partir du moment où une forme s'est détachée des Eaux, tout lien organique immédiat entre celles-ci et celle-là est rompu ; entre le préformel et la forme il y a un hiatus. Cette rupture n'a pas lieu lorsqu'il s'agit de formes engendrées par la Terre et de la Terre ; celles-ci restent solidaires de leur matrice, dont elles ne se sont d'ailleurs détachées que provisoirement, à laquelle elles retourneront pour se reposer, se fortifier et, finalement, reparaître au grand jour. C'est pour cela qu'il y a entre la terre et les formes organiques par elle engendrées un lien magique de sympathie. Toutes ensembles, elles constituent un système. Les fils invisibles qui relient la végétation, le règne animal et les hommes d'une certaine région, au sol qui les a produits et qui les porte et les nourrit, ont été tissés par la vie qui palpite aussi bien dans la Mère que dans ses créatures. La solidarité qui existe entre le tellurique d'un côté, le végétal, l'animal, l'humain de l'autre, est due à la *vie* qui est la même partout. Leur unité est d'ordre biologique. Et lorsque l'un quelconque des modes de cette vie est souillée ou stérilisée par un crime contre la vie, tous ses autres modes sont atteints, en vertu de leur solidarité organique.
>
> Mircea Eliade, 1949 « Traité d'histoire des religions », bibliothèque historique Payot (édition de 1994), Paris.

Les quelques lignes placées en exergue de cette introduction permettent de mieux comprendre le rôle fondamental des sols et des surfaces altérées vis-à-vis des être humains, des points de vue religieux, sociologiques, biologiques, et économiques. La mise en culture de plantes utiles, le développement de l'agriculture et la sédentarisation des cultivateurs ont influencé de manière décisive le développement des cités et des civilisations occidentales. Cette importance des ressources alimentaires a conduit progressivement à l'optimisation des pratiques agricoles. Cette recherche agronomique a eu pour objet les plantes, mais aussi les sols et leur capacité à retenir l'eau et les nutriments essentiels [1]. On s'est ainsi intéressé aux propriétés texturales et structurales des sols, ainsi qu'à leur composition chimique et minéralogique. Ces recherches ont permis de mettre en évidence le rôle fondamental joué par les minéraux de la fraction argileuse, notamment les phyllosilicates [2].

Les phyllosilicates sont abondants dans les sols et les profils d'altération [3-6]. Ces minéraux présentent une grande réactivité dans les milieux naturels, notamment vis-à-vis des éléments métalliques présents en solution. En effet, certains phyllosilicates comme les smectites et vermiculites présentent une morphologie lamellaire, une surface spécifique élevée et une charge structurale permanente [3, 7, 8]. Ces propriétés confèrent aux smectites et vermiculites la capacité de retenir les cations métalliques à proximité de leur surface par interaction électrostatique [9]. En milieu hydraté, ces cations peuvent être échangés facilement et rapidement avec d'autres cations présents en solution. Les cations métalliques peuvent aussi perdre tout ou partie de leur sphère d'hydratation, et former avec la surface des phyllosilicates des liaisons iono-covalentes fortes. Ils peuvent également diffuser dans le réseau cristallin des phyllosilicates, et occuper des lacunes dans ce réseau. Enfin, les cations métalliques peuvent être intégrés dans la structure des phyllosilicates lors de processus de néoformation argileuse et de croissance cristalline [10]. L'ensemble de ces mécanismes d'adsorption sur les solides minéraux a pour effet de réduire la concentration et la mobilité des espèces chimiques cationiques dans le milieu naturel. Identifier le mécanisme d'adsorption pour un couple cation-argile donné est alors un préalable nécessaire à l'étude de la mobilité et de la biodisponibilité des cations métalliques [11]. À cet effet, les techniques de spectroscopie d'absorption des rayons X, et notamment la spectroscopie de structure fine étendue d'absorption des rayons X (acronyme anglais : EXAFS) ont donné de précieuses informations sur les états physico-chimiques de polluants dans des milieux contaminés [12, 13]. La spectroscopie EXAFS notamment permet de déterminer l'environnement chimique et structural sur quelques angströms autour d'un élément cible, et ce à de faibles teneurs en cet élément. De plus, l'interprétation de cette information structurale en termes de mécanismes d'adsorption est facilitée par l'étude de ces mécanismes au laboratoire.

Cette étude a pour objet la caractérisation des mécanismes d'adsorption des cations divalents Co et Zn par les phyllosilicates, et de néoformation de phyllosilicates zincifère et cobaltifères. Les expériences d'adsorption ont été menées principalement sur l'hectorite, une smectite magnésienne de taille analogue à celle des smectites présentes dans les sols [14]. Pour bien caractériser les différents mécanismes de fixation des cations, des techniques macroscopiques et spectroscopiques ont été employées simultanément. La spectroscopie EXAFS utilisée dans le cadre de cette étude permet d'identifier la nature du complexe cation-solide, et donc de reconstituer le mécanisme moléculaire de fixation des cations. De plus, l'application de l'EXAFS polarisé (P-EXAFS) à l'étude de films auto-supportés de smectites permet de reconstituer l'environnement cristallochimique des cations cibles avec très peu d'ambiguïté [15, 16]. Cette étude spectroscopique fournit en outre des spectres de référence utiles pour l'analyse ultérieure d'échantillons naturels. L'étude chimique macroscopique permet (1) d'estimer la cinétique et l'amplitude de l'adsorption en fonction de paramètres de la solution tels que son pH, sa force ionique, sa composition chimique, et (2) de mesurer l'impact de cette fixation sur la stabilité de la phase solide. À partir de ces informations, il est possible de déterminer la stabilité chimique des complexes formés entre le cation et la phase solide, et de prédire plus précisément le devenir des cations dans ces milieux dynamiques que sont les systèmes naturels [17].

Ce mémoire est divisé en neuf chapitres, regroupés en cinq parties. La première partie (chapitres 1 et 2) consiste en des rappels généraux sur la structure des smectites, et leurs propriétés chimiques en solution. La deuxième partie (chapitre 3) détaille les opérations de purification de l'hectorite, ainsi que les protocoles chimiques mis en œuvre pour les expériences en solution. Les résultats de l'étude d'adsorption des cations Co et Zn sur l'hectorite à pH modéré et faible rapport cation/solide sont présentés dans la troisième partie (chapitres 4 et 5). La quatrième partie présente les résultats de nucléation et cristallisation de phyllosilicates zincifères sur l'hectorite (chapitre 6) et cobaltifères sur le quartz (chapitre 7) à température ambiante. Les résultats obtenus permettent finalement de discuter dans la cinquième partie la notion d'échange cationique dans les sols (chapitre 8).

note : dans la suite du texte français, le mot « adsorption » (et tous les termes qui s'y rattachent) désigne l'ensemble des mécanismes de fixation d'un cation à la surface d'une phase solide. Ce mot est donc pris comme un équivalent français du terme anglais « sorption », tel qu'il a été employé par Scheidegger & al [18].

Première partie : les smectites

Introduction

Les phyllosilicates sont des composés hydratés de silice et de cations métalliques di- ou trivalents. Ils ont pour dénominateur commun une organisation élémentaire bidimensionnelle, qui résulte de l'agencement de leurs constituants chimiques au niveau atomique. Cette anisotropie structurale a pour conséquences une forte anisotropie des propriétés physico-chimiques, en particulier des différences notables de réactivité de faces cristallographiques distinctes des feuillets élémentaires. Pour bien comprendre ces différences de propriétés chimiques, il est important de connaître la structure cristallochimique des phyllosilicates.

Les phyllosilicates contenus dans les sols et les profils d'altérations présentent une grande variété de compositions chimiques, notamment en termes de nature des cations (Al, Fe, Mg...) et de proportions cation/silice. Ces différences chimiques ont un impact sur la structure des phyllosilicates, mais aussi sur leur réactivité en solution, notamment en termes de stabilité, de solubilité, de rétention et d'échange de cations interfoliaires. Ces relations entre composition élémentaire, organisation structurale et réactivité de surface des phyllosilicates sont illustrées dans le cas des smectites, phyllosilicates ubiquistes dans les milieux naturels.

Cette partie est divisée en deux sections. La première section (chapitre 1) décrit la structure élémentaire des particules de smectites, et l'organisation structurale de l'espace interfoliaire et des bordures des feuillets. La seconde section (chapitre 2) présente les différents mécanismes de fixation des cations à la surface des smectites, ainsi que les modèles macroscopiques utilisés jusqu'à présent pour décrire cette adsorption.

1. Propriétés structurales des smectites

1.1. Structure et propriétés du feuillet élémentaire

1.1.1. Structure cristalline idéale

Les smectites sont des silicates hydratés d'aluminium, de magnésium, ou de fer. Elles possèdent une structure lamellaire ou phyllitique, formée par l'assemblage de deux couches tétraédriques (notées T) autour d'une couche octaédrique (notée O; fig. 1.1.a). Les octaèdres sont assemblés entre eux exclusivement par les arêtes. Les tétraèdres sont reliés entre eux exclusivement par les sommets, et partagent chacun un sommet avec la couche octaédrique. Les oxygènes basaux partagés seulement par les tétraèdres forment des réseaux bidimensionnels plus ou moins plans (fig. 1.1b). Ces oxygènes délimitent des cavités dites siloxanes, dont le rayon est légèrement inférieur à 1.4 Å [2]. Les oxygènes de la couche d'octaèdres non partagés avec des tétraèdres sont protonés, et forment des groupes hydroxyles. Ces groupes hydroxyles de constitution sont situés à l'aplomb des cavités siloxanes.

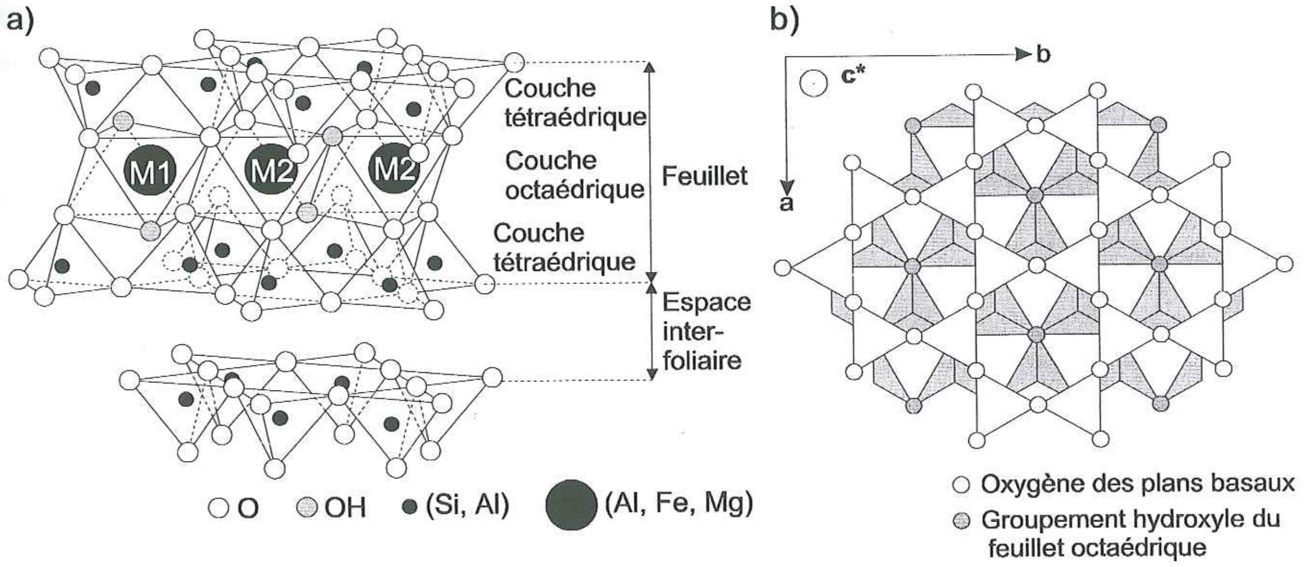

Figure 1.1. Structure tridimensionnelle d'un feuillet de smectite [16]. a) Visualisation des polyèdres de co-ordination des cations structuraux, avec nomenclature des sites octaédriques trans (M1) et cis (M2). b) Vue de la structure dans la direction normale au feuillet, permettant de voir l'arrangement des oxygènes de la cavité siloxane et la position des groupements hydroxyles.

Les sites tétraédriques d'une smectite sont tous occupés par des cations, généralement des ions Si^{4+}, mais qui peuvent être substitués par des ions Fe^{3+} ou Al^{3+}. Les sites octaédriques peuvent être occupés par des cations, mais selon leur charge formelle certains sites octaédriques peuvent être vacants.

- Si les cations de la couche octaédrique sont principalement trivalents, alors seuls deux sites octaédriques sur trois sont occupés. Les smectites sont dites dioctaédriques. Leur composition chimique par demi-maille est $\mathrm{Me}_2^{3+}\mathrm{Si}_4\mathrm{O}_{10}(\mathrm{OH})_2$ (Me^{3+} = Al^{3+}, Fe^{3+}, Cr^{3+}...). Les groupements hydroxyles de la couche octaédrique sont alors inclinés en direction des sites vacants [19, 20]. Les smectites sont dites « trans-vacantes » si les groupes hydroxyles sont localisés aux deux extrémités opposés des octaèdres vacants (sites M1; fig.1.1.a), ou « cis-vacantes » si les groupes hydroxyles sont localisés le long d'une arête partagée par deux octaèdres (sites M2 ; fig. 1.1.a).

- Si les cations octaédriques sont divalents, alors tous les sites octaédriques sont occupés. Les smectites sont dites trioctaédriques. Leur composition chimique par demi-maille est $\mathrm{Me}_3^{2+}\mathrm{Si}_4\mathrm{O}_{10}(\mathrm{OH})_2$ (Me^{2+} = Mg^{2+}, Fe^{2+}, Ni^{2+}, Zn^{2+}, ...). Les groupements hydroxyles du feuillet pointent alors vers l'extérieur du feuillet, selon une direction normale à la couche octaédrique [19, 21].

Les différents cations octaédriques ont des rayons ioniques distincts [22] et, par conséquent, la taille de la couche octaédrique isolée, mesurée par ses paramètres de maille (a, b), est fonction de la nature du cation. Ces paramètres (a, b) sont souvent différents de ceux de la couche tétraédrique isolée. L'ajustement des dimensions des couches octaédriques et tétraédriques se fait par le biais de modifications structurales des deux types de couches, modifications qui ont une amplitude différente selon la nature du cation octaédrique.

- Les cations octaédriques trivalents (Al^{3+}, Fe^{3+}...) des smectites dioctaédriques ont des rayons ioniques relativement petits ($R_{\mathrm{Al}} = 0.53$ Å; $R_{\mathrm{Fe}} = 0.55$ Å). Par conséquent, les paramètres (a, b) de la couche octaédrique isolée sont nettement plus petits que ceux de la couche tétraédrique isolée. L'ajustement de ces deux couches se fait en partie grâce à une augmentation des paramètres (a, b) de la couche octaédrique par un aplatissement des octaèdres avec conservation des distances cation-oxygène (fig. 1.2). Cet aplatissement est mesuré par l'angle ψ, entre la normale au feuillet et le vecteur joignant deux oxygènes diamétralement opposés. La valeur de cet angle est de 54.7° pour des octaèdres non déformés (symétrie Oh), et d'environ 57° dans le cas de smectites dioctaédriques [3, 16, 23]. De plus les paramètres (a, b) de la couche tétraédrique sont réduits par d'une rotation des tétraèdres autour d'axes parallèles à **c*** (fig. 1.3.a). La rotation des tétraèdres est mesurée par l'angle α, qui peut valoir jusqu'à 15° [3, 24]. Cette rotation est corrélée à un basculement des oxygènes des plans de base vers les sites octaédriques vacants (fig. 1.3.b). La symétrie hexagonale de la cavité siloxane est alors perdue au profit d'une symétrie pseudo-ditrigonale, et le rayon de la cavité diminue légèrement.

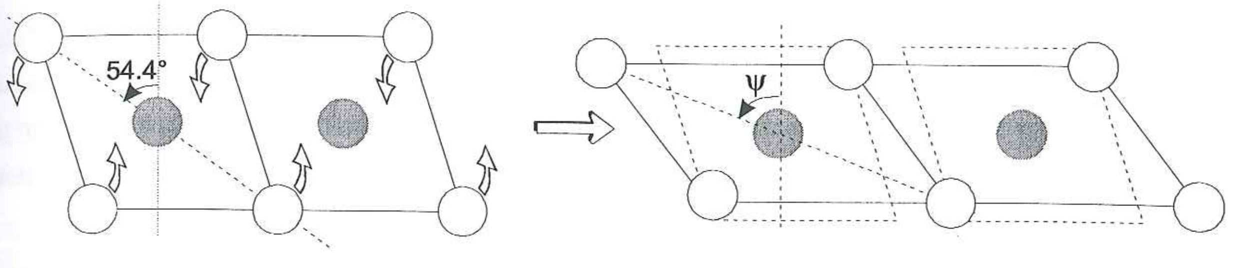

Figure 1.2. Illustration de l'aplatissement de la couche octaédrique d'une smectite et de son impact sur les distances entre cations. Les sphères sombres représentent les cations et les blanches les oxygènes de l'octaèdre de coordination.

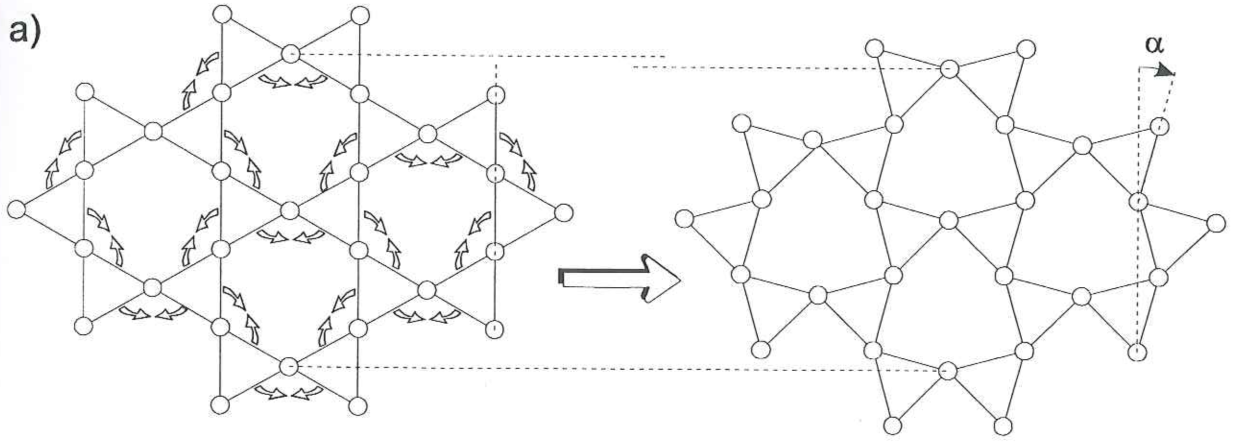

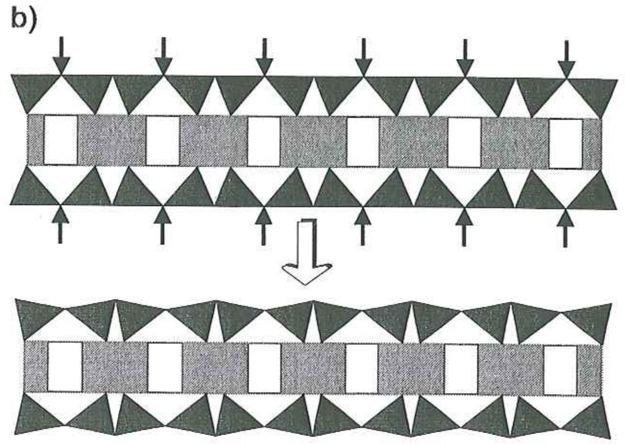

Figure 1.3. (a) Mécanisme de raccourcissement de la couche tétraédrique des smectites par rotation conjugée des tétraèdres autour d'axes parallèles à **c***. Le sens de rotation est indiqué par les petites flèches. En raison de la symétrie pseudo-ditrigonale de la couche, le raccourcissement a lieu dans toutes les directions du plan. (b) Basculement des oxygènes des plans de base vers les sites octaédriques vacants.

- Dans les phyllosilicates trioctaédriques, les cations de la couche octaédrique ont des rayons ioniques plus élevés, entre 0.6 et 0.75 Å. L'angle ψ peut atteindre des valeurs élevées, jusqu'à 60° [3]. La déformation de la couche tétraédrique est alors nettement moins importante, avec des valeurs de α inférieures à 7°, et même parfois nulles [3, 24, 25]. Enfin, il n'y pas de basculement des oxygènes des plans de base.

1.1.2. Charge structurale des smectites

Les smectites présentent toutes un déficit de charge électrique du feuillet, de l'ordre de 0.2 à 0.6 charge par demi-maille [3, 7, 26, 27]. Dans la plupart des cas, ce déficit résulte de la substitution partielle de cations structuraux par des cations de valence inférieure. Par exemple, les ions Si^{4+}

peuvent être remplacés par des ions Al^{3+}. Dans les smectites dioctaédriques, les cations Al^{3+}et Fe^{3+} des sites octaédriques peuvent être remplacés par des ions Mg^{2+} et Fe^{2+}... Ce déficit peut aussi provenir de la présence de lacunes dans la couche octaédrique (cas des stévensites). La nature et la localisation du déficit de charge du feuillet, ainsi que la nature du cation octaédrique dominant, sont utilisées pour classifier les smectites (tableau 1.1).

Tableau 1.1. Classification et formule structurale des principales smectites, basée sur la localisation de la charge et la nature des cations octaédriques. Le déficit de charge structural est équilibré par un cation E^+ retenu auprès du feuillet.

Localisation de la charge	Smectites dioctaédriques	Smectites trioctaédriques
Octaédrique	Montmorillonite $E_x^+(Al_{2-x}Mg_x)Si_4O_{10}(OH)_2$	Hectorite $E_x^+(Mg_{3-x}Li_x)Si_4O_{10}(OH)_2$ Stévensite $E_{2x}^+(Mg_{3-x}\ \ _x)Si_4O_{10}(OH)_2$ (= site vacant)
Tétraédrique	Beidellite $E_x^+Al_2(Si_{4-x}Al_x)O_{10}(OH)_2$ Nontronite $E_x^+Fe_2(Si_{4-x}Al_x)O_{10}(OH)_2$	Saponite $E_x^+Mg_3(Si_{4-x}Al_x)O_{10}(OH)_2$

Le déficit de charge est compensé par des cations, hydratés ou non, retenus à proximité des plans de base des feuillets. Ces cations peuvent lier simultanément deux feuillets, et initier ainsi des empilements d'ordre et d'amplitude variable, comme cela est illustré dans la partie suivante.

1.2. Empilement des feuillets

Des particules tridimensionnelles de smectites peuvent être obtenues par empilement de feuillets. Le nombre de feuillets empilés varie selon la nature du cation interfoliaire et le degré d'hydratation de l'espace interfoliaire [28-30]. Il peut varier de plusieurs dizaines d'unités (cas des smectites calciques) à un feuillet isolé (cas de certaines smectites sodiques ; [2]). La cohésion entre les feuillets d'une même particule est assurée par la couche interfoliaire (cations et éventuellement eau d'hydratation). Trois modes d'empilement sont observés pour les phyllosilicates (fig. 1.4) [31].

- Dans un empilement ordonné, les feuillets ont les mêmes directions cristallographiques (aux propriétés de symétrie de la maille près). Ils sont positionnés les uns par rapport aux autres de sorte que les centres des cavités siloxanes se font face et sont rigoureusement alignés dans la direction **c***. Ce mode d'empilement n'a jamais été observé pour les smectites.

- Dans un empilement semi-ordonné, les feuillets successifs sont décalés par des translations et des rotations « semi-définies » (e.g., de valeurs ± n $2\pi/3$, ou ± n.b/3). Ces empilements ne sont observés que pour les smectites dont le déficit de charge est d'origine tétraédrique.

- Dans un empilement turbostratique, les feuillets sont décalés par des rotations et/ou des translations quelconques. Les axes **a** et **b** de feuillets successifs sont ainsi désorientés les uns par rapport aux autres, et la particule ne présente pas d'ordre dans la direction **c***. Ce type d'empilement est le plus fréquent chez les smectites.

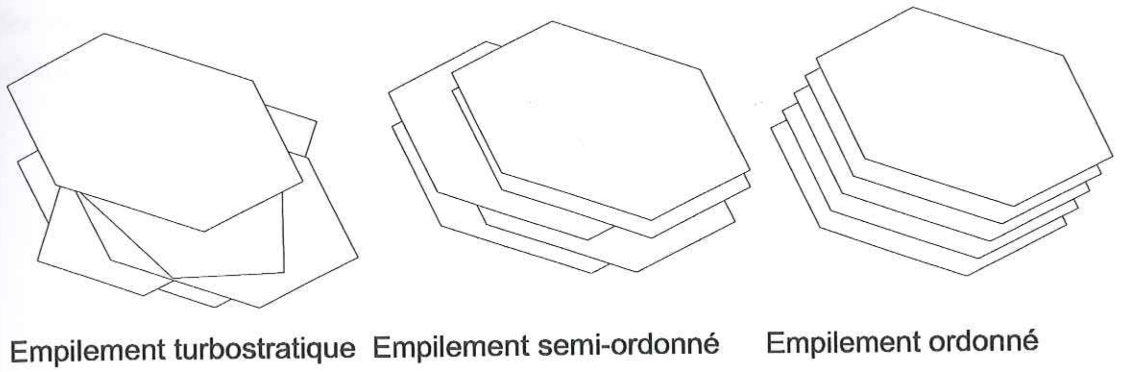

Figure 1.4. Les différents modes d'empilement des feuillets argileux.

La morphologie des feuillets peut avoir un impact sur l'importance du désordre dans les empilements turbostratiques. Par exemple, les feuillets allongé selon une direction cristallographique particulière tendent à s'aligner entre eux au sein d'une même particule. De telles particules présentent alors un ordre plus important que des particules formés par l'empilement de feuillets trapus. Il est possible d'augmenter l'ordre au sein des empilements, et de passer ainsi d'un empilement turbostratique à un empilement semi-ordonné, par des cycles d'humectation-dessication (HD) répétés [32-34]. Cette augmentation de l'ordre est facilitée avec les gros cations alcalins comme K^+, Rb^+ et Cs^+ [34], et nettement moins avec les alcalino-terreux comme Ca^{2+} (V.A. Drits, communication personnelle). Ces disparités dans le mode d'empilement des feuillets suggère que ces cations interfoliaires n'interagissent pas tous de la même manière avec les feuillets. Ce point est développé dans la section suivante.

1.3. Organisation de l'espace interfoliaire

1.3.1. Interactions entre cations interfoliaires et feuillets

Les cations interfoliaires peuvent interagir de différentes manières avec les plans de base des feuillets de smectites [8, 35]. (fig. 1.5). Ils peuvent conserver leur sphère d'hydratation, et sont alors retenus à la surface des feuillets par des interactions faibles (interactions électrostatiques, pont H, etc...). Dans ce cas, ils peuvent résider soit dans la couche diffuse, soit au voisinage immédiat des oxygènes des plans de base, pour former des complexes hors sphère (CHS). Les cations interfoliaires peuvent aussi perdre plusieurs molécules d'eau d'hydratation, et leur polyèdre de coordination est alors complété par des oxygènes des plans de base. Ces cations forment alors des complexes de sphère interne (CSI)[1].

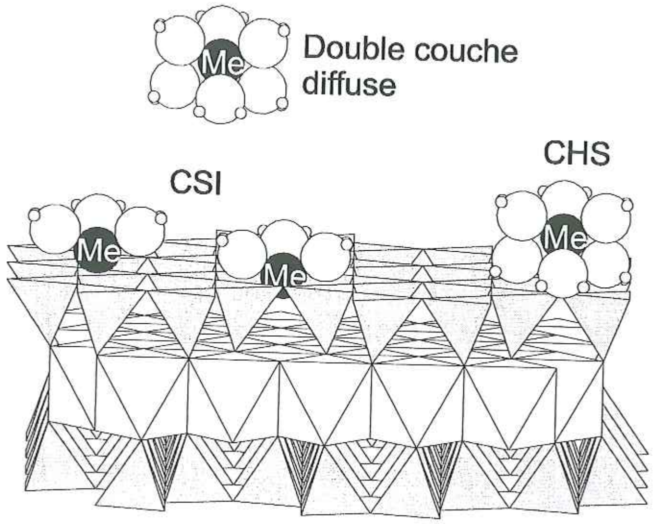

Figure 1.5. Mécanismes de fixation d'un cation Me^{m+} sur le plan de base d'une smectite [35].

Le mode de fixation d'un cation dépend essentiellement de sa charge, de sa taille, de l'état d'hydratation de l'espace interfoliaire, du facteur d'ordre dans l'empilement des feuillets de la particule, et de l'origine tétraédrique ou octaédrique du déficit de charge [2]. Si le déficit de charge a une origine octaédrique, alors une grande partie de ce déficit est délocalisée par le biais des tétraèdres liés à cet octaèdre sur environ 10 oxygènes des plans de base. Le déficit de charge positive par oxygène est faible (de l'ordre de 0.12-0.15 unité), ce qui favorise des interactions faibles et délocalisées (interactions électrostatiques, pont H...). Par contre, si la substitution a lieu dans un tétraèdre, alors le déficit de charge est localisé principalement sur les 3 oxygènes basaux de ce tétraèdre. La fraction de charge par oxygène est plus importante et les interactions fortes, comme la formation de CSI, sont favorisées. D'autre part, la déshydratation partielle ou totale de l'espace interfoliaire tend à rapprocher les plans de base des feuillets et à favoriser la formation de complexes dans lesquels les cations sont liés aux deux feuillets [21, 34].

1.3.2. Environnements structuraux des cations interfoliaires

Les cations et les molécules d'eau localisés dans un espace interfoliaire hydraté sont mobiles [36-42] et peuvent diffuser sur les plans de base avec des taux de diffusion généralement très supérieurs à ceux des cations du feuillet. Ils peuvent par conséquent être remplacés par des cations de la solution dans de brefs délais (moins de 24 h), et sont donc échangeables. La mobilité (et par conséquent l'échangeabilité) de certains cations interfoliaires peut être restreinte par des cycles HD, ou par déshydratation à haute température ou sous vide [43, 44]. Cependant, cette déshydratation modifie l'environnement structural du cation interfoliaire par rapport aux conditions hydratées. Ceci souligne l'intérêt des techniques permettant une caractérisation structurale des cations interfoliaires en présence d'eau : spectroscopie infrarouge, spectroscopie de résonance magnétique nucléaire, diffraction des rayons X, spectroscopie EXAFS. Les modes possible d'organisation de l'espace interfoliaire peuvent aussi être abordés de façon théorique, notamment par dynamique moléculaire [45-48]. Cependant, ces études théoriques posent problème, cas elles ne prennent pas en compte de manière explicite l'impact de l'empilement des feuillets (turbostratiques ou semi-ordonnés) sur la nature des complexes interfoliaires. De fait, elles demeurent sujettes à caution. Les résultats des études expérimentales et théoriques pour des smectites ne contenant qu'un seul type de cation interfoliaire (systèmes dit homoioniques) peuvent être résumés comme suit.

- Les cations alcalins K^+, Rb^+ et Cs^+ ont des enthalpies d'hydratation relativement faibles en valeur absolue (tableau 1.2), et des rayons ioniques égaux (K^+) ou supérieures (Rb^+, Cs^+) à celui de la cavité siloxane ($r < 1.4$ Å; [2]). Ces cations peuvent donc perdre facilement une partie de leurs molécules d'eau d'hydratation au profit des oxygènes des plans de base. À pression partielle de vapeur d'eau P_{H20} inférieure à la pression saturante, P_{sat}, des CSI sont observés par RMN [41]. Les simulations par dynamique moléculaires suggèrent que de ces CSI se forment par liaison des cations avec les oxygènes basaux d'un tétraèdre (fig. 1.6.a) [45]. La quantité d'eau localisée dans l'espace interfoliaire est faible, de l'ordre d'une couche d'eau [29]. En conditions anhydres, les cations forment des CSI stables [21, 34] par interaction avec deux feuillets successifs. Le Cs est alors localisé dans les cavités siloxanes d'un feuillet (fig. 1.6.b). Le mode d'interaction de ce CSI avec l'autre feuillet dépend du mode d'empilement des feuillets. Dans un empilement turbostratique, les cavités siloxanes peuvent éventuellement faire face à d'autres cavités siloxanes, mais plus généralement aux plans basaux des tétraèdres du second feuillet [34]. Après plusieurs cycles HD, l'empilement des feuillets tend à s'ordonner, et le nombre de cations formant des CSI par interaction avec deux cavités siloxanes augmente [34]. Cette formation de tactoïdes, avec départ de toute l'eau interfoliaire, s'accompagne d'une réduction significative de la mobilité et de l'échangeabilité des cations [33, 49].

- Les cations Ba^{2+}, Na^+, et Li^+, ont une enthalpie d'hydratation plus forte (en valeur absolue) que celle de K^+, Rb^+ et Cs^+, et leur rayon ionique est égale ou inférieur à celui de la cavité siloxane. En conditions « déshydratées », on a pu montrer que le Li localisé dans l'espace interfoliaire est en fait piégé avec une molécule d'eau au voisinage des cavités siloxanes (fig. 1.6.c) [20, 21]. Pour des états d'hydratation intermédiaires, à une ou deux couches d'eau, les études par diffraction des rayons X [44] et spectroscopie infrarouge [50] suggèrent que Na et Li sont partiellement engagés dans les cavités siloxanes des feuillets (fig. 1.6.b). Ces résultats ne semblent pas coïncider avec ceux de modélisations par dynamique moléculaire, qui suggèrent que Na et Li forment alors des CHS dans l'espace interfoliaire (fig. 1.6.d), ou des CSI au-dessus des plans de base des tétraèdres substitués par Al^{3+} (fig. 1.5.b) [45, 47]. L'espace interfoliaire peut contenir une ou plusieurs couches d'eau selon la P_{H2O} [29].

---

[1] Les termes « complexes hors sphère » et « complexes de sphère interne » sont ici des définitions purement structurales.

- Les cations divalents Mg^{2+}, Ca^{2+} et Sr^{2+} ont des rayons ioniques faibles et des enthalpies d'hydratation élevées (en valeur absolue) (tableau 1.2). Ils sont donc fortement liés à leur sphère d'hydratation, et forment des CHS [36-38, 51-57] jusqu'à des P_{H2O} faibles (10 % de P_{sat} ; [51]) (fig. 1.6.d). Les molécules d'eau de la sphère d'hydratation peuvent établir des ponts H avec les oxygènes des plans basaux [51]. L'espace interfoliaire est hydraté à une couche d'eau à faible P_{H20} (< 10 % de P_{sat}) et présente entre une et deux couches d'eau pour des conditions de P_{H20} modérément insaturées [29]. La mobilité des cations dans cet espace hydraté est toujours importante, bien que réduite par rapport à une solution [36].

Tableau 1.2. Quelques propriétés physiques des cations [58]. Les rayons ioniques sont donnés pour une coordinance octaédrique [22].

Ion	Enthalpie d'hydratation (kJ mol^{-1})	Rayon ionique (Å)	ion	Enthalpie d'hydratation (kJ mol^{-1})	Rayon ionique (Å)
Cations alcalins			Cations alcalino-terreux		
Li^+	-515	0.76	Be^{2+}	-2487	0.45
Na^+	-405	1.02	Mg^{2+}	-1922	0.72
K^+	-321	1.38	Ca^{2+}	-1592	1.00
Rb^+	-296	1.52	Sr^{2+}	-1445	1.18
Cs^+	-263	1.67	Ba^{2+}	-1304	1.35
Divers					
			Cu^{2+}	-2100	0.73
Ag^+	-476	1.15	Cd^{2+}	-1806	0.95

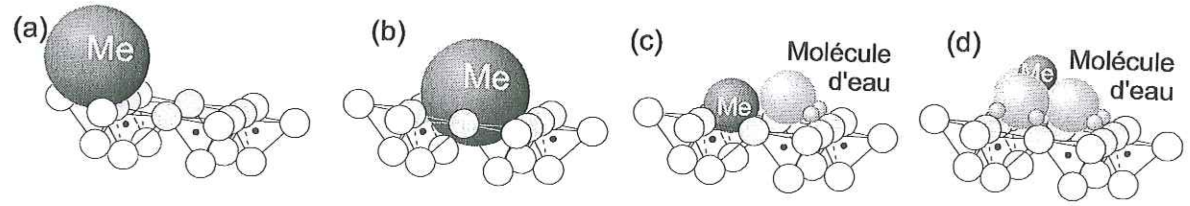

Figure 1.6. Modes possibles d'interaction des cations avec le plan de base des smectites. Pour faciliter la visualisation, les oxygènes du feuillet sont représentés avec une taille réduite, et seules les interactions avec l'un des deux feuillets sont illustrés. a) Formation de CSI avec les oxygènes d'un plan basal de tétraèdre. b) Formation de CSI dans les cavités siloxanes. c) Formation de CSI avec une partie des oxygènes d'une cavité siloxane. Une molécule d'eau reste attachée au cation et interagit avec des oxygènes de la cavité par le biais de ponts H. d) Formation de CHS interagissant avec le plan de base par des liaisons H.

Ces différents modes de fixation des cations dans l'espace interfoliaire ont un impact considérable sur la réversibilité de la déshydratation. K^+, Rb^+ et Cs^+ peuvent réaliser des liaisons avec les oxygènes de deux cavités siloxanes se faisant face, et former des CSI stables en l'absence de molécules d'eau. Il est possible d'augmenter la quantité de ces CSI par des cycles HD, au cours desquels les directions cristallographiques des feuillets s'alignent progressaient, pour aboutir à un empilement semi-ordonné dans lequel tous les cations interfoliaires forment des complexes stables. Il y a alors occlusion de l'espace interfoliaire, et la cinétique de réhydratation peut être très lente (irréversible sur une durée de l'ordre du jour). Na^+ et Li^+ ne peuvent former de tels CSI stables en l'absence de molécules d'eau. Ceci explique la cinétique de réhydratation toujours très rapide des smectites-Na déshydratées [28, 44].

Quelques études structurales ont porté sur des systèmes contenant deux types de cations interfoliaires [33, 59, 60]. L'étude d'une montmorillonite calco-sodique a montré que cette montmorillonite a un comportement typique d'une montmorillonite sodique pour des rapports Ca/(Ca + Na) inférieures à une valeur critique f (≈ 0,3 pour la montmorillonite de Camp-Berteaux); alors que pour Ca/(Ca + Na) > f, il y a ségrégation d'espaces interfoliaires sodiques et calciques [59, 60]. Il est possible d'interpréter ces résultats en supposant que les cations Ca peuvent migrer dans les cavités siloxanes comme les Na, pour neutraliser localement le déficit de charge du feuillet lié à deux substitutions au voisinage immédiat de cette cavité. f est alors la fraction du déficit de charge du feuillet pouvant être neutralisé de cette manière par les cations Ca.. Par contre, les cations Ca ne peuvent pas neutraliser localement les déficits de charge liés à une seule substitution par cavité ; ils restent alors localisés dans l'espace interfoliaire pour assurer une neutralisation globale du déficit de charge du feuillet.

Dans le cas d'une montmorillonite calco-potassique, les cations K^+ et Ca^{2+} se répartissent aléatoirement dans l'espace interfoliaire de la smectite hydratée [33]. Après quelques cycles HD, K^+ est de moins en moins échangeable. Des domaines homoioniques apparaissent, et certains espaces interfoliaires sont probablement occupés uniquement par des K^+.

1.4. Les bordures des feuillets

La rupture du réseau cristallin en bordure des feuillets argileux est à l'origine d'un déficit de liaisons cristallines pour les oxygènes de bordure [8, 61]. Ce déficit peut être quantifié à partir du modèle dit de force de liaison introduit par Pauling [62]. Dans ce modèle, chaque cation de valence V_M forme avec chacun des anions X de son polyèdre de coordination une liaison électrostatique de force $f_{M\text{-}X} = V_M/n$, où n est le nombre d'anions du polyèdre de coordination. Dans une structure stable, la valence V_X d'un anion est compensée par la somme des forces de liaisons établies avec ses m cations voisins,

$$\sum_m f_{M_m\text{-}X} = V_X . \qquad (1.1)$$

On peut illustrer le modèle de force de liaison pour les oxygènes structuraux d'une smectite alumineuse (fig. 1.7). Dans cette smectite, un Si de la couche tétraédrique forme des liaisons de force $f_{Si\text{-}O} = 4/4 = 1$, et chaque Al de la couche octaédrique forme des liaisons de force $f_{Al\text{-}O} = 3/6 = 0{,}5$. La somme des forces de liaison reçues par un oxygène du plan basal lié à deux tétraèdres de Si vaut donc

2, et compense exactement la charge de cet oxygène. De même, la somme des forces de liaison reçues par un oxygène de la couche octaédrique lié à un Si et deux Al vaut également 2. Enfin, la somme des forces de liaison reçues par un groupe hydroxyle lié à deux Al de la couche octaédrique vaut 1, et compense donc la charge de ce groupe.

Figure 1.7. Illustration du modèle de valence de liaison pour une smectite dioctaédrique alumineuse. La valence d'un atome d'oxygène est égale à 2, celle d'un groupement hydroxyle égale à 1.

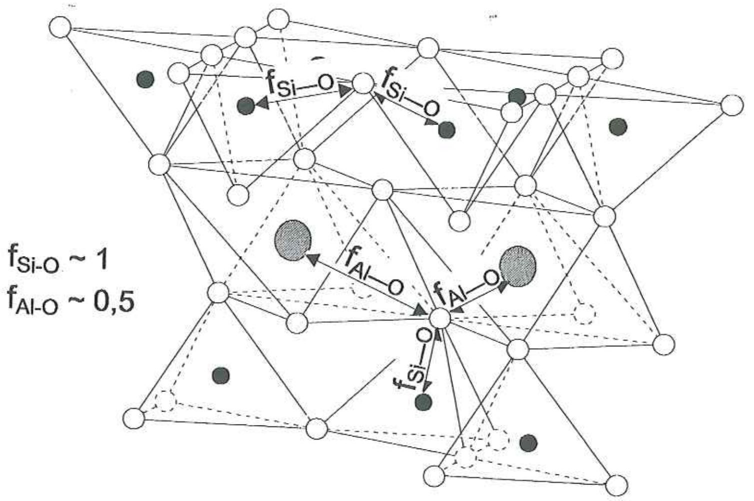

Pour quantifier le degré d'insaturation d'un oxygène de bordure de feuillet, il suffit alors de calculer la somme des forces de liaison établies par cet oxygène avec les cations proches voisins. Ce calcul aboutit à des différences importantes selon la localisation des oxygènes de surface. Ainsi,

– le degré d'insaturation d'un oxygène lié à un seul Al est très élevé, de l'ordre de -1,5 ;

– le degré d'insaturation d'un oxygène d'un groupe silanol reste élevé, de l'ordre de -1 ;

– le degré d'insaturation d'un oxygène lié à un Al et un Si, ou d'un groupe hydroxyle lié à un Al, est plus faible de l'ordre de -0,5 ;

– les groupes hydroxyles liés à deux Al ne sont pas insaturés.

Cette insaturation peut être compensée de différentes manières.

- Les distances entre les oxygènes de surface et les cations structuraux deviennent plus courtes. Cette compensation de charge peut être décrite à l'aide du modèle de valence de liaison, qui est une généralisation du modèle de Pauling [63-71]. Dans ce modèle, les atomes M et X d'un cristal établissent entre eux des liaisons dont la valence ν_{M-X} est fonction de la distance interatomique R_{M-X}:

$$\nu_{M-X} = \exp\left(\frac{R^0_{M-X} - R_{M-X}}{0,37}\right), \tag{1.2}$$

où R^0_{M-X} est une constante qui dépend uniquement de la nature de X et de M. Par analogie avec le modèle de Pauling, la structure est stable quand la somme des valences de liaison pour un atome donné compense sa valence formelle V_i. Cependant, seule une réduction significative d'une distance interatomique peut résulter en une augmentation appréciable de la valence de liaison correspondante. Par exemple, la distance moyenne Al-O dans un octaèdre est d'environs 1,91 Å, ce qui, pour une valeur R^0_{Al-O} = 1,651 Å [65], donne $\nu_{Al-O} = 0,5$ par application de l'équation (1.2). Pour obtenir $\nu_{Al-O} = 1$, R_{Al-O} doit être réduit à 1,65 Å. D'autre part, en augmentant la valence de liaison de l'oxygène de surface, on augmente par la même la somme des valences de liaisons apportées au cation structural qui lui est attaché. Cette augmentation peut à être limitée par un allongement des distances entre ce cation et les oxygènes du volume structural, qui, à leurs tours, deviennent insaturés, etc... Cette relaxation de la structure de surface du solide est donc forcément limitée et ne permet pas de compenser la totalité de l'insaturation des oxygènes de bordure [72].

- Les oxygènes de surface peuvent réaliser des ponts hydrogène avec les molécules d'eau [2]. La valence de liaison de ces ponts hydrogène est de l'ordre de 0,1-0,2 unités [69, 73]. Le nombre possible de liaisons par oxygène de surface est limité à 2-3, du fait de l'encombrement stérique des molécules d'eau au voisinage de la surface. Ce mode de compensation ne suffit donc pas à neutraliser l'insaturation des oxygènes de bordure.

- Les oxygènes de surface peuvent se protoner [74-77]. La valence de la liaison O-H vaut typiquement 0,8. Une double protonation peut avoir lieu dans le cas de déficit très important [72]. Le cation surfacique est alors partiellement hydraté.

- Les oxygènes de surface peuvent éventuellement se lier à des cations présent en solution, pour lesquels ils peuvent avoir une forte affinité [2, 8]. La valence de liaison est alors fonction de la nature du cation, selon l'équation (1.2). cependant, le cation adsorbé peut être considéré comme faisant partie du solide, et sa sphère d'hydratation peut alors être perçue comme une nouvelle interface. D'une certaine manière, ce mode de compensation a pour résultat de créer de nouveaux oxygènes de surface.

La compensation des oxygènes de surface qui sont sous-saturés du fait de la rupture du réseau cristallin peut donc être réalisée par différents phénomènes. Certains d'entre eux peuvent aboutir à la fixation de molécules d'eau, de protons et de cations en bordure des argiles. Ces réactions de fixation font de l'interface eau-particule un lieu privilégié d'échange de matière entre le solide et la solution. Du fait de la surface spécifique (rapport surface/masse) élevée des particules d'argiles, qui peut atteindre plusieurs centaines de mètre carrés par gramme, ces réactions à l'interface peuvent être facilement étudiées à l'aide de méthodes chimiques. Ces études ont servi de base à l'établissement de modèles chimiques de réactivité des smectites.

2. Réactivité de surface des smectites

La réactivité de surface des smectites comprend les réactions de protonation-déprotonation, précipitation-dissolution, fixation ou libération de cations organiques et inorganiques. Ces réactions peuvent être couplées ou non à des réactions d'oxydoréduction. La réactivité des smectites dépend donc du pH et de la composition chimique de la solution, ainsi que de la stabilité des espèces chimiques de surface qui se forment durant les réactions. Pour mieux comprendre et quantifier cette réactivité, on a recours à des modèles macroscopiques et, notamment, à une décomposition de la surface en sites réactifs.

2.1. Les sites à la surface des smectites

On appelle site une entité chimique de la surface susceptible de réagir avec des espèces chimiques de la solution (protons, cations, anions, molécules neutres...). Dans le cas des smectites, on distingue de manière classique deux types de sites [2, 8].

- Les oxygènes des cavités siloxanes constituent le premier type de site de surface. La charge structurale des feuillets est délocalisée sur ces oxygènes. Cette charge est dite permanente car elle est indépendante du pH, et de la concentration en électrolytes (ou force ionique) de la suspension. En revanche, elle peut varier avec le potentiel redox de la solution, suite à des réactions d'oxydo-réduction impliquant des cations structuraux, notamment le couple Fe^{2+}/Fe^{3+} [78]. Du fait de cette charge, les sites interfoliaires sont susceptibles d'attirer et de retenir des cations de la solution.

- Les oxygènes insaturés présents en bordure des feuillets constituent le deuxième type de sites de surface. L'insaturation des oxygènes est compensée par des interactions de différents types, soit avec les molécules du solvant, soit avec des cations (ou anions) présents en solution. Les réactions ayant lieu sur ces sites de bordure des feuillets dépendent fortement du pH de la composition chimique de la solution.

Les sites des plans de base et les sites de bordure présentent donc des propriétés réactives contrastées. Cependant, certaines réactions chimiques sont susceptibles de se produire sur chacun des deux types de site (fig. 2.1). Par exemple, les cations retenus sous forme de CHS sur les sites de plan de base peuvent être échangés, mais c'est aussi le cas pour les cations retenus sur les sites de bordure sous forme de CHS (un CHS de bordure peut aussi être décrit comme une paire ionique entre un site de bordure charge négative, et un cation hydraté; [79-81]). De même, des réactions difficilement réversibles de fixation de cations sous forme de CSI peuvent se produire sur les sites de bordure et dans les cavités siloxanes.

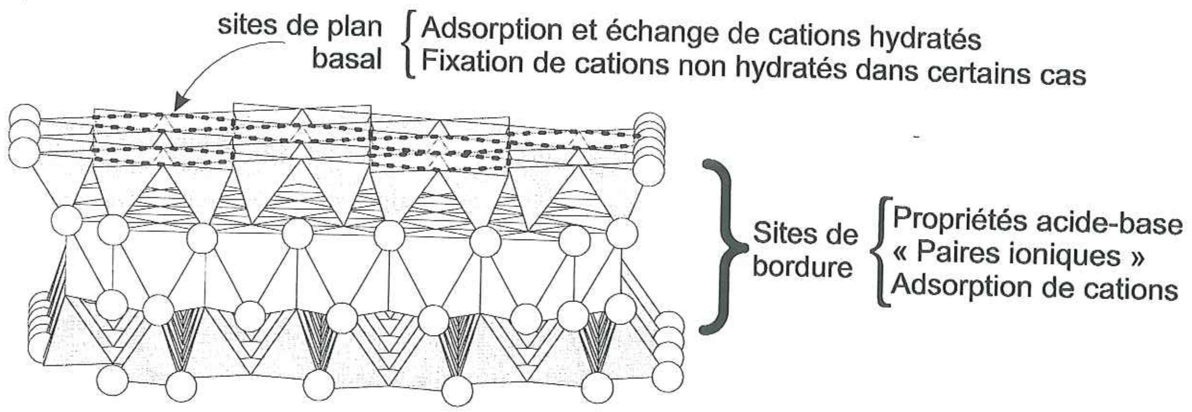

Figure 2.1. Les différents types de sites de surface d'une smectite.

2.2. Propriétés acido-basiques et stabilité des smectites

2.2.1. Réactions acido-basiques à la surface des smectites

Figure 2.2. Exemple de titration d'une suspension de montmorillonite [82]. La quantité de protons fixée (adsorbée) à la surface de la montmorillonite augmente avec la diminution du pH. Montmorillonite 10 g/L, KCl 0.1 M, 25°C.

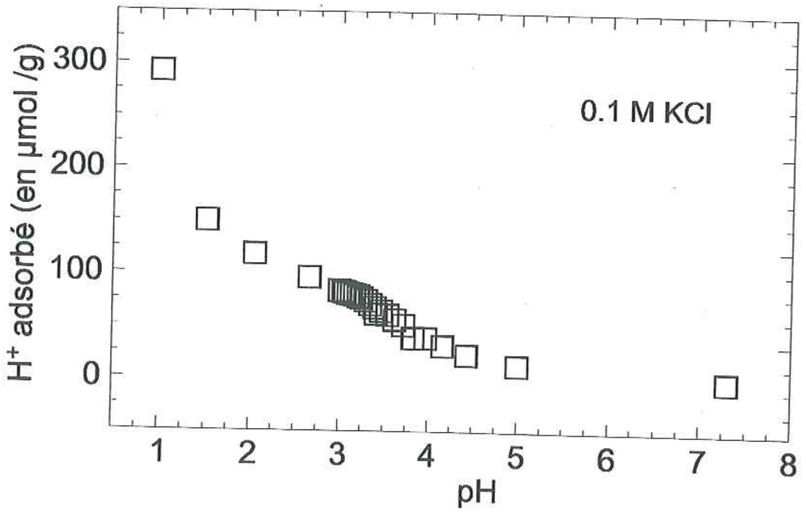

La titration d'une suspension de montmorillonite (fig. 2.2) montre que les smectites possèdent des propriétés acido-basiques. Différents modèles ont été développés pour décrire ces propriétés de manière quantitative [80, 81, 83-87]. Ces modèles sont généralement dérivés des modèles développés pour les oxydes et les hydroxydes [88]. Le modèle le plus simple rend compte de ces réactions par le biais de deux étapes de déprotonation d'un groupe amphotère unique. Le gain ou la perte d'un proton s'accompagne d'une modification de la charge électrostatique portée par le groupe amphotère SOH, selon les réactions

$$\mathrm{SOH_2^+ \Leftrightarrow SOH + H^+} \quad (\mathrm{K_{A1,int}}) \tag{2.1}$$

$$\mathrm{SOH \Leftrightarrow SO^- + H^+} \quad (\mathrm{K_{A2,int}}) \tag{2.2}$$

avec une concentration de sites de surface SOH de l'ordre de 10^{-5} mol g^{-1} de smectite [82]. Dans des modèles un peu plus complexes, on fait intervenir au moins deux types de sites amphotères afin de bien décrire les résultats de titration, SOH et TOH, ayant des constantes acido-basiques distinctes [85, 87]. Ces sites ne sont pas identifiés aux différents groupes fonctionnels (e.g. aluminols, silanols...) présents en bordure des smectites. Le lien entre propriétés chimiques et propriétés structurales est fait dans un troisième type de modèle, qui décrit explicitement les réactions acido-basiques sur les oxygènes de surface des octaèdres et des tétraèdres [80, 81, 84]. Par exemple, les propriétés acido-basiques de la montmorillonite du Wyoming SWy-1 ont été décrites à l'aide de réactions faisant intervenir explicitement des sites aluminols

$$\mathrm{AlOH_2^+ \Leftrightarrow AlOH + H^+} \quad (\mathrm{K_{A1,int}^{AlOH}}) \tag{2.3}$$

$$\mathrm{AlOH \Leftrightarrow AlO^- + H^+} \quad (\mathrm{K_{A2,int}^{AlOH}}) \tag{2.4}$$

et silanols,

$$\mathrm{SiOH_2^+ \Leftrightarrow SiOH + H^+} \quad (\mathrm{K_{A1,int}^{SiOH}}) \tag{2.5}$$

$$\mathrm{SiOH \Leftrightarrow SiO^- + H^+} \quad (\mathrm{K_{A2,int}^{SiOH}}) \tag{2.6}$$

Les constantes acido-basiques utilisées dans ce cas sont dérivées de la titration de phases alumineuses (gibbsite $\mathrm{Al(OH)_3}$) et siliceuses (quartz) [80, 81]. De plus, ces groupes fonctionnels chargés positivement ou négativement peuvent également former des paires ioniques (CHS) avec les ions présents en solution,

$$\mathrm{SiO^- + B^+ \Leftrightarrow SiO^- \cdots B^+} \quad (\mathrm{K_{A1',int}^{SiOH}}) \tag{2.7}$$

$$\mathrm{SiOH_2^+ + X^- \Leftrightarrow SiOH_2^+ \cdots X^-} \quad (\mathrm{K_{A2',int}^{SiOH}}) \tag{2.8}$$

Les sites acido-basiques localisés sur une particule étant relativement proches les uns des autres, une réaction acido-basique sur l'un des sites influence la réactivité des sites voisins [89]. Par exemple, la fixation ou le départ de protons ou d'autres ions conduit à des excès ou des déficits de charge électrique en bordure du feuillet. Cette charge a pour effet d'attirer (charge négative) ou de repousser (charge positive) les protons. Par conséquent, l'activité des protons au voisinage de cette surface chargée, $\{H^+\}$, est différente de celle des protons en solution, (H^+). Cet impact d'une densité de charge de surface σ_0 non nulle sur l'activité $\{H^+\}$ peut être décrit à l'aide du potentiel électrostatique moyen à la surface crée par σ_0, ψ_0. La différence entre $\{H^+\}$ et (H^+) à l'équilibre est alors donnée par la loi de répartition de Boltzmann [90],

$$\{\mathrm{H^+}\} = (\mathrm{H^+}) \cdot \exp\left(-\frac{F\psi_0}{RT}\right) \tag{2.9}$$

La constante intrinsèque de déprotonation $\mathrm{K_{A1,int}}$ s'écrit

$$\mathrm{K_{A1,int}} = \frac{\{\mathrm{H^+}\}\{\mathrm{SOH}\}}{\{\mathrm{SOH_2^+}\}} \tag{2.10}$$

où {SOH} et $\{SOH_2^+\}$ sont les activités des groupes de surface SOH et SOH_2^+. Or, l'activité des protons est généralement mesurée dans la solution, par le biais du pH, et non à la surface. La constante acido-basique de surface *apparente* pour un potentiel de surface donné, K_{A1}, s'écrit alors :

$$K_{A1,int} = \frac{(H^+)\{SOH\}}{\{SOH_2^+\}} \exp\left(-\frac{F\psi_0}{RT}\right) = K_{A1} \exp\left(-\frac{F\psi_0}{RT}\right) \qquad (2.11)$$

Pour une adsorption de quantité croissante de protons avec la diminution du pH, ψ_0 croît, et la constante apparente de protonation $1/K_{A1}$ devient de plus en plus faible par rapport à $K_{A1,int}$. Autrement dit, tout se passe comme si la charge positive croissante à la surface liée à l'adsorption d'une quantité croissante de protons, rendait l'adsorption d'une quantité plus importante de protons de plus en plus difficile.

La charge de surface peut être compensée par une accumulation d'ions au voisinage de la surface, de manière analogue à la compensation des charges permanentes du feuillet. Cette accumulation peut se faire soit dans la double couche diffuse, soit sous forme de complexes de surface. Plusieurs modèles de neutralisation des charges de surface ont été proposés pour décrire les résultats de titration [91].

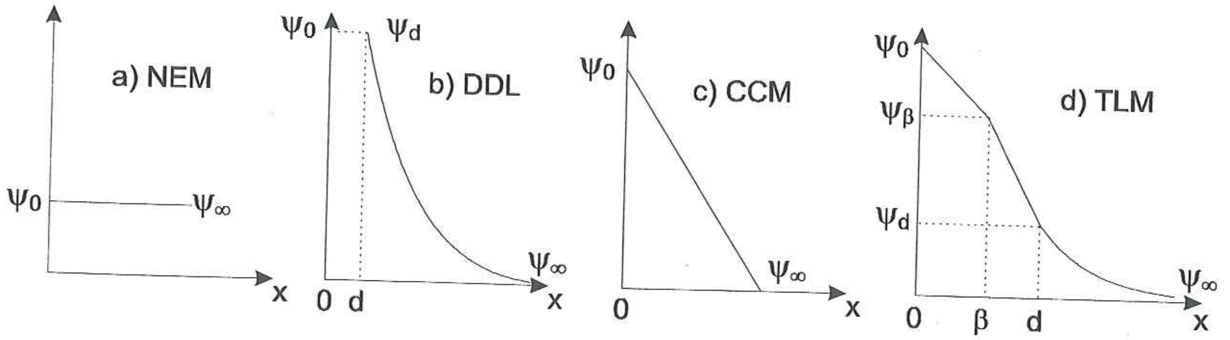

Figure 2.3. Illustration de la décroissance du potentiel électrique avec l'éloignement de la surface, dans le cas d'un électrolyte ne formant pas de complexes de surface de sphère interne. a) Modèle non électrostatique. b) Modèle à double couche diffuse. c) Modèle à capacitance constante. d) Modèle à triple couche.

- Dans le modèles non électrostatique (« non electrostatic model » ; acronyme NEM), les réactions acido-basiques sont décrites de manière purement thermochimique [92-96]. Aucune correction électrostatique n'est introduite pour les concentrations d'espèces chimiques chargés à la surface (fig. 2.3a).

- Dans le modèle à double couche diffuse (« diffuse double layer » ; acronyme DDL), on suppose que la densité de charge de surface σ_0 est répartie selon une couche plane et qu'elle est compensée par l'accumulation de cations en solution dans une double couche diffuse de type Gouy-Chapman [90, 97]. La décroissance du potentiel en solution jusqu'à une valeur ψ_∞ = 0 loin de la surface est alors décrite par la loi de Gouy-Chapman, qui donne la valeur du potentiel ψ_x à une distance donnée x de la surface en fonction de la quantité de charges accumulées dans la double couche diffuse (fig. 2.3b). Dans le cas d'un électrolyte symétrique (i.e., cations et anions ont la même charge absolue z) de concentration en solution C_{sol}, ψ_x s'écrit [2, 90] :

$$\psi_x = \frac{4RT}{zF\tanh\left(ae^{-z\kappa x}\right)}, \text{avec } a = \tanh\left(\frac{zF\psi_0}{4RT}\right) \text{et } \kappa = 2F\sqrt{\frac{2C_{sol}}{\varepsilon\varepsilon_0 RT}} \qquad (2.12)$$

où ε_0 est la permittivité diélectrique du vide, ε est la permittivité du milieu considéré (ici l'eau à la surface), F est la constante de Faraday, R est la constante des gaz parfaits, T est la température. La charge de surface est limitée par le nombre de sites de protonation-déprotonation en surface [98]. Le modèle DDL tient compte de la taille finie des ions en définissant une distance de moindre approche, d. Les relations de Gouy-Chapman sont appliquées à partir de ce point d, en postulant $\psi_d = \psi_0$. [99]. En pratique, cela revient à translater l'ensemble de la double couche diffuse d'une distance d vers la solution (fig. 2.3b).

- Dans le modèle à capacitance constante (« constant capacitance model » ; acronyme CCM), on considère que le potentiel créé par σ_0 est compensé par une accumulation d'ions en solution à une distance constante de la surface, telle que la différence entre ψ_0 et ψ_∞ est directement liée à la valeur de σ_0 par le biais d'une capacitance spécifique κ (en $C\ V^{-1}\ m^{-2}$) :

$$\psi_0 - \psi_\infty = \frac{\sigma_0}{\kappa} \qquad (2.13)$$

avec κ ne dépendant que de la force ionique de la solution [88]. Ce modèle est en fait une approximation du modèle DDL dans le cas de hautes forces ioniques, et donc de concentrations en électrolytes élevées (fig. 2.3c).

- Dans le modèle de triple couche (« triple layer model », acronyme TLM) [80, 81, 100], la charge de surface est compensée par l'accumulation d'ions selon deux couches distinctes (fig. 2.3d) :
  - une première couche plane β correspondant aux ions X^- et B^+ retenus à proximité de la surface lors de la formation des paires ioniques $SOH_2^+\cdots X^-$ et $SO^-\cdots B^+$ (équations 2.7 et 2.8). La différence entre ψ_0 et ψ_β est liée à σ_0 par le biais d'une capacitance spécifique constante κ_1

$$\psi_0 - \psi_\beta = \frac{\sigma_0}{\kappa_1} \qquad (2.14)$$

  - une deuxième couche diffuse, de type Gouy-Chapman, à partir d'une distance d de la surface. La différence entre ψ_β et ψ_d, le potentiel à la limite de la couche diffuse, est liée à la densité de charge σ_d (obtenue par différence entre σ_0 et la densité de charges au plan β, σ_β) par le biais d'une capacitance spécifique constante κ_2

$$\psi_d - \psi_\beta = \frac{\sigma_d}{\kappa_2} \qquad (2.15)$$

2.2.2. Dissolution des smectites

Lorsqu'une smectite est mise dans une solution d'eau pure, elle libère des espèces chimiques en solution. Par exemple, la dissolution de l'hectorite $Na_{0.40}(Mg_{2.65}Li_{0.35})(Si_{3.95}Al_{0.05})O_{10}OH_2)$ à pH 6 résulte en l'augmentation des éléments Si, Mg et Li en solution en proportions proches de la composition stoechiométrique du minéral (fig. 2.4). Ce rapport stoechiométrique n'est pas compatible avec une dissolution localisée sur les faces basales des feuillets : on s'attendrait alors plutôt à un large excès de silice en solution. Les sites de dissolution aux pH modérés sont donc localisés en bordure de feuillet, là où la rupture du feuillet facilite l'hydrolyse des cations de la surface [101-106]. Cette localisation a été confirmée récemment par une étude de dissolution in situ par microscopie à force atomique [107].

Figure 2.4. Cinétique de dissolution de l'hectorite à pH 6.0 et 25°C dans un fond ionique $NaNO_3$ 0.3 M; [hectorite] = 0.65 g L^{-1}. Voir la deuxième partie de ce mémoire pour les détails expérimentaux.

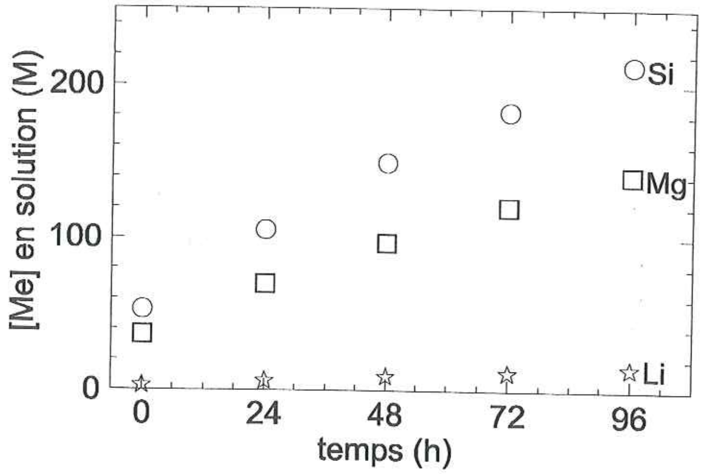

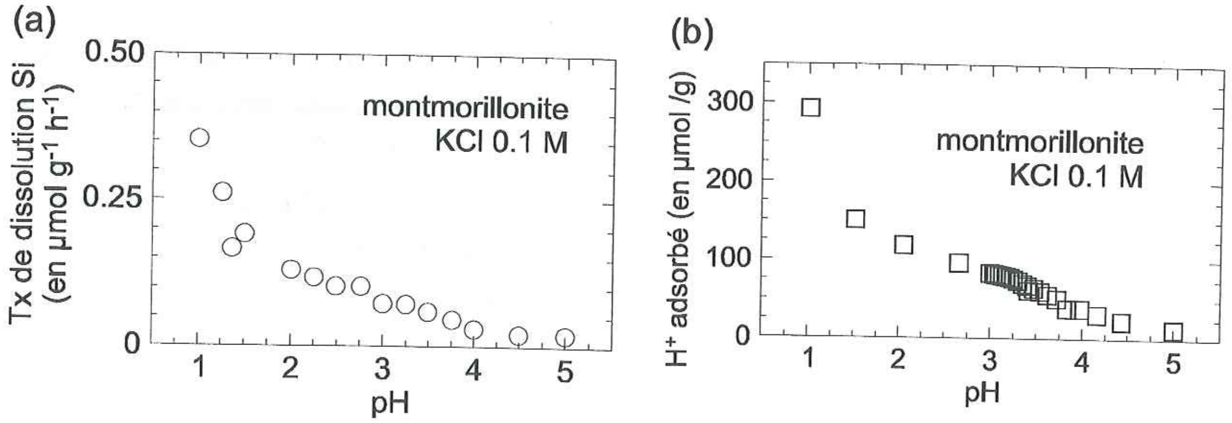

Figure 2.5. a) Cinétique de dissolution d'une montmorillonite alumineuse (mesurée par le taux de libération de silice en solution) en fonction du pH [82]. Ce taux de dissolution est très nettement corrélé avec la concentration de sites de surface protonés (b).

La mesure du taux cinétique de dissolution pour une montmorillonite (fig. 2.5.a) montre que ce taux augmente fortement quand le pH diminue. Cet accroissement de la cinétique aux faibles pH est corrélé à l'augmentation du nombre de sites protonés à la surface (fig. 2.5.b). Le taux cinétique v de libération de Si en solution et la quantité de sites SOH_2^+ protonés peuvent être reliés par

$$v = \frac{d[Si]}{dt} = k.\{SOH_2^+\} \qquad (2.16)$$

avec k = (9.3 ± 0.5)x10^{-4} h^{-1} pour les données présentées ici [82]. Cette corrélation entre le taux cinétique de dissolution et la quantité de sites protonés suggère que la protonation des oxygènes de surface active le détachement de la surface des cations qui leur sont liés [82, 104]. Pour expliquer cette activation, on a proposé que la protonation de groupes fonctionnels de surface polarisait et ainsi fragilisait les liaisons chimiques entre les atomes de surface et le solide cristallin [104, 108, 109]. Le taux cinétique de dissolution dépend également de la composition chimique des smectites. Par exemple, le taux de dissolution en milieu acide de smectites dioctaédriques alumineuses augmente avec la teneur en Fe et Mg de la couche octaédrique [110].

2.3. Fixation de cations à la surface des smectites

2.3.1. Mécanismes macroscopiques de fixation

La fixation macroscopique ou adsorption de cations est influencée par la composition et la concentration de l'électrolyte, et par le pH de la solution [2, 8, 79-81, 84-87, 93, 111-119]. L'importance de ces deux facteurs est illustrée ici par l'adsorption de Al dans une suspension de montmorillonite en présence de KCl (fig. 2.6) [86].

- A bas pH, l'adsorption de cations augmente quand la force ionique diminue. Cette observation indique que l'adsorption est fonction des concentrations relatives en Al et K. Cette dépendance est caractéristique de l'adsorption par échange cationique.
- A haute force ionique, l'adsorption par échange cationique est inhibée. On observe alors que l'adsorption d'Al augmente quand le pH augmente. De plus, cette adsorption s'accompagne de libération de protons en solution [86]. Cette dépendance en pH est caractéristique d'une adsorption spécifique de cations à la surface d'oxydes et d'hydroxydes [2, 8, 88, 114, 120-123]. Elle est interprétée dans le case des argiles par la formation de complexes de surface du cation sur les sites acido-basiques situés en bordure des feuillets.

Figure 2.6. Adsorption d'Al sur la montmorillonite en présence de KCl à différentes concentrations (d'après [86]).

Conditions expérimentales : [Al] = 34.8 µM ; montmorillonite 1,86 g L^{-1} (KCl 1 M), 2,03 g L^{-1} (KCl 0,1 M), ou 1,95 g L^{-1} (KCl 0,03 M) ; 25°C.

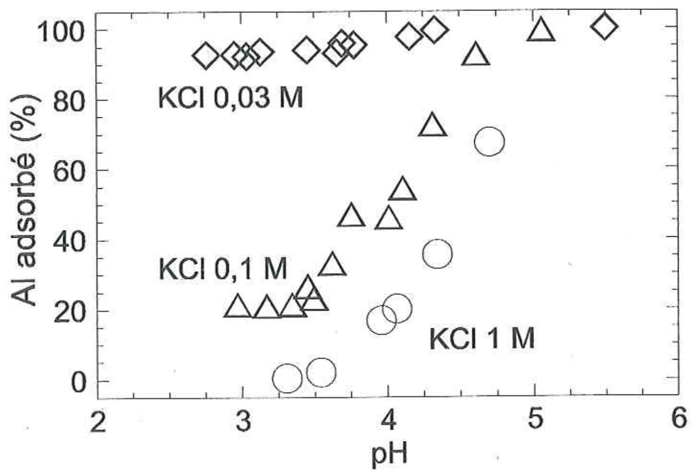

2.3.2. Fixation de cations en fonction du pH

L'adsorption de cations métalliques (Co, Cd, Zn, Cu) par les smectites (montmorillonite, hectorite) est un phénomène fréquemment observé [79-81, 84, 86, 87, 94, 111, 116, 124-127]. Plusieurs descriptions thermochimiques de cette adsorption ont été proposées. Les modèles les plus anciens suggèrent que cette adsorption correspond à la formation de paires ioniques entre le cation et un site de surface déprotoné de charge négative [79]. Par exemple, dans le cas de Co^{2+}

$$SiO^- + Co^{2+} \Leftrightarrow SiO^- \cdots Co^{2+} \qquad (K) \qquad (2.17)$$

où le cation Co^{2+} retenu à la surface reste hydraté et n'interagit avec la surface que par le biais de liaisons faibles (forces électrostatiques et ponts hydrogènes). Cette description a été reprise ultérieurement pour rendre compte d'une partie de l'adsorption de Cd^{2+} sur la montmorillonite [80, 81].

Des modèles plus récents décrivent l'adsorption de cations comme une réaction entre un site de sites de surface et un cation pour former un complexe de surface. Ces réactions peuvent être couplées à des départs de protons, afin de rendre compte des libérations de protons observées lors de l'adsorption de cations. Par exemple, l'adsorption de Cu^{2+} sur la montmorillonite a été décrite par les réactions suivantes [87]

$$SOH + Cu^{2+} \Leftrightarrow SOHCu^{2+} \qquad (2.18)$$

$$SOH + Cu^{2+} \Leftrightarrow SOCu^{+} + H^{+} \qquad (2.19)$$

$$SOH + Cu^{2+} + H_2O \Leftrightarrow SOCu(OH) + 2H^{+} \qquad (2.20)$$

La formation de complexes de surface est à l'origine d'un apport de charge susceptible d'influencer toute adsorption ultérieure, de manière analogue à ce qui se passe lors de la protonation des sites de surface. Cet apport de charge est pris en compte de diverses manières dans les modèles d'adsorption. Dans le cadre des modèles DDL et CCM, toutes les charges liées à la formation de CSI sont supposées être localisées dans le plan de la surface [85-87], et sont prises en compte dans le calcul de σ_0. Dans le TLM, une partie des charges dans le plan β du fait de la modélisation de paires ioniques entre les sites déprotonés et les cations [80, 81, 84]. Enfin, dans certains modèles, ces effets électrostatiques sont purement ignorés [94-96]. Ces modèles ont tous permis de reproduire les résultats expérimentaux. Cependant, l'utilisation de modèles thermochimiques implique que toutes les réactions chimiques sont à l'équilibre, *y compris celles de dissolution des smectites*. Or, cet équilibre n'est en général pas atteint avant des durées de l'ordre du mois [82, 104, 128], voire de l'année [129]. D'autre part, ces modèles supposent que les cations sont fixés à la surface de la smectite par le biais de la formation de complexes de surface en bordure des feuillets, ce qui n'a pas été démontré à l'échelle atomique jusqu'à présent. Enfin, ces modèles ne prennent pas en compte la possible précipitation des cations métalliques avec des espèces dissoutes comme Si et Al. Pourtant, des études récentes [18, 125, 130-132] ont montré que ce mécanisme d'immobilisation peut être prépondérant pour des pH supérieurs à 7 (fig. 2.7). En conclusion, les modèles macroscopiques présentés sont basés sur une description structurale de l'adsorption, mais ils ne semblent pas toujours en mesure de discriminer le mécanisme d'adsorption effectif. Il est donc nécessaire de caractériser d'abord le mécanisme d'adsorption à l'échelle atomique pour être en mesure de décrire avec exactitude l'adsorption des cations sur les phyllosilicates en fonction du pH.

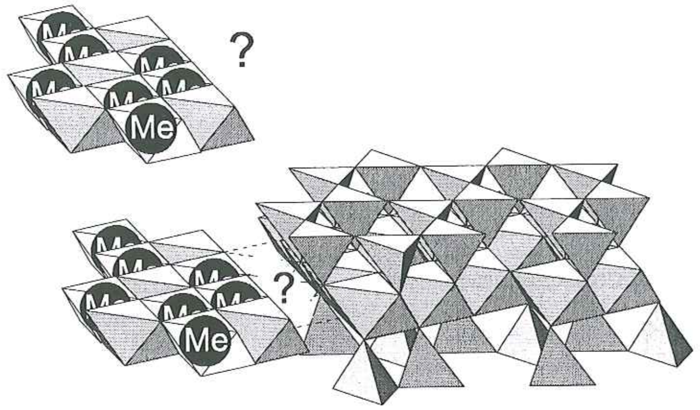

Figure 2.7. Immobilisation de cations métalliques par précipitation avec des espèces chimiques libérées lors de la dissolution des smectites comme dans le cas du nickel en présence de montmorillonite [18, 131]. Le lieu de formation du précipité (dans le surnageant ou à la surface de la smectite) n'est pas encore connue.

2.3.3. Échange cationique à la surface des smectites

2.3.3.1. Le phénomène d'échange

Les propriétés d'échange cationique des sols et des minéraux argileux ont été identifiées dès le milieu du 19^e siècle (voir [133]). Dans le cas de smectites, cet échange est dominé par le remplacement des cations interfoliaires. Par exemple, l'interaction de cations Na^+ et K^+ avec la surface d'une smectite peut être décrit de la façon suivante :

$$Smc - Na^{+}_{(s)} + K^{+}_{(aq)} \Leftrightarrow Smc - K^{+}_{(aq)} + Na^{+}_{(aq)} \qquad (2.21)$$

où $Smc - Na^{+}_{(s)}$ et $Smc - K^{+}_{(s)}$ désignent respectivement une mole de cations Na^+ et une mole de cations K^+ échangeables. La somme des charges des ions échangeables à la surface des smectites est nommée capacité d'échange cationique (CEC). Dans l'exemple donné ci-dessus, la CEC est égale à :

$$Q = \left[Smc - Na^{+}_{(s)}\right] + \left[Smc - K^{+}_{(s)}\right] \qquad (2.22)$$

où $[Smc - Na^{+}_{(s)}]$ et $[Smc - K^{+}_{(s)}]$ désignent les nombres de mole de cations Na^+ et K^+ échangeables par unité de masse de smectite. Bien que la charge structurale des smectites ne dépende pas du pH, la CEC globale augmente légèrement avec le pH (tableau 2.1). Cette augmentation peut être expliquée par l'importance croissante des paires ioniques de type $SO^- \cdots A^+$ qui se forment en bordure des feuillets (équation 2.7). La plupart des méthodes de mesure de la CEC tentent de s'affranchir de cette dépendance en excluant de la quantité mesurée la contribution des cations retenus sur les bordures [35, 134].

Tableau 2.1. Variation de la CEC de quelques montmorillonites avec le pH [79]. La CEC a été mesurée par la méthode de dilution isotopique de ^{22}Na, un cation qui ne s'adsorbe pas à la surface de manière spécifique.

Origine	CEC à « bas » pH (meq / 100g)		CEC à « haut » pH (meq / 100g)	
	pH	CEC	pH	CEC
Camp Berteau (Maroc)	4,30	91,5	6,16	105
Wyoming	4,26	77,1	6,00	91,1
Marnia (Algérie)	4,05	92,7	5,91	103,9
Grèce (non précisée)	3,72	89,0	5,71	97,5
Moosburg (Allemagne)	3,93	84,6	5,92	96,5

2.3.3.2. *Approche thermochimique de l'échange cationique*

Du fait de la conservation de la CEC à pH donné, on peut décrire l'échange cationique comme une réaction chimique, avec une loi d'action de masse associée. Par exemple, une réaction d'échange entre un cation monovalent A^+ et un cation divalent B^{2+}

$$2\,\mathrm{Smc}-\mathrm{A}^{+}_{(s)}+\mathrm{B}^{2+}_{(aq)}\Leftrightarrow\mathrm{Smc}-\mathrm{B}^{2+}_{(s)}+2\,\mathrm{A}^{+}_{(aq)}\qquad(2.23)$$

admet comme loi d'action de masse

$$\mathrm{K}=\frac{\left(\mathrm{Smc}-\mathrm{B}^{2+}_{(aq)}\right)\left(\mathrm{A}^{+}_{(aq)}\right)^{2}}{\left(\mathrm{Smc}-\mathrm{A}^{+}_{(s)}\right)^{2}\left(\mathrm{B}^{2+}_{(aq)}\right)}\qquad(2.24)$$

où $\left(\mathrm{Smc}-\mathrm{B}^{2+}_{(aq)}\right)$, $\left(\mathrm{Smc}-\mathrm{A}^{+}_{(aq)}\right)$, $\left(\mathrm{B}^{2+}_{(aq)}\right)$, et $\left(\mathrm{A}^{+}_{(aq)}\right)$ désignent les activités des espèces chimiques considérées. Cette description purement thermochimique ne nécessite à priori aucune donnée sur la nature structurale des sites d'échange cationique [133, 135]. L'équilibre chimique (2.24) peut être traité selon différentes conventions (tableau 2.2). Dans toutes ces conventions, l'échangeur est décrit comme une espèce chimique hypothétique X^-, symbolisant une mole de charge de surface. On suppose de plus que l'activité des cations adsorbés par échange cationique (ou cations échangeables) peut être calculée à l'aide d'un modèle simple. Dans la convention de Vanselow, par exemple, on traite la fraction échangeable comme une solution solide idéale et homogène. L'activité des cations échangeables est alors égale à la fraction molaire N de ces cations au sein de l'échangeur, multiplié par un coefficient d'activité égale à 1, soit [123, 136-138] :

$$\mathrm{N_A}=\frac{\mathrm{n_A}}{\mathrm{n_A}+\mathrm{n_B}}\quad\text{et}\quad\mathrm{N_B}=\frac{\mathrm{n_B}}{\mathrm{n_A}+\mathrm{n_B}}\qquad(2.25)$$

où n_A et n_B sont les nombres de moles de cations A et B adsorbés par échange cationique. Dans la convention de Gaines & Thomas, par contre, l'activité est égale à la fraction E de la charge totale compensée par les cations adsorbés, multiplié par un coefficient d'activité égale à 1, soit [139] :

$$\mathrm{E_A}=\frac{\mathrm{N_A}}{\mathrm{N_A}+2\,\mathrm{N_B}}\quad\text{et}\quad\mathrm{E_B}=\frac{\mathrm{N_B}}{\mathrm{N_A}+2\,\mathrm{N_B}}.\qquad(2.26)$$

Tableau 2.2. Différents modèles chimiques d'échange cationique à la surface des smectites. pour tous ces modèles, le coefficient d'activité des espèces échangeables est égale à 1.

Convention	Equilibre chimique	Expression de K	Références
Vanselow	$2\,XA + BCl_2 \Leftrightarrow X_2B + 2\,ACl$	$K_V=\frac{N_B(ACl)^2}{N_A^2(BCl_2)}$	[136, 137]
Gaines et Thomas	$2\,XA + BCl_2 \Leftrightarrow X_2B + 2\,ACl$	$K_{GT}=\frac{E_B(ACl)^2}{E_A^2(BCl_2)}$	[139]
Gapon	$2\,XA + BCl_2 \Leftrightarrow 2\,XB_{½} + 2\,ACl$	$K_G^2=\frac{E_B^2(ACl)^2}{E_A^2(BCl_2)}$	[135]
Rothmund et KornFeld†	$XA + BCl_2 \Leftrightarrow 2\,XB_{½} + 2\,ACl$	$K_{RK}=\frac{E_B^{2/\beta}(ACl)^2}{E_A^{2/\beta}(BCl_2)}$	[140]

† le coefficient β est choisi arbitrairement

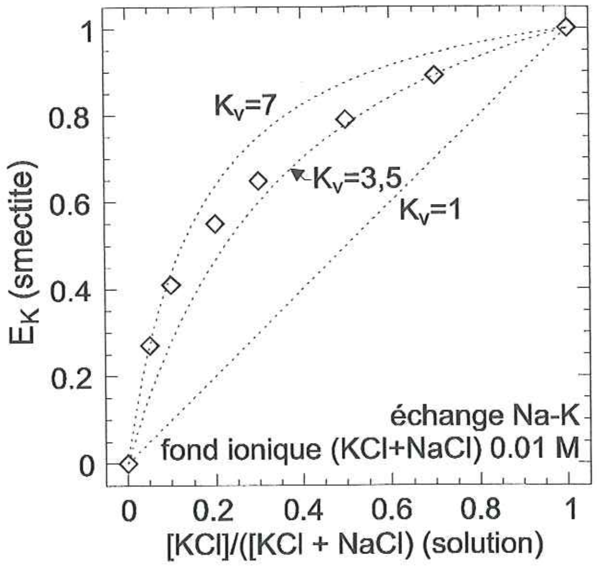

Figure 2.8. Exemple d'isotherme d'échange cationique pour un échange Na-K. On constate d'une part que l'échange est préférentiel, et d'autre part que les données d'échange ne peuvent être modélisées à l'aide d'un coefficient de sélectivité K_v unique. Ces données, ainsi que le protocole expérimental, sont exposées dans [141].

Les différentes conventions (tableau 2.2) diffèrent essentiellement par la définition de l'activité des cations dans la fraction échangeable, ainsi que par le poids relatif de ces activités dans l'expression de K. Elles sont toutes identiquement valides d'un point de vue thermodynamique [2, 123]. Cependant, les valeurs de K calculées avec ces conventions ne sont valables que pour des rapports constants des coefficients d'activité des espèces de surface, et donc des concentrations données des espèces chimiques dans la phase échangeuse et dans la solution (fig. 2.8). Les valeurs de K calculées représentent en fait des coefficients de sélectivité de l'échange pour des conditions chimiques données [123, 141, 142].

En dépit de leur domaine de validité restreint, les coefficients de sélectivité permettent d'avoir une idée de la dépendance de l'échange avec les compositions de la fraction échangeable et de la solution. Ils permettent aussi de quantifier les ordres croissants d'affinité de cations pour l'échange cationique [115, 143]. On a ainsi pu montrer que l'affinité des cations monovalents pour les sites d'échange croît avec la décroissance (en valeur absolue) de l'enthalpie d'hydratation (fig. 2.9). Ceci peut s'expliquer par une réduction de la distance entre le cation et la charge de surface délocalisée lors de la déshydratation, ce qui stabilise le complexe de surface de manière accrue.

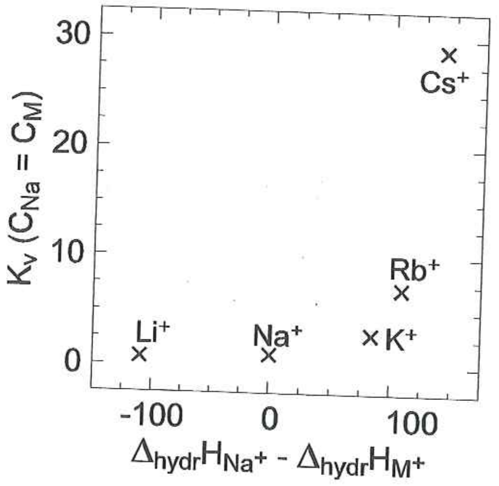

Figure 2.9. Dépendance entre le coefficient de sélectivité K_v pour l'échange entre Na et un autre cation monovalent M (M = Li, K, Rb, ou Cs) avec l'enthalpie d'hydratation du cation M. Les concentrations de en solution Na et de M (C_{Na} et C_M) sont prises égales entre elles. Les conditions expérimentales sont détaillées dans [115, 143].

Pour obtenir une vraie constante thermodynamique vraie à partir d'un coefficient de sélectivité, il faut tenir compte des coefficients d'activité des espèces de surface. Par exemple, dans la convention de Vanselow,

$$(XA) = f_A N_A \text{ et } (X_2B) = f_B N_B , \qquad (2.27)$$

et constante d'équilibre thermodynamique non conditionnelle s'écrit :

$$K_{ex} = \frac{f_B N_B (ACl)^2}{f_A^2 N_A^2 (BCl_2)} = \frac{f_B}{f_A^2} K_V \qquad (2.28)$$

Les coefficients d'activité sont calculés par rapport à un état standard qui, dans le cas de l'échange cationique, correspond à un échangeur homoionique à l'équilibre avec une solution infiniment diluée du cation échangeable [2, 123]. Le coefficient d'activité du cation dans l'échangeur homoionique est alors égale à 1.

2.3.3.3. Approche électrochimique de l'échange cationique

Le développement de modèles électrostatiques de l'échange cationique [85, 90, 144] résulte de la volonté de replacer l'interaction électrostatique au cœur de la modélisation de l'échange. Dans le modèle le plus simple [85], l'échangeur est décrit comme un milieu homogène constitué de charges négatives fixes et compensées par des cations mobiles et échangeables. Pour un déficit de charges structurales élevé, et donc une quantité importante de charges structurales négatives, la concentration d'anions libres dans ce milieu est négligeable, et le potentiel électrochimique Ψ_0 à l'intérieur de ce milieu est uniforme. Dans ces conditions, l'espace interfoliaire a un comportement dit de phase de Donnan [145, 146]. Le nombre de moles $[M^{z+}]$ d'un cation M^{m+} adsorbé sur l'échangeur est lié à Ψ_0 et à l'activité de M^{m+} en solution, (M^{m+}), par

$$\frac{[M^{m+}]}{(M^{m+})} = \text{Exp}\left(\frac{-mF\Psi_0}{RT}\right). \qquad (2.29)$$

Cette description simple ne prend en compte que la charge des cations, et non leur nature. Elle ne permet pas de rendre compte des affinités différentes de cations de même charge, comme celle observée pour les cations monovalents (fig. 2.9). D'autre part, cette approche suppose que le déficit de charge est élevé et réparti de manière uniforme à la surface de la smectite. Or, le déficit de charge est de l'ordre de 0.6 à 2 charges électroniques nm^{-2} (1-3 meq m^{-2}), et est délocalisé sur seulement quelques oxygènes des plans de base. La distance moyenne entre deux sites chargés est donc de l'ordre de 1 nm, ce qui est supérieur au diamètre moyen d'un cation hydraté (entre 0.3 et 0.6 nm), et invalide l'hypothèse d'un potentiel uniforme.

2.3.3.4. Approche physico-chimique

Dans l'approche physico-chimique [144], les sites d'échange cationiques ont une charge unitaire et sont considérés comme des sites d'adsorption de cations analogues aux sites de bordures (fig. 2.10). Ces sites sont localisés formellement sur les mêmes plans que les sites acido-basiques des particules. La réaction d'échange est alors décrite comme la somme de deux ou plusieurs réactions d'adsorption de cations M^{z+} sur des sites S_p de charge permanente,

$$S_p^- + M^{m+} \Leftrightarrow S_pM^{(m-1)+} \quad (K_{Sp,int}) \qquad (2.30)$$

Une constante spécifique de formation du complexe de surface $K_{Sp,int}$ est définie pour chaque cation échangeable. Comme dans le cas de l'adsorption sur les sites de bordures des smectites, cette formation de complexes de surface modifie le potentiel ψ_0. Cette modification est prise en compte par l'introduction d'un terme correcteur dépendant de ψ_0 [144] :

$$K_{Sp,int} = \frac{\left\{S_pM^{(m-1)+}\right\}}{\left\{S_p^-\right\}(M^{m+})} \exp\left(\frac{(m-1)F\psi_0}{RT}\right). \qquad (2.31)$$

La densité de charge à l'origine de ψ_0 est calculée à partir de la somme des charges des sites de charge permanente et des sites acido-basiques. Enfin, les cations accumulés dans la double couche diffuse sont considérés comme étant également retenus à la surface des particules, et donc constituent aussi des espèces cationiques échangeables. Cette description chimique des réactions d'échange est en accord avec la réalité physique de la localisation des cations échangeables dans la double couche diffuse et sous forme de complexes de surface, CHS ou CSI.

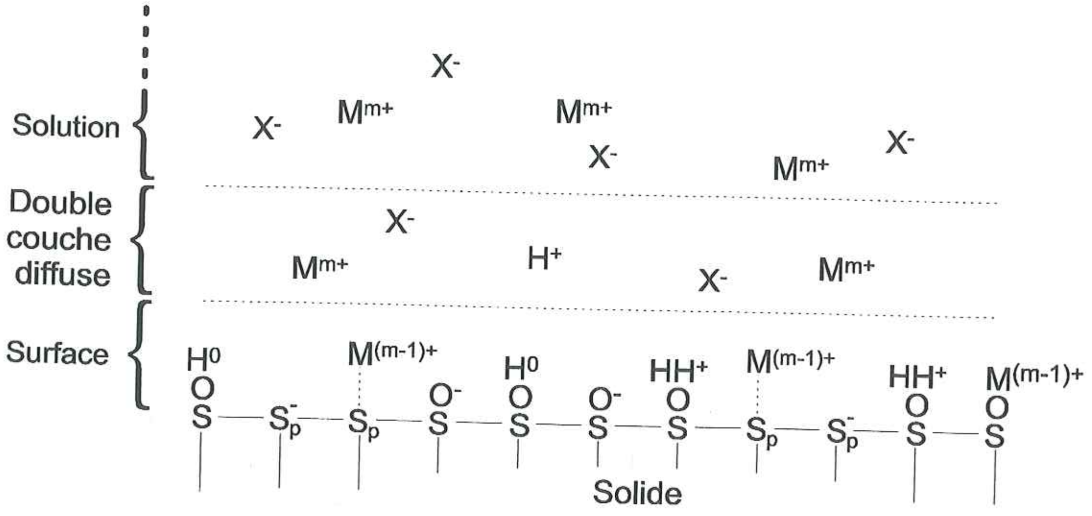

Figure 2.10. Illustration du modèle physico-chimique d'échange cationique. Les cations peuvent être retenus à la surface soit par formation de complexes de surface avec des sites acido-basique, soit par fixation sur des sites de charge permanente, soit dans la double couche diffuse. L'électroneutralité globale de la particule est assurée par la somme des cations présents sous forme de complexes de surface et dans la double couche diffuse.

Conclusion

Les smectites présentent une réelle diversité de mécanismes de fixation des cations métalliques, des points de vue thermodynamiques, cinétiques, et structuraux. Les modèles chimiques macroscopiques ont été développés afin de prédire l'état macroscopique de ces systèmes à l'équilibre. Cependant, ces modèles ne permettent pas de remonter directement au mécanisme structurale d'adsorption des cations [17]. La détermination de ce mécanisme nécessite l'emploi de techniques cinétiques, microscopiques et spectroscopiques [17, 147]. D'autre part, ces modèles ne prennent pas en compte les réactions du substrat avec la solution, notamment les réactions de dissolution et de précipitation. Or, ces réactions sont susceptibles d'affecter de manière sensible la quantité de cations fixée sur la surface du substrat [148]. Enfin, ces modèles n'offrent pas de description du devenir des cations en fonction de leur temps de résidence dans un système géochimique. Or, l'équilibre est rarement atteint dans les systèmes naturels à température ambiante, ne serait-ce que parce que certaines réactions, comme la diffusion des cations dans le réseau cristallin, et la néoformation de nouvelles phases solides, sont lentes et ne conduisent à une immobilisation détectable de cations qu'au bout de quelques mois [18, 149].

Deuxième partie : matériel et méthodes

Introduction

Le substrat utilisé pour les expériences d'adsorption a été sélectionné dans le but de caractériser la réactivité des sites de bordure des smectites et de relier les aspects macroscopiques et microscopiques de cette réactivité. L'hectorite, une smectite trioctaédrique magnésienne qui se forme dans les environnements alcalins [4, 150], présente des propriétés qui permettent d'atteindre facilement cet objectif. Les particules d'hectorite ont un rapport de surface de bordure sur surface de plan basal plus important que la plupart des smectites modèles employées dans les études d'adsorption [107]. De ce fait, il est possible d'étudier les réactions ayant lieu sur les bordures des argiles à des rapports de concentration de cation sur quantité de substrat élevés. Les quantités élevées de cations adsorbés en bordure de ces feuillets permettent également d'obtenir des données de spectroscopie EXAFS sur ces complexes de surface avec un meilleur rapport signal sur bruit. Enfin, comme toute smectite, l'hectorite peut être préparée sous forme de films auto-supportés dont l'étude par spectroscopie EXAFS polarisée (P-EXAFS) permet de caractériser avec une grande précision l'environnement cristallochimique des cations adsorbés. Il est ainsi possible d'identifier avec peu d'ambiguïté la nature du mécanisme d'adsorption.

Cette partie est divisée en deux sections. La première section (chapitre 3) présente les protocoles de purification de l'hectorite, de réalisation des expériences chimiques, et de préparation des films auto-supportés destinés au P-EXAFS. La deuxième section (chapitre 4) expose brièvement quelques aspects expérimentaux de la goniométrie de texture et de la spectroscopie EXAFS. Les aspects théoriques de ces deux méthodes sont développés dans l'article intitulé « *Sorption of metal ions on clay minerals. I. Polarized EXAFS evidence for the adsorption of cobalt on the edges of hectorite particles* » situé dans la troisième partie de la thèse.

3. Matériels et méthodes expérimentales

3.1. Purification et caractérisation de l'hectorite

L'hectorite utilisée dans le cadre de cette étude est la SHCa-1 provenant de la mine d'Hector, Californie. Elle est distribuée par le « Source Clay Project » de la Clay Mineral Society of America. Avant son envoi par le « Source Clay Project », le matériel a été séché à basse température et légèrement broyé (http://cms.lanl.gov/sourcecl.html). Ce matériel contient de l'hectorite mélangée à des impuretés minérales (calcite, minéraux ferriques...). Certaines de ces impuretés sont des particules de grande taille qui peuvent être séparées des petites particules d'hectorite par fractionnement granulométrique. L'élimination des autres impuretés, comme les grains de calcite colloïdaux, ou les encroûtements d'hydroxydes de fer et de manganèse, nécessite l'emploi de traitements chimiques. L'objectif de la procédure de purification est d'éliminer ces impuretés et d'obtenir une suspension d'hectorite homoionique.

3.1.1. Dispersion du sédiment dans l'eau et fractionnement granulométrique

Environ 12 g de sédiment sont dispersés dans 1 L d'eau ultra-pure par agitation sur table tournante pendant 24 h (180 rotations par minute; rpm). La fraction granulométrique fine (<2 μm) de cette suspension est ensuite séparée à l'aide de techniques de sédimentation. La première méthode employée consiste à verser la suspension dans une éprouvette graduée de 2 L, et à compléter ce volume de suspension jusqu'à une hauteur d'eau de 40 cm. Après homogénéisation, la suspension est laissée au repos pendant 14,25 h. Durant cette période de repos, les particules sédimentent au fond du tube, avec une vitesse de sédimentation v donnée par la loi de Stockes,

$$v = \frac{d_s^2(\rho_H - \rho_W)g}{18\eta} \tag{3.1}$$

où g est l'accélération de la pesanteur (9,81 m s^{-2}), ρ_H et ρ_W sont les masses volumiques de l'hectorite et de l'eau (respectivement 2600 et 997 kg m^{-3} à 25°C), η est la viscosité de l'eau (8.904x10^{-4} kg m^{-1} s^{-1}), et d_s est le diamètre de Stokes de la particule, égal à son diamètre réel en première approximation. Les particules de grande taille sédimentent rapidement au fond du tube et les particules de petite taille restent dans la fraction supérieure de la suspension. Au bout de 14,25 h les 20 cm supérieurs du tube, ne contenant plus que des particules de diamètre inférieur à 2 μm, sont siphonnés à l'aide d'une pipette pasteur dont le bout est recourbé vers le haut. Cette fraction fine est floculée à l'aide d'une solution NaCl 1 M, puis centrifugée légèrement pour éliminer une partie de l'eau, et finalement stockée sous forme de suspension brute au réfrigérateur avant traitement chimique. Le cycle de sédimentation est répété entre 6 et 8 fois, jusqu'à ce que la quantité d'hectorite collectée de cette manière devienne négligeable.

Afin de réduire le temps de fractionnement granulométrique, on a été amené à utiliser une technique de fractionnement plus rapide par centrifugation. Dans cette méthode, la suspension obtenue après agitation est répartie en fractions de 45 ml dans des tubes à centrifuger de 50 ml. Ces tubes sont fermés, agités pendant une heure, puis sont mis à centrifuger pendant 7 minutes à 500 rpm dans une centrifugeuse à berceaux pivotants (fig. 3.1), pour laquelle l'accélération centrifuge est toujours parallèle au tube. La fraction supérieure des tubes, ne contenant que des particules de diamètre inférieure à 2 µm, est ensuite collectée à l'aide d'une pipette pasteur au bout recourbé, floculée, et stockée au réfrigérateur, comme pour la première méthode. Les tubes à centrifuger sont complétés à 45 ml avec de l'eau bidistillée, agités à nouveau pendant une heure, et le fractionnement granulométrique par centrifugation est de nouveau réalisé. Ce cycle est répété 6 à 8 fois, jusqu'à ce que la quantité d'hectorite collectée de cette manière devienne négligeable.

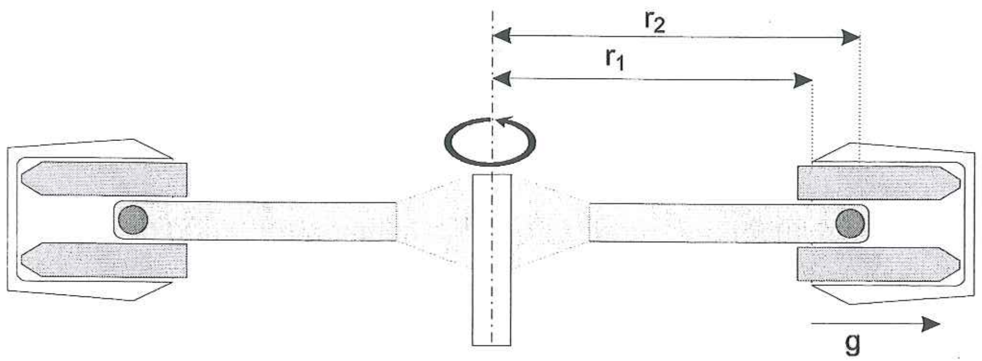

Figure 3.1. Principe de fractionnement granulométrique par centrifugation sur centrifugeuse à berceau pivotant. Durant la centrifugation, les particules de plus grande taille sédimentent au fond des tubes. À la fin de la sédimentation, la fraction localisée entre les rayons r_1 (surface de l'eau dans le tube) et r_2 est collectée. Dans la présente étude, r_1 = 86 mm et r_2 = 136 mm, et la fraction récoltée ne contient plus que des particules de taille inférieure à 2 µm.

3.1.2. Purification par traitement chimique

L'objectif de ce traitement chimique est d'éliminer les carbonates, les hydroxydes de fer et de manganèse, ainsi que la matière organique qui pourrait éventuellement contaminer la suspension brute. Le traitement débute avec le transfert de fractions de 100 ml (contenant 1 à 2 g d'hectorite) de la suspension brute dans des pots à centrifuger de 250 ml. Trois étapes se succèdent ensuite.

Traitement par acide HCl. Cette attaque a pour but d'éliminer les carbonates de calcium. Chaque pot à centrifuger est complété à 200 ml avec une solution HCl 10^{-4} M, NaCl 0,5 M (la haute teneur en NaCl a pour but d'éviter que les ions libérés par dissolution des carbonates ne se réadsorbent sur l'hectorite par échange cationique). Les pots sont fermés et agités sur table rotative pendant une heure (180 rpm). Ils sont ensuite centrifugés (2 000 rpm pendant 15 min). Le surnageant (environ 150 ml par pot) est éliminé, et les pots sont de nouveau complétés à 200 ml avec la solution acide. Ce traitement est répété trois fois. À la fin du troisième cycle, les pots à centrifuger sont complétés avec une solution NaCl 0,5 M, agités pendant 1 h, centrifugés, et le surnageant éliminé. Ce cycle de lavage est répété environ deux fois (trois lavages au total). Il a pour but de ramener l'hectorite à des conditions de pH relativement neutres.

Traitement par dithionite-citrate-bicarbonate (DCB). Ce traitement a pour but d'éliminer les hydroxydes de fer et de manganèse par dissolution en conditions réductrices. Le contenu de chaque pot est complété à 200 ml avec une solution de citrate 0,2 M, bicarbonate 0,1 M, NaCl 0,5 M. Le citrate est un complexant des ions Fe^{2+} en solution, et le bicarbonate tamponne le pH de la suspension. Une pincée de dithionite de sodium ($Na_2S_2O_4$), un puissant réducteur, est ajoutée dans chaque pot juste avant fermeture, puis les pots sont agités pendant 1 h à température ambiante, centrifugés, et le surnageant éliminé. Le cycle est répété une fois. Il est suivi de trois cycles de lavage par NaCl 0,5 M additionné d'une pincée de dithionite, et d'un cycle de lavage par NaCl 0,5 M uniquement. Ce lavage a pour but d'éliminer Fe et Mn réduits contenus dans l'eau associée à l'argile.

Traitement par H_2O_2. Ce traitement a pour but d'éliminer toute trace de matière organique. Le contenu de chaque pot est complété à 200 ml avec une solution H_2O_2 3 %, NaCl 0.5 M. Les pots sont ensuite agités pendant ¼ h pour disperser l'hectorite dans la suspension, puis les suspensions sont transférées dans un grand bêcher de 2 L. Les pots à centrifuger sont soigneusement rincés avec le restant de la solution H_2O_2, et les solutions de lavage transférées dans le bêcher. La suspension est ensuite chauffée à 50°C durant 1 h, tout en étant agitée à l'aide d'un barreau aimanté, puis à 70°C pendant 1 h pour éliminer les traces de H_2O_2. On laisse ensuite la suspension refroidir, et on la transfère dans des pots à centrifuger de 200 ml. Après centrifugation, on élimine le surnageant. La suspension est alors prête pour l'étape finale de conditionnement.

3.1.3. Conditionnement et stockage

Le protocole initial de conditionnement consistait à laver l'hectorite par dialyse. Pour cela, on prépare des cylindres de membrane semi-perméable, que l'on remplit de suspension. Ces cylindres sont immergés dans un bêcher contenant de l'eau bidistillée, qui est changée tous les jours, jusqu'à ce qu'on ne puisse plus déceler la présence d'ions Cl^- dans l'eau de dialyse par test au nitrate d'argent. La suspension-mère d'hectorite est alors transférée dans un flacon en polyéthylène et stockée à 4°C dans un réfrigérateur. La teneur en hectorite de la suspension-mère est déterminée par pesée d'un volume connu de cette suspension porté à sec par chauffage à 120°C pendant 48 h. Ce mode de conditionnement permet de réaliser des expériences de chimie à des conditions de faibles forces ioniques (jusqu'à 0.0015 M). Néanmoins, on s'est rendu compte que cette suspension-mère contenait un excès de cations Mg par rapport à la stoechiométrie de l'hectorite. Cette accumulation de Mg peut s'expliquer par le fait que l'hectorite se dissout durant la dialyse et libère des cations Mg^{2+}, lesquels remplacent les cations Na^+ sur les sites d'échange. Par la suite, on a préféré modifier le protocole de conditionnement afin de prévenir cette accumulation.

Le nouveau protocole de conditionnement consiste en des cycles répétés d'agitation et lavage de la suspension avec une solution $NaNO_3$ 0,3 M, jusqu'à ce que qu'on ne puisse plus déceler la présence d'ions Cl^- par test au nitrate d'argent (8 cycles au total). La suspension est alors transférée dans un flacon en polyéthylène et stockée à 4°C dans un réfrigérateur. Dans ces conditions, on n'observe pas d'excès de Mg par rapport à la stoechiométrie de l'hectorite, et on peut réaliser facilement des expériences de chimie à force ionique haute ou modérée. Cependant, la concentration importante de $NaNO_3$ dans la suspension-mère ne permet pas, pour une concentration d'hectorite donnée, de travailler à des forces ioniques aussi faibles que dans le cas précédent.

3.1.4. Caractérisation de l'hectorite

L'hectorite purifiée a été caractérisée par diffraction des rayons X sur un diffractomètre D-5000 Siemens. Le diffractogramme présente les raies et bandes caractéristiques de l'hectorite, et ne présente aucun pic d'une autre phase minérale.

La capacité d'échange cationique correspondant à la charge structurale permanente de la smectite a été déterminée à l'aide de la méthode d'Anderson [134]. Dans la méthode employée, une fraction (20 ml) de suspension-mère d'hectorite est transférée dans un tube à centrifuger de 50 ml et saturée au Cs par des cycles répétés d'agitation dans des solutions de CsCl 0,05 M régulièrement renouvelées. À la fin du dernier cycle, il reste un peu de solution CsCl 0,05 M dans la pâte d'hectorite contenue au fond du tube; cette solution est éliminée par lavage de l'hectorite dans une solution d'éthanol. Un lavage supplémentaire avec LiCl 0,5 M permet d'éliminer le Cs retenu en bordure des feuillets, tout en évitant de désorber le Cs retenu sur les sites d'échange cationique. Enfin, le Cs encore retenu par l'hectorite est désorbé par des cycles répétés d'échange avec NH_4^+ contenu dans solution de NH_4OAc 0,2 M. Les solutions contenant le Cs désorbé sont réunies dans une fiole jaugée de 250 ml. Après avoir complété le volume de la fiole jaugée, la concentration de Cs dans cette fiole est mesurée par ICP-MS. La valeur de la CEC déduite de cette mesure est égale à 840 mol_c kg^{-1} d'hectorite.

La stabilité de l'hectorite en suspension a été évaluée par le biais d'expériences cinétiques de dissolution sous atmosphère inerte et sous conditions contrôlées de température et de pH (voir la section suivante pour le protocole expérimental). Ces expériences ont été menées à une teneur en hectorite de 0,65 g L^{-1}, à une force ionique élevée ($NaNO_3$ 0,3 M) pour éviter que les cations Mg et Li libérés lors de la dissolution ne se réadsorbent par échange cationique, et à des conditions de faibles concentrations de Mg, Si, et Li en solution, pour minimiser l'impact de la réaction inverse de reprécipitation. Pour les pH étudiés ($4 \leq pH \leq 10$), on observe deux domaines (fig. 3.2).

- Pour des pH acides et neutres ($4 \leq pH \leq 7$), la dissolution est congruente ou légèrement incongruente, avec une libération préférentielle des cations de la couche octaédrique. La cinétique de dissolution augmente avec la diminution du pH. Ce comportement est compatible avec un mécanisme de dissolution par protonation et détachement des cations octaédriques [82, 103, 151, 152].

- Pour des pH basiques ($8 \leq pH \leq 10$), la dissolution est incongruente, avec des taux de libération élevés pour Si et des taux beaucoup plus faibles pour Mg et Li. Ces faibles taux sont observés pour Mg alors que sa concentration en solution n'est à saturation ni avec la brucite $Mg(OH)_2$, ni avec les carbonates de Mg. Pour expliquer cette faible cinétique de dissolution, on peut supposer que la couche octaédrique de l'hectorite est relativement métastable à ce domaine de pH élevé, alors que les couches tétraédriques se dissolvent facilement en raison de la formation facilitée d'espèces silicatées déprotonées à haut pH [108]. Des études ultérieures permettront de discuter cette hypothèse.

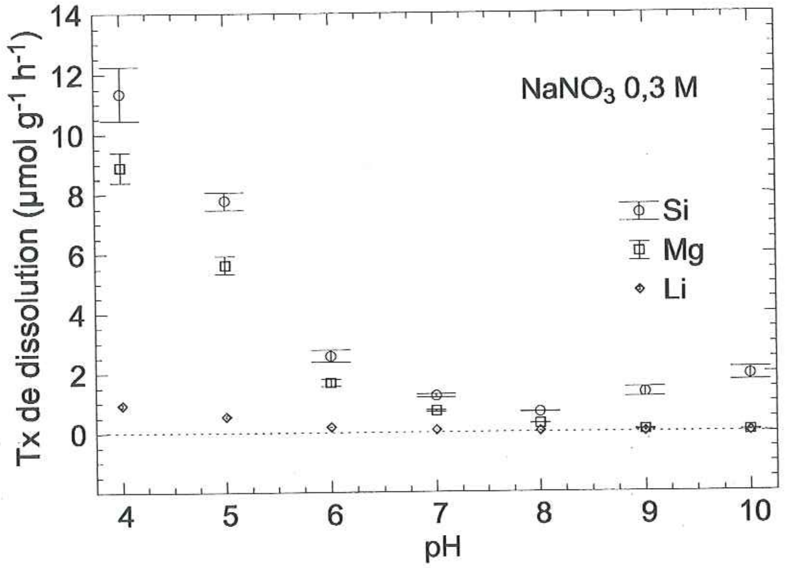

Figure 3.2. Cinétique de dissolution de l'hectorite en fonction du pH à 25°C. La dissolution devient fortement incongruente à $pH \geq 8$ avec très peu de Mg libéré.

3.2. Expériences chimiques d'adsorption de cations

Toutes les solutions utilisées dans le cadre de ce travail ont été préparées avec de l'eau ultra-pure. Le système de purification comprend une cartouche de déionisation de l'eau, une source UV le long de laquelle l'eau déionisée circule afin de détruire les bactéries et d'oxyder la matière organique, une résine retenant les ions et la matière organique oxydée, et un filtre terminal de porosité 0,22 µm. Les sels commerciaux utilisés sont tous de qualité supérieure et n'ont subi aucune purification supplémentaire avant utilisation.

Toutes les expériences ont été réalisées dans un réacteur en polyéthylène, afin de minimiser les interactions des cations et de la silice avec les parois (fig. 3.3). Ce réacteur est plongé dans un bain d'eau thermostaté à 25 ±0.1°C. La suspension est agitée à l'aide d'un barreau aimanté de section triangulaire, reposant sur le fond du réacteur. Une atmosphère inerte est maintenue en permanence dans le réacteur, en faisant buller de l'argon à travers la suspension, le gaz ayant auparavant traversé successivement trois solutions de lavage :

- une solution H_2SO_4 0,5 M destinée à débarrasser le gaz de ses impuretés basiques ;

- une solution NaOH 1 M destinée à débarrasser le gaz de ses impuretés acides ;

- une solution $NaNO_3$ à la force ionique de la suspension, pour humidifier le gaz à la bonne P_{H2O}.

Le pH est mesuré à l'aide d'une électrode combinée en verre Metrohm. Cette électrode est étalonnée à l'aide de solutions tampons (Merk), et recalibrée tous les deux jours. La valeur du potentiel est lue par un pH-mètre Metrohm 713 et enregistrée sur un PC. Dans les expériences menées à pH constant, une burette automatique pilotée par le PC délivre des petites quantités d'acide et de base. Des échantillons de la suspension peuvent être prélevés à l'aide d'une aiguille en polyéthylène plongeant dans la suspension, et reliée à un robinet sur lequel on peut adapter une seringue de prélèvement.

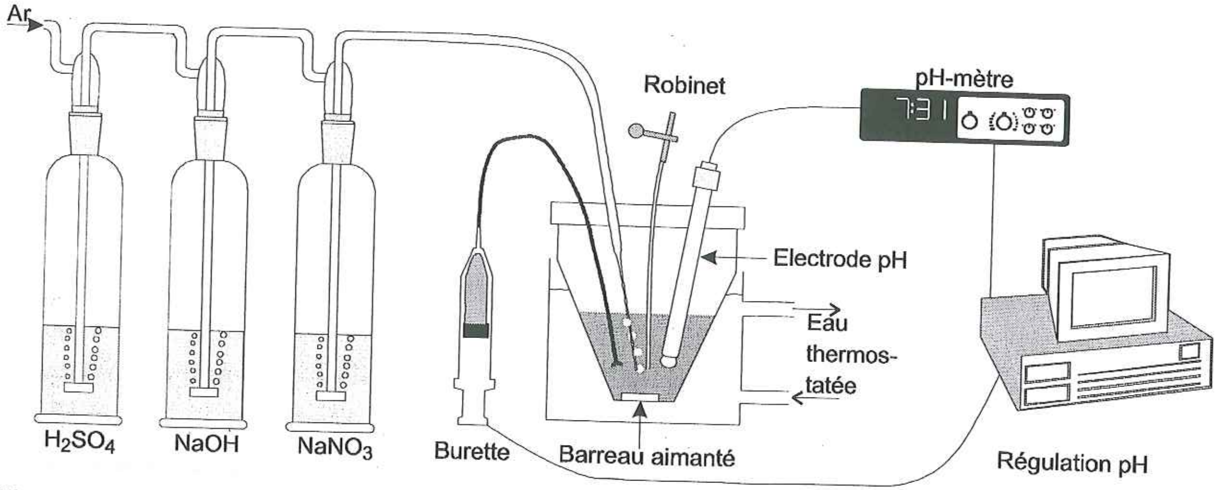

Figure 3.3. Schéma du montage expérimental utilisé pour les réactions d'adsorption des cations et de dissolution cinétique de l'hectorite.

Les suspensions d'hectorite utilisées pour les expériences cinétiques d'adsorption sont obtenues par mélange de la suspension-mère, de solutions $NaNO_3$, et d'eau ultra-pure, de manière à obtenir des valeurs finales de concentration en $NaNO_3$ et de teneur en hectorite connues. Ces suspensions sont pré-équilibrées au pH de l'expérience durant un laps de temps minimum de 1 h. L'expérience proprement dite d'adsorption de cation, ou de mesure de la dissolution de l'hectorite, commence au terme de ce pré-équilibrage.

3.3. Préparation de films auto-supportés

Les films auto-supportés d'hectorite sont obtenus par filtration des suspensions sur filtre de nitrate de cellulose de porosité 0,05 µm. Une vitesse de filtration lente est souhaitable pour obtenir une bonne orientation des particules dans le plan du filtre. Les durées totales de filtration varient typiquement de 1 h, pour des faibles volumes de suspension diluée, à 6 h, pour des volumes importants de suspension concentrée. Afin d'éviter les problèmes de contamination par le CO_2 atmosphérique tant que la phase liquide est encore importante, les filtrations sont effectuées dans un appareil de filtration clos, sous atmosphère d'argon humidifié. Les films auto-supportés sont ensuite séchés à température ambiante, et stockés dans des boîtes individuelles.

3.4. Méthodes physique d'étude des films auto-supportés

3.4.1. Goniométrie de texture

La goniométrie de texture a été utilisée pour vérifier que le film présente une texture de fibre, c'est-à-dire que les axes c* des particules individuelles d'hectorite sont idéalement orientés dans la direction normale au film, et les axes (a, b) répartis dans toutes les directions du plan du film. La distribution d'orientation des axes cristallographiques des particules dans le film est obtenue à partir de la mesure, par diffraction des rayons X, des distributions d'orientation de plusieurs familles de plans réticulaires. Le dispositif expérimental utilisé à cette fin (fig. 3.4) est constitué d'une source de rayons X à anode tournante, d'un goniomètre de texture 4 cercles sur lequel est fixé le film, et d'un détecteur. Le faisceau produit par l'anode de cuivre est monochromatisé par un polycristal de graphite plan. Deux fentes collimatrices croisées permettent de réduire la divergence du faisceau. Le goniomètre de texture est constitué d'un goniomètre θ-2θ classique, et d'une platine permettant des rotations autour de deux axes X et Y (fig. 3.4). L'axe X est défini par l'intersection entre le plan du film et le plan de diffraction, et l'axe Y est perpendiculaire au film. La mesure de la distribution des intensités diffractées est réalisée en fixant les angles θ et 2θ aux valeurs correspondant à une réflexion d'indice connu. L'intensité de cette réflexion dans les différentes directions de l'espace est ensuite mesurée en faisant tourner l'échantillon autour des axes X et Y.

Dans les films auto-supportés, l'empilement des feuillets est turbostratique. Les plans {hkl} pour lesquels l'intensité diffractée est non nulle sont parallèles (plans {00l}) ou perpendiculaires (plans {hk0}) à l'empilement. Pour déterminer complètement les distributions d'orientation des axes a, b et c* des feuillets individuels il faut choisir au moins trois réflexions non parallèles deux à deux. Dans le cadre de cette étude, les réflexions sélectionnées sont 020/110, 200/130 et 004 (fig. 3.5).

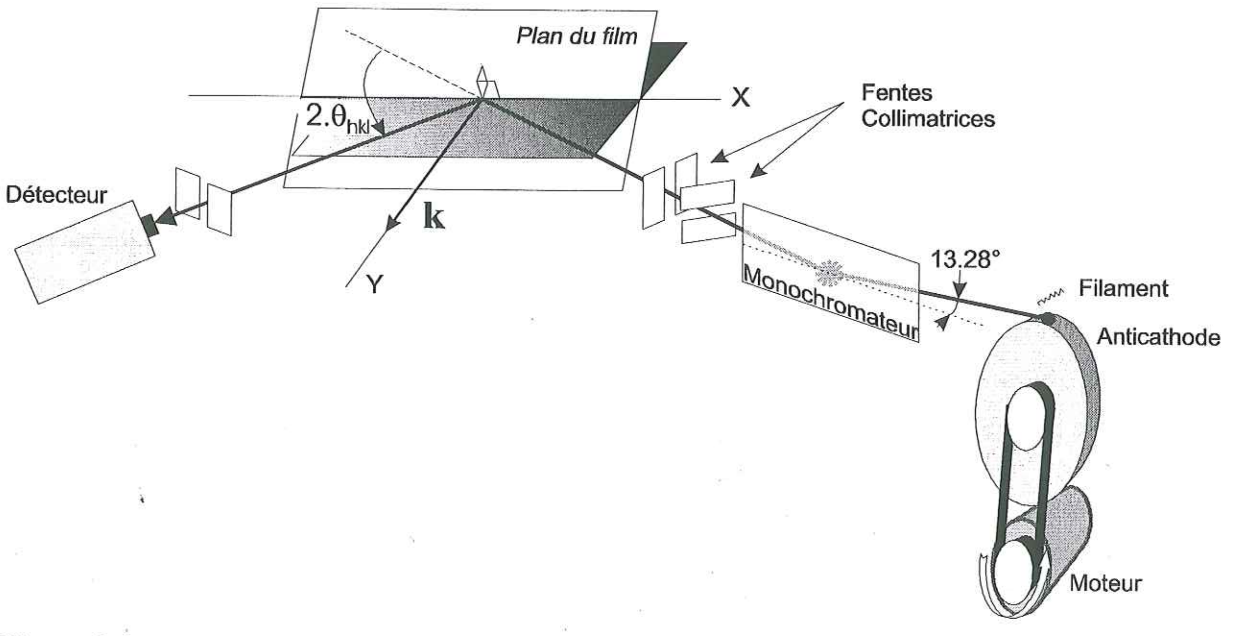

Figure 3.4. Représentation schématique du montage expérimental de diffraction des rayons X utilisé pour la goniométrie de texture.

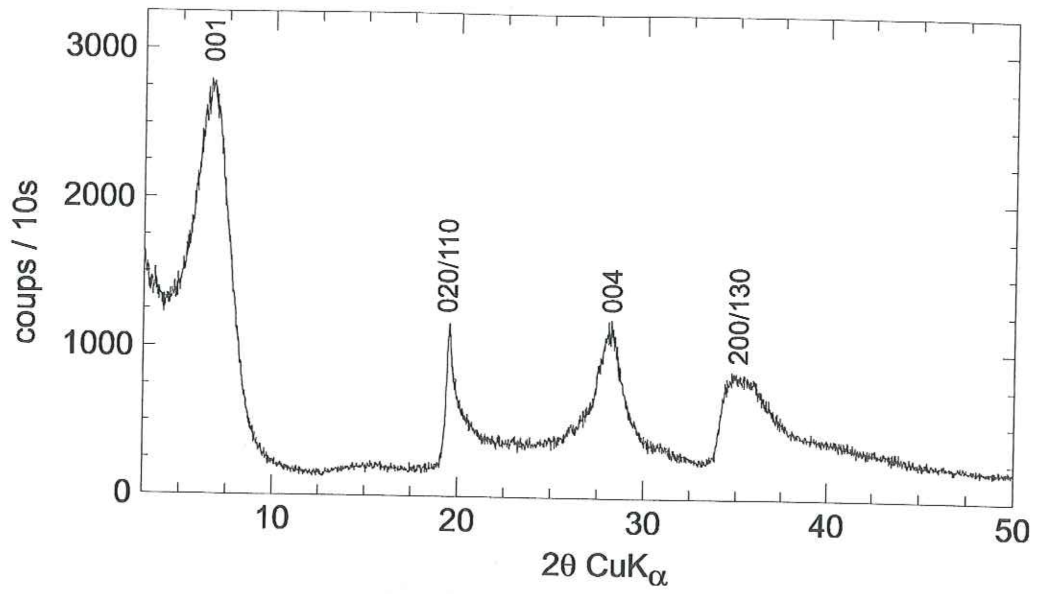

Figure 3.5. Diagramme de diffraction X d'une préparation de poudre d'hectorite. Les différentes réflexions utilisées pour la goniométrie de texture sont indexées.

Les aspects théoriques de l'analyse quantitative de texture sont détaillés dans l'article intitulé « *Sorption of metal ions on clay minerals. I. Polarized EXAFS evidence for the adsorption of cobalt on the edges of hectorite particles* » situé dans la troisième partie de la thèse.

3.4.2. Spectroscopie EXAFS

Les mesures d'absorption des rayons X ont été réalisées sur les spectromètres des lignes 8.1 du Synchrotron Radiation Source de Daresbury (Royaume Uni) [153, 154] et BM 32 de l'European Synchrotron Radiation Facility (France). Le rayonnement synchrotron est produit par des électrons relativistes accélérés dans un champs magnétique. La radiation est très intense et présente un spectre continu « blanc » allant de l'infrarouge lointain aux rayons γ. Le vecteur champ électrique ε du rayonnement est polarisé linéairement dans le plan de l'orbite des électrons. Lorsque l'on s'écarte du plan, il apparaît une composante de polarisation verticale, d'intensité généralement faible par rapport à la composante horizontale. Cette faible composante verticale est négligeable dans nos expériences de dichroïsme car, d'une part, on sélectionne la partie centrale du faisceau X grâce à un jeu de fentes collimatrices et, d'autre part, la composante de polarisation verticale est atténuée par la double diffraction de Bragg sur les cristaux du monochromateur [155]. Le taux de polarisation linéaire (défini comme la différence entre les intensités des composantes horizontales et verticales du faisceau, normalisée par la somme de ces intensités) est toujours supérieur à 95 %.

Le faisceau incident polychromatique est collimaté par deux jeux de fentes, (fig. 3.6). Le faisceau blanc est monochromatisé par double diffraction de Bragg sur des cristaux de silicium taillés suivant le plan cristallin (111). Le faisceau incident est ensuite collimaté sur l'échantillon à l'aide d'un jeu de fentes verticales et horizontales. Son intensité I_0 est mesurée avec une chambre à ionisation (station 8.1) ou par deux diodes (BM 32). Le film auto-supporté est positionné dans le faisceau à l'aide d'une platine goniométrique, de façon à contrôler précisément l'angle α entre ε et le plan du film. L'intensité I_1 de la fluorescence émise par l'échantillon est mesurée à l'aide d'un multi-détecteur solide au germanium résolu en énergie. Lorsque l'élément étudié est dilué ($\Delta\mu/\mu < 0.1$), cette intensité est proportionnelle à la section efficace d'absorption des rayons X de l'élément dont le spectre est mesuré [156].

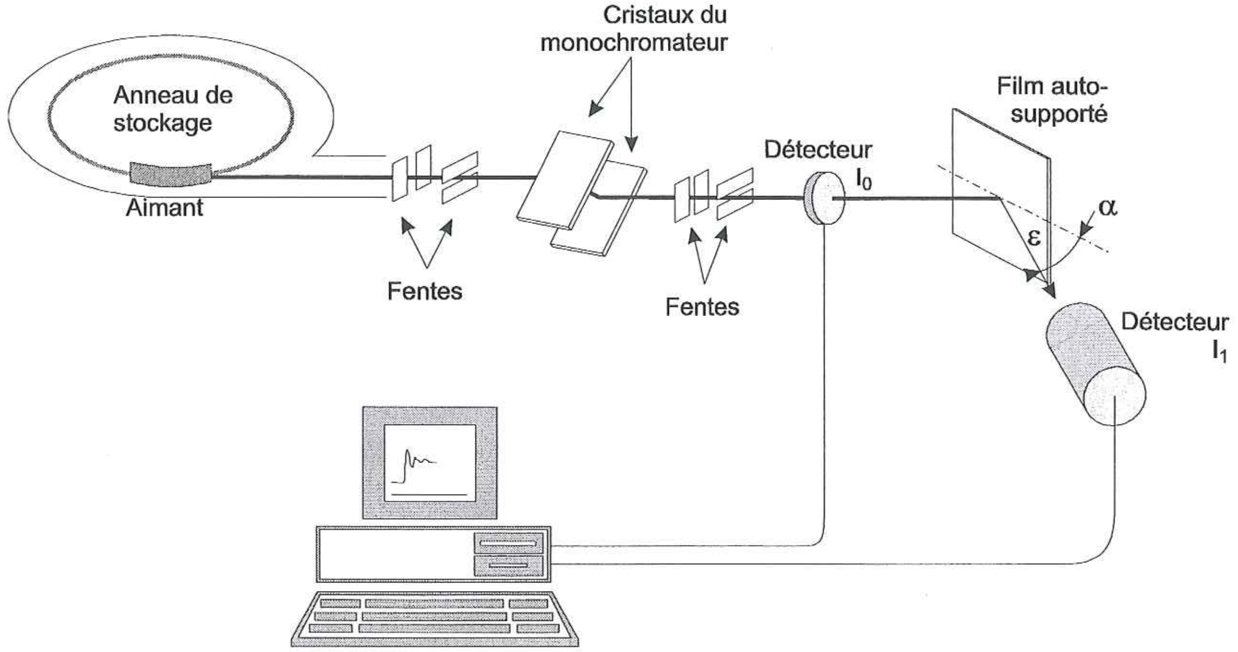

Figure 3.6. Schéma d'un spectromètre d'absorption des rayons X.

Les spectromètres BM 32 et 8.1 sont tous les deux équipés d'un système de focalisation qui permet de réduire la taille du faisceau sur l'échantillon. Sur la ligne BM32, un miroir situé en amont du monochromateur focalise le faisceau verticalement, et un courbeur sur le second cristal le focalise sagittalement. Sur la ligne 8.1 de SRS, les focalisations verticales et sagittales sont réalisées simultanément par un miroir de surface toroïdale situé en aval du monochromateur. La petite taille du faisceau permet de réaliser des mesures en polarisation à des angles α élevés car la largeur h' du faisceau X sur l'échantillon varie comme $h' = h/\cos\alpha$ (fig. 3.7), où h est la largeur du faisceau. Du fait de la valeur extrêmement réduite de h sur BM32 ($h < 1$ mm), on a pu mesurer des spectres EXAFS pour des échantillons de 10 mm de largeur à des angles α de 80° ($h' < 6$ mm pour $\alpha = 80°$). La valeur de h plus élevée sur 8.1 ($h \sim 2$ mm), n'a permis la mesure de spectres que pour des valeurs α inférieures à 70° ($2/\cos 70° = 5.8$ mm).

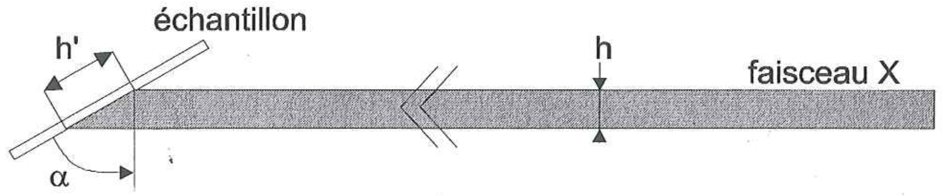

Figure 3.7. Relation entre la largeur h du faisceau incident et sa largeur h' sur l'échantillon

Les aspects théoriques de la spectroscopie P-EXAFS sont détaillés dans l'article intitulé « *Sorption of metal ions on clay minerals. I. Polarized EXAFS evidence for the adsorption of cobalt on the edges of hectorite particles* » situé dans la troisième partie de la thèse.

Conclusion

Le protocole de purification de l'hectorite a permis d'obtenir un matériau de pureté satisfaisante pour la réalisation des expériences de dissolution et d'adsorption de cations. Néanmoins, l'utilisation de techniques encore plus sélective vis-à-vis des phases indésirables (carbonates, hydroxydes de fer) est souhaitable, notamment en raison de la faible stabilité et de la cinétique de dissolution élevée de l'hectorite en solution. Par exemple, l'attaque acide des carbonates peut être remplacée par une technique « douce », de dissolution des carbonates à un pH de 5-6 contrôlé par ajout d'acide, avec élimination par dégazage du CO_2 libéré lors de cette dissolution. À ces valeurs de pH moins élevées que dans le cas d'une attaque acide simple, la cinétique de dissolution de l'hectorite est moins rapide, et l'hectorite est ainsi davantage préservée. On pourrait également envisager de conditionner l'hectorite après traitement dans une solution de $NaNO_3$ 0,3 M dégazée et ajustée préalablement à pH 8 afin de limiter les réactions de dissolution durant le stockage de la suspension-mère. À terme, l'objectif reste toujours l'obtention d'une suspension homoionique d'hectorite-Na pure, dans laquelle les propriétés morphologiques et physico-chimiques du phyllosilicate présent dans le matériau de départ ont été préservées au maximum.

La cinétique de dissolution de l'hectorite observée à température ambiante et pour des valeurs de pH proches de celles des milieux naturels, est très supérieure à celle des montmorillonites alumineuses [82, 104]. Cette cinétique importante en fait cependant un matériau de choix pour l'étude des relations existant entre l'adsorption des cations et la stabilité du solide, et ce pour des laps de temps très courts. D'autre part, la stabilité de l'hectorite semble plus importante en conditions basiques qu'en conditions acides.

Troisième partie : mécanisme d'adsorption de Co et Zn sur l'hectorite à pH modéré (pH $\leq$ 6,5)

Introduction

Bien que de nombreuses études aient été consacrées à la réactivité de surface des smectites, bien peu d'entre elles se sont attachées à relier les aspects macroscopiques et structuraux de cette réactivité. D'une part, la plupart des modèles basés sur les études chimiques macroscopiques postulent la formation de complexes de surface sur les argiles, soit sur les plans de base, soit sur les bordures des smectites. Or, jusqu'à présent, l'existence de CSI en bordure des argiles n'a pu être établie avec certitude. D'autre part, de nombreuses études spectroscopiques, microscopiques, et diffractométriques (e.g. [36-39, 41, 42, 52-54, 157-162] ont eu pour objectif de caractériser la structure des complexes formés par échange cationique. Ces études ont été souvent réalisées à saturation de la capacité d'échange des smectites, autrement dit à des concentrations den cations qui sont plutôt exceptionnelles dans les milieux naturels. Les mécanismes moléculaires d'adsorption dépendant du pH, et leur rapport avec les comportements macroscopiques d'adsorption, n'ont été étudiés de manière explicite que dans quelques cas [18, 131, 132]. Les différents modes de fixation des cations à la surface des solides (CHS, CSI...) ont un impact à long terme sur le devenir du substrat, notamment en termes d'activation ou d'inhibition de la dissolution. Or, jusqu'à présent, ces relations entre structure du complexe et stabilité de la surface minérale ont été peu étudiées [163], et à notre connaissance aucun de ces travaux n'a porté sur l'hectorite.

Les objectifs de cette partie sont (1) de définir les conditions chimiques pour lesquelles les cations Co et Zn forment des CSI, (2) de déterminer la structure de ces CSI en bordure des feuillets de l'hectorite, et (3) de déterminer l'impact de ces CSI sur la stabilité de l'hectorite. Cette partie est subdivisée en trois sections. Dans la première section, (chapitre 4) la spectroscopie P-EXAFS est utilisée pour déterminer la structure des CSI formés par adsorption de Co sur l'hectorite à haute force ionique ($NaNO_3$ 0,3 M) et pH modéré (pH 6,5). Le mécanisme d'adsorption de Co en fonction de la force ionique et de la concentration totale en Co à pH 6,5 est ensuite étudiée en couplant les approches spectroscopiques (EXAFS) et cinétiques. Dans le deuxième section (chapitre 5), les méthodes de spectroscopie P-EXAFS et de cinétique chimique sont appliquées à l'étude du mécanisme d'adsorption de Zn, un oligo-élément important pour les organismes vivants, sur l'hectorite, à des pH modérés (pH 4 et 6,5).

4. Adsorption de Co sur l'hectorite à pH 6,5

4.1. Structure du complexe de surface formé par adsorption spécifique

L'environnement cristallochimique de Co fixé à pH modéré (pH 6,5) et haute force ionique ($NaNO_3$ 0,3 M), dans des conditions d'inhibition de l'échange cationique, a été déterminé par P-EXAFS sur un film auto-supporté préparé avec une concentration en solution de Co égale à TotCo = 100 μM et un temps de réaction de 120 h. Les résultats de cette étude sont détaillés dans l'article intitulé « *Sorption of metal ions on clay minerals. I. Polarized EXAFS evidence for the adsorption of cobalt on the edges of hectorite particles* » situé à la fin de cette section.

La figure 4.1 montre que les spectres EXAFS enregistrés en polarisation présentent plusieurs fréquences distinctes, indiquant la présence de plusieurs couches atomiques entourant le Co adsorbé. Les amplitudes et les phases des oscillations EXAFS varient fortement avec l'angle α entre le champ électrique $\boldsymbol{\varepsilon}$ et le plan du feuillet smectitique, ce qui indique que l'environnement du Co est anisotrope. Les transformées de Fourier (TF) de ces spectres présentent plusieurs pics, provenant des contributions des couches atomiques entourant le cobalt (fig. 4.2). Le premier pic (`A`) provient de la contribution des oxygènes de l'octaèdre de coordination de Co, et le deuxième pic (`B`), des contributions des couches cationiques les plus proches. Ce pic `B` présente une dépendance angulaire importante: son amplitude diminue pour α compris entre 0 et 35°, puis augmente pour $\alpha > 35°$. Cette dépendance angulaire ne peut être expliquée que par l'existence de deux sous-couches atomiques ayant des orientations distinctes. L'analyse quantitative a montré que le cobalt était entouré de 1.6 ± 0.4 Mg à 3.03 Å dans le plan du film, et de 2.2 ± 0.5 Si à environ 3.27 Å en-dehors du plan. Ces distances interatomiques sont typiques de liaisons par arêtes entre les octaèdres de Co et de Mg, et de liaisons par sommet entre les octaèdres de Co et les tétraèdres de Si. La dépendance angulaire des contributions Mg et Si, ainsi que le nombre réduit de voisins, indiquent que le cobalt forme des complexes de sphère interne (CSI) mononucléaires localisés en bordure du feuillet, en continuité structurale de la couche (Mg, Li) octaédrique de l'hectorite (fig. 4.3).

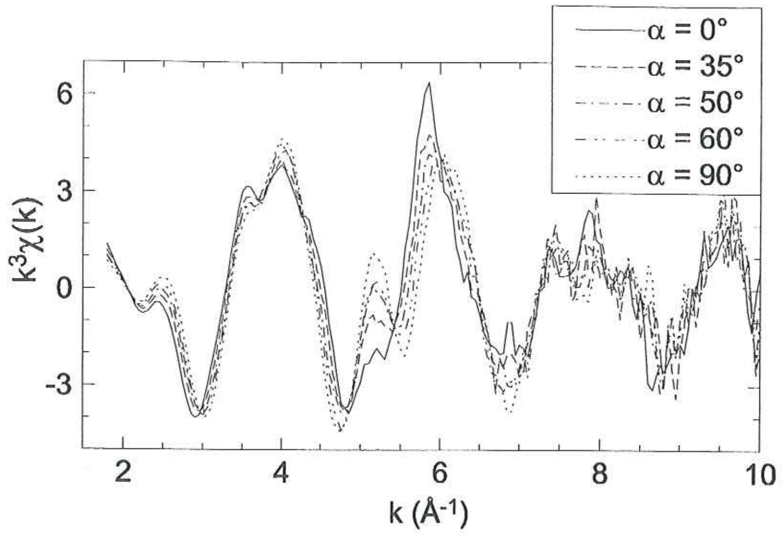

Figure 4.1. Dépendance angulaire des spectres EXAFS au seuil K du cobalt adsorbé sur l'hectorite à pH 6,5 et $NaNO_3$ 0,3 M.

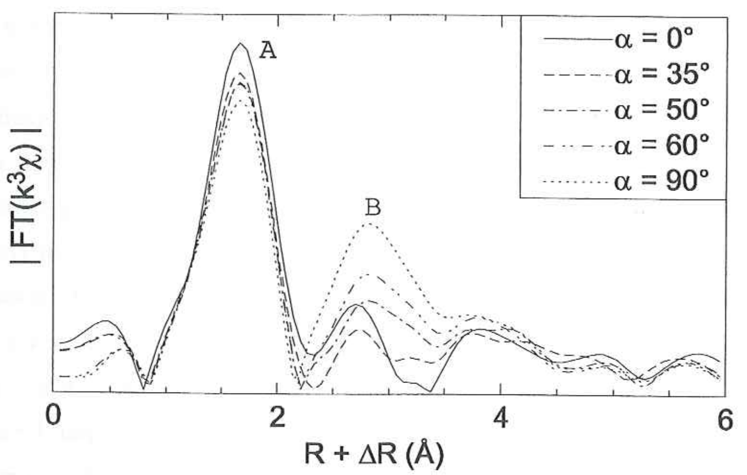

Figure 4.2. Dépendance angulaire du module de la TF des spectres EXAFS pour le cobalt adsorbé sur l'hectorite à pH 6,5 et $NaNO_3$ 0,3 M.

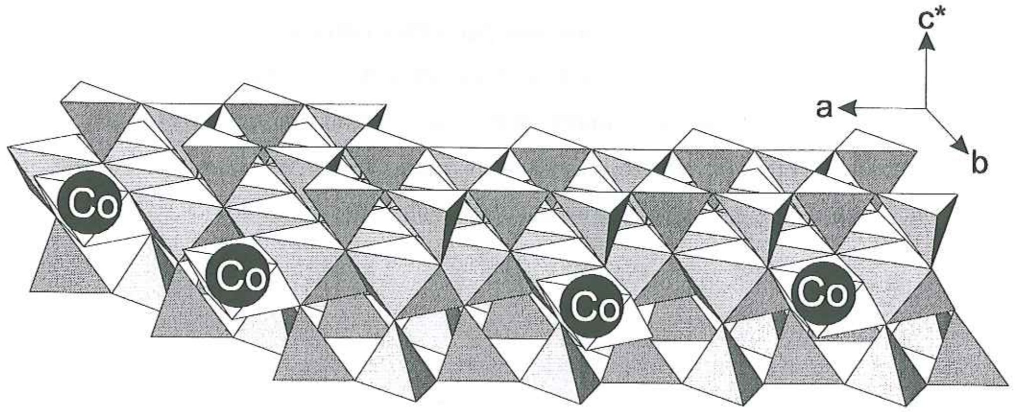

Figure 4.3. Exemples de complexes de sphère interne formés par adsorption de Co en bordure des feuillets d'hectorite. Les octaèdres de Co partagent des arêtes avec des octaèdres de Mg, et des sommets avec des tétraèdres de Si comme dans une structure phyllosilicate.

(*Sorption of metal ions on clay minerals. I. Polarized EXAFS evidence for the adsorption of cobalt on the edges of hectorite particle.* Article paru dans Journal of Colloid and Interface Science)

Journal of Colloid and Interface Science **215,** 140–158 (1999)
Article ID jcis.1999.6253, available online at http://www.idealibrary.com on IDEAL®

Sorption of Metal Ions on Clay Minerals

I. Polarized EXAFS Evidence for the Adsorption of Co on the Edges of Hectorite Particles

Michel L. Schlegel,*,[1] Alain Manceau,* Daniel Chateigner,† and Laurent Charlet*

**Environmental Geochemistry Group, LGIT-IRIGM, University of Grenoble, BP 53, F-38 041 Grenoble Cedex 9, France; and*
†Laboratoire de Physique de l'État Condensé, Université du Maine, BP535, F-72085 Le Mans Cedex 9, France

E-mail: Michel.Schlegel@ujf-grenoble.fr

Received November 25, 1998; accepted March 30, 1999

The local structural environment of Co sorbed on hectorite (a magnesian smectite) has been investigated by polarized EXAFS (P-EXAFS) spectroscopy on a self-supporting film of Co-sorbed hectorite. This sorption sample was prepared by contacting Co and hectorite at pH 6.5 and at high ionic strength (0.3 M $NaNO_3$) to favor pH-dependent sorption reaction over cation exchange. A self-supporting film was elaborated after 120 h of reacting time, when apparent quasi-equilibrium conditions were attained. The half-width at half maximum of the orientation distribution of c* axis of individual clay platelets off the film normal was determined by quantitative texture analysis, and found to be equal to 18.9°. Co K-edge P-EXAFS spectra were recorded at angles between the incident beam and the film normal equal to 0°, 35°, 50°, and 60°; the 90° spectrum was obtained by extrapolation. Spectral analysis led to the identification of the two nearest cationic subshells containing 1.6 ± 0.4 Mg at 3.03 Å and 2.2 ± 0.5 Si at 3.27 Å. These distances are respectively characteristic of edge-sharing linkages between Mg and Co octahedra and of corner-sharing linkages between Co octahedra and Si tetrahedra, as in clay structures. The angular dependence of the Co–Mg and Co–Si contributions indicates that Co–Mg pairs are oriented parallel to the film plane, whereas Co–Si pairs are not. These results are interpreted by the formation of Co inner-sphere mononuclear surface complexes located at the edges of hectorite platelets, in the continuity of the (Mg, Li) octahedral sheet. © 1999 Academic Press

Key Words: **Co; hectorite; adsorption; EXAFS; polarized EXAFS; surface complex.**

INTRODUCTION

Smectites are widespread minerals of weathering formations and sediments (1). They possess a large specific surface area and a high structural charge (up to 1000 meq per kg). Therefore, these clay minerals much influence the physico-chemical properties of geological formations where they are present. The retention properties of smectites are also of interest for the setup of geochemical barriers for nuclear waste repositories. These barrier systems are foreseen to limit leaching of hazardous chemicals or radionuclides (2). Industrial applications of smectites encompass heterogeneous catalysis on modified clays (3) and pharmacological technologies. For all these reasons, a good understanding of the surface stability and sorptive reactivity of smectites is highly desirable.

The high surface reactivity of smectites is a direct consequence of their lamellar and defective structure. Smectites are built of layers made by the condensation of one central octahedral sheet and two tetrahedral sheets (4). Heteroionic cationic substitutions impart to smectites a permanent negative structural charge, which is compensated by the adsorption of cations on basal planes. Divalent cations sorbed on these planes form outer-sphere (OS) surface complexes (5–10) and are easily exchanged with solute ions by varying the cationic composition of the solution. Besides these cation exchange properties, smectites also possess pH-dependent sorption properties (11–17). The pH-dependent sorption was inferred to take place at layer edges, where truncation of the bulk structure leads to the formation of oxygen dangling bonds. However, no definite structural evidence for the adsorption of cations on edge sites has been reported yet. Extended X-ray absorption fine structure (EXAFS) studies rather suggested that the pH-dependent sorption of cations on phyllosilicates leads to the precipitation of mixed (18, 19) or pure (9, 20) hydroxide phases, without definite evidence for spatial association between the precipitated and the sorbent phases. Furthermore, a recent reevaluation of EXAFS data on a similar sorbate–sorbent system (21) emphasized the relatively high uncertainty on structural parameters (interatomic distance, number of neighboring atoms) obtained by powder-EXAFS, which could eventually bring the reliability of several sorption structural models in question. One origin for these uncertainties is the relatively limited reciprocal space explored by EXAFS (at best $\Delta k = 14$ Å^{-1}), which prevents the discrimination of atomic shells separated by less than 0.10–0.15 Å (22). This is typically the case in phyllosilicates, where absorbing atoms of the octahedral sheet are surrounded by neighboring cations from the octahe-

---

[1] To whom correspondence should be addressed.

0021-9797/99 $30.00

dral and tetrahedral sheets at $R \sim 3.05–3.10$ Å and $R \sim 3.20–3.25$ Å, respectively. Manceau and co-workers (23, 24) showed that this limitation can be overcome by performing polarized-EXAFS (P-EXAFS) experiments on phyllosilicate single crystals. The contribution of cations from the tetrahedral sheets can be minimized by orienting the phyllosilicate plane parallel to the electric field vector ϵ of the incident X-ray beam (Fig. 1, left). Conversely, the contribution of cations from the octahedral sheet is extinguished in the perpendicular orientation of ϵ (Fig. 1, right). Recently, this P-EXAFS technique was successfully applied for the first time to well-textured self-supporting clay films (25, 26). These studies demonstrated the unique ability of P-EXAFS to probe highly anisotropic environments with an enhanced precision, as compared to powder EXAFS. The discriminating capacity of P-EXAFS can be used to differentiate cations precipitated in solution from cations adsorbed on the edges of smectite layers.

In the present study, the sorption mechanism of Co on hectorite, a magnesian smectite, was investigated by P-EXAFS spectroscopy performed on a self-supporting film of Co-sorbed hectorite. Adsorption of Co on the edge sites of hectorite was favored by carefully controlling the chemical conditions of the sorption process. In particular, sorption was carried out at high ionic strength ($I = 0.3$ M) to inhibit Co adsorption on cation exchange sites, and at moderate pH (pH 6.5) and Co concentration ([Co] = 10^{-4} M) to avoid as much as possible the precipitation of either pure $Co(OH)_{2(s)}$ or of Co hydrous phyllosilicates such as Co-rich kerolite (hereafter referred to as CoKer) (21). The orientation distribution of hectorite crystallites in the self-supporting film plane was determined by quantitative texture analysis (QTA). Mg and Si cationic shells surrounding sorbed Co were unambiguously identified by P-EXAFS spectroscopy, and the orientation of the Co–Mg and Co–Si pairs with respect to the basal plane of hectorite particles were determined. Based on these results, a structural model for the adsorption mechanism of Co on the layer edges of hectorite is proposed.

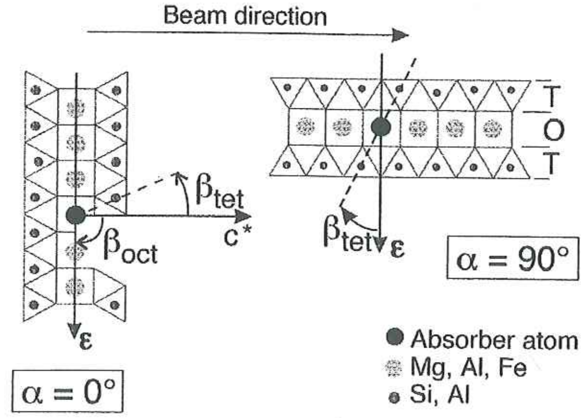

FIG. 1. Principle of polarized EXAFS measurements on phyllosilicates: (left) electric field vector ϵ parallel to the layer plane; (right) ϵ perpendicular to the layer plane.

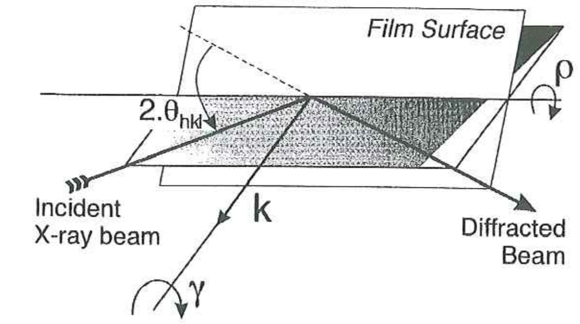

FIG. 2. X ray diffraction geometry used for texture analysis in the reflection mode. A θ_{hkl} pole figure can be measured by fixing θ_{hkl} and then rotating the sample around γ and ρ (both rotations conserving θ_{hkl}).

BACKGROUND

Quantitative Texture Analysis

The quantitative texture analysis of a polycrystalline aggregate is based on the concept of orientation distribution (OD), which represents a statistical description of the individual crystallite orientations within this aggregate (27). This orientation can be evaluated by determining the pole distribution of $\{hkl\}$ diffracting planes (i.e. the orientation distribution of the vectors $\langle hkl\rangle^*$ perpendicular to these planes) with respect to the sample referential. Figure 2 illustrates the principle of a pole distribution measurement on an X-ray diffractometer. Three rotation movements, θ_{hkl} (Bragg angle), γ (azimuthal angle), and ρ (tilt angle) are available. In this geometry, only $\{hkl\}$ planes whose poles are aligned with the **k** direction are in diffracting conditions, provided θ_{hkl} fulfills the Bragg condition. The diffracted intensity $I_{hkl}(\gamma, \rho)$ is proportional to the number of crystallite planes that satisfy these orientation and Bragg conditions. Rotation of the sample in every position around γ and ρ conserves θ_{hkl} and allows for all crystallites of the sample to be brought successively in a diffracting position. A pole density $P_{hkl}(\gamma, \rho)$ is then obtained by normalizing measured diffracted intensities with respect to an average value obtained by integrating all intensities over γ and ρ This normalization procedure enables the comparison of several samples regardless of their porosity and purity, under the assumption that the average diffracted intensity is constant whatever the true texture is. Finally, a pole figure is obtained by projecting the pole density on the film plane using an equal-area projection for qualitative visual representation of the textural quality of the sample.

In the case of smectite samples, only a few $\{hkl\}$ reflections are experimentally accessible, because some are too low θ_{hkl} angles to ensure a constant irradiation of the sample, and others are systematically extinct. Furthermore, the measurable peaks consist of several overlapped reflections, as a result of the crystal symmetry (26), and the resulting multipole figures are of complex visual interpretation. To derive a quantitative information on the sample texture, it is then necessary to calculate the complete OD that would best fit the measured pole density, using a refinement technique. The quality of the fit between the experimental and the OD-recalculated pole density can be evaluated by the reliability factor,

$$RP = \frac{1}{I}\sum_{hkl}\sum_{j}\frac{P_{hkl}^{\mathrm{calc}}(j) - P_{hkl}^{\mathrm{obs}}(j)}{P_{hkl}^{\mathrm{obs}}(j)}, \qquad [1]$$

where $P_{hkl}^{\mathrm{obs}}(j)$ and $P_{hkl}^{\mathrm{calc}}(j)$ refer to the observed and recalculated pole densities, and j runs for all γ and ρ values. A similar reliability factor R_W, in which observed and recalculated intensities are weighed, can be defined. R_W enables the comparison of the refinement quality for samples with different texture strengths. Once the OD has been refined, every desired single pole figure can be recalculated for much simpler interpretation. More details on QTA refinements can be found elsewhere (26, 28).

Polarized EXAFS

In an EXAFS experiment, the absorption coefficient μ of an element present in the studied material is measured as a function of the energy of the incident X-ray beam. For a linearly polarized X-ray beam and a layered compound having a threefold or higher symmetry axis perpendicular to the layer plane, this absorption coefficient can be written (23–26, 29)

$$\mu^{\alpha} = \mu^{\parallel}\cos^2\alpha + \mu^{\perp}\sin^2\alpha, \qquad [2]$$

where α is the angle between the electric field vector ϵ and the layer plane (Fig. 1). The notations $\parallel$ and $\perp$ denote orientations of ϵ parallel ($\alpha = 0°$) and perpendicular ($\alpha = 90°$) to the layer plane, respectively. The net EXAFS oscillations are derived from X-ray absorption spectra by the normalization equation

$$\chi = \frac{\mu - \mu_0}{\mu_0} \Rightarrow \mu = \mu_0(1 - \chi), \qquad [3]$$

where μ_0 is the absorption coefficient of an isolated atom. As μ_0 does not depend on α, χ exhibits a dichroic angular dependence described by

$$\chi^{\alpha} = \chi^{\parallel}\cos^2\alpha + \chi^{\perp}\sin^2\alpha = \chi^{\perp} + (\chi^{\parallel} - \chi^{\perp})\cos^2\alpha. \qquad [4]$$

Equation [4] is rigorously correct for the total macroscopic EXAFS signal (i.e. for the sum of single and multiple scattering contributions). From the knowledge of $\chi^{\parallel}$ and $\chi^{\perp}$, Eq. [4] allows the calculation of χ^{α} for any value of α in dichroic systems. Conversely, if $\chi^{\perp}$ is not accessible experimentally, then it can be calculated via linear regression of EXAFS spectra obtained for $\alpha < 90°$ and extrapolation to $\alpha = 90°$. In a perfectly disordered (isotropic) powder, χ^{α} is averaged over all space directions and reduces to an α-independent spectrum, χ^{iso}.

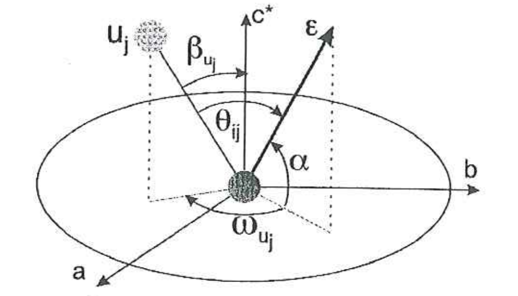

FIG. 3. Definition of the angles θ_{ij}, ω_{u_j}, α, and β_{u_j} in polarized experiments.

The EXAFS oscillations are interpreted microscopically as resulting from the interference between photoelectronic waves outgoing from the absorbing atom (i) and waves backscattered by neighboring atoms (j); therefore it can be decomposed into contributions of successive atomic shells, χ_{ij}. For a powder, the amplitude of χ_{ij}^{iso} is of course proportional to the number of atoms present in the j shell; N_j^{real} and χ_{ij}^{iso} can be written

$$\chi_{ij}^{\mathrm{iso}} = S_0^2 N_j^{\mathrm{real}} A_{ij}(k, \lambda, R_{ij}, \sigma_{\mathrm{j}}) \cdot \sin(2kR_{ij} + \phi_{ij}(k)), \qquad [5]$$

where k is the norm of the photoelectron wavevector, R_{ij} is the absorber–backscatterer distance, $\phi_{ij}(k)$ is a phase shift function depending on the nature of the ij pair, S_0^2 is an amplitude reduction factor which is characteristic of the absorber, and $A_{ij}(k, \lambda, R_{ij}, \sigma_j)$ is a damping function which depends on R_{ij}, on the mean free path of the photoelectron (λ), and on the structural and thermal disorder of the j shell, expressed as a Debye–Waller factor σ_j. At a given temperature, the more disordered the shell, the higher σ_j.

In contrast to powder EXAFS, in P-EXAFS the amplitude of χ_{ij}^{P} is not only dependent on N_j^{real}, but also on the orientation of ϵ with respect to the vectors $\mathbf{R}_{iu_j}$ that connects the absorbing i atom to the u_j^{th} atom of the j shell. At the K-edge and in the plane-wave approximation, this relationship can be written

$$\chi_{ij}^{\mathrm{P}} = 3\chi_{ij}^{\mathrm{iso}}\sum_{u_j=1}^{N_j^{\mathrm{real}}}\cos^2\theta_{iu_j} = 3\langle\cos^2\theta_{iu_j}\rangle\chi_{ij}^{\mathrm{iso}}, \qquad [6]$$

where θ_{iu_j} is the angle between ϵ and $\mathbf{R}_{iu_j}$. The summation is made over all the N_j^{real} atoms of the j shell. For layered compounds, θ_{iu_j} can be expressed as a function of α, of the β_{u_j} angle between $\mathbf{R}_{iu_j}$ and $\mathbf{c}^*$, and of the ω_{u_j} angle between the in-plane projections of ϵ and $\mathbf{R}_{iu_j}$ (Fig. 3). The existence of a threefold or higher symmetry axis normal to the layer plane indicates that the j^{th} shell contains several u_j backscattering atoms with the same β_{u_j} orientation (except for $\beta_{u_j} = 0°$).

Thus, the $\langle\cos^2\theta_{iuj}\rangle$ term can be reduced to a function of only α and β_j by averaging the in-plane ω_{uj} angles (29). This results in

$$3\langle\cos^2\theta_{iuj}\rangle = 1 - \frac{(3\cos^2\beta_j - 1)(3\cos^2\alpha - 2)}{2}. \quad [7]$$

Hence the angular dependence of χ_{ij}^{P} can be described by a simple affine function of $\cos^2\alpha$:

$$\chi_{ij}^{P} = \chi_{ij}^{iso}\cdot\left[1 - \frac{(3\cos^2\beta_j - 1)(3\cos^2\alpha - 2)}{2}\right]. \quad [8]$$

Equation [8] confirms that only the amplitude of χ_{ij}^{P} is modified by varying α. It is then possible to define for each α angle an apparent number of neighboring backscatterers, N_j^{app}, which is proportional to χ_{ij}^{P}, so that

$$\frac{N_j^{app}}{N_j^{real}} = \frac{\chi_{ij}^{P}}{\chi_{ij}^{iso}}. \quad [9]$$

N_j^{app} can be calculated from β_j and N_j^{real} for any α value by combining Eqs. [8] and [9]:

$$N_j^{app} = N_j^{real}\cdot\left[1 - \frac{(3\cos^2\beta_j - 1)(3\cos^2\alpha - 2)}{2}\right]. \quad [10]$$

Equation [10] resumes to a simple expression in two cases. First, when $\alpha = 35.3°$, then $N_j^{app} = N_j^{real}$ regardless of β_j, and the polarized and powder EXAFS spectra are identical. Second, when $\beta_j = 53.7°$, $N_j^{app} = N_j^{real}$ regardless of α, and the EXAFS contribution of the *j* shell has no angular dependence. $\alpha = 35.3°$ and $\beta_j = 54.7°$ are "magic angles." Equation [10] also indicates that N_j^{app} increases with increasing α for $\beta_j < 54.7°$ and decreases with increasing α for $\beta_j > 54.7°$. Thus, the orientation of the *ij* pairs with respect to $\beta = 54.7°$ can be determined from the angular dependence of N_j^{app}.

How these theoretical considerations apply to phyllosilicates will now be shown taking Fe in biotite as a example (23, 24). Biotite is a trioctahedral phyllosilicate like hectorite (Fig. 1). Fe is located in the octahedral sheet and is surrounded by 6 (Fe, Mg) neighbors of the octahedral sheet ($\beta = 90°$) and 4 (Si, Al) neighbors of the tetrahedral sheets ($\beta \approx 33°$). These two shells are located at close distances (~3.04–3.10 Å vs 3.25–3.30 Å), and their EXAFS contributions cannot be discriminated by conventional EXAFS analysis (22), thereby decreasing the accuracy of the spectral quantitative analysis (30). In contrast, Eq. [10] shows that in P-EXAFS, the contribution from the (Fe, Mg) shell extinguishes for $\alpha = 90°$ ($N_{Fe,Mg}^{app} = 0$), and the analysis of the enhanced contribution of the single (Si, Al) shell is facilitated ($N_{Si,Al}^{app} = 8.4$). Likewise, for $\alpha = 0°$, the apparent number of (Si, Al) neighbors is diminished ($N_{Si,Al}^{app} = 1.8$), which makes easier the analysis of the enhanced contribution of the (Fe, Mg) shell ($N_{Fe,Mg}^{app} = 9$). Manceau and co-workers (23) confirmed experimentally these theoretical predictions and demonstrated that P-EXAFS measurements allow the determination of structural parameters (R_{ij}, N_j) for close atomic shells with an enhanced precision.

For an absorbing element whose structural environment is not known, the inclination angle β_j of a backscattering *j* shell with respect to **c*** can be ideally determined from the angular dependence of N_j^{app}. For this purpose, Eq. [10] can be rewritten as an affine function of $\cos^2\alpha$:

$$\frac{N_j^{app}}{N_j^{real}} = \frac{3}{2}(1 - 3\cos^2\beta_j)\cdot\cos^2\alpha + 3\cos^2\beta_j. \quad [11]$$

The slope (*B*) of this function depends only on β_j, and the β_j value can be readily determined from a linear regression of N_j^{app}/N_j^{real} with respect to $\cos^2\alpha$.

Eqs. [2], [4], [7]–[11] hold true for dichroic single crystals. They can be applied to textured self-supporting clay films, provided a symmetry axis of order greater than two exists normal to the film plane. For example, a C_∞ axis can be obtained by perfectly orienting the basal planes of individual platelets parallel to the film surface, and then dispersing the **a** and **b** axis randomly in the film plane. In this case, all **c*** axes point perpendicular to the film plane, and β_j are the same for all crystallites. For real films, in which the basal planes of platelets are disoriented off the film plane, a C_∞ axis can still be defined, if **a** and **b** axes are distributed randomly around the film normal. In this case, however, disorientation of the platelets causes a dispersion of the β_j angles and results in angular dependencies of N_j^{app} that are weaker than in the case of a perfect orientation. As a corollary, β_j determined experimentally from Eq. [11] on these real films tends to be underestimated for $\beta_j > 54.7°$ and overestimated for $\beta_j < 54.7°$.

EXPERIMENTAL

Hectorite Purification and Characterization

Hectorite $Na_{0.40}(Mg_{2.65}Li_{0.35})(Si_{3.95}Al_{0.05})O_{10}(OH)_2$ was purchased from the Clay Mineral Repository (SHCa-1). In this magnesian smectite, the Mg and Li atoms are located in the octahedral sheet and Si atoms in the tetrahedral sheets. Approximately 25 g of the raw material were suspended in 1 L of deionized Milli-Q water and shaken at 180 rpm for 48 h. The <2 μm fraction was then separated by sedimentation techniques. This fraction was treated several times with a 10^{-4} mol L^{-1} (M) HNO_3 solution to remove carbonate minerals, and subsequently washed 5 times with 0.5 M NaCl to exchange interlayer cations with sodium. No concentrated inorganic acid solutions were used, since hectorite appears to dissolve quickly in strong acidic media (31, 32). Afterwards the clay suspension was treated 1 h with a 5×10^{-3} M dithionite, 0.2 M citrate, 0.1 M bicarbonate, 0.5 M NaCl solution at pH 6.5 to remove possibly remaining ferric oxides, and 1 h with a 3% H_2O_2, 0.5 M NaCl solution at 50°C to remove organic matter (17, 33, 34). Remaining H_2O_2 was destroyed by heating the suspension for more than 1 h at 70°C. Dialysis against Milli-Q water was then performed until no Cl^- anions could be detected ($AgNO_3$ test). The final 2 wt% stock suspension was stored at 4°C in the dark prior to use. Measurements of aqueous SiO_2 concentrations at different preparation stages showed that the amorphous-SiO_2 solubility limit was never reached.

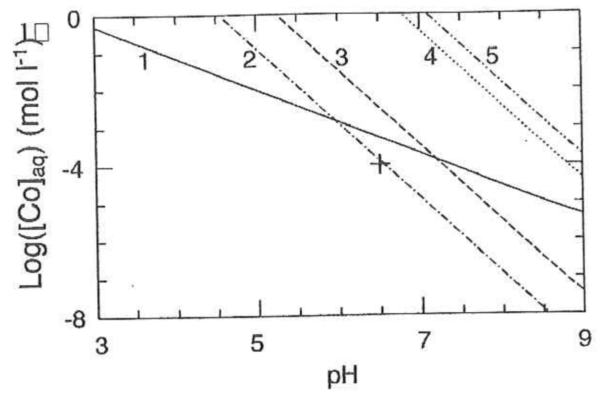

FIG. 4. Solubility of Co in solution with respect to Co hydroxides and Co-rich kerolite (CoKer). Solubility constants are taken from Refs. (21, 74). Plots of solubility limits are given for (1) stoichiometric dissolution of CoKer, (2) CoKer solubility controlled by amorphous silica, (3) CoKer solubility controlled by quartz, (4) solubility of pink active Co hydroxide, and (5) solubility of blue Co hydroxide. The cross refers to the maximal experimental [Co] in the hectorite suspension.

The purified clay suspension was characterized by X-ray diffraction on a Siemens D-500 X-ray diffractometer. No trace of crystallized carbonate mineral could be detected. The cation exchange capacity (CEC), measured by Cs exchange (35), is 840 meq kg^{-1}. Specific surface area determined by BET equals 114 m^2 g^{-1}.

Co sorption and Film Preparation

General Considerations

Chemical reactions such as hectorite dissolution, formation of pure or mixed Co hydroxide, or Co adsorption on exchange sites may strongly interfere with Co adsorption on pH-dependent sites. Therefore, the chemical conditions (pH, ionic strength) for Co sorption were carefully determined to avoid these interferences.

The lower limit of the possible pH value for Co sorption was imposed by the dissolution kinetics of hectorite. At pH 6.5, it takes about 10 days for the working clay suspension to reach a free Si concentration of 400 μM. Since the dissolution rate of hectorite is enhanced at lower pH (36), pH 6.0 was chosen as a lower limit. Also, as a prerequisite, pH has to be high enough to allow for a sufficient amount of Co to sorb on hectorite within a reasonable period of time. The upper pH limit was selected to avoid precipitation of pure $Co(OH)_{2(s)}$ and CoKer. Plots of the Co solubility with respect to CoKer and $Co(OH)_{2(s)}$ (Fig. 4) indicate that the upper pH limit for Co sorption is ~6.7 for a Co concentration of 100 μM. Sorption experiments were thus conducted at pH 6.5.

Ionic strength (*I*) and equilibration time for Co sorption were defined on the basis of kinetic results obtained at two different ionic strengths (Fig. 5). At low ionic strength (0.01 M $NaNO_3$), an important Co sorption occurred within the first 5 min of contact time between the cation and the clay surface. At high ionic strength (0.3 M $NaNO_3$), this rapid cation sorption was far less pronounced, which suggests that it corresponds to Co adsorption on exchange sites (37). Following this initial step, sorption went on at slower rates. The relaxation time associated with this second sorption step is not compatible with a cation exchange process (37). Based on these results, Co was sorbed at high ionic strength ($I = 0.3$ M) to inhibit cation exchange, and the self-supporting film was elaborated after 120 h of reacting time, when Co sorption was significantly slowed down.

Experimental Design

All chemicals were of ACS reagent grade. All solutions were prepared with Milli-Q water. A constant Na concentration of 0.3 M was maintained throughout the experiment by preparing the working solutions with the appropriate amounts of $NaNO_3$ salt (Fluka). pH measurements were made using a Metrohm combined electrode connected to a Metrohm pH-meter. This electrode was calibrated with buffers (Merck, titrisol) and recalibrated at least every 48 h. The pH of the suspension was continuously adjusted to 6.5 (±0.05) by software-controlled additions of small volumes of acid (0.1 M HNO_3, 0.3 M $NaNO_3$) or base (0.02 M NaOH, 0.28 M $NaNO_3$) solutions.

The sorption experiment was conducted at 25 ± 0.1°C in a

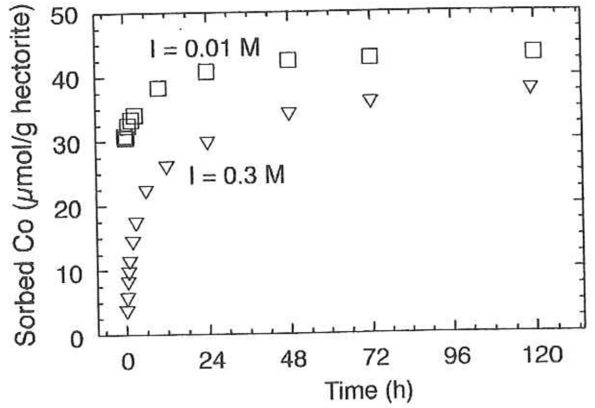

FIG. 5. Kinetics of Co sorption on hectorite at high ($I = 0.3$ M, ▽) and low ($I = 0.01$ M, □) ionic strengths. Chemical conditions are: pH 6.5, solid concentration [hectorite] = 1.95 g L^{-1}, total Co concentration $[Co]_{tot}$ = 100 μM.

polyethylene vessel immersed in a thermostated water bath. Solid concentration in the suspension was 1.95 g L^{-1}. Vigorous stirring of the suspension was achieved by a rotating magnetic bar. An inert atmosphere was maintained by bubbling argon throughout the suspension. Prior to use, Ar was acid- and base-washed by bubbling through 10% H_2SO_4 and 0.1 M NaOH solutions, and bubbled through a 0.3 M $NaNO_3$ solution to ensure a constant P_{H_2O} partial pressure. After a preequilibration time of 48 h at pH 6.5, an aliquot of a 0.21 M $Co(NO_3)_2$, 10^{-3} M HNO_3, 0.3 M $NaNO_3$ solution was added to the clay suspension to obtain a final Co concentration of 100 μM. The pH of the suspension was then readjusted to 6.5 within 5 min by gentle addition of the base solution and kept at this value until the end of the experiment. At the end of the sorption period (120 h), Co and Si concentrations in the supernatant were measured by spectrophotometry (38), and Mg was analyzed by inductively coupled plasma-atomic emission spectrometry. The amount of Co sorbed on hectorite at the end of the experiment was equal to 37 μmol g^{-1} of hectorite, i.e. a weight concentration of 2.23×10^{-3} g g^{-1} of hectorite. The free Si concentration in solution amounted to 333 μM at the time of Co introduction in the suspension, and reached a concentration of 394 μM at the end of the sorption period. Dissolved Si was always undersaturated with respect to amorphous silica (solubility of ~2000 μM (39)), and supersaturated with respect to quartz (solubility of 183 μM (40)). This supersaturation can be neglected, owing to the very slow crystallization rate of quartz at room temperature (41).

A 60-μm thick self-supporting film of Co-sorbed hectorite was prepared by slowly filtering 60 mL of the suspension on a 0.05-μm Sartorius cellulose nitrate filter in a closed filtration vessel. In order to avoid atmospheric carbonate contamination, a continuous flow of humidified argon was maintained over the sample throughout the whole filtration stage. Excess of salt and aqueous Co were washed with a few milliliters of Milli-Q water. When dry enough, the thin film was moved into a desiccator. This last drying stage is not believed to have substantially modified the sorption mode of Co, as hectorite is known to retain at least two layers of water molecules, even under low pressure of water vapor (42). Seven slices of the same film were cut and stacked on a sample holder, in order to get a thick sample for fluorescence-yield EXAFS measurements. Upon stacking, these slices were successively rotated around an axis perpendicular to the film plane to ensure a completely random in-plane orientation of hectorite crystallites in the EXAFS sample. The concentration of Co in the sample was low enough ($\Delta\mu/\mu < 0.01$ at $\alpha = 60°$) to eliminate self-absorption effects (43, 44).

Synthesis of Reference Compounds

CoKer of formula $Co_3Si_4O_{10}(OH)_2$, and Co-doped Mg-rich kerolite (CoMgKer) of formula $Co_{0.03}Mg_{2.97}Si_4O_{10}(OH)_2$ were synthesized by aging fresh precipitate of the desired chemical compositions at 75°C for 15 days, according to the procedure described by Decarreau (45, 46). Their b unit cell parameters, as calculated from the position of the (060) diffraction peak, equal 9.30 Å and 9.24 Å, respectively. In these precipitates, Co is located within the phyllosilicate octahedral sheet, and is surrounded by 6 Co and 4 Si (CoKer), or 6 Mg and 4 Si (CoMgKer), respectively. $Co(OH)_{2(s)}$ was obtained by titrating a 0.05 M $Co(NO_3)_2$ solution with 0.2 M NaOH under an argon atmosphere. The fresh pink precipitate was allowed to age for 15 days at room temperature in an anoxic glove box. These reference compounds were loaded in sample holders sealed with Kapton windows for EXAFS measurements.

Quantitative Texture Analysis

QTA was carried out by X-ray diffraction experiments on a four-circle goniometer mounted on a rotating copper anode (Rikagu RU 300-E). The X-ray incident beam was monochromatized using a flat graphite monochromator and collimated, giving a final beam cross section of 1*1 mm^2. Pole densities were measured on a single portion of the hectorite film by scanning the tilt angle ρ between 0 and 85° and the azimuthal angle γ between 0 and 360° with angle increments $\Delta\rho$ and $\Delta\gamma$ of 5°. In order to minimize defocusing effects, relatively open (4 mm) detecting slits were used. Three pole figures were measured: {004}, {020/110}, and {200/130}. Data were corrected for background defocusing. The pole densities were normalized and the OD was refined using the WIMV algorithm (47) of BEARTEX (28). The reflection overlaps are not the exact ones from a theoretical random powder, because defocusing limits the pole figure extent accessible to measurements (ρ only up to 85°). Thus all overlaps were considered as unknowns and were resolved during the OD refinement procedure. The OD was iteratively refined up to a velocity of convergence of 0.3%. Multiple and single pole densities were then recalculated. Visual evaluation of the OD simulation was allowed by comparison of experimental and recalculated pole figures, whereas the quality of the OD refinement was quantified by *RP* and R_W values (26).

EXAFS Data Collection and Reduction

Polarized Co K-EXAFS spectra for the Co-sorbed hectorite film were recorded at the SRS synchrotron radiation facility in Daresbury, UK, on the EXAFS 8.1 station. The optic of the spectrometer consists of a Si(111) double crystal monochromator and a focusing mirror (48). The second crystal of the monochromator was detuned by 30% to increase the rejection rate of harmonics. The clay film was mounted on a goniometer, and EXAFS spectra were recorded at α = 0°, 35°, 50°, and 60° in fluorescence detection mode using a 13-element array Ge detector (Canberra).

EXAFS spectra for $Co(OH)_{2(s)}$ and CoKer were recorded in transmission mode at the LURE synchrotron radiation facility, France, on the D42 station, with the plane of the sample holder positioned at the magic angle to get rid of any textural effect (24). Measurements were performed using a Si(331) channel-cut monochromator, and gaz ionization chambers filled with an air–helium mixture dosed to attenuate the beam intensity by ~20% before and ~50% after the sample entry. The EXAFS spectrum for CoMgKer was recorded in fluorescence mode at ESRF, France, on the BM32 CRG/IF station. Measurements were performed using a Ni-coated focusing mirror, a Si(111) monochromator, and a 30-element array Ge detector, with the plane of the sample positioned at the magic angle.

TABLE 1

Quantitative EXAFS Analysis for Reference Compounds

	First peak					Second peak												
		Co–O shell					Co–Co shell			Co–Mg shell			Co–Si shell					
	IFT range[a] (Å)	*R* (Å)	*N*	σ (Å)	R_p	IFT range[a] (Å)	*R* (Å)	*N*	σ (Å)	*R* (Å)	*N*	σ (Å)	*R* (Å)	*N*	σ (Å)	R_P	ΔE_0^b (eV)
$Co(OH)_{2(s)}$	1.1–2.2	2.10	6.0[c]	0.08	0.003	2.2–3.5	3.19[d]	6.0[c]	0.08							0.008	−0.1
CoKer	0.9–2.2	2.09	6.0[c]	0.09	0.012	2.3–3.5	3.12[e]	6.0[c]	0.09				3.27	4.0[c]	0.09	0.003	−0.8
CoMgKer	0.9–2.2	2.08	6.0[c]	0.09	0.005	2.2–3.1				3.07	6.0[c]	0.09	3.21	4.0[c]	0.10	0.035	−0.7

[a] Ranges for inverse Fourier transforms (IFT) in the real space.

[b] The threshold energy E_0 was taken at the half-height of the absorption edge ($\Delta\mu/2$). ΔE_0 given here for FEFF7.02 theoretical functions.

[c] Value held fixed during the fitting procedure.

[d] Crystallographic $R_{Co\text{-}Co}$ = 3.17 Å (56).

[e] Crystallographic $R_{Co\text{-}Co}$ = 3.10 Å (calculated from the position of the (060) diffraction peak).

EXAFS data reduction was accomplished following a standard procedure (22), using a software package implemented by D. Bonnin (ESPCI, Paris). As a preliminary step, absorption spectra were given the shape of the semi-empirical model of Lengeler (49, 50). $\chi(k)$ for $\alpha = 90°$ was extrapolated from $0° \leq \alpha \leq 60°$ measurements following Eq. [4] (23, 26). Fourier transformation was performed on $k^3\chi(k)$ between 2 and 10 $Å^{-1}$ using a Kaiser apodization window (51), resulting in a radial structure function (RSF) in the distance space. RSF peaks are located at apparent distances ($R + \Delta R$), which differ from crystallographic absorber-backscatterer distances (R) by ~ −0.3 Å, owing to the existence of the phase shift term $\phi_{ij}(k)$ in the EXAFS formula (Eq. [5]) (22). RSF's structural peaks of interest were selected in the distance space, and Fourier-back-transformed in k space. Interatomic distances (R) and number of atomic neighbors (N) were determined by least-square fitting these Fourier-filtered contributions with theoretical phase and amplitude functions calculated with FEFF7.02 (52), using talc, hectorite (Co–Mg and Co–Si pairs) and $Co(OH)_{2(s)}$ (Co–O and Co–Co pairs) as model structures (53–56). The amplitude reduction factor S_0^2 was set to 0.85, in accordance with previous experimental studies (57). The goodness of the fit was quantified by the reliability factor R_P, defined as

$$R_p = \frac{\sum_k \left(k^3 \cdot \chi_{calc}(k) - k^3 \cdot \chi_{exp}(k)\right)^2}{\sum_k \left(k^3 \cdot \chi_{exp}(k)\right)^2}. \qquad [12]$$

The accuracy of the interatomic distances obtained by using theoretical FEFF functions was assessed by fitting the experimental contributions of the first and second atomic shells for $Co(OH)_{2(s)}$, CoKer and CoMgKer references. Examination of Table 1 shows that EXAFS $R_{Co\text{-}O}$ values for the first oxygen shell of the three references are very similar to crystallographic values for divalent and oxygen-hexacoordinated Co (e.g., $R_{Co\text{-}O}$ = 2.097 Å for $Co(OH)_{2(s)}$ (56)). EXAFS-derived $R_{Co\text{-}Co}$ values for $Co(OH)_{2(s)}$ (3.19 Å) and CoKer (3.12 Å) are both larger than crystallographic distances (3.17 and 3.10 Å, respectively; Table 1). The same difference of 0.02 Å was previously reported (58) and likely originates from uncertainty in theoretical phase shift functions. The EXAFS-derived $R_{Co\text{-}Mg}$ value for CoMgKer (3.07 Å) is similar to crystallographic $R_{Mg\text{-}Mg}$ distances in talc (3.05–3.06 Å (53)) and to the distance calculated from the b unit cell parameter of CoMgKer (=9.24/3 = 3.08 Å). Finally, EXAFS-derived $R_{Co\text{-}Si}$ for CoMgKer (3.21 Å) is lower by 0.03 Å than $R_{Mg\text{-}Si}$ in talc (3.24 Å (53)). This result is surprising, as the Co octahedra have a larger size (e.g., $R_{Co\text{-}O}$ = 2.097 Å in $Co(OH)_{2(s)}$), compared to Mg octahedra ($R_{Mg\text{-}O} \approx$ 2.05–2.08 Å in talc), which should cause Si tetrahedra to be repelled at higher distances. This relatively large uncertainty on $R_{Co\text{-}Si}$ cannot be attributed to the use of theoretical FEFF functions (26), but rather results from the overlap of the Mg and Si shells in powder-EXAFS spectra (21, 59). In conclusion, the uncertainty on EXAFS-derived distances resulting from the use of theoretical phase shift functions is about 0.01 Å for Co–O pairs, probably about 0.02 Å for Co–Co and Co–Mg pairs. The uncertainty in distance for Co–Si pairs cannot be estimated with accuracy on powder samples but has been shown to be as good as 0.03 Å in former P-EXAFS experiments (26). The uncertainty on the number of neighboring atoms will be discussed later.

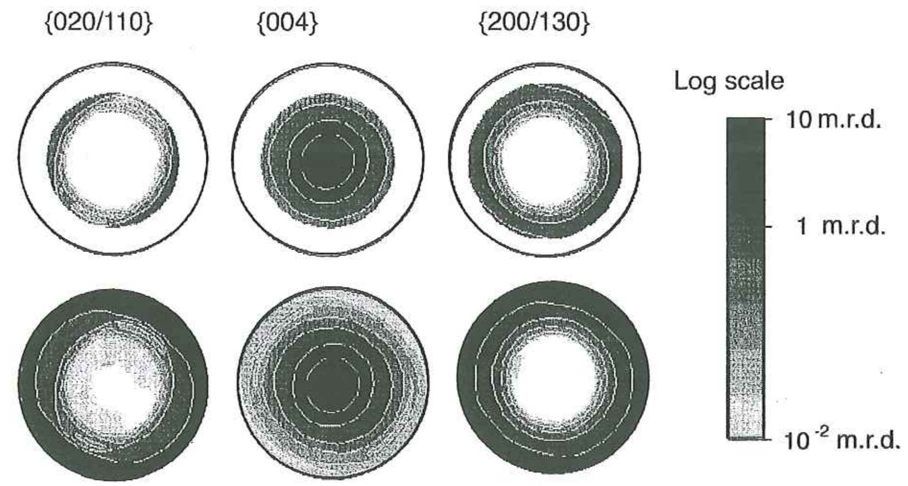

FIG. 6. Normalized, experimental (above) and recalculated (below) pole figures for Co-sorbed hectorite (logarithmic density scale, equal area projection). Note that experimental pole figures are satisfactorily reproduced by the computation.

RESULTS AND INTERPRETATION

Texture Analysis

Normalized experimental and OD-recalculated pole figures are presented in Fig. 6. Pole densities are expressed in multiple of a random distribution (m.r.d.). Experimental and recalculated patterns look similar to each other, with low (i.e., good) reliability factors. Reliability factors for density values above 1 m.r.d. of $RP_1 = 2.3\%$, and for all densities of $RP_0 = 5\%$, were obtained at the end of the refinement. The corresponding weighted factors are $R_{\mathrm{W1}} = 1.4\%$ and $R_{\mathrm{W0}} = 6.1\%$ (26).

Zones of iso-densities form nonconstant rings on the {020/110} pole figure and to some extent on the {200/130} pole figure as well. One would see in such density variations an effect of preferential orientations of **a** and **b** axes in the film plane. However, these irregularities affect only the peripheral part of each pole figure, where the beam may not hit regularly the sample, and are located at the same azimuthal angle for all pole figures. This observation is not consistent with a texture effect for different {*hkl*} reflections; we therefore conclude to a geometrical effect due to a nonregular irradiation of the sample during γ rotation. Thus, it can be concluded that **a** and **b** axes of crystallites are randomly distributed in the film plane. This observation, combined with the high density at the center of the {004} pole figure, indicates that the distribution of crystallites in the thin film is axisymmetrical, or, in other words, that a C_∞ symmetry axis exists perpendicular to the film plane. The presence of this axisymmetry indicates that it is possible to apply Eqs. [4] and [7]–[11]. Manceau *et al.* (26) drew the same conclusion on a self-supporting film of nontronite.

Figure 7a represents the {001} distribution recalculated from the OD. This reflection has a maximum orientation density of 11 m.r.d., which is an indication of a highly textured film, but is lower than the value of 39 m.r.d. reported for a nontronite self-supporting film (26). The difference of texture strength of the two films possibly originates from the greater thickness of the hectorite film (~60 μm) as compared to that of nontronite (~20 μm). The increase in thickness allowed us to increase the intensity of the fluorescence signal during EXAFS acquisition.

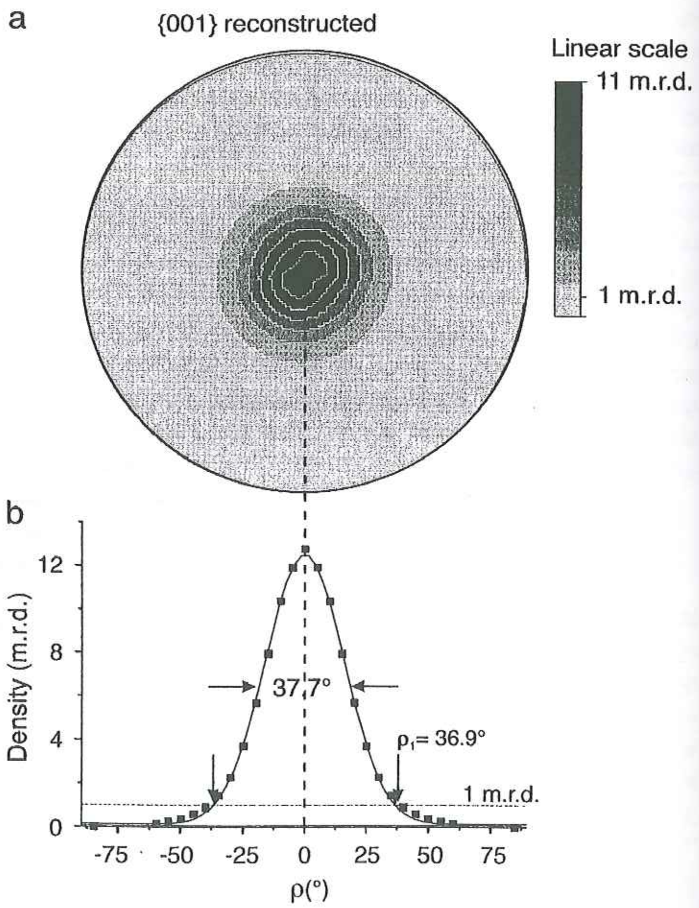

FIG. 7. (a) Recalculated {001} pole figure for hectorite (linear density scale, equal area projection). (b) Integrated ρ scan of the {001} pole figure. The 1 m.r.d. density is represented by an horizontal dashed line and the gaussian fit to the ρ scan by a solid line.

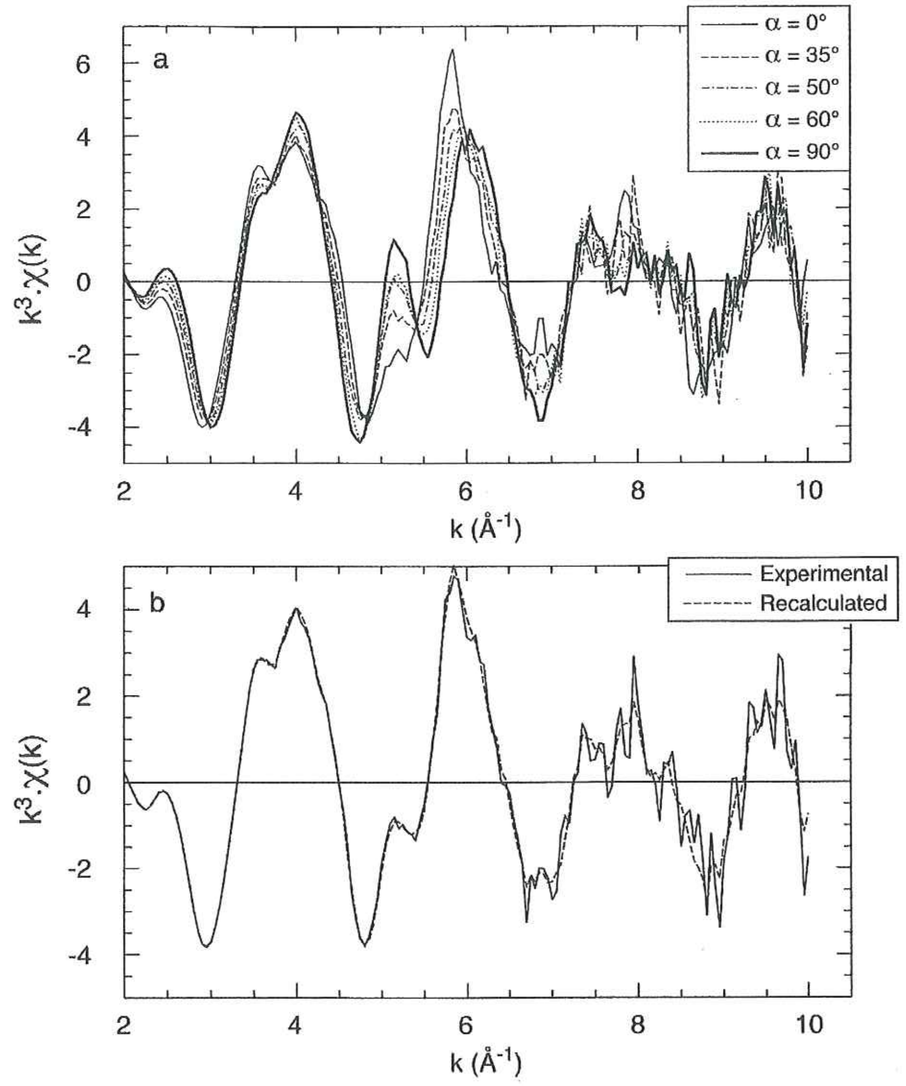

FIG. 8. (a) k^3-weighted Co K-edge EXAFS spectra at α angles of 0°, 35°, 50°, 60°, and 90°. The 90° spectrum has been obtained by regression of the experimental data for $0 \leq \alpha \leq 60°$ and extrapolation to $\alpha = 90°$. (b) Comparison of the experimental (solid line) and extrapolated-recalculated (dashed line) k^3-weighted EXAFS spectra for $\alpha = 35°$.

A ρ-transect of the {001} density distribution was obtained by averaging for each ρ value the normalized densities of the {001} pole figure over all γ angles (Fig. 7b). The dispersion of **c*** axes of individual platelets off the film normal can be quantified by the full width at half maximum (FWHM) of this ρ-transect. Here the FWHM is equal to 37.7°, as compared to 19.8° for Garfield nontronite (26). This lower orientation is expected to diminish slightly the angular dependence of P-EXAFS spectra. The difference between N_j^{app} obtained for an ideal texture (Eq. [10]) and the value obtained for real samples (N_j^{exp}) was calculated by Manceau *et al.* (25) in the case of a step-shaped distribution of **c*** axis symmetrically around the film normal. These calculations showed that for a distribution having a step-shaped width of 40°, $(N_j^{\mathrm{app}} - N_j^{\mathrm{exp}})/N_j^{\mathrm{app}}$ is equal to 11% at $\alpha = 90°$ for $\beta = 33°$, and equals 4% at $\alpha = 0°$ for $\beta = 90°$. Consequently, N_j^{exp} can be considered equal to N_j^{app} as a first approximation.

EXAFS Spectra

The EXAFS spectra recorded at different α angles and the extrapolated spectrum at $\alpha = 90°$ are displayed in Fig. 8a. The quality of the extrapolation procedure was estimated by comparing the experimental spectrum at $\alpha = 35°$, $\chi_{\mathrm{exp}}^{35°}(k)$ to that recalculated from the regression procedure, $\chi_{\mathrm{calc}}^{35°}(k)$ (Fig. 8b). The agreement between these two spectra is very good at low k and decreases at high k, as a result of the increase of the signal to noise ratio. Close examination of Fig. 8b shows that $\chi_{\mathrm{calc}}^{35°}(k)$ is less noisy than $\chi_{\mathrm{exp}}^{35°}(k)$, especially at high k. One can see in this observation an effect of the calculation of $\chi_{\mathrm{calc}}^{35°}(k)$ via linear regression of independent experimental points. This inference can be checked by comparing the uncertainty of the measurements for $\chi^{35°}_{\rm exp}(k)$ ($s^{\alpha}_{\rm exp}(k)$) and for $\chi^{35°}_{\rm calc}(k)$ ($s^{\alpha}_{\rm calc}(k)$) with the assumption that $s^{\alpha}_{\rm exp}(k)$ is independent on α, i.e. that $s_{\rm exp}(k)$ is the same for all experimental spectra; $s_{\rm exp}(k)$ and $s^{\alpha}_{\rm calc}(k)$ are then related by (60)

$$s^{\alpha}_{\rm calc} = s_{\rm exp}(k) \cdot \left[\frac{1}{n} + \frac{(\cos^2\alpha_{\rm calc} - \langle\cos^2\alpha_{\rm exp}\rangle)^2}{\sum_{\alpha_{\rm exp}} (\cos^2\alpha_{\rm exp} - \langle\cos^2\alpha_{\rm exp}\rangle)^2}\right]^{1/2}, \quad [13]$$

where $\alpha_{\rm exp}$ is the experimental angle ($\alpha_{\rm exp} = 0°, 35°, 50°$, and $60°$), n is the number of experimental spectra (here $n = 4$), and $\alpha_{\rm calc}$ is the angle of the calculated spectrum. Application of Eq. [13] results in $s^{35°}_{\rm calc}(k) = 0.52 * s_{\rm exp}(k)$, which means that the recalculated spectrum is theoretically about half as noisy as the experimental one. This calculation compares favorably with the reduction of noise observed for $\chi^{35°}_{\rm calc}(k)$ (Fig. 8b). Furthermore, for $\alpha = 90°$, $s^{90°}_{\rm calc}(k) = 1.14 * s_{\rm exp}(k)$, which suggests that $\chi^{90°}_{\rm calc}(k)$ has a similar signal to noise ratio as the experimental spectra. This result allows us to place confidence in the regression and calculation procedure.

P-EXAFS spectra (Fig. 8a) contain several distinct frequencies having a large amplitude, even at high k. Multiple scattering paths do not have a large amplitude at high k. Hence, the observed multifrequency indicates the presence of several backscattering shells around Co. The position and amplitude of several oscillation maxima vary as a function of α. For example, the maximum centered near 6 Å^{-1} ($\alpha = 0°$) shifts to higher k with increasing α, whereas the opposite trend is observed for the maximum near 4.2 Å^{-1}. These modifications cannot be interpreted by the variation of a hypothetical self-absorption effect with α, as this effect solely modifies the amplitude of $\chi^{\alpha}(k)$ (43, 61), and also because of the low concentration of Co within the sample ($\Delta\mu/\mu < 0.01$). Instead, these angular variations originate from a polarization dependence of the EXAFS contributions. It has been seen in the background section that the amplitude of the contribution of an atomic j shell ($\chi_{\text{Co-}j}$) depends on its β_j angle. Therefore, the occurrence of multiple wave frequencies, together with the polarization dependence of EXAFS spectra, indicate that Co atoms are surrounded by several atomic shells oriented differently with respect to **c***. The angular dependence of EXAFS spectra also suggests that sorbed Co atoms are associated structurally to hectorite platelets.

EXAFS spectra recorded at the magic angle for Co-sorbed hectorite and reference compounds are contrasted in Fig. 9. Co-sorbed hectorite has a markedly different EXAFS spectrum from CoKer and $\rm Co(OH)_{2(s)}$, which points to distinct crystallochemical environments. This simple comparison indicates that sorbed Co did not precipitate as pure $\rm Co(OH)_{2(s)}$ or CoKer, as expected from the careful choice of sorption chemical conditions. Instead, EXAFS spectra of Co-sorbed hectorite and CoMgKer bear strong similarities, which suggests that sorbed Co is located, at least partially, in a Mg clay-like environment.

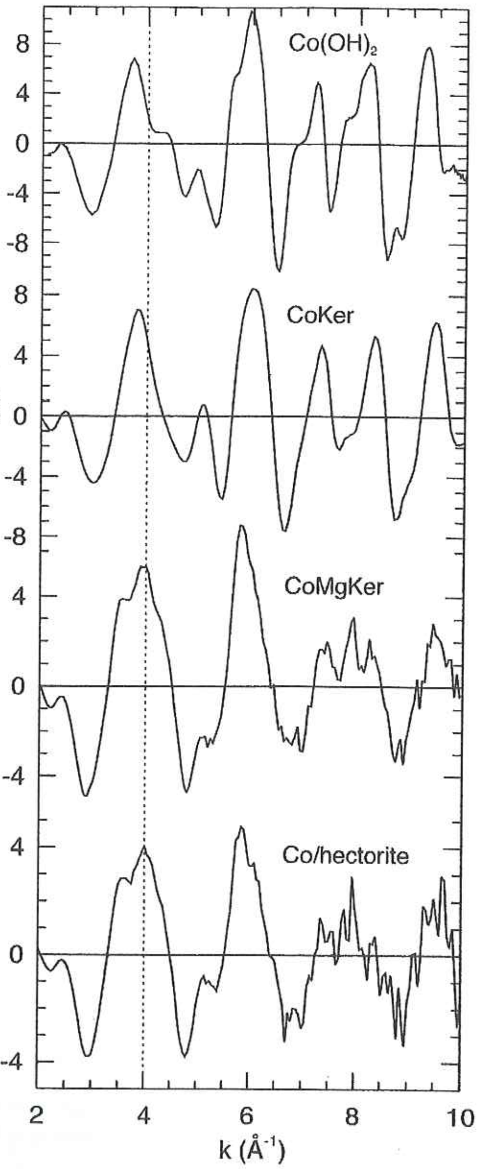

FIG. 9. k^3-weighted Co K-edge EXAFS spectra for $\rm Co(OH)_{2(s)}$, Co-rich kerolite (CoKer), Co-doped Mg-rich kerolite (CoMgKer), and Co-sorbed hectorite. All spectra were recorded at the magic angle.

Radial Structure Functions (RSFs)

RSFs corresponding to the P-EXAFS spectra in Fig. 8a are plotted in Fig. 10. Several intense peaks are observed at $R + \Delta R$ distances of 1.8 Å and 2.7–2.8 Å. These peaks point to the presence of several atomic shells in the vicinity of sorbed Co, which is fully consistent with the occurrence of several wave frequencies noted previously in P-EXAFS spectra. Figure 11 shows that the RSFs of $\rm Co(OH)_{2(s)}$, CoKer, and Co-sorbed hectorite at $\alpha = 35°$ differ by the position and amplitude of their second structural peaks, which confirms that Co has a different structural environment in Co-sorbed hectorite and in these references. A significant difference of amplitude can also be observed between Co-sorbed hectorite and CoMgKer, which suggests that either the number or the nature of neighboring cations are different in these two compounds.

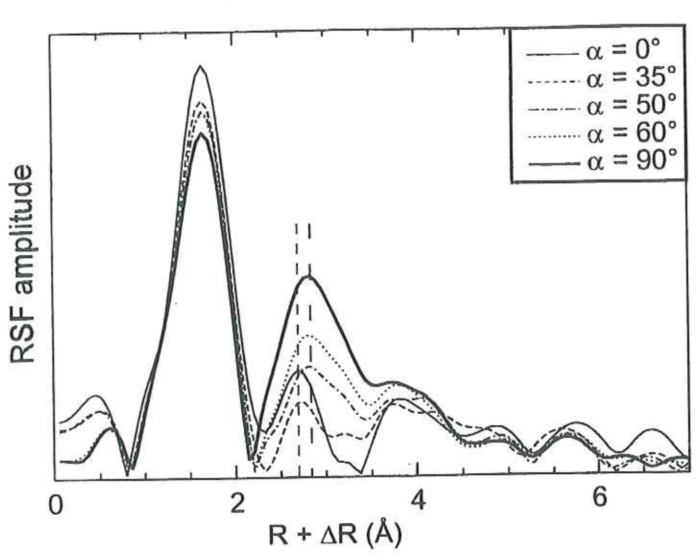

FIG. 10. Polarization dependence of the Co K-edge RSF for Co-sorbed hectorite at α angles of 0°, 35°, 50°, 60° (experimental), and 90° (extrapolated).

First RSF Peak

The first RSF peak at $R + \Delta R = 1.8$ Å corresponds to the contribution of oxygen atoms coordinated to Co. The $R_{\text{Co-O}}$ distance was determined by least-squares fitting the partial EXAFS contribution obtained by Fourier back-transforming this RSF peak. Good fits ($R_{\rm P} \leq 0.006$ for $0° \leq \alpha \leq 60°$, and $R_{\rm P} = 0.010$ for $\alpha = 90°$) were obtained by assuming 5.6 ($\alpha = 0°$) to 4.3 ($\alpha = 90°$) oxygen atoms at $R_{\text{Co-O}} = 2.08$ Å ($\sigma = 0.10$ Å) (Table 2). The uncertainty on $R_{\text{Co-O}}$ and $N_{\rm O}$ resulting from experimental measurements and spectral analysis were estimated at $\alpha = 35°$ by successively varying and fixing these structural parameters during the least-squares fit. A 0.02 Å shift of $R_{\text{Co-O}}$ from its best-fit value, or an increase of $N_{\rm O}$ from 5.1 to 6 (20%), led to a two-time increase of $R_{\rm P}$. However, this estimation procedure does not take into account the possible offset of $R_{\text{Co-O}}$ resulting from the use of theoretical phase shift functions. This $R_{\text{Co-O}}$ offset was previously inferred to 0.01 Å from the analysis of references. Therefore, the experimental uncertainty on $R_{\text{Co-O}}$ and $N_{\rm O}$ are typically ±0.03 Å and ±20%, respectively.

The value of $R_{\text{Co-O}}$ confirms that sorbed Co is divalent and hexacoordinated to oxygen (62), as fourfold coordinated Co or sixfold coordinated Co(III) would have resulted in shorter Co–O distances of 1.9–2.0 Å. It can therefore be concluded that no redox reaction occurred during the sample preparation. The relatively high value of σ ($\sigma = 0.10$ Å), and the low number of detected oxygens ($4.3 \leq \rm N_O \leq 5.6$), in comparison to CoKer and $\rm Co(OH)_{2(s)}$, point to an increase in the dispersion of Co–O bond lengths in the sorption sample. The larger spread of $R_{\text{Co-O}}$ likely results from difference of bond strengths, possibly because oxygens coordinated to Co belong to distinct chemical entities, such as $\rm H_2O$ molecules, OH groups, and oxygens of the sorbent surface. This structural disorder causes a damping of the EXAFS signal, which is not fully compensated by an increase of σ, so that the number of oxygens detected by EXAFS is lower than the actual number coordinated to Co. Since this difference between the detected and the actual number of oxygens is structural in origin, it was not taken into account in the previous estimate of the experimental uncertainty. Therefore, the real uncertainty on $N_{\rm O}$, which sums up the experimental uncertainty and the effects of structural disorder, is probably higher than 20%.

The amplitude of first RSF peaks decreases with increasing α (Fig. 10), and this lowering is reflected in Table 2 by a reduction of $N^{\rm app}_{\rm O}$ from 5.6 at $\alpha = 0°$ to 4.3 at $\alpha = 90°$. As exposed in the background section, the sense of this variation indicates that $\beta_{\rm O} > 54.7°$, i.e. that the coordination octahedron is flattened (26). To quantify this flattening, $\beta_{\rm O}$ has been estimated as follows. First, a linear regression of $N^{\rm app}_{\rm O}$ with respect to $\cos^2\alpha$ was performed for $0° \leq \alpha \leq 60°$ (Fig. 12). Second, $N^{\rm real}_{\rm O} = 5.18$ was calculated from this regression equation at the magic angle $\alpha = 35.3°$. Third, application of Eq.

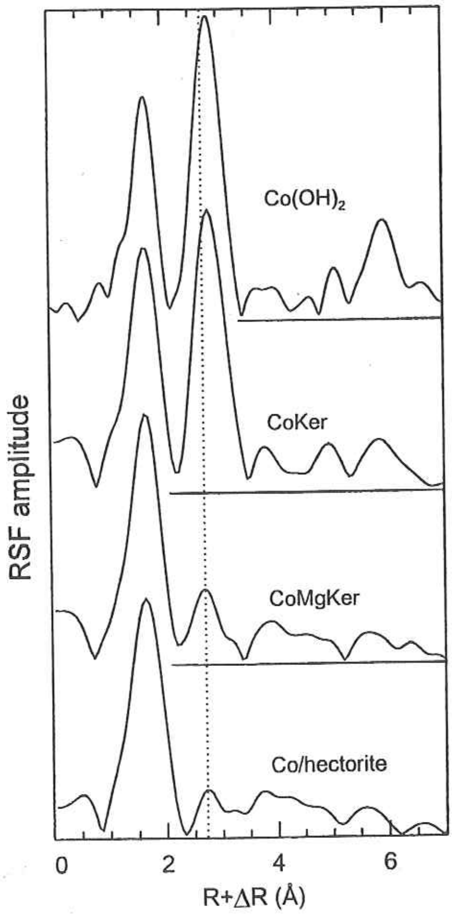

FIG. 11. Co K-edge RSF for $\rm Co(OH)_{2(s)}$, Co-rich kerolite (CoKer), Co-doped Mg-rich kerolite (CoMgKer), and Co-sorbed hectorite.

TABLE 2
Quantitative EXAFS Analysis for Co-Sorbed Hectorite

	First peak					Second peak								
		Co–O shell					Co–Mg shell			Co–Si shell				
α	IFT range[b] (Å)	R (Å)	N_O^{app}	σ (Å)	R_p	IFT range[b] (Å)	R (Å)	N_{Mg}^{app}	σ (Å)	R (Å)	N_{Si}^{app}	σ (Å)	R_P	ΔE_0^a (eV)
0°	0.9–2.2	2.08[c]	5.6	0.10[c]	0.004	2.3–3.3	3.03	2.3	0.10[c]	3.27[c]	0.5	0.11[c]	0.022	−0.1
35°	0.9–2.2	2.08	5.1	0.10	0.002	2.3–3.3	3.03[c]	1.6	0.10[c]	3.27[c]	2.2	0.11[c]	0.015	−0.1
50°	0.9–2.2	2.08[c]	4.9	0.10[c]	0.005	2.2–3.3	3.03[c]	1.1	0.10[c]	3.27[c]	3.6	0.11[c]	0.031	−0.1
60°	0.9–2.2	2.08[c]	4.7	0.10[c]	0.006	2.2–3.4	3.03[c]	0.6	0.10[c]	3.27[c]	4.4	0.11[c]	0.029	−0.1
90°	0.9–2.2	2.08[c]	4.35	0.10[c]	0.010	2.2–3.4				3.27	5.8	0.11	0.029	−0.1

[a] The threshold energy E_0 was taken at the half-height of the absorption edge ($\Delta\mu/2$). ΔE_0 given here for FEFF7.02 theoretical functions.

[b] Ranges for inverse Fourier transforms (IFT) in the real space.

[c] Value held fixed during the fitting procedure.

[11] with $N_O^{real} = 5.18$ yielded $\beta_O^{exp} = 57.9°$. The statistical uncertainty on β_O^{exp} was obtained from the dispersion of N_O^{app} off the regression line (60) and was equal to $\pm 1°$ at the 95.5% confidence level. As discussed in the background section, the real β_O value (β_O^{real}) is probably slightly higher than the experimental β_O^{exp} value, because of the disorientation of individual platelets off the film plane. Nevertheless, β_O^{exp} compares well with β_O for edge-sharing octahedra in Co-substituted synthetic mica (~58.2° (63)).

Second RSF Peak

The high amplitude of the RSF peak near $R + \Delta R = 2.7$–2.8 Å for $\alpha = 0°$ and 90° suggests that it originates from the contribution of nearest cationic shells, which may consist of either Co, Si, or Mg. This peak displays a complex angular dependence, decreasing from $\alpha = 0°$ to $\alpha = 35°$, and then increasing from $\alpha = 35°$ to $\alpha = 90°$. Meantime, its maximum shifts from $R + \Delta R = 2.7$ Å to 2.8 Å as α increases. If this peak arised from a *single* atomic shell contribution, then its position would be invariant with α (Eq. [8]). Therefore, the shift in position with α indicates that this peak is made of the contributions of at least two atomic subshells, consisting either of chemically identical atoms located at different distances from Co, or of chemically different atoms. Furthermore, this angular effect can only be observed if the contribution of one subshell predominates at $\alpha = 0°$ and the other at $\alpha = 90°$, i.e., if these two subshells have different β_j angles.

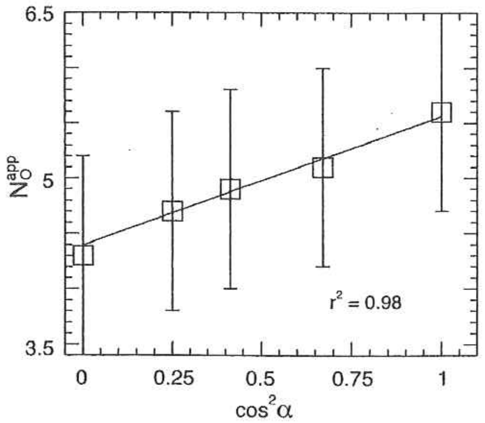

FIG. 12. Angular dependence of the apparent number of oxygen neighbors (N_O^{app}) for Co-sorbed hectorite. Squares: experimental data. Linear regression of experimental data (solid line) for $0 \leq \alpha \leq 60°$ yielded $N_O^{app} = 1.17{*}\cos^2\alpha + 4.39$.

Back-Fourier transforms of second RSF peaks for $\alpha = 0°$, 35°, and 90° are contrasted in Fig. 13a. Of significance is the presence of isosbestic points, for which χ_{ij}^{P} is independent of α. These points are much sensitive to defaults in spectral normalization, and their observation over the entire k-span attests for the reliability of the data analysis. This reliability can be further assessed by comparing the experimental $\chi_{2nd\ peak}^{35°}$ contribution to that recalculated from $\chi_{2nd\ peak}^{0°}$ and $\chi_{2nd\ peak}^{90°}$ by the theoretical expression derived from Eq. [4],

$$\chi_{2nd\ peak}^{35°} = \tfrac{2}{3} \cdot \chi_{2nd\ peak}^{0°} + \tfrac{1}{3} \cdot \chi_{2nd\ peak}^{90°}. \qquad [14]$$

Figure 13b shows that experimental and recalculated $\chi_{2nd\ peak}^{35°}$ are hardly distinguishable. This very good quantitative agreement ($R_P = 8 \times 10^{-3}$) deserves to be emphasized and denotes the fair precision of measurements in the $3 \leq k \leq 10$ Å^{-1} interval.

Chemical nature of the predominant contributions at $\alpha = 0°$ and 90°. That the second shell contains at least two subshells whose contributions alternatively predominate at $\alpha = 0°$ and $\alpha = 90°$ has been shown in the previous section. The simplest hypothesis consists of assuming that this second shell comprises *only* two subshells, denoted M1 and M2. According to Eq. [5], the EXAFS contribution of M1 and M2 can be written as a damped sinusoid with a frequency that depends on the absorber-backscatterer distance ($2kR_{ij}$ term), and on the chemical nature of the backscatterer (ϕ_{ij} term). Therefore, the phase difference between the $\chi_{Co\text{-}M1}(k)$ and $\chi_{Co\text{-}M2}(k)$ waves is given by

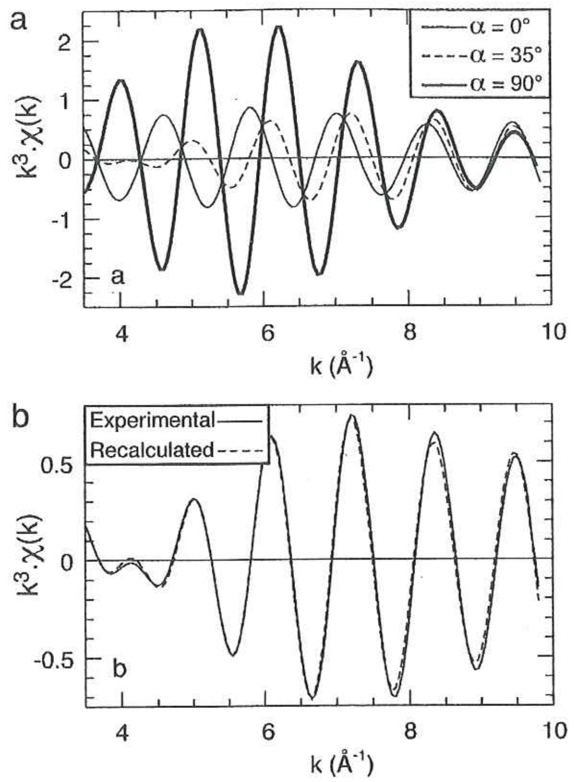

FIG. 13. Fourier-filtered EXAFS spectra of the second shell ($\chi_{2nd\ shell}(k)$) for Co-sorbed hectorite. (a) Comparison of $\chi_{2nd\ shell}(k)$ for $\alpha = 0°$, 35°, and 90°. (b) Comparison of the experimental $\chi_{2nd\ peak}^{35°}$ contribution (solid line) and the $\chi_{2nd\ peak}^{35°}$ contribution recalculated from $\chi_{2nd\ peak}^{0°}$ and $\chi_{2nd\ peak}^{90°}$ (dashed line).

$$\begin{aligned}\Delta\varphi(k) &= \varphi_{M2}(k) - \varphi_{M1}(k)\\ &= 2k(R_{Co\text{-}M2} - R_{Co\text{-}M1})\\ &\quad + (\phi_{Co\text{-}M2}(k) - \phi_{Co\text{-}M1}(k)); \qquad [15]\end{aligned}$$

$\Delta\varphi$ can be estimated experimentally by supposing that $\chi_{2nd\ peak}^{0°}$ contains only the contribution of M1 and $\chi_{2nd\ peak}^{90°}$ contains only the contribution of M2, so that $\Delta\varphi$ is simply the phase difference between $\chi_{2nd\ peak}^{0°}$ and $\chi_{2nd\ peak}^{90°}$. This phase difference can be read out on Fig. 13a and equals π at $k = 4$ Å^{-1}, and 2π at $k = 9.5$ Å^{-1}. In the following, M1 and M2 will be identified by their ability to verify Eq. [15] at $k = 4$ and 9.5 Å^{-1}.

Let us first assume that $R_{Co\text{-}M2} = R_{Co\text{-}M1}$ and that the two subshells are chemically different. Equation [15] then reduces to $\Delta\varphi(k) = \phi_{Co\text{-}M2}(k) - \phi_{Co\text{-}M1}(k)$. Theoretical $\Delta\varphi$ functions corresponding to the various combinations of possible M1 and M2 subshells were obtained from $\phi_{Co\text{-}Co}(k)$, $\phi_{Co\text{-}Mg}(k)$ and $\phi_{Co\text{-}Si}(k)$ phase shift functions (Fig. 14a) computed with FEFF7.02. Examination of Fig. 14b shows that none of the $\Delta\varphi$ functions verify $\Delta\varphi = \pi$ at $k = 4$ Å^{-1} and $\Delta\varphi = 2\pi$ at $k = 9.5$ Å^{-1}. Therefore, this hypothesis should be ruled out.

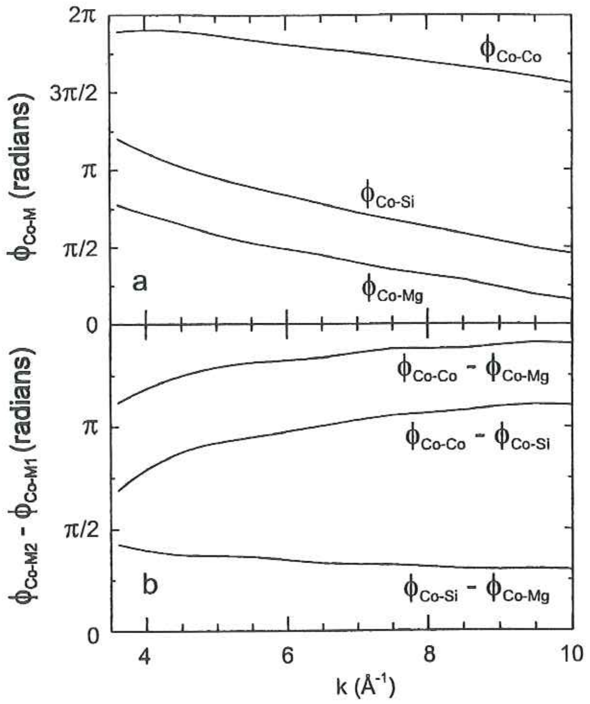

FIG. 14. FEFF7.02 calculated phase shift functions for Co–Co, Co–Si, and Co–Mg pairs and interatomic distances of 3.10 Å. (a) Plot of the phase shift functions. (b) Plot of the difference of phase ($\Delta\varphi$) for various combinations of atomic pairs.

Let us then assume that the two subshells are chemically different and that $R_{Co\text{-}M2} \neq R_{Co\text{-}M1}$. Equation [15] can then be rewritten

$$R_{M2} - R_{M1} = \frac{\Delta\varphi - (\phi_{Co\text{-}M2}(k) - \phi_{Co\text{-}M1}(k))}{2k}. \qquad [16]$$

$R_{M2} - R_{M1}$ values calculated for the different combinations of atomic pairs are listed in Table 3 for $k = 4$ and 9.5 Å^{-1}. There is no atomic pair for which $R_{M2} - R_{M1}$ is completely indepen-

TABLE 3
Calculated Differences of Distance between M1 and M2 Subshells at $k = 4$ and 9.5 Å^{-1} and for Different Combinations of M1 and M2 Subshells

M1	M2	$(R_{M2} - R_{M1})$ for $k = 4$ Å^{-1}	$(R_{M2} - R_{M1})$ for $k = 9.5$ Å^{-1}	$\Delta(R_{M2} - R_{M1})^a$ (Å)
Co	Mg	0.85	0.56	−0.29
Co	Si	0.70	0.51	−0.19
Si	Co	0.08	0.15	0.07
Si	Mg	0.54	0.38	−0.16
Mg	Co	−0.07	0.09	0.16
Mg	Si	0.24	0.28	0.04

[a] Calculated as follows: $\Delta(R_{M2} - R_{M1}) = (R_{M2} - R_{M1})_{k=9.5Å^{-1}} - (R_{M2} - R_{M1})_{k=4Å^{-1}}$.

dent of k. This suggests that at least one of the $\chi^{0^\circ}_{\mathrm{2nd\ peak}}$ or $\chi^{90^\circ}_{\mathrm{2nd\ peak}}$ functions does not originate from a single subshell. The smallest variation of $R_{\mathrm{M2}} - R_{\mathrm{M1}}$ from $k = 4$ to $k = 9.5$ Å^{-1} corresponds to M1 = Mg and M2 = Si (Table 3). All other combinations of atomic pairs (including pairs of chemically identical atoms) result in variations of $R_{\mathrm{M2}} - R_{\mathrm{M1}}$ at least 1.5 times larger. Therefore, this preliminary analysis suggests that predominant backscatterers are Mg at 0° and Si at 90°. The sign of $R_{\mathrm{Si}} - R_{\mathrm{Mg}}$ indicates that the Si subshell is more distant from Co than the Mg one. The exact nature of the atomic contributions contained in $\chi^{0^\circ}_{\mathrm{2nd\ peak}}$ and $\chi^{90^\circ}_{\mathrm{2nd\ peak}}$ will be identified below.

Quantitative analysis. At first, $\chi^{\alpha}_{\mathrm{2nd\ peak}}(k)$ functions were tentatively fitted by assuming only Mg backscatterers at $\alpha = 0°$ and Si backscatterers at $\alpha = 90°$. Only three parameters (N, R, and σ) were allowed to vary for each shell. This single shell analysis yielded a good fit at $\alpha = 90°$ ($R_{\mathrm{P}} = 0.029$), with $N^{\mathrm{app}}_{\mathrm{Si}} = 5.8$ and $R_{\mathrm{Co\text{-}Si}} = 3.27$ Å ($\sigma_{\mathrm{Si}} = 0.11$ Å). The agreement was not as good at $\alpha = 0°$ ($R_{\mathrm{P}} = 0.059$), and a two-shell fit was therefore performed with Mg and Si neighbors, by fixing σ_{Si} and $R_{\mathrm{Co\text{-}Si}}$ to their value at $\alpha = 90°$. A good agreement ($R_{\mathrm{P}} = 0.022$) was obtained with $N^{\mathrm{app}}_{\mathrm{Si}} = 0.5$, $N^{\mathrm{app}}_{\mathrm{Mg}} = 2.3$, and $R_{\mathrm{Co\text{-}Mg}} = 3.03$ Å ($\sigma_{\mathrm{Mg}} = 0.10$ Å) (Fig. 15 and Table 2). Finally, $\chi^{\alpha}_{\mathrm{2nd\ peak}}(k)$ for $35° \leq \alpha \leq 60°$ were fitted by varying only $N^{\mathrm{app}}_{\mathrm{Mg}}$ and $N^{\mathrm{app}}_{\mathrm{Si}}$ and fixing σ and R identical to their value at $\alpha = 0°$ and 90° (Fig. 15). The experimental uncertainty on the structural parameters was estimated at $\alpha = 35°$ by varying and fixing successively $R_{\mathrm{Co\text{-}Si}}$, $R_{\mathrm{Co\text{-}Mg}}$, N_{Mg}, and N_{Si}. This procedure showed that the figure of merit, R_{P}, increased from 0.015 to 0.022 and that the spectral fit was visually substantially degraded as N_{Mg} was varied from 1.6 to 2, or from 1.6 to 1.3. Thus, the estimated uncertainty on $N^{\mathrm{app}}_{\mathrm{Mg}}$ resulting from experimental data collection and analysis is ±0.4 (i.e., 25% of $N^{\mathrm{app}}_{\mathrm{Mg}}$). Application of the same procedure to the other adjusted parameters yielded an estimated experimental uncertainty on $N^{\mathrm{app}}_{\mathrm{Si}}$ of ±0.5 and on (R_{Mg}, R_{Si}) of ±0.02 Å. A small $\chi_{\mathrm{Co\text{-}Co}}$ component was also introduced during the fit to detect the possible presence of Co polynuclear complexes. The quality of the fit was significantly altered upon the introduction of a Co content as low as 0.1 ($\sigma = 0.11$ Å), leading to an increase of R_{P} from 0.015 to 0.020, and a shift to high k of the maximum of the $\chi(k)$ envelope (data not shown). This shift can be accounted for by observing that the amplitude of $\chi_{\mathrm{Co\text{-}Co}}(k)$ (Fig. 15, $Co(OH)_{2(s)}$ reference) peaks at 7–8 Å^{-1}, whereas the amplitude of $\chi^{\alpha}_{\mathrm{2nd\ peak}}(k)$ peaks at 6 Å^{-1} for Co-sorbed hectorite. Therefore, $N_{\mathrm{Co}} = 0.1$ can be taken as an upper limit, which indicates that less than 10% of sorbed Co is present as dimers, or less than 1.8% as a Co precipitate.

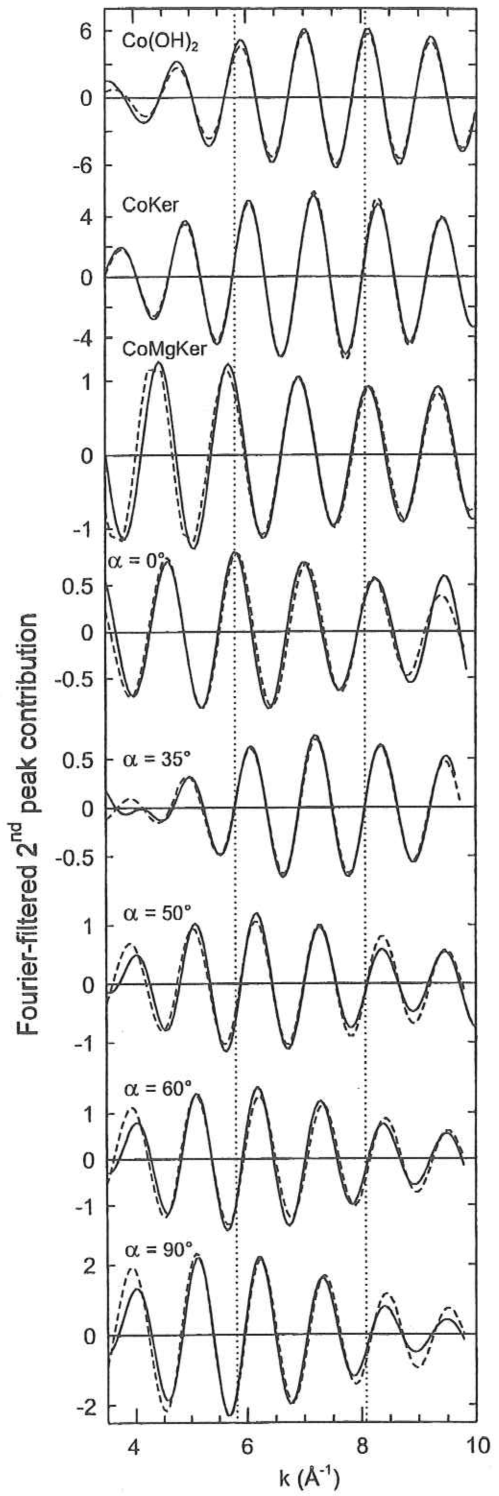

FIG. 15. Comparison between experimental and modeled $\chi_{\mathrm{2nd\ shell}}(k)$ contributions for $Co(OH)_{2(s)}$, Co-rich kerolite (CoKer), Co-doped Mg-rich kerolite (CoMgKer), and Co-sorbed hectorite from $\alpha = 0°$ to $\alpha = 90°$.

Relatively high σ values ($\sigma = 0.10–0.11$ Å) were required to fit $\chi^{\alpha}_{\mathrm{2nd\ peak}}(k)$ for Co-sorbed hectorite, as compared to reference compounds ($\sigma = 0.09–0.10$ Å). As previously discussed for the oxygen shell, these high σ values are symptomatic of a significant dispersion of interatomic distances, and EXAFS may not be sensitive to their full distribution, yielding a lower number of detected backscatterers than actually present. Since this loss of atomic neighbors is of structural origin, it should be added to the uncertainty coming from data collection and analysis. The total uncertainty on $N^{\mathrm{app}}_{\mathrm{Mg}}$ and $N^{\mathrm{app}}_{\mathrm{Si}}$ are thus probably higher than 25%.

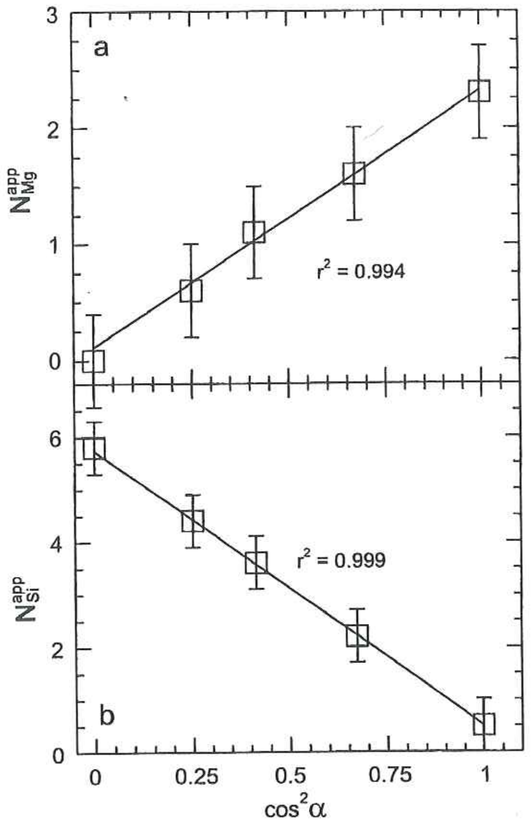

FIG. 16. Angular dependence of the apparent number of nearest Mg ($N^{\mathrm{app}}_{\mathrm{Mg}}$) (a) and Si ($N^{\mathrm{app}}_{\mathrm{Si}}$) (b) atoms for Co-sorbed hectorite. Squares: experimental data. Linear regression of experimental data for $0 \leq \alpha \leq 60°$ (solid lines) yielded $N^{\mathrm{app}}_{\mathrm{Mg}} = 2.21{*}\cos^2\alpha + 0.11$ and $N^{\mathrm{app}}_{\mathrm{Si}} = -5.22{*}\cos^2\alpha + 5.72$.

$N^{\mathrm{app}}_{\mathrm{Mg}}$ and $N^{\mathrm{app}}_{\mathrm{Si}}$ are plotted in Fig. 16 as a function of $\cos^2\alpha$. Good linear correlations between N^{app} and $\cos^2\alpha$ are found for the two subshells, with regression coefficients $r^2 > 0.99$. $\beta^{\mathrm{exp}}_{\mathrm{Mg}}$ and $\beta^{\mathrm{exp}}_{\mathrm{Si}}$ were calculated in the same way as $\beta^{\mathrm{exp}}_{\mathrm{O}}$, and the uncertainty on $\beta^{\mathrm{exp}}_{\mathrm{Mg}}$ and $\beta^{\mathrm{exp}}_{\mathrm{Si}}$ were estimated from the dispersion of $N^{\mathrm{app}}_{\mathrm{Mg}}$ and $N^{\mathrm{app}}_{\mathrm{Si}}$ off the regression lines. This calculation yielded $\beta^{\mathrm{exp}}_{\mathrm{Mg}} = 80.1 \pm 10.2°$, and $\beta^{\mathrm{exp}}_{\mathrm{Si}} = 22.2° \pm 1.4°$. Consequently, Co–Mg pairs are, to the precision of the method, parallel to the film plane, whereas Co–Si pairs are inclined by ~20° off the normal to this plane.

DISCUSSION

Mechanism of Co Sorption

P-EXAFS showed that the structural environment of Co atoms sorbed on hectorite is highly anisotropic. This structural anisotropy concerns the coordination octahedron of Co, which is flattened, and the second shell, made of in-plane Mg and out-of-plane Si atoms located at $R_{\mathrm{Co\text{-}Mg}} = 3.03$ Å and $R_{\mathrm{Co\text{-}Si}} = 3.27$ Å. This structural information will serve to determine the sorption mechanism(s) of Co among the several ones that are consistent with the structural association between the sorbate and the sorbent: (a) outer-sphere surface adsorption, (b) inner-sphere surface adsorption, (c) surface precipitation of $Co(OH)_{2(s)}$ or of phyllosilicate-like compounds, and (d) diffusion within octahedral vacancies of hectorite (64).

In an outer-sphere adsorption mechanism, the sorbate is held in the vicinity of the sorbent surface without loosing its hydration shell. Neighboring cations from the sorbent are then relegated at distances higher than ~4 Å (65, 66). In the present study, the occurrence of cationic shells at 3.0–3.3 Å is not compatible with the exclusive formation of outer-sphere Co complexes.

The formation of inner-sphere surface complexes involves the creation of chemical bonds between the sorbate and the surface oxygens of the sorbent. Surface cations of the sorbent thus enter the second coordination sphere of the sorbate. If this next-nearest coordination sphere contains only cations from the sorbent, then adsorbed species are isolated on the sorbent surface and form mononuclear surface complexes (67). Here, only Mg and Si shells were detected at 3.03 and 3.27 Å, suggesting that Co form mononuclear inner-sphere surface complexes.

Polymerization of the sorbate in the vicinity of an inner-sphere surface complex may lead to the precipitation of a pure hydroxide phase, or a mixed one if dissolved species from the sorbent phase are incorporated in the precipitate (21). In the present study, this surface precipitate would be either $Co(OH)_{2(s)}$ or a neoformed (Co, Mg) hydrous silicate. Results from the quantitative spectral analysis, and the dissimilarity of EXAFS spectra for Co-sorbed hectorite, $Co(OH)_{2(s)}$ and CoKer (Fig. 9) suggest that no CoKer or $Co(OH)_{2(s)}$ did precipitate. The neoformation of a CoMgKer-like phase seems more possible, as EXAFS spectra for the sorption sample and CoMgKer are similar. However, these two compounds clearly have different $\chi_{\mathrm{2nd\ peak}}(k)$ functions (Fig. 15), which indicates that Co do not have the same structural environments. Furthermore, if Co sorption resulted in the neoformation of a CoMgKer-like phase, then the amount of dissolved Mg would be expected to decrease, or its release rate by hectorite would be at least significantly slowed down shortly after Co introduction in the suspension. Instead, chemical experiments (68) showed that the release rate of Mg dramatically increases. Compelling neoformation of a (Co, Mg) hydrous silicate can thus be rejected.

Following its adsorption, the sorbed cation may also diffuse to vacant sites of the sorbent. For example, in dioctahedral smectites, where one third of octahedral sites are vacant, Ni(II) was shown to diffuse within empty sites upon heating at 150°C (8). The proportion of vacant sites is not known in hectorite, but it can be taken to 1% as in trioctahedral magnesian stevensites (69) which are isostructural to hectorite. For 1% of vacant sites, the amount of vacancies equals ~80 μmol g^{-1}, which is clearly higher than the amount of sorbed Co (37 μmol g^{-1}). Co diffused into vacant octahedra would be surrounded by 6 (Mg, Li) octahedral neighbors (N_{oct}) and 4 Si tetrahedral neighbors (N_{tet}), leading to a $N_{\mathrm{oct}}/N_{\mathrm{tet}}$ ratio of 1.5. In the sorption sample, $N_{\mathrm{tet}} = N_{\mathrm{Si}} = 2.2 \pm 0.5$, but N_{oct} is probably higher than N_{Mg}, because structural Li atoms are too light to contribute to the EXAFS signal. Assuming a random distribution of Li in the octahedral sheet, N_{oct} can be calculated from the stoichiometric composition of hectorite and is equal to $N^{*}_{\mathrm{Mg}}(3/2.65) = 1.8 \pm 0.45$ for the sorption sample. $N_{\mathrm{oct}}/N_{\mathrm{tet}}$ is thus equal to 0.8 ± 0.3, which is significantly different from the 1.5 expected if Co were in octahedral vacancies. This $N_{\mathrm{oct}}/N_{\mathrm{tet}}$ value is also not consistent with a mixing of Co outer-sphere complexes and Co in vacancy sites. This discussion on the different possible sorption mechanisms of Co allows us to conclude that Co form inner-sphere mononuclear complexes at the surface of hectorite.

Location of Inner-Sphere Surface Complexes

Angular P-EXAFS measurements indicated that Co–Mg pairs are parallel to the plane of the hectorite film, whereas Co–Si pairs are inclined by ~70° from this plane. Since texture analysis showed that (Mg, Li) octahedral sheets are parallel to the film plane, then the only possible location for Co surface complexes is at the edges of hectorite platelets, in the prolongation of the octahedral sheet.

This conclusion is further supported by structural parameters derived from the quantitative analysis of EXAFS spectra. The $R_{\mathrm{Co\text{–}Mg}}$ and $R_{\mathrm{Co\text{–}Si}}$ distances of 3.03 and 3.27 Å are very close to the structural distances $d_{(\mathrm{Mg,Li})\text{–}(\mathrm{Mg,Li})} = 3.03$ Å and $d_{(\mathrm{Mg,Li})\text{–}\mathrm{Si}} = 3.23$ Å for hectorite (54, 55). In addition, $\beta^{\mathrm{exp}}_{\mathrm{Mg}} \sim 80°$ and $\beta^{\mathrm{exp}}_{\mathrm{Si}} \sim 22°$ compare well with crystallographic β values for Mg–Mg ($\beta_{\mathrm{Mg}} = 90°$) and Mg–Si ($\beta_{\mathrm{Si}} \sim 30°$) pairs in hectorite. These similarities in distance and angle between surface Co and structural Mg indicate that these two atoms have similar (but not identical) structural environments. Based on these results, it is concluded that Co octahedra are located on the edges of hectorite platelets and share one or several edges with structural (Mg, Li) octahedra (E-type linkage) and one or several corners with Si tetrahedra (C-type linkage), like in a clay structure.

Structure of Co Surface Complexes on Hectorite

Surface Structure of Platelet Edges

Electron microphotography indicated that hectorite crystallites have a lath-type morphology and are elongated along the a direction (54, 70). The large (001) basal planes are bounded predominantly by (010) planes (90%), and, to a lesser extent, by (110), (120), and (100) planes. How the atomic structure of these boundary planes can be modeled from the crystal structure of hectorite will be developed for the (010) layer edge.

Idealized pristine surfaces can be obtained by truncating the hectorite bulk structure along planes perpendicular to the (001) surface and then by completing the broken coordination polyhedra with oxygens. For energetic reasons, truncation planes having the minimum number of broken Me–O–Me bonds (Me = Si or Mg) are likely favored. Two different surface configurations are obtained (Fig. 17): B1, in which surface oxygens of the octahedral sheet are uniquely coordinated to Mg, and B2, which is depleted in surficial Mg in comparison to B1, so that half of surface oxygens coordinated to Mg are also coordinated to Si.

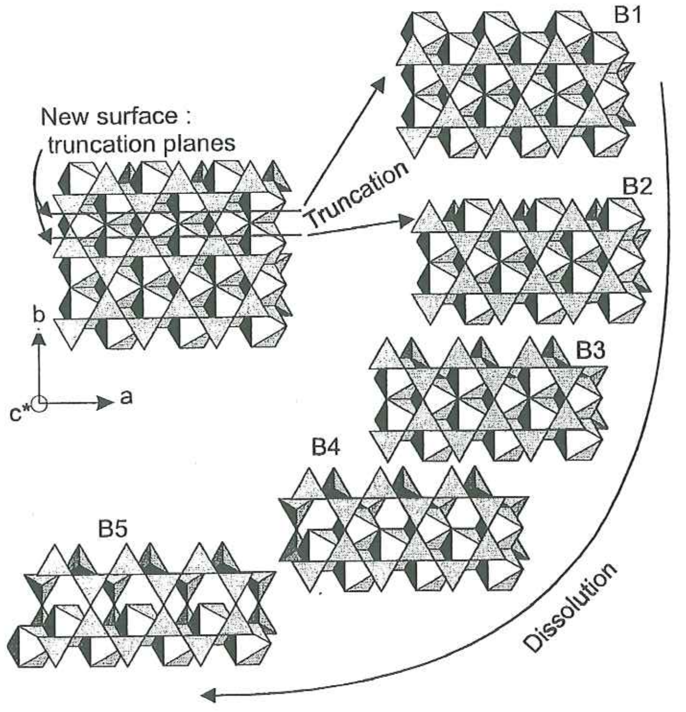

FIG. 17. Modeled formation of possible (010) layer edges from the bulk structure of hectorite. B1–B2 morphologies are obtained by truncation of the bulk structure, and B2–B5 are obtained by a progressive leaching of Mg.

These pristine surfaces can be altered by noncongruent dissolution, as dissolution takes place at layer edges. For example, chemical and microscopic studies on the dissolution of biotite in acidic conditions pointed to a rapid depletion of octahedral cations, leading eventually to the formation of amorphous silica fringes at layer edges (71). Preferential leaching of Mg was also observed for hectorite under slightly acidic conditions, but no silica fringes were identified (72). This preferential leaching can be modeled by deleting successive Mg rows at layer edges while leaving the tetrahedral sheets unaffected (Fig. 17). Obviously, most protruding Mg will be more easily removed, so that the B1 configuration is not expected to exist at pH ~6.5. But the absence of detected silica fringes on hectorite precludes an extensive depletion of surface Mg atoms. Finally, it can be assumed that layer edges have ideally a B2 surface structure in some places, and a more Mg-depleted structure elsewhere (B3 to B5). Figure 18 represents such an idealized surface structure for the (010) edge, which will be used in the following for modeling the structure of Co surface complexes.

Structure of Surface Complexes on a (010) Edge

Several types of surface complexes may exist for each surface configuration. These complexes differ from each other by the number of E and C linkages, i.e., by the number of next-nearest cations from the octahedral and the tetrahedral sheets. For example, in the B2 configuration, adsorbed Co can form 3E and 2C linkages, or 1E and no C linkages (Fig. 19). These surface complexes will be denoted $S^{(010),\mathrm{B2}}_{3\mathrm{E}+2\mathrm{C}}$ and $S^{(010),\mathrm{B2}}_{1\mathrm{E}+0\mathrm{C}}$, respectively, where (010) is the plane index, B2 is the configuration index, and the subscript refers to the number of E and C linkages. For these two surface complexes, the number of E linkages exceeds that of C linkages by one, and therefore these complexes cannot account alone for experimental $N_{\mathrm{oct}} = 1.8 \pm 0.45$ and $N_{\mathrm{tet}} = 2.2 \pm 0.5$ values.

In the B3 surface configuration, sorbed Co can be bridged to either 3 (Mg, Li) and 4 Si ($\mathrm{S}^{(010),\mathrm{B3}}_{3\mathrm{E}+4\mathrm{C}}$), or to 1 (Mg, Li) and 2 Si ($\mathrm{S}^{(010),\mathrm{B3}}_{1\mathrm{E}+2\mathrm{C}}$) (Fig. 18). Assuming the formation of these two surface complexes only, with relative fractions x and y, respectively, the following set of equations is obtained:

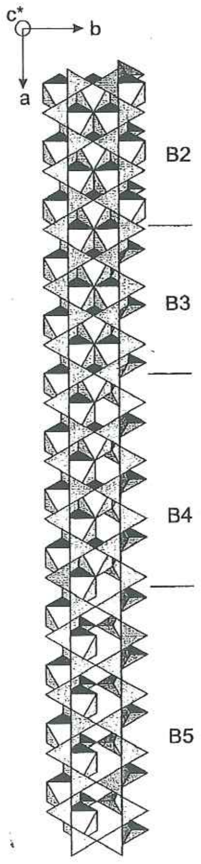

FIG. 18. Idealized (010) surface structure for hectorite projected along the c* direction.

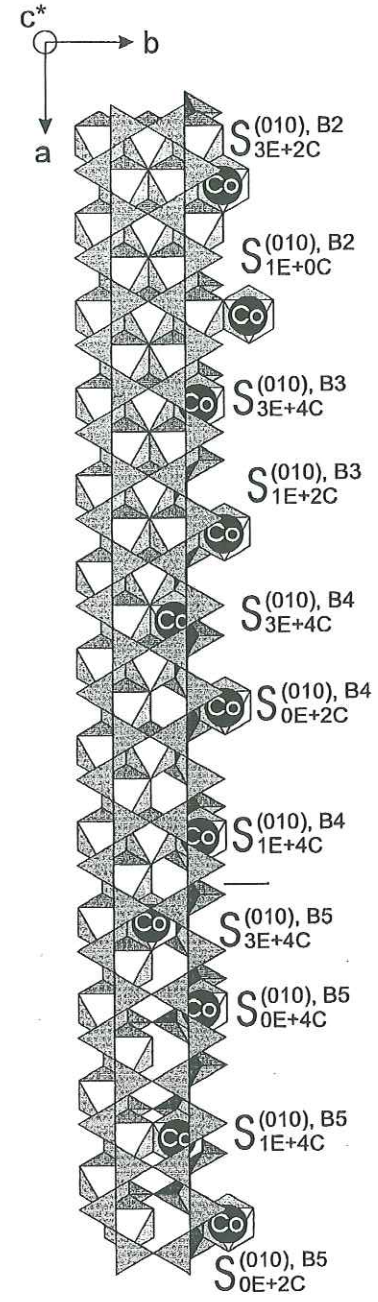

FIG. 19. Possible structure of mononuclear Co surface complexes on the (010) surface of hectorite. Co atoms are located in the plane of the (Mg, Li) octahedral sheet.

$$x + y = 1 \tag{17}$$

$$3x + y = N_{\mathrm{oct}} \pm 0.45 \tag{18}$$

$$4x + 2y = N_{\mathrm{tet}} \pm 0.5. \tag{19}$$

Expressing y as a function of x in Eq. [17] and substituting y for x in Eqs. [18] and [19] yields $x = 0.4 \pm 0.2$ (Eq. [18]) and $x = 0.1 \pm 0.25$ (Eq. [19]). Thus, x is comprised between 0.2 and 0.35, which means that, in this surface configuration,

$S^{(010),B3}_{3E+4C}$ and $S^{(010),B3}_{1E+2C}$ surface complexes would represent 20–35% and 65–80% of sorbed Co, respectively.

Three and four surface complexes may exist in B4 and B5 configurations, respectively: $S^{(010),B4}_{3E+4C}$, $S^{(010),B4}_{0E+2C}$, $S^{(010),B4}_{1E+4C}$, $S^{(010),B5}_{3E+4C}$, $S^{(010),B5}_{0E+4C}$, $S^{(010),B5}_{1E+4C}$, and $S^{(010),B5}_{0E+2C}$. None of these surface complexes can account alone for N_{oct} and N_{tet} values. Indeed, several types of surface complexes, possibly from different surface configurations (e.g., $S^{(010),B2}_{3E+2C}$, $S^{(010),B4}_{0E+2C}$, and $S^{(010),B5}_{1E+4C}$) are needed simultaneously to reproduce EXAFS results.

That EXAFS analysis yielded higher σ and lower N_O values for the sorption sample than for the references can now be explained by the coexistence of several types of surface complexes. Each type of surface complex differs from the others by N_{oct}, N_{tet}, and by the number of sorbent oxygens of the surface coordinated to Co. Therefore, Co–O bond strengths are expected to be scattered, which would eventually result in a slight dispersion of interatomic distances by some thousandths of Å. This dispersion provides a plausible explanation to the observed structural disorder.

Comparison with Previous EXAFS Studies

EXAFS results for Co sorbed on hectorite at moderate pH (pH 6.5) and surface coverage ($\Gamma = 0.32\ \mu\text{mol g}^{-1}$) suggest that the percentage of Co–Co pairs is at most 10%, or that less than 2% of Co can be embedded in large polynuclear Co complexes. Mononuclear Co complexes were also observed on rutile for moderate chemical conditions (pH 5.9, $\Gamma = 0.62\ \mu\text{mol g}^{-1}$). At higher pH (pH >6.7) and surface coverage ($\Gamma > 0.63\ \mu\text{mol g}^{-1}$) the formation of polynuclear Co complexes was reported for quartz (20, 73), kaolinite (66), alumina (65), and montmorillonite (9). In some studies these polynuclear complexes corresponded to mixed precipitates, having incorporated chemical species from the sorbent phase. For example, Towle *et al.* (65) suggested that Co sorption in an alumina suspension resulted in the formation of a Co–Al mixed hydroxide. Similarly, sorption of Co on quartz was shown to result in the neoformation of a Co-rich hydrous phyllosilicate (21). That no such precipitation did occur in the present study can be ascribed to the careful choice and control of chemical conditions throughout the whole sorption experiment.

CONCLUDING REMARKS

This study has demonstrated the potential of P-EXAFS for elucidating the geometrical arrangement of cations sorbed on clay minerals. Carefully controlled chemical conditions, and the elaboration of well-textured self-supporting films, are prerequisites to the successful application of this new method. In the present study, high ionic strength ($I = 0.3$ M) was chosen to favor pH-dependent sorption over cation-exchange adsorption, and a moderate pH of 6.5 allowed hindering the formation of polynuclear Co complexes as reported in previous studies.

P-EXAFS results indicate that, in the conditions of our experiments, Co form inner-sphere mononuclear surface complexes and are surrounded by two next-nearest cationic shells which are oriented differently with respect to the clay basal plane. The first subshell is parallel to the (001) plane and consists of ~1.6 ± 0.4 Mg atoms at 3.03 Å ($\beta_{Mg} = 80 \pm 10°$). The second is inclined by ~22.2° ± 1.4° to the **c*** direction and consists of 2.2 ± 0.5 Si atoms at 3.27 Å. No Co neighboring cations were detected, allowing us to disregard the presence of significant amounts of pure $Co(OH)_{2(s)}$ or Co-rich neoformed phyllosilicate. This whole set of structural results is consistent with the formation of Co mononuclear surface complexes located at the edges of hectorite platelets, in the continuity of the (Mg, Li) octahedral sheets.

ACKNOWLEDGMENTS

W. P. Gates is warmly thanked for fruitful discussions on clay mineral properties and sample preparations. The SRS, LURE, and ESRF staffs are acknowledged for providing the X-ray beam and for their technical assistance. D.C. acknowledges Professor M. Pernet for the opportunity of using the texture experiment at Laboratoire de Cristallographie-CNRS, Grenoble, France.

REFERENCES

1. McBride, M. B., "Environmental Chemistry of Soils." Oxford Univ. Press, Oxford, 1994.
2. Bruno, G., Decarreau, A., Proust, D., and Lajudie, A., *Appl. Clay Sci.* **7,** 169 (1992).
3. Konta, J., *in* "Euroclay Meeting" (J. Konta, Eds.), p. 11. Univerzita Karlova Praha, Prague, 1985.
4. Bailey, S. W., *in* "Crystal structures of clay minerals and their X-ray identification" (G. W. Brindley and G. Brown, Eds.). Mineralogical Society, London, 1980.
5. McBride, M. B., Pinnavaia, T. J., and Mortland, M. M., *Amer. Mineral.* **60,** 66 (1975).
6. McBride, M. B., *Clays Clay Min.* **27,** 91 (1979).
7. McBride, M. B., *Clays Clay Min.* **30,** 200 (1982).
8. Muller, F., Besson, G., Manceau, A., and Drits, V. A., *Phys. Chem. Minerals* **24,** 159 (1997).
9. Papelis, C., and Hayes, K. F., *Coll. and Surf. A: Physicochem. Engineer. Aspects* **107,** 89 (1996).
10. Chisholm-Brause, C. J., Conradson, S. D., Buscher, C. T., Eller, P. G., and Morris, D. E., *Geochim. Cosmochim. Acta* **58,** 3625 (1994).
11. Peigneur, P., Maes, A., and Cremers, A., *Clays Clay Min.* **23,** 71 (1975).
12. Inskeep, W. P., and Baham, J., *Soil Sci. Soc. Am. J.* **47,** 660 (1983).
13. Charlet, L., Schindler, P. W., Spadini, L., Furrer, G., and Zysset, M., *Aquatic Sci.* **55,** 291 (1993).
14. McKinley, J. P., Zachara, J. M., Smith, S. C., and Turner, G. D., *Clays Clay Min.* **43,** 586 (1995).
15. Zachara, J. M., Smith, S. C., Resh, C. T., and Cowan, C. E., *Soil Sci. Soc. Am. J.* **57,** 1491 (1993).
16. Zachara, J. M., and McKinley, J. P., *Aquatic Sci.* **55,** 250 (1993).
17. Zachara, J. M., and Smith, S. C., *Soil Sci. Soc. Am. J.* **58,** 762 (1994).
18. Scheidegger, A. M., Lamble, G. M., and Sparks, D. L., *Environ. Sci. Technol.* **30,** 548 (1996).
19. Scheidegger, A. M., Lamble, G. M., and Sparks, D. L., *J. Colloid Interface Sci.* **186,** 118 (1997).
20. O'Day, P. A., Brown, G. E. r., and Parks, G. A., *Geol. Soc. Amer. Abstr. Prog.* (1990).
21. Manceau, A., Schlegel, M. L., Nagy, K. L., and Charlet, L., submitted.

22. Teo, B. K., "EXAFS: Basic Principles and Data Analysis." Springer-Verlag, Berlin, 1986.
23. Manceau, A., Bonnin, D., Kaiser, P., and Fretigny, P., *Phys. Chem. Minerals* **16,** 180 (1988).
24. Manceau, A., Bonnin, D., Stone, W. E. E., and Sanz, J., *Phys. Chem. Minerals* **17,** 363 (1990).
25. Manceau, A., Schlegel, M. L., Chateigner, D., Lanson, B., Bartoli, C., and Gates, W. P., *in* "Synchrotron X-ray Methods in Clay Science" (D. Schulze, P. Bertsch, and J. Stucki, Eds.). Clay Mineral Society of America, in press.
26. Manceau, A., Chateigner, D., and Gates, W. P., *Phys. Chem. Minerals* **25,** 347 (1998).
27. Bunge, H. J., "Textures in Material Science." Butterworth, London, 1981.
28. Wenk, H. R., Chateigner, D., Pernet, M., Bingert, J., Hellstrom, E., and Ouladdiaf, B., *Physica C* **272,** 1 (1996).
29. Bonnin, D., Bouat, J., Kaiser, P., Frétigny, C., and Béguin, F., *J. Phys. C* **8,** 865 (1986).
30. Manceau, A., *Can. Miner.* **28,** 321 (1990).
31. Komadel, P., Madejova, J., Janek, M., Gates, W. P., Kirkpatrick, R. J., and Stucki, J. W., *Clays Clay Min.* **44,** 228 (1996).
32. Kreit, J. F., Shainberg, I., and Herbillon, A. J., *Clays Clay Min.* **30,** 223 (1982).
33. Jackson, M. L., "Soil Chemical Analysis." Prentice–Hall, Englewood Cliffs, NJ, 1964.
34. Zachara, J. M., Smith, S. C., and Kuzel, L. S., *Geochim. Cosmochim. Acta* **59,** 4825 (1995).
35. Anderson, S. J., and Sposito, G., *Soil Sci. Soc. Am. J.* **55,** 1569 (1991).
36. Tiller, K., *Clay Min.* **7,** 245 (1968).
37. Verburg, K., and Baveye, P., *Clays Clay Min.* **43,** 637 (1995).
38. Jeffery, G. H., Bassett, J., Mendham, J., and Denney, R. C., "Vogel's Textbook of Quantitative Chemical Analysis." Wiley, New York, 1978.
39. Iler, R. K., "The Chemistry of Silica," Wiley, New York, 1979.
40. Rimstidt, J. D., *Geochim. Cosmochim. Acta* **61,** 2553 (1997).
41. Stumm, W., and Morgan, J. J., "Aquatic Chemistry." Wiley, New York, 1996.
42. Cases, J-M., Berend, I., Delon, J. F., François, M., Grillet, I., Michot, L., Poirier, J. E., and Yvon, J., *in* "Matériaux argileux" (A. Decarreau, Eds.). Société française de minéralogie et de cristallographie, Paris, 1990.
43. Tröger, L., Zschech, E., Arvanitis, D., and Baberschke, *Jpn. J. Appl. Phys.* **32,** 144 (1992).
44. Castañer, R., and Prieto, C., *J. Phys. III France* **7,** 337 (1997).
45. Decarreau, A., *C.R. Acad. Sci. Paris* **292,** 61 (1981).
46. Decarreau, A., *Geochim. Cosmochim. Acta* **49,** 1537 (1985).
47. Matthies, S. M., Vinel, G. W., and Helming, K., "Standard Distributions in Texture Analysis." Akad. Verlag, Berlin, 1987.
48. Van der Hoek, M. J., Werner, W., and Van Zuylen, P., *Nucl. Instr. Meth. in Phys. Res. A* **246,** 380 (1986).
49. Aberdam, D., *J. Synchrotron Rad.* **5,** 1287 (1998).
50. Lengeler, B., and Eisenberger, P., *Phys. Rev. B* **21,** 4507 (1980).
51. Manceau, A., and Combes, J-M., *Phys. Chem. Minerals* **15,** 283 (1988).
52. Rehr, J. J., Albers, R. C., and Zabinsky, S. I., *Phys. Rev. Lett.* **69,** 3397 (1992).
53. Rayner, J. H., and Brown, G., *Clays Clay Min.* **21,** 103 (1973).
54. Oberlin, A., and Mering, J., *Bull. Soc. Franç. Minér. Crist.* **89,** 29 (1966).
55. Kadi-Hanifi, M., and Mering, J., *C.R. Séanc. Acad. Sc. Paris D* **274,** 149 (1972).
56. Lotmar, W., and Feitknecht, W., *Z. Kristallograph. Kristallogeom. Krystallphys. Krystallchem.* **93,** 368 (1936).
57. O'Day, P. A., Rehr, J. J., Zabinsky, S. I., and Brown Jr., G. E., *J. Am. Chem. Soc.* **116,** 2938 (1994).
58. Vaarkamp, M., Dring, I., Oldman, R. J., Stern, E. A., and Koningsberger, D. C., *Phys. Rev. B* **50,** 7872 (1994).
59. Scheidegger, A. M., Strawn, D. G., Lamble, G. M., and Sparks, D. L., *Geochim. Cosmochim. Acta* **62,** 2233 (1998).
60. Bowker, A. H., and Liebermann, G. J., "Engineering Statistics." Prentice–Hall, Englewood Cliffs, NJ, 1959.
61. Tröger, L., Arvanitis, D., Baberschke, K., Michaelis, H., Grimm, U., and Zschech, E., *Phys. Rev. B* **46,** 2383 (1992).
62. Shannon, R. D., *Acta Cryst. A* **32,** 751 (1976).
63. Hazen, R. M., and Wones, D. R., *Amer. Mineral.* **57,** 103 (1972).
64. Charlet, L., and Manceau, A., *in* "Environmental particles" (J. Buffle and H. P. Van Leeuwen, Eds.), Vol. 2, p. 117. Lewis, London, 1993.
65. Towle, S. N., Bargar, J. R., Brown Jr., G. E., and Parks, G. A., *J. Colloid Interface Sci.* **187,** 62 (1997).
66. O'Day, P. A., Parks, G. A., and Brown Jr., G. E., *Clays Clay Min.* **42,** 337 (1994).
67. Spadini, L., Manceau, A., Schindler, P. W., and Charlet, L., *J. Colloid Interface Sci.* **168,** 73 (1994).
68. Schlegel, M. L., Charlet, L., and Manceau, A., *J. Colloid Interface Sci.*, submitted.
69. Güven, N., *in* "Hydrous Phyllosilicates" (S. W. Bailey, Eds.), Reviews in Mineralogy, Vol. 19. Mineralogical Society of America, Washington, DC, 1988.
70. Mathieu-Sicaud, A., and Mering, J. *Bull. Soc. Franç. Minér. Crist.* **74,** 439 (1951).
71. Turpault, M.-P., and Trotignon, L., *Geochim. Cosmochim. Acta* **58,** 2761 (1994).
72. Tiller, K., *Clay Min.* **7,** 261 (1968).
73. O'Day, P. A., Chisholm-Brause, C. J., Towle, S. N., Parks, G. A., and Brown, G. E. J., *Geochim. Cosmochim. Acta* **60,** 2515 (1996).
74. Baes, C. F. J., and Mesmer, R. E., "The Hydrolysis of Cations." Wiley, New York, 1976.

4.2. Mécanisme d'adsorption à haute et basse force ionique, et stabilité de l'hectorite

Des expériences de cinétique d'adsorption de Co sur l'hectorite ont été menées à pH 6,5 et avec une teneur en hectorite de 1,95 g L^{-1}. On a étudié l'influence de la concentration totale en Co ($20 \leq$ TotCo ≤ 200 µM) pour une force ionique élevée ($NaNO_3$ 0,3 M), et l'influence de la force ionique à TotCo = 100 µM. La nature des complexes de surface formés à basse force ionique a par ailleurs été caractérisée par spectroscopie EXAFS de poudre. Les résultats obtenus sont détaillés dans l'article intitulé « *Sorption of metal ions on clay minerals. II. Mechanism of Co sorption on hectorite at high and low ionic strength, and impact on the sorbent stability* » situé à la fin de cette section.

4.2.1. Mécanisme d'adsorption à haute force ionique et impact sur la stabilité de l'hectorite

Les résultats de cinétique d'adsorption à pH 6,5 et différents TotCo permettent d'identifier deux étapes cinétiques distinctes à haute force ionique ($NaNO_3$ 0,3 M). Lors de la première heure de contact, la cinétique d'adsorption est la même pour toutes les concentrations étudiées (fig. 4.4). Pour des temps de réaction plus longs, les courbes de cinétique divergent. À TotCo = 20 µM, pratiquement tout le cobalt est fixé au bout de 6 h. Par contre, à ToTCo ≥ 50 µM l'adsorption du cobalt se poursuit, avec un taux cinétique qui croît avec TotCo. À partir des concentrations de Co adsorbé, il est possible de tracer des « isothermes » d'adsorption de Co pour des temps de réaction donnés (fig. 4.5). Pour t = 12 h, l'isotherme a la forme d'un isotherme de Langmuir. Ceci suggère que le Co en solution est à l'équilibre avec un type de site de surface dont la concentration, estimée à partir des paramètres d'un isotherme de Langmuir ajusté à la courbe expérimentale, est égale à environ 27,5 µmol par gramme d'hectorite. Pour des temps de réaction plus longs, la forme des isothermes est différente, indiquant que de nouvelles réactions d'adsorption se manifestent. Les résultats d'EXAFS polarisé exposés précédemment pour TotCo = 100 µM et t = 120 h suggèrent que toutes ces réactions correspondent à l'adsorption de Co sur différents types de sites de surface avec des cinétiques de réaction plus ou moins rapides.

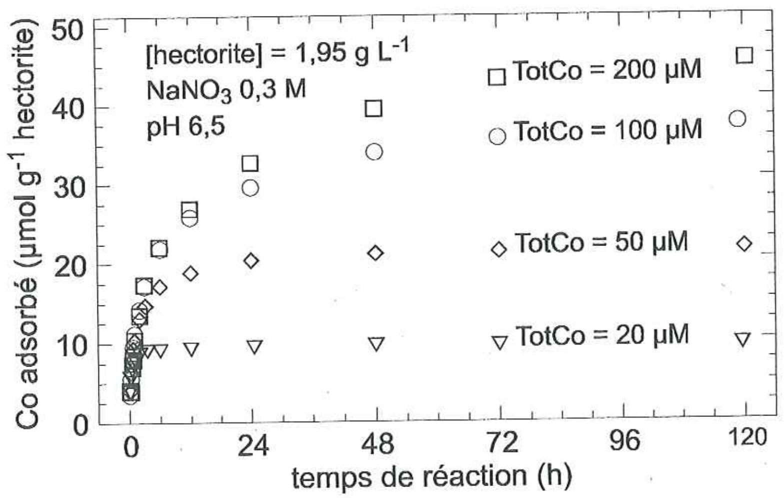

Figure 4.4. Cinétique d'adsorption de Co sur l'hectorite à pH 6,5 pour un fond ionique de $NaNO_3$ 0,3 M, et pour différentes valeurs de concentration totale de Co (TotCo).

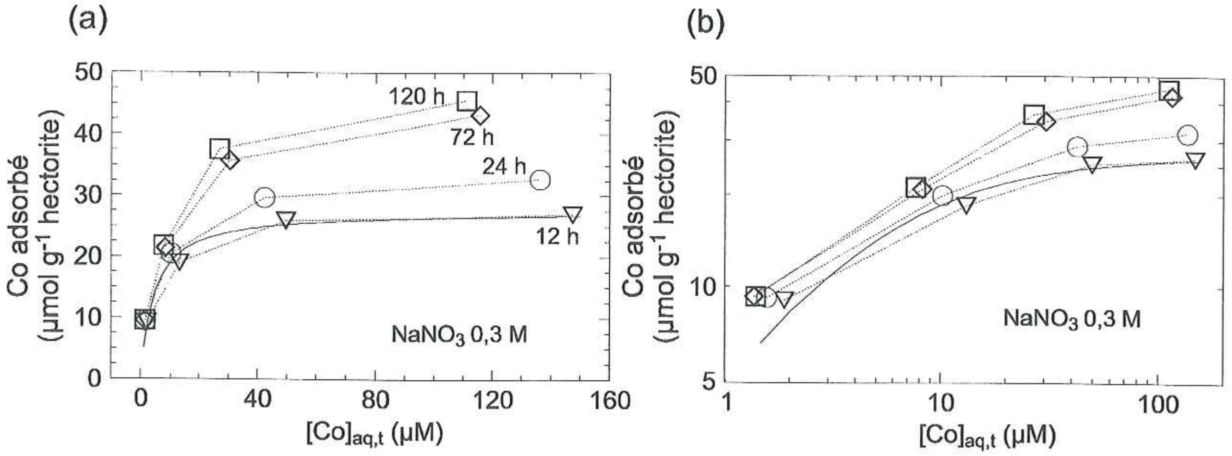

Figure 4.5. « Isothermes » d'adsorption de Co sur l'hectorite à pH 6,5, NaNO$_3$ 0,3 M, et pour des temps de réaction de 12 h (∇), 24 h (○), 72 h (◇), et 120 h (□). Les pointillés permettent de mieux visualiser les isothermes expérimentaux. La ligne pleine représente l'isotherme de Langmuir obtenu par meilleur ajustement des données à t = 12 h. (a) Echelle linéaire des concentrations. (b) Echelle logarithmique des concentrations.

La cinétique de dissolution de l'hectorite à pH 6,5 est sensiblement modifiée par l'adsorption de Co (fig. 4.6). Cette adsorption a pour impact une accélération importante du taux de libération de Mg en solution, corrélée avec le taux de fixation de Co. On peut rendre compte de cette accélération en supposant que des sites de fixation de Co en bordure des feuillets sont aussi susceptibles d'adsorber Mg, mais sans lier fortement ce cation. Tant que Co est absent du système, Mg est adsorbé sur ces sites, mais dès que Co est ajouté, il chasse Mg de ces sites, ce qui accroît subitement sa concentration en solution. Après environ 24 h, le taux de libération de Mg diminue sensiblement. Contrairement à Mg, le taux de libération de Si diminue sensiblement dès l'introduction de Co dans la suspension. Cette diminution suggère que les CSI de Co observés par spectroscopie P-EXAFS inhibent la dissolution de l'hectorite, par exemple en bloquant les sites de dissolution localisés en bordure des feuillets.

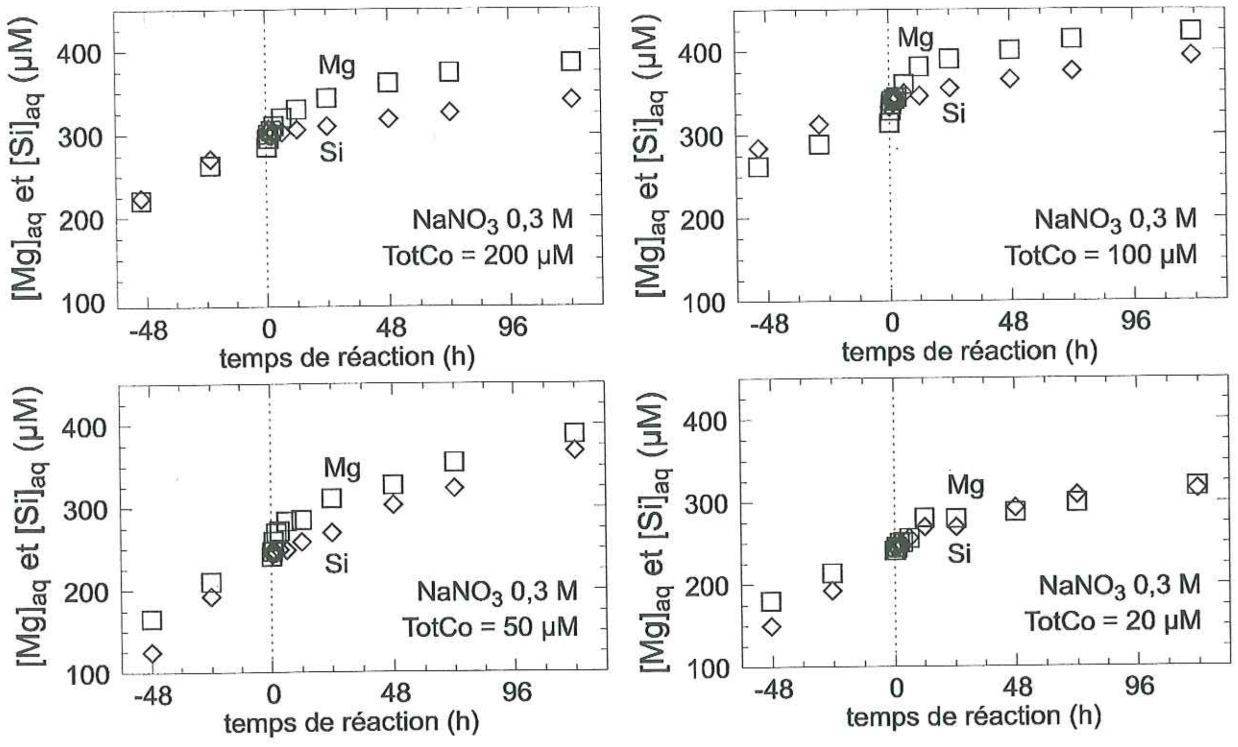

Figure 4.6. Impact de l'addition de Co sur les cinétiques de libération de Mg et Si dans la suspension à pH 6,5 et pour différentes valeurs de concentration totale de Co (20 ≤ TotCo ≤ 200 µM). [Mg]$_{aq}$ et [Si]$_{aq}$ sont respectivement les concentrations totales de Mg et Si mesurées en solution. t = 0 correspond au temps d'addition du Co en solution.

4.2.2. Mécanisme d'adsorption de Co à basse force ionique

À basse force ionique (NaNO$_3$ 0,01 M) et pH 6,5, une proportion importante de Co présent dans la solution est adsorbée pendant les cinq premières minutes de la réaction (fig. 4.7). Cette cinétique très rapide est caractéristique d'une adsorption sur les sites d'échange cationique. Après cette étape initiale, la fixation de Co sur l'hectorite se poursuit à une vitesse moins grande. Cette cinétique plus lente est semblable à celle observée à haute force ionique (fig. 4.4), ce qui suggère qu'une partie du Co restant en solution après l'échange cationique initial est progressivement fixée par adsorption spécifique sur les sites de bordure de l'hectorite.

Figure 4.7. Cinétique d'adsorption de Co sur l'hectorite à pH 6,5 et à haute (NaNO$_3$ 0,3 M ; ○) et basse (NaNO$_3$ 0,01 M ; +) force ionique.

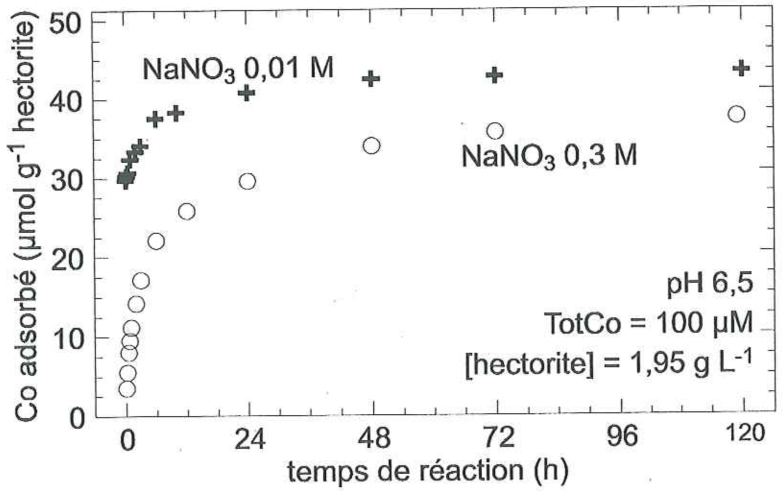

Afin de vérifier cette hypothèse, des spectres EXAFS ont été enregistrés sur des films d'hectorite ayant réagi avec Co à basse force ionique et pour des temps de réaction égaux ou supérieurs à 6 h. Ces spectres sont similaires à ceux obtenus à haute force ionique, ce qui indique que l'environnement cristallochimique moyen du Co est le même à haute et basse force ionique. Ce résultat est surprenant car on s'attendait plutôt à observer une prédominance de Co adsorbé par échange cationique et formant des CHS à basse force ionique. Pour rendre compte de ce résultat, la quantité de Co échangeable à l'équilibre avec Co en solution et en présence de Mg (libéré par dissolution de l'hectorite) a été calculée, en prenant comme coefficients de sélectivité pour les échanges Na-Co et Na-Mg $K^{c}_{Na-Mg} = 0{,}34 \pm 0{,}06$ et $K^{c}_{Na-Co} = 0{,}18 \pm 0{,}06$. Les résultats de ce calcul (fig. 4.8) montrent que la fraction de Co échangeable diminue avec le temps, alors que la quantité totale de Co adsorbée augmente. La combinaison de ces calculs et des résultats de spectroscopie EXAFS indique que le cobalt adsorbé initialement par échange cationique (t < 5 min) est progressivement transféré sur des sites de bordure (5 min ≤ t ≤ 120 h). L'échangeur cationique joue par conséquent le rôle de réservoir tampon provisoire du métal adsorbé.

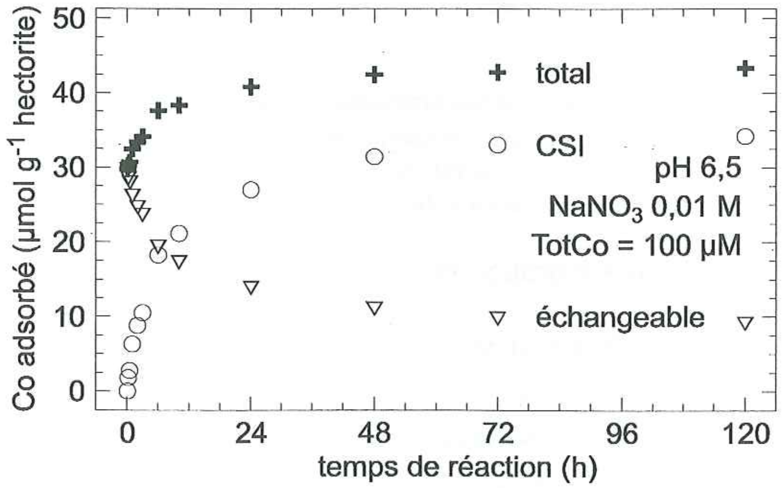

Figure 4.8. Évolution de la concentration calculée de Co adsorbé par échange cationique (▽) à l'équilibre avec Co en solution, et pour un coefficient de sélectivité $K^{c}_{Na-Co} = 0{,}18$ selon la convention de Vanselow. Sont également représentées la concentration totale (mesurée) de Co fixé par l'hectorite (+), et la différence (calculée) entre cette concentration totale et la concentration de Co échangeable (○). Les résultats d'EXAFS indiquent que cette différence correspond à la formation de complexes de sphère interne (CSI) en bordure des feuillets d'hectorite.

(*Sorption of metal ions on clay minerals. II. Mechanism of Co sorption on hectorite at high and low ionic strength, and impact on the sorbent stability.* Article paru dans Journal of Colloid and Interface Science)

Journal of Colloid and Interface Science **220**, 392–405 (1999)
Article ID jcis.1999.6538, available online at http://www.idealibrary.com on IDEAL®

Sorption of Metal Ions on Clay Minerals

II. Mechanism of Co Sorption on Hectorite at High and Low Ionic Strength and Impact on the Sorbent Stability

Michel L. Schlegel,[1] Laurent Charlet, and Alain Manceau

Environmental Geochemistry Group, LGIT-IRIGM, University of Grenoble, BP 53 F-38 041 Grenoble Cedex 9, France

Received May 19, 1999; accepted September 10, 1999

The mechanism of Co uptake from aqueous solution onto hectorite (a magnesian smectite) and its impact on the stability of this clay mineral were investigated as a function of Co concentration (TotCo = 20 to 200 µM, 0.3 M NaNO$_3$) and ionic strength (0.3 and 0.01 M NaNO$_3$, TotCo = 100 µM) by combining kinetics measurements and Co K-edge extended X-ray absorption fine structure (EXAFS) spectroscopy. The morphology of the sorbent phase was characterized by atomic force microscopy (AFM) and consists of lath-type particles bounded by large basal planes and layer edges.

At low ionic strength (0.01 M NaNO$_3$), important Co uptake occurred within the first 5 min of reaction, consistent with Co adsorption on exchange sites of hectorite basal planes. Thereafter, the sorption rate dramatically decreased. In contrast, at high ionic strength (0.3 M NaNO$_3$), Co uptake rate was much slower within the first 5 min and afterward higher than at 0.01 M NaNO$_3$, consistent with Co adsorption on specific surface sites located on the edges of hectorite. Time-dependent isotherms for Co uptake at high ionic strength indicated the existence of several sorption mechanisms having distinct equilibration times. The dissolution of hectorite was monitored before and after Co addition. A congruent dissolution regime was observed prior to Co addition. Just after Co addition, an excess release of Mg relatively to congruent dissolution rates occurred at both high and low ionic strengths. At high ionic strength, this excess release nearly equaled the amount of sorbed Co. The dissolution rate of hectorite then decreased at longer Co sorption times.

EXAFS spectra of hectorite reacted with Co at high and low ionic strengths and for reaction times longer than 6 h, exhibited similar features, suggesting that the local structural environments of Co atoms are similar. Spectral simulations revealed the occurrence of ~2 Mg and ~2 Si neighboring cations at interatomic distances characteristic of edge-sharing linkages between Co and Mg octahedra and corner-sharing linkages between Co octahedra and Si tetrahedra, respectively. This local structure is characteristic of inner sphere mononuclear surface complexes at layer edges of hectorite platelets. The occurrence of these complexes even at low ionic strength apparently conflicts with kinetics results, as exchangeable divalent cations are known to form outer sphere surface complexes. To clarify this issue, the amount of Co adsorbed on exchange sites was calculated from the solute Co concentration, assuming that cation exchange was always at equilibrium. These calculations showed that sorbed Co was transferred within 48 h from exchange sites to edge sorption sites.

Key Words: **Co; hectorite; kinetics; adsorption; dissolution; cation exchange; EXAFS; surface complex.**

INTRODUCTION

Among the inorganic phases that are common in surficial environments, smectites deserve special attention. These minerals possess large specific surface areas and permanent electrostatic charges, which enable them to sorb organic and inorganic cations. Therefore, they are thought to dominate many of the physicochemical properties of soils (1), recent sediments, and geological fractures (2). They also have found industrial applications in catalysis, pharmacology, waste management, and water treatment (3). Therefore, characterization of the smectite–water interface properties has been the topic of countless studies. However, few of them addressed the relationship between the sorption mechanism and the stability of the sorbent surface.

Studies of smectite sorption properties have long focused on major ions in pH-buffered systems and thus on cation exchange processes (1, 4–12). Exchangeable cations balance the smectite negative charges generated by isomorphic substitution within the clay structure (1). For a given cation at a given total concentration, adsorption on exchange sites is favored when the hydration enthalpy of the sorbate is low, when the background electrolyte concentration is low, and when the clay concentration is high (1, 12). The kinetics of cation exchange is fast, and steady-state concentration of the sorbate is attained within a few minutes (13–15). Exchangeable cations were shown by X-ray diffraction to be located in the smectite interlayer (16). Studies using electron-spin resonance (ESR), X-ray photoelectron spectroscopy, and extended X-ray adsorption

---

[1] To whom correspondence should be addressed. E-mail: Michel.Schlegel@ujf-grenoble.fr.

0021-9797/99 $30.00

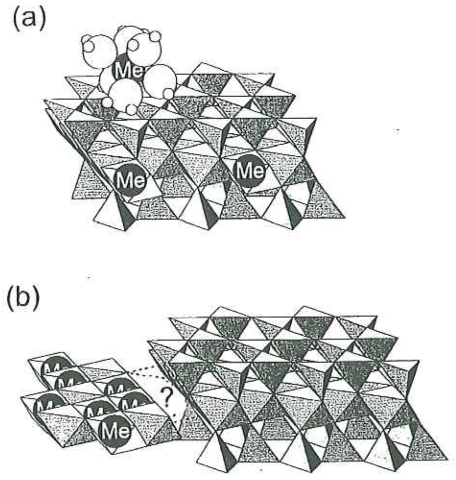

FIG. 1. Illustration of different sorption mechanisms of metal ions on clay minerals. (a) Adsorption of metal ions as outer sphere surface complexes on exchange sites located on basal planes and as inner sphere surface complexes on crystallite edges. (b) Coprecipitation of the sorbate and sorbent species liberated by dissolution. The question mark indicates that the structural relationship between the neoformed and the sorbent phases is unknown.

fine structure (EXAFS) spectroscopy further indicated that many exchangeable divalent cations keep a complete hydration sphere in water-saturated media (Fig. 1a). Outer sphere (OS) surface complexes are thus formed near the basal plane of smectites (17–25). More recently, studies of cation sorption performed at low cation concentration showed that uptake increases with pH, especially under high ionic strength conditions (26–37). This pH-dependent uptake results in proton release, as for metal ion sorption on oxide and hydroxide mineral surfaces (31), and has been interpreted in terms of inner sphere (IS) complex formation on surface sites at the edges of clay crystallites (30–32, 34, 36, 38). Previous EXAFS studies of Co sorbed at near-neutral pH and low surface coverage on hectorite, a magnesian smectite, have demonstrated the formation of IS complexes, in which Co octahedra are located in the continuity of the magnesium octahedral sheet (Fig. 1a) (39). In contrast, Ni sorbed at high pH and high initial concentrations on montmorillonite forms (Ni, Al) coprecipitates (Fig. 1b), with sorption going on over days, possibly weeks (40, 41). This slow sorption rate contrasts with the implicit assumption of equilibrium embedded in most surface chemical models.

Adsorbed cations can further affect the surface stability and dissolution kinetics of oxides. Inhibition of smectite dissolution has been shown to occur upon addition of Al to a montmorillonite suspension (42). Such inhibition phenomena may account for the low dissolution rates observed in the field compared to laboratory measurements (43, 44). In some cases, however, cation uptake does not result in a simple inhibition or enhancement of dissolution. For instance, adsorption of divalent metal cations (Zn, Co, Ni, Mn) on hectorite enhances the release of Mg with respect to Si over a timescale of weeks (45) and thus has a long-term effect on the stability of this smectite mineral. Deciphering dynamic relationships between cation uptake and mineral stability is thus mandatory to understand the long-term interactions of dissolved elements and mineral surfaces in natural systems.

The present paper aims at clarifying the mechanistic and kinetic features of Co uptake by hectorite and its impact on the dissolution of this magnesian smectite. The mechanism of Co adsorption at near-neutral pH (pH 6.5) and high and low ionic strength was determined first by combined wet kinetics chemistry and magic-angle EXAFS (MA-EXAFS) spectroscopy. The consequence of Co adsorption on hectorite dissolution was then studied. Macroscopic and microscopic results were finally rationalized by a single mechanistic model.

MATERIALS AND METHODS

Hectorite Purification and Characterization

A detailed description of hectorite purification and properties has been given in the companion paper (39). Briefly, 25 g of hectorite ($Na_{0.40}(Mg_{2.65}Li_{0.35})(Si_{3.95}Al_{0.05})O_{10}(OH)_2$) from the Source Clays Repository of the Clay Minerals Society (SHCa-1) was dispersed in 1 L of milli-Q water. The <2 μm fraction was isolated by sedimentation techniques, then successively saturated with Na (0.5 M NaCl), treated with a weakly acidic solution (10^{-4} M HCl), a dithionite-citrate-bicarbonate (DCB) solution, a 3% H_2O_2 solution to remove mineral impurities and organic matter, and finally dialyzed and stored at 4°C in the dark. Discarded solutions corresponding to these different stages were analyzed for Mg, Li, and Si to assess the impact of this purification procedure on the stability of hectorite. The cation exchange capacity of the purified clay, measured at pH 6 by Cs^+ exchange (46), equaled 840 μmol g^{-1}, and the specific surface area determined by N_2 BET was 114 m^2 g^{-1}.

Adsorption and Dissolution Experiments

All solutions were made with milli-Q water and chemicals of ACS reagent grade. A constant Na concentration and a slightly fluctuating nitrate concentration ($[NO_3^-] = [Na^+] \pm 5\%$) were maintained throughout the experiments by preparing the working suspensions with the appropriate amounts of $NaNO_3$ salt (Fluka). As Co concentrations were negligible with respect to Na, ionic strength (I) hereafter refers to $[Na^+]$.

Sorption experiments were conducted at 25 ± 0.1°C in polyethylene vessels immersed in a thermostatic water bath. Polyethylene was chosen to avoid interactions of dissolved cations and silica with the vessel walls. A rotating magnetic bar ensured vigorous stirring of the suspension. A water vapor-saturated inert atmosphere was maintained by bubbling humidified Ar that had passed beforehand through a purification setup (10% H_2SO_4, then 0.1 M NaOH, and finally $NaNO_3$ at the ionic strength of the suspension). The pH of the suspension was maintained at 6.5 ± 0.05 by a PC-controlled pH-stat that delivered acid (0.1 M HNO_3) or base (0.02 M NaOH) solutions adjusted at the sodium concentration of the suspension, as needed. The combined pH electrode was calibrated against buffers (Merck titrisol) and recalibrated at least every 48 h.

1□

TABLE 1
Chemical Conditions and Results of EXAFS Analysis for Co-Sorbed Hectorite Samples

Sample name	Ionic strength (M)	Equilibration time (h)	g Co_{ads}[a] / g hectorite (‰)	Γ (μmol g^{-1} hectorite)	Co–O shell R (Å)	Co–O shell N_O^{EXAFS}	Co–O shell σ (Å)	Co–Mg shell R (Å)	Co–Mg shell N_{Mg}^{EXAFS}	Co–Mg shell σ (Å)[c]	Co–Si shell R (Å)	Co–Si shell N_{Si}^{EXAFS}	Co–Si shell σ (Å)[c]	R_p	ΔE_0[b] (eV)
#0.3M-120h	0.3	120	2.38	37	2.07	5.1	0.10	3.03	1.6	0.10	3.27	2.2	0.11	0.015	−0.8
#0.01M-6h	0.01	6	2.27	38	2.08	5.3	0.10	3.03	1.6	0.10	3.76	2.2	0.11	0.015	−0.8
#0.01M-72h	0.01	72	2.66	43	2.08	5.4	0.10	3.04	2.0	0.10	3.27	2.6	0.11	0.017	−0.8

[a] TotCo = 100 μM for all experiments.
[b] Threshold energy E_0 taken at the half-height of the absorption edge ($\Delta\mu/2$). ΔE_0 for FEFF7.02 theoretical functions.
[c] Fixed parameter.

A 1.95 g L^{-1} hectorite suspension was obtained by mixing the appropriate amounts of hectorite stock suspension and $NaNO_3$ solution. The pH of this suspension was raised to 6.5 and kept at this value for at least 48 h prior to Co addition. Meanwhile, suspension samples were periodically taken to measure Mg and Si release, the first sample having been taken after a delay ranging from few hours to two days. Kinetics experiments of Co uptake were initiated by adding an aliquot of a 0.21 M $Co(NO_3)_2$, 10^{-3} M HNO_3, 0.3 M $NaNO_3$ solution to the preequilibrated suspension, so as to obtain the desired total Co concentration TotCo in the reactor. The time of Co addition is hereafter referred to as $t = 0$. The pH was then immediately readjusted to 6.5 by addition of the base solution. At given times, 5-ml samples were withdrawn from the reaction vessel with a plastic syringe connected to a polyethylene needle, centrifuged, and filtered (Sartorius 0.05-μm cellulose nitrate filter). The first milliliter of the filtered supernatant was discarded to limit losses due to sorption on the filter. Co and Si total concentrations in the filtered supernatant, $[Co]_{aq,t}$ and $[Si]_{aq,t}$, were measured by spectrophotometry (47, 48), and dissolved total Mg concentration $[Mg]_{aq,t}$ by inductively coupled plasma-atomic emission spectrometry. In all experiments, $[Si]_{aq,t}$ remained below 420 μM. Consequently, silicic acid is undersaturated with respect to amorphous silica and is assumed to remain in a predominantly monomeric form (49). Under all chemical conditions, more than 99.9% of cobalt dissolved in the supernatant was present as $Co^{2+}_{(aq)}$ (50). Thus the $Co^{2+}_{(aq)}$ concentration $[Co^{2+}_{(aq)}]$ in the supernatant equals $[Co]_{aq,t}$ within experimental uncertainties. Likewise, $[Mg^{2+}_{(aq)}] \approx [Mg]_{aq,t}$.

EXAFS

Co-sorbed hectorite samples for EXAFS spectroscopy were prepared at both high and low ionic strength (Table 1), following the same chemical protocol as for the kinetics experiments. Reaction times ranged from 6 h to 5 days. Hectorite particles were separated from the supernatant by filtration, rinsed with a few milliliters of deionized water, and air-dried, as described in the companion paper (39). Due to long filtration times (up to 6 h), no sample was prepared for reaction times shorter than 6 h.

Co K-edge EXAFS spectra were recorded on the EXAFS 8.1 station at the SRS synchrotron radiation facility in Daresbury, UK. A Si(111) double crystal monochromator and a focusing mirror were used. The second crystal of the monochromator was detuned by 30% to increase the rejection rate of high-order harmonics. Samples were mounted on a goniometer and positioned at the magic angle (35°) with respect to the incident beam to avoid textural effects (51). Absorption spectra were measured in fluorescence detection mode using a 13-element Ge detector (Canberra).

EXAFS data reduction was carried out following a standard procedure (52), using a software package implemented by D. Bonnin (ESPCI, Paris). As a preliminary step, absorption spectra were given the shape of the semiempirical model of Lengeler (53, 54). Fourier transformations were performed on $k^3 \cdot \chi(k)$ between 2 and 10 $Å^{-1}$ using a Kaiser apodization window (55), resulting in a radial structure function (RSF) in the distance space. RSF structural peaks are located at apparent distances ($R + \Delta R$) that differ from structural distances by $\Delta R \approx -0.3$ Å. Peaks of interest were selected in the distance space and Fourier back-transformed in k space. Numbers of neighboring atoms and interatomic distances were determined by least-squares fitting these Fourier-filtered spectra with theoretical phase and amplitude functions calculated with FEFF7.02 (56) by using talc, hectorite (Co–Mg and Co–Si pairs), and $Co(OH)_2$ (Co–O pairs) as model structures (39, 57–60). The goodness of the fit was assessed by the reliability factor R_p, defined as

$$R_p = \frac{\sum_k \left(k^3 \cdot \chi_j^{calc}(k) - k^3 \cdot \chi_j^{exp}(k)\right)^2}{\sum_k \left(k^3 \cdot \chi_j^{exp}(k)\right)^2}, \qquad [1]$$

where $\chi_j^{exp}(k)$ and $\chi_j^{calc}(k)$ are the experimental and simulated contributions for one given j shell, respectively. Total uncertainty on the EXAFS-derived structural distances for powder

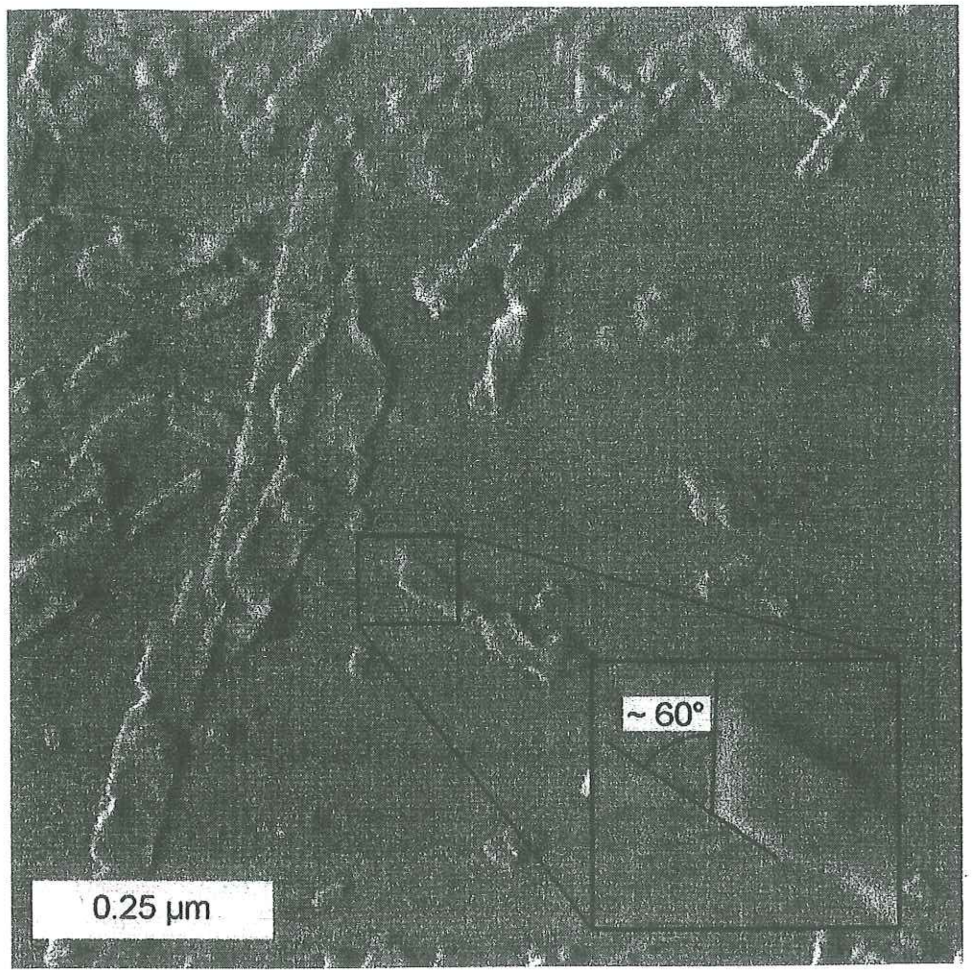

FIG. 2. AFM image of hectorite. This image was acquired in the contact mode under water in a flow-through cell by using a Si_3N_4 tip (Digital Instruments) (62). Note that not all particles in this picture are representative of the average width to length ratio of hectorite. Insert: close view of particle, showing the respective orientations of the (010) and (110) edges.

samples was estimated in the companion paper (39) to ±0.02 Å for $R_{\text{Co-O}}$, ±0.04 Å for $R_{\text{Co-Mg}}$, and probably more than ±0.06 Å for $R_{\text{Co-Si}}$. The uncertainty in the number of neighboring atoms is estimated to ±20% for $N_{\text{O}}^{\text{EXAFS}}$, ±25% for $N_{\text{Mg}}^{\text{EXAFS}}$, and ±30% for $N_{\text{Si}}^{\text{EXAFS}}$ (39).

RESULTS AND INTERPRETATION

Morphology and Surface Site Density of Hectorite

Individual crystallites observed by atomic force microscopy (Fig. 2) display the typical lath-type morphology of hectorite (58, 59, 61). The measured height of individual particles equals ~1 nm (62), which corresponds to the thickness of one single smectite layer. This observation indicates that Na-exchanged hectorite platelets are well dispersed. As for other Na-exchanged smectites (1), no stacking of individual platelets is observed. The elongation direction of the particles is known to run parallel to the **a** axis (Fig. 2; (58)). The particles are bounded predominantly by (010) and (100) planes and by another plane oriented at 60° off the **a** direction (Fig. 2, insert). From the knowledge of unit cell parameters (a = 5.25 Å and b = 9.09 Å), this third plane can be indexed as (110). A distribution analysis over 100 particles yielded an average length and width of 200 nm and 65 nm (62). These values point to the small dimensions of sorbent particles. From these observations, a model morphology for hectorite particles can be proposed (Fig. 3a). This model assumes that individual crystallites are, on average, 200 nm long by 65 nm wide and are bounded by their (001) basal faces and by (010), (110), and (100) edges. The ratio of the (110) to (100) edge lengths is difficult to determine without further detailed image analyses which are beyond the scope of this paper. However, it can be inferred from visual inspection of Fig. 2 that (010) and (110) are approximately of equal area. Therefore, the length of the (100) edge will be taken to be half the crystallite width, 32.5 nm. It turns out that the average length of individual (110) and (010) edges equals $32.5/(2*\cos(\pi/6)) \approx 18.7$ nm, and $200-(32.5*\tan(\pi/6)/2) \approx 181.2$ nm, respectively. Then, the number

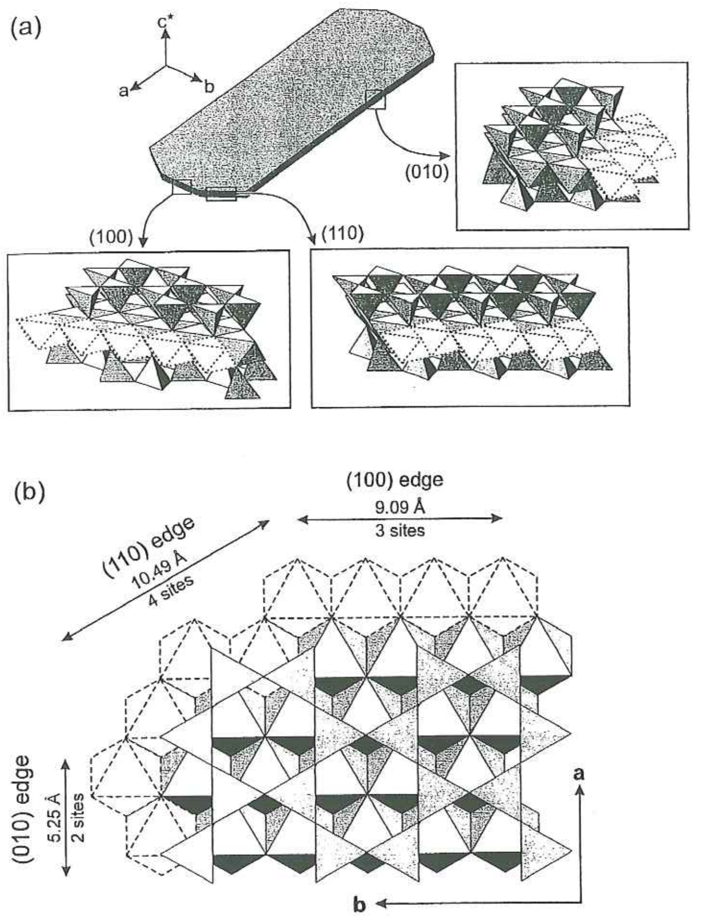

FIG. 3. (a) Idealized morphology of a hectorite particle. Morphologies of layer edges and edge surface sites (dashed octahedra) are shown in inserts. (b) Projection of hectorite down to **c*** and visualization of edge adsorption sites. Also displayed are numerical values used for the calculation of the number of edge sites.

of surface octahedral sites at the edges of hectorite particles can be calculated from the length of layer edges and from unit cell parameters. This calculation yields 3.81, 3.81, and 3.30 sites nm^{-1} for (010), (110), and (100) edges (Fig. 3b), respectively, which sums up to a total number of $(181.2*2*3.81) + (32.5*2*3.81) + (18.7*4*3.30) \approx 1879$ sites per particle. Finally, the amount of edge sites per gram of hectorite, as obtained from the mass of individual particles, equals ~92.5 $\mu mol\ g^{-1}$.

This estimate can be affected by a number of factors, including the statistical uncertainty in the average particle length and width, the relative size of the (110) and (100) edges, or the occurrence of small edge features (pitches, peninsulas) that may have been overlooked by AFM. For example, the calculated amount of surface sites diminishes to ~82.5 $\mu mol\ g^{-1}$ by increasing the particle length to 400 nm or the width to 75 nm (i.e., to values substantially high, but observed for a few hectorite particles (62)). Furthermore, by keeping constant crystallite dimensions to $200*65\ nm^2$, the site concentration increases to 95.8 $\mu mol\ g^{-1}$ in the absence of (100) edges, reaches a minimum of 92.4 $\mu mol\ g^{-1}$ when (100) edges comprise 60% of the particle width, and equals 93.7 $\mu mol\ g^{-1}$ in the absence of (110) edges. The spatial resolution of AFM is also limited by the radius of the tip (~10 nm (62)), which does not enable the detection and quantification of very small edge features. The occurrence of such features likely results in an increase in the edge surface (63, 64) and, hence, of the number of surface sites. Finally, 92.5 $\mu mol\ g^{-1}$ represents an average density of surface sites, but every site is not necessarily reactive. P-EXAFS results (39) showed that Co atoms form isolated surface complexes on hectorite edges (i.e., an absence of Co–Co pairing), which implies that the maximum density of Co sorption sites is to be halved, thus equal to 46.2 $\mu mol\ g^{-1}$ hectorite.

Structure of Co Surface Complexes

EXAFS spectra. Magic-angle EXAFS spectra obtained for Co-sorbed hectorite after various reaction times and contrasted ionic strengths (Table 1) look similar (Fig. 4a). This suggests that the crystallochemical environments of sorbed Co are similar regardless of the experimental conditions. One of these samples (#0.3M-120h) was studied in detail by P-EXAFS (39), and Co octahedra were shown to form IS surface complexes on the border of hectorite (Mg, Li) octahedral sheets by sharing edges (E) with (Mg, Li) octahedra and corners (C) with Si tetrahedra. The spectral likeness observed here among the various samples suggests a predominance of this type of surface complex at all ionic strengths and reaction times.

Radial structure functions. Moduli and imaginary parts of the Fourier transforms of MA-EXAFS spectra are displayed in

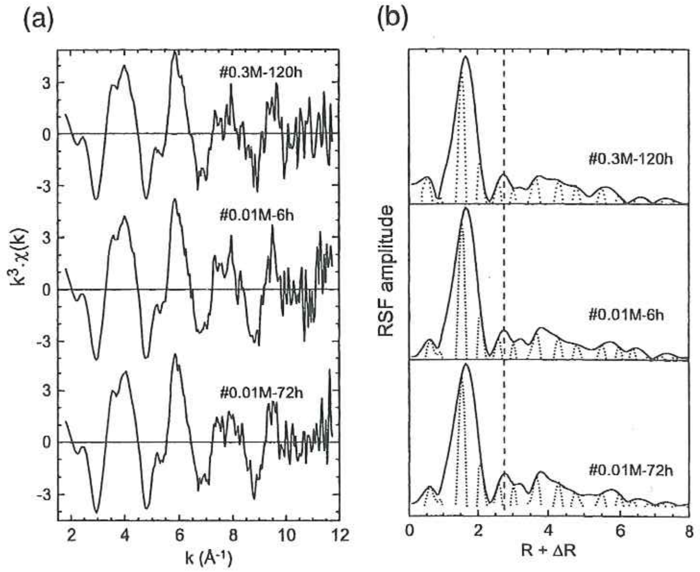

FIG. 4. (a) k^3-weighted Co K-edge EXAFS spectra for Co-sorbed hectorite samples. All spectra were recorded at the magic angle. (b) Co K-edge radial structure functions (RSF; solid lines) and imaginary parts of the Fourier transforms (dotted lines) for Co-sorbed hectorite samples. Ionic strengths and equilibration times are listed in Table 1.

Fig. 4b. Several peaks can be observed at $R + \Delta R$ distances of 1.7, 2.7, and 4 Å, confirming that several atomic shells are present in the neighborhood of Co. The first RSF peaks located at $R + \Delta R = 1.7$ Å originate from the contribution of oxygen atoms from the Co coordination spheres. Their quantitative analysis yielded $R_{\text{Co-O}} \approx 2.07$–$2.08$ Å, and $N_{\text{O}}^{\text{EXAFS}} \approx 5.1$–$5.4$ ($\sigma = 0.10$ Å; Table 1). These $R_{\text{Co-O}}$ values indicate that sorbed Co is divalent and hexacoordinated to oxygens. The second RSF peaks located at $R + \Delta R \approx 2.7$ Å arise from the contribution of the nearest cationic shells. These peaks have their maxima at the same $R + \Delta R$ value for all samples, and their imaginary parts are in phase, indicating similar cationic environments. This finding is further substantiated by the likeness of spectral contributions obtained by Fourier back-transforming second RSF peaks ($R + \Delta R$ window $= 2.2$–3.2 Å) (Fig. 5a). These results support the hypothesis that, in the whole sample series, sorbate Co ions are surrounded by the same types of backscatterers located at the same distances from Co. It has been demonstrated by P-EXAFS for sample #0.3M-120h that these backscatterers consist of Mg atoms at $R_{\text{Co-Mg}} = 3.03$ Å and of Si atoms at $R_{\text{Co-Si}} = 3.27$ Å (39). Quantitative spectral analysis for the two new spectra was therefore performed by taking $R_{\text{Co-Mg}}$, $R_{\text{Co-Si}}$, $N_{\text{Mg}}^{\text{EXAFS}}$, and $N_{\text{Si}}^{\text{EXAFS}}$ from #0.3M-120h as starting parameters and allowing them to float during least-squares fits. Good fits were obtained (Fig. 5b) by assuming $R_{\text{Co-Mg}}$, $R_{\text{Co-Si}}$, $N_{\text{Mg}}^{\text{EXAFS}}$, and $N_{\text{Si}}^{\text{EXAFS}}$ values which did not differ from one sample to one another within statistical uncertainty (Table 1). As in the companion article (39), Co–Co pairs were included in the spectral model to test whether a detectable fraction of Co polymerized upon sorption. The quality of the fit was significantly altered, as attested by an increase in R_p from 0.015 to 0.020, for N_{Co} as low as 0.1 ($\sigma = 0.11$ Å). $N_{\text{Co}} = 0.1$ is therefore considered to be the highest possible value for N_{Co}, which indicates that less than 10% of sorbed Co is contained in dimers, or less than 5% in trimers, or less than 1.8% in a Co-clay-like compound. Thus, adsorption of Co on adjacent edge sites is clearly limited, and compelling formation of pure or mixed hydroxides of large size hampered. Note that the maximum amount of sorbed Co (43 μmol g^{-1}; Table 1) compares fairly well with the calculated amount of nonadjacent edge sites (46.2 μmol g^{-1}), which provides further indirect support to the sorption of Co on every two surface sites.

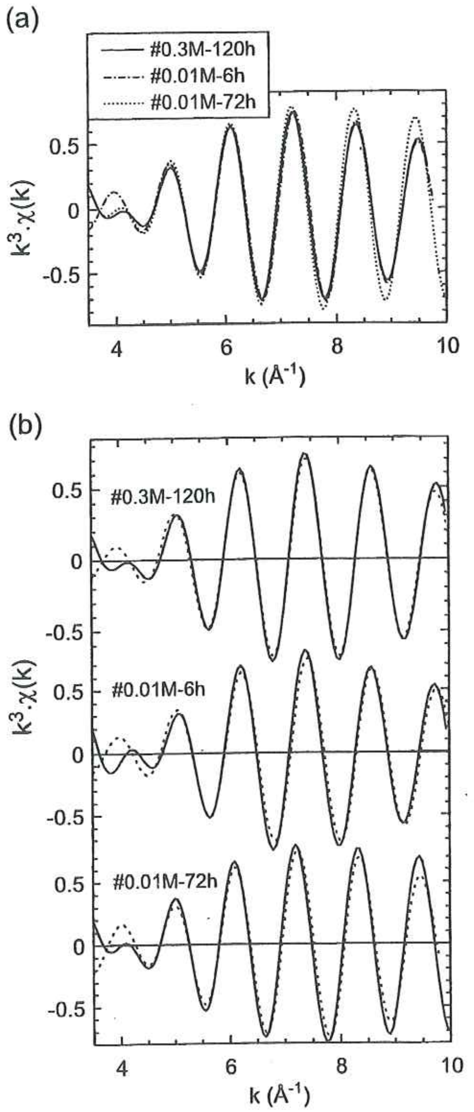

FIG. 5. Fourier-filtered EXAFS spectra of the second shell ($\chi_{\text{2nd shell}}(k)$) for Co-sorbed hectorite. (a) Comparison of $\chi_{\text{2nd shell}}(k)$ for the different sorption samples. (b) Comparison between experimental and modeled $\chi_{\text{2nd shell}}(k)$ contributions.

Structural environment of sorbed Co. Several types of IS surface complexes having different numbers of Mg and Si neighbors can fit both structural (EXAFS) and morphological (AFM) results. These surface complexes can form on (100), (110), and (010) platelet edges (Fig. 6), and Co complexes having distinct number of neighboring sorbent cations may coexist on the same edge. For example, Co adsorbed on (010) planes can form either 3 edge (E) and 4 corner (C) linkages ($\text{S}_{\text{3E+4C}}^{(010)}$ surface complex) or 1 E and 2 C linkages ($\text{S}_{\text{1E+2C}}^{(010)}$ surface complex), where the (010) superscript is the plane index and the subscript refers to the number of E and C linkages (Fig. 6). As EXAFS spectroscopy averages the contribution from all existing surface complexes, the proportion of each surface complex can be calculated from the average number of neighboring cations. For instance, let us consider #0.3M-120h (Table 1). $N_{\text{Si}}^{\text{EXAFS}} = 2.2 \pm 0.6$ and $N_{\text{Mg}}^{\text{EXAFS}} = 1.6 \pm 0.4$ correspond to the average number of C linkages with Si tetrahedra and E linkage with Mg octahedra, respectively. EXAFS is not sensitive to light elements, such as Li, hence, the number of structural Mg *and* Li octahedra sharing edges with adsorbed Co is probably higher than $N_{\text{Mg}}^{\text{EXAFS}}$. Assuming a random distribution of Li within the octahedral sheet, this number approximately equals $N_{\text{oct}}^{\text{EXAFS}} = N_{\text{Mg}}^{\text{EXAFS}} *3/2.65 \approx 1.8 \pm 0.45$. Thus, $N_{\text{Si}}^{\text{EXAFS}} = 2.2 \pm 0.6$ and $N_{\text{oct}}^{\text{EXAFS}} = 1.8 \pm 0.45$ fits with 20–35% of $\text{S}_{\text{3E+4C}}^{(010)}$ surface complexes and 65–80% of $\text{S}_{\text{1E+2C}}^{(010)}$ surface complexes (39).

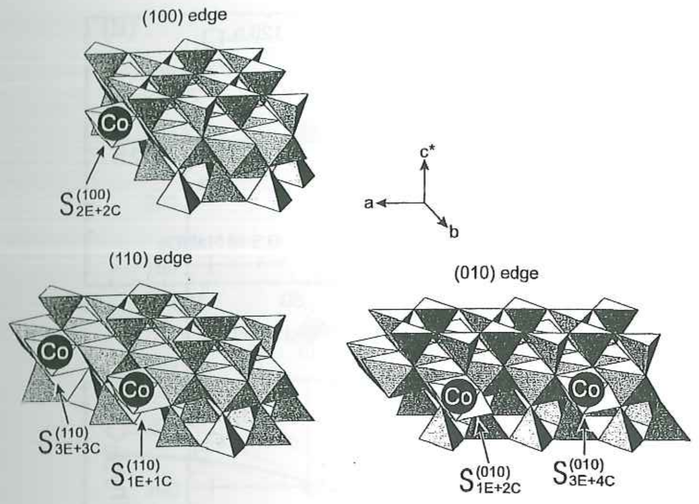

FIG. 6. Possible structures of mononuclear Co surface complexes on hectorite edges. Co atoms are located in the plane of the hectorite octahedral sheets.

Previous EXAFS studies contemplated the exclusive formation of OS metal ion complexes at low ionic strength and moderate pH conditions (23–25). Sorbed cations were shown to hold their hydration shells, and no metal sorbent backscatterer was observed within ~4 Å around adsorbed ions. In contrast, in the present study, (Mg, Si) shells were unambiguously detected at 3.0–3.3 Å, and the comparable amplitude of these contributions at high and low ionic strengths indicates that these IS surface complexes are also present in substantial amount at low ionic strength. However, comparable $N_{\text{oct}}^{\text{EXAFS}}$ and $N_{\text{Si}}^{\text{EXAFS}}$ values at high and low ionic strength does not preclude the occurrence of OS complexes at low ionic strength, as the absence of neighboring cations for OS complexes can be balanced by a higher number of neighboring cations surrounding edge-sorbed Co. This consideration will be exemplified with sample #0.01M-6h (Table 1). $N_{\text{oct}}^{\text{EXAFS}} = 1.8 \pm 0.45$ and $N_{\text{Si}}^{\text{EXAFS}} = 2.2 \pm 0.6$ can be obtained by assuming either (a) 20–35% of $\text{S}_{\text{3E+4C}}^{(010)}$ surface complexes and 65–80% of $\text{S}_{\text{1E+2C}}^{(010)}$ surface complexes or (b) ~60% of $\text{S}_{\text{3E+4C}}^{(010)}$ surface complexes and ~40% of OS Co complexes (no neighboring cations). Hence, EXAFS analysis alone does not allow discrimination between two distinct IS complexes and a mixture of IS and OS surface complexes.

In conclusion, EXAFS results indicate that Co surface complexes have, on average, the same local structure for reaction times higher than 6 h and for ionic strengths $I = 0.3$ M and $I = 0.01$ M. Co atoms form predominantly isolated IS surface complexes in the continuity of hectorite octahedral sheets. Polynuclear surface complexes are marginal, if present at all, whereas the presence of OS complexes on exchange sites at low ionic strength cannot be dismissed. How a diversity of macroscopic sorption mechanisms can compare with this apparent uniformity of sorbate molecular environments will now be addressed.

Kinetics and Mechanism of Co Sorption and Hectorite Dissolution

Kinetics of Co sorption. The kinetics of Co uptake by hectorite at various ionic strengths and total Co concentrations is illustrated in Fig. 7a and 7b. For any value of TotCo investigated, the maximum amount of sorbed Co (45.5 μmol g^{-1}) never exceeded the number of edge sites derived from AFM (46.2 μmol g^{-1}). At low ionic strength (0.01 M $NaNO_3$), significant Co uptake (up to 30 μmol g^{-1} of hectorite) occurred within the first 5 min of reaction time between sorbate cations and clay particles (Fig. 7a). A cation exchange mechanism is presumably responsible for this fast cation uptake (15), inasmuch as the amount of sorbed Co within the first 5 min drastically decreased as the ionic strength increased. This cation exchange likely occurred on exchange sites located on (001) basal planes of clay platelets (1).

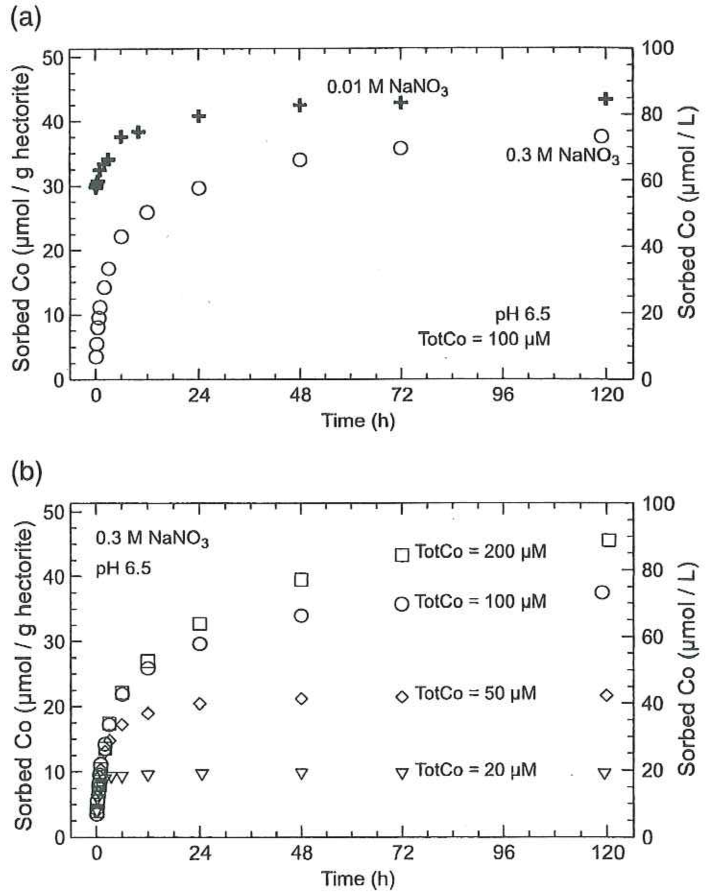

FIG. 7. Kinetics of Co adsorption on hectorite. (a) Adsorption as a function of ionic strength. TotCo = 100 μM; hectorite 1.95 g L^{-1}, pH 6.5; I = 0.3 M (○), and 0.01 M (✚). (b) Adsorption as a function of TotCo. I = 0.3 M, hectorite 1.95 g L^{-1}, pH 6.5. TotCo = 200 μM (□), 100 μM (○), 50 μM (◇), and 20 μM (▽).

Following this fast reaction step, uptake at low ionic strength went on at a much slower rate. The sorption rates observed within this second step are too slow to be accounted for by cation exchange (13, 15), which suggests the existence of a second uptake mechanism. Sorption experiments at high ionic strength (I = 0.3 M) and for different TotCo allowed better characterization of this second step (Fig. 7b). Initial sorption rates (5 min $\leq t <$ 1 h) were roughly independent of TotCo (~30.8 μmol g^{-1} h^{-1}). After 1 and 2 h of sorption time, sorption rates for TotCo = 20 and 50 μM, respectively, leveled off. After 12 h, Co sorption reached a plateau for TotCo < 50 μM, whereas sorption still went on for TotCo ≥ 50 μM, with higher sorption rates observed for higher TotCo.

For all experiments, addition of Co was followed by addition of base to prevent the pH from shifting to lower values. Between 2.4 and 20.2 μmol of NaOH per g hectorite was needed to keep the pH at the targeted value. The amounts of acid delivered with Co aliquots were too low to account alone for the corresponding excess of protons in the suspensions. It is thus assumed that this proton release resulted from Co sorption. Interference of base addition with proton consumption resulting from ongoing hectorite dissolution hampers any further detailed analysis, especially for long reaction times. Note, however, that base addition was also required at low ionic strength and over a time span of 3 h.

To gain further insight into the uptake mechanism at $t \geq 5$ min, "pseudoisotherms" of Co uptake were drawn at high ionic strength for different reaction times (Fig. 8a–b). At t = 12 h, a Langmuir-type pseudoisotherm can be observed, suggesting that equilibrium has been approached for at least one surface site. To check this qualitative inference, experimental data were fitted with a Langmuir equation (Fig. 8). Good agreement was obtained for a concentration of surface sites equal to 27.5 μmol g^{-1} hectorite. Attempts to model this isotherm with the Freundlich equation (15) did not improve the fit. At longer reaction times, the shapes of these pseudoisotherms are modified, indicating that overall equilibrium conditions were not attained (49). Nonequilibrium can result from the occurrence of a new Co uptake mechanism, which could be (a) nucleation of pure Co or mixed (Co, Si) precipitates, (b) diffusion into the hectorite structure, (c) a slow buildup of a mixed (Co, Si, Mg) clayey fringe at the hectorite edge, or (d) adsorption on another kind of surface site. Precipitation of pure or mixed (Co, Si) hydroxides can be precluded in view of the EXAFS results obtained for long sorption times and high Co concentrations (e.g., #0.3M-120h) (39). Also, significant diffusion of divalent metal ions within clay octahedral vacancies has been shown to occur only at temperatures greater than 100°C (25). Discrimination between (c) and (d) is more difficult, as the incorporation of significant amounts of Mg and Si in clay fringes can result in the formation of a (Mg, Si)-dominated Co molecular environment. In this case, significant amounts of Si and Mg, at least equal to the amount of sorbed Co, are needed to form the new solid phase in order to avoid Co–Co pairing. As a result, the mass balance of dissolved Si and Mg would be greatly affected by the buildup of (Co, Mg, Si) clayey fringes, in contrast to what can be expected in the case of the adsorption of isolated Co atoms on layer edges. Therefore, in order to clarify this issue, the kinetics of hectorite dissolution before and after Co adsorption was studied.

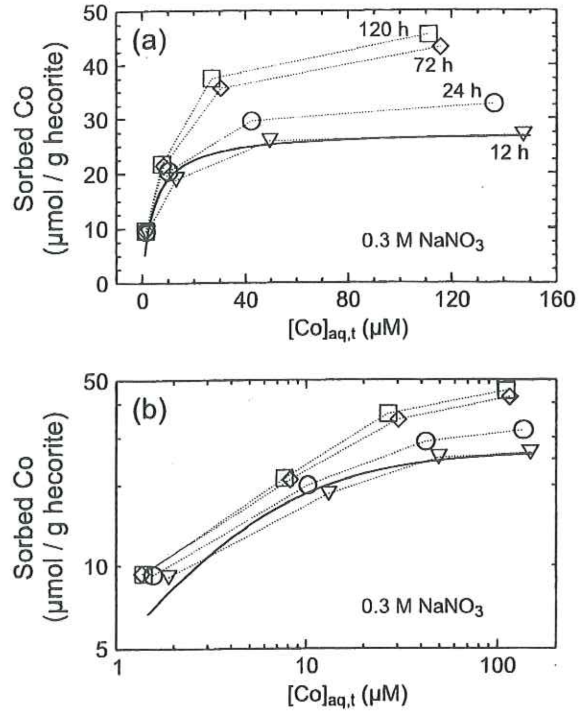

FIG. 8. Nonequilibrium "isotherms" for Co sorption at contact times of 12 h (▽), 24 h (○), 72 h (◇), and 120 h (□). TotCo from 20 to 200 μM, I = 0.3 M, hectorite 1.95 g L^{-1}, pH 6.5. "Isotherms" are given with (a) linear and (b) logarithmic scales. Thin dotted lines are displayed for the sake of clarity. Solid line: modeled Langmuir isotherm for Co uptake at t = 12 h.

Kinetics of hectorite dissolution in absence of Co. At I = 0.3 M and just before Co addition, the ratio of Mg to Si release rates (=0.54 ± 0.07 and 0.85 ± 0.37 μmol h^{-1} g^{-1}, respectively) was equal to 0.66 (Fig. 9). This value is similar to the Mg to Si ratio in hectorite (=2.65/3.95 = 0.67) and points to a congruent dissolution regime. This inference, however, runs counter to $[\mathrm{Mg}]_{\mathrm{aq,t}}$ to $[\mathrm{Si}]_{\mathrm{aq,t}}$ ratios between 0.95 and 1.0 (t = 0), which suggests a larger Mg release than what could be expected from hectorite stoichiometry. To explain this apparent discrepancy, $[\mathrm{Mg}]_{\mathrm{aq,t}}$ values for $t \leq 0$ were plotted as a function of $[\mathrm{Si}]_{\mathrm{aq,t}}$ (Fig. 9b). A fair linear correlation can be observed with a regression slope of 0.68 ± 0.05 (r^2 = 0.985). Thus, only limited deviation to a congruent dissolution regime is actually observed over the sampled preequilibration time. Extrapolation of the regression line to $[\mathrm{Si}]_{\mathrm{aq,t}}$ = 0 yields a positive concentration of $[\mathrm{Mg}]_{\mathrm{aq,t}} \approx$ 77 μM. One would see in this excess of Mg an evidence for initial incongruent dissolution of hectorite with a preferential release of Mg with respect to Si (65). However, it seems unlikely that dissolution changes so rapidly from a strongly incongruent to a congruent regime (66). Alternatively, hectorite may have been enriched in Mg with respect to Si during the dialysis pretreatment. As dialysis proceeded, dissolution of hectorite resulted in the release of Si neutral species, which were readily removed from the dialysis bag, while Mg cations may have exchanged for Na cations on exchange sites of hectorite. These Mg ions would then have been removed from exchange sites, as hectorite was suspended in the background electrolyte medium. Indeed, $[\mathrm{Mg}]_{\mathrm{aq,t}}$ to $[\mathrm{Si}]_{\mathrm{aq,t}}$ ratios in late dialysis solutions were lower than the Mg:Si stoichiometric ratio of hectorite.

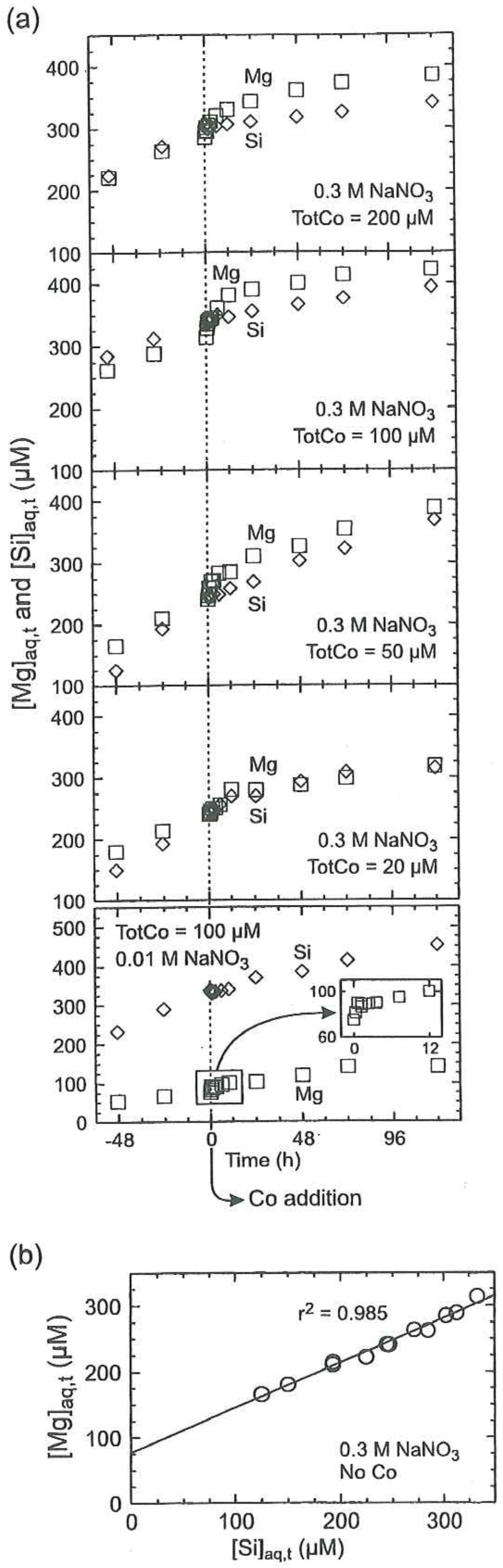

FIG. 9. Kinetics of Mg and Si release before and after Co uptake at high ionic strength. Hectorite 1.95 g L^{-1}, pH 6.5. (a) Dissolution trends for Mg (□) and Si (◇) before and after Co addition to the suspension. (b) Plot of $[\mathrm{Mg}]_{\mathrm{aq,t}}$ versus $[\mathrm{Si}]_{\mathrm{aq,t}}$ for I = 0.3 M and $t \leq 0$.

TABLE 2

Si Release Rates and Si Concentrations at t = 0 and I = 0.3 M

$[\mathrm{Si}]_{\mathrm{aq,t}}$ (μM)	Reaction time (h)	Release rate (μmol of Si h^{-1} g^{-1} hectorite)	TotCo at $t \geq 0$ (μM)[a]
330	130	0.39	100
297	82	0.73	200
240	57	1.18	50
239	57	1.11	20

[a] For information.

The Mg and Si release rates at I = 0.3 M were not constant throughout the preequilibration period, indicating that the net dissolution rate of hectorite was somewhat time-dependent. This observation was further supported by the confrontation of the Si release rates at t = 0, with distinct $[\mathrm{Si}]_{\mathrm{aq,t}}$ values obtained after different preequilibrium periods (Table 2): the longer the reaction time, the higher $[\mathrm{Si}]_{\mathrm{aq,t}}$, and the lower the release rate. This correlation between high dissolution rates and low $[\mathrm{Si}]_{\mathrm{aq,t}}$ is commonly observed at the beginning of dissolution experiments (67–69), and several hypotheses have been proposed. First, smaller particles with high interfacial energy may dissolve preferentially at the beginning of the dissolution experiments (70). Second, highly reactive dissolution sites may occur at the mineral surface and yet be active only under high undersaturation conditions (71). Third, the onset of the reverse reaction of precipitation of the solid may gradually occur as the products of dissolution gradually build up in the supernatant (72).

Dissolution results at low ionic strength were conspicuously different from those at high ionic strength. Both ratios of $[\mathrm{Mg}]_{\mathrm{aq,t}}$ to $[\mathrm{Si}]_{\mathrm{aq,t}}$ (=0.22) and of Mg to Si release rates (=0.19) are markedly lower than the Mg to Si atomic ratio in hectorite. This departure from congruent dissolution probably results from a cation exchange mechanism, in which Mg released upon dissolution adsorbs on cation exchange sites (73).

Kinetics of hectorite dissolution after Co addition. Distinct trends for the release of Mg and Si were observed after Co addition ($t \geq 0$) (Fig. 9a). On the one hand, Si release was inhibited immediately after Co addition. This inhibiting effect is more pronounced for TotCo = 200 μM, as the release rate of Si decreased from 0.83 μmol h^{-1} g^{-1} at t = 0 to 0.19 μmol h^{-1} g^{-1} at t = 24 h. Interestingly, the Si release rate at low ionic strength also decreased from 1.01 μmol h^{-1} g^{-1} at $t \leq 0$ to 0.89 μmol h^{-1} g^{-1} at $t = 24$ h. On the other hand, the release rate of Mg was enhanced during the first 12 h of Co sorption. At high ionic strength ($I = 0.3$ M), the excess of released Mg relative to $t \leq 0$ was nearly equal to the amount of sorbed Co. The Mg release rate then gradually decreased. For example, the Mg release rate at TotCo = 200 μM jumped from 0.50 μmol h^{-1} g^{-1} at $t \leq 0$ to 50.1 μmol h^{-1} g^{-1} at $t =$ 5 min and decreased afterward (0.57 μmol h^{-1} g^{-1} at $t = 24$ h) to eventually reach values below that observed at $t = 0$ (0.20 μmol h^{-1} g^{-1} at $t = 72$ h). The Mg release pattern observed at low ionic strength ($I = 0.01$ M) qualitatively followed the pattern described at higher ionic strength, yet two major differences could be observed. First, the excess of Mg in solution relative to $t \leq 0$ (~15 μmol g^{-1}; Fig. 9, insert) was significantly lower than the amount of sorbed Co (more than 30 μmol g^{-1}; Fig. 7a). Second, Co uptake and excess release of Mg did not occur simultaneously, as opposed to what was observed at high ionic strength. Indeed, the enhanced Mg release lasted for the first hour of reaction, whereas most of Co uptake occurred within the first 5 min.

The release behavior of Mg at high ionic strength gives clues to the long-term mechanism of Co uptake. Part of the excess release of Mg upon Co addition can be unambiguously correlated to the short-term adsorption of Co ($0 \leq t \leq 12$ h). Afterward, a second mechanism has to be invoked. The hypothetical buildup of a (Co, Mg, Si) solid precipitate would be expected to result in a rapid decrease of both Mg *and* Si apparent release rates due to Mg and Si incorporation in the new solid phase. This hypothesis is at variance with the observed concomitant removal of Co *and* excess release of Mg for reaction times as long as 24 h. Alternatively, a long-term adsorption mechanism similar to the short-term mechanism, but on distinct sites, provides a fair explanation for the enhanced Mg release for the first 24 h of reaction time. Therefore, it can be assumed from the dissolution results that long-term ($t \geq 12$ h) sorption of Co on hectorite results from adsorption on new surface sites.

DISCUSSION

Mechanism of Co Uptake at Low Ionic Strength

The kinetics investigations point to very rapid Co uptake within the first 5 min of contact time at low ionic strength, compared to the slower adsorption rate at high ionic strength (Fig. 7a). This enhanced initial uptake is a strong indication of cation exchange processes. Divalent cations adsorbed on exchange sites are known to form OS surface complexes (17–19, 23–25). The sorption observed for $t \geq 5$ min at high ionic strength and coinciding with proton release can be connected to specific uptake of Co. The sorption rate associated with this mechanism does not depend on $[\mathrm{Co}]_{\mathrm{aq},t}$ during the first hour of contact time, yet the influence of TotCo can be observed for longer reaction times. In contrast, EXAFS results indicate that formation of IS Co surface complexes at the edges of hectorite particles occurs at both high and low ionic strengths. EXAFS results do not preclude the occurrence of OS complexes at low ionic strength, but such complexes are clearly not of paramount importance. For further discussion it is important to note that EXAFS measurements were preceded by at least 6 h of reaction time.

Both retention of Mg ions released by hectorite dissolution (Fig. 9a) and rapid sorption kinetics of Co for $0 \leq t \leq 5$ min (Fig. 7a) point to the importance of cation exchange for divalent solute cations at low ionic strength. Cation exchange is known to occur very rapidly and reaches equilibrium within minutes (13). Thus, any increase of $[\mathrm{Co}^{2+}_{(\mathrm{aq})}]$ results in nearly simultaneous adsorption of Co on exchange sites, according to the reaction

$$2\,X\mathrm{Na} + \mathrm{Co}^{2+}_{(\mathrm{aq})} \Leftrightarrow X_2\mathrm{Co} + 2\,\mathrm{Na}^{+}_{(\mathrm{aq})}, \qquad [2]$$

where X^- refers to one mole of exchange sites. As a result, after a given reaction time, the amount of exchangeable Co corresponds to an equilibrium value with respect to $[\mathrm{Co}^{2+}_{(\mathrm{aq})}]$ (which has been shown equal to $[\mathrm{Co}]_{\mathrm{aq},t}$ within uncertainty). This value can be calculated using the equilibrium constant for reaction [2], which can be written in the Vanselow approach (15, 31, 74),

$$K^{\mathrm{c}}_{\mathrm{Na\text{-}Co}} = \frac{(X_2\,\mathrm{Co})[\mathrm{Na}^{+}_{(\mathrm{aq})}]^2}{(X\mathrm{Na})^2[\mathrm{Co}^{2+}_{(\mathrm{aq})}]}, \qquad [3]$$

where $K^{\mathrm{c}}_{\mathrm{Na=Co}}$ is the conditional exchange constant for given exchanger and solute compositions, $(X_2\mathrm{Co})$ and $(X\mathrm{Na})$ are the activities of exchangeable cations, which are given in the Vanselow approach by (74)

$$(X_mM) = \frac{[X_mM]}{\sum_k [X_{m_k} M_k]}, \qquad [4]$$

where $[X_mM]$ is the molar concentration of M^{m+} ions adsorbed on exchange sites and the summation is taken over all exchangeable cations. In the present system, exchangeable cations include not only monovalent Na and divalent Co, but also divalent Mg released by the dissolution of hectorite. The exchanger is not a binary, but a ternary system. It is therefore necessary to calculate first the amount of exchangeable Mg. This can be done, based on the equilibrium constant for Mg–Na exchange:

$$K^{\mathrm{c}}_{\mathrm{Na\text{-}Mg}} = \frac{(X_2\mathrm{Mg})[\mathrm{Na}^{+}_{(\mathrm{aq})}]^2}{(X\mathrm{Na})^2[\mathrm{Mg}^{2+}_{(\mathrm{aq})}]}. \qquad [5]$$

At $t < 0$, only Na and Mg cations were present on the exchange sites. It is thus possible to calculate $K^{\mathrm{c}}_{\mathrm{Na\text{-}Mg}}$, provided that $[\mathrm{Mg}^{2+}_{(\mathrm{aq})}]$ and $X_2\mathrm{Mg}$ can be determined (as stated above, $[\mathrm{Mg}^{2+}_{(\mathrm{aq})}] \approx [\mathrm{Mg}]_{\mathrm{aq},t}$). The amount of exchangeable Mg has not been measured directly. It can be calculated however, from the difference between observed $[\mathrm{Mg}]_{\mathrm{aq},t}$ and the theoretical amount expected if no Mg were retained on exchange sites. This last value was obtained by summing the initial excess of Mg present in the suspension (~77 μM) to Mg released upon hectorite dissolution, assuming congruent release of Si and Mg (e.g., ~226 μM at $t = 0$). Comparison to observed $[\mathrm{Mg}]_{\mathrm{aq},t}$ (=75 μM) indicates that ~228 μM of Mg out of a total of 303 μM (i.e., 75%) was adsorbed on exchange sites. Equating the amount of X sites to the measured cation exchange capacity of the clay (=840 μmol g^{-1}), enabled us to calculate $K^{\mathrm{c}}_{\mathrm{Na\text{-}Mg}}$. The obtained value (0.34) is low compared to what is usually obtained for aluminum smectites (e.g., $K^{\mathrm{c}}_{\mathrm{Na\text{-}Mg}} \approx 5.8\text{–}0.7$ for Wyoming montmorillonite; (75)), but, to our knowledge, no other Na–Mg cation exchange coefficient for trioctahedral smectites has been measured yet. The amount of exchangeable Mg can be calculated from $[\mathrm{Mg}]_{\mathrm{aq},t}$ for $t > 0$, under the assumption that Co addition had little impact on the $K^{\mathrm{c}}_{\mathrm{Na\text{-}Mg}}$ value, i.e., that the value of the exchange constant remained roughly the same in binary and ternary systems. Assuming that Co uptake within the first 5 min of contact time was solely due to cation exchange at $I = 0.01$ M and that $[\mathrm{Co}^{2+}_{(\mathrm{aq})}] \approx [\mathrm{Co}]_{\mathrm{aq},t}$, $K^{\mathrm{c}}_{\mathrm{Na=Co}}$ is found to be equal to 0.18. Finally, for $t > 5$ min, the amounts of exchangeable Co and Mg in equilibrium with solute concentrations can be calculated using the Na-Co and Na-Mg exchange constants calculated above, assuming that the cation exchange coefficients are constant. Although this approximation is valid for an only limited range of solute chemical compositions (15), it can provide useful insight into the behavior of the present system. Indeed, calculations indicate that the amount of exchangeable Co did not remain constant but decreased as the total amount of sorbed Co increased with time (Fig. 10). For example, for TotCo = 100 μM, the amount of Co adsorbed on exchange sites decreased from 29.7 μmol g^{-1} (100%) at $t = 5$ min to 19 μmol g^{-1} (50%) at $t = 6$ h, and 11 μmol g^{-1} (28%) at $t = 72$ h. Hence, the decline of Co adsorption on cation exchange sites and the rise of one or several additional uptake mechanisms occur in conjunction. This inference can be further scrutinized by subtracting the contribution of cation exchange from the total amount of sorbed Co at low ionic strength (Fig. 10). The striking likeness between this kinetic pattern (Fig. 10) and those for Co sorption at high ionic strength (Fig. 7b) suggests that the same specific sorption mechanism takes place in both cases. EXAFS results confirm the formation of IS surface complexes on the edge of hectorite platelets after more than 6 h of reaction time and, hence, reveal that the reactivity of edge sorption sites is not altered upon modification of the ionic strength. This edge sorption mechanism invites comparison with the sorption properties of oxide minerals.

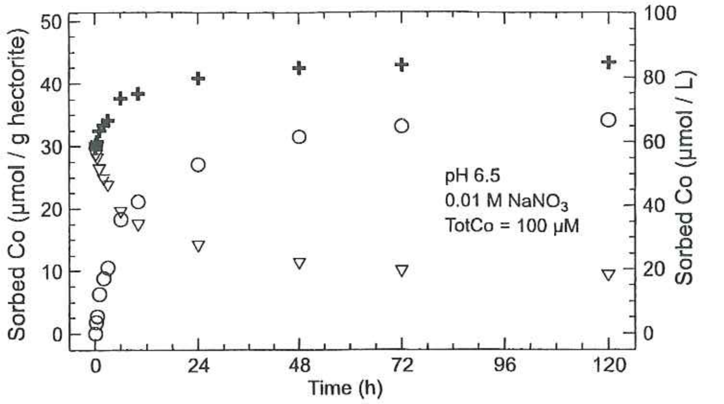

FIG. 10. Concentrations of adsorbed Co species as a function of time for TotCo = 100 μM and $I = 0.01$ M. (▽): Co adsorbed on cation exchange sites, assuming a Na-Co cation exchange coefficient $K^{\mathrm{c}}_{\mathrm{Na\text{-}Co}} = 0.18$; (○): Co assumed to be adsorbed on edge sites. (✚): Total amount of sorbed Co.

The mechanism of Co sorption at low ionic strength can now be deciphered from complementary EXAFS and solution chemistry results. Rapid Co uptake occurs first by cation exchange. After 5 min of contact time, the exchange reaction can be assumed to be near equilibrium, yet high amounts of solute Co are still present (~40 μM for TotCo = 100 μM). IS surface complexes are then forming on the edges, but this sorption mechanism is much slower than cation exchange (compare kinetics trends at $I = 0.01$ M and $I = 0.3$ M; Fig. 7a), and near-equilibrium conditions are attained only after several hours of reaction time (Fig. 7b). Hence, $[\mathrm{Co}]_{\mathrm{aq},t}$ steadily decreases as a consequence of edge sorption (Fig. 10). This decrease of $[\mathrm{Co}]_{\mathrm{aq},t}$ leads in turn to release of Co from cation exchange sites into solution, as a consequence of fast cation exchange reactions. Steady-state conditions are eventually attained when $[\mathrm{Co}]_{\mathrm{aq},t}$ is at equilibrium with both exchangeable and edge-sorbed Co ions.

In conclusion, although the total amount of Co sorbed on hectorite at $I = 0.01$ M varies by only 15 μmol g^{-1} between $t = 5$ min and 120 h, the amount of edge-adsorbed Co is inferred to increase by more than 30 μmol g^{-1}. Co ions initially adsorbed on exchange sites are transferred to IS edge sites (Fig. 11). Exchange sites act as an extemporaneous cation buffer system, which is able to control the concentration of solute Co. Furthermore, all of these computations were performed assuming that edge-adsorption started after only 5 min of contact time, although the onset of this adsorption mechanism probably coincides with $t = 0$. Thus not all sorbed Co at $t = 5$ min are present as OS surface complexes, and, according to Eq. [3], this implies that the amounts of exchangeable Co calculated above are slightly overestimated and should be regarded as upper limits.

Structure of IS Surface Complexes at Low Ionic Strength

Cation exchange considerations indicated that the fraction of Co adsorbed on exchange sites does not decrease below ~20%

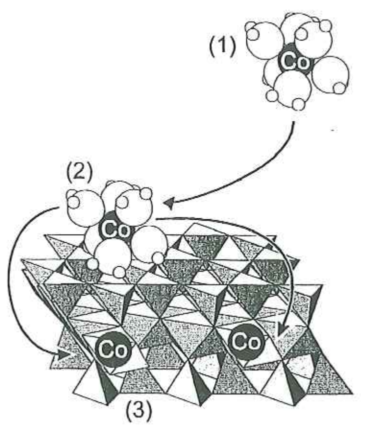

FIG. 11. Proposed mechanism of Co sorption at low ionic strength. (1) Dissolved Co. (2) Co adsorption as an outer sphere surface complex on the basal planes of hectorite. (3) Transfer and adsorption of Co on layer edges as inner sphere surface complexes.

at $I = 0.01$ M (Fig. 10) and therefore that OS surface complexes do coexist with IS edge complexes in the samples probed by EXAFS. As stated previously, EXAFS spectroscopy averages the contribution of Co atoms present as OS surface complexes, for which there is no nearest cationic shell, and those present as IS surface complexes. Because the OS complex contribution increases as ionic strength decreases, the average $N_{\mathrm{Mg}}^{\mathrm{EXAFS}}$ and $N_{\mathrm{Si}}^{\mathrm{EXAFS}}$ should be smaller at lower ionic strengths, provided the number of sorbent cation neighbors in IS surface complexes does not change. This runs counter to the similarity of $N_{\mathrm{Mg}}^{\mathrm{EXAFS}}$ and $N_{\mathrm{Si}}^{\mathrm{EXAFS}}$ values obtained at high and low ionic strengths (Table 1). Therefore, higher numbers of Mg and Si neighboring atoms surrounding edge-sorbed Co ($N_{\mathrm{Mg}}^{\mathrm{IS}}$ and $N_{\mathrm{Si}}^{\mathrm{IS}}$, respectively) are required to account for N^{EXAFS} values observed at low ionic strength. $N_{\mathrm{Mg}}^{\mathrm{IS}}$ and $N_{\mathrm{Si}}^{\mathrm{IS}}$ can be estimated from $N_{\mathrm{Mg}}^{\mathrm{EXAFS}}$ and $N_{\mathrm{Si}}^{\mathrm{EXAFS}}$ and from the fraction F of Co adsorbed on edge sites, according to

$$F = \frac{\mathrm{TotCo} - [\mathrm{Co}]_{\mathrm{aq},t} - [X_2\mathrm{Co}]}{\mathrm{TotCo} - [\mathrm{Co}]_{\mathrm{aq},t}}, \qquad [6]$$

$$N_{\mathrm{Mg}}^{\mathrm{IS}} = \frac{N_{\mathrm{Mg}}^{\mathrm{EXAFS}}}{F}, \qquad [7]$$

$$N_{\mathrm{Si}}^{\mathrm{IS}} = \frac{N_{\mathrm{Si}}^{\mathrm{EXAFS}}}{F}. \qquad [8]$$

Values of F at $I = 0.01$ M obtained from $K_{\mathrm{Na-Co}}^{\mathrm{c}} = 0.18$ are 0.50 at $t = 6$ h and 0.72 at $t = 72$ h, which gives $N_{\mathrm{Mg}}^{\mathrm{IS}} = 3.2 \pm 0.8$, $N_{\mathrm{Si}}^{\mathrm{IS}} = 4.4 \pm 1$ at $t = 6$ h, and $N_{\mathrm{Mg}}^{\mathrm{IS}} = 2.7 \pm 0.6$, $N_{\mathrm{Si}}^{\mathrm{IS}} = 3.6 \pm 0.7$ at $t = 72$ h. Comparatively, at $I = 0.3$ M, $F = 1.0$ results in $N_{\mathrm{Mg}}^{\mathrm{IS}}$ and $N_{\mathrm{Si}}^{\mathrm{IS}}$ equal to 1.6 ± 0.4 and 2.2 ± 0.5, respectively (Table 3). The dependence of $N_{\mathrm{Mg}}^{\mathrm{IS}}$ and $N_{\mathrm{Si}}^{\mathrm{IS}}$ on ionic strength contrasts with the likeness of raw EXAFS spectra at different ionic strengths.

The above line of evidence suggests that the first-formed edge Co surface complexes have a higher number of Mg and Si neighbors (the so-called "high-energy sites" (76)). These surface complexes could be $S_{\mathrm{3E+4C}}^{(010)}$ on (010) planes (Fig. 6). Then Co surface complexes having lower numbers of Mg and Si neighbors, such as $S_{\mathrm{1E+2C}}^{(010)}$, would be formed at increasing loadings. The *kinetically* favored formation of $S_{\mathrm{3E+4C}}^{(010)}$ over $S_{\mathrm{1E+2C}}^{(010)}$ can be contrasted to purely *structural* considerations (Fig. 3) suggesting that $S_{\mathrm{3E+4C}}^{(010)}$ and $S_{\mathrm{1E+2C}}^{(010)}$ surface complexes could form in approximately equal amounts.

Impact of Co Adsorption on Dissolution of Hectorite

Short-term release of Mg upon Co sorption. The increased release of Mg correlated to Co sorption at $t > 0$ was unexpected and deserves further discussion. Tiller (45) also described an excess release of Mg upon sorption of metal cations, but he did not observe the simultaneity of both phenomena. Valsami-Jones and co-workers (77) noticed that the adsorption of Pb on hydroxylapatite resulted in an equimolar release of Ca in suspension. They correlated this release with the formation of Pb hydroxylapatite. Van Cappellen and Qiu (71) observed an enhanced release of dissolved silica in the first 6 h of Co uptake on biogenic silica and attributed it to an exchange reaction. The replacement of edge-exposed Mg by adsorbing Co could account for the observed near-equimolarity between Co sorption and Mg excess release (Fig. 9a). The replacement could be favored when chemical bonds between edge-exposed Mg and bulk hectorite are weakened. For example, protonation of surface octahedral cations is known to promote their detachment from smectite edges (49, 67, 72, 73). The higher lability of protonated surface Mg octahedra is a feasible explanation for the observed simultaneity between proton release, Co adsorption, and Mg-enhanced release.

TABLE 3
Calculated Number of Mg and Si Neighboring Cations for Edge-Sorbed Co as a Function of Edge Coverage

Sample name	Edge site coverage (μmol g^{-1})	Fraction of sorbed Co on edge sites	$N_{\mathrm{Mg}}^{\mathrm{IS}}$	$N_{\mathrm{Si}}^{\mathrm{IS}}$
#0.3M-120h	37	0[a]	1.6 (±0.4)[a]	2.2 (±0.5)[a]
#0.01M-6h	19	0.5[b]	3.2 (±0.8)[b]	4.4 (±1)[b]
#0.01M-72h	34	0.72[b]	2.7 (±0.6)[b]	3.6 (±0.7)[b]

[a] Cation exchange is assumed to be completely inhibited.

[b] Derived from the total Co uptake and the conditional cation exchange constant calculated after 5 min of contact time at $I = 0.01$ M.

Long-term inhibition of hectorite dissolution by Co sorption. As apparent in Fig. 9, the release rate of Si markedly diminished after addition of Co to the suspension. One could see in this apparent inhibition an effect of the coprecipitation of Si and Co to form a Co-rich clay mineral. However, EXAFS results unequivoqually show that such a precipitation process does not occur. It may also be assumed that the higher amount of Mg in the supernatant, resulting from Co adsorption, caused a slowing of hectorite dissolution rate due to the saturation state effect (78). However, this hypothesis implies that high concentrations of dissolved Mg at constant $[\mathrm{Si}]_{\mathrm{aq},t}$ have an impact on the apparent dissolution rate of hectorite, which runs counter to previous evidence for unchanging Si release rates with $[\mathrm{Mg}]_{\mathrm{aq},t}$ increasing up to 0.05 M (79). Dissolution inhibition may instead be a direct consequence of the incorporation of high amounts of Co at layer edges of hectorite. Because Co-clays have been shown to be more stable than Mg-clays (80), the adsorption of Co likely results in the formation of Co edges of higher stability than Mg edges with respect to dissolution. As a consequence, Co adsorption would limit the extent of layer edges accessible to dissolution, thus causing the measured decrease of dissolution rates.

CONCLUSION

The combination of EXAFS spectroscopy and kinetics chemical studies proved crucial in the elucidation of the Co sorption mechanism on hectorite at $I = 0.01$ M. Whereas a very rapid cation exchange reaction on hectorite exchange sites (within minutes) was substantiated by kinetics results, EXAFS spectroscopy confirmed the formation of IS Co surface complexes on edge sites for reaction times longer than 6 h. The interpretation of kinetics measurements in the light of structural results showed that, at low ionic strength, cation exchange sites act as a transient cation buffer, from which initially sorbed cations can further migrate to hectorite edge sites. Edge-sorbed Co form various IS Co surface complexes in the continuity of hectorite octahedral sheets.

Co adsorption on edge surface sites correlated with (a) an initial excess of Mg release with respect to dissolution of pure hectorite ($0 \leq t \leq 12$ h) and (b) a longer-term inhibition of Mg and Si release rates ($t > 12$ h). The complexity of the Co sorption mechanism and its impact on hectorite stability would not have been reckoned from the sole determination of the average structure of Co surface complexes as obtained from EXAFS spectroscopy. This work therefore emphasizes the importance of coupling chemical and spectroscopic studies to better understand the role of chemical parameters such as sorbate concentration, ionic strength, residence and reaction times on the mechanism rate and reversibility of trace metal uptakes in natural systems.

ACKNOWLEDGMENTS

The Daresbury staff are acknowledged for providing the X-ray beam and for their technical assistance. D. Bosbach is also acknowledged for providing the AFM image of hectorite. The authors are grateful to P. Van Cappellen for invaluable comments and suggestions and to K. L. Nagy and an anonymous reviewer for careful reading of the manuscript. Financial support from the MAE-DAAD Procope project (#780-/ST/1/EU) is acknowledged.

REFERENCES

1. Sposito, G., "The Surface Chemistry of Soils." Oxford Univ. Press, Oxford, 1984.
2. Degueldre, C., Grauer, R., and Laube, A., *Appl. Geochem.* **11,** 697 (1996).
3. Konta, J., *in* "Euroclay Meeting" (J. Konta, Eds.), p. 11. Univerzita Karlova Praha, Prague, 1985.
4. Vanselow, A. P., *J. Am. Chem. Soc.* **54,** 1307 (1932).
5. Vanselow, A. P., *Soil Sci.* **33,** 95 (1932).
6. Gapon, E. N., *J. Gen. Chem. (U.S.S.R.)* **3,** 144 (1933).
7. Jenny, H., "Properties of Colloids." Stanford Univ. Press, Stanford, 1938.
8. Kelley, W. P., "Cation Exchange in Soils." Reinhold, New York, 1948.
9. Gaines, G. L., and Thomas, H. C., *J. Chem. Phys.* **21,** 714 (1953).
10. Maes, A., Stul, M. S., and Cremers, A., *Clays Clay Min.* **27,** 387 (1979).
11. Landelout, H., *in* "Chemistry of Clays and Clay Minerals" (A. C. D. Newman, Eds.), vol. 6. Longman Scientific & Technical, Harlow, 1987.
12. McBride, M. B., "Environmental Chemistry of Soils." Oxford Univ. Press, Oxford, 1994.
13. Tang, L., and Sparks, D. L., *Soil Sci. Soc. Am. J.* **57,** 42 (1993).
14. Verburg, K., Baveye, P., and McBride, M. B., *Soil Sci. Soc. Am. J.* **59,** 1268 (1995).
15. Sposito, G., "Chemical Equilibria and Kinetics in Soils." Oxford Univ. Press, Oxford, 1994.
16. MacEwan, D. M. C., and Wilson, M. J., *in* "Crystal Structure of Clay Minerals and their X-ray Identification" (G. Brindley and G. Brown, Eds.), p. 197. Mineralogical Society, London, 1980.
17. McBride, M. B., Pinnavaia, T. J., and Mortland, M. M., *Amer. Mineral.* **60,** 66 (1975).
18. McBride, M. B., *Clays Clay Min.* **27,** 91 (1979).
19. McBride, M. B., *Clays Clay Min.* **30,** 200 (1982).
20. Davison, N., McWhinnie, W. R., and Hooper, A., *Clays Clay Min.* **39,** 22 (1991).
21. Dillard, J. D., and Koppelman, M. H., *J. Colloid Interface Sci.* **87,** 46 (1982).
22. Siantar, D. P., and Fripiat, J. J., *J. Colloid Interface Sci.* **169,** 400 (1995).
23. Papelis, C., and Hayes, K. F., *Coll. Surf. A: Physicochem. Eng. Aspects* **107,** 89 (1996).
24. Dent, A. J., Ramsay, J. D. F., and Swanton, S. W., *J. Colloid Interface Sci.* **150,** 45 (1992).
25. Muller, F., Besson, G., Manceau, A., and Drits, V. A., *Phys. Chem. Minerals* **24,** 159 (1997).
26. Peigneur, P., Maes, A., and Cremers, A., *Clays Clay Min.* **23,** 71 (1975).
27. Egozy, Y., *Clays Clay Min.* **28,** 311 (1980).
28. Inskeep, W. P., and Baham, J., *Soil Sci. Soc. Am. J.* **47,** 660 (1983).
29. Scheidegger, A. M., and Sparks, D. L., *Chem. Geol.* **132,** 157 (1996).
30. Stadler, M., and Schindler, P. W., *Clays Clay Min.* **41,** 288 (1993).
31. Charlet, L., Schindler, P. W., Spadini, L., Furrer, G., and Zysset, M., *Aquatic Sci.* **55,** 291 (1993).
32. Zachara, J. M., and McKinley, J. P., *Aquatic Sci.* **55,** 250 (1993).
33. Zachara, J. M., Smith, S. C., Resh, C. T., and Cowan, C. E., *Soil Sci. Soc. Am. J.* **57,** 1491 (1993).
34. Zachara, J. M., and Smith, S. C., *Soil Sci. Soc. Am. J.* **58,** 762 (1994).
35. Degueldre, C., Ulrich, H. J., and Silby, H., *Radiochimica Acta* **65,** 173 (1994).

36. McKinley, J. P., Zachara, J. M., Smith, S. C., and Turner, G. D., *Clays Clay Min.* **43,** 586 (1995).
37. Baeyens, B., and Bradbury, M. H., "A Quantitative Mechanistic Description of Ni, Zn and Ca Sorption on Na-Montmorillonite. Part II: Sorption measurements." Report 95-11, Paul Scherrer Institut, Zürich, 1995.
38. Kraepiel, A. M. L., Keller, K., and Morel, F. M. M., *J. Colloid Interface Sci.* **210,** 43 (1999).
39. Schlegel, M. L., Manceau, A., Chateigner, D., and Charlet, L., *J. Colloid Interface Sci.* **215,** 140 (1999).
40. Scheidegger, A. M., Lamble, G. M., and Sparks, D. L., *J. Colloid Interface Sci.* **186,** 118 (1997).
41. Scheidegger, A. M., Strawn, D. G., Lamble, G. M., and Sparks, D. L., *Geochim. Cosmochim. Acta* **62,** 2233 (1998).
42. Fürrer, G., Zysset, M., and Schindler, P. W., *in* "Geochemistry of Clay-Pore-Fluids Interactions" (D. A. C. Manning, P. L. Hall and C. R. Hughes, Eds.), p. 243. Chapman & Hall, London, 1993.
43. Schnoor, J. L., *in* "Aquatic Chemical Kinetics" (W. Stumm, Eds.). Wiley Interscience, New York, 1990.
44. Drever, J. I., "The Geochemistry of Natural Waters." Prentice-Hall, Upper Saddle River, NJ, 1997.
45. Tiller, K. G., *Clay Min.* **7,** 409 (1968).
46. Anderson, S. J., and Sposito, G., *Soil Sci. Soc. Am. J.* **55,** 1569 (1991).
47. Jeffery, G. H., Bassett, J., Mendham, J., and Denney, R. C., "Vogel's Textbook of Quantitative Chemical Analysis." Wiley, New York, 1978.
48. Charlot, G., "Dosages absorptiométriques des éléments minéraux." Masson, Paris, 1978.
49. Stumm, W., "Chemistry of the Solid-Water Interface." Wiley, New York, 1992.
50. Baes, C. F. J., and Mesmer, R. E., "The Hydrolysis of Cations." Wiley, New York, 1976.
51. Manceau, A., Bonnin, D., Stone, W. E. E., and Sanz, J., *Phys. Chem. Minerals* **17,** 363 (1990).
52. Teo, B. K., "EXAFS: Basic Principles and Data Analysis." Springer-Verlag, Berlin, 1986.
53. Aberdam, D., *J. Synchrotron Rad.* **5,** 1287 (1998).
54. Lengeler, B., and Eisenberger, P., *Phys. Rev. B* **21,** 4507 (1980).
55. Manceau, A., and Combes, J.-M., *Phys. Chem. Minerals* **15,** 283 (1988).
56. Rehr, J. J., Albers, R. C., and Zabinsky, S. I., *Phys. Rev. Lett.* **69,** 3397 (1992).
57. Rayner, J. H., and Brown, G., *Clays Clay Min.* **21,** 103 (1973).
58. Oberlin, A., and Mering, J., *Bull. Soc. Franç. Minér. Crist.* **89,** 29 (1966).
59. Kadi-Hanifi, M., and Mering, J., *C. R. Séanc. Acad. Sc. Paris* **274 D,** 149 (1972).
60. Lotmar, W., and Feitknecht, W., *Z. Kristallograph. Kristallogeom. Krystallphys. Krystallchem.* **93,** 368 (1936).
61. Güven, N., *in* "Hydrous Phyllosilicates" (S. W. Bailey, Eds.). Reviews in Mineralogy, vol. 19, p. 497. Mineralogical Society of America, Washington, DC, 1988.
62. Bosbach, D., Charlet, L., Bickmore, B., and Hochella, M. F., Jr., submitted.
63. Brady, P. V., and Walther, J. V., *Chem. Geol.* **82,** 253 (1990).
64. Hochella, M. F., Jr., and Banfield, J. F., *in* "Chemical Weathering Rates of Silicate Minerals" (A. F. White and S. L. Brantley, Eds.). Reviews in Mineralogy, vol. 31, p. 353. Mineralogical Society of America, Washington, DC, 1995.
65. Nagy, K. L., *in* "Chemical Weathering Rates of Silicate Minerals" (A. F. White and S. L. Brantley, Eds.). Reviews in Mineralogy, vol. 31, p. 173. Mineralogical Society of America, Washington, DC, 1995.
66. Malmstrom, M., and Banwart, S., *Geochim. Cosmochim. Acta* **61,** 2779 (1997).
67. Carroll-Webb, S. A., and Walther, J. V., *Geochim. Cosmochim. Acta* **52,** 2609 (1988).
68. Fürrer, G., and Stumm, W., *Geochim. Cosmochim. Acta* **50,** 1847 (1986).
69. Wieland, E., Wehrli, B., and Stumm, W., *Geochim. Cosmochim. Acta* **52,** 1969 (1988).
70. Tester, J. W., Worley, W. G., Robinson, B. A., Grigsby, C. O., and Feerer, J. L., *Geochim. Cosmochim. Acta* **58,** 2407 (1994).
71. Van Cappellen, P., and Qiu, L., *Deep-Sea Res. II* **44,** 1129 (1997).
72. Walther, J. V., *Am. J. Sci.* **296,** 693 (1996).
73. Zysset, M., and Schindler, P. W., *Geochim. Cosmochim. Acta* **60,** 921 (1996).
74. Sposito, G., "The Thermodynamics of Soil Solutions." Oxford Univ. Press, Oxford, 1981.
75. Sposito, G., Holtzclaw, K. M., Charlet, L., Jouany, C., and Page, L., *Soil Sci. Soc. Am. J.* **47,** 51 (1983).
76. Benjamin, M. M., and Leckie, J. O., *J. Colloid Interface Sci.* **79,** 209 (1981).
77. Valsami-Jones, E., Ragnarsdottir, K. V., Putnis, A., Bosbach, D., Kemp, A. J., and Cressey, G., *Chem. Geol.* **151,** 215 (1998).
78. Lasaga, A. C., "Kinetic Theory in the Earth Sciences." Princeton Univ. Press, Princeton, 1998.
79. Tiller, K. G., *Clay Min.* **7,** 245 (1968).
80. Decarreau, A., *Geochim. Cosmochim. Acta* **49,** 1537 (1985).

5. Adsorption de Zn sur l'hectorite à pH ≤ 6,5

La cinétique d'adsorption macroscopique de Zn sur l'hectorite a été étudiée à deux forces ioniques ($NaNO_3$ 0,01 et 0,3 M) et deux pH (pH 6,5 et 4), pour une concentration totale en Zn (TotZn) de 100 µM. Les expériences ont été réalisées à des teneurs en hectorite de 1,95 g L^{-1} (pH 6,5) et 2,2 g L^{-1} (pH 4). Les concentrations en solution des espèces chimiques Zn, Mg, et Si ont été mesurées pour des temps de réaction croissants. La nature des complexes de surface formés à pH 6,5 a été déterminée par spectroscopie P-EXAFS sur films auto-supportés, et par spectroscopie EXAFS sur des pâtes humides. Les résultats obtenus sont détaillés dans l'article intitulé « *Adsorption mechanism of Zn on hectorite as a function of time, pH, and ionic strength* » situé à la fin de cette section.

5.1. Cinétique d'adsorption macroscopique

À basse force ionique, une proportion importante de Zn est adsorbée pendant les cinq premières minutes de réaction, quel que soit le pH (fig. 5.1). Cette cinétique très rapide est caractéristique d'une adsorption sur les sites d'échange cationique. Après cette étape initiale, la fixation du zinc sur l'hectorite se poursuit à une vitesse plus faible à pH 6,5 (fig. 5.1.b) alors qu'à pH 4 lZn est progressivement relâché en solution (fig. 5.1.a). L'inhibition de l'échange cationique à haute force ionique permet de mettre en évidence une fixation de Zn sur une échelle de temps plus longue, d'environ 48 h, et de plus forte amplitude à haut pH. Après 72 h de réaction, pratiquement tout le Zn introduit à pH 6,5 est adsorbé, alors que seulement 35 % de TotZn l'est à pH 4.

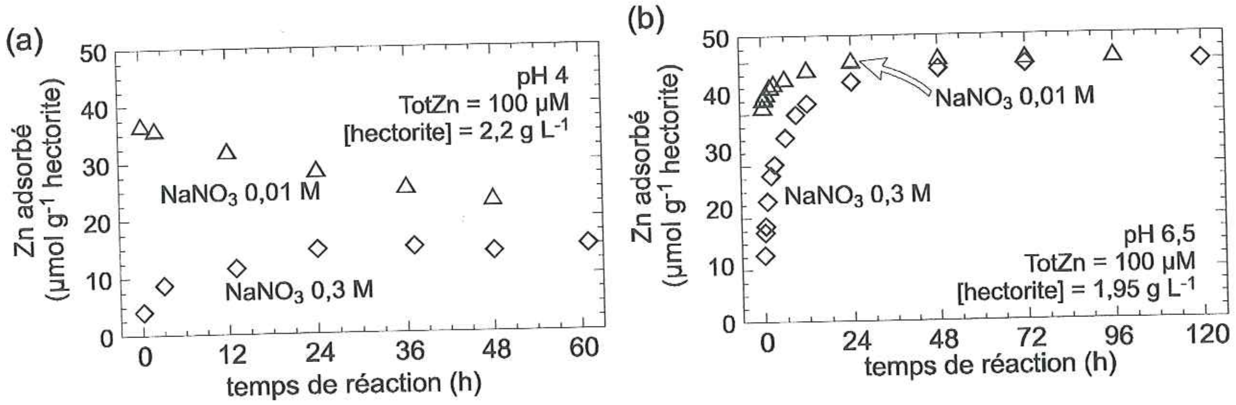

Figure 5.1. Cinétique d'adsorption de Zn sur l'hectorite en fonction du pH dans un fond ionique de $NaNO_3$ 0,3 M (◇) et 0,01 M (△). (a) pH 4. (b). pH 6,5.

À pH 4 et à haute force ionique, le taux de dissolution de l'hectorite en présence de Zn est légèrement inférieur au taux de dissolution en absence de Zn, suggérant que l'adsorption de Zn à ce pH ralentit un peu la cinétique de dissolution. La cinétique de dissolution de l'hectorite à pH 6,5 est par contre fortement modifiée par l'addition de Zn. Ces modifications sont similaires à celles observées lors de l'addition de Co (fig. 4.6) avec, d'une part, une inhibition immédiate et durable du taux de libération de Si, et, d'autre part, une libération de Mg accélérée durant les premières heures d'adsorption de Zn, puis inhibée après environ 24 h de contact. Les résultats obtenus de cinétique d'adsorption du zinc, et de l'impact de cette adsorption sur la stabilité de l'hectorite, présentent donc des similitudes importantes avec ceux obtenus pour le cobalt.

5.2. Structure des complexes de surface à pH 6,5

Afin de caractériser l'environnement cristallochimique du Zn adsorbé, des films auto-supportés d'hectorite ayant réagi avec Zn à pH 6,5 ont été caractérisés par spectroscopie P-EXAFS. Les spectres enregistrés à haute et basse force ionique, et pour des temps de réaction en solution de 6 h ou plus, présentent tous une dépendance angulaire semblable à celle observée pour le cobalt, ce qui indique que les environnements structuraux de ces deux cations sont comparables. Les TF de ces spectres présentent plusieurs pics provenant des contributions des couches atomiques entourant le zinc (fig. 5.2). L'analyse de ces contributions montre que les cations Zn sont hexacoordonnés et entourés d'une couche de 1,5-1,8 (± 0,5) Mg à environ 3,08 Å dans le plan du film, et d'une couche de 1,8-2,7 (± 0,5) Si à environ 3.26 Å hors du plan du film. Ces données structurales indiquent que le zinc forme des CSI localisés en bordure des feuillets d'hectorite, en continuité structurale de la couche octaédrique (Mg, Li), comme dans le cas du cobalt.

Figure 5.2. Modules des TF des spectres P-EXAFS enregistrés sur un film auto-supporté de Zn adsorbé sur l'hectorite à haute force ionique.

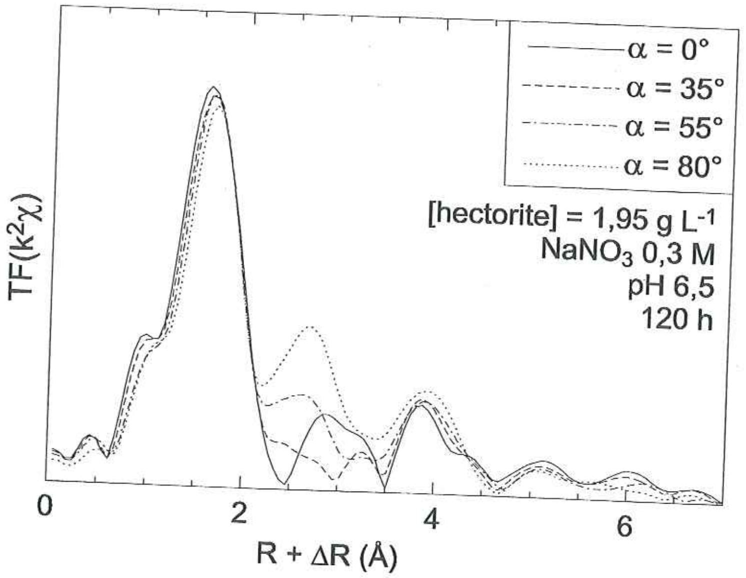

Les spectres EXAFS enregistrés sur des pâtes humides d'hectorite ayant réagi avec le Zn à haute force ionique sont semblables à ceux obtenus pour les films auto-supportés. Ceci confirme que les CSI observés par spectroscopie P-EXAFS à haute force ionique se sont formés lors des réactions d'adsorption en suspension. En revanche, le spectre enregistré sur une pâte humide pour une basse force ionique et pour un temps de réaction en solution court (t = 5 min) à pH 6,5 est semblable au spectre de Zn hydraté : tous deux ne présentent qu'une seule fréquence dont l'amplitude décroît de manière monotone (fig. 5.3). Cela indique que le zinc adsorbé dans ces conditions forme des CHS, en accord avec les résultats de l'étude cinétique montrant une adsorption initiale rapide par échange cationique. Pour des temps de réaction croissants (t = 6 h et 96 h), les spectres présentent de nouvelles fréquences d'amplitude de plus en plus importante, et au bout de 96 h de temps de réaction le spectre EXAFS est comparable à celui d'un CSI en bordure de feuillet. Cette évolution spectrale indique que la proportion de zinc adsorbée sur les sites d'échanges cationiques décroît, et celle formant des CSI en bordure de feuillets croît, pour des temps de réaction croissants.

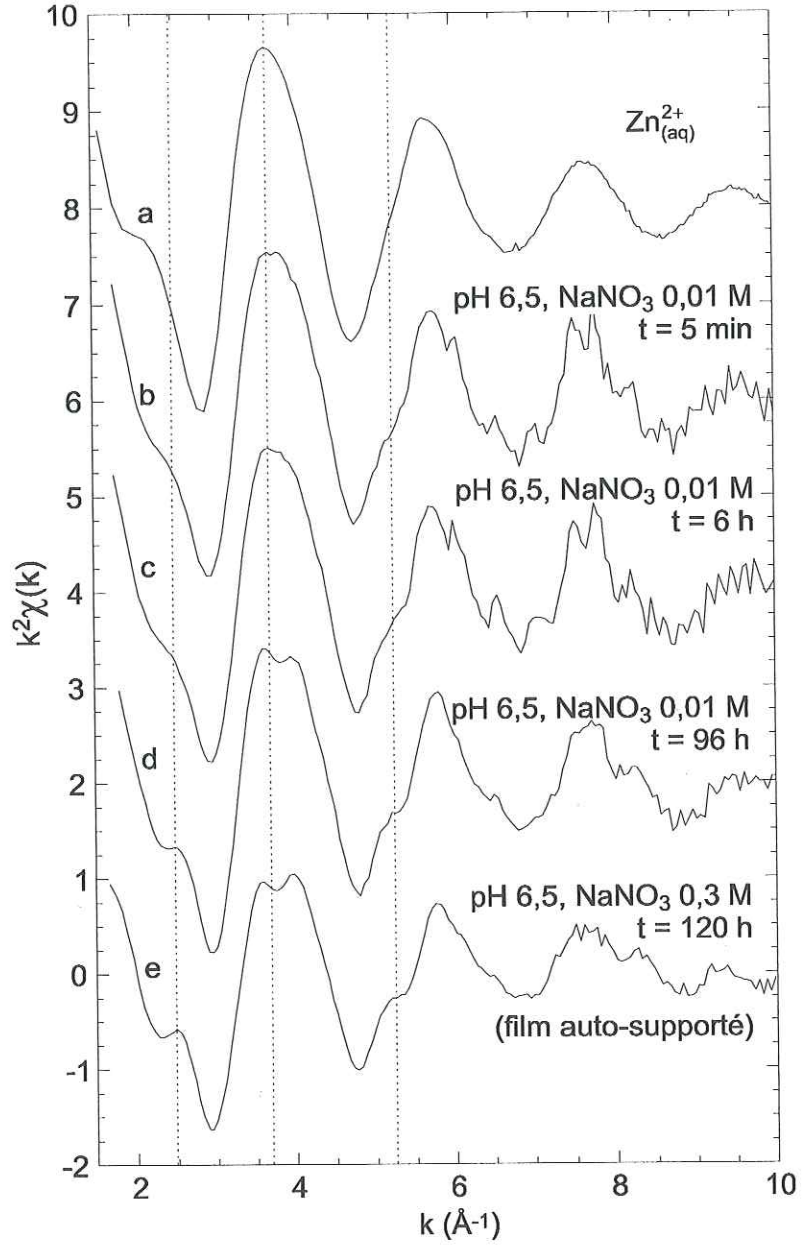

Figure 5.3. Spectres EXAFS (a) du zinc solvaté, (b-d) des échantillons de pâte humide d'hectorite ayant réagi avec Zn à basse force ionique, et (e) d'un film auto-supporté de Zn ayant réagi avec l'hectorite à haute force ionique. Tous les spectres ont été enregistrés à l'angle magique. À cet angle, le spectre enregistré sur un film est identique à celui obtenu avec une poudre isotrope.

Ces résultats démontrent que le zinc adsorbé initialement sur les *sites d'échange cationique* à pH 6,5 est transféré ultérieurement sur *les sites de bordure* de l'hectorite, soit par migration sur les plans de base depuis les sites d'échange cationique vers les sites de bordure, soit par désorption du zinc échangeable et réadsorption directe sur les sites de bordure depuis le surnageant (fig. 5.5). La cinétique du premier mécanisme n'est pas connue, celle du deuxième peut être estimée à partir de la cinétique d'adsorption directe du zinc sur les sites de bordure à haute force ionique. Cependant, pour ces deux mécanismes, la quantité de Zn échangeable après un temps de réaction donné peut être calculée en prenant un coefficient de sélectivité pour l'échange Na-Zn de $K^{c}_{Na-Zn} = 0,41 \pm 0,06$. Ce calcul montre que la quantité de Zn échangeable à l'équilibre avec le Zn en solution diminue avec le temps, jusqu'à devenir négligeable au bout de 96 h (moins de 5 % du Zn adsorbé). Les données EXAFS obtenues sur des pâtes humides à des temps de réaction croissants confirment que la fraction croissante de zinc fixée par l'hectorite et non échangeable est adsorbée sur les sites de bordure des feuillets d'hectorite. La cinétique (calculée) de cette adsorption spécifique de Zn à basse force ionique (fig. 5.4) semble un peu plus lente qu'à haute force ionique. Cette observation montre que le mécanisme de migration du zinc échangeable vers les sites de bordure n'est pas significativement plus rapide que le mécanisme d'adsorption directe. On pourrait expliquer cela par l'existence d'une étape cinétiquement limitante unique et commune à ces deux mécanismes.

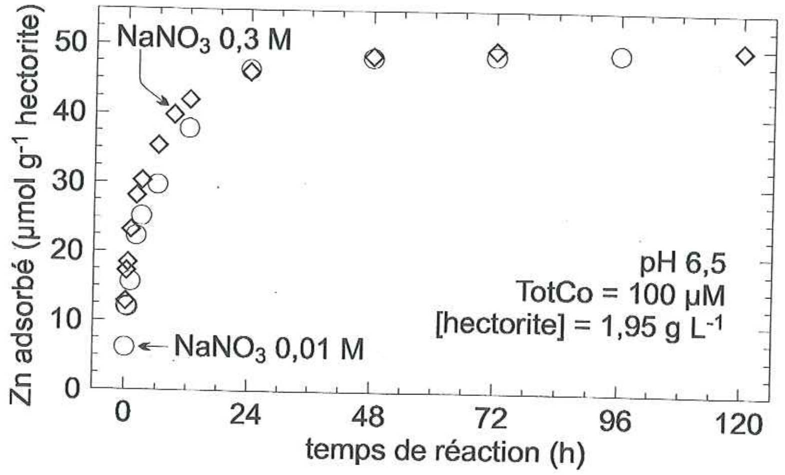

Figure 5.4. Comparaison des cinétiques d'adsorption spécifique de Zn sur l'hectorite à basses (○) et hautes (◇) forces ioniques.

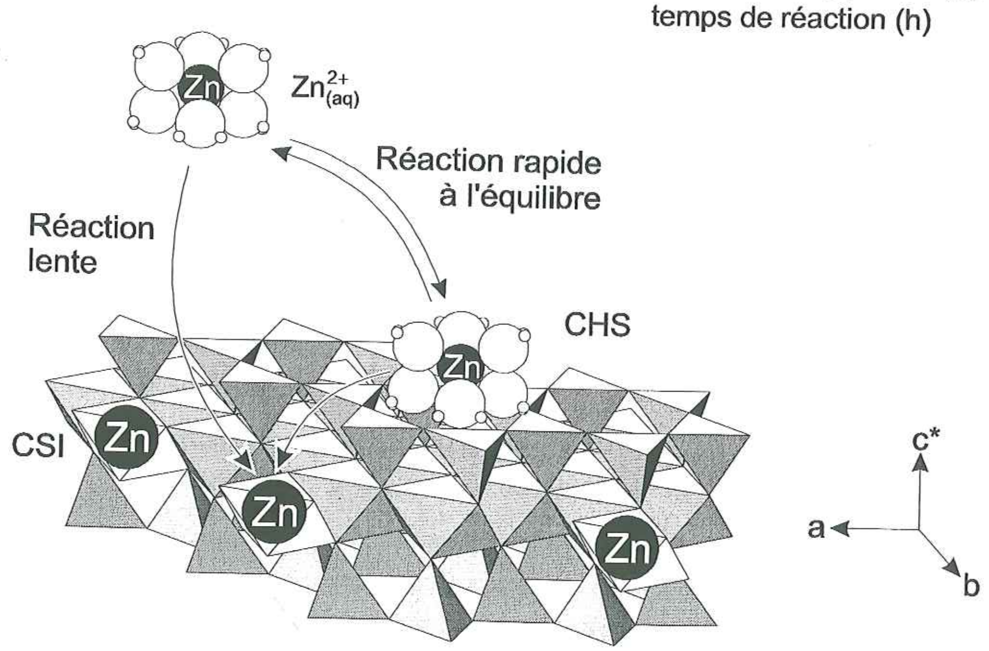

Figure 5.5. Mécanisme d'adsorption du zinc sur l'hectorite à pH 6,5 et basse force ionique. Le Zn est adsorbé initialement sur des sites d'échange cationique où il forme des complexes hors sphère (CHS). Il est ensuite transféré des sites d'échange vers les sites de bordure des feuillets, où il forme des complexes de sphère interne (CSI).

(*Adsorption mechanism of Zn on hectorite as a function of time, pH, and ionic strength.* Article soumis à American Journal of Science)

ADSORPTION MECHANISM OF ZN ON HECTORITE AS A FUNCTION OF TIME, PH, AND IONIC STRENGTH

Michel L. Schlegel, Alain Manceau, Laurent Charlet, Jean-Louis Hazemann

Environmental Geochemistry Group, LGIT-IRIGM, University of Grenoble and CNRS, BP 53

F-38 041 Grenoble cedex 9, France

Corresponding author: Alain Manceau

e-mail: Alain.Manceau@ujf-grenoble.fr

Key Words: Zn, hectorite, adsorption, kinetics, EXAFS, Polarized EXAFS, in-situ EXAFS, surface complex, cation exchange

ABSTRACT

The mechanism of Zn uptake in dilute suspensions (~2 g L^{-1}) of hectorite was investigated by kinetics chemical experiments and extended X-ray absorption fine structure (EXAFS) spectroscopy on wet pastes and self-supporting films of Zn-sorbed hectorite. Kinetics experiments were performed at various pH (4 and 6.5), ionic strengths (0.3 and 0.01 M $NaNO_3$), and at a total Zn concentration of 100 µM.

At low ionic strength (0.01 M $NaNO_3$), an important Zn uptake occurred within the first 5 min of reaction, whatever the pH. This rapid kinetics is consistent with Zn adsorption on exchange sites located on basal planes of hectorite. After this fast sorption, the amount of sorbed Zn either slowly increased (pH 6.5) or decreased (pH 4). At high ionic strength (0.3 M $NaNO_3$), Zn uptake within was less rapid than at low ionic strength the first 5 min, and the amount of sorbed Zn gradually increased afterwards at both pH 4 and 6.5, with higher uptake being observed at higher pH. This behavior is consistent with Zn adsorption on pH-dependent sites. The dissolution of hectorite was monitored during Zn sorption. At pH 6.5 and 0.3 M $NaNO_3$, an initial correlation was observed between Zn uptake and an excess release of Mg relative to pure hectorite suspension. In contrast, Si release was inhibited immediately after Zn addition. At pH 4, the dissolution of hectorite seemed unaffected by Zn addition.

At pH 6.5, similar polarized-EXAFS (P-EXAFS) spectra were obtained on self-supporting films for the two ionic strengths (0.01 and 0.3 M $NaNO_3$) and for reaction times comprised between 6 h and 120 h, suggesting a similarity in the crystallochemical environment of Zn. Four atomic shells were identified from the quantitative analysis of P-EXAFS spectra: a nearest O shell at $R_{Zn-O} = 2.06 \pm 0.01$ Å, a Mg shell at $R_{Zn-Mg} = 3.06\text{-}3.09 \pm 0.03$ Å, a Si shell at $R_{Zn-Si} = 3.23\text{-}3.26 \pm 0.03$ Å, and a next-nearest O shell at $R_{Zn-O} = 3.69\text{-}3.74 \pm 0.06$ Å. R_{Zn-Mg} and R_{Zn-Si} values are characteristic of edge-sharing linkages between Zn and Mg octahedra, and of corner-sharing linkages between Zn octahedra and Si tetrahedra, respectively. The angular dependence of the Zn-Mg and Zn-Si contributions indicates that Zn-Mg pairs are oriented parallel to the film plane, whereas Zn-Si pairs are not. These results are indicative of the formation of Zn inner-sphere (IS) surface complexes at layer edges of hectorite platelets, in continuity to octahedral sheets. Magic-angle EXAFS spectra recorded on wet pastes and self-supporting films obtained at pH 6.5 and 0.3 M $NaNO_3$ bear strong similarity, confirming the validity of this IS uptake mechanism under full wet conditions at high ionic strength. At 0.01 M $NaNO_3$, a continuous evolution with increasing reaction time from predominant outer-sphere (OS) to predominant IS complexes was observed for wet pastes. A two-step sorption mechanism is proposed from the combination of structural and chemical results at 0.01 M $NaNO_3$ and pH 6.5: solute Zn initially sorbs as OS exchangeable complex on interlayer sites, and then migrates to layer edge where it forms IS surface complex.

SYMBOLS

OS = outer-sphere

IS = inner-sphere

EXAFS = extended X-ray absorption fine structure

P-EXAFS = polarized extended X-ray absorption fine structure

FT = Fourier transform of the EXAFS spectrum

RSF = radial structure function

α = angle between the X-ray polarization vector and the phyllosilicate plane

β_j = angle between the **c*** axis of the phyllosilicate layer and the vectors connecting the X-ray absorbing atom to backscattering atoms in the j shell

k = modulus of the wavevector in EXAFS spectroscopy

$\chi(k)$ = EXAFS function

χ_j^α = EXAFS contribution of a j shell at the α angle

χ_j^{iso} = EXAFS contribution of a j shell at the magic angle

N_j^α = apparent number of backscatterers in the j shell at the α angle

$N_j^{35°}$ = structural number of backscatterers in the j shell

R_{Zn-j}^{EXAFS} = EXAFS-derived interatomic distance between Zn absorber and backscattering atoms in the j shell

σ = Debye-Waller term in EXAFS spectroscopy. Account for the atomic disorder

S_0^2 = amplitude reduction factor in EXAFS spectroscopy

R_P = reliability factor used to adjust model to sample EXAFS spectra

ZnKer = Zn-containing kerolite

ZnKer300 = Zn-kerolite $Zn_3Si_4O_{10}(OH)_2{\cdot}nH_2O$

ZnKer070 = Zn-containing kerolite $Zn_{0.7}Mg_{2.3}Si_4O_{10}(OH)_2{\cdot}nH_2O$

ZnKer003 = Zn-containing kerolite $Zn_{0.03}Mg_{2.97}Si_4O_{10}(OH)_2{\cdot}nH_2O$

E linkage = edge-sharing linkage

C linkage = corner-sharing linkage

I = ionic strength

$Zn^{2+}_{(aq)}$ = fully solvated Zn^{2+} cation

$[Zn]_{aq,tot}$ = concentration of Zn in the supernatant

$[Si]_{aq,tot}$ = concentration of Si in the supernatant

$[Mg]_{aq,tot}$ = concentration of Mg in the supernatant

TotZn = Total Zn concentration in the suspension

TotCo = Total Co concentration in the suspension

INTRODUCTION

At low concentration, Zn is a micronutrient for living organisms (Stout, 1956; Reed and Martens, 1996). Because plants absorb Zn from soil solution, maintaining adequate levels of dissolved Zn in soils is essential to the optimal growth of crops (Reed and Martens, 1996). At high concentration, this element can accumulate in organic matter and reach toxic levels, causing for example leaf chlorosis and necrosis, plant death, and articular diseases to vertebrate organisms (Beyer and Storm, 1995). High Zn levels in the environment can result from sewage sludge deposition, smelter emission, mine drainage, and industrial waste dispersion (O'Neill, 1993; Reed and Martens, 1996). To satisfy both agricultural requirements and public health policies, it is important to understand the mechanisms regulating the solute concentration and bioavailability of Zn in soils.

It is currently admitted that the fate of Zn in natural systems is mainly controlled by reactions with both organic matter and mineral surfaces (Sposito, 1984; McBride, 1994). At low concentration and low pH, Zn is complexed by organic matter or held up by clay minerals in an exchangeable form (McBride, 1994; Sarret, 1998). At higher concentration, or higher pH, the solute concentration of Zn is thought to be controlled by sorption on (hydr)oxide minerals (McBride, 1994) or precipitation of Zn hydroxycarbonates (Schindler, 1991). Structural association of Zn with smectite minerals was also inferred (McBride, 1994), and was recently observed in contaminated soils (Manceau and others, 2000c). The high affinity of Zn for phyllosilicates in natural systems (Ross, 1946; Rivière and others, 1985; Manceau and others, 2000c) agrees with the relatively low solubility of synthetic Zn-containing phyllosilicates (Decarreau, 1985; Manceau and others, 2000c). This affinity appeals for a detailed characterization of the possible interactions between Zn and phyllosilicates, such as smectites.

Like many divalent cations, the retention of Zn on smectites can be achieved by various molecular mechanisms. Divalent metal cations can adsorb as outer-sphere (OS) surface complexes on basal planes to balance the structural layer charge (McBride, Pinnavaia, and Mortland, 1975; McBride, 1979; MacEwan and Wilson, 1980; McBride, 1982; Dent, Ramsay, and Swanton, 1992; Papelis and Hayes, 1996; Muller and others, 1997). The exchangeability of interlayer cations depends on their hydration enthalpies, the cationic composition and concentration of the solution (fig. 1), the phyllosilicate concentration, and the location of the charge deficit in the phyllosilicate structure (Vanselow, 1932a, Vanselow, 1932b, Gapon, 1933, Jenny, 1938, Kelley, 1948, Gaines and Thomas, 1953, Maes, Stul, and Cremers, 1979, Sposito, 1984, Laudelout, 1987, McBride, 1994). The kinetics of the cation exchange is fast, and the steady-state aqueous concentration of the sorbate is attained within a few minutes (Tang and Sparks, 1993; Sposito, 1994; Verburg, Baveye, and McBride, 1995). Divalent metal cations can also sorb on smectites via a pH-dependent mechanism, as on oxide and hydroxide mineral surfaces (Peigneur, Maes, and Cremers, 1975; Egozy, 1980; Inskeep and Baham, 1983; Charlet and others, 1993; Stadler and Schindler, 1993; Zachara and McKinley, 1993; Zachara and others, 1993; Degueldre, Ulrich, and Silby, 1994; Zachara and Smith, 1994; McKinley and others, 1995; Scheidegger and Sparks, 1996; Bradbury and Baeyens, 1999). At pH_1 in figure 1, only a small fraction of Zn is retained by this sorption mechanism, and this amount can fluctuate, owing to competitive sorption by cation exchange. At $pH_2 > pH_1$, nearly 100 percent of Zn is adsorbed, whatever the ionic strength. This pH-dependent uptake is interpreted at the atomic scale by the formation of inner-sphere (IS) complexes on oxygen dangling bonds at the edges of smectite crystallites (Charlet and others, 1993; Stadler and Schindler, 1993; Zachara and McKinley, 1993; Zachara and Smith, 1994; McKinley and others, 1995; Kraepiel, Keller, and Morel, 1999; Schlegel, Charlet, and Manceau, 1999; Schlegel and others, 1999). The increase in pH and sorbate concentration can also lead to the formation of sorbate-containing precipitates (Scheidegger, Lamble, and Sparks, 1997; Ford and Sparks, 1998; Scheidegger and others, 1998), and, therefore, to the long-term occlusion of Zn from soil solutions (O'Neill, 1993; Manceau and others, 2000c).

The distinction between cation exchange, layer edge adsorption, and sorbate precipitation is of crucial importance, inasmuch as these uptake mechanisms influence the time scale of Zn desorption, and, thus, of Zn bioavailability in soils. The various uptake mechanisms are usually differentiated macroscopically from the dependence on pH and ionic strength and from the reversibility of the cation uptake. However, the dependence of sorption/desorption kinetics on pH and ionic strength, and the competition between distinct uptake mechanisms are generally overlooked in macroscopic studies (Sposito, 1994; Scheidegger and others, 1998). Conversely, sorption mechanisms of divalent cations on clay minerals can be studied directly at the molecular level by extended X-ray absorption fine structure (EXAFS) spectroscopy (Scheidegger, Lamble, and Sparks, 1997; Scheidegger and others, 1998; Schlegel, Charlet, and Manceau, 1999; Schlegel and others, 1999). The structural information (interatomic distances and the nature and number of atomic neighbors) obtained from the analysis of EXAFS spectra is limited by the extension of the explored reciprocal space (generally $\Delta k \leq 14$ Å^{-1}), which precludes the discrimination of close atomic shells (Teo, 1986). The uncertainty on structural parameters for overlapping atomic contributions is relatively high, and seriously limits the characterization of the sorbate crystallochemical environment (Stern, 1988; Manceau and others, 1999b). The overlap of contributions is a problem for phyllosilicates, because X-ray absorbing atoms in the octahedral sheet are surrounded by neighboring cations at R ~ 3.00-3.12 Å in the octahedral sheet and R ~ 3.20-3.30 Å in tetrahedral sheets (Manceau, 1990). In an effort to overcome this limitation, Manceau and coworkers (Manceau and others, 1988; Manceau and others, 1990) performed polarized-EXAFS (P-EXAFS) experiments on biotite single crystals (fig. 2). In P-EXAFS, the contribution of (Si, Al) cations in tetrahedral sheets is minimized and the contribution of (Fe, Mg) cations in the octahedral sheet enhanced, when the experimental angle α between the X-ray polarization vector and the phyllosilicate plane equals 0° (parallel orientation; fig. 2, left). Conversely, the contribution of (Fe, Mg) cations is extinguished, and that of (Si, Al) cations enhanced, for α = 90° (normal orientation; fig. 2, right). Magnifying alternatively the contributions of octahedral and tetrahedral shells increases the precision on structural parameters. P-EXAFS was extended recently to fine-grained layer minerals (Manceau, Chateigner, and Gates, 1998; Manceau and others, 1999a), and successfully applied to the crystal chemistry of oxidized and reduced nontronite (Manceau and others, 2000a; Manceau and others, 2000b), to the sorption mechanism of Co on the phyllomanganate buserite (Manceau and others, 1997) and on the trioctahedral smectite hectorite (Schlegel and others, 1999), and to the speciation of Zn in soils (Manceau and others, 2000c). These studies showed that P-EXAFS on self-supporting films of fine-grained minerals allows the characterization of the

anisotropic structural environment of cations sorbed on, or occluded in, layered structures with an enhanced precision as compared to powder EXAFS.

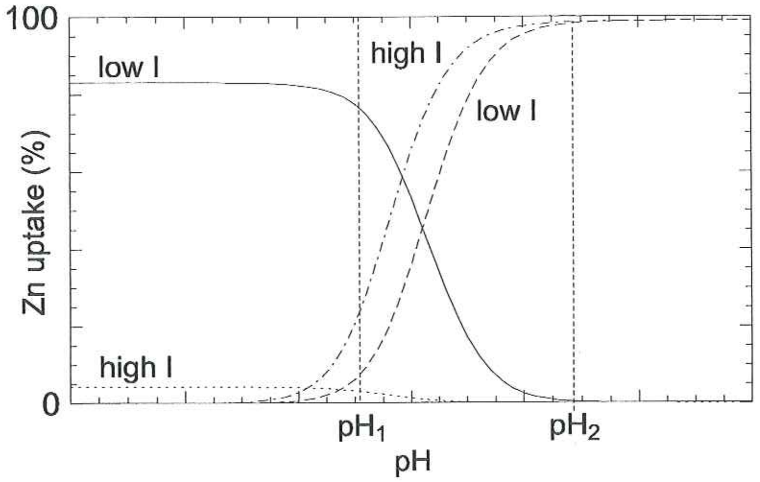

Fig. 1. Influence of pH and ionic strength (I) on the steady-state mechanism of cation sorption on smectites at low sorbate/sorbent ratio, as inferred from batch experiments (Charlet and others, 1993). Solid line: sorption by cation exchange at low I. Dotted line: sorption by cation exchange at high I. Dashed line: pH-dependent sorption at low I. Dash-dotted line: pH-dependent sorption at high I. Only a small fraction of the sorbate is sorbed via a pH-dependent mechanism at pH_1, whereas almost all sorbate cations are fixed by this mechanism at pH_2.

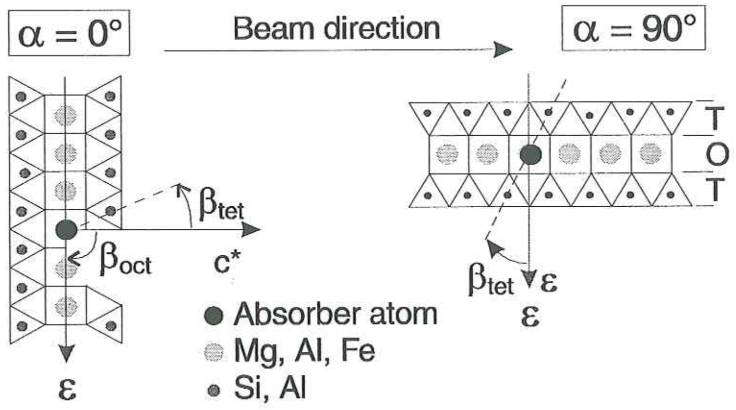

Fig. 2. Principle of polarized EXAFS measurements on phyllosilicates. Left: electric field vector **ε** parallel to the layer plane (α = 0°). Right: **ε** perpendicular to the layer plane (α = 90°).

This study aims at determining the mechanism(s) of Zn uptake in suspensions of hectorite. The influence of pH and ionic strength on Zn uptake are studied first by batch kinetics experiments, and interpreted in terms of cation exchange and specific sorption reactions. Then, the molecular environment of Zn sorbed at high and low ionic strength at pH 6.5, is determined by combining magic-angle EXAFS (MA-EXAFS) spectroscopy on wet pastes, and P-EXAFS spectroscopy on self-supporting films of Zn-sorbed hectorite. Finally, EXAFS-derived structural models are used to interpret mechanistically macroscopic data.

EXPERIMENTAL

Hectorite purification and characterization

Hectorite $Na_{0.40}(Mg_{2.65}Li_{0.35})(Si_{3.95}Al_{0.05})O_{10}(OH)_2$ was purchased from the Clay Mineral Repository (SHCa-1). (Mg, Li) atoms are located in the octahedral sheet and (Si, Al) atoms in the tetrahedral sheets of the magnesian smectite. Approximately 25 g of the raw material were suspended in 1 L of deionized Milli-Q water, and shaken at 180 rpm for 48 h. The <2 μm fraction was extracted by sedimentation techniques, treated several times with a 10^{-4} mol L^{-1} (M) HNO_3, 0.5 M NaCl solution to remove carbonate minerals, and subsequently washed five times with a 0.5 M NaCl solution to exchange interlayer cations with Na. No concentrated inorganic acid solutions were used, because hectorite dissolves quickly in strong acidic media (Kreit, Shainberg, and Herbillon, 1982; Komadel and others, 1996). Afterwards the clay suspension was treated for 1 h with a 5.10^{-3} M dithionite, 0.2 M citrate, 0.1 M bicarbonate, 0.5 M NaCl solution at pH 6.5 and room temperature to remove possibly remaining ferric oxides, and for 1 h with a 3 percent H_2O_2, 0.5 M NaCl solution at 50°C to remove organic matter (Jackson, 1964; Zachara and Smith, 1994). Remaining H_2O_2 was destroyed by heating the suspension for more than 1 h at 70°C. Dialysis against Milli-Q water was then performed until no Cl^- anions could be detected ($AgNO_3$ test). The final 2 percent weight stock suspension was stored at 4°C in the dark prior to use. Measurements of aqueous $Si(OH)_4$ released during the purification procedure showed that the amorphous-SiO_2 solubility limit was never reached. The purified clay suspension was characterized by X-ray diffraction on a Siemens D-500 X-ray diffractometer. No trace of crystallized carbonate mineral could be detected. The cation exchange capacity (CEC), measured by Cs exchange (Anderson and Sposito, 1991), is 840 meq kg^{-1}, and the specific surface area measured by BET equals 114 m^2 g^{-1}.

Zn sorption experiments

All solutions were prepared with Milli-Q water and chemicals of ACS reagent grade. Sorption experiments were conducted at 25°C (±0.1°C) in polyethylene vessels immersed in a thermostatic water bath. Polyethylene was chosen to avoid interactions of dissolved cations and silica with the vessel walls. A Teflon-coated rotating magnetic bar ensured vigorous stirring of the suspension. A water vapor-saturated inert atmosphere was maintained by bubbling humidified Ar that had passed beforehand through a purification setup (10 percent H_2SO_4, then 0.1 M NaOH, and finally $NaNO_3$ at the ionic strength of the suspension). Constant concentrations of the background $NaNO_3$ electrolyte were maintained throughout the experiments by preparing the working solutions with the appropriate amounts of $NaNO_3$ salt (Fluka). pH measurements were performed with a Metrohm combined electrode connected to a Metrohm pH-meter. This electrode was calibrated with buffers (Merck, titrisol), and recalibrated at least every 72 h. During kinetics experiments, the pH of the suspension was maintained at the desired value ±0.05 (pH 4 or 6.5) by a PC-controlled pH-stat that delivered small aliquots of acid (0.1 M HNO_3) or base (0.01 M NaOH) solutions adjusted at the Na concentration of the suspension, as needed. The base solution was prepared with CO_2-free deionized water. The hectorite concentrations in suspensions were 1.95 g L^{-1} (pH 6.5), and 2.2 g L^{-1} (pH 4).

After a pre-equilibration time of 48 h at pH 6.5, or 3 h at pH 4, an aliquot of a 0.21 M $Zn(NO_3)_2$, 10^{-3} M HNO_3 solution was added to the clay suspension to obtain a total Zn concentration of TotZn = 100 μM. The time of Zn addition is referred to as t = 0. Following Zn addition, pH was immediately readjusted to the target value (± 0.05), and maintained to this value by adding some base solution. At given times ($0 < t \leq 120$ h), 5 ml of the suspension were withdrawn with a plastic syringe connected to a polyethylene needle, centrifuged, and filtered (Sartorius 0.1 μm cellulose nitrate filter) for chemical analysis. The first milliliter of the filtered supernatant was discarded to limit losses due to sorption on the filter. Zn and Mg total concentrations in the filtered supernatant, $[Zn]_{aq,tot}$ and $[Mg]_{aq,tot}$, were measured by inductively coupled plasma-atomic emission spectrometry, and total Si concentration, $[Si]_{aq,tot}$, by spectrophotometry (Charlot, 1978; Jeffery and others, 1978). In experiments conducted at pH 6.5, $[Si]_{aq,tot}$ never exceeded 400 μM, hence silicic acid was assumed to remain predominantly in monomeric form (Stumm, 1992). In contrast, $[Si]_{aq,tot}$ at the end of experiments conducted at pH 4 (1550-1700 μM) were not far from the solubility limit of amorphous SiO_2 (~2000 μM; (Iler, 1979), and polymerization of silicate species may have occurred in solution (Stumm, 1992). Supersaturation with respect to quartz (solubility of 183 μM; (Rimstidt, 1997) was observed for all experiments, but was neglected owing to the slow crystallization rate of quartz at room temperature (Stumm and Morgan, 1996). In all experiments, more than 99.9 percent of Zn dissolved in the supernatant was present as $Zn^{2+}_{(aq)}$ (Baes and Mesmer, 1976). Thus $[Zn^{2+}_{(aq)}] \approx [Zn]_{aq,tot}$ within experimental uncertainties. Likewise, $[Mg^{2+}_{(aq)}] \approx [Mg]_{aq,tot}$.

Preparation of sorption samples for EXAFS

Preparation of self-supporting films.-Zn-sorbed hectorite samples were prepared following the chemical protocol used for kinetics experiments. 60 μm thick self supporting films were obtained by slowly filtering 60 ml of the suspension on a 0.05 μm Sartorius cellulose nitrate filter in a closed filtration vessel. Filtration was performed under a continuous flow of humidified argon to limit contamination by atmospheric carbonate. Excess of salt and aqueous Zn were washed with a few milliliters of Milli-Q water before drying. Several slices of the same film were cut and stacked on a sample holder, in order to get a thick sample for fluorescence-yield P-EXAFS measurements. Upon stacking, the slices were successively rotated around an axis perpendicular to the film plane to improve the in-plane disorientation of hectorite crystallites. Self-absorption effects are negligible owing to the low concentration of Zn in the sample ($\Delta\mu/\mu < 0.01$ at $\alpha = 60°$; (Tröger and others, 1992; Castañer and Prieto, 1997).

Preparation of wet pastes.-Aliquots for self-supporting films and wet pastes were withdrawn from the reaction vessel simultaneously. Wet pastes were obtained by centrifuging 30 ml of the clay suspension (15 min at 10,000 rpm), and removing the clear supernatant. Pastes were then loaded in Teflon sample holders and sealed with Kapton windows. Samples prepared at 0.3 M $NaNO_3$ were stored at 2°C for 15 days before EXAFS measurements, whereas those at 0.01 M $NaNO_3$ were measured approximately 30 min after centrifugation. An additional sample was prepared by dispersing hectorite in bidistilled water ([hectorite] = 2 g L^{-1}) at pH 3.7, then spiking the suspension with 0.21 M $Zn(NO_3)_2$ to a final TotZn = 995 μM, and finally centrifuging 30 ml of the clay suspension after 30 min of reaction time. These extreme chemical conditions (pH 3.7, ionic strength of 0.0015 M) were chosen to favor the formation of OS Zn surface complexes on cation exchange sites. For all wet pastes, more than 95 percent of total Zn was sorbed on hectorite. Hence, the EXAFS signal from the Zn fraction present in the residual supernatant is negligible. Chemical conditions for samples studied by EXAFS are summarized in table 1.

Reference compounds

General considerations.-The structural environment of sorbed Zn depends on the sorption mechanism, which can be (1) a cation exchange, (2) a specific adsorption, (3) a lattice diffusion, and (4) a precipitation of a new solid phase (Charlet and Manceau, 1993; Manceau and others, 1999b). Zn adsorbed on cation exchange sites retains its first hydration sphere, and nearest cations are repelled at distances greater than 4 Å (Manceau and others, 1999b; Schlegel and others, 1999). Thus, the Zn EXAFS spectrum of this OS complex should resemble that of solvated $Zn^{2+}_{(aq)}$. Zn adsorbed on specific adsorption sites of hectorite is likely located in a phyllosilicate structural environment, as observed for divalent Co (Schlegel and others, 1999). The Zn EXAFS spectrum should then resemble that of a Zn-doped magnesian phyllosilicate, such as kerolite ($Mg_3Si_4O_{10}(OH)_2{\cdot}nH_2O$). Zn diffused in the octahedral sheet of hectorite also has a typical phyllosilicate short-range order. Finally, a poorly crystallized kerolite-like mineral (hereafter referred to as ZnKer) may form by a coprecipitation of Zn and Si, possibly together with Mg. Consequently, a preliminary EXAFS study of $Zn^{2+}_{(aq)}$ and various ZnKer references is warranted to assist us in the discrimination of the possible Zn sorption mechanisms on hectorite.

Preparation of references.-OS complexes were modeled with a solvated $Zn^{2+}_{(aq)}$ reference obtained by dissolving $Zn(NO_3)_3$ in bidistilled water to a total Zn concentration of 0.1 M. This solution was acidified to pH 4 to prevent any polymerization. A series of ZnKer minerals of formula $Zn_xMg_{3-x}Si_4O_{10}(OH)_2{\cdot}nH_2O$ (x = 3: ZnKer300; x = 0.7: ZnKer070; x = 0.03: ZnKer003) was prepared by aging fresh (Zn, Mg, Si) precipitates of the desired chemical compositions at 75°C for 15 days (Decarreau, 1981; Decarreau, 1985). The purity and crystallinity of these references were checked by X-ray diffraction, and b unit-cell parameters were calculated from the position of (060) diffraction peaks.

EXAFS data collection and reduction

Zn K-edge EXAFS spectra ($\chi(k)$) of Zn-sorbed hectorite films and pastes, and of ZnKer070 and ZnKer003 references, were recorded at ESRF, France, on the BM32 CRG/IF station. Clay films were mounted on a goniometer, and EXAFS spectra were recorded at α = 0°, 35°, 55°, and 80° in fluorescence detection mode with a 30 element array Ge detector. EXAFS spectra for wet pastes and reference powders were recorded at the magic angle (α = 35°; (Manceau and others, 1990). At this angle textural effects are cancelled, and, therefore, $\chi^{35°}(k)$ is identical to the spectrum obtained for a perfectly isotropic powder ($\chi^{iso}(k)$; (Manceau and others, 1990). Recording conditions for sorption samples are summarized in table 1. MA-EXAFS spectra of $Zn^{2+}_{(aq)}$ and ZnKer300 references were recorded in transmission mode at the LURE synchrotron radiation facility, France, on the D42 station. Measurements were performed with gas ionization chambers filled with an air-helium mixture dosed to attenuate the beam intensity by ~20 percent before and ~50 percent after the sample entry.

EXAFS data were reduced with the SEDEM software (Aberdam, 1998). As a preliminary step, absorption spectra were given the shape of the Stobbe function, which is a quantum-mechanically derived formula for atomic absorption at the K-edge. Fourier transformation was performed on $k^2\chi(k)$ between 2 and 10 $Å^{-1}$ using a Kaiser apodization window (Manceau and Combes, 1988), resulting in a radial structure function (RSF) in the distance space. RSF peaks are located at apparent absorber-backscatterer distances (R + ΔR), which differ from interatomic structural distances (R) by $\Delta R \sim$ -0.3-0.4 Å (Teo, 1986). RSF structural peaks of interest were windowed and Fourier back-transformed in k space by using a software package implemented by D. Bonnin (ESPCI, Paris). R values and numbers of atomic neighbors (N) were determined by least-squares fitting the Fourier-filtered experimental contributions ($\chi_{exp}(k)$) with theoretical phase and amplitude functions calculated with FEFF7.02 (Rehr, Albers, and Zabinsky, 1992), and using talc and Zn-doped hectorite as model structures for Zn-O, Zn-Mg and Zn-Si pairs (Oberlin and Mering, 1966; Kadi-Hanifi and Mering, 1972; Rayner and Brown, 1973). The amplitude reduction factor S_0^2 was set to 0.85 (O'Day and others, 1994; Manceau, Chateigner, and Gates, 1998). The goodness of the fit between experimental $\chi_{exp}(k)$ and model $\chi_{calc}(k)$ was quantified by the reliability factor R_P, defined as

$$R_p = \frac{\sum_k \left(k^2 \cdot \chi_{calc}(k) - k^2 \cdot \chi_{exp}(k)\right)^2}{\sum_k \left(k^2 \cdot \chi_{exp}(k)\right)^2}. \qquad (1)$$

TABLE 1

Zn-sorbed hectorite samples analyzed by EXAFS spectroscopy

Samples	[hectorite] ($g\ L^{-1}$)	TotZn (μM)	pH	Ionic strength (M)	Reaction time (h)	Sample type	EXAFS acquisition
#H001_30min_WP	2.0	995	3.7	0.0015	0.5	wet paste	MA-EXAFS$^{\text{Þ}}$
#H01_5min_WP	1.95	100	6.5	0.01	0.08	wet paste	MA-EXAFS$^{\text{Þ}}$
#H01_6h_WP	1.95	100	6.5	0.01	6	wet paste	MA-EXAFS$^{\text{Þ}}$
#H01_6h_SSF	1.95	100	6.5	0.01	6	self-supporting film	P-EXAFS$^{\text{ÞÞ}}$
#H01_96h_WP	1.95	100	6.5	0.01	96	wet paste	MA-EXAFS$^{\text{Þ}}$
#H01_96h_SSF	1.95	100	6.5	0.01	96	self-supporting film	P-EXAFS$^{\text{ÞÞ}}$
#H30_6h_WP	1.95	100	6.5	0.3	6	wet paste	MA-EXAFS$^{\text{Þ}}$
#H30_6h_SSF	1.95	100	6.5	0.3	6	self-supporting film	P-EXAFS$^{\text{ÞÞ}}$
#H30_120h_WP	1.95	100	6.5	0.3	120	wet paste	MA-EXAFS$^{\text{Þ}}$
#H30_120h_SSF	1.95	100	6.5	0.3	120	self-supporting film	P-EXAFS$^{\text{ÞÞ}}$

Þ Measurements performed at the magic angle (α = 35°)

ÞÞ Measurements performed at α = 0°, 35°, 55°, and 80°

RESULTS AND INTERPRETATION

Chemistry

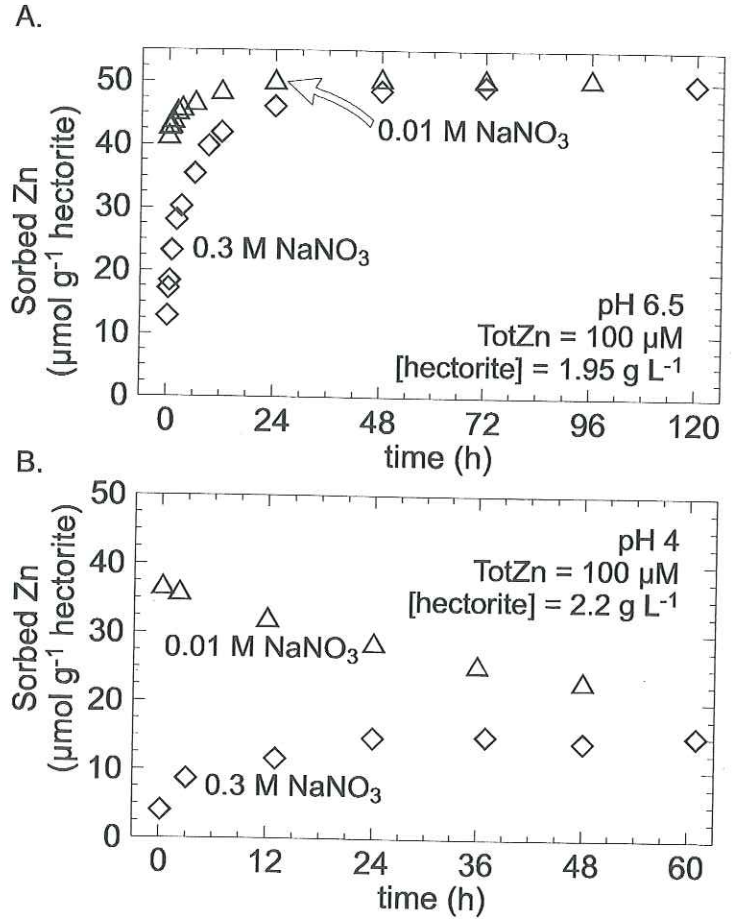

Fig. 3. Sorption of Zn on hectorite at high (0.3 M NaNO$_3$: ◇) and low (0.01 M NaNO$_3$: △) ionic strength as a function of pH and reaction time, for a total Zn concentration of TotZn = 100 µM. (A) pH 6.5, [hectorite] = 1.95 g L^{-1}. (B) pH 4, [hectorite] = 2.2 g L^{-1}. (A) and (B) have distinct time scales.

Kinetics of Zn sorption.-Distinct kinetics trends of Zn uptake by hectorite are observed upon variations of pH and ionic strength (fig. 3A and B). At 0.01 M NaNO$_3$ an important Zn uptake occurred within the first 5 min of reaction time at pH 4 and 6.5, leading to a Zn uptake of 72 percent (pH 4) and 82 percent (pH 6.5) of TotZn. The rapid uptake was strongly reduced at higher ionic strength. This sorption behavior is typical of a cation exchange mechanism, resulting in the formation of Zn OS complexes on basal planes of hectorite (Sposito, 1984; Sposito, 1994). Following this fast reaction step, uptake still went on at pH 6.5, but at a much slower rate (fig. 3A). This slow reaction step can no longer be interpreted in terms of a cation exchange mechanism (Tang and Sparks, 1993; Sposito, 1994). In contrast to pH 6.5, at pH 4 Zn slowly desorbed consecutively to the fast initial uptake (fig. 3B). At 0.3 M NaNO$_3$, the kinetics of Zn uptake was slow at pH 6.5 and pH 4. After 48 h of equilibration time, nearly 100 percent of TotZn was sorbed at pH 6.5 (fig. 3A), and only 35 percent of TotZn at pH 4 (fig. 3B). The higher uptake at higher pH is typical of pH-dependent adsorption mechanism, which supposedly resulted in the formation of IS Zn complexes at the edges of hectorite platelets at both pH (Charlet and others, 1993).

At pH 6.5, identical amounts of base (37 µmol NaOH per g hectorite) were added at high and low ionic strengths to prevent a pH shift to lower values after Zn addition. The amounts of acid introduced with Zn spikes (0.24 µmol HNO$_3$ per g hectorite) were too low to account alone for the excess of protons in suspensions. It is thus assumed that this proton release resulted from Zn sorption, a phenomenon which is characteristic of an oxide-like sorption mechanism. Consequently, the pH-dependent sorption mechanism observed at high ionic strength probably also occurred at low ionic strength and pH 6.5 after the fast initial cation exchange.

Impact of Zn addition on hectorite stability.-The impact of Zn sorption on the dissolution of hectorite at pH 6.5 was assessed by following Mg and Si release rates before and after Zn addition (fig. 4A and B). At 0.3 M NaNO$_3$ and t ≤ 0, the ratio of Mg (0.56 ± 0.09 µmol h^{-1} g^{-1}) to Si (0.82 ± 0.09 µmol h^{-1} g^{-1}) release rates (0.68 ± 0.13) was close to the atomic Mg/Si ratio of hectorite (0.67), but the $[Mg]_{aq,tot}/[Si]_{aq,tot}$ ratio at t = 0 was significantly higher (1.02 ± 0.02). As discussed by Schlegel and coworkers (Schlegel, Charlet, and Manceau, 1999), this arose from an excess of $[Mg]_{aq,tot}$ likely caused by a partial exchange of interlayer Na by Mg cations during the dialysis stage of the hectorite purification. At t ≤ 0, lower amounts of $[Mg]_{aq,tot}$ were found at low than at high ionic strength for similar $[Si]_{aq,tot}$, (fig.4: see data at pH 6.5 and t = -24 h), owing to the probable readsorption of dissolved Mg on cation exchange sites of Na-hectorite. Higher Si release rates were observed at low ionic strength (1.56 ± 0.09 µmol h^{-1} g^{-1} at t = 0 and 0.01 M NaNO$_3$), in keeping with previous results on hectorite dissolution (Kreit, Shainberg, and Herbillon, 1982).

Adding Zn induced a change in Mg and Si release rates at pH 6.5 and 0.3 M NaNO$_3$ (fig. 4A). The Si release rate slowed down from 0.82 ± 0.09 µmol h^{-1} g^{-1} at t ≤ 0, to 0.24 ± 0.09 µmol h^{-1} g^{-1} at t = 24 h, and to 0.13 ± 0.03 at t = 120 h. In contrast, the release rate of Mg abruptly increased following Zn addition, from 0.56 ± 0.09 µmol h^{-1} g^{-1} at t ≤ 0 to 2.05 ± 0.4 µmol h^{-1} g^{-1} at t = 3 h. The excess of Mg release for t > 0 can be calculated from the difference between experimental $[Mg]_{aq,tot}$ and theoretical $[Mg]_{aq,tot}$ obtained by extrapolation of the Mg release rate measured at t = 0. The excess of Mg equals 24.2 ± 4 µmol g^{-1} at t = 6 h, and is of the same order, though significantly lower, than the amount of sorbed Zn (35.4 ± 1.5 µmol g^{-1}). Both Zn sorption and excess of Mg release occurred simultaneously, suggesting a replacement of layer edge-exposed Mg by sorbed Zn. For t ≥ 6 h, the Mg release rate gradually decreased to reach at t = 120 h a value (0.09 ± 0.04 µmol h^{-1} g^{-1}) lower than at t = 0. Therefore, the adsorption of Zn via a pH-dependent mechanism (pH 6.5, 0.3 M NaNO$_3$) seems to result in a long-term inhibition of hectorite dissolution. At 0.01 M NaNO$_3$, a decrease of the Si release rate (from 1.56 ± 0.09 µmol h^{-1} g^{-1} at t = 0 to 0.56 ± 0.09 µmol h^{-1} g^{-1} at t = 96 h) was observed, as for 0.3 M NaNO$_3$ (fig. 4B). However, there was no abrupt enhancement of Mg release after Zn addition. The high uncertainty on release rates for Mg (0.12 ± 0.9 and 0.10 ± 0.09 µmol h^{-1} g^{-1} at t = 0 h and 96 h, respectively) hampers any interpretation.

At pH 4 (fig. 4C and D), neither Mg nor Si dissolution rates changed significantly during Zn uptake, which is at variance with results at pH 6.5. Mg and Si dissolution rates at 0.3 M NaNO$_3$ for t ≥ 24 h (7.6 ± 0.1 and 11.1 ± 0.2 µmol h^{-1} g^{-1}, respectively) are only slightly lower than those of pure hectorite at the same ionic strength (8.2 ± 0.5 and 12.2 ± 0.9 µmol h^{-1} g^{-1}, respectively; data not shown). Therefore, even if some specific adsorption likely occurred on layer edges at 0.3 M NaNO$_3$ and pH 4, this adsorption had little effect on the dissolution rate of hectorite. At 0.01 M $NaNO_3$, the release rate of Mg and Si for t ≥ 24 h (9.7 ± 0.2 and 16.4 ± 0.4 μmol h^{-1} g^{-1}) are significantly higher than at 0.3 M $NaNO_3$. A similar behavior was observed for Si at pH 6.5. The ratio of Mg to Si release rate was lower at 0.01 M $NaNO_3$ than at 0.3 M $NaNO_3$, (respectively 0.59 ± 0.02 and 0.68 ± 0.02). This likely results from readsorption of dissolved Mg on cation exchange sites, as observed at pH 6.5 and low ionic strength.

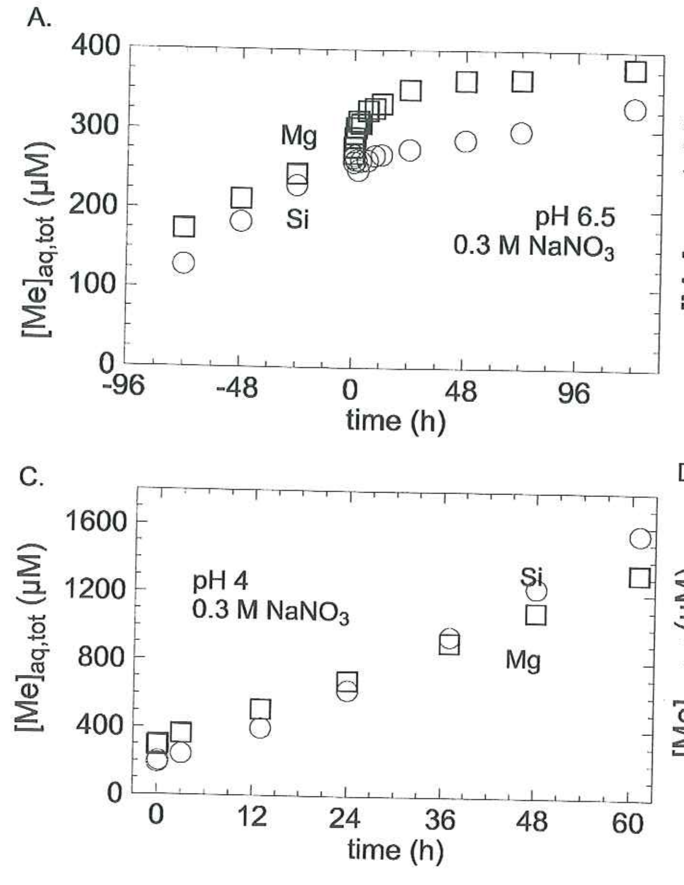

Fig. 4. Kinetics of Mg (□) and Si (○) release in the supernatant before (t < 0) and after (t > 0) Zn addition. TotZn = 100 μM for all experiments. [hectorite] = 1.95 g L^{-1} at pH 6.5 (A and B) and 2.2 g L^{-1} at pH 4 (C and D). (A) pH 6.5, 0.3 M $NaNO_3$. (B) pH 6.5, 0.01 M $NaNO_3$. (C) pH 4, 0.3 M $NaNO_3$. (D) pH 4, 0.01 M $NaNO_3$. Experiments at pH 4 and 6.5 have different time and $[Me]_{aq,tot}$ scales.

EXAFS spectroscopy

Reference compounds.-χ(k) for model compounds can be used to fingerprint the structural environment of Zn. The EXAFS spectrum for $Zn^{2+}_{(aq)}$ has a single wave frequency for k > 3 $Å^{-1}$, and its amplitude decreases monotonously with k (fig. 5). This spectral feature is consistent with the presence of only one ordered coordination sphere (i.e., 6 H_2O) around $Zn^{2+}_{(aq)}$. Instead, EXAFS spectra for clay minerals contain wave frequencies (arrows in fig. 5) which are absent in $Zn^{2+}_{(aq)}$. Hence, they do not arise from multiple scattering (MS) paths within the first coordination sphere of Zn, but rather from the contribution of higher shells.

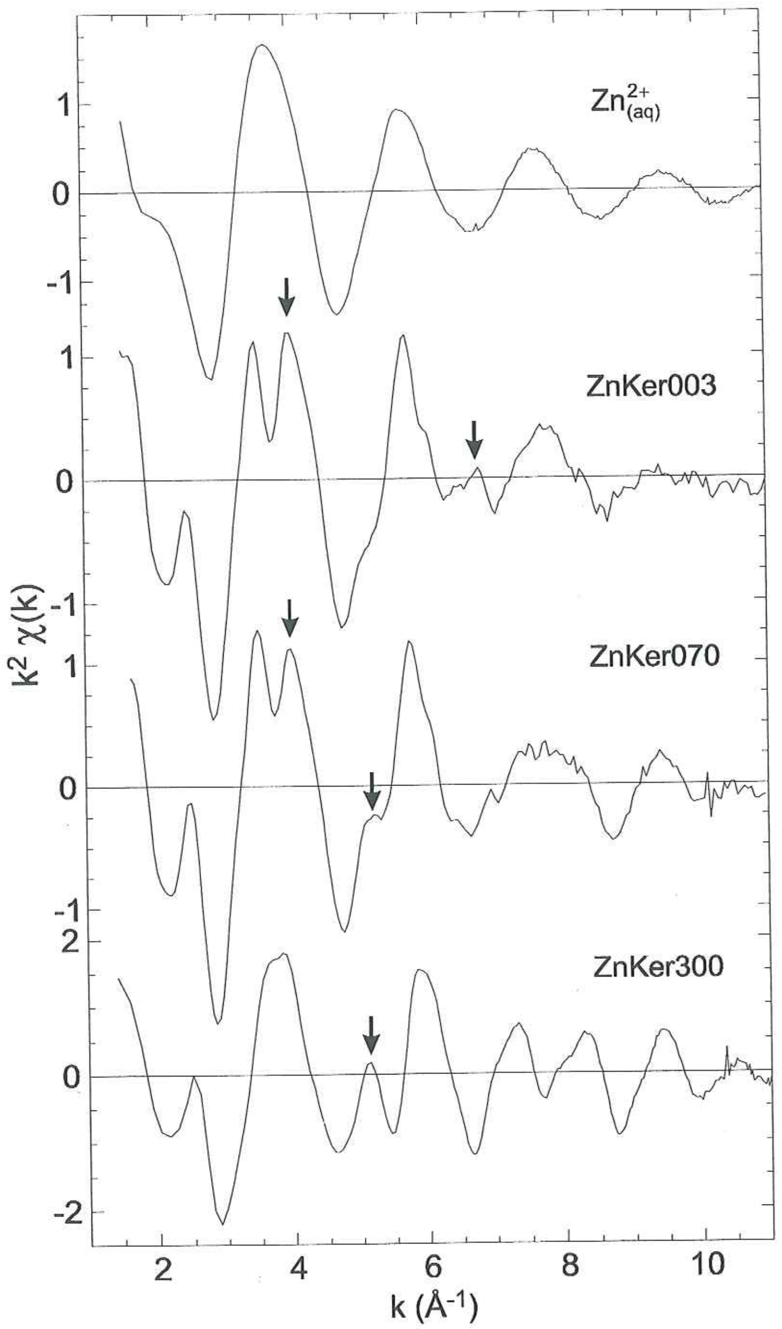

Fig. 5. k^2-weighted Zn K-edge EXAFS spectra for $Zn^{2+}_{(aq)}$, Zn-doped kerolite (ZnKer003), (Zn,Mg)-kerolite (ZnKer070), and Zn-kerolite (ZnKer300). All spectra were recorded at the magic angle to prevent texture effects.

All Fourier transforms (FTs) display a first RSF peak (labeled A) located near R + ΔR = 1.6 Å, corresponding to the EXAFS contribution of nearest oxygen atoms coordinated to Zn (fig. 6). Two RSF peaks at R + ΔR = 2.9 and 3.8 Å are observed for $Zn^{2+}_{(aq)}$. They were tentatively assigned to MS contributions within the first hydration sphere (Kuzmin and Grisenti, 1994), and to single-scattering contributions of the second hydration sphere at ~4.1 Å (Munoz-Paez, Pappalardo, and Sanchez Marcos, 1995). However, *ab initio* FEFF6 calculations suggested that the single scattering contribution of the second oxygen shell is canceled by double scattering paths between oxygens in the first and second shells (Kuzmin, Obst, and Purans, 1997). Thus RSF peaks at R + ΔR = 2.9 and 3.8 Å for $Zn^{2+}_{(aq)}$ are likely dominated by MS contributions. The RSFs for Zn-containing kerolites display maxima at R + ΔR = 2.7-2.9 (peak B) and 3.8 Å (peak C). Their high amplitude, compared to $Zn^{2+}_{(aq)}$, indicates that they correspond essentially to single scattering contributions beyond the first oxygen shell. Their structural origin was determined by combining P-EXAFS measurements and FEFF7.02 calculations (Manceau, Chateigner, and Gates, 1998; Manceau and others, 1999a; Manceau and others, 1999b). Peak B corresponds to the mixed contribution of the 6 nearest octahedral (Oct1) and 4 nearest tetrahedral (Tet1) cations, and of higher oxygen shells (table 2). Its amplitude depends on the Zn/(Zn + Mg) ratio in the octahedral sheet of ZnKer (fig. 6). Not only do the amplitudes vary, but imaginary parts of FTs for ZnKer003 and ZnKer300 are almost out-of-phase (fig. 7). Manceau and Calas (1986) related this phase contrast to the π-dephasing between EXAFS waves backscattered by Mg, one the one hand, and by transition elements such as Fe, Ni, and Zn, on the other hand. The sensitivity of the imaginary part of the FT to the relative proportion of Mg and Zn atoms in the Oct1 shell can be used to identify the nature of the predominant backscatterer in Zn-sorbed hectorite. Peak C originates from the contribution of next-nearest Si cations (Tet2), and from higher oxygen shells (table 2) (Manceau and others, 1999a; Manceau and others, 2000c). It has a large amplitude in trioctahedral layer silicates (Manceau and others, 1999b), and neither its amplitude nor imaginary part significantly change with the chemical composition of the clay, in contrast to peak B (fig. 7).

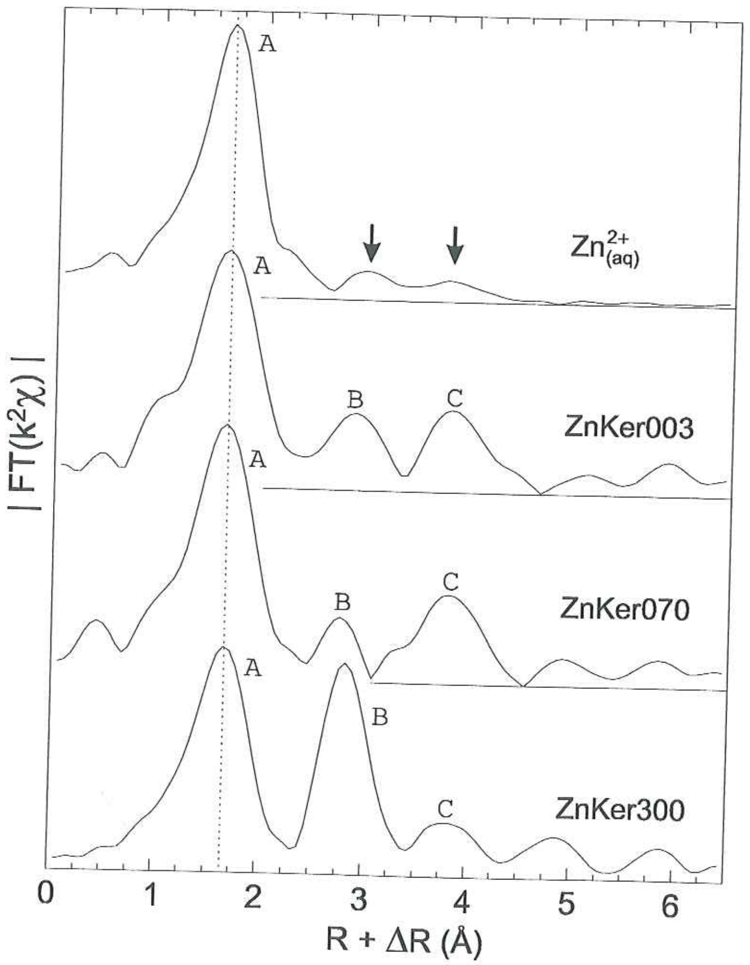

Fig. 6. Zn K-edge k^2-weighted radial structure functions (RSFs) for $Zn^{2+}_{(aq)}$, ZnKer003, ZnKer070, and ZnKer300.

TABLE 2

Successive atomic shells surrounding Mg in hectorite

(Kadi-Hanifi and Mering, 1972, Oberlin and Mering, 1966)

Shell	Element	N	R (Å)	β (deg)[þ]
O1	O	6	2.05	58.7
Oct1	Mg	6	3.03	90
Tet1	Si	4	3.23	32.8
O2	O	2	3.47	19.5
O3	O	6	3.66	73.2
O4	O	2	3.79	30.2
O5	O	2	4.01	35.3
Tet2	Si	4	4.43	52.2
O6	O	2	4.54	44.0
O7	O	12	4.75	77.1

[Þ] Angle between **c*** and the vector binding Mg to the atoms in the shell

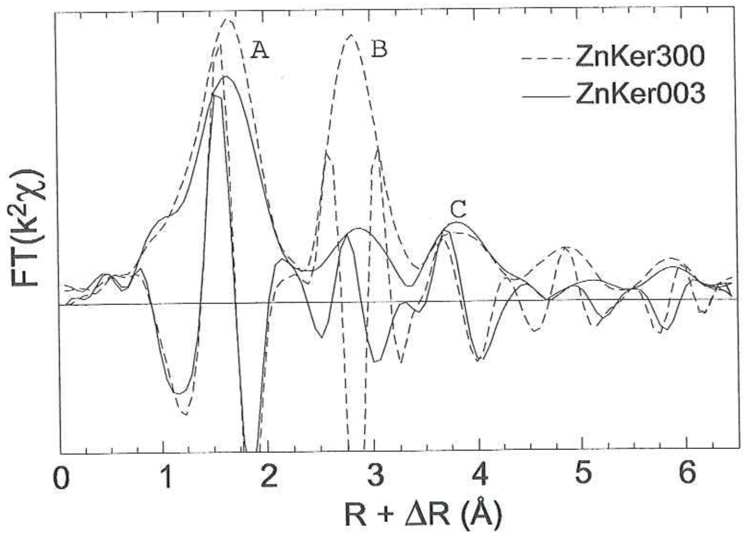

Fig. 7. Moduli (RSFs) and imaginary parts of the k^2-weighted Fourier transforms for ZnKer003 and ZnKer300. Note the good similarity of peaks C.

For all kerolites, an EXAFS-derived R^{EXAFS}_{Zn-O} value of 2.07 Å typical of oxygen-hexacoordinated Zn was obtained (table 3; (Kuzmin, Obst, and Purans, 1997). The precision on R^{EXAFS}_{Zn-O} and N_O was estimated by successively varying and fixing these structural parameters during the least-squares fit. A 0.01 Å shift of R^{EXAFS}_{Zn-O} from its best-fit value, or a decrease of N_O from 6 to 5 (20 percent), resulted in a two-time increase of R_p. The Fourier-filtered EXAFS contributions corresponding to peak B, $\chi_B(k)$, were fitted by assuming only cationic (Mg, Zn, Si) backscatterers. The numbers of nearest cations were fixed to $N_{Zn} = 6$ and $N_{Mg} = 0$ for ZnKer300, $N_{Zn} = 1.4$ and $N_{Mg} = 4.6$ for ZnKer070, and $N_{Zn} = 0$ and $N_{Mg} = 6$ for ZnKer003, based on chemical compositions. Optimal spectral simulations were obtained ($0.002 \leq R_p \leq 0.032$) for $R^{EXAFS}_{Zn-Zn} = 3.10$ Å and $R^{EXAFS}_{Zn-Mg} = 3.07$-3.08 Å (table 4 and fig. 8), as compared to X-ray diffraction (b/3) values of 3.08 and

3.06 Å, respectively. The systematic difference in distance likely originates from uncertainty in theoretical phase shift functions for these particular atomic pairs (Vaarkamp and others, 1994; Schlegel and others, 1999). Interestingly, R^{EXAFS}_{Zn-Si} markedly decreased with increasing Mg/(Zn + Mg) ratio from 3.30 Å for ZnKer300 to 3.20 Å for ZnKer003 (table 4). This 0.10 Å reduction in distance is hardly accountable for by the difference of ionic radii between Zn and Mg (that is, the contraction of the unit cell), as R^{EXAFS}_{Zn-Zn} and R^{EXAFS}_{Zn-Mg} differ by only 0.03 Å. Instead, the observed correlation between R^{EXAFS}_{Zn-Si} and Mg/(Zn + Mg) is due to a large uncertainty on EXAFS-derived distances for this particular shell (± 0.06 Å). The uncertainty occurs because the χ_{Si} and χ_{Mg} waves are out-of-phase and the χ_{Si} and χ_{Zn} waves are in-phase (Scheidegger and others, 1998; Manceau and others, 1999b; Schlegel and others, 1999). The uncertainty is lower in P-EXAFS (±0.03 Å) because χ_{Si} is singled out in the perpendicular orientation (Manceau, Chateigner, and Gates, 1998). The uncertainty on R^{EXAFS}_{Zn-Zn} and R^{EXAFS}_{Zn-Mg} were evaluated to ± 0.03 Å, and the uncertainty on N_{Zn}, N_{Mg}, and N_{Si} to ± 0.5.

TABLE 3

Quantitative EXAFS analysis of the first Zn-O coordination shell

	α	IFT range[Þ]	Zn-O shell				ΔE$_0$[ÞÞ]
		(Å)	R (Å)	N	σ (Å)	R_p	(eV)
References							
$Zn^{2+}_{(aq)}$	35°	1.0-2.1	2.07	6.0[†]	0.09	0.001	-1.1
ZnKer300	35°	1.1-2.2	2.07	6.0[†]	0.09	0.002	-2.6
ZnKer070	35°	1.1-2.2	2.07	6.0[†]	0.10	0.003	-2.2
ZnKer003	35°	1.1-2.2	2.07	6.0[†]	0.10	0.003	-3.6
P-EXAFS samples							
#H30_6h_SSF	0°	1.1-2.3	2.06	4.8	0.10	0.004	-2.5
	80°	1.1-2.2	2.06	4.4	0.10	0.006	-2.5
#H30_120h_SSF	0°	1.1-2.2	2.06	4.8	0.10	0.004	-2.5
	80°	1.1-2.2	2.06	4.4	0.10	0.006	-2.5
#H01_6h_SSF	0°	1.1-2.2	2.06	4.7	0.10	0.003	-1.6
	80°	1.1-2.1	2.06	4.6	0.10	0.002	-1.6
#H01_96h_SSF	0°	1.2-2.1	2.06	5.5	0.10	0.002	-1.4
	80°	1.1-2.3	2.06	5.4	0.10	0.009	-1.4

[Þ] R + ΔR intervals for inverse Fourier transforms (IFTs)

[ÞÞ] The threshold energy E_0 was taken at the half-height of the absorption edge (Δμ/2)

[†] Value held fixed during the fitting procedure

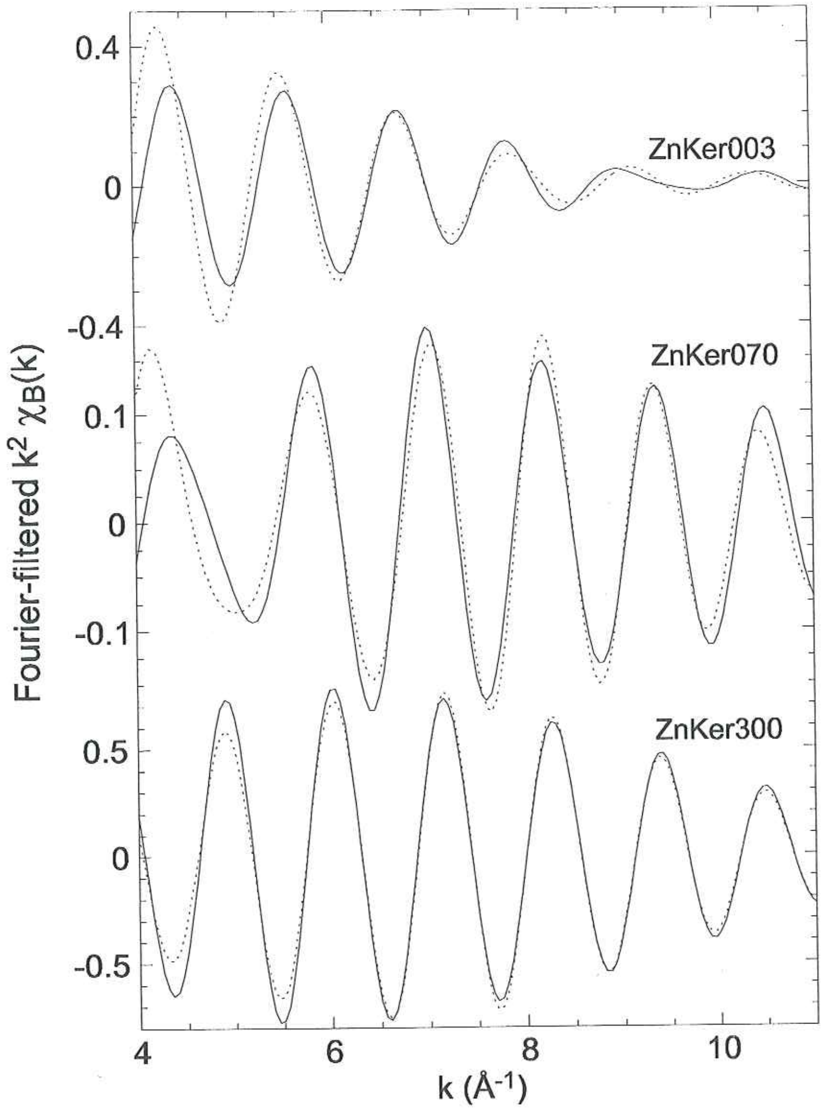

Fig. 8. Comparison of experimental (solid line) and simulated (dotted line) Fourier-filtered EXAFS contribution of peak B ($\chi_B(k)$) for ZnKer003, ZnKer070, and ZnKer300.

P-EXAFS of self-supporting films.-Figure 9A shows P-EXAFS spectra for a short contact time (t = 6 h) at 0.3 M $NaNO_3$ and pH 6.5 (#H30_6h_SSF; table1). Several frequencies are observed up to 7 Å^{-1}, suggesting the presence of several backscattering shells around Zn. The angular dependence of EXAFS spectra is clearly apparent from the variations in amplitude and position of EXAFS oscillations. For example, the wave maximum near 5.2 Å^{-1} gradually increases with α, whereas the maximum near 5.9 Å^{-1} drops and shifts to higher k. This angular dependence indicates that the structural environment of sorbed Zn is anisotropic, and suggests that sorbed Zn atoms are structurally associated to hectorite platelets. Owing to the axisymmetrical symmetry of the self-supporting film (Schlegel and others, 1999), the polarization dependence of K-edge EXAFS spectra can be written:

$$\chi^{\alpha} = \chi^{\parallel}\cos^2\alpha + \chi^{\perp}\sin^2\alpha = \chi^{\perp} + (\chi^{\parallel} - \chi^{\perp})\cos^2\alpha \qquad (2)$$

where χ^{α} is the P-EXAFS spectrum at any α value, and $\chi^{\parallel}$ and $\chi^{\perp}$ are P-EXAFS spectra in the parallel (α = 0°) and perpendicular (α = 90°) orientations (fig. 2). A good linear correlation between χ^{α} and $\cos^2\alpha$

(equation 2) is observed for 35° ≤ α ≤ 80° (fig. 9B and C), thus attesting for the good quality of the data and the reliability of the EXAFS normalization. However, $\chi^{0°}(k)$ significantly deviates from regression lines. Figure 9A shows that these deviations are due to the poorer quality of this particular spectral record. The same amplitude problem is encountered in all $\chi^{0°}$ spectra, and, consequently, $\chi^{0°}$ were systematically recalculated from linear regressions of χ^{α} for 35° ≤ α ≤ 80°. Schlegel and others (1999) showed that experimental and recalculated $\chi^{0°}$ have similar uncertainties. Experimental (35° ≤ α ≤ 80°) and recalculated (α = 0°) P-EXAFS spectra for all self-supporting films are shown in figure 10. At given α, only minor differences are observed from one sample to another, although they were prepared under contrasted chemical conditions (table 1). This observation suggests that the crystallochemical environments of sorbed Zn are similar in all samples. $\chi^{35°}(k)$ spectra clearly do not resemble ZnKer300 (fig. 5), indicating that sorbed Zn did not precipitate as Zn-rich kerolite. Instead, Zn-sorbed hectorite and Zn-doped kerolite (ZnKer070, ZnKer003) bear strong spectral similarities, which suggests that sorbed Zn is located, at least partly, in a phyllosilicate structural environment.

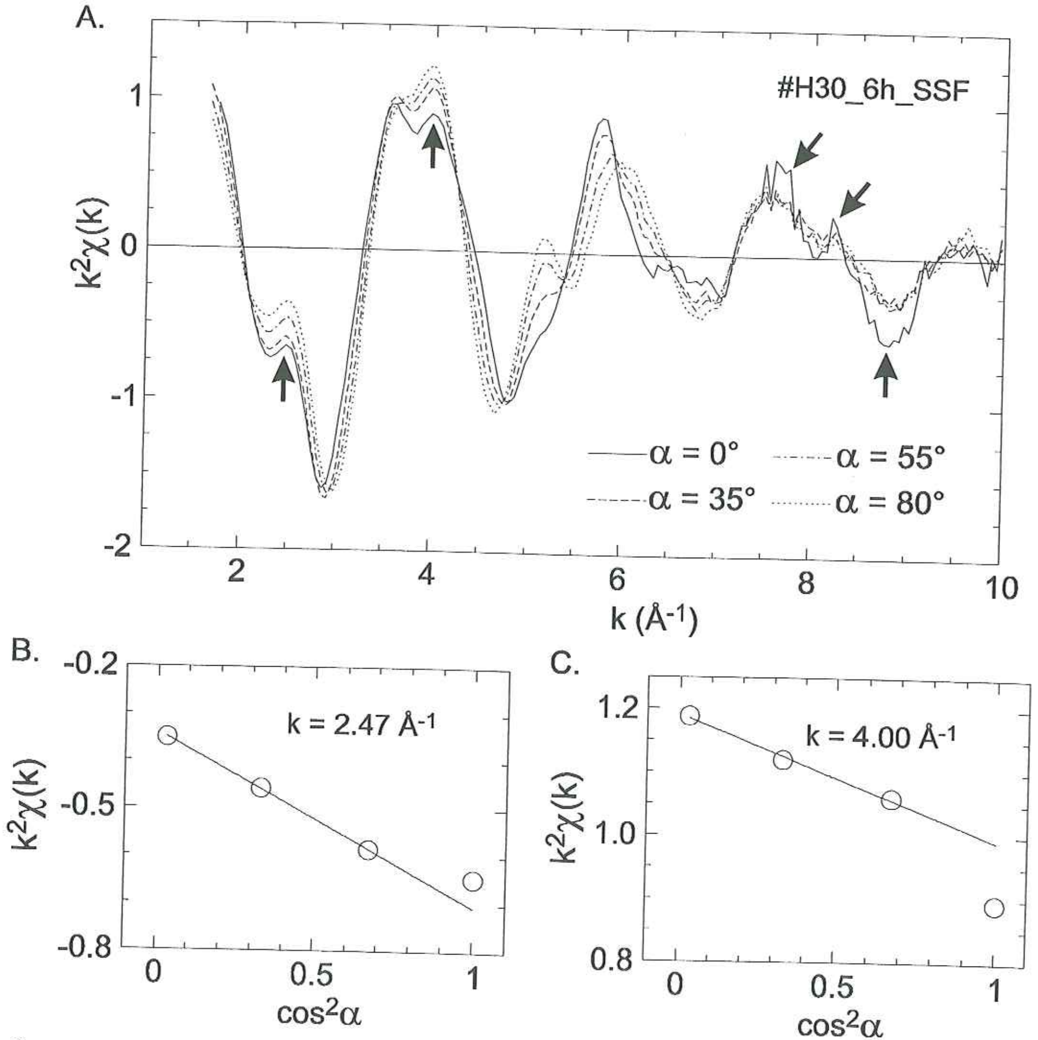

Fig. 9. (A) k^2-weighed Zn K-edge polarized-EXAFS (P-EXAFS) spectra at α angles of 0°, 35°, 55°, and 80°, for Zn-sorbed hectorite at high ionic strength (0.3 M $NaNO_3$) and short reaction time (t = 6 h) (#H30_6h_SSF). Arrows point to amplitude pitfalls affecting $\chi^{0°}$. (B) and (C) are examples of experimental linear correlations between $\chi^{\alpha}(k)$ and $\cos^2\alpha$ for two selected k values. $\chi^{0°}(k)$ obviously deviates from the linear regression.

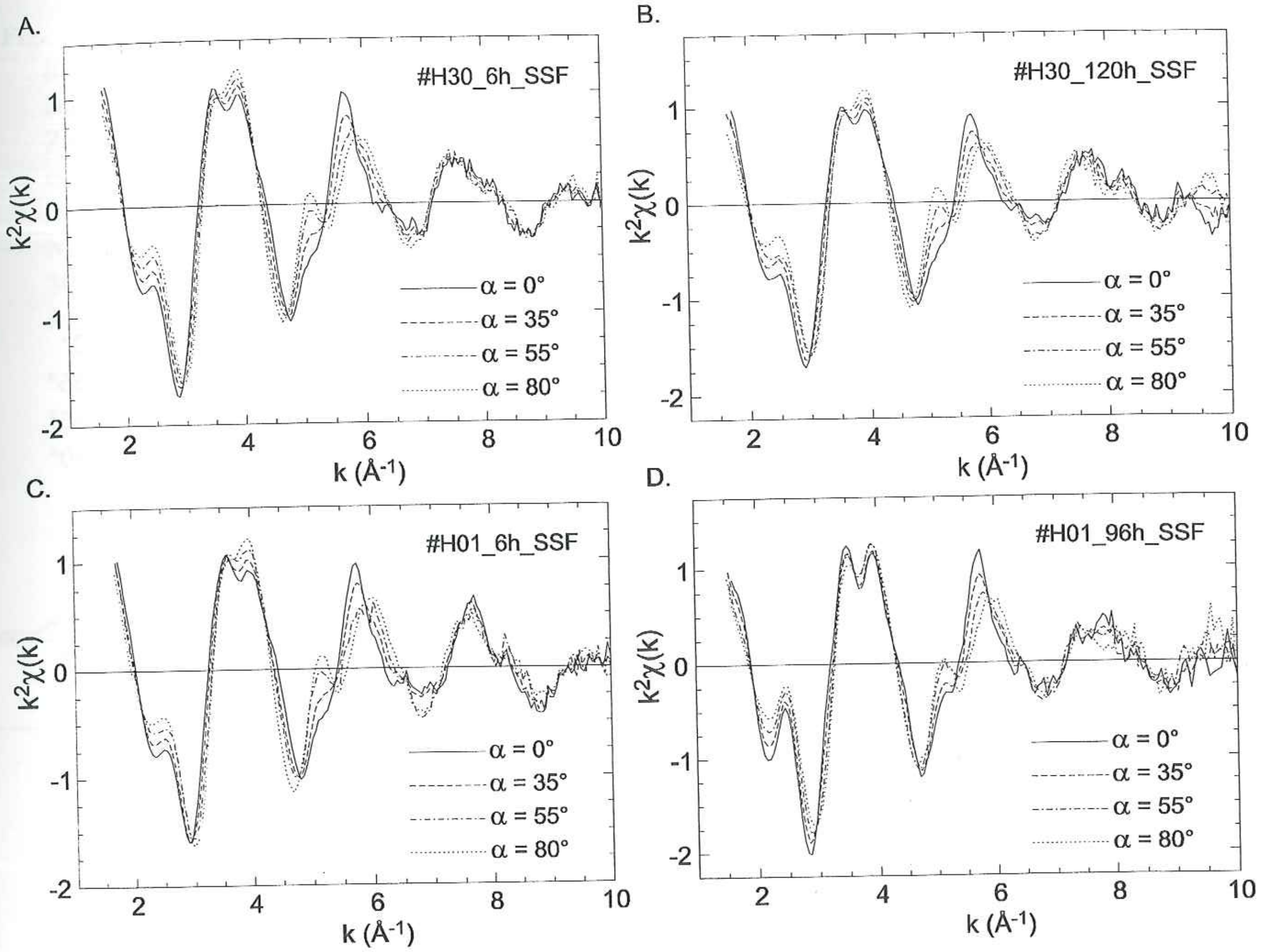

Fig. 10. k^2-weighted P-EXAFS spectra at α angles of 0°, 35°, 55°, and 80°. The 0° spectra were obtained by regression of experimental data for 35° ≤ α ≤ 80° and extrapolation to α = 0°. (A) Reaction time t = 6 h, ionic strength 0.3 M $NaNO_3$. (B) t = 120 h, 0.3 M $NaNO_3$. (C) t = 6 h, 0.01 M $NaNO_3$. (D) t = 96 h, 0.01 M $NaNO_3$.

Polarized-RSFs (P-RSFs) exhibit several intense peaks at R + ΔR distances near 1.6 Å (peak `A`), 2.6-2.8 Å (peak `B1`), 3.2 (peak `B2`), and 3.8 Å (peak `C`) (fig. 11). The position and imaginary part of peaks `A` coincide with those in ZnKer003, implying that Zn is hexacoordinated to oxygen atoms in sorption samples, as in the reference (fig. 12A). The quantitative analysis yielded R_{Zn-O}^{EXAFS} = 2.06 Å for all sorption samples and α values ($R_P \leq 0.009$; table 3). The relatively high σ values (σ = 0.10 Å), and the low numbers of oxygen atoms ($N_O^{iso} \leq 5.5$) can be explained by the coordination of Zn to distinct chemical entities, such as H_2O molecules, OH groups, and possibly O atoms of the sorbent surface (Schlegel and others, 1999). The position and imaginary part of peaks `C` in sorption samples also coincide with those in ZnKer003 (Tet2 shell, predominantly; table 2 and fig. 12A). The noteworthy angular invariance of this peak (fig. 12B and C) indicates that Zn-Tet2 pairs are inclined by $\beta \approx 54.7°$ with respect to **c*** (the "magic angle"; Manceau and others, 1990), that is, to a value close to β_{Tet2} in phyllosilicate structures (table 2). This result strongly supports a phyllosilicate environment for sorbed Zn. The lower amplitude of peak `C` in sorption samples as compared to clay references (fig. 12A) results either from an increase in structural disorder, or a decrease of the number of next-nearest Si atoms.

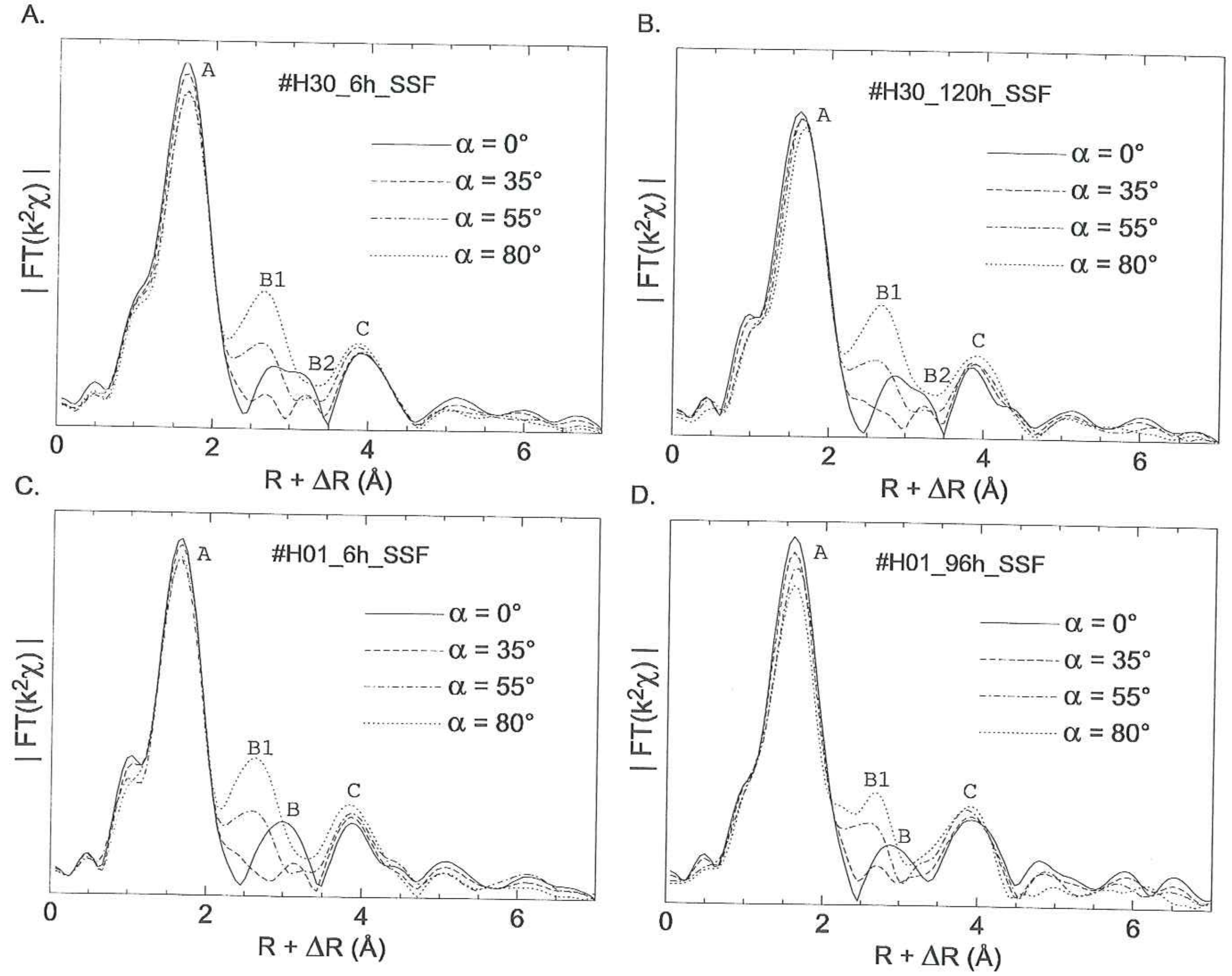

Fig. 11. Polarization dependent RSFs for Zn-sorbed hectorite at α angles of 35°, 55°, 80° (experimental), and 0° (extrapolated). (A) Reaction time t = 6 h, ionic strength 0.3 M $NaNO_3$. (B) t = 120 h, 0.3 M $NaNO_3$. (C) t = 6 h, 0.01 M $NaNO_3$. (D) t = 96 h, 0.01 M $NaNO_3$. At 0.01 M $NaNO_3$ and α = 0°, peaks `B1` and `B2` merge in a single peak `B`.

Fig. 12. (A) Comparison of Fourier transforms (FTs) at α = 35° (magic angle) for #H30_6h_SSF and ZnKer003. (B, C) Angular dependence of moduli (RSFs) and imaginary parts of FTs for Zn sorbed hectorite at 0.3 M $NaNO_3$ (#H30_6h_SSF). (B) α = 0° and 80°. (C) α = 0° and 35°. Peak `C` is invariant with α angles.

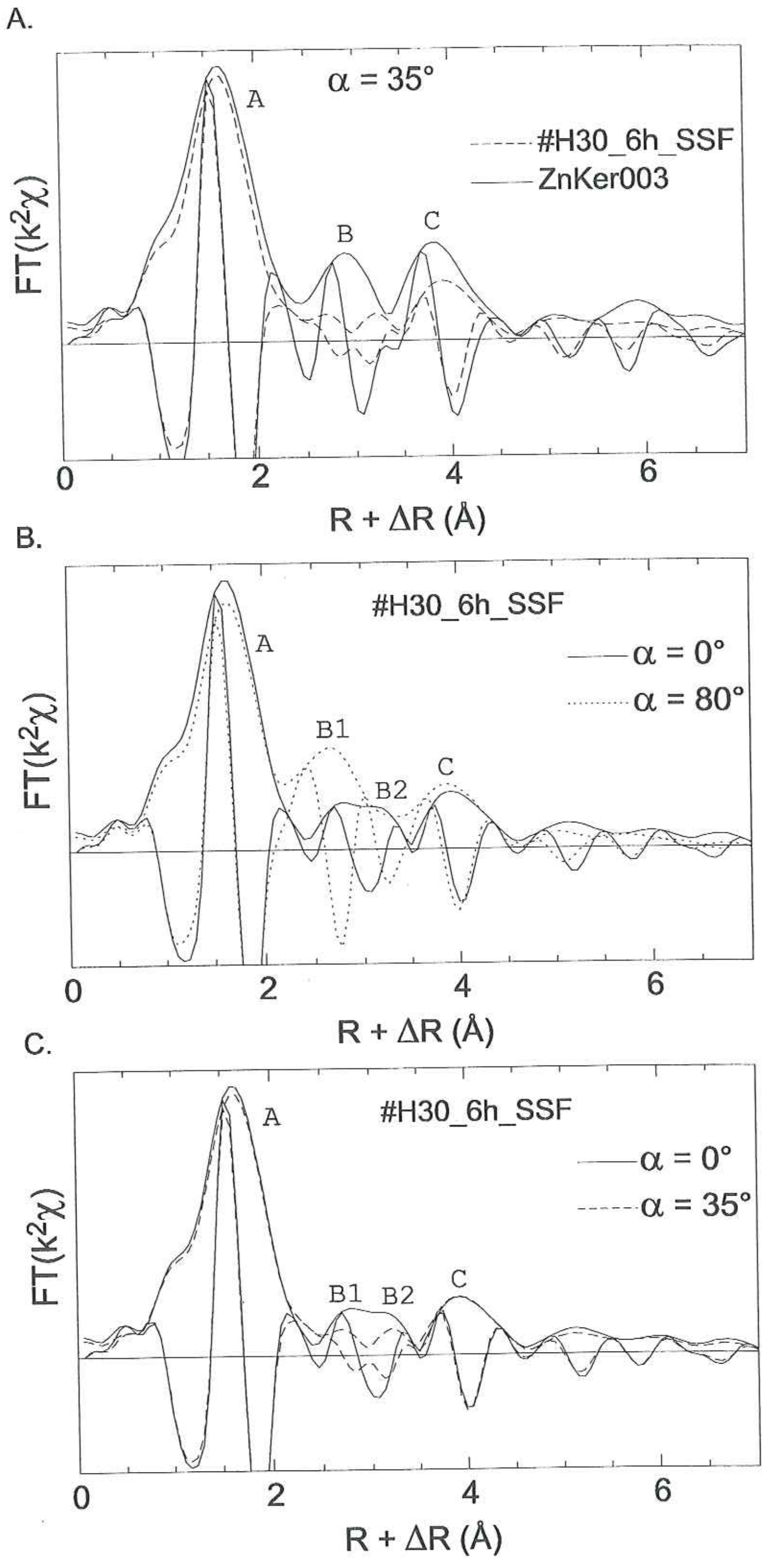

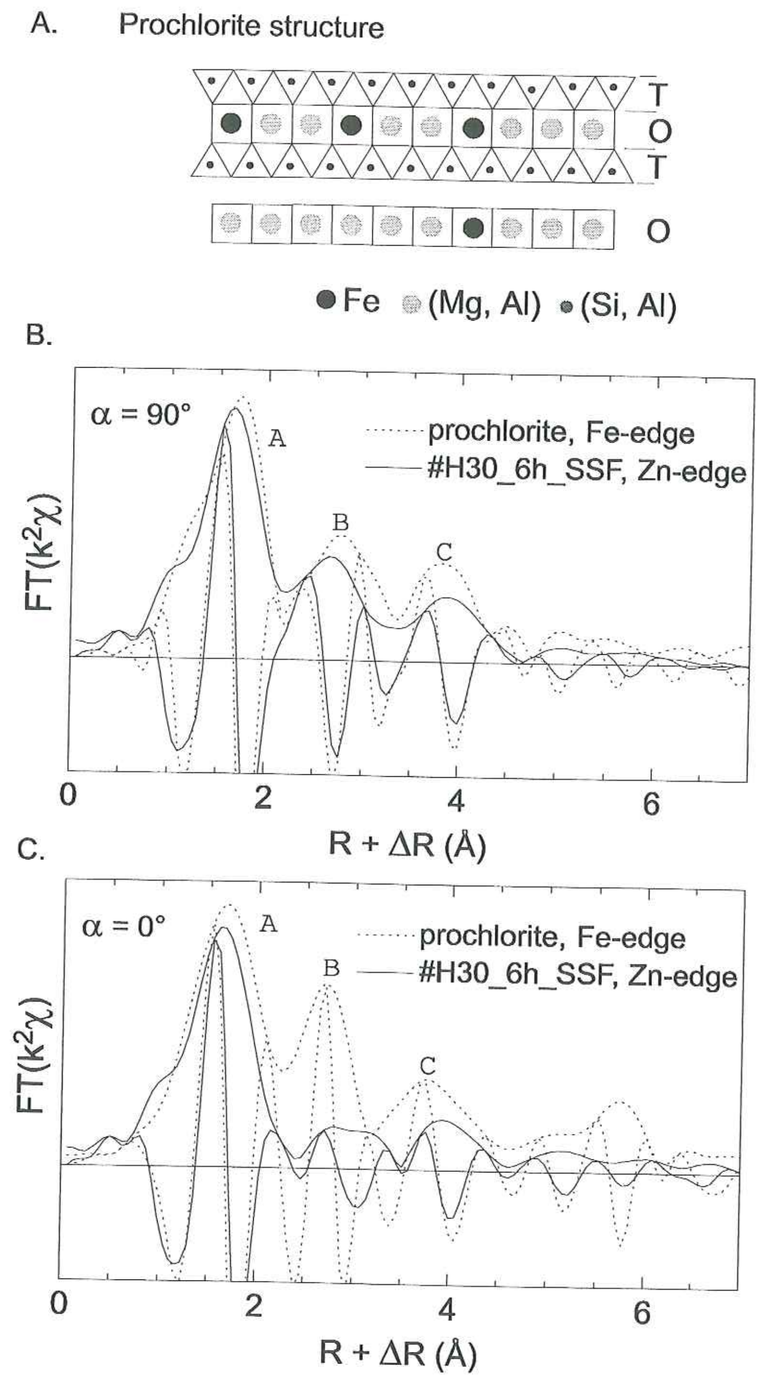

Fig. 13 (A) Schematic structure of prochlorite. TOT phyllosilicate layers alternate with brucitic octahedral sheets (O). Fe(II) atoms are distributed in the two types of octahedral sheets. (B and C) Comparison of moduli and imaginary parts of FTs for Zn-sorbed hectorite (#H30_6h_SSF, Zn K-edge) and Fe(II) dispersed in Mg-rich prochlorite (Fe K-edge) at α = 90° (B) and 0° (C).

Peaks `B1` and `B2` have a strong angular dependence. For instance, the amplitude of peak `B1` for #H30_6h_SSF decreases from α = 0° to α = 35°, and then increases from α = 35° to α = 80°, whereas its maximum shifts from R + ΔR = 2.8 Å to 2.6 Å (fig. 11A). This angular behavior indicates the presence of at least two atomic shells having distinct inclinations relative to **c*** (Schlegel and others, 1999). The angular dependence of the EXAFS contribution for a j shell (χ_j^α) can be written:

$$\chi_j^\alpha = \chi_j^{iso} \cdot \left[1 - \frac{(3\cos^2\beta_j - 1)(3\cos^2\alpha - 1)}{2} \right] \quad (3)$$

From equation (3), the amplitude of χ_j^α increases with increasing α for β_j values lower than the magic angle (54.7°), and decreases with increasing α for β_j values higher than 54.7°. The apparent number of backscatterers in the j shell as a function of α (N_j^α) is (Manceau, Chateigner, and Gates, 1998; Schlegel and others, 1999)

$$N_j^\alpha = N_j^{iso} \cdot \left[1 - \frac{(3\cos^2\beta_j - 1)(3\cos^2\alpha - 1)}{2} \right] \quad (4)$$

where N_j^{iso} is the crystallographic value obtained in MA-EXAFS. These theoretical considerations can be exemplified by taking prochlorite as a case study (Manceau and others, 1988). This phyllosilicate contains divalent Fe dispersed in magnesian sheets with ~75 percent of Fe located in the octahedral sheet of the TOT layer and ~25 percent of Fe located in the interlayer brucitic sheet (fig. 13A). Hence, Fe is surrounded on average by 6 in-plane Mg neighbors in TOT and brucitic octahedral sheets (β = 90°) at R ~ 3.05 Å, and by 4*0.75 = 3 out-of plane (Si, Al) neighbors in tetrahedral sheets (β ≈ 33°) at R ~ 3.25 Å. Therefore, $N_{Mg}^{35°} = 6$ and $N_{Si,Al}^{35°} = 3$. From equation (4), $N_{Si,Al}^{0°} = 1.4$, $N_{Si,Al}^{90°} = 6.3$, $N_{Mg}^{0°} = 9$, and $N_{Mg}^{90°} = 0$. As divalent Fe and Zn have a similar number of electrons and ionic radius (Shannon, 1976), their EXAFS signals are similar for a comparable structural environment. Therefore, the similarity in position and imaginary parts of peaks B and C for prochlorite and Zn-sorbed hectorite at α = 90° observed in figure 13B offers evidence for the presence of nearest (TeT1) and next-nearest (Tet2) Si shells in sorption samples. In contrast, the amplitude, position and imaginary part of peak `B` in prochlorite differ from those of peaks `B1` and `B2` in sorption samples at α = 0° (fig. 13C). The nature of in-plane nearest atomic neighbors is determined below from the hectorite structure (table 2) and spectral simulations.

As expected from the comparison with prochlorite, Fourier-filtered $\chi_{B1,B2}^{80°}(k)$ for all sorption samples were successfully fitted ($0.005 \le R_P \le 0.015$) with a Si shell of 3.5 to 4.5 atoms at $R_{Zn-Si}^{EXAFS} = 3.23$-3.26 Å (fig. 14; table 4). $\chi_{B1,B2}^{0°}(k)$ could not be fitted with a combination of only Mg as Oct1 and Si as Tet1 shells, and a third shell, corresponding to peak `B2`, had to be added. The fading of peak `B2` at high α values indicates that this shell has a β value greater than 54°. A previous P-EXAFS study on nontronite, a ferric dioctahedral smectite, showed that the O3 shell at R ~ 3.7 Å significantly contributed to the EXAFS signal and had to be added to Oct1+ Tet1 contributions during the spectral simulation (Manceau, Chateigner, and Gates, 1998). To decrease the degree of freedom of the spectral fit, the three-shell fits were performed by fixing R_{Zn-Si}^{EXAFS} and σ_{Si} to their values at α = 80°. Correct fits were obtained with R_{Zn-Mg}^{EXAFS} and R_{Zn-O3}^{EXAFS} values comparable (within uncertainty) to those in clay references, and in hectorite (table 2 and 4; fig. 14). Adding even a small χ_{Zn} contribution at R ~ 3.10 Å to the spectral model did not improve the quality of the simulation, leading to the conclusion that Zn-Zn pairs are marginal, if not absent.

TABLE 4

Quantitative EXAFS analysis of higher coordination shells

	α	IFT range^Þ (Å)	Zn-Zn shell R (Å)	N_{Zn}	σ (Å)	Zn-Mg shell R (Å)	N_{Mg}	σ (Å)	Zn-Si shell R (Å)	N_{Si}	σ (Å)	Zn-O3 shell R (Å)	N_{O3}	σ (Å)	ΔE_0^ÞÞ (eV)	R_P
References																
ZnKer300	35°	2.3 - 3.4	3.10§	6.0†	0.10				3.30	4.0†	0.09				-2.6†	0.002
ZnKer070	35°	2.3 - 3.4	3.10	1.4†	0.10	3.07	4.6†	0.10	3.24	4.0†	0.11				-2.2†	0.032
ZnKer003	35°	2.3 - 3.4				3.08§§	6.0†	0.10	3.20	4.0†	0.10				-3.6†	0.016
P-EXAFS samples																
#H30_6h_SSF	0°	2.3 - 3.5				3.06	2.4	0.10	3.25†	1.9	0.11†	3.72	4.6	0.10	-2.5†	0.025
	80°	2.2 - 3.4							3.25	4.4	0.11				-2.5†	0.008
#H30_120h_SSF	0°	2.3 - 3.5				3.08	2.2	0.10	3.26†	1.4	0.10†	3.74	3.4	0.10	-2.5†	0.045
	80°	2.2 - 3.4							3.26	4.5	0.10				-2.5†	0.005
#H01_6h_SSF	0°	2.3 - 3.5				3.09	2.4	0.11	3.23†	0.8	0.11†	3.69	4.7	0.10	-1.6†	0.011
	80°	2.2 - 3.4							3.23	3.8	0.11				-1.6†	0.011
#H01_96h_SSF	0°	2.3 - 3.5				3.06	2.7	0.10	3.26†	1.2	0.10†	3.71	3.8	0.10	-1.4†	0.007
	80°	2.2 - 3.4							3.26	3.5	0.10				-1.4†	0.015

Þ R + ΔR interval for the inverse Fourier transforms (IFTs)

ÞÞ The threshold energy E_0 is taken at the half-height of the absorption edge (Δμ/2)

† Value held fixed during the fitting procedure

§ The crystallographic distance, calculated from the position of the (060) diffraction peak, is 3.08 Å

§§ The crystallographic distance, calculated from the position of the (060) diffraction peak, is 3.06 Å

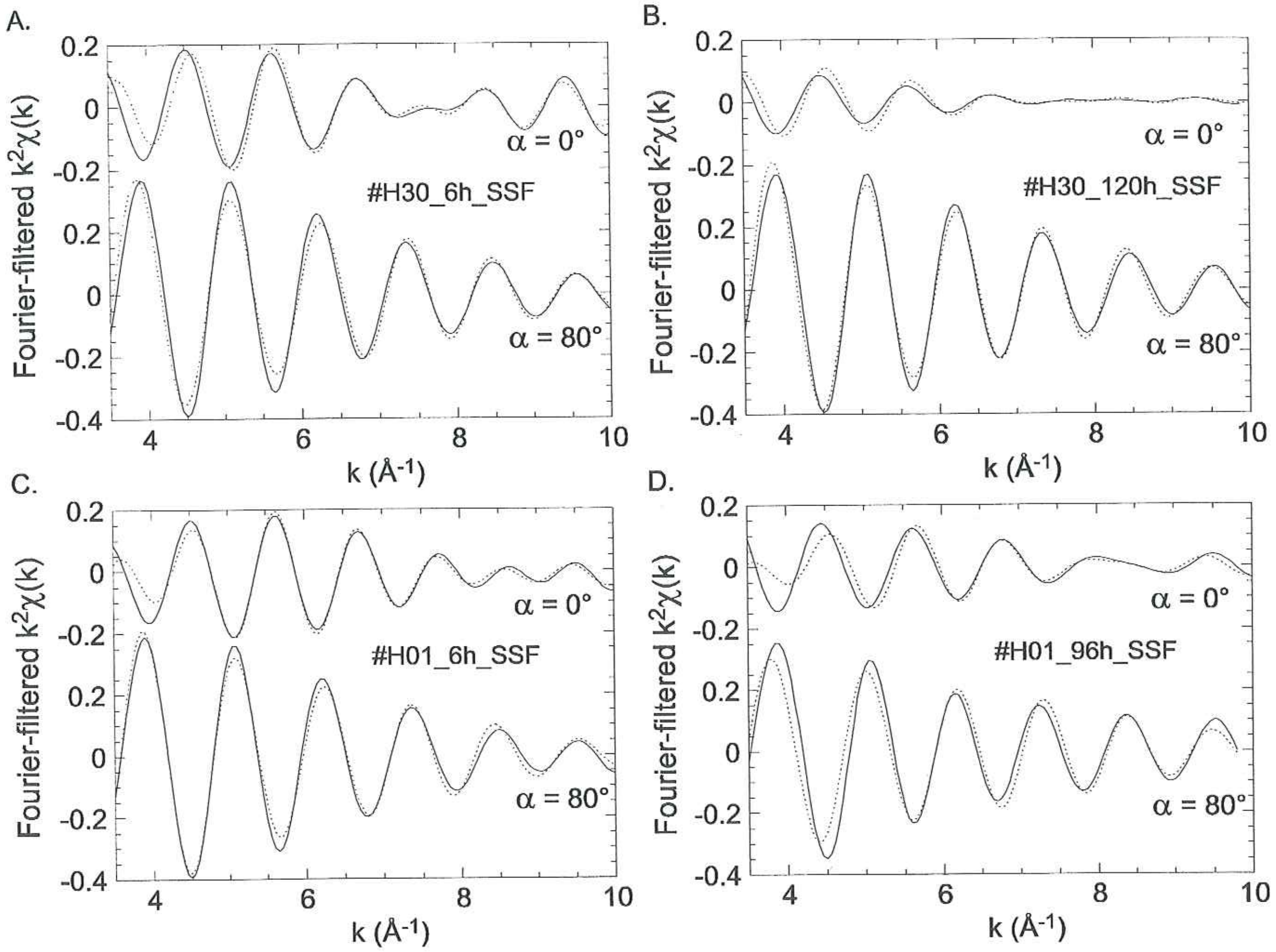

Fig. 14. Comparison between experimental and simulated Fourier-filtered EXAFS contributions of peaks `B1,B2` for Zn-sorbed hectorite at α = 0° ($\chi^{0°}_{B1,B2}(k)$) and 80° ($\chi^{80°}_{B1,B2}(k)$). (A) Reaction time t = 6 h, ionic strength 0.3 M $NaNO_3$. (B) t = 120 h, 0.3 M $NaNO_3$. (C) t = 6 h, 0.01 M $NaNO_3$. (D) t = 96 h, 0.01 M $NaNO_3$.

Figure 11 shows that peaks `B1,B2` are almost canceled at α = 35°. From equation (3), $\chi^{35°}_{B1,B2}$ can be expressed as

$$\chi^{35°}_{B1,B2} = \frac{\chi^{\alpha°}_{B1,B2} + (3\sin^2\alpha - 1)\chi^{0°}_{B1,B2}}{3\sin^2\alpha} \quad (\alpha \neq 0°) \qquad (5)$$

For α = 80°, this equation reads

$$\chi^{35°}_{B1,B2} \approx 0.345 * \chi^{80°}_{B1,B2} + 0.656 * \chi^{0°}_{B1,B2} \qquad (6)$$

Figure 15 shows that $\chi^{0°}_{B1,B2}$ and $\chi^{80°}_{B1,B2}$ are out-of-phase in the [3.5-6 Å^{-1}] k-range, with the amplitude of $\chi^{80°}_{B1,B2}$ being about twice as intense as that of $\chi^{0°}_{B1,B2}$. Consequently, equation (6) predicts that $\chi^{80°}_{B1,B2}$ and $\chi^{0°}_{B1,B2}$ should be nearly cancelled at the magic angle, as observed experimentally in figure 15. The consequence of this wave extinction is that no stable fit could be obtained at α = 35°. Yet, owing to the angular magnification of cationic contribution, $N_{Mg}^{35°}$, $N_{Si}^{35°}$, and $N_{O3}^{35°}$ can be accurately determined from values obtained at $\alpha = 0$ and 80° by using equation (4) (table 5).

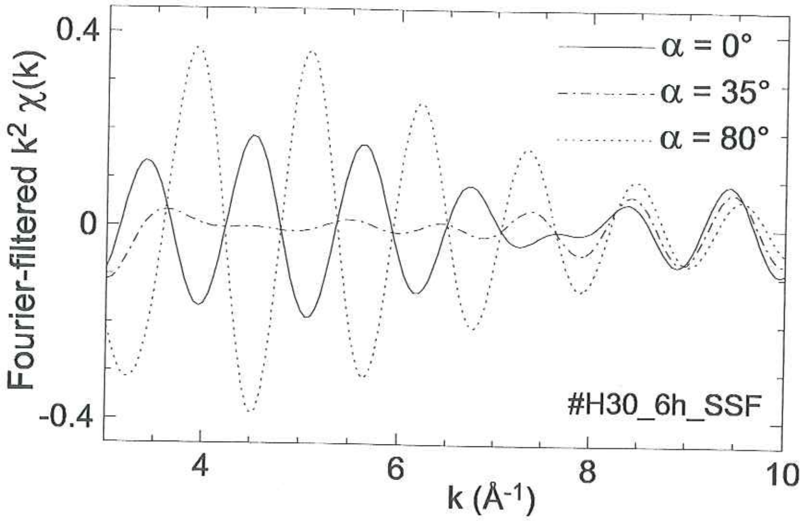

Fig. 15. Comparison of $\chi_{B1,B2}^{\alpha}(k)$ for $\alpha = 0°$, 35° and 80°. Note the extinction of $\chi_{B1,B2}^{35°}(k)$ for $3 \le k \le 7$ Å^{-1}.

TABLE 5

Calculated number of neighbor atoms at 35° for self-supporting films

P-EXAFS samples	$N_{Mg}^{35°}$	N_{oct} Þ	$N_{Si}^{35°}$	$N_{O3}^{35°}$
#H30_6h_SSF	1.6	1.8	2.7	3.1
#H30_120h_SSF	1.5	1.7	2.4	2.3
#H01_6h_SSF	1.6	1.8	1.8	3.1
#H01_96h_SSF	1.8	2.0	2.0	2.5

Þ Calculated as $N_{oct} = N_{Mg}^{35°} * 3/2.65$

Structural environment of Zn in self-supporting films.-P-EXAFS results indicate that sorbed Zn octahedra are surrounded by in-plane Mg and out-of-plane Si atoms at R_{Zn-Mg}^{EXAFS} and R_{Zn-Si}^{EXAFS} distances matching those in ZnKer and characteristic of edge-sharing (E) linkages with Mg octahedra and corner-sharing (C) linkages with Si tetrahedra. That Si tetrahedra are not isolated, but polymerized in a tetrahedral framework as in phyllosilicate structure, is supported by the detection of the next-nearest Si shell (Tet2). In addition, the angular dependence of EXAFS spectra provides strong evidence for a physical association of Zn atoms to the clay sorbent, and indicates that the Mg, Si (Tet1 + Tet2) and O3 shells belong to hectorite. Consequently, this whole set of results demonstrates that Zn octahedra are located in structural continuity of the hectorite octahedral sheet. As EXAFS is not sensitive to Li, the actual number of nearest octahedral cations sharing edges with Zn octahedra (N_{oct}) is probably higher than $N_{Mg}^{35°}$. From the structural formula of hectorite, and assuming a random distribution of Li within the octahedral sheet, $N_{oct} \approx N_{Mg}^{35°} * 3/2.65$ (table 5). N_{oct} ranges between 1.7 and 2.0 (±0.8), and is significantly lower than if all Zn had diffused in octahedral

sheets of hectorite ($N_{oct} = 6$). A fraction of Zn could have migrated into octahedral sheets while another would form OS complexes on hectorite basal planes, but in this case $N_{oct}/N_{Si}^{35°} \approx 6/4 = 1.5$, which is significantly different from experimental values ($0.7 \le N_{oct}/N_{Si}^{35°} \le 1.0$). Only the attachment of Zn octahedra at the edges of hectorite platelets complies with both a clay-like environment and a low number of neighboring sorbent cations. Consequently, it is concluded from the analysis of P-EXAFS spectra that Zn forms IS surface complexes at layer edges of hectorite, as for Co in similar sorption conditions (Schlegel and others, 1999).

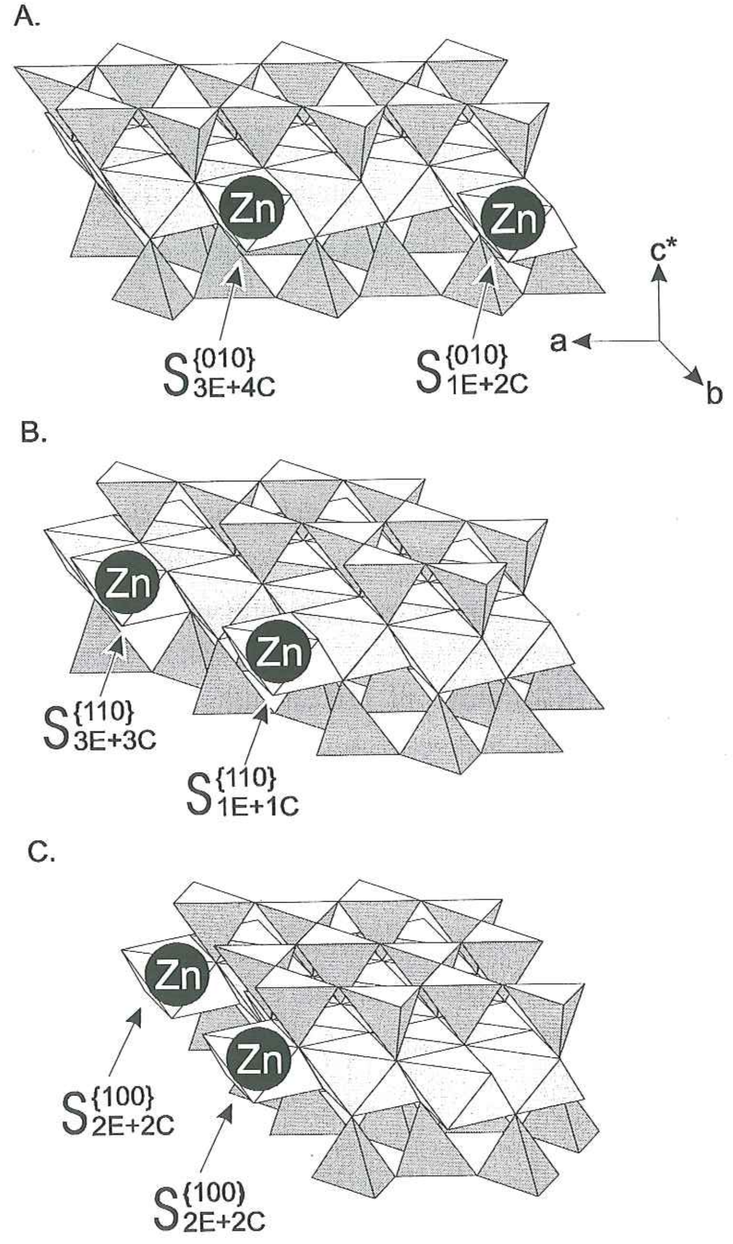

Fig. 16. Possible structures of mononuclear Zn surface complexes on the edges of hectorite platelets. (A) {010} layer edges. (B) {110} layer edges. (C) {100} layer edges. Zn octahedra are located in the continuity of the (Mg, Li) octahedral sheet.

The structure of Zn surface complexes depends on the morphology of hectorite layer edges. Hectorite platelets have a lath-type morphology, and their {001} basal faces are bounded by {010}, {110} and {100} edge faces (Mathieu-Sicaud, Mering, and Perrin-Bonnet, 1951; Oberlin and Mering, 1966; Bosbach and others, 1999). Several types of Zn surface complexes, having distinct numbers of nearest sorbent cations, can form on a given edge face. For instance, figure 16A shows the formation of $S^{\{010\}}_{3E+4C}$ and $S^{\{010\}}_{1E+2C}$ surface complexes on {010} planes. Other surface complexes can form on the {110} and {100} faces (for example, $S^{\{110\}}_{1E+1C}$, $S^{\{110\}}_{3E+3C}$, and $S^{\{100\}}_{2E+2C}$; fig. 16 B and C). It is possible to account for experimental N_{oct} and $N^{35°}_{Si}$ values for each film sample (table 5) by assuming adequate combinations of $S^{\{010\}}_{3E+4C}$, $S^{\{010\}}_{1E+2C}$, $S^{\{110\}}_{1E+1C}$, $S^{\{110\}}_{3E+3C}$, and $S^{\{100\}}_{2E+2C}$ surface complexes (Schlegel and others, 1999).

The identification of IS Zn complexes in self-supporting films at pH 6.5, low ionic strength (0.01 M $NaNO_3$), and for relatively short reaction times ($t \geq 6$ h) is the most salient result of P-EXAFS. The formation of these complexes is consistent with kinetics results (that is, slow Zn uptake for $t > 5$ min and proton release) , which suggested a pH-dependent sorption of Zn even at low ionic strength. However, the coexistence of IS and OS complexes at low ionic strength cannot be precluded, as the presence of OS complex would simply lower N_{oct} and $N^{35°}_{Si}$. This issue is addressed below by the analysis of EXAFS spectra obtained on fully hydrated samples.

MA-EXAFS of wet pastes.-Figure 17 compares MA-EXAFS spectra for wet pastes of Zn-sorbed hectorite. At pH 3.7, 0.0015 M $NaNO_3$, and 30 min of reaction time (#001_30min_WP) the EXAFS spectrum is nearly identical to that of $Zn^{2+}_{(aq)}$ (fig. 18A), indicating the formation of OS surface complexes on exchange sites. At pH 6.5 and 0.3 M $NaNO_3$, no spectral evolution with increasing reaction time (t = 6 h and 120 h) is observed (fig. 17), and MA-EXAFS spectra resemble that of the self-supporting film (fig. 18B) indicating the presence of IS complexes in wet samples. In contrast, at pH 6.5 and 0.01 M $NaNO_3$, a conspicuous spectral evolution is discernible from t = 5 min to t = 96 h: the oscillation maximum near 3.7 $Å^{-1}$ (#H01_5min_WP) progressively splits (#H01_6h_WP and #H01_96h_WP), and shoulders at 2.5 and 5.3 $Å^{-1}$ show up (fig. 17, arrows). The #H01_5min_WP spectrum clearly resembles those for #H001_30min_WP and $Zn^{2+}_{(aq)}$, indicating the presence of OS surface complexes for short sorption time (t = 5 min). This spectral likeness decreases with increasing reaction time, and, at t = 6 h (#H01_6h_WP) and 96 h (#H01_96h_WP), spectra increasingly resemble those recorded on self-supporting films, indicating that OS surface complexes are progressively replaced by IS surface complexes upon aging.

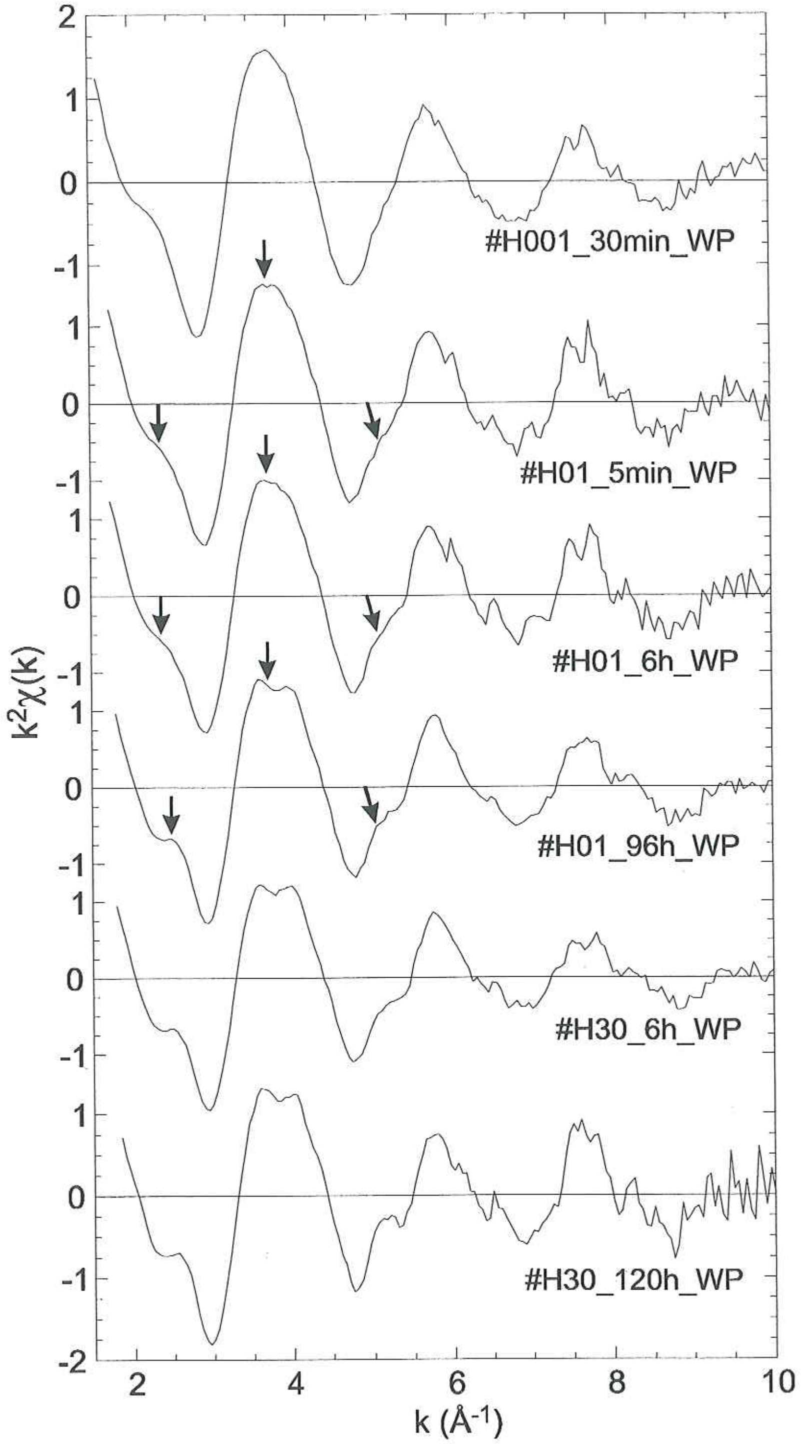

Fig. 17. k^2-weighted magic-angle EXAFS spectra for wet pastes of hectorite reacted with Zn under various ionic strength and reaction time conditions. Sorption conditions are listed in table 1.

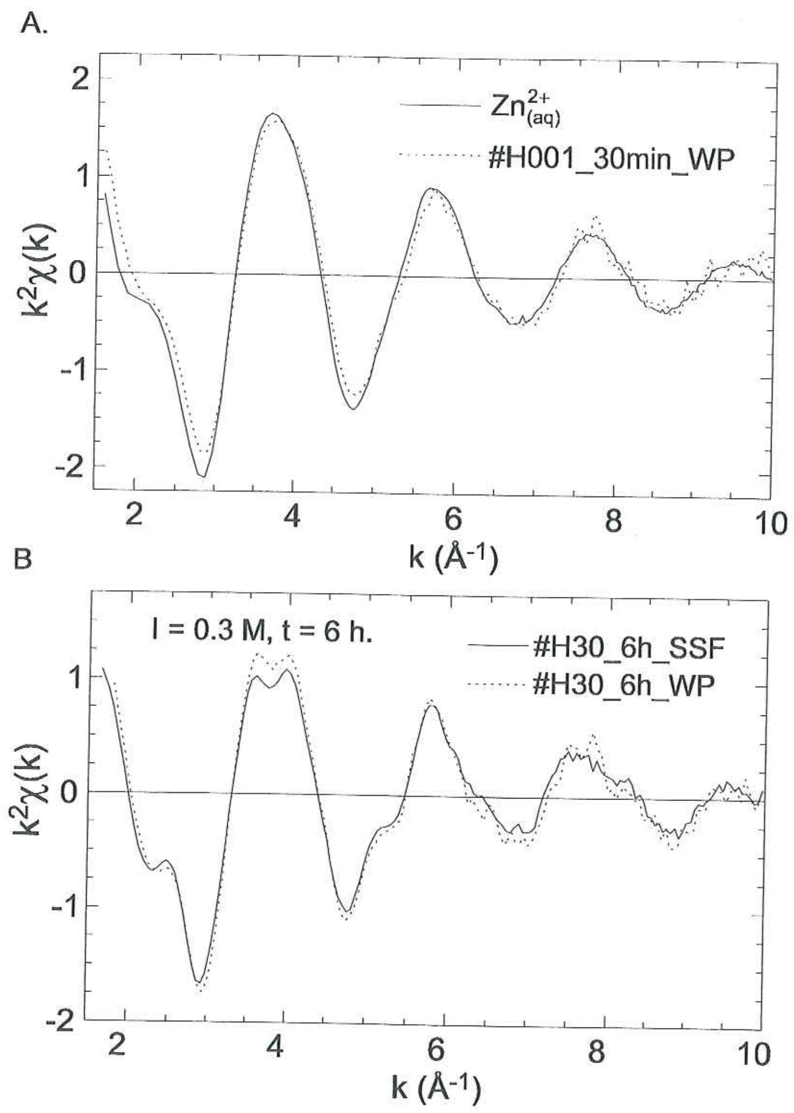

Fig. 18. (A) Comparison of k^2-weighted EXAFS spectra for $Zn^{2+}_{(aq)}$ and #H001_30min_WP (t = 30 min, 0.0015 M $NaNO_3$). (B) Comparison of k^2-weighted EXAFS spectra for #H30_6h_WP and #H30_6h_SSF (t = 6 h, 0.3 M $NaNO_3$).

DISCUSSION

Zn uptake at high ionic strength

Zn adsorption at 0.3 M $NaNO_3$ and pH 6.5 is concomitant with an excess of Mg release, which differs somehow from a true oxide-like sorption mechanism (Charlet and others, 1993). An increased release of sorbent species upon sorbate uptake was observed for the uptake of Co on hectorite (Schlegel, Charlet, and Manceau, 1999) and of Pb on hydroxylapatite (Ca-HAP) (Lower, Maurice, and Traina, 1998; Valsami-Jones and others, 1998). In the latter case, this phenomenon was explained by the dissolution of Ca-HAP and precipitation of Pb-HAP. In the present study, the partial dissolution of hectorite and parallel precipitation of Zn-rich kerolite can be ruled out owing to the absence of Zn-Zn pairs. Furthermore, exchange of Mg by Zn on interlayer sites is unlikely because cation exchange is inhibited at high ionic strength. A third hypothesis consists to assume that, prior to Zn addition, Mg cations adsorb and form edge surface complexes on hectorite like Zn. Yet, as chemical conditions favor hectorite dissolution, these surface complexes would have a low stability, hence Mg would adsorb and desorb dynamically. The net accumulation of Mg in solution *at the beginning* of Zn sorption can then be explained by the preferential sorption of Zn over Mg on reactive edge sites, owing to the higher stability of Zn phyllosilicates with respect to Mg ones (Decarreau, 1985; Manceau and others, 2000c). The formation of stable Zn fringes should then result in a *long-term* inhibition of hectorite dissolution, as observed experimentally, since the release rates of Si and Mg at pH 6.5 and 0.3 M $NaNO_3$ decrease from respectively 0.82 ± 0.09 and 0.56 ± 0.09 µmol h^{-1} g^{-1} at $t \leq 0$ to respectively 0.13 ± 0.03 and 0.09 ± 0.04 µmol h^{-1} g^{-1} at t = 120 h (fig. 3A and B).

Cation exchange and Zn uptake at low ionic strength and pH 6.5

At pH 6.5 and 0.01 M $NaNO_3$, the proportion of Zn IS complexes increases over that of OS ones with reaction time, suggesting a quantitative transfer of Zn from exchange sites to edge sites. These EXAFS-based structural results confirm the sorption mechanism inferred from kinetics sorption data, that is, initial fast Zn sorption by cation exchange followed by Zn fixation on edge sites. To better link spectroscopic and macroscopic observations, the time-dependent amount of exchangeable Zn can be estimated from chemical data. For this purpose, the rapid initial ($t \leq 5$ min) adsorption of Zn observed at 0.01 M $NaNO_3$ is described by the cation exchange reaction

$$2\,XNa + Zn^{2+}_{(aq)} \Leftrightarrow X_2Zn + 2\,Na^{+}_{(aq)} \qquad (7)$$

where X^- refers to one mole of exchange sites. This reaction is known to occur rapidly, and to reach equilibrium within minutes (Tang and Sparks, 1993). For this reason, exchangeable Zn (X_2Zn) is believed to be always near, or at equilibrium with $[Zn^{2+}_{(aq)}]$ ($\approx[Zn]_{aq,tot}$), *whatever the reaction time*. This equilibrium can be written in the Vanselow approach (Sposito, 1981; Charlet and others, 1993; Sposito, 1994)

$$K^{c}_{Na-Zn} = \frac{(X_2Zn)\left[Na^{+}_{(aq)}\right]^2}{(XNa)^2\left[Zn^{2+}_{(aq)}\right]} \qquad (8)$$

where K^{c}_{Na-Zn} is the Vanselow selectivity coefficient, which depends on both exchanger and solute compositions, and (X_2Zn) and (XNa) are the molar fractions of exchangeable cations. These molar fractions are calculated from the molar concentrations of Zn and Na adsorbed on exchange sites (respectively $[X_2Zn]$ and $[XNa]$) as

$$(X_2Zn) = \frac{[X_2Zn]}{\sum_j \left[X_{m_j}M_j\right]} \qquad (9)$$

and

$$(XNa) = \frac{[XNa]}{\sum_j \left[X_{m_j} M_j\right]} \qquad (10)$$

where the summation runs over all M_j^{m+} cations which can sorb on exchange sites. In the present system, M_j = Na, Zn, Mg, and Li. Thus $[X_{mj}M_j]$ must be known to calculate exchangeable Zn as a function of $[Zn]_{aq,tot}$. Solute Na is roughly constant, and [XNa] can be calculated from the difference between the total concentration of exchange sites and [XLi] + 2 $[X_2Zn]$ + 2 $[X_2Mg]$. [XLi] can be neglected, because Li is known to have a lower affinity for exchange sites than Na (McBride, 1994), and the sum of exchangeable and dissolved Li concentrations never exceeded 100 µM, being two orders of magnitude lower than $[Na]_{aq,tot}$. $[X_2Mg]$ cannot be neglected, and, in addition, it is not constant because $[Mg]_{aq,tot}$ increases with reaction time. Exchangeable Mg is calculated from $[Mg]_{aq,tot}$ by using equations similar to equations (8-10) and taking $K^c_{Na-Mg} = 0.34 \pm 0.06$ (Schlegel, Charlet, and Manceau, 1999). Then, $K^c_{Na-Zn} = 0.41 \pm 0.06$ was obtained from chemical data at 0.01 M $NaNO_3$, pH 4, and t = 5 min, by assuming that all sorbed Zn cations are retained in an exchangeable form. Because specific sorption occurs even at pH as low as 4, as visible in figure 3B, the calculated K^c_{Na-Zn} value actually represents an upper limit for the real selectivity coefficient. Finally, the time-dependent amount of exchangeable Zn and Mg at pH 6.5 and 0.01 M $NaNO_3$ was obtained by solving simultaneously, for each kinetics data point, the equations for Na-Zn and Na-Mg exchanges from the experimental values of $[Na]_{aq,tot}$, $[Zn]_{aq,tot}$, $[Mg]_{aq,tot}$.

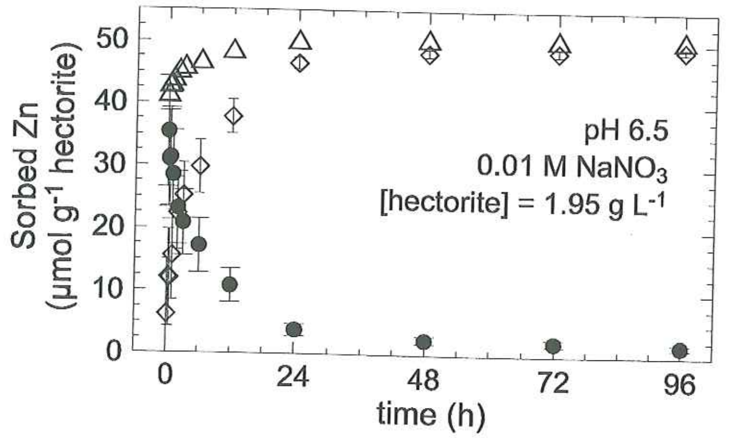

Fig. 19. Sorption of Zn as a function of time for pH 6.5 and 0.01 M $NaNO_3$. (△): Total amount of sorbed Zn. (●): Zn adsorbed on cation exchange sites. (◇): Difference between total amount of sorbed Zn and exchangeable Zn.

Figure 19 shows that the fraction of TotZn sorbed on exchange sites steadily decreased with increasing reacting time from 70 percent at t = 5 min to 4 percent at t = 96 h, whereas the total amount of sorbed Zn increased from ~ 80 percent of TotZn at t = 5 min to nearly 100 percent at t = 96 h. The decrease of the proportion of Zn OS complexes with increasing reaction time agrees with EXAFS results on wet pastes, and allows us to precise the mechanism of Zn sorption at pH 6.5 and 0.01 M $NaNO_3$ (fig. 20A to D). First, solute Zn (fig. 20A) rapidly adsorbs as OS complexes on cation exchange sites (fig. 20B). Then, Zn IS complexes form at layer edges, either by diffusion of Zn from basal surfaces (fig. 20C) or by direct sorption of solute Zn to edge sites (fig. 20D). Direct specific sorption being much slower than cation exchange, it causes a steadily decrease of $[Zn]_{aq,tot}$, which is immediately balanced by the rapid release of Zn from exchange sites to solution. After 96 h of sorption reaction, the proportion of Zn retained on exchange sites (4 percent) is well below the detection limit of EXAFS estimated to ~ 20 percent. Therefore, OS complexes remaining at the end of sorption experiments were overlooked in wet pastes and self-supporting films.

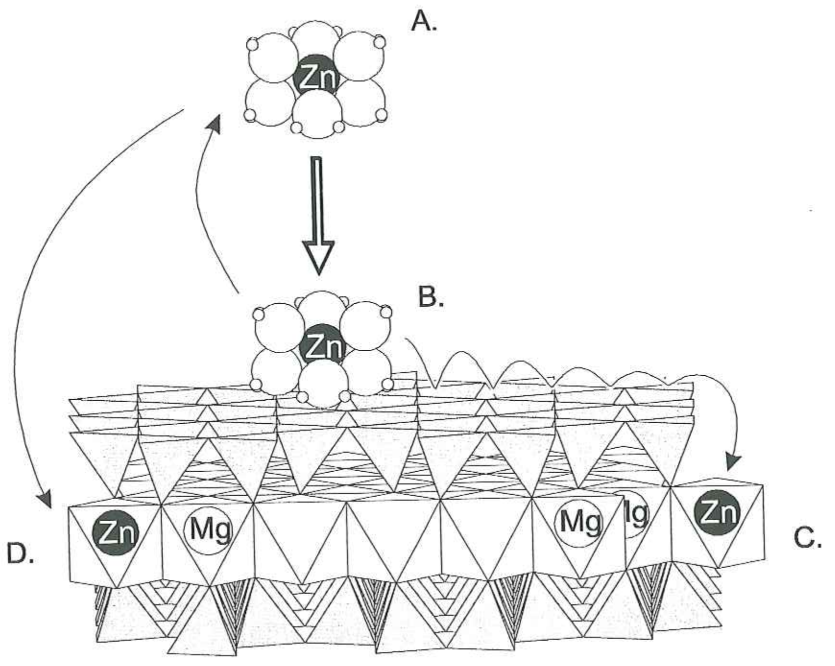

Fig. 20. Proposed mechanism of Zn sorption at 0.01 M $NaNO_3$ and pH 6.5. (A) Solute Zn. (B) Zn adsorption as OS surface complexes on the basal planes of hectorite, in equilibrium with solute Zn. (C, D) Zn adsorption as IS complexes on layer edges. This second step can result either from a surface diffusion of OS complexes from basal to edge sites (C), or from the direct adsorption of solute Zn (D).

The agreement between chemical calculations and MA-EXAFS results on wet pastes suggests that a fraction of the predominant IS complexes observed on dry samples for t = 6 h, pH 6.5 and 0.01 M $NaNO_3$ (#H01_6h_SSF) formed during the film preparation, because about 37 percent of Zn should be normally present as OS complexes. This excess of IS complex likely formed during the 6 h of the filtration stage.

Cation exchange at low ionic strength and pH 4

At pH 4 and 0.01 M $NaNO_3$, Zn initially sorbed by a cation exchange mechanism, but, in contrast to pH 6.5, the amount of sorbed Zn afterwards decreased with increasing reaction time (fig. 3B). The fraction of exchangeable Zn was calculated with the same set of equations as for pH 6.5. It always represented more than 87 percent of sorbed Zn, indicating that Zn sorption was mainly controlled by a cation exchange mechanism of Zn for Na and Mg. The amount of exchangeable Mg calculated from the exchange model increased from 77 µmol g^{-1} at t = 5 min (that is, $(X_2Mg) \approx 0.11$) to ≈ 270 µmol g^{-1} at t = 48 h ($(X_2Mg) \approx 0.51$), because of the increase of Mg in solution due to the fast dissolution of hectorite at pH 4. The increase of exchangeable Mg reduced the number of exchange sites accessible to Zn, thus accounting for the observed Zn desorption.

The sorption mechanism of Zn on hectorite at pH 6.5 is qualitatively similar to Co (Schlegel and others, 1999; Schlegel, Charlet, and Manceau, 1999). Indeed, these two cations form IS surface complex on hectorite edges at high ionic strength, and OS and then IS complex at low ionic strength. However, their sorption kinetics are different. Figure 21 shows that for identical chemical conditions (that is, pH 6.5, ionic strength 0.3 M $NaNO_3$, hectorite concentration 1.95 g L^{-1}, and total sorbent concentrations TotZn = 100 µM or TotCo = 100 µM), Zn is always quantitatively more sorbed than Co, the amount of sorbed cation reaching nearly 100 percent of TotZn, as compared to 72 percent of TotCo, at t = 120 h. The higher chemical affinity of Zn for hectorite edge sites is in keeping with the higher stability (that is, lower Gibbs free energy of formation) of Zn-kerolite compared to Co-kerolite (Decarreau, 1985).

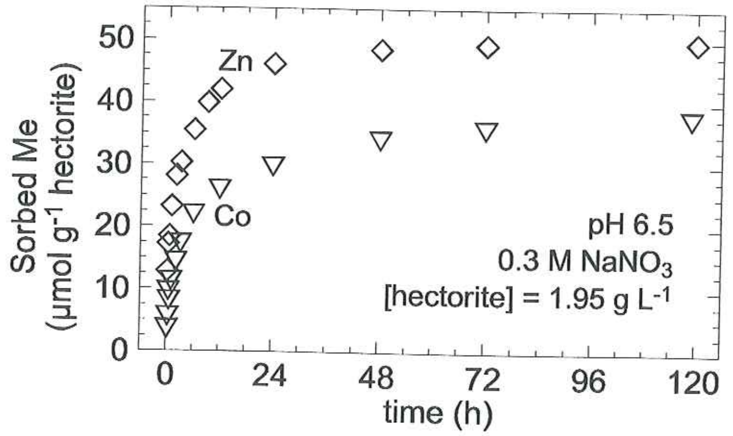

Fig. 21. Comparison between kinetics of Zn (◇) and Co (▽ sorption on hectorite at high ionic (0.3 M $NaNO_3$), and for total Zn and Co concentrations of 100 µM. [hectorite] = 1.95 g L^{-1}.

CONCLUDING REMARKS

The successful identification of the sorption mechanisms of Zn on hectorite is essentially due to the combination of four factors: (1) the detailed characterization of the complete chemistry of the sorbate-sorbent system, including the role of chemical parameters such as ionic strength and reaction time, (2) the preparation of appropriate Zn structural references mimicking the possible sorbate structural environments, (3) the application of MA-EXAFS to the determination of Zn sorption mechanisms under full wet conditions, and (4) the application of P-EXAFS to the determination of the spatial orientation of nearest atomic neighbors around sorbed Zn.

The present study highlights the importance of pH, ionic strength, and sorbate-smectite contact time on the fate of Zn in soils. Under low ionic strength conditions, Zn can be temporarily held in an exchangeable form by smectite particles and thereafter released, owing to the fast reversibility of this sorption mechanism. Released Zn can migrate to plant roots, be sorbed on surface sites of higher energy, such as those present on clay edges and (oxihydr)oxide minerals, or be incorporated in neoformed solids, such as Zn-containing phyllosilicates. Clearly, the uptake of trace elements to soil constituents is a time-dependent process and the study of natural samples usually provides only a crystal chemical snapshot. Kinetics studies at macroscopic and microscopic scales are therefore required to improve transfer models of trace elements in natural systems.

ACKNOWLEDGMENTS

The LURE and ESRF staffs are acknowledged for the provision of the synchrotron beam time. J.J. Menthonnex, Y. Soldo, O. Prost and O. Ulrich are commended for their technical assistance in the collection of EXAFS spectra on BM 32 at ESRF.

REFERENCES

Aberdam, D., 1998, SEDEM, a software package for EXAFS data extraction and modeling: Journal of Synchrotron Radiation, v. 5, p. 1287-1297.

Anderson, S. J., and Sposito, G., 1991, Cesium-adsorption method for measuring accessible structural surface charge: Soil Science Society of America Journal, v. 55, p. 1569-1576.

Baes, C. F. J., and Mesmer, R. E., 1976, The hydrolysis of cations: New York, John Wiley & Sons, 489 p.

Beyer, W. N., and Storm, G., 1995, Ecotoxicological damage from zinc smelting at Palmerton, Pennsylvania, *in* Hoffman, D. J., Rattner, B. A., Burton, G. A. Jr., and Cairns, J. Jr., editors, Handbook of ecotoxicology: Boca Raton, Lewis Publisher.

Bosbach, D., Charlet, L., Bickmore, B., and Hochella, M. F., Jr., 1999, The dissolution of hectorite: In-situ, real-time observations using atomic force microscopy: The American Mineralogist, submitted.

Bradbury, M. H., and Baeyens, B., 1999, Modelling the sorption of Zn and Ni on Ca-montmorillonite: Geochimica et Cosmochimica Acta, v. 63, p. 325-336.

Castañer, R., and Prieto, C., 1997, Fluorescence detection of extended X-ray absorption fine structure in thin films: Journal de Physique III, v. 7, p. 337-349.

Charlet, L., and Manceau, A., 1993, Structure, formation and reactivity of hydrous oxides particles: insights from X-ray absorption spectroscopy, *in* Buffle, J., and Van Leeuwen, H. P., editors, Environmental particles: London, Lewis Publishers, p. 117-163.

Charlet, L., Schindler, P. W., Spadini, L., Furrer, G., and Zysset, M., 1993, Cation adsorption on oxides and clays: the aluminium case: Aquatic Science, v. 55, p. 291-303.

Charlot, G., 1978, Dosages absorptiométriques des éléments minéraux: Paris, Masson.

Decarreau, A., 1981, Cristallogenèse à basse température de smectites trioctaédriques par vieillissement de coprécipités silicométalliques de formule $(Si_{4-x}Al_x)M_3^{2+}O_{11},nH_2O$, où x varie de 0 à 1 et où M^{2+} = Mg-Ni-Co-Zn-Fe-Cu-Mn: Comptes Rendus de l'Académie des Sciences, Série II, v. 292, p. 61-64.

Decarreau, A., 1985, Partitioning of divalent transition elements between octahedral sheets of trioctahedral smectites and water: Geochimica et Cosmochimica Acta, v. 49, p. 1537-1544.

Degueldre, C., Ulrich, H. J., and Silby, H., 1994, Sorption of ^{241}Am onto montmorillonite, illite and hematite colloids: Radiochimica Acta, v. 65, p. 173-179.

Dent, A. J., Ramsay, J. D. F., and Swanton, S. W., 1992, An EXAFS study of uranyl ion in solution and sorbed onto silica and montmorillonite clay suspensions: Journal of Colloid and Interface Science, v. 150, p. 45-60.

Egozy, Y., 1980, Adsorption of cadmium and cobalt on montmorillonite as a function of solution composition: Clays and Clay Minerals, v. 28, p. 311-318.

Ford, R. G., and Sparks, D. L., 1998, Potential formation of secondary hydrotalcite-like precipitates during Zn and Cu sorption to pyrophyllite: Mineralogical Magazine, v. 62A, p. 462-463.

Gaines, G. L., and Thomas, H. C., 1953, Adsorption studies on clay minerals. II. A formulation of the thermodynamics of exchange adsorption: Journal of Chemical Physics, v. 21, p. 714-718.

Gapon, E. N., 1933, Theory of exchange adsorption in soils: J. Gen. Chem. (U.S.S.R.), v. 3, p. 144-152.

Iler, R. K., 1979, The chemistry of silica: New York, John Wiley & Sons.

Inskeep, W. P., and Baham, J., 1983, Adsorption of Cd(II) and Cu(II) by Na-montmorillonite at low surface coverage: Soil Science Society of America Journal, v. 47, p. 660-665.

Jackson, M. L., 1964, Soil chemical analysis: Englewood Cliffs, N.J., Prentice-hall, inc, 498 p.

Jeffery, G. H., Bassett, J., Mendham, J., and Denney, R. C., 1978, Vogel's textbook of quantitative chemical analysis: New York, John Wiley and sons.

Jenny, H., 1938, Properties of colloids: Stanford, Stanford university press, 136 p.

Kadi-Hanifi, M., and Mering, J., 1972, Précisions sur la structure de l'hectorite: Comptes Rendus Hebdomadaires des Séances de l'Académie des Sciences, v. 274D, p. 149-151.

Kelley, W. P., 1948, Cation exchange in soils: ACS monographs, v. 109: New York, Reinhold publishing corporation, 144 p.

Komadel, P., Madejova, J., Janek, M., Gates, W. P., Kirkpatrick, R. J., and Stucki, J. W., 1996, Dissolution of hectorite in inorganic acids: Clays and Clay Minerals, v. 44, p. 228-236.

Kraepiel, A. M. L., Keller, K., and Morel, F. M. M., 1999, A model for metal adsorption on montmorillonite: Journal of Colloid and Interface Science, v. 210, p. 43-54.

Kreit, J. F., Shainberg, I., and Herbillon, A. J., 1982, Hydrolysis and decomposition of hectorite in dilute salt solutions: Clays and Clay Minerals, v. 30, p. 223-231.

Kuzmin, A., and Grisenti, R., 1994, Evaluation of multiple-scattering contributions in extended X-ray absorption fine structure for MO_4 and MO_6 clusters: Philosophical Magazine B, v. 70, p. 1161-1175.

Kuzmin, A., Obst, S., and Purans, J., 1997, X-ray absorption spectroscopy and molecular dynamics studies of Zn^{2+} hydration in aqueous solutions: Journal of Physics Condensed Matter, v. 9, p. 10065-10078.

Laudelout, H., 1987, Cation exchange equilibria in clays, *in* Newman, A. C. D., editor, Chemistry of clays and clay minerals: Harlow, Longman scientific & technical, p. 225-236.

Lower, S. K., Maurice, P. A., and Traina, S. J., 1998, Simultaneous dissolution of hydroxylapatite and precipitation of hydroxypyromorphite: direct evidence of homogenous nucleation: Geochimica et Cosmochimica Acta, v. 62, p. 1773-1780.

MacEwan, D. M. C., and Wilson, M. J., 1980, Interlayer and intercalation complexes of clay minerals, *in* Brindley, G., and Brown, G., editors, Crystal structure of clay minerals and their X-ray identification: London, Mineralogical Society, p. 197-248.

Maes, A., Stul, M. S., and Cremers, A., 1979, Layer charge-cation exchange capacity relationships in montmorillonite: Clays and Clay Minerals, v. 27, p. 387-392.

Manceau, A., 1990, Distribution of cations among the octahedra of phyllosilicates: insight from EXAFS: Canadian Mineralogist, v. 28, p. 321-328.

Manceau, A., Bonnin, D., Kaiser, P., and Fretigny, P., 1988, Polarized EXAFS of biotite and chlorite: Physics and Chemistry of Minerals, v. 16, p. 180-185.

Manceau, A., Bonnin, D., Stone, W. E. E., and Sanz, J., 1990, Distribution of Fe in the octahedral sheet of trioctahedral micas by polarized EXAFS. Comparison with NMR results: Physics and Chemistry of Minerals, v. 17, p. 363-370.

Manceau, A., and Calas, G., 1986, Nickel-bearing clay minerals: II. Intracrystalline distribution of nickel: an X-ray absorption study: Clay Minerals, v. 21, p. 341-360.

Manceau, A., Chateigner, D., and Gates, W. P., 1998, Polarized EXAFS, distance-valence least-squares modeling (DVLS) and quantitative texture analysis approaches to the structural refinement of Garfield nontronite: Physics and Chemistry of Minerals, v. 25, p. 347-365.

Manceau, A., and Combes, J.-M., 1988, Structure of Mn and Fe oxides and oxyhydroxides: a topological approach by EXAFS: Physics and Chemistry of Minerals, v. 15, p. 283-295.

Manceau, A., Drits, V. A., Silvester, E., Bartoli, C., and Lanson, B., 1997, Mechanism of Co^{2+} oxidation by the phyllomanganate buserite: The American Mineralogist, v. 82, p. 1150-1175.

Manceau, A., Lanson, B., Chateigner, D., Wu, J., Huo, D., Gates, W. P., and Stucki, J. W., 2000a, Oxidation-reduction mechanism of iron in dioctahedral smectites. 2. Structural chemistry of reduced Garfield nontronite: The American Mineralogist, v. 85, p. 153-172.

Manceau, A., Lanson, B., Drits, V. A., Chateigner, D., Gates, W. P., Wu, J., Huo, D., and Stucki, J. W., 2000b, Oxidation-reduction mechanism of iron in dioctahedral smectites. 1. Structural chemistry of oxidized reference nontronites: The American Mineralogist, v. 85, p. 133-152.

Manceau, A., Lanson, B., Schlegel, M. L., Hargé, J.-C., Musso, M., Hazemann, J.-L., Chateigner, D., and Lamble, G. M., 2000c, Quantitative speciation Zn speciation in smelter-contaminated soils by EXAFS spectroscopy: American Journal of Science, under press.

Manceau, A., Schlegel, M. L., Chateigner, D., Lanson, B., Bartoli, C., and Gates, W. P., 1999a, Application of Polarized EXAFS to Fine-Grained Layered Minerals, *in* Schulze, D. G., Stucki, J. W., and Bertsch, P. M., editors, Synchrotron X-ray Methods in Clay Science: Clay Mineral Society of America, p. 69-114.

Manceau, A., Schlegel, M. L., Nagy, K. L., and Charlet, L., 1999b, Evidence for the formation of trioctahedral clay upon sorption of Co^{2+} on quartz: Journal of Colloid and Interface Science, v. 220, p. 181-197.

Mathieu-Sicaud, A., Mering, J., and Perrin-Bonnet, I., 1951, Étude au microscope électronique de la montmorillonite et de l'hectorite saturées par différents cations: Bulletin de la Société française de Minéralogie et Cristallographie, v. 74, p. 439-456.

McBride, M. B., 1979, Mobility and reactions of VO^{2+} on hydrated smectite surfaces: Clays and Clay Minerals, v. 27, p. 91-96.

McBride, M. B., 1982, Hydrolysis and dehydration reaction reactions of exchangeable Cu^{2+} on hectorite: Clays and Clay Minerals, v. 30, p. 200-206.

McBride, M. B., 1994, Environmental chemistry of soils: Oxford, Oxford University Press.

McBride, M. B., Pinnavaia, T. J., and Mortland, M. M., 1975, Electron spin relaxation and the mobility of manganese(II) exchange ions in smectites: The American Mineralogist, v. 60, p. 66-72.

McKinley, J. P., Zachara, J. M., Smith, S. C., and Turner, G. D., 1995, The influence of uranyl hydrolysis and multiple site-binding reactions on adsorption of U(VI) to montmorillonite: Clays and Clay Minerals, v. 43, p. 586-598.

Muller, F., Besson, G., Manceau, A., and Drits, V. A., 1997, Distribution of isomorphous cations within octahedral sheets in montmorillonite from Camp-Berteaux: Physics and Chemistry of Minerals, v. 24, p. 159-166.

Munoz-Paez, A., Pappalardo, R. R., and Sanchez Marcos, E., 1995, Determination of the second hydration shell of Cr^{3+} and Zn^{2+} in aqueous solutions by extended X-ray absorption fine structure: Journal of the American Chemical Society, v. 117, p. 11710-11720.

Oberlin, A., and Mering, J., 1966, Observations sur l'hectorite (étude en microscopie et diffraction électroniques): Bulletin de la Société française de Minéralogie et Cristallographie, v. 89, p. 29-40.

O'Day, P. A., Rehr, J. J., Zabinsky, S. I., and Brown, G. E. Jr., 1994, Extended X-ray Absorption Fine Structure (EXAFS) analysis of disorder and multiple-scattering in complex crystalline solids: Journal of the American Chemical Society, v. 116, p. 2938-2949.

O'Neill, P., 1993, Environmental chemistry: London, Chapman & Hall, 268 p.

Papelis, C., and Hayes, K. F., 1996, Distinguishing between interlayer and external sorption sites of clay minerals using X-ray absorption spectroscopy: Colloids and Surfaces A: Physicochemical and engineering aspects, v. 107, p. 89-96.

Peigneur, P., Maes, A., and Cremers, A., 1975, heterogeneity of charge density distribution in montmorillonite as inferred from cobalt adsorption: Clays and Clay Minerals, v. 23, p. 71-75.

Rayner, J. H., and Brown, G., 1973, The crystal structure of talc: Clays and Clay Minerals, v. 21, p. 103-114.

Reed, S. T., and Martens, D. C., 1996, Copper and Zinc, *in* Sparks, D. L., editor, Methods of soil analysis. Part 3-Chemical methods: Madison, Soil Science Society of America, Inc.

Rehr, J. J., Albers, R. C., and Zabinsky, S. I., 1992, High-order multiple-scattering calculations of X-ray absorption fine structure: Physical Review Letters, v. 69, p. 3397-3400.

Rimstidt, J. D., 1997, Quartz solubility at low temperatures: Geochimica et Cosmochimica Acta, v. 61, p. 2553-2558.

Rivière, M., Rautureau, M., Besson, G., Steinberg, M., and Amour, M., 1985, Complémentarité des rayons X et de la microscopie électronique pour la détermination des diverses phases d'une argile zincifère: Clay Minerals, v. 20, p. 53-67.

Ross, C. S., 1946, Sauconite-a clay mineral of the montmorillonite group: The American Mineralogist, v. 31, p. 411-424.

Sarret, G., ms., 1998, Biogéochimie structurale du zinc et du plomb par spectroscopie EXAFS : interactions avec des acides humiques, des parois cellulaires de champignon, et des lichens, Laboratoire de géophysique interne et tectonophysique: Ph.D. Thesis, Université Joseph Fourier-Grenoble 1, p. 189.

Scheidegger, A. M., Lamble, G. M., and Sparks, D. L., 1997, Spectroscopic evidence for the formation of mixed-cation hydroxide phases upon metal sorption on clay and aluminium oxides: Journal of Colloid and Interface Science, v. 186, p. 118-128.

Scheidegger, A. M., and Sparks, D. L., 1996, Kinetics of the formation and the dissolution of nickel surface precipitates on pyrophyllite: Chemical Geology, v. 132, p. 157-164.

Scheidegger, A. M., Strawn, D. G., Lamble, G. M., and Sparks, D. L., 1998, The kinetics of mixed Ni-Al hydroxide formation on clay and aluminium oxide minerals: a time-resolved XAFS study: Geochimica et Cosmochimica Acta, v. 62, p. 2233-2245.

Schindler, P. W., 1991, A solution chemists view of surface chemistry: Pure and Applied Chemistry, v. 63, p. 1697-1704.

Schlegel, M. L., Charlet, L., and Manceau, A., 1999, Sorption of metal ions on clay minerals. II. Mechanism of Co sorption on hectorite at high and low ionic strength, and impact on the sorbent stability: Journal of Colloid and Interface Science, v. 220, p. 392-405.

Schlegel, M. L., Manceau, A., Chateigner, D., and Charlet, L., 1999, Sorption of metal ions on clay minerals. I. Polarized EXAFS evidence for the adsorption of cobalt on the edges of hectorite particles: Journal of Colloid and Interface Science, v. 215, p. 140-158.

Shannon, R. D., 1976, Revised effective ionic radii and systematic studies of interatomic distances in halides and chalcogenides: Acta Crystallographica, v. A32, p. 751-767.

Sposito, G., 1981, The thermodynamics of soil solutions: Oxford, Oxford University Press.

Sposito, G., 1984, The surface chemistry of soils: Oxford, Oxford University Press.

Sposito, G., 1994, Chemical equilibria and kinetics in soils: Oxford, Oxford University Press.

Stadler, M., and Schindler, P. W., 1993, Modeling of H^+ and Cu^{2+} adsorption on calcium-montmorillonite: Clays and Clay Minerals, v. 41, p. 288-296.

Stern, E. A., 1988, Theory of EXAFS, *in* Koningsberger, D. C., and Prins, R., editors, X-ray absorption: Principles, applications, techniques of EXAFS, SEXAFS and XANES: Chemical Analysis: New York, Wiley-Interscience, p. 3-51.

Stout, P. R., 1956, Micronutrients in crop vigor: J. Agric. Food Chem., v. 4, p. 1000-1006.

Stumm, W., 1992, Chemistry of the solid-water interface: New York, John Wiley & sons.

Stumm, W., and Morgan, J. J., 1996, Aquatic chemistry: New York, John Wiley & Sons, 780 p.

Tang, L., and Sparks, D. L., 1993, Cation-exchange kinetics on montmorillonite using pressure-jump relaxation: Soil Science Society of America Journal, v. 57, p. 42-46.

Teo, B. K., 1986, EXAFS: basic principles and data analysis: Berlin, Springer-Verlag.

Tröger, L., Zschech, E., Arvanitis, D., and Baberschke, K., 1992, Quantitative fluorescence EXAFS analysis of concentrated samples-correction of the self-absorption effect, 7th. International Conference on X-Ray Absorption Fine Structure: Kobe, Jpn. J. Appl. Phys., p. 144-146.

Vaarkamp, M., Dring, I., Oldman, R. J., Stern, E. A., and Koningsberger, D. C., 1994, Comparison of theoretical methods for the calculation of extended x-ray absorption fine structure: Physical Review B, v. 50, p. 7872-7883.

Valsami-Jones, E., Ragnarsdottir, K. V., Putnis, A., Bosbach, D., Kemp, A. J., and Cressey, G., 1998, The dissolution of apatite in the presence of aqueous metal cations at pH 2-7: Chemical Geology, v. 151, p. 215-233.

Vanselow, A. P., 1932a, Equilibria of the base-exchange reaction of bentonites, permutites, Soil colloids and zeolites: Soil Science, v. 33, p. 95-113.

Vanselow, A. P., 1932b, The utilization of the base-exchange reaction for the determination of activity coefficients in mixed electrolytes: Journal of American Chemical Society, v. 54, p. 1307-1311.

Verburg, K., Baveye, P., and McBride, M. B., 1995, Cation exchange hysteresis and dynamics of formation and breakdown of montmorillonite quasi-crystals: Soil Science Society of America Journal, v. 59, p. 1268-1273.

Zachara, J. M., and McKinley, J. P., 1993, Influence of hydrolysis on the sorption of metal cations by smectites: importance of edge coordination reactions: Aquatic Science, v. 55, p. 250-261.

Zachara, J. M., and Smith, S. C., 1994, Edge complexation reactions of cadmium on specimen and soil-derived smectite: Soil Science Society of America Journal, v. 58, p. 762-769.

Zachara, J. M., Smith, S. C., Resh, C. T., and Cowan, C. E., 1993, Cadmium sorption on specimen and soil smectites in sodium and calcium electrolytes: Soil Science Society of America Journal, v. 57, p. 1491-1501.

Discussion et conclusion.

Les résultats de chimie de solution et de spectroscopie EXAFS pour le cobalt et le zinc montrent que les mécanismes d'adsorption de ces deux cations à pH modéré (6,5) sont comparables. À haute force ionique, Co et Zn forment tous deux des CSI localisés en bordure des feuillets d'hectorite, en continuité structurale des couches octaédriques (Mg, Li). À basse force ionique, les mécanismes d'adsorption de Co et Zn présentent tous deux une étape initiale d'adsorption rapide par échange cationique, puis une étape plus lente de transfert des cations vers les sites de bordure des feuillets. Quelques différences quantitatives entre Co et Zn peuvent être relevées, notamment en terme de cinétique d'adsorption spécifique et de quantité de cation adsorbé pour des conditions chimiques identiques. Par exemple, pour une haute force ionique ($NaNO_3$ 0,3 M), une concentration totale en cation de 100 µM, et une concentration en hectorite de 1,95 g L^{-1}, les quantités de cation adsorbées après 120 h de réaction sont égales à plus de 97% de TotZn, et seulement 72% de TotCo. Par ailleurs, la réaction d'adsorption de Zn semble atteindre l'équilibre (i.e., pratiquement tout le zinc est adsorbé) après seulement 72 h, alors qu'au bout de 120 h l'adsorption de Co n'est pas achevée. Ces résultats suggèrent que l'affinité du zinc pour les sites d'adsorption spécifique en bordure des feuillets d'hectorite est supérieure à celle du cobalt. Un parallèle peut être fait entre cette différence d'affinité et la plus grande stabilité (ΔG) des argiles zincifères par rapport aux argiles cobaltifères [164, 165].

Du fait de la mise en œuvre d'un protocole expérimental relativement lourd, et de la volonté de contrôler les expériences du début à la fin, les études cinétiques ont été limitées dans le temps. Il aurait été souhaitable de poursuivre ces études cinétiques sur de plus longues périodes, par exemple, dans le cas de Co, jusqu'à ce que toutes les réactions d'adsorption du cobalt aient atteint l'équilibre. Cependant, il n'est pas certain que les résultats alors obtenus eussent permis d'approfondir la compréhension des systèmes étudiés. En revanche, la nature des complexes de surface formés lors de l'adsorption spécifique de Zn et Co à bas pH (e.g. 4) et haute force ionique reste à déterminer. Il est probable, mais pas certain, que ces complexes soient des CSI de structure similaire à ceux observés à plus haut pH (i.e., 6,5).

L'étude de la stabilité de l'hectorite avant et après addition de Co ou Zn a permis de mettre en évidence une accélération importante et temporaire de la libération de Mg en solution, et directement corrélée à la cinétique d'adsorption des cations métalliques. Cette corrélation peut s'expliquer soit par des interactions entre adsorption des cations et dissolution de l'hectorite, soit par une compétition entre Mg et les cations additionnés pour l'adsorption sur les mêmes sites de bordure. Le mécanisme moléculaire de cette libération accrue pourrait être élucidé en étudiant l'influence de paramètres susceptibles de modifier les proportions de Mg adsorbé et de sites de dissolution actifs, comme le pH, et le degré de sous-saturation de la suspension vis-à-vis de l'hectorite.

Quatrième partie : nucléation hétérogène et croissance de phyllosilicates zincifères sur l'hectorite et cobaltifères sur le quartz

Introduction

L'origine des phyllosilicates présents dans les sols et les profils d'altération a fait l'objet de nombreuses études [4-6, 166]. Dans les formations superficielles, les phyllosilicates peuvent être hérités de la roche-mère, résulter de la transformation à l'état solide de phyllosilicates instables dans les conditions physico-chimiques de la surface, ou encore être néoformés à partir d'espèces chimiques dissoutes [6, 166]. Les processus de néoformation par précipitation d'éléments dissous sont susceptibles de piéger les cations métalliques, que ce soit dans les gisements [167, 168], dans les profils latéritiques [10], ou dans les zones polluées [13]. Ces néoformations de phyllosilicates s'effectuent généralement par nucléation hétérogène, soit en continuité structurale d'autres phyllosilicates (épitaxie), soit à la surface de minéraux d'organisation structurale différente (topotaxie) [4, 169]. L'identification au laboratoire des conditions physico-chimiques favorisant cette nucléation hétérogène permet alors de préciser les conditions géochimiques dans lesquelles ces processus sont susceptibles de se produire dans les milieux naturels.

Les études d'adsorption de cations sur des phyllosilicates à des pH supérieurs ou égaux à 7 ont montré qu'il y avait néoformation d'hydroxydes lamellaires simples ou doubles [18, 125, 130, 131, 170]. Ces résultats sont surprenants, car ces hydroxydes sont assez rares dans le milieu naturel, alors que les phyllosilicates y sont au contraire abondants. Cette disparité pourrait résulter de concentrations de silice en solution $[Si]_{aq}$ différentes dans les expériences en laboratoire et dans le milieu naturel. En effet, les valeurs de $[Si]_{aq}$ mesurées (quand elles le sont) au début des expériences d'adsorption et lors de la nucléation des hydroxydes sont généralement faibles (moins de 100 µM, soit 6 ppm SiO_2), et n'atteignent des valeurs de 200-300 µM (12-18 ppm SiO_2) que lorsque la majeure partie des cations a déjà été adsorbée [18]. Or, plus de 90% des eaux terrestres ont une concentration en SiO_2 dissous comprise entre 180 µM (11 ppm SiO_2) et 1300 µM (80 ppm SiO_2) [171], ces valeurs étant comprises entre la solubilité du quartz ($[Si(OH)_4] = 183$ µM; [172]) et celle de la silice amorphe ($[Si(OH)_4] \approx 2\,000$ µM; [173]). La disparité entre les concentrations expérimentales et naturelles de silice dissoute d'une part, et l'abondance des phyllosilicates par rapport aux hydroxydes lamellaires dans les milieux naturels d'autre part, suggère que $[Si]_{aq}$ pourrait jouer un rôle crucial dans les mécanismes de nucléation et de néoformation des phyllosilicates.

Les objectifs de cette partie sont (1) de définir les conditions chimiques (notamment $[Si]_{aq}$) pour lesquelles on peut avoir hétéronucléation et néoformation de phyllosilicates à la surface de l'hectorite, et (2) de montrer que de telles néoformations sont aussi possibles lors de l'adsorption de cations sur le quartz, un minéral très abondant dans les milieux naturels. Dans la première section (chapitre 6), on montre qu'il est possible de réaliser une épitaxie de phyllosilicates zincifères sur l'hectorite à condition de maintenir une concentration en SiO_2 dissous comparable aux concentrations naturelles. Dans la deuxième section (chapitre 7), la néoformation de phyllosilicates cobaltifères à la surface du quartz est démontrée en réanalysant les résultats de chimie et de spectroscopie EXAFS déjà publiés [174].

6. Néoformation de phyllosilicates zincifères sur l'hectorite

Le mécanisme de néoformation d'un phyllosilicate zincifère dans une suspension d'hectorite (0,65 g L^{-1}) a été étudié à haute force ionique ($NaNO_3$ 0,3 M) afin d'inhiber l'échange cationique, à pH 7,3, à une concentration totale en zinc (TotZn) de 520 µM (soit plus de 5 fois la concentration de sites de bordure calculée à partir des données d'AFM;), et à des valeurs de $[Si]_{aq}$ de 30~60 µM (expérience désignée par H30_Zn) ou 500-550 µM (H30_SiZn). À haute $[Si]_{aq}$, une solution de $SiO_2.Na_2O$ 0,01 M, $NaNO_3$ 0,28 M (silice-base) a été ajoutée durant l'expérience pour maintenir le pH à la valeur cible de 7,3 et $[Si]_{aq}$ à une valeur élevée. À basse $[Si]_{aq}$, le pH a été régulé à l'aide de NaOH 0,02 M, $NaNO_3$ 0,28 M. Une expérience de contrôle (NoH_SiZn) a été réalisée à une haute $[Si]_{aq}$ (~540 µM) et en absence d'hectorite, pour vérifier que la disparition de Zn en solution mesurée en présence d'hectorite était bien due à l'adsorption de ce cation sur la smectite. La nature des complexes de surface formés lors de ces expériences a été déterminée par spectroscopie P-EXAFS sur des films auto-supportés. Les résultats de cette étude sont détaillés dans l'article en préparation intitulé « *Sorption of metal ions on clay minerals. III. Epitaxial growth of Zn-rich clay minerals at the edges of hectorite particles* » situé à la fin de cette section.

6.1. Impact de Si sur l'adsorption de Zn

En absence d'hectorite, les concentrations de Zn et Si en solution restent constantes, indiquant qu'il n'y a pas de précipitation homogène d'un solide mixte Zn-Si. En présence d'hectorite, et à basse concentration en Si ($[Si]_{aq}$ ~ 30-60 µM), une fraction modérée de Zn (5,8% de TotZn) est adsorbée au cours de trois premières heures de contact, ensuite l'adsorption se poursuit lentement, et la quantité de Zn adsorbée au bout de 168 h est inférieure à 15% (fig. 6.1). À haute concentration en Si ($[Si]_{aq}$ ~ 540 µM), la fraction de Zn adsorbée au cours des trois premières heures est plus importante (15,2% de TotZn) qu'à basse concentration en Si, et au bout de 120 h de réaction, plus de 90% de TotZn est adsorbé. Durant cette réaction, $[Si]_{aq}$ reste pratiquement constant en dépit de l'addition de larges quantités de silice-base (fig. 6.2), ce qui indique que Si est adsorbé en même temps que Zn. Au-delà de 9 h de temps de réaction, le rapport Si/Zn adsorbé est constant (1,09 ± 0,05), et légèrement inférieur à celui d'un phyllosilicate TOT trioctaédrique (~ 1,33).

6.2. Environnement moléculaire des cations adsorbés

L'environnement atomique du zinc adsorbé a été déterminé par P-EXAFS sur des films auto-supportés. Des effets angulaires importants ont été observés pour tous les films, ce qui suggère une association structurale entre Zn et les particules d'hectorite. La comparaison de ces spectres avec ceux de phyllosilicates TOT de synthèse, ayant des proportions variables de Mg et Zn, indique que l'environnement de Zn adsorbé est comparable à celui de Zn dans un phyllosilicate (fig. 6.3).

L'analyse quantitative des spectres EXAFS montre que pour une valeur de $[Si]_{aq}$ faible et un temps de réaction de 96 h, le zinc est entouré dans le plan du film par 1,7 ± 0,5 Zn et 1,4 ± 0,5 Mg à des distances $R_{Zn\text{-}Zn}$ et $R_{Zn\text{-}Mg}$ de 3,08 Å, et par 0,6 ± 0,5 Si à $R_{Zn\text{-}Si} \approx 3{,}28$ Å hors du plan. Ces données structurales indiquent l'existence de clusters d'octaèdres de Zn reliés par arêtes en bordure des feuillets d'octaèdres de l'hectorite. À haute concentration en Si et pour un temps de réaction nettement plus court (t = 9 h), les nombres de voisins Zn et Si sont plus importants (3,8 ± 0,5 et 1,5 ± 0,5, respectivement), tandis que le nombre de voisins Mg diminue (0,8 ± 0,5). L'augmentation du nombre de voisins Zn suggère que le zinc forme des clusters d'octaèdres de plus grande taille qu'à basse concentration en silice. D'autre part, la diminution du nombre de voisins Mg indique que la fraction de Zn attachée directement en bordure des feuillets est moins importante. L'augmentation du nombre de voisins Si ne peut être alors expliquée que par la fixation des tétraèdres de Si sur les couches octaédriques de Zn. Enfin, pour un temps de réaction de 120 h, le spectre EXAFS enregistré est très proche de celui d'une kérolite zincifère. Le zinc est alors entouré de 6 ± 0.5 voisins Zn à $R_{Zn\text{-}Zn} = 3.10$ Å dans la direction du plan, et de 3.6 ± 0.5 Si à $R_{Zn\text{-}Si} \approx 3.26$ Å orientés hors du plan. Ces nombres de voisins élevés indiquent que les nucléi de phyllosilicates zincifères ont un diamètre moyen supérieur à 30 Å [175].

Figure 6.1. Cinétique d'adsorption de Zn à pH 7,3, $NaNO_3$ 0,3 M et pour différentes concentrations d'hectorite et de $[Si]_{aq}$. (☆) : $[Si]_{aq} \approx 540$ µM, [hectorite] = 0 g L^{-1}. (△) : $[Si]_{aq} \approx 30\text{-}60$ µM, [hectorite] = 0,65 g L^{-1}. (◇) : $[Si]_{aq} \approx 540$ µM, [hectorite] = 0,65 g L^{-1}.

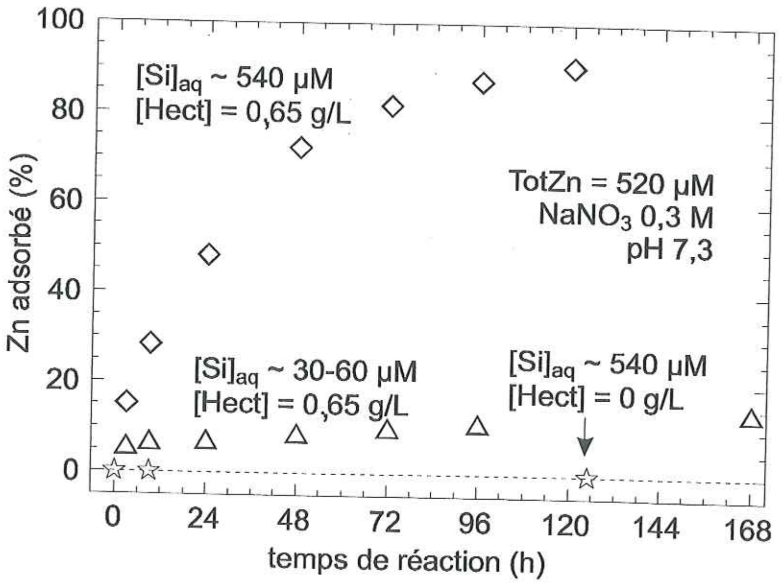

Figure 6.2. Variations de $[Si]_{aq}$ lors de l'adsorption de Zn sur l'hectorite pour l'expérience H30_SiZn. (○) : $[Si]_{aq}$ expérimentale. (◌) : $[Si]_{aq}$ hypothétique, calculée en faisant l'hypothèse que tout le Si apporté dans la suspension lors des ajouts de silice-base reste dans le surnageant.

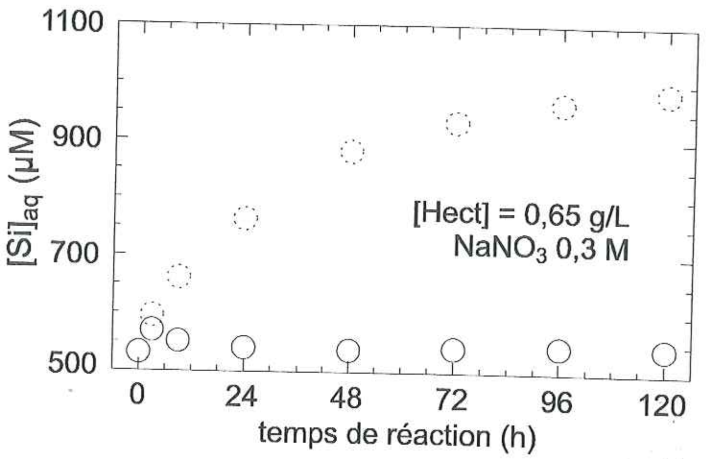

Figure 6.3. Comparaison des spectres EXAFS mesurés à l'angle magique pour des kérolites zincifères de synthèse et des échantillons de Zn adsorbé sur l'hectorite à différents temps de réaction et $[Si]_{aq}$. ZnKer300 = $Zn_3Si_4O_{10}(OH)_2{\cdot}nH_2O$; ZnKer135 = $Zn_{1,35}Mg_{1,65}Si_4O_{10}(OH)_2{\cdot}nH_2O$. Noter les grandes similitudes en fréquence des différents spectres.

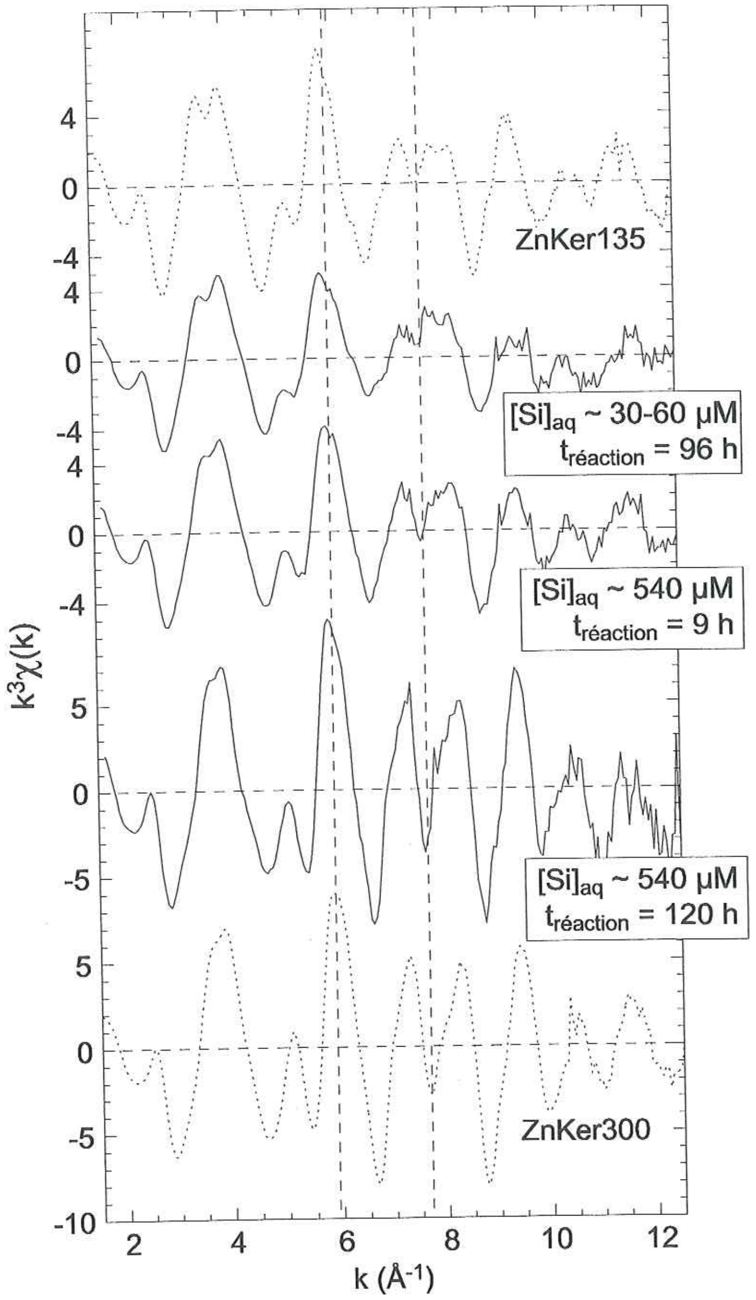

(Sorption of metal ions on clay minerals. III. Epitaxial growth of Zn-rich clay minerals at the edges of hectorite particles. Article en préparation)

Sorption of metal ions on clay minerals. III. Epitaxial growth of Zn-rich clay minerals on the edges of hectorite particles

Michel L. Schlegel,[1,*,†] Alain Manceau,[1] Laurent Charlet,[1] Daniel Chateigner,[2]
and Jean-Louis Hazemann[2,3]

1: Environmental Geochemistry Group, LGIT-IRIGM, University of Grenoble, BP 53
F-38 041 Grenoble cedex 9, France

2: Laboratoire de Physique de l'État Condensé, Université du Maine, BP535
F- 72085 Le Mans cedex 9, France

3 :Laboratoire de Cristallographie, CNRS, 25, avenue des Martyrs, BP 166
F-38 042 Grenoble Cedex 9, France

Short running title: P-EXAFS study of Zn-sorbed hectorite

*: Corresponding author: Michel L. Schlegel

e-mail: Michel.Schlegel@ujf-grenoble.fr

Abstract

In terrestrial waters, dissolved Si can influence the sorption of trace metals by mineral surfaces. The impact of dissolved Si ($[Si]_{aq,t}$) on Zn uptake in dilute suspensions (0.65 g L^{-1}) of hectorite ($(Na_{0.40}(Mg_{2.65}Li_{0.35})(Si_{3.95}Al_{0.05})O_{10}(OH)_2)$) was investigated at pH 7.3, at a total Zn concentration of TotZn = 520 µM, and at high ionic strength (0.3 M $NaNO_3$) by combining kinetics chemical experiments and polarized extended X-ray absorption fine structure (P-EXAFS) spectroscopy.

At low $[Si]_{aq,t}$ (~30-60 µM), 5.8% of TotZn was adsorbed within the first 3 h of reaction. The sorption rate was lower afterwards, and Zn uptake amounted to 14.8% of TotZn after 168 h of reaction. This kinetics is consistent with Zn sorption on pH-dependent edge sites of hectorite platelets. Higher sorption rates were systematically observed at high $[Si]_{aq,t}$ (~530 µM), the fraction of Zn removed amounting to 15.2% of TotZn at t = 3 h and to 90.7% at t = 120 h. After 9 h of reaction time, Si uptake also occurred, and the Si/Zn uptake ratio (1.09 ± 0.03) was close to those of TO (~0.67) and TOT (~1.33) trioctahedral phyllosilicates, which suggests the neoformation of a Zn phyllosilicate. In the absence of hectorite, neither Zn nor Si were removed from solution, even at high $[Si]_{aq,t}$, indicating that Zn uptake occurred by sorption on hectorite surface.

The angular dependence observed for all P-EXAFS spectra confirms that Zn cations are structurally associated to hectorite platelets. Further comparison of spectra for sorption samples and Zn references shows that sorbed Zn was always located in a clay environment. Zn polymers were detected in all sorption samples. The size and structure of these Zn surface complexes varies with $[Si]_{aq,t}$ and reaction time. At low $[Si]_{aq,t}$, and after a long reaction time (t = 96 h), Zn is surrounded by in-plane 1.9 ± 0.5 Zn and at 1.4 ± 0.5 at 3.08 Å, and 0.6 ± 0,5 Si at 3.28 Å. These results point to formation of small polymers containing 2-3 Zn cations, and located at the layer edges of hectorite, in structural continuity of the hectorite octahedral sheet. At high $[Si]_{aq,t}$, higher number of Zn and Si neighbors, and lower numbers of Mg neighbors, were detected, and at the end of the sorption (t = 120h), Zn is surrounded by 6.0 ± 0.5 Zn at 3.10 Å and 3.6 ± 0.5 Si at 3.27 Å. These results at high $[Si]_{aq,t}$, can be interpreted by the nucleation and growth of large Zn phyllosilicates of TOT structure at the edges of hectorite platelets.

1. INTRODUCTION

Silica is one of the most widespread chemical species at the Earth's surface. The aqueous concentration of silicic acid in terrestrial waters typically ranges between 10 and 80 ppm (Davies and De Wiest, 1966), and is controlled by the dissolution of silicate minerals, such as quartz (Rimstidt, 1997), olivine, pyroxene, amphibole and feldspar (Drever, 1997), and the dissolution and precipitation of secondary phases, including phyllosilicates. Heterogeneous nucleation of these phyllosilicate phases is commonly observed, and clay minerals grow either epitaxially on detrital, inherited, or secondary phyllosilicates (Nagy et al., 1999; Robarge, 1998), or topotactically on dissimilar phases such as quartz (Davis et al., 1998), silica (Banfield et al., 1991), and even organic matter (Fortin et al., 1997). These reactions of phyllosilicate neoformation can significantly affect the cycling of major and trace cationic elements in soils and weathering profiles (Drever, 1997; Harder, 1977; Manceau et al., 2000b; Righi and Meunier, 1995; Robarge, 1998). Because of this environmental importance, characterization of the mechanisms by which phyllosilicates nucleate at mineral-water interfaces is warranted.

Recent microscopic and spectroscopic studies on the surface reactivity of silicate minerals in laboratory conditions (Farquhar et al., 1997; O'Day et al., 1996; O'Day et al., 1994a; Papelis and Hayes, 1996; Scheidegger et al., 1996; Scheidegger et al., 1997; Scheidegger et al., 1998) concluded to the neoformation of pure, and mixed hydroxide phases. Yet, these compounds are seldom identified in natural systems. Neoformation of clay minerals upon cation uptake in quartz (Manceau et al., 1999b) and silica suspensions (Charlet and Manceau, 1994; Espinose de la Caillerie et al., 1995a) was detected by powder extended X-ray absorption fine structure (EXAFS) spectroscopy. However, the structural information which can be retrieved from powder EXAFS spectroscopy is limited to the immediate vicinity of the target atom, which hampers the discrimination between homogeneous and heterogeneous nucleation (Manceau et al., 1999b). Manceau & al (Manceau et al., 1999b) propose to overcome this limitation of EXAFS by performing polarized EXAFS on highly textured self-supporting films of fine-grained layer minerals. This method was successfully applied by Schlegel & al (Schlegel et al., 1999) to identify Co sorption sites at the edges of hectorite, a magnesian smectite (Fig. 1). The contribution from Mg cations of the octahedral sheet at R ~ 3.03 Å was enhanced for parallel orientation between the X-ray polarization vector and the phyllosilicate plane ($\alpha = 0$; Fig. 1, left), and extinguished for normal orientation ($\alpha = 90°$; Fig. 1, right), whereas the opposite polarization dependence was observed for Si contributions. Thus, the formation of Co surface complexes in the continuity of the smectite octahedral sheets was successfully demonstrated. The ability of P-EXAFS to identify and characterize highly anisotropic environment can be used to differentiate solids precipitated in the bulk solutions from that neoformed in structural continuity to the smectite layers. The theory of P-EXAFS and its application to fine-grained minerals are presented elsewhere (Manceau et al., 1998; Manceau et al., 1999a).

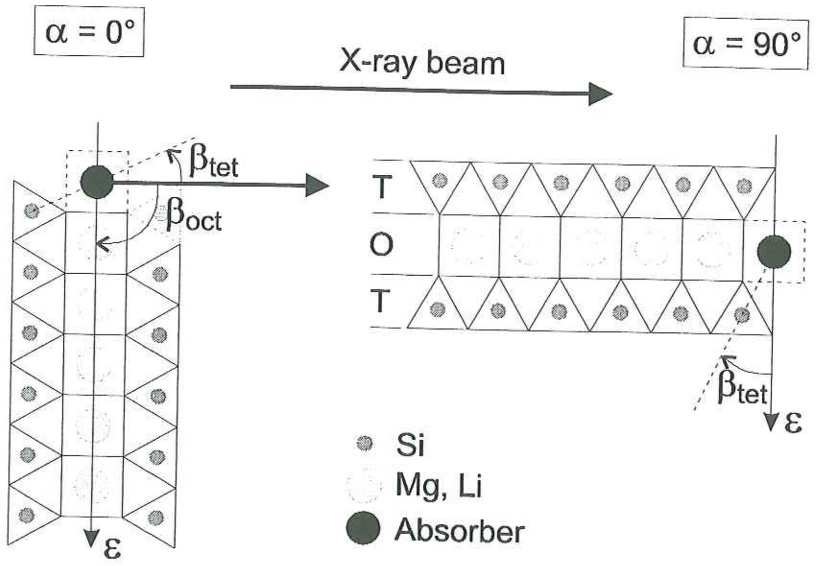

Fig. 1. Application of polarized EXAFS measurements to the characterization of sorbent surface complexes located at the edges of phyllosilicate platelets. Left: electric field vector **ε** parallel to the layer plane. Right: **ε** perpendicular to the layer plane.

In this paper, P-EXAFS was employed to study the nucleation and growth mechanism of Zn phyllosilicate on hectorite. Emphasis is placed on the catalytic role of the sorbent surface and the importance of dissolved Si. The uptake of Zn and Si at near-neutral pH (7.3) and high Zn/hectorite ratio (520 μmol Zn/0.65 g hectorite) were followed by kinetics chemical methods. Self-supporting films were carefully prepared from these hectorite suspensions, and the orientation distribution of hectorite crystallites in these films quantified by texture analysis. Zn-containing solid phases were successfully identified, and their structural relationship with the hectorite sorbent determined. Based on these results, the impact of dissolved Si on the structural mechanism of Zn uptake can be discussed. In this paper, "uptake" refers to the partitioning of dissolved species to a solid phase, regardless of the partition mechanism (i.e., adsorption on a solid phase or bulk precipitation) (Towle et al., 1997).

2. MATERIALS AND METHODS

2.1. Hectorite purification and characterization

Hectorite $Na_{0.40}(Mg_{2.65}Li_{0.35})(Si_{3.95}Al_{0.05})O_{10}(OH)_2$ was purchased from the Clay Mineral Repository (SHCa-1). 10 g of the raw material was dispersed in 500 ml of milli-Q water. The <2 μm fraction was isolated by centrifugation, treated several times with a 10^{-4} mol L^{-1} (M) HNO_3, 0.5 M NaCl solution to remove carbonates, and subsequently washed five times with a 0.5 M NaCl solution to exchange interlayer cations with Na. No concentrated inorganic acid was used, because hectorite dissolves quickly at low pH (Komadel et al., 1996; Kreit et al., 1982). Then the clay suspension was treated with a dithionite, citrate, bicarbonate solution for 1 h at pH 6.5 to remove possibly remaining ferric oxides, and with a 3% H_2O_2, 0.5 M NaCl solution for 1 h at 50°C to remove organic matter (Jackson, 1964; Schlegel et al., 1999; Zachara and Smith, 1994; Zachara et al., 1995). Remaining H_2O_2 was destroyed by heating the suspension for more than 1 h at 70°C. Finally, hectorite was repeatedly washed with a 0.3 M $NaNO_3$ solution until no Cl^- could be detected by $AgNO_3$ test, and then stored as a 1.3% wt stock suspension at 4°C in dark. The purified clay was characterized by X-ray diffraction on a Siemens D-5000 X-ray diffractometer. No trace of crystallized carbonate mineral could be detected. The cation exchange capacity (CEC), measured by Cs exchange (Anderson and Sposito, 1991), is 840 meq kg^{-1}. Specific surface area determined by BET equals 114 m^2 g^{-1}.

2.2. Zn uptake experiments

All solutions were prepared with Milli-Q water and chemicals of ACS reagent grade. Sorption experiments were conducted at 25°C (±0.1°C) in polyethylene vessels immersed in a thermostatic water bath. Polyethylene was chosen to avoid interactions of dissolved cations and silica with the vessel walls. A rotating magnetic bar ensured vigorous stirring of the suspension. A water vapor-saturated inert atmosphere was maintained by bubbling humidified Ar that had passed beforehand through a purification setup (10% H_2SO_4, then 0.1 M NaOH, and finally $NaNO_3$ at the ionic strength of the suspension). A constant high Na concentration of 0.3 M was maintained throughout the experiments by preparing the working solutions with the appropriate amounts of $NaNO_3$ salt (Fluka). pH measurements were performed with a combination electrode (Metrohm) calibrated with buffers (Merck, titrisol), and recalibrated at least every 48 h. pH values were adjusted by adding small aliquots of acid (0.1 M HNO_3, 0.3 M $NaNO_3$), base (0.02 M NaOH, 0.28 M $NaNO_3$), or silica-base (0.01 M SiO_2, 0.02 M NaOH, 0.28 M $NaNO_3$) solutions, according to experimental conditions.

Three experiments were performed to assess the role of hectorite surface and the importance of dissolved Si in uptake of Zn. In the first experiment [H30_SiZn], a dilute hectorite suspension (0.65 g L^{-1}) with a solute Si concentration, $[Si]_{aq,t}$, of ~530 μM was prepared at pH 4 by mixing the hectorite stock suspension with acid, silica-base, and $NaNO_3$ solutions. Prior to Zn addition, this suspension was allowed to react overnight without pH control. In the second experiment [NoH_SiZn], a Si-enriched hectorite suspension was prepared likewise, allowed to react overnight, and then centrifuged (30 min at 5 000 rpm). A 100 ml aliquot of the supernatant was acidified with 50 μl of the acid solution, filtered (Millipore 0.05 μm cellulose nitrate filter) to remove any remaining hectorite particle, poured back in a clean reaction vessel, and outgassed with humidified Ar for 1 h prior to Zn addition. Hence, NoH_SiZn differs from H30_SiZn only by the absence of hectorite particles. In the third experiment [H30_Zn], a hectorite suspension (0.65 g L^{-1}) with a "low" $[Si]_{aq,t}$ (~30 μM) was prepared at pH 4 by mixing the hectorite stock suspension with only acid and $NaNO_3$ solutions, and allowed to react overnight. In all experiments, pH was adjusted to 7.3 prior to Zn addition. Zn uptake was then initiated by adding an aliquot of a 0.21 M $Zn(NO_3)_2$, 10^{-3} M HNO_3

solution to obtain a total Zn concentration (TotZn) of 520 μM. The time of Zn addition is hereafter referred to as t = 0. Following Zn addition, pH was adjusted to 7.3 (±0.05) within 2 h, and kept at this value by adding silica-base (H30_SiZn and NoH_SiZn) or base (H30_Zn) solutions at a slow rate (~50 μl min^{-1}) to avoid local supersaturation. At given times, ($0 < t \leq 168$ h), 5 ml of the suspensions were withdrawn from the reaction vessel with a plastic syringe connected to a polyethylene needle, centrifuged, and filtered (Millipore 0.05 μm cellulose nitrate filter). The first milliliter of the filtered supernatant was discarded to limit losses due to sorption on the filter. filtered supernatants were acidified with a drop of 0.1 M HNO_3, and stored in the dark. Zn, Si and Mg concentrations in the filtered supernatant ($[Zn]_{aq,t}$ and $[Si]_{aq,t}$, and $[Mg]_{aq,t}$) were measured by inductively coupled plasma-atomic emission spectrometry. $[Si]_{aq,t}$ never exceeded 600 μM. Therefore, silicic acid was undersaturated with respect to amorphous silica (solubility of ~2000 μM; (Iler, 1979)), and was assumed to remain predominantly in monomeric form (Stumm, 1992). Zn uptake was determined from the difference between TotZn and $[Zn]_{aq,t}$, taking into account the dilution caused by addition of base or silica-base. The dilution factor for the i^th^ sample was calculated as

$$D_i = \prod_{j=1}^{i-1} \frac{v_j - v_{sample,j}}{v_j - v_{sample,j} + v_{b,j}} \qquad (1)$$

where v_j is the suspension volume before withdrawing the j^th^ sample, $v_{sample,j}$ is the volume of the j^th^ sample, and $v_{b,j}$ is the volume of base or silica-base solution added after withdrawal of the j^th^ sample. D = 1 in the absence of dilution, and D = 0 for an infinite dilution. Calculations of D_i for H30_SiZn yielded D = 0.993 at t = 3 h and D = 0.952 at t = 120 h. Dilution was less important for H30_Zn (D = 0.996 at t = 168 h) and NoH_SiZn (D > 0.999 at t = 125 h). Speciation calculations at t = 0 showed that 94.7% of Zn in the supernatant was present as $Zn^{2+}_{(aq)}$, 1.8% as $ZnOH^{+}_{(aq)}$, and 3.7% as $Zn_2OH^{3+}_{(aq)}$ dimers (Baes and Mesmer, 1976). At no moment did $[Zn]_{aq,t}$ reach the solubility limit of ZnO, the stable precipitated form of Zn in solutions. Possible complexation of Zn by dissolved Si in solution was not considered in these calculations, because no thermodynamic data are available for such complexes, to our knowledge.

2.3. Sample preparation for EXAFS spectroscopy

15 μm thick self supporting films of Zn-sorbed hectorite were obtained by slowly filtering 40 ml of the suspension withdrawn from reaction vessels at t = 9 h, 120 h (H30_SiZn) and 96 h (H30_Zn) on 0.05 μm Sartorius cellulose nitrate filters. Filtration was performed in a closed filtration vessel under a continuous flow of humidified Ar to limit contamination by atmospheric carbonate. Excess of salt and aqueous Zn were washed with a few milliliters of Milli-Q water before drying. Previous experiments showed that drying does not modify the atomic environment of Zn sorbed at high ionic strength (Schlegel et al., 2000). Several slices of the same film were cut and stacked on a sample holder. Upon stacking, the slices were successively rotated around an axis perpendicular to the film plane to improve the in-plane disorientation of hectorite crystallites. A fraction of NoH_SiZn at t = 125 h (NoH_SiZn_125h) was pipetted in a Teflon sample holder sealed with kapton windows for fluorescence-yield EXAFS measurements. Chemical conditions for the preparation of EXAFS samples are summarized in table 1.

Table 1.Samples analyzed by EXAFS spectroscopy.

Samples	[hectorite]	Zn uptake[a]	Γ^b (μmol g^{-1}	$\frac{g\ Zn_{uptake}}{g\ hectorite}$	$[Si]_{aq,t}$	Time
	(g L^{-1})	%	hectorite)	(%)	(μM)	(h)
H30_SiZn_9h	0.65	28.4	227	1.43	551	9
H30_SiZn_120h	0.65	90.7	725	4.56	544	120
H30_Zn_96h	0.65	11.4	91.1	0.57	51	96
NoH_SiZn_125h	0	0	/	/	572	125

(a) Initial Zn concentration TotZn = 520 μM.

(b) Ratio of the Zn uptake to the weight concentration of hectorite.

2.4. EXAFS data collection and reduction

Zn K-edge EXAFS spectra were recorded at the European synchrotron radiation facility (ESRF, France) on the BM32 CRG/IF station. The optics of the spectrometer consists of a Ni-coated focusing mirror, and a Si(111) double crystal monochromator. Clay films were mounted on a goniometer, and EXAFS spectra were recorded at α = 10°, 35°, 55°, and 80°. The most concentrated sample (H30_SiZn_120) was recorded in transmission mode by using photodiode detectors. The three other samples (H30_SiZn_9h, H30_Zn_96h, and NoH_SiZn_125h) were recorded in fluorescence detection mode, by using a 30 element array Ge detector. The EXAFS spectrum of NoH_SiZn_125h was recorded immediately after its transfer to the Teflon cell.

EXAFS data were reduced with the SEDEM software (Aberdam, 1998). As a preliminary step, absorption spectra were given the shape of the Stobbe function, which is a quantum-mechanically derived formula for atomic absorption. Fourier transformations were performed on $k^3\chi(k)$ functions between k = 2.5 $Å^{-1}$ and k = 12 $Å^{-1}$ using a Kaiser apodization window (Manceau and Combes, 1988). Fourier transforms (FTs) display amplitude maxima (peaks) located at apparent absorber-backscatterer distances (R + ΔR), which differ from interatomic structural distances (R) by ΔR ~ -0.3-0.4 Å (Teo, 1986). FTs structural peaks of interest were selected in the distance space and Fourier-back-transformed in k space by using a software package implemented by D. Bonnin (ESPCI, Paris). R values and number of atomic neighbors (N^{α}) were determined by least-squares fitting Fourier-filtered EXAFS contributions $\chi^{exp}(k)$ with theoretical phase and amplitude functions calculated with FEFF7.02 (Rehr et al., 1992), using talc and Zn-doped hectorite as model structures for Zn-O, Zn-Mg and Zn-Si pairs (Kadi-Hanifi and Mering, 1972; Oberlin and Mering, 1966; Rayner and Brown, 1973). The amplitude reduction factor S_0^2 was set to 0.85 (Manceau et al., 1998; O'Day et al., 1994b). The goodness of the fit was quantified by the reliability factor R_P, defined as

$$R_p = \frac{\sum_k \left(k^3 \cdot \chi^{calc}(k) - k^3 \cdot \chi^{exp}(k)\right)^2}{\sum_k \left(k^3 \cdot \chi^{exp}(k)\right)^2} \qquad (2)$$

where $\chi^{exp}(k)$ and $\chi^{calc}(k)$ are the experimental and simulated EXAFS contributions, respectively. The precision on EXAFS distances (R^{EXAFS}) was estimated to ± 0.02 Å for R^{EXAFS}_{Zn-O}, ± 0.03 Å for R^{EXAFS}_{Zn-Mg}, and ± 0.03 Å for R^{EXAFS}_{Zn-Si} (Schlegel et al., 2000), and the precision on N^{α} to ± 0.5 (Schlegel et al., 2000).

2.5. Quantitative texture analysis

Orientation distributions of c* axes normal to hectorite particles within the self-supporting films were determined by texture goniometry on a HUBER Cradle 500 diffractometer. The incident beam (Cu Kα) was monochromatized and collimated on the sample (1 x 1 mm slits), with a divergence of 7 x 7 mrad in the asymmetric reflection mode. Single portions of hectorite films were mounted on a two-circle goniometer. {004} pole figures of hectorite were obtained by tilting the film normal off the diffraction plane by $\Delta\rho = 5°$ increments over the [-80°, 80°] ρ-range, and recording the diffraction pattern for each ρ step over $\Delta 2\theta = 120°$ with a position sensitive curved detector (INEL CPS 120; counting time: 1800 seconds per step). Since self-supporting films of fine-grained layer minerals have an axisymmetrical fiber-like texture (i.e., with random in-plane distribution of crystallite a and b axes) the distribution density of c* off the film normal is simply retrieved from the integrated intensity I(ρ) of the {004} reflection as a function of ρ after background subtraction (Manceau et al., 2000b). Details on the calculation of distribution densities from these net integrated intensities are given elsewhere (Manceau et al., 2000a).

3. RESULTS AND INTERPRETATION

3.1. Kinetics results

On the one hand, no Zn uptake was observed for NoH_SiZn, even after 125 h of reaction time (Fig. 2). Since this sample was prepared without hectorite, this result indicates that Zn-rich precipitates did not nucleate in solution, or that such nuclei were too small to be removed by centrifugation and filtration. On the other hand, Zn uptake was observed for H30_SiZn and H30_Zn, and actually corresponded to a true sorption process. Distinct kinetics of Zn uptake were observed for H30_SiZn and H30_Zn. When no Si was added (H30_Zn), 5.8% of TotZn (46.6 μmol g^{-1} hectorite) were sorbed during the first 3 h of reaction time; afterwards, Zn sorption slowed on, and only 14.6% of TotZn (116.9 μmol g^{-1} hectorite) were removed at t = 168 h. Initial Zn sorption was more rapid for H30_SiZn, as sorbed Zn amounted to 15.2% of TotZn (121.7 μmol g^{-1} hectorite) at t = 3 h. Furthermore, Zn sorption steadily went on, and as much as 90.7% of Zn were removed at t = 120 h. The influence of Zn uptake on the dissolution of hectorite and on the fluctuations of $[Si]_{aq,t}$ was also examined. In absence of hectorite (NoH_SiZn), $[Si]_{aq,t}$ and $[Mg]_{aq,t}$ kept constant (data not shown). In H30_Zn, $[Si]_{aq,t}$ and $[Mg]_{aq,t}$ steadily increased with time, indicating that hectorite kept on dissolving during Zn uptake (Fig. 3a). The ratio of Mg to Si release (= (43 ± 7)/(40 ± 7) = 0.93 ± 0.23) slightly differs from the Mg:Si ratio in hectorite (=2.65/3.95 = 0.67), suggesting an uncongruent dissolution. This uncongruence can result either from an excess of Mg release, or from back uptake of dissolved Si. A slow increase of $[Mg]_{aq,t}$ was also observed for H30_SiZn, indicating that the suspension is undersaturated with respect to hectorite, even at "high" $[Si]_{aq,t}$ (Fig. 3b). In contrast, $[Si]_{aq,t}$ values at the beginning and at the end of the H30_SiZn experiment were comparable, although large volumes of silica-base were added during the whole reaction time to keep the pH at 7.3 (Fig. 3c). To clarify this point, let us assume that all Si added with the silica-base had accumulated in the supernatant. Theoretical $[Si]_{aq,t}$ as a function of time can be calculated from the increments of added silica-base, taking measured $[Si]_{aq,t}$ at t = 0 as a starting value. Contrasting these theoretical $[Si]_{aq,t}$ to experimental concentrations of dissolved Si Si shows that Si uptake occurs *during* Zn uptake. Further contrasting the calculated Si uptake to the experimental Zn uptake for t ≥ 3 h yields a fair linear correlation (Fig. 3d), with a regression slope of 1.09 (±0.08), suggesting that the same molecular mechanism is responsible for uptake of both Zn and Si. The nature of this mechanism will be determined by P-EXAFS spectroscopy.

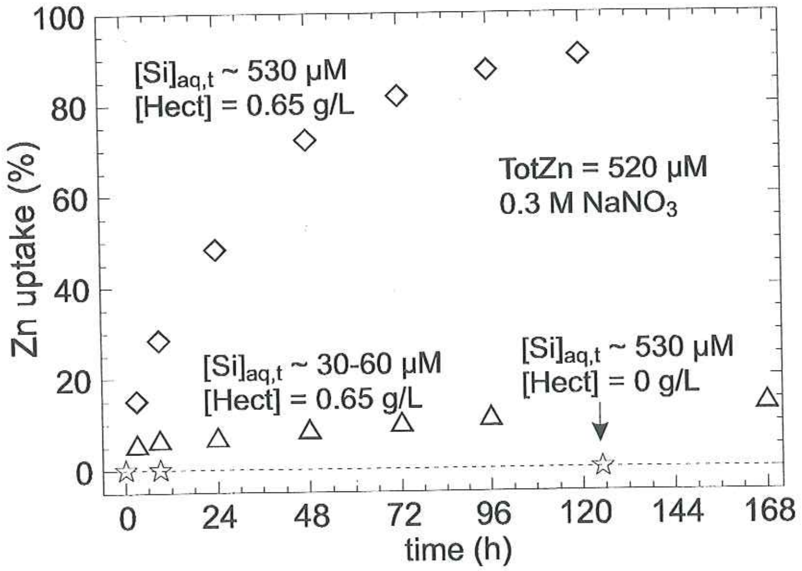

Fig. 2. Zn uptake as a function of the initial $[Si]_{aq,t}$ concentration. TotZn = 520 μM and pH 7.3 for all experiments. (◇): Solid concentration of hectorite [hectorite] = 0.65 g L^{-1}, $[Si]_{aq,t} \approx 530$ μM, titration by 0.01 M Na_2SiO_3, 0.28 M $NaNO_3$ (H30_SiZn). (△): [hectorite] = 0.65 g L^{-1}, $[Si]_{aq,t} \approx$ 30-60 μM, titration by 0.02 M NaOH, 0.28 M $NaNO_3$ (H30_Zn); (☆): [hectorite] = 0 g L^{-1}, $[Si]_{aq,t} \approx 530$ μM, titration by 0.01 M Na_2SiO_3 0.28 M $NaNO_3$ (NoH_SiZn).

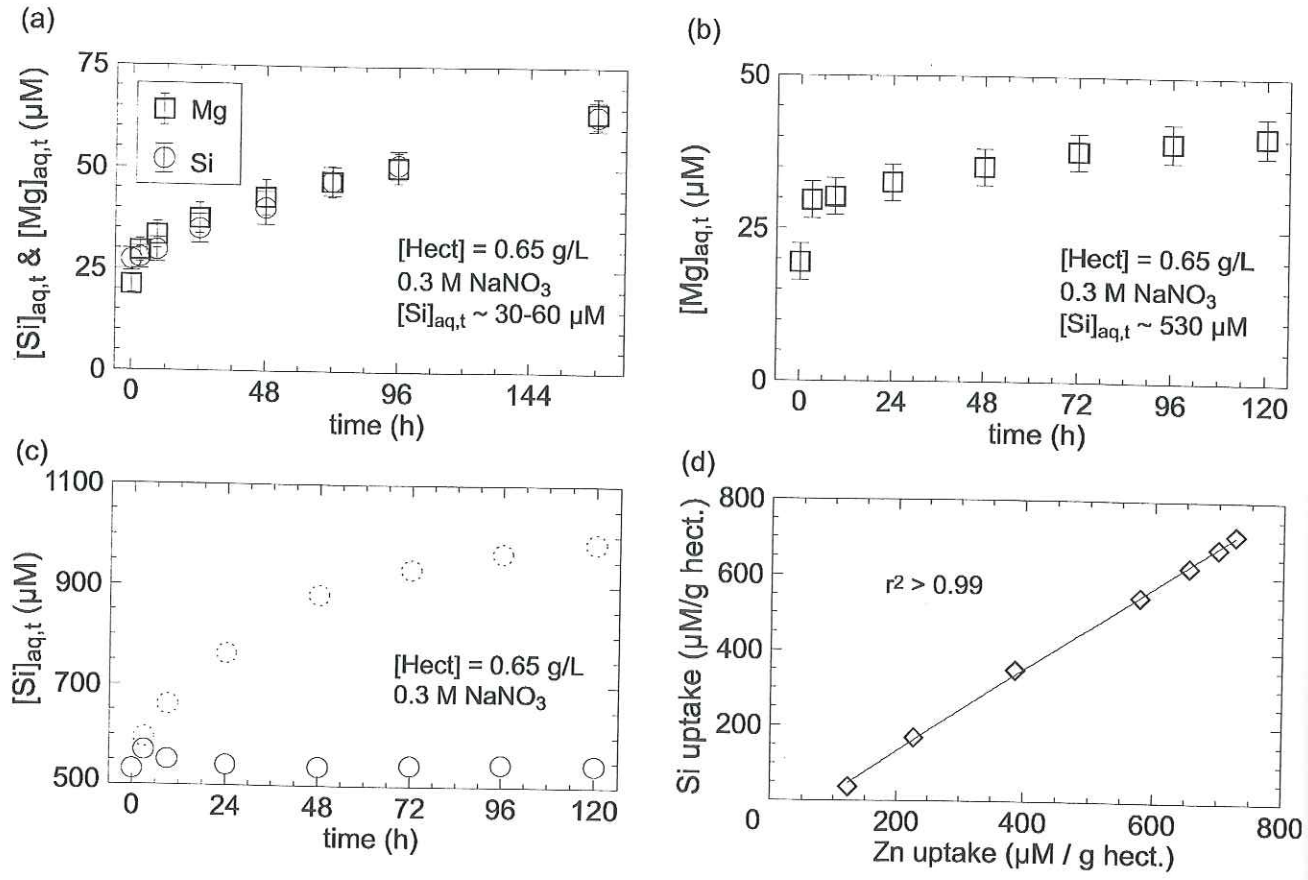

Fig. 3. Impact of Zn uptake on Mg and Si concentrations in the suspension. (a) $[Mg]_{aq,t}$ (□) and $[Si]_{aq,t}$ (○) released by hectorite dissolution for $[Si]_{aq,t} \approx 30\text{-}60$ µM (H30_Zn). (b) $[Mg]_{aq,t}$ (□) released by hectorite dissolution at $[Si]_{aq,t} \approx 530$ µM (H30_SiZn). (c) $[Si]_{aq,t}$ (H30_SiZn): (○) observed concentration; (◌) calculated concentration assuming that all Si added remain in the supernatant. (d) Plot of Zn uptake versus Si uptake for H30_SiZn; regression slope of 1.09 ± 0.03.

3.2. Quantitative texture analysis

The distribution density of crystallite c* axes off the film normal is visualized in Fig. 4 by the radial distribution density of {004} poles. In an isotropic powder, crystallites are distributed over all possible orientations, and consequently I(ρ) is constant after correction of the X-ray defocusing. Here, narrow distributions with maxima near ρ = 0° are observed, which indicates that most platelets have their c* axes normal to the film plane (i.e., ab planes parallel to the film plane). H30_Zn_9h is highly textured, with a measured maximum of distribution density (P_{max}) equal to 14 m.r.d., and a full width at half-maximum (FWHM) of the distribution equal to 33.3°. c* axes have larger angular spread in H30_SiZn_9h (P_{max} = 8.7 m.r.d., FWHM = 46.4°) and H30_SiZn_120h (P_{max} = 7.5 m.r.d., FWHM = 48.4°). The decrease in texturation parallels the increase in Zn content, and offers direct evidence for the modification of the surface properties of clay particles in the film, as a result of the sorption mechanism of Zn. It will be shown below that this higher disorientation diminishes, but not suppresses, the angular dependence of P-EXAFS spectra.

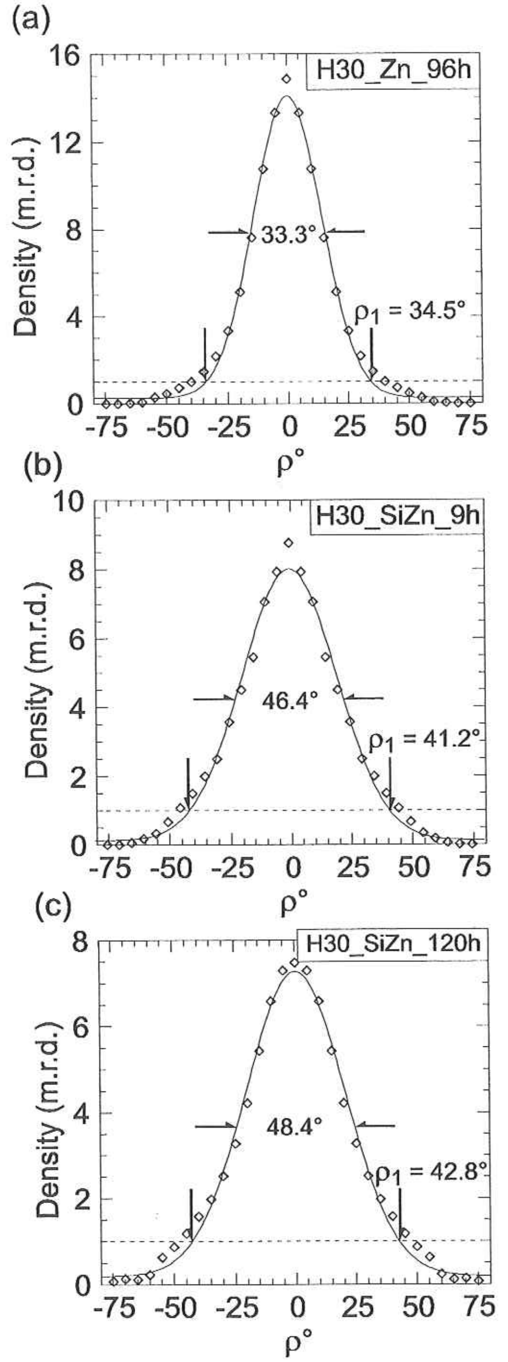

Fig. 4. Integrated radial distribution densities of c* axes from hectorite crystallites with respect to the normal of the self-supporting film (ρ = 0°). The distribution maxima are given for the center of the pole figure (ρ = 0°). The 1 m.r.d. (perfectly random powder) is indicated by a dashed line. Linear density scales and equal area projections are used for the pole figures. (a): H30_Zn_96h. (b) H30_SiZn_9h. (c) H30_SiZn_120h. Note the decrease in texture quality from H30_Zn_96h to H30_SiZn_120h, presumably reflecting changes in textural properties of the clay platelets.

3.3. EXAFS spectroscopy

3.3.1. EXAFS spectra

k^3-weighted P-EXAFS spectra for sorption samples are displayed in Fig. 5. The presence of multiple frequencies having a high amplitude at high k (e.g. k = 8 $Å^{-1}$) indicates the existence of several structurally ordered atomic shells around Zn. The strong polarization dependence of the amplitude and position of EXAFS oscillations, e.g., near 5.0 and 5.8 $Å^{-1}$, indicates that Zn atoms are epitaxially or topotactically associated to hectorite platelets. However, the three EXAFS spectra have distinct spectral features (e.g. at k = 5 $Å^{-1}$), angular dependencies (e.g. arrows in Fig. 5), and even amplitudes. These dissimilarities point to a diversity of Zn crystallochemical environments. Spectral modifications between samples are also shown in Fig. 6, which compares EXAFS spectra for sorption samples at $\alpha = 35°$ (at this angle, P-EXAFS spectra and powder EXAFS spectra are similar; (Manceau et al., 1990)) to structural references. These references include a Zn-rich kerolite $Zn_3Si_4O_{10}(OH)_2$ (ZnKer300), and a mixed (Zn, Mg)-rich kerolite. $Zn_{1.35}Mg_{1.65}Si_4O_{10}(OH)_2$ (ZnKer135). Both compounds have an hectorite-like structure in which Zn is located in the octahedral sheet and surrounded by 4 Si neighbors of the tetrahedral sheets at R ≈ 3.25 Å, and either 6 Zn (ZnKer300) or 2.7 Zn + 3.3 Mg (ZnKer135) neighbors of the octahedral sheet at R ≈ 3.10 Å (Decarreau, 1985; Schlegel et al., 2000). ZnKer135 and H30_Zn_96h have a similar shape, indicating that Zn in the clay film is located in a phyllosilicate environment, with both Mg and Zn octahedral neighbors, as in Ker135 (Fig. 6). Likewise, the spectral resemblance between ZnKer300 and H30_SiZn_120h is noteworthy, and suggests that the crystallochemical environments of Zn in the two solids are alike.

The EXAFS spectrum for NoH_SiZn_125h is quite different from those of the films and displays a single wave frequency, as the solvated $Zn^{2+}_{(aq)}$ reference. This result shows that the homogenous nucleation of Zn solid phases in the bulk solution is a marginal process, and it proves that Zn directly reacted with hectorite surfaces in sorption samples.

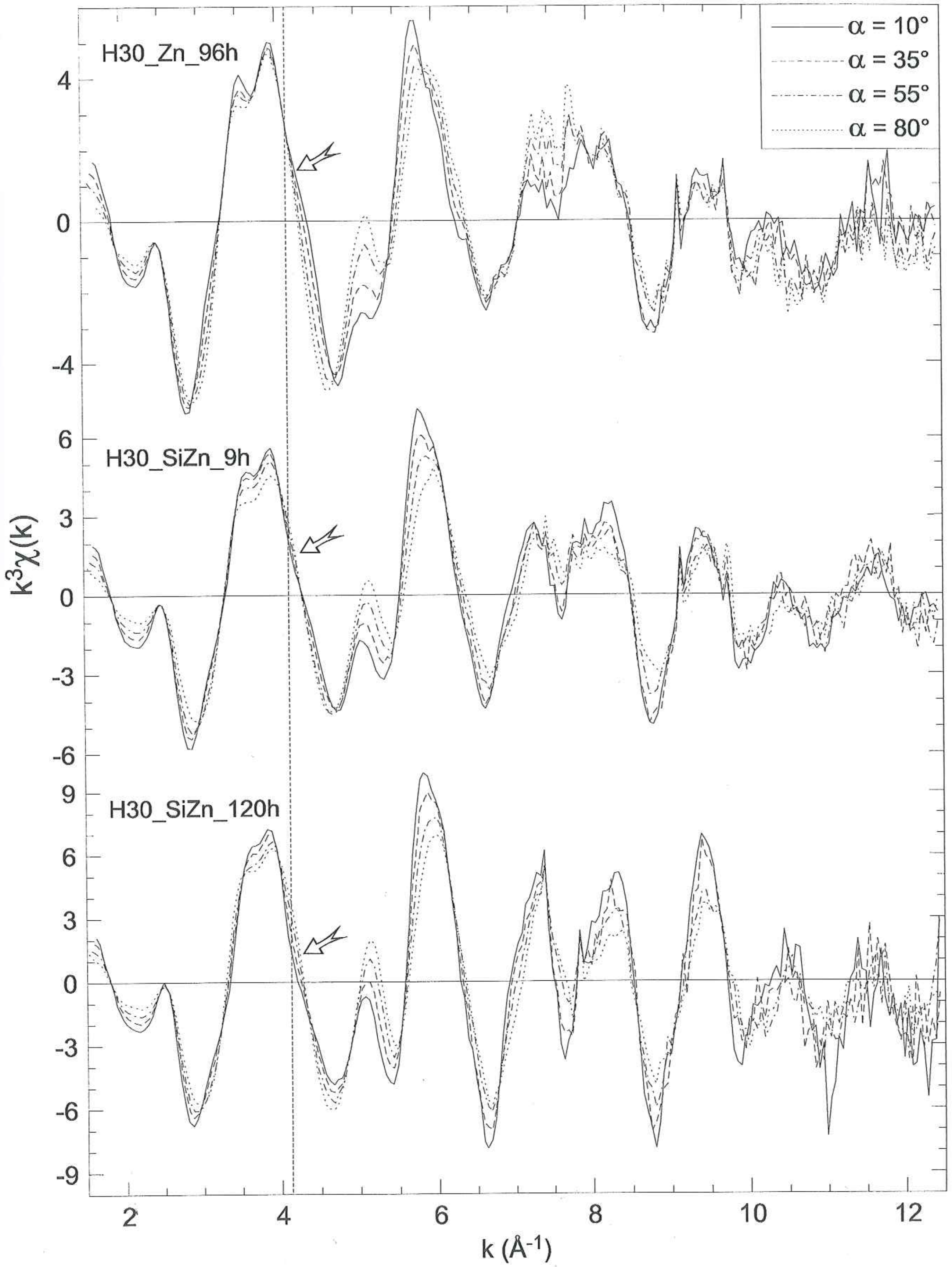

Fig. 5. k^3-weighted Zn K-edge P-EXAFS spectra for Zn in hectorite films at α angles of 10°, 35°, 55°, and 80°. Chemical conditions for samples are listed in Table 1.

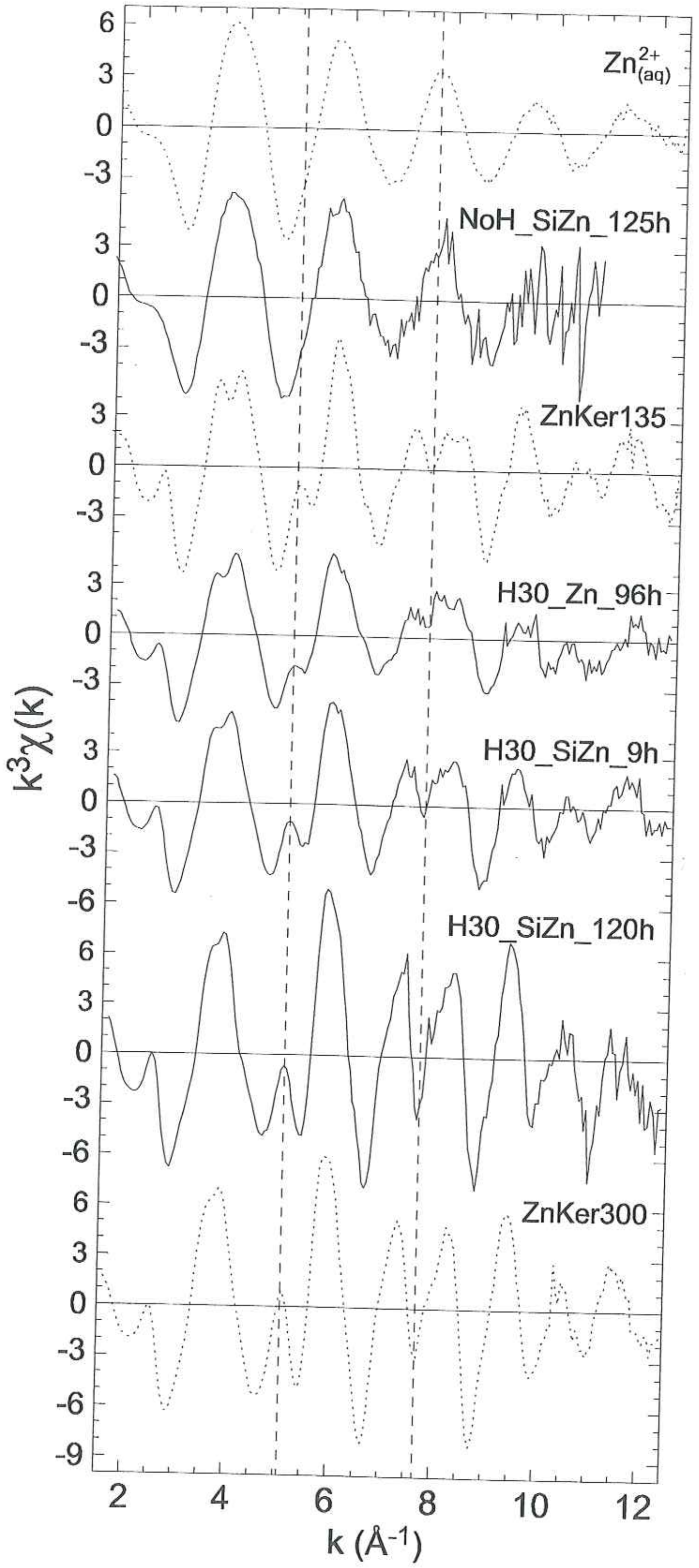

Fig. 6. k^3-weighted EXAFS spectra for Ma EXAFS spectra for aqueous Zn ($Zn^{2+}_{(aq)}$), Zn-rich kerolite (ZnKer135, ZnKer300) references, and for Zn in hectorite films. All spectra recorded at the magic angle (α = 35°).

Fig. 7. Moduli of the Fourier transforms (|FTs|) for Zn in hectorite films at α angles of 10°, 35°, 55°, and 80°. Chemical conditions for samples are listed in Table 1.

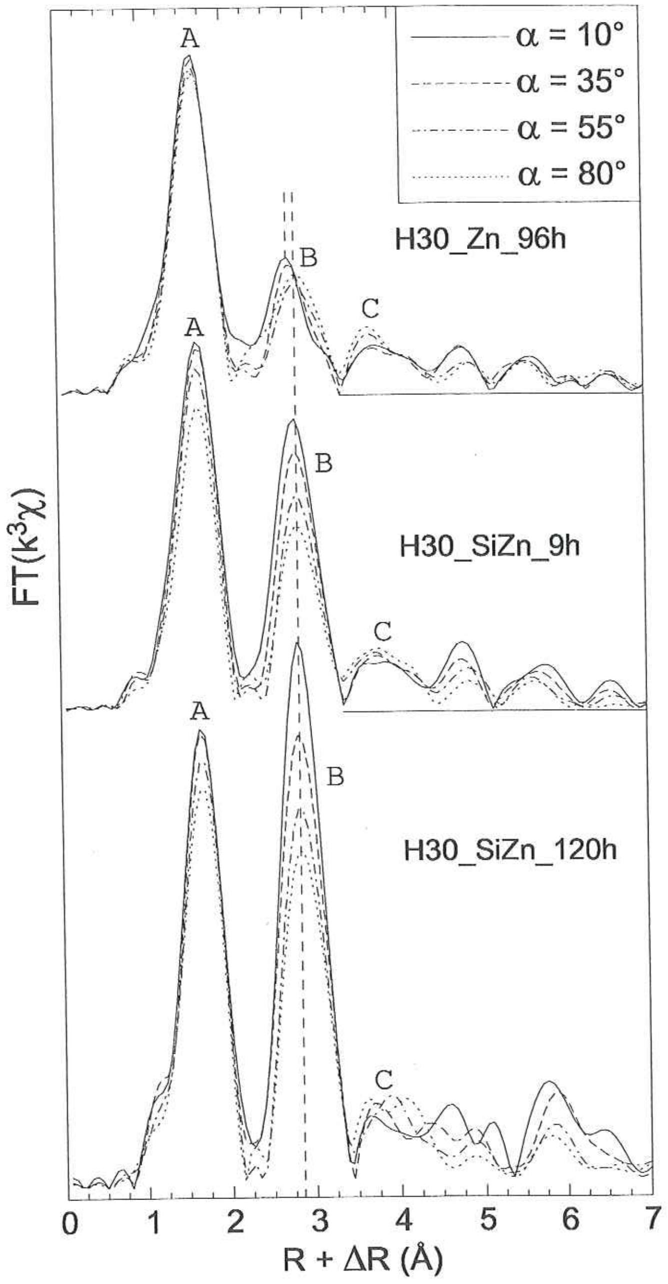

3.3.2. *Fourier Transforms (FTs)*

FTs for sorption samples (Fig. 7) display several high amplitude maxima at R + ΔR = 1.7 Å (peak A), 2.7-2.8 Å (peak B), and 3.8 Å (peak C). Insight on the nature of atomic shells contributing to these peaks can be obtained by comparing moduli (|FT|s) and imaginary parts in sorption samples and kerolite references (Fig. 8a, b). The imaginary part of both H30_SiZn_120h and ZnKer300 coincide over the entire R-range, and only local differences of |FT|s can be observed, confirming that Zn in H30_SiZn_120h is located in the octahedral sheet of a phyllosilicate structure, as in ZnKer300 (Fig. 8a). Imaginary parts of H30_Zn_96h and ZnKer135 also coincide in position over the entire R-range, and FT peaks have identical shape, differing only by absolute amplitudes (Fig. 8b). Again, this similarity provides strong evidence for the location of sorbed Zn in clay-like environment, with both Zn, Si, and presumably Mg cationic neighbors. These observed similarities greatly simplify the identification of predominant contributions, because the structural origins of the different FT peaks for a phyllosilicate were previously identified by Manceau and coworkers (Manceau et al., 1998; Manceau et al., 1999a; Manceau et al., 1999b).

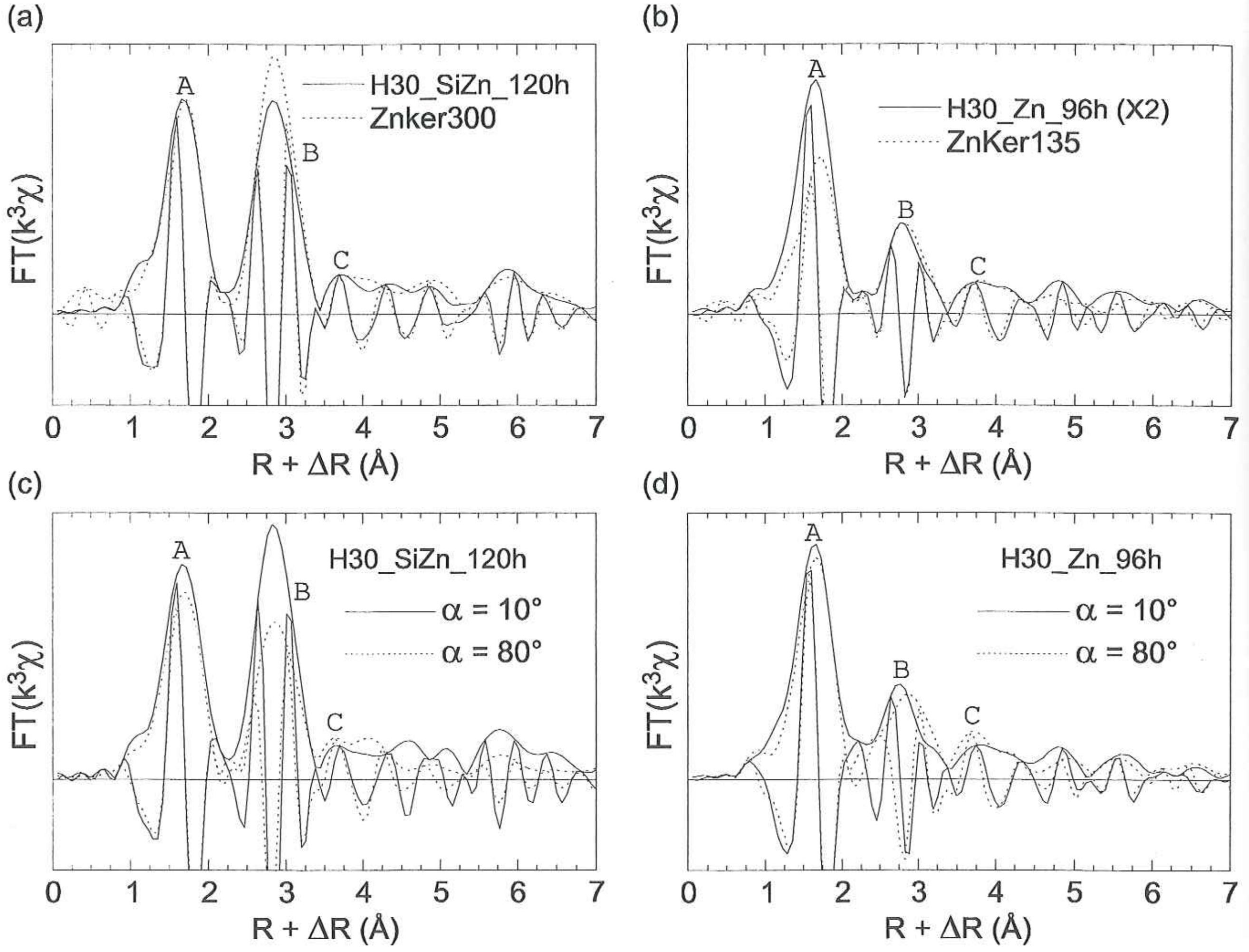

Fig. 8. Comparison of k^3-weighted FTs (moduli and imaginary parts) for (a) ZnKer300 and H30_SiZn_120h at α = 35°, (b) ZnKer135 and H30_Zn_96h at α = 35°, (c) H30_SiZn_120h at α = 10° and 80°, and (d) H30_Zn_96h at α = 10° and 80°.

Peak A.- Peak A originates from the contribution of oxygen atoms ligated to Zn (Manceau et al., 2000b). R^{EXAFS}_{Zn-O} obtained by least-square fitting the Fourier-filtered χ^{α}_{O} contributions increase from 2.04 Å for H30_Zn_96h (σ = 0.10 Å) to 2.05 Å for H30_SiZn_9h (σ = 0.10 Å) and 2.06 Å for H30_SiZn_120h (σ = 0.09 Å), with good figures of merit ($R_p \leq 0.010$; table 2). Distance values are typical of six-fold coordinated Zn, as four-fold coordination would result in R^{EXAFS}_{Zn-O} shorter than 2 Å (Kuzmin et al., 1997). The increase of R^{EXAFS}_{Zn-O} and decrease of σ correlate with an increase of N^{α}_{O} at given α (table 2), which can be traced to a decrease in structural disorder within Zn coordination octahedra, i.e., a more narrow dispersion of Zn-O bond lengths. The relatively high incoherency of Zn-O bond lengths for H30_Zn_96h probably results from Zn ligation to oxygen of distinct chemical entities with distinct binding strengths, such as H_2O molecules, OH groups, and possibly the sorbent surface (Schlegel et al., 1999). Alternatively, the lower structural disorder observed for Zn in H30_SiZn_9h and H30_SiZn_96h suggests that most oxygen ligands are structurally equivalent.

Table 2. Quantitative EXAFS analysis of the FT Zn-O coordination shell.

P-EXAFS samples	α	IFT range[a] (Å)	Zn-O shell R (Å)	Zn-O shell N^{α}_{O}	Zn-O shell σ (Å)	ΔE0[b] (eV)	RP
H30_Zn_96h	10°	1.1-2.2	2.04[c]	4.5	0.10[c]	-1.5[c]	0.010
	35-	1.0-2.2	2.04	4.4	0.10	-1.4	0.006
	55°	1.0-2.2	2.04[c]	4.3	0.10[c]	-1.4[c]	0.007
	80°	1.1-2.2	2.04[c]	4.4	0.10	-1.4[c]	0.002
H30_SiZn_9h	10°	1.1-2.2	2.05[c]	5.1	0.10[c]	-1.5[c]	0.002
	35°	1.1-2.2	2.05	5.0	0.10	-1.5	0.002
	55°	1.1-2.2	2.05[c]	4.8	0.10[c]	-1.5[c]	0.001
	80°	1.1-2.1	2.05[c]	4.2	0.10[c]	-1.5[c]	0.004
H_SIZn_120h	10°	1.2-2.2	2.06[c]	6.1	0.09[c]	-1.4[c]	0.007
	35°	1.2-2.2	2.06	6.0	0.09	-1.4	0.010
	55°	1.2-2.2	2.06[c]	5.9	0.09[c]	-1.4[c]	0.002
	80°	1.1-2.2	2.06[c]	5.5	0.09[c]	-1.4[c]	0.002

(a) R + ΔR interval for inverse Fourier transforms (IFTs) in the real space.
(b) The threshold energy E_0 was taken at the half-height of the absorption edge (Δμ/2).
(c) Value held fixed during the fitting procedure.
(d) Distance parameters coupled at the same value during the fit of $\chi^{35°}_{B}$.
(e) σ parameters coupled at the same value during the fit of $\chi^{35°}_{B}$.
(f) Parameters optimized at α = 10° and 80°, simultaneously.

A systematic decrease of N^{α}_{O} with increasing α can be noticed for every film sample. This angular dependence of the oxygen EXAFS contribution ($\chi^{\alpha}_{O}(k)$) can be related to the inclination β_O of this shell relatively to c*, and can be written at the K-edge, in the plane-wave approximation and for a threefold or higher symmetry axis (Bonnin et al., 1986; Manceau et al., 1998; Schlegel et al., 1999):

$$\chi^{\alpha}_{O} = \chi^{iso}_{O} \cdot \left[1 - \frac{(3\cos^2\beta_O - 1)(3\cos^2\alpha - 1)}{2}\right] \tag{3}$$

where χ^{iso}_{O} is the EXAFS in a isotropic powder sample. N^{α}_{O} can then be retrieved from

$$N^{\alpha}_{O} = N^{iso}_{O} \cdot \left[\frac{3}{2}.(1 - 3\cos^2\beta_O)\cos^2\alpha + 3\cos^2\beta_O\right] \tag{4}$$

where N_O^{iso} is the number of backscatterers detected in a powder sample. Eqn. 4 shows that and no angular variation of N_O^α is expected for $\beta_O = 54.7°$, the inclination angle in a symmetric octahedron. N_O^α decreases with increasing α when $\beta_O > 54.7°$. β_O can be further quantified experimentally by rewriting Eqn. 4 as:

$$\frac{N_j^\alpha}{N_j^{iso}} = \frac{3}{2}\cdot\left(1-3\cos^2\beta_j\right)\cos^2\alpha + 3\cos^2\beta_j \qquad (5)$$
$$= S\cdot\cos^2\alpha + O$$

where O and S are regression coefficients. How experimental β_0^{exp} are calculated from this affine function is detailed now. First, linear regression of N^α with respect to $\cos^2\alpha$ is performed, and S is obtained by normalizing the regression slope with $N^{35°}$ (Fig. 9; Table 4). β_0^{exp} is then obtained by

$$\beta_0^{exp} = \mathrm{Arc}\cos\sqrt{\frac{3-2S}{9}} = f(S) \qquad (6)$$

Eqn. (6) can be applied only if $-3 < S < 3/2$, which is the case for oxygen shells (Table 3). The uncertainty on β_0^{exp} ($\delta\beta_0^{exp}$) resulting from the uncertainty on S (δS) is obtained by (Taylor, 1997)

$$\delta\beta_0^{exp} = \left|\frac{\delta f(S)}{\delta S}\right|\delta S \qquad (7)$$

β_0^{exp} range between 55.1° and 56.5° (±0.4°). Note that β_0^{exp} may differ from the real crystallographic β_O, because the disorientation of crystallites planes within the film sample is expected to diminish the angular dependence of P-EXAFS contributions, and, thus decrease the absolute magnitude of S in Eqn. 6. Hence, β_O tends to be underestimated for $\beta_O > 54.7°$, and overestimated for $\beta_O < 54.7°$. Manceau et al. (Manceau et al., 1999a) evaluated the decrease of the apparent polarization dependence for a P-EXAFS contribution in the case of a step-shaped distribution of absorber-backscatterers pairs symmetrically around β. They showed that such dispersion has little impact on β^{exp} for $50 \leq \beta \leq 60°$. In conclusion, EXAFS-derived β_0^{exp} are consistent with slight flattening of coordination octahedra (Table 4). Such flattening is commonly observed in edge-sharing octahedral sheets (Güven, 1988).

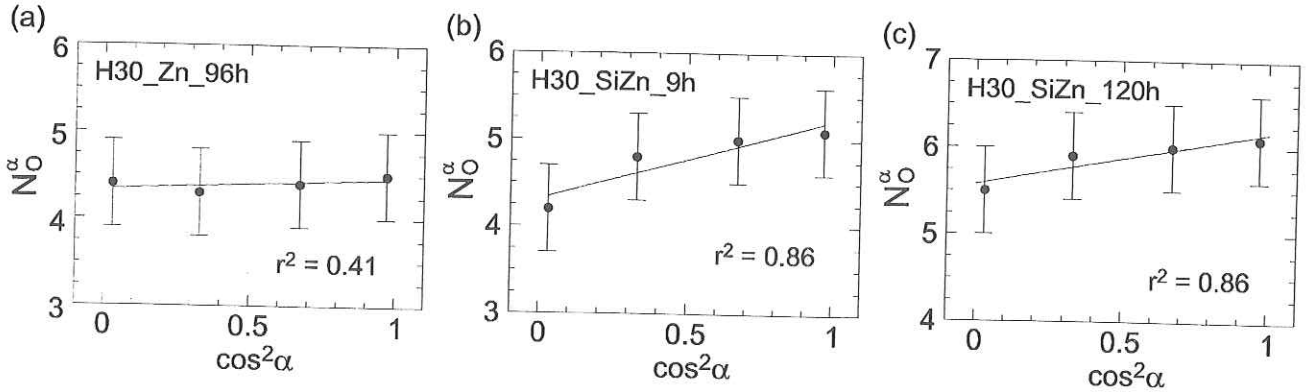

Fig. 9. Angular dependence of the number of nearest O atoms (N_O^α) for Zn in hectorite films. (a) H30_Zn_96h; (b) H30_SiZn_9h; (c) H30_SiZn_120h.

Peak B.- Peaks B originate from the predominant contributions of several cations in the octahedral and tetrahedral sheets. All peaks B display an angular dependence, which results from the angular variation of EXAFS contributions to peak B originating from in-plane and out-of-plane backscatterers. The overlap of EXAFS contributions predominating in the parallel (α = 0°; $\chi_B^{//}(k)$) and perpendicular (α = 90°; $\chi_B^{\perp}(k)$) orientations can be written at a given α:

$$\chi_B^\alpha(k) = \chi_B^\perp(k) + \left(\chi_B^{//}(k) - \chi_B^\perp(k)\right)\cos^2\alpha \qquad (8)$$

Hence, depending on the phase relation between $\chi_B^{//}(k)$ $\chi_B^\perp(k)$, only the amplitude of $\chi_B^\alpha(k)$, or both the amplitude and phase of $\chi_B^\alpha(k)$ may vary with α. For instance, the amplitude of peak B markedly decreases for H30_SiZn_120h (Fig. 7), but both peak maxima and imaginary parts coincide in position at α = 10° and at α = 80° (Fig. 8c), suggesting that similar (but not necessarily identical) backscattering waves predominate at both in-plane and out-of-plane orientations of ε. This situation is observed for phyllosilicates in which EXAFS waves backscattered by in plane (Co, Zn) cations from the octahedral sheets and out-of-plane Si are in phase over most of the k-range (Manceau et al., 1999b; O'Day et al., 1996). Amplitude and imaginary parts for peak B in H30_SiZn_9h display a similar angular behavior, also suggesting the presence of predominant Zn and Si backscatterers. In contrast, peak B in H30_Zn_96h displays a complex angular behavior; its amplitude decreases from α = 10° to α = 55°, and then increases as α converges to 80°, and its maximum shifts from R + ΔR = 2.75 Å to 2.9 Å, whereas the imaginary part is shifted to lower R + ΔR values (Fig. 8d). Schlegel & al (Schlegel et al., 1999) demonstrated that such an angular behavior of peak B can originate from the overlap of out-of-phase EXAFS waves from in-plane Mg and out-of-plane Si. Indeed, EXAFS contributions from Mg, Zn and Si cations can be expected, based on the FT similarity between H30_Zn_96h and ZnKer135. Accurate determination of cationic contributions to peak B is completed now by spectral quantitative analysis.

An optimal fit of the Fourier-filtered $\chi_B^{80°}(k)$, was obtained for H30_Zn_96h ($R_p = 0.019$) with a Si shell of 3.6 atoms at $R_{Zn-Si}^{EXAFS} = 3.28$ Å ($\sigma_{Si} = 0.10$ Å; Fig. 10). From previous results on Zn-sorbed-hectorite, contributions from this Si shell is expected at α as low as 10° (Schlegel et al., 1999). Attempts to fit $\chi_B^{10°}(k)$ assuming combination of either (Mg + Si) or (Zn +Si) backscatterers yield no acceptable results. $\chi_B^{10°}(k)$ is then fitted assuming Zn, Mg, and Si contributions, with R_{Zn-Si}^{EXAFS} and σ_{Si} fixed to values at α = 80°, $R_{Zn-Mg}^{EXAFS} = R_{Zn-Zn}^{EXAFS}$ and $\sigma_{Zn} = \sigma_{Mg}$, to decrease the degree of freedom of the spectral fit. A correct fit is obtained ($R_p = 0.025$) with $R_{Zn-Zn}^{EXAFS} = R_{Zn-Mg}^{EXAFS} = 3.10$ Å ($\sigma_{Zn} = \sigma_{Mg} = 0.10$ Å; Table 3 and Fig. 10). $\chi_B^\alpha(k)$ are then fitted at α = 35° and 55° by varying only N_{Zn}^α, N_{Mg}^α, and N_{Si}^α (Table 3).

Tentative fit of $\chi_B^{80°}(k)$ for H30_SiZn_120h by assuming only Si neighbors was not successful, indicating the presence of an additional backscattering shell besides Si. The shift in position of the $\chi_B^{80°}(k)$

maximum from ~5 Å^{-1} for H30_Zn_96h to ~7 Å^{-1} for H30_SiZn_120h suggests that this additional contribution originates from heavy backscatterers, such as Zn atoms (Fig. 10). Such Zn contributions were expected to dominate in-plane $\chi_{B}^{10^\circ}(k)$. therefore, $\chi_{B}^{10^\circ}(k)$ and $\chi_{B}^{80^\circ}(k)$ were simultaneously fitted assuming Zn and Si contributions, with R_{Zn-Zn}^{EXAFS}, R_{Zn-Si}^{EXAFS}, σ_{Zn} and σ_{Si} kept identical at α = 10° and 80°. Good fits were obtained ($R_p = 0.004$ at α = 10° and 0.008 at α = 80°) with $R_{Zn-Zn}^{EXAFS} = 3.10$ Å and $R_{Zn-Si}^{EXAFS} = 3.28$ Å ($\sigma_{Zn} = \sigma_{Si} = 0.10$ Å; Table 3). $\chi_{B}^{\alpha}(k)$ are then fitted at α = 35° and 55° by varying only N_{Zn}^{α}, and N_{Si}^{α} (Table 3). Adding an Mg contribution ($R_{Zn-Zn}^{EXAFS} = R_{Zn-Mg}^{EXAFS}$; $\sigma_{Zn} = \sigma_{Mg}$) improved the fit neither at α = 10° (R_p = 0.004 for $N_{Mg}^{10^\circ} = 1$) nor at α = 35° (R_p = 0.011 for $N_{Mg}^{35^\circ} = 0.5$), suggesting that Mg backscatterers, if present, are clearly not of paramount importance.

$\chi_{B}^{80^\circ}(k)$ and $\chi_{B}^{10^\circ}(k)$ for H30_SiZn_9h were also fitted simultaneously, assuming two shells of Si and Zn, with R_{Zn-Zn}^{EXAFS}, R_{Zn-Si}^{EXAFS}, σ_{Zn} and σ_{Si} kept identical at α = 10° and 80°. A correct fit was obtained at α = 80° (R_p = 0.023) with $R_{Zn-Si}^{EXAFS} = 3.26$ Å, $\sigma_{Si} = 0.10$ Å, $R_{Zn-Zn}^{EXAFS} = 3.10$ Å and $\sigma_{Zn} = 0.10$ Å, but not at α = 10°. Adding an third shell of Mg at α = 10° ($R_{Zn-Zn}^{EXAFS} = R_{Zn-Mg}^{EXAFS}$ and $\sigma_{Zn} = \sigma_{Mg}$) significantly improved the fit (R_p = 0.002) without modification of R_{Zn-Zn}^{EXAFS}, σ_{Zn}, R_{Zn-Si}^{EXAFS}, σ_{Si} (Table 3). A three-shell fit of $\chi_{B}^{\alpha}(k)$ at α = 35° and 55° was then performed, by varying only N_{Zn}^{α}, N_{Mg}^{α}, and N_{Si}^{α} (Table 3). R_{Zn-Zn}^{EXAFS} and R_{Zn-Si}^{EXAFS} values for every probed sample are close to interatomic distances previously reported for ZnKer300 ($R_{Zn-Zn}^{EXAFS} = 3.10$ Å and $R_{Zn-Si}^{EXAFS} = 3.30$ Å; (Schlegel et al., 2000).

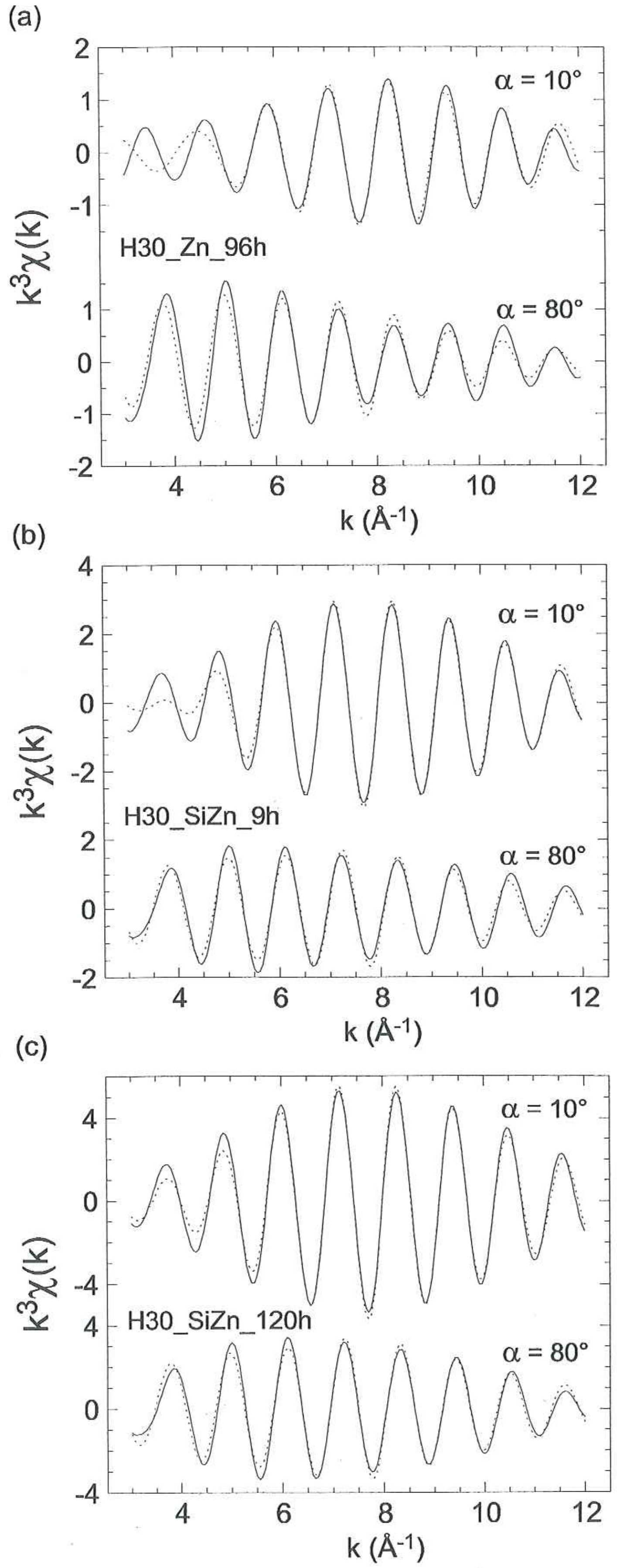

Fig. 10. Fourier-filtered EXAFS contributions of peak B at α = 80°. (a) H30_Zn_96h; (b) H30_SiZn_9h; (c) H30_SiZn_120h.

Table 3. Quantitative EXAFS analysis of the FT second peaks.

P-EXAFS samples	α	IFT range[a] (Å)	Zn-Zn shell			Zn-Mg shell			Zn-Si shell			ΔE0[b] (eV)	RP
			R (Å)	*N*	σ (Å)	*R* (Å)	*N*	σ (Å)	*R* (Å)	*N*	σ (Å)		
H30_Zn_96h	10°	2.3-3.4	3.08[d]	1.9	0.10[e]	3.08[d]	1.9	0.10[e]	3.28[c]	0.4	0.10[c]	-1.5[c]	0.025
	35°	2.4-3.4	3.08[c]	1.7	0.10[c]	3.08[c]	1.4	0.10[c]	3.28[c]	0.6	0.10[c]	-1.4[c]	0.033
	55°	2.3-3.4	3.08[c]	0.5	0.10[c]	3.08[c]	0.8	0.10[c]	3.28[c]	2.8	0.10[c]	-1.4[c]	0.015
	80°	2.2-3.4						0.10	3.28	3.6	0.10	-1.4[c]	0.019
H30_SiZn_9h	10°	2.1-3.5	3.10[d]	4.7	0.10[e]	3.10[d]	1.1	0.10[e]	3.26[c]	0.5	0.10[c]	-1.5[c]	0.002
	35°	2.3-3.4	3.10[c]	3.8	0.10[c]	3.10[c]	0.8	0.10[c]	3.26[c]	1.5	0.10[c]	-1.5[c]	0.005
	55°	2.4-3.4	3.10[c]	2.6	0.10[c]	3.10[c]	0.4	0.10[c]	3.26[c]	2.4	0.10[c]	-1.5[c]	0.016
	80°	2.3-3.4	3.10	1.4	0.10				3.26	3.8	0.10	-1.5[c]	0.023
H_SIZn_120h	10°	2.3-3.4	3.10[f]	8	0.10[f]				3.26[f]	2.2	0.10[f]	-1.4[c]	0.004
	35°	2.3-3.4	3.10[c]	6.0	0.10[c]				3.26[c]	3.6	0.10[c]	-1.4[c]	0.011
	55°	2.3-3.4	3.10[c]	4.2	0.10[c]				3.26[c]	4.8	0.10[c]	-1.4[c]	0.006
	80°	2.3-3.4	3.10[f]	2.7	0.10[f]				3.26[f]	6.4	0.10[f]	-1.4[c]	0.008

(a) R + ΔR interval for inverse Fourier transforms (IFTs) in the real space.
(b) The threshold energy E_0 was taken at the half-height of the absorption edge (Δμ/2).
(c) Value held fixed during the fitting procedure.
(d) Distance parameters coupled at the same value during the fit of $\chi_B^{35°}$.
(e) σ parameters coupled at the same value during the fit of $\chi_B^{35°}$.
(f) Parameters optimized at α = 10° and 80°, simultaneously.

Systematic variations of the number of Zn, Mg, and Si neighboring atoms (N^α) were observed with increasing α for every film sample, and can be related to the inclination angle β of the backscattering shells (Table 3). For example, N^α_{Zn} and N^α_{Mg} decrease and N^α_{Si} increase with increasing α suggests that both β_{Zn} and β_{Mg} are higher than 54.7°, whereas β_{Si} < 54.7°. β^{exp} and $\delta\beta^{exp}$ were further calculated by applying equations identical to Eqn (3-7) to all identified shells (Table 4). As for the oxygen shell, the dispersion of crystallite planes off the film plane presumably results in β^{exp} different from crystallographic β, e.g. $\beta^{exp}_{Zn} < \beta_{Zn}$. Nevertheless, β^{exp}_{Zn}, β^{exp}_{Mg} and β^{exp}_{Si}, when obtained, are consistent with Zn-Mg and Zn-Zn pairs oriented parallel or slightly inclined with respect to the film plane, and with Zn-Si pairs inclined by ~50-70° off this plane (Table 4).

Table 4. Reduced sloped of linear regressions and calculated inclination of backscattering shells.

P-EXAFS samples	Zn-O shell				Zn-Zn shell			
	S[a]	δS[b]	β_O[c]	$\delta\beta_O$[d]	S[a]	δS[b]	β_{Zn}[c]	$\delta\beta_{Zn}$[d]
H30_Zn_96h	0.03	0.02	55.1	0.5	1.29	0.31	77.6	12
H30_SiZn_9h	0.13	0.02	56.5	0.5	0.92	0.04	69.0	1.0
H_SIZn_120h	0.10	0.03	56.1	0.5	0.93	0.06	69.2	1.1

P-EXAFS samples	Zn-Mg shell				Zn-Si shell			
	S[a]	δS[b]	β_{Zn}[c]	$\delta\beta_{Zn}$[d]	S[a]	δS[b]	β_{Zn}[c]	$\delta\beta_{Zn}$[d]
H30_Zn_96h	1.42	0.14	82.4	8.8	-4.6	0.7		
H30_SiZn_9h	1.46	0.08	84.8	7.0	-2.27	0.26	23.7	6.0
H_SIZn_120h					-1.12	0.11	40.1	1.9

(a) Slope of the regression line normalized by $N^{35°}$.
(b) Mean square deviation of the regression line.
(c) Uncertainty on the normalized slope, calculated at the 68 % (1σ) confidence level.
(d) Uncertainty on β, calculated at the 68% (1σ) confidence level.

Peak C.- Peak C in (Zn, Mg)-rich kerolite originates from the predominant contributions of next-nearest Si cations (Tet2) at ~ 4.4-4.5 Å, and from higher oxygen shells (Manceau et al., 2000b; Manceau et al., 1999a). This EXAFS contribution has a large amplitude in layered silicates, where Si tetrahedra are polymerized in a two-dimensional framework bridged to the octahedral sheet (Manceau et al., 1999b). This peak is present in all FTs, and in addition, FT imaginary parts for Zn samples coincide in position with that of clay references, indicating the presence of such Si tetrahedral networks in the sorption samples. Furthermore, comparable amplitudes of peak C in H30_SiZn_120h and in ZnKer300, suggest that nearly complete Si tetrahedral sheets formed in the sorption sample. In contrast, the lower amplitude of peak C in H30_Zn_96h relatively to ZnKer135 may result either from a higher structural disorder, or from a lower number of next-nearest Si in the sorption sample.

4. DISCUSSION

4.1. Structural environment of sorbed Zn

The occurrence of sorbed in a phyllosilicate environment et pH 7.3 is supported by the strong similarity of EXAFS spectra for sorption samples and phyllosilicate references, and by the identification of in-plane (Zn, Mg) and out-of-plane Si at distances and orientations typical of phyllosilicates structure

(Manceau et al., 1998). In such environments, Zn octahedra share corner (C) with neighboring Si tetrahedra, and edges (E) with neighboring (Zn, Mg) octahedra. In addition, the detection of more than 1 in-plane Zn backscatterers points to the formation of Zn octahedral sheets parallel to hectorite platelets. Location of these sheets in structural continuity to hectorite platelets is supported by two lines of evidence. First, no evidence for compelling polymerization of Zn in solution could be obtained in absence of hectorite surface, even after 125 h of reaction time. In contrast, Zn polymers were observed, when the sorbate was *physically* in contact with the sorbent surface. Second, neighboring Mg cations may correspond either to Mg exposed at the edge surfaces of hectorite platelets, or to solute cations incorporated upon growth of Zn sheets. In the latter case, the proportion of Mg in the sheet, and thus the structural $N_{Mg}^{35°}/N_{Zn}^{35°}$, is expected to increase with increasing Mg/Zn ratio in solutions, especially for H30_SiZn. However, a decrease of $N_{Mg}^{35°}/N_{Zn}^{35°}$ from t = 9 h to t = 120h is observed for this sample, although the $[Zn]_{aq,t}/[Mg]_{aq,t}$ ratio keeps increasing with reaction time. Therefore, incorporation of Mg in Zn octahedral sheet can be dismissed, leading to the conclusion that Zn octahedral sheets are located in structural continuity of (Mg, Li) octahedral sheets of the hectorite platelets.

The occurrence of peaks C indicate that neighbor Si atoms detected by EXAFS polymerized to form tetrahedral sheets (T) bridged to Zn octahedral sheets (O). N_E values significantly lower than 6 indicate that Zn sheets are of limited size, as is the case for H30_SiZn_9h and H30_Zn_96h. The average number of E linkages in such sheets, N_{Zn}, is a function of the number of Zn atoms, Q_{Zn} (Fig. 11; (Manceau and Calas, 1986)). Several Zn polymers of distinct size, and distinct N_{Zn}, are likely to coexist at the clay surface, and the information retrieved from EXAFS is a weighed average Zn atoms located in these surface complexes, hence only the average size of Zn sheets can be obtained from N_E. For example, $N_E = N_{Zn}^{35°} = 1.7$ for H30_Zn_96h (Table 3) can be obtained by assuming either 30% of Zn included in dimers ($N_{Zn} = 1$) and 70% in Zn trimers ($N_{Zn} = 2$; Fig. 12), or 28% of Zn included in large octahedral sheets ($N_{Zn} = 6$), and 78 % of Zn monomers ($N_{Zn} = 0$). Likewise, $N_{Zn}^{35°} = 3.8$ can be obtained assuming only polymers with an average $Q_{Zn} \approx$ 7-18, or 33 % of monomers and 67 % Zn in large sheets. Hence, the occurrence of small-sized surface complexes cannot be ruled out for both H30_Zn_96h and H30_SiZn_9h. In contrast, $N_{Zn} = 6 \pm 0.5$ for H30_SiZn_120h, indicates that almost all Zn are included in large-sized Zn octahedral sheets with $Q_{Zn} \geq$ 200, hence, with diameters equal or higher than 30 Å.

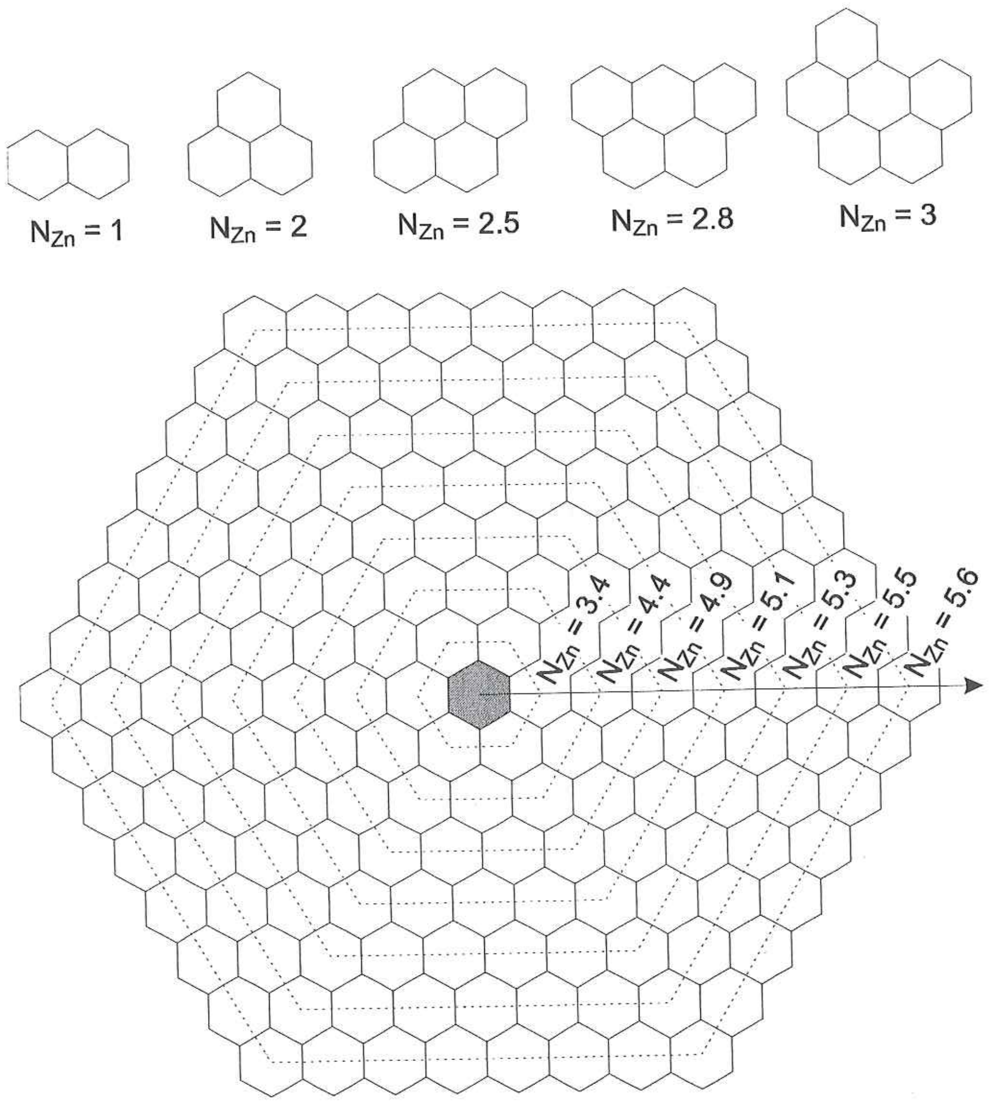

Fig. 11. Average number of neighbor atoms (N_{Zn}) in Zn octahedral sheets as a function of the number of Zn cations contained in this sheet (Q_{Zn}).

4.2. Mechanism of Zn sorption

4.2.1. Zn sorption at low concentration of dissolved Si

After 3 hours of contact time, the amount of sorbed Zn at low $[Si]_{aq,t}$ reaches 46 µmol g^{-1}, and this initial sorption coincide with a rapid release of Mg in the suspension. This rapid adsorption and the concomitant release of Mg compare with sorption data at pH 6.5, where sorbed Zn were shown to form mononuclear surface complexes at the layer edges of hectorite (Schlegel et al., 2000). At t = 9 h, the amount of sorbed Zn reaches 91 µmol g^{-1} hectorite, and Zn polymers of small mean size (Q_{Zn} = 2-3) are detected, which are presumably confined to immediate vicinity of hectorite edges, thus bridging edge exposed Mg octahedral and Si tetrahedra (Fig. 12a). As exposed above, the occurrence of Zn monomers in conjunction with large Zn domains cannot be dismissed. However, such large domains, if present, would amount to less than 20% of sorbed Zn. Hence, Zn can be inferred to remain in predominantly oligomeric form. Incorporation of dissolved Si in Zn polymers to neoform ZnKer nuclei might account for the slight uncongruency observed for hectorite dissolution. However, part of this uncongruency likely originates from an excess release of Mg upon adsorption of Zn (Schlegel et al., 2000). In conclusion, Zn uptake at low $[\mathrm{Si}]_{aq,t}$ likely results in the formation of small oligomers, located at the layer edges of hectorite, in structural continuity of the octahedral sheet.

4.2.2. *Zn sorption at high concentration of dissolved Si*

After only 9 h of reaction time at $[\mathrm{Si}]_{aq,t} \approx 530$ µM, both the amount of sorbed Zn (227 µmol g^{-1}) and the mean size of Zn polymers ($Q_{Zn} \approx$ 10-20) are significantly higher than at t = 96 h for H30_Zn. Thus larger polymers (or higher amounts of large polymers) form in comparatively shorter time. Also, $N_{\mathrm{Mg}}^{35^\circ}$ decreases to 0.8, indicating lower proportions of E linkages between Zn atoms and hectorite octahedral sheets. In contrast, $N_{\mathrm{Si}}^{35^\circ}$ increases from H30_Si_96h to H30_SiZn_9h (Table 3). This higher $N_{\mathrm{Si}}^{35^\circ}$ may be accounted for by assuming that a minimum of 25% of Zn octahedra (57 µmol g^{-1}) are located in contact to the hectorite edges, and share 4 C with Si tetrahedra of hectorite (0.25*4 = 1 ≈ 1.5 ± 0.5), while the remainder form large hydroxide platelets devoid of Si. However, previous results show that for surface coverage of ~ 50 µmol g^{-1} hectorite at pH 6.5, experimental $N_{\mathrm{Si}}^{35^\circ} = 2.4$, i.e., well below the expected value. In addition, if all Si contributions originate from tetrahedra at the layer edges of hectorite, then an increase of both $N_{\mathrm{Si}}^{35^\circ}$ and $N_{\mathrm{Mg}}^{35^\circ}$ would have been expected, which is at variance with present results (Table 3). Alternatively, assuming that Si polymerized with Zn to form Zn-rich clay nuclei not only explains the relatively high $N_{\mathrm{Si}}^{35^\circ}$, but also accounts for Si uptake at t = 9 h (169 µmol g^{-1}; Fig. 3d). The ratio of Zn to Si (Zn:Si) neighbor atoms in such nuclei, as estimated by the ratio of $N_{\mathrm{Zn}}^{35^\circ}/N_{\mathrm{Si}}^{35^\circ}$, equals (3.7 ± 0.5)/(1.5 ± 0.5) = 2.4 ± 0.9. This value is different from both ratios expected for TO ($N_{\mathrm{Zn}}^{35^\circ}/N_{\mathrm{Si}}^{35^\circ} = 6/2 = 3$) and TOT ($N_{\mathrm{Zn}}^{35^\circ}/N_{\mathrm{Si}}^{35^\circ} = 6/4 = 1.5$) clay structures. Furthermore, the chemical Zn/Si ratio, as estimated by the ratio of Zn to Si uptakes, equals (169 ± 6)/(227 ± 6) = 0.74 ± 0.03, which compares neither with Si/Zn = 2/3 = 0.67 for TO structure, nor with Zn/Si = 4/3 = 1.33 for TOT ones. Hence, Zn nuclei may have either an Si-enriched TO structure, or a Si-depleted TOT one (Fig. 12b).

An important increase of the mean size of octahedral sheets occurs between t = 9 h ($Q_{Zn} \approx 20$) t = 120 h ($Q_{Zn} \geq 200$), in conjunction with a comparatively smaller increase of surface coverage (from 227 to 725 µmol g^{-1}). If all particles had grown at the same rate, then only $Q_{Zn} \approx 60$ would have been expected at t = 120 h.. The comparatively higher experimental Q_{Zn} can be explained either by the growth of selected nuclei and the dissolution of other ones through Ostwald ripening (Robarge, 1998), or by the coalescence upon growth of nuclei located at the same layer edges of hectorite platelets. In these large nuclei, Zn is surrounded by neighboring 6 ± 0.5 in-plane Zn and 3.6 ± 0.5 out-of-plane Si, as can be expected for a TOT phyllosilicate. Further knowledge about the structure and chemical composition of these Zn nuclei can be obtained from the ratio of Si/Zn uptake of 1.09 ± 0.08 (Fig. 3d). This ratio is somewhat lower than the 4/3 ratio expected for a perfect TOT phyllosilicate. Including the amount of Si released upon hypothetical stoichiometric dissolution of hectorite (=92 ± 7 µmol/ g hectorite) enhances this ratio to 1.21 ± 0.09, which is still slightly lower than the expected value. This depletion in Si relatively to TOT clay minerals may corresponds either to coexistence of TO and TOT layers, or to the presence of defects in T sheets in TOT clay minerals. Indeed, a deficit in Si relatively to TOT structure was already reported for "hydrated talc" minerals (Brindley and Hang, 1973; Imai et al., 1973), and this deficit was later suggested to arise from defects in T sheets (Drits and Tchoubar, 1990). This model might also apply to Zn nuclei at the layer edges of hectorite platelets (Fig. 12c). In conclusion, combination of P-EXAFS and chemical data clearly demonstrates that Zn-rich phyllosilicates of TOT structure nucleate on hectorite particles after only 5 days of reaction time, but only at $[\mathrm{Si}]_{aq,t}$ relevant to field conditions.

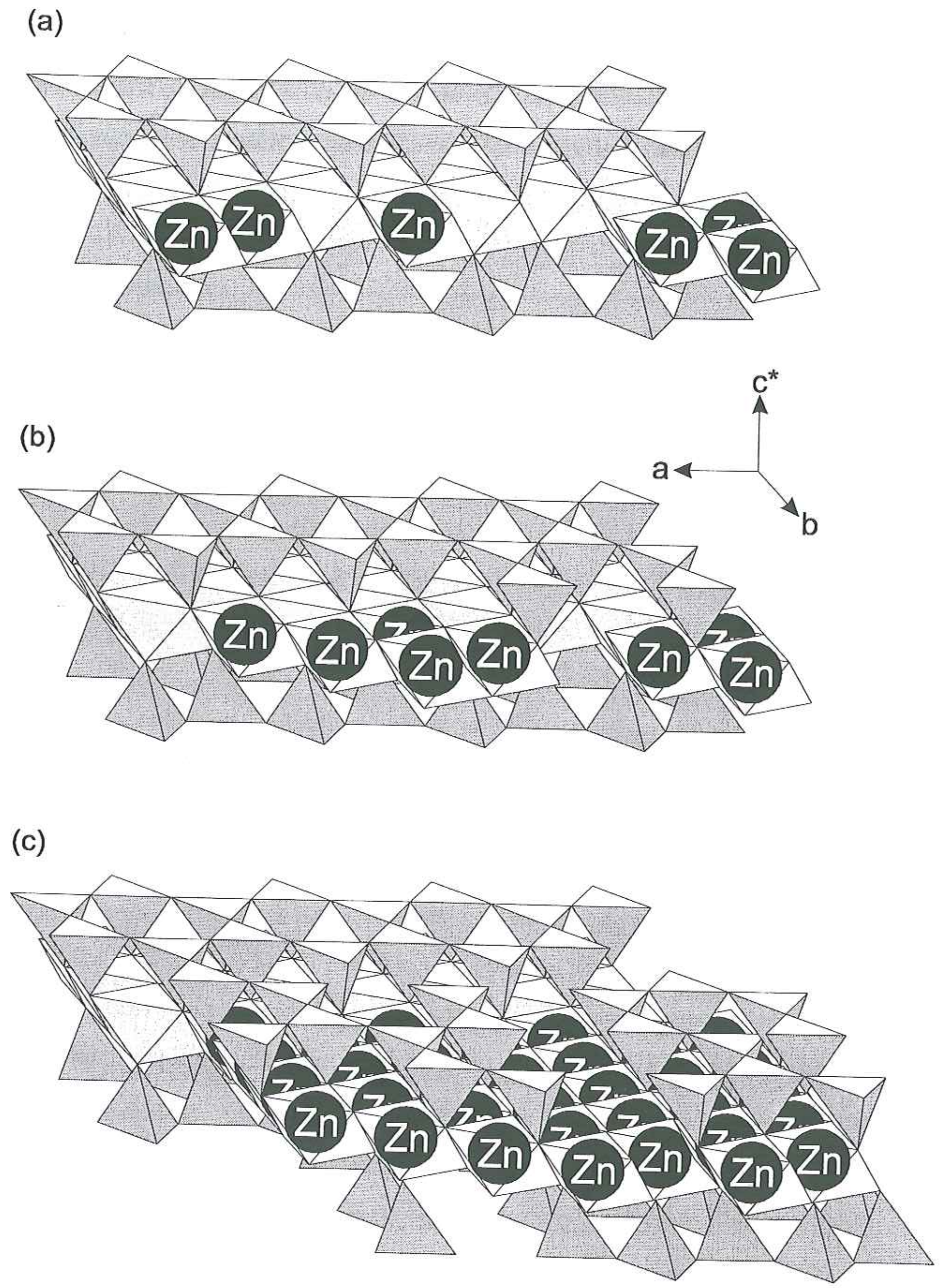

Fig. 12. Structural models for Zn polymers forming at the layer edges of hectorite, as a function of $[Si]_{aq,t}$ and reaction time. (a) H30_Zn_96h; formation of small polymers at layer edges of hectorite platelets. (b) H30_SiZn_9h; formation of Zn phyllosilicate nuclei by structural association of Zn octahedra and Si tetrahedra. (c) H30_SiZn_120h; growth of large clusters of Zn phyllosilicates.

4.3. Mechanisms of clay heteronucleation and growth

Studies devoted to the growth mechanism of phyllosilicates usually start by nucleating stable seeds of the clay minerals, either homogeneously in the bulk solution, over a given supersaturation state, or heterogeneously at a mineral surface. Study of heterogeneous nucleation has long been hampered by the difficulty to detect and characterize small particle seeds on a mineral substrate. Solid precipitation in presence of large minerals surfaces has been reported in a number of recent studies (Charlet and Manceau, 1992; Charlet and Manceau, 1994; Espinose de la Caillerie et al., 1995b; O'Day et al., 1996; O'Day et al., 1994a; Scheidegger et al., 1997; Scheidegger et al., 1998; Towle et al., 1997), however, it was not clear whether precipitates did form at the mineral surface, or nucleate in solution and subsequently bind to the sorbent. Recently, Nagy & al (Nagy et al., 1999) were able to characterize heteronucleation of gibbsite on kaolinite and muscovite surfaces by combining chemical (flow through reactor) and structural (X-ray powder diffraction and tapping-mode atomic force microscopy) methods. In the present study, deciphering the initial steps of Zn phyllosilicate nucleation and growth has been made possible by the use of P-EXAFS spectroscopy at the K-edge of Zn, and by chemical conditions of high $[Si]_{aq,t}$, yet undersaturated with respect to amorphous silica.

Analysis of samples obtained during the reaction time suggests that the ratio $N^{35°}_{Zn} / N^{35°}_{Si}$ increases during the early stage of nucleation (H30_ZnSi_9h), suggesting that early nuclei are depleted in Si. This depletion is consistent with a nucleation mechanism initiated by the formation of small octahedral sheets of brucite-like structure. Further growth of these domains is then enhanced by the formation of Si tetrahedral sheets. Simultaneous uptake of Zn and Si for longer sorption times suggests that phyllosilicate growth from solute compounds is a cooperative process, with Zn and Si sheets growing at about the same rate.

4.4. Application to field studies

The rapid formation of Zn phyllosilicate close to field conditions suggests that this mechanism of Zn immobilization be plausible in terrestrial systems. Indeed, P-EXAFS analysis of the soil clay fraction in areas heavily polluted by smelter emissions enabled the unambiguous identification of Zn phyllosilicates (Manceau et al., 2000b). In addition, the angular dependence observed upon P-EXAFS analysis of these minerals suggested a structural association of these neoformed clay minerals to charged clay particles (smectites, illite, chlorite...) of the soil. Alternatively, a mechanism of phyllosilicate neoformation via homogeneous nucleation in a gel would have led to the formation of disoriented clay particles within the gel, hence no angular dependence would have been expected.

These results also allow to discuss possible mechanisms of Ni-rich phyllosilicates associated to weathering formations of ultrabasic rocks. High levels of Ni are observed in neoformed magnesian phyllosilicates of either TO or TOT structure, often called "garnierites" (Brindley and Hang, 1973), which are present in cracks of the weathering profiles. These garnierites were believed to result from neoformation of solid phases incorporating Ni, Mg and Si elements released upon alteration of rock-forming minerals (Pelletier, 1983). Manceau & Calas (Manceau and Calas, 1985; Manceau and Calas, 1986) showed that Ni contained in garnierite is concentrated within large Ni-rich domains, even for Ni/(Ni + Mg) ratios as low as 0.07. As the affinity of Ni for phyllosilicate structure compares with that of Zn (Decarreau, 1981; Decarreau, 1985), the neoformation mechanism of Ni domains in garnierites might be reasonably compared with that of Zn domains on hectorite: Ni domains may have likely formed by heteronucleation and growth of Ni-rich phyllosilicate clusters.

5. CONCLUDING REMARKS

The present study highlights the impact of $[Si]_{aq,t}$ on the immobilization mechanism of Zn on mineral surfaces at Zn concentrations undersaturated with respect to both hydroxide and ZnO oxide phases. At low $[Si]_{aq,t}$, $\approx$30-60 μM (< 4 ppm SiO_2), formation of Zn polymers is observed at the layer edges of hectorite, yet the mean size of these polymers is limited to a few Zn atoms, suggesting that hectorite surface cannot promote the precipitation of large Zn hydroxide layers, or Zn oxide, for undersaturated conditions. In contrast, nucleation and extensive growth of clay particles is observed at $[Si]_{aq,t}$, $\approx$530 μM ($\approx$32 ppm SiO_2), i.e. at concentrations that can be found in terrestrial systems, and well undersaturated with respect to amorphous silica. Dissolved Si thus may play a pivotal role in the fate of transition metal ions in natural systems, by governing both the extent and the mechanism of uptake. Hence, studies devoted to cation sorption on clay particles may greatly benefit from taking $[Si]_{aq,t}$ into account.

Acknowledgements

The LURE and ESRF staffs are acknowledged for providing the synchrotron X-ray beam. J-L Hazemann, J.J. Menthonnex, Y. Soldo, O. Prost and O. Ulrich are commended for their technical assistance in the collection of EXAFS spectra on BM 32 at the European Synchrotron Radiation Facility (ESRF).

Bibliography

Aberdam D. (1998) SEDEM, a software package for EXAFS data extraction and modelling. *J. Synchrotron Rad.* **5**, 1287-1297.

Anderson S. J. and Sposito G. (1991) Cesium-adsorption method for measuring accessible structural surface charge. *Soil Sci. Soc. Am. J.* **55**, 1569-1576.

Baes C. F. J. and Mesmer R. E. (1976) *The hydrolysis of cations*. John Wiley & Sons.

Banfield J. F., Jones B. F., and Veblen D. R. (1991) An AEM-TEM study of weathering and diagenesis, Albert Lake, Oregon: I. Weathering reactions in the volcanics. *Geochim. Cosmochim. Acta* **55**, 2781-2793.

Bonnin D., Bouat J., Kaiser P., Frétigny C., and Béguin F. (1986) Bond angle determination by angular EXAFS study and Deby-Waller anistropy in 2D graphite intercalation compounds. *J. Phys.* **C8**, 865-868.

Brindley G. W. and Hang P. T. (1973) The nature of garnierite. I. Structures, chemical compositions and color characteristics. *Clay Min.* **21**, 27-40.

Charlet L. and Manceau A. (1992) X-ray absorption spectroscopic study of the sorption of Cr(III) at the oxide-water interface. II. Adsorption and surface precipitation on hydrous ferric oxide. *J. Colloid Interface Sci.* **148**, 443-458.

Charlet L. and Manceau A. (1994) Evidence for the neoformation of clays upon sorption of Co(II) and Ni(II) on silicates. *Geochim. Cosmochim. Acta* **58**, 2577-2782.

Davies S. N. and De Wiest R. C. M. (1966) *Hydrogeology*. John Wiley & sons.

Davis J. A., Coston J. A., Kent D. B., and Fuller C. C. (1998) Application of the surface complexation concept to complex mineral assemblages. *Environ. Sci. Technol.* **32**, 2820-2828.

Decarreau A. (1981) Mesure expérimentale des coefficients de partage solide/solution pour les éléments de transition A^{2+} dans les smectites magnésiennes (A= Ni, Co, Zn, Fe, Cu, Mn). *C. R. Acad. Sc. Paris* **292**, 459-462.

Decarreau A. (1985) Partitioning of divalent transition elements between octahedral sheets of trioctahedral smectites and water. *Geochim. Cosmochim. Acta* **49**, 1537-1544.

Drever J. I. (1997) *The geochemistry of natural waters*. Prentice Hall.

Drits V. A. and Tchoubar C. (1990) *X-ray diffraction by disordered lamellar structures*. Springer verlag.

Espinose de la Caillerie J.-B. d., Kermarec M., and Clause O. (1995a) ^{29}Si NMR observation of an aqueous magnesium silicate formed during impregnation of silica with Mg(II) in aqueous solution. *J. Phys. Chem.* **99**, 17273-17281.

Espinose de la Caillerie J.-B. d., Kermarec M., and Clause O. (1995b) Impregnation of γ-alumina with Ni(II) or Co(II) at neutral pH: hydrotalcite-type coprecipitate formation and characterization. *J. Am. Chem. Soc.* **117**, 11471-11481.

Farquhar M. L., Vaughan D. J., Hughes C. R., Charnock J. M., and England K. E. R. (1997) Experimental studies of the interaction of aqueous metal cations with mineral substrates: lead, cadmium and copper with perthitic feldspar, muscovite and biotite. *Geochim. Cosmochim. Acta* **61**, 3051-3064.

Fortin D., Ferris F. G., and Beveridge T. G. (1997) Surface-mediated mineral development by bacteria. In *Interactions between microbes and minerals*, Vol. 35 (ed. J. F. Banfield and K. H. Nealson), pp. 161-180. Mineralogical Society of America.

Güven N. (1988) Smectites. In *Hydrous Phyllosilicates*, Vol. 19 (ed. S. W. Bailey), pp. 497-559. Mineralogical society of America.

Harder H. (1977) Clay mineral formation under lateritic weathering conditions. *Clay Min.* **12**, 281-288.

Iler R. K. (1979) *The chemistry of silica*. John Wiley & Sons.

Imai N., Otsuka R., Nakamura T., Tsunashima A., and Sakamoto T. (1973) Hydrated talc: alteration product of wollastonite by reaction with magnesium-bearing hydrothermal solutions. *Clay Sci.* **4**, 175-191.

Jackson M. L. (1964) *Soil chemical analysis*. Prentice-hall, inc.

Kadi-Hanifi M. and Mering J. (1972) Précisions sur la structure de l'hectorite. *C. R. Séanc. Acad. Sc. Paris* **274D**, 149-151.

Komadel P., Madejova J., Janek M., Gates W. P., Kirkpatrick R. J., and Stucki J. W. (1996) Dissolution of hectorite in inorganic acids. *Clays Clay Min.* **44**, 228-236.

Kreit J. F., Shainberg I., and Herbillon A. J. (1982) Hydrolysis and decomposition of hectorite in dilute salt solutions. *Clays Clay Min.* **30**, 223-231.

Kuzmin A., Obst S., and Purans J. (1997) X-ray absorption spectroscopy and molecular dynamics studies of Zn2+ hydration in aqueous solutions. *Journal of Physics: Condensed Matter* **9**, 10065-10078.

Manceau A., Bonnin D., Stone W. E. E., and Sanz J. (1990) Distribution of Fe in the octahedral sheet of trioctahedral micas by polarized EXAFS. Comparison with NMR results. *Phys. Chem. Minerals* **17**, 363-370.

Manceau A. and Calas G. (1985) Heterogeneous distribution of nickel in hydrous silicates from New Caledonia ore deposits. *Amer. Mineral.* **70**, 549-558.

Manceau A. and Calas G. (1986) Nickel-bearing clay minerals: II. Intracrystalline distribution of nickel: an X-ray absorption study. *Clay Min.* **21**, 341-360.

Manceau A., Chateigner D., and Gates W. P. (1998) Polarized EXAFS, distance-valence least-squares modeling (DVLS) and quantitative texture analysis approaches to the structural refinement of Garfield nontronite. *Phys. Chem. Minerals* **25**, 347-365.

Manceau A. and Combes J.-M. (1988) Structure of Mn and Fe oxides and oxyhydroxides: a topological approach by EXAFS. *Phys. Chem. Minerals* **15**, 283-295.

Manceau A., Lanson B., Drits V. A., Chateigner D., Gates W. P., Wu J., Huo D., and Stucki J. W. (2000a) Oxidation-reduction mechanism of iron in dioctahedral smectites. 1. Structural chemistry of oxidized reference nontronites. *Amer. Mineral.* **85**, 133-152.

Manceau A., Lanson B., Schlegel M. L., Hargé J.-C., Musso M., Hazemann J.-L., Chateigner D., and Lamble G. M. (2000b) Quantitative Zn speciation in smelter-contaminated soils by EXAFS spectroscopy. *American Journal of Science*, under press.

Manceau A., Schlegel M. L., Chateigner D., Lanson B., Bartoli C., and Gates W. P. (1999a) Application of Polarized EXAFS to Fine-Grained Layered Minerals. In *Synchrotron X-ray Methods in Clay Science* (ed. D. G. Schulze, J. W. Stucki, and P. M. Bertsch), pp. 69-114. Clay Mineral Society of America.

Manceau A., Schlegel M. L., Nagy K. L., and Charlet L. (1999b) Evidence for the formation of trioctahedral clay upon sorption of Co^{2+} on quartz. *J. Colloid Interface Sci.* **220**, 181-197.

Nagy K. L., Cygan R. T., Hanchar J. M., and Sturchio N. C. (1999) Gibbsite growth kinetics on gibbsite, kaolinite, and muscovite substrates: atomic force microscopy evidence for epitaxy and an assessment of reactive surface area. *Geochim. Cosmochim. Acta* **63**, 2337-2351.

Oberlin A. and Mering J. (1966) Observations sur l'hectorite (étude en microscopie et diffraction électroniques). *Bull. Soc. Franç. Minér. Crist.* **89**, 29-40.

O'Day P. A., Chisholm-Brause C. J., Towle S. N., Parks G. A., and Brown G. E., Jr. (1996) X-ray absorption spectroscopy of Co(II) sorption complexes on quartz (α-SiO_2) and rutile (TiO_2). *Geochim. Cosmochim. Acta* **60**, 2515-2532.

O'Day P. A., Parks G. A., and Brown G. E., Jr. (1994a) Molecular structure and binding of Cobalt(II) surface complexes on kaolinite from x-ray absorption spectroscopy. *Clays Clay Min.* **42**, 337-355.

O'Day P. A., Rehr J. J., Zabinsky S. I., and Brown G. E., Jr. (1994b) Extended X-ray Absorption Fine Structure (EXAFS) analysis of disorder and multiple-scattering in complex crystalline solids. *J. Am. Chem. Soc.* **116**, 2938-2949.

Papelis C. and Hayes K. F. (1996) Distinguishing between interlayer and external sorption sites of clay minerals using X-ray absorption spectroscopy. *Coll. Surf. A: Physicochem. Engineer. Aspects* **107**, 89-96.

Pelletier B. (1983) Localisation du nickel dans les minerais 'garniéritiques' de la Nouvelle Calédonie. *Sci. Géol. Mém.* **73**, 173-183.

Rayner J. H. and Brown G. (1973) The crystal structure of talc. *Clays Clay Min.* **21**, 103-114.

Rehr J. J., Albers R. C., and Zabinsky S. I. (1992) High-order multiple-scattering calculations of X-ray absorption fine structure. *Phys. Rev. Lett.* **69**, 3397-3400.

Righi D. and Meunier A. (1995) Origin of clays by rock weathering and soil formation. In *Origin and mineralogy of clays* (ed. B. Velde), pp. 43-161. Springer.

Rimstidt J. D. (1997) Quartz solubility at low temperatures. *Geochim. Cosmochim. Acta* **61**, 2553-2558.

Robarge W. P. (1998) Precipitation/dissolution reactions in soils. In *Soil physical chemistry, second edition* (ed. D. L. Sparks), pp. 193-238. CRC Press.

Scheidegger A. M., Lamble G. M., and Sparks D. L. (1996) Investigation of Ni adsorption on pyrophyllite: an XAFS study. *Environ. Sci. Technol.* **30**, 548-554.

Scheidegger A. M., Lamble G. M., and Sparks D. L. (1997) Spectroscopic evidence for the formation of mixed-cation hydroxide phases upon metal sorption on clay and aluminium oxides. *J. Colloid Interface Sci.* **186**, 118-128.

Scheidegger A. M., Strawn D. G., Lamble G. M., and Sparks D. L. (1998) The kinetics of mixed Ni-Al hydroxide formation on clay and aluminium oxide minerals: a time-resolved XAFS study. *Geochim. Cosmochim. Acta* **62**, 2233-2245.

Schlegel M. L., Manceau A., Chateigner D., and Charlet L. (1999) Sorption of metal ions on clay minerals. I. Polarized EXAFS evidence for the adsorption of cobalt on the edges of hectorite particles. *J. Colloid Interface Sci.* **215**, 140-158.

Schlegel M. L., Manceau A., Hazemann J.-L., and Charlet L. (2000) Adsorption mechanism of Zn on hectorite as a function of time, pH, and ionic strength. *American Journal of Science*, submitted.

Stumm W. (1992) *Chemistry of the solid-water interface*. John Wiley & sons.

Taylor J. R. (1997) *An introduction to error analysis*. University Science books.

Teo B. K. (1986) *EXAFS: basic principles and data analysis*. Springer-Verlag.

Towle S. N., Bargar J. R., Brown G. E., Jr., and Parks G. A. (1997) Surface precipitation of Co(II)(aq) on Al_2O_3. *J. Colloid Interface Sci.* **187**, 62-82.

Zachara J. M. and Smith S. C. (1994) Edge complexation reactions of cadmium on specimen and soil-derived smectite. *Soil Sci. Soc. Am. J.* **58**, 762-769.

Zachara J. M., Smith S. C., and Kuzel L. S. (1995) Adsorption and dissociation of Co-EDTA complexes in iron oxide-containing subsurface sands. *Geochim. Cosmochim. Acta* **59**, 4825-4844.

7. Néoformation de phyllosilicates cobaltifères

Les expériences d'adsorption du cobalt sur le quartz ont été réalisées par O'Day & al [174]. Le quartz a subi au préalable un traitement de surface éprouvant, consistant en des lavages répétés à l'acide et à l'eau bidistillée, suivis d'un séchage à 60°C avant utilisation. Dans ces conditions, une couche de silice amorphe a pu se développer à la surface du quartz [176, 177]. Les suspensions ont été préparées dans des tubes en polypropylène par mise en contact de Co (TotCo $\leq$ 2000 µM) et de quartz, à une concentration en solide comprise entre 240 et 250 g L^{-1}. Ces suspensions ont ensuite été conditionnées dans un excès de base initial, et agitées sous atmosphère inerte. Le pH n'a donc pas été contrôlé au cours de la réaction. L'analyse des valeurs de pH et de $[Co]_{aq}$ à la fin des réactions a montré que toutes les solutions étaient sous-saturées vis-à-vis de $Co(OH)_2$. Enfin, les valeurs de $[Si]_{aq}$ en fin d'expérience n'ont pas été publiées, ce qui limite l'exploitation des données chimiques.

7.1. Environnement cristallochimique de Co adsorbé

Les spectres EXAFS pour le cobalt adsorbé sur le quartz à différents taux de couverture Γ ($0,77 \leq \Gamma \leq 9,9$ µmol m^{-2}) sont comparables, indiquant que les environnements cristallochimiques du cobalt dans tous les échantillons sont identiques. L'analyse quantitative de ces spectres montre que Co est hexacoordonné et entouré de 6 voisins Co à environ 3,12 Å et d'un nombre variable de voisins Si à des distances EXAFS de 3,3-3,4 Å [174]. Dans le modèle structural d'adsorption proposé à partir de ces résultats, Co était censé former des CSI mononucléaires à la surface du quartz, et des feuillets d'hydroxyde $Co(OH)_2$ [174]. La formation d'hydroxydes de cobalt en conditions de sous-saturation de la solution vis-à-vis de $Co(OH)_2$ est difficile à expliquer [178]. De plus, le mécanisme d'adsorption proposé par O'Day diffère sensiblement de la néoformation de phyllosilicates observée lors de l'adsorption de Co à la surface de la silice amorphe, un solide dont l'ordre local est pourtant similaire à celui du quartz [179]. Par conséquent, les spectres EXAFS de Co adsorbé sur le quartz ont fait l'objet d'une réanalyse approfondie. Les résultats de cette étude sont détaillés dans l'article intitulé « *Evidence for the formation of trioctahedral clay upon sorption of* Co^{2+} *on quartz* » situé à la fin de cette section.

Les spectres EXAFS de Co adsorbé sur l'hectorite (Γ = 5,21 µmol m^{-2} ; échantillon Γ521), et de $Co(OH)_2$ ont une structure semblable mais des phases différentes pour $k \geq 5$ $Å^{-1}$ (fig. 7.1.a). Les similitudes entre les spectres de Γ521 et d'une kérolite cobaltifère $Co_3Si_4O_{10}(OH)_2{\cdot}nH_2O$ (CoKer) sont bien plus prononcées, indiquant que l'environnement du cobalt adsorbé est plutôt comparable à celui d'un phyllosilicate qu'à celui d'un hydroxyde (fig. 7.1.b). Ce résultat est confirmé par la comparaison des TF (fig. 7.2). Les TF de Γ521 et $Co(OH)_2$ présentent des différences de phases et de parties imaginaires remarquables (notamment entre 3 et 6 Å), alors que celles de Γ521 et CoKer sont remarquablement superposées de 0 à 7 Å. L'origine structurale des contributions EXAFS de $Co(OH)_2$ et CoKer a été déterminée par spectroscopie EXAFS polarisée de composés de références, et par des simulations FEFF. Il a été montré que les domaines de TF compris entre 3,5 et 5,5 Å contiennent des contributions d'origines structurales distinctes pour $Co(OH)_2$ et CoKer :

- pour $Co(OH)_2$, les pics `A`, `B`, `C` proviennent des contributions d'atomes d'oxygène des feuillets adjacents (`A`), d'atomes de cobalt des feuillets adjacents (`B`), et d'un mélange de contributions d'atomes de cobalt deuxièmes voisins du feuillet et des feuillets adjacents (`C`) (fig. 7.3.a) ;
- pour CoKer, les pics `A`, `B`, `C` proviennent des contributions des oxygènes basaux des couches tétraédriques (`A`), des atomes de silicium deuxièmes voisins Si_2 (`C`) et de la contribution mixte de cobalt deuxièmes voisins et silicium troisièmes voisins Si_3 du feuillet (`C`) (fig. 7.3.a). Ces trois contributions n'ont une amplitude significative que lorsque les tétraèdres de silice sont organisés en couches liées aux couches octaédriques de cobalt, comme dans les phyllosilicates.

La similitude des TF de Γ521 et CoKer, notamment des pics `A`, `B`, et `C`, montre que le cobalt dans Γ521 et CoKer ont le même ordre à courte et moyenne distance. En particulier, la détection des contributions provenant des couches atomiques Si_2 et Si_3 indiquent que les tétraèdres de Si forment des couches tétraédriques. Cette organisation structurale des tétraèdres est incompatible avec la topologie des tétraèdres de silicate dans le quartz. Ce résultat permet de confirmer que le Co adsorbé sur le quartz est localisé dans une structure de type phyllosilicate.

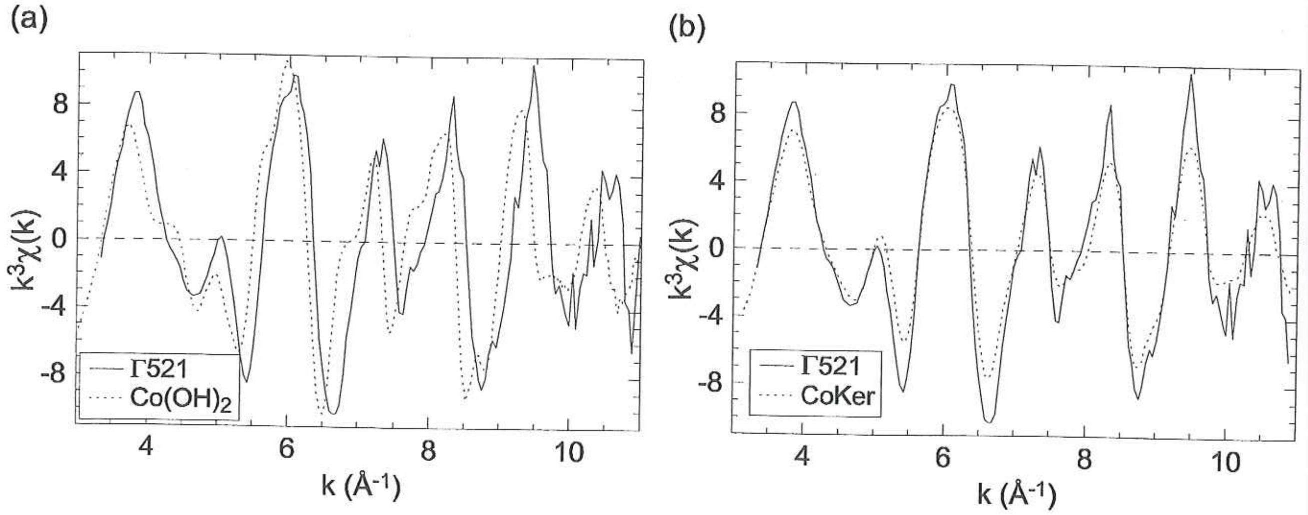

Figure 7.1. (a) Comparaison des spectres EXAFS de cobalt adsorbé sur le quartz à un taux de couverture de 5,21 µmol m^{-2} (Γ521) et de $Co(OH)_2$. (b) Comparaison des spectres EXAFS de Γ521 et de la kérolite cobaltifère ($Co_3Si_4O_{10}(OH)_2{\cdot}nH_2O$; CoKer).

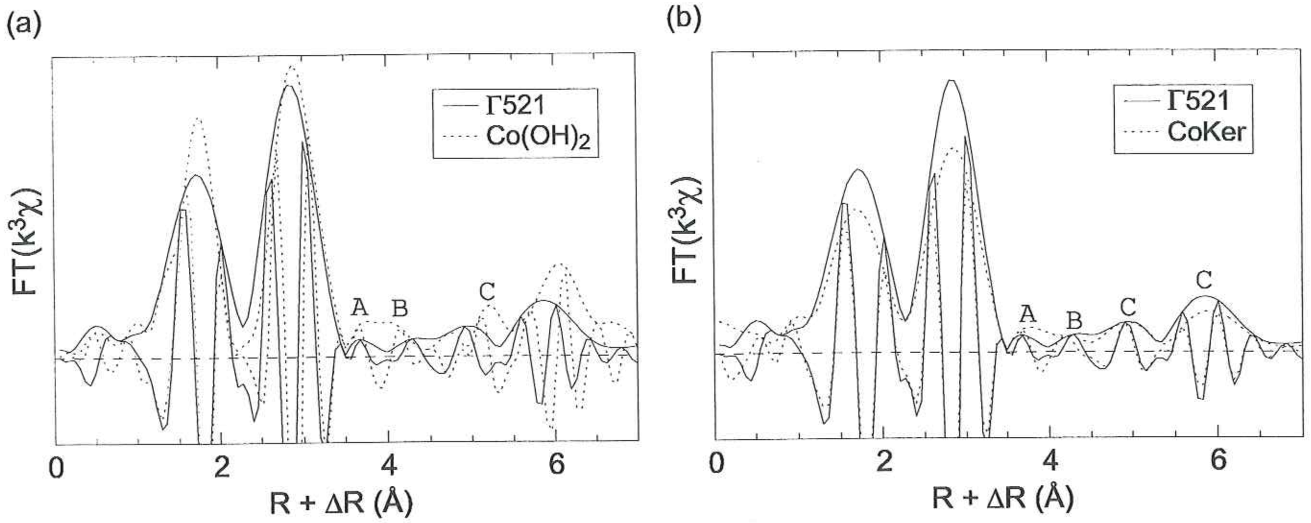

Figure 7.2. Comparaison des transformés de Fourier (a) de Γ521 et $Co(OH)_2$, et (b) de Γ521 et CoKer.

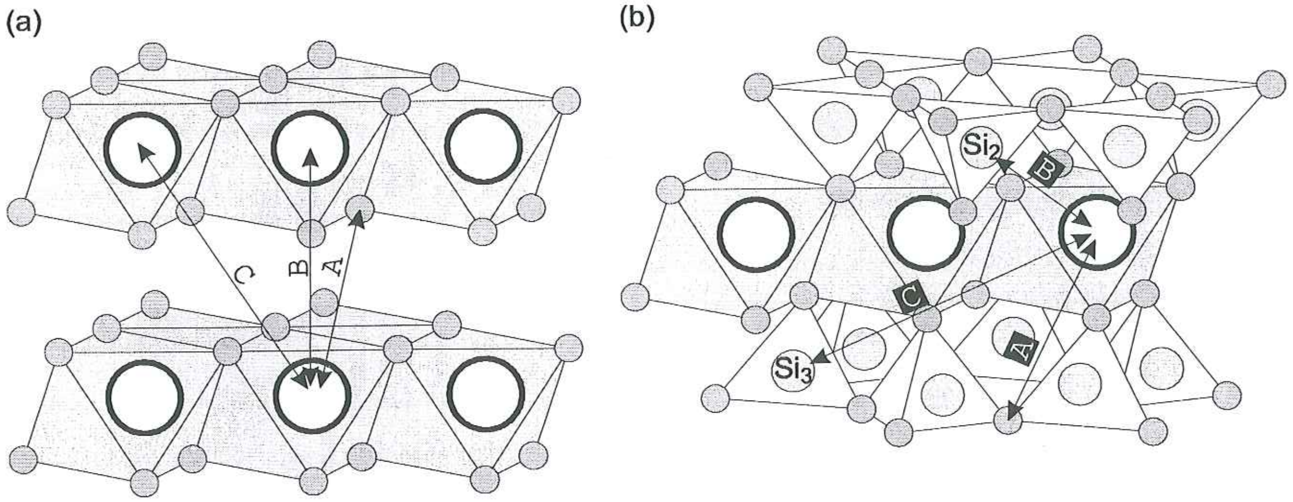

Figure 7.3. Origines structurale des différentes contributions pour les pics des transformées de Fourier de (a) $Co(OH)_2$, et (b) CoKer.

7.2. Stabilité thermodynamique des phyllosilicates cobaltifères

Afin de vérifier si la solution est sursaturée ou non vis-à-vis d'une kérolite cobaltifère, la solubilité de CoKer a été calculée. Pour cela, la constante de solubilité de CoKer a été estimée de manière indirecte par détermination de l'enthalpie libre de formation de CoKer en utilisant la méthode développée par Tardy et al. [180-182]. A partir de cette constante (Log K = 15.11), les valeurs de $[Co]_{aq}$ à l'équilibre avec CoKer à pH donné ont été calculées pour deux situations possibles :

- une dissolution congruente de CoKer, sans précipitation de silice amorphe pour $[Si(OH)_4] >$ 2 000 µM;
- une dissolution à concentration de $Si(OH)_4$ contrôlée par la solubilité du quartz ($[Si(OH)_4] =$ 183 µM; [172]).

Les courbes de solubilité obtenues ont été comparées aux valeurs expérimentales de $[Co]_{aq}$ mesurées par O'Day & al à la fin des expériences d'adsorption [174]. La figure 7.4 montre que les valeurs de $[Co]_{aq}$ sont proches des conditions d'équilibre avec une kérolite cobaltifère et confirme que ces suspensions sont très sous-saturées vis-à-vis de $Co(OH)_2$. Pour pousser plus loin cette analyse, il faudrait disposer des valeurs de $[Si]_{aq}$, mais celles-ci n'ont malheureusement pas été publiées.

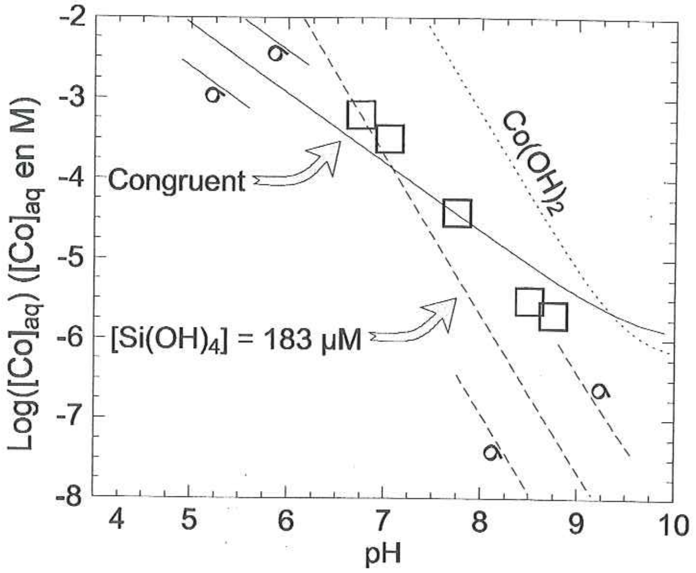

Figure 7.4. Courbes de solubilité théorique de CoKer dans le cas d'une dissolution congruente (trait plein) et d'une dissolution à $[Si(OH)_4]$ constante, contrôlée par la solubilité du quartz (tirets). La comparaison de ces courbes avec la solubilité de $Co(OH)_2$ indique que CoKer est plus stable que l'hydroxyde pur en présence de silice en solution. Le bon accord entre les valeurs théoriques de solubilité et les valeurs de $[Co]_{aq}$ à la fin des expériences d'adsorption (□) suggère que les phyllosilicates cobaltifères identifiés par EXAFS se sont formés dans des conditions de stabilité vis-à-vis de la solution.

(*Evidence for the formation of trioctahedral clay upon sorption of Co^{2+} on quartz.* Article paru dans Journal of Colloid and Interface Science)

Journal of Colloid and Interface Science **220,** 181–197 (1999)
Article ID jcis.1999.6547, available online at http://www.idealibrary.com on IDEAL®

Evidence for the Formation of Trioctahedral Clay upon Sorption of Co^{2+} on Quartz

Alain Manceau,*,[1] Michel Schlegel,* Kathryn L. Nagy,† and Laurent Charlet*

**Environmental Geochemistry Group, LGIT-IRIGM, University Joseph Fourier and CNRS, 38041 Grenoble Cedex 9, France; and †Department of Geological Sciences, University of Colorado, Boulder, Colorado 80309-0399*

Received May 24, 1999; accepted September 15, 1999

The sorption mechanism of Co on quartz at room temperature has been investigated by an in-depth analysis of published extended X-ray absorption fine structure (EXAFS) spectroscopy and solution chemistry data. In particular, the 3.5–5 Å mid-range atomic environment of Co has been determined with unprecedented precision by combining *ad initio* FEFF7.02 calculations and results obtained by polarized EXAFS on the mid-distance structure of sheet silicate minerals. The local atomic environment around sorbed Co atoms is identical to that of Co in trioctahedral clays and substantially different from that in the cobalt hydroxide $Co(OH)_{2(s)}$. Neoformation of a trioctahedral clay is consistent with calculated thermodynamic solubilities, which indicate that 2:1 and 1:1 Co-rich hydrous silicates, similar to kerolite and chrysotile, are less soluble than $Co(OH)_{2(s)}$. Consequently, precipitation of Co-rich clay is favored over that of $Co(OH)_{2(s)}$ at pH values below 9 and for a dissolved Si concentration equal to quartz solubility. New experimental data show that dissolved Si concentrations can approach, and even exceed, that of quartz solubility during the short times of sorption experiments. Based on the available data, it is not possible to conclude unequivocally if the Co layer silicate grew epitaxially on the quartz surface, topotactically in a surface amorphous layer, or independently of the quartz framework structure. The structural and chemical interpretation is supported by recent published studies in which sorption of a hydrolyzable cation leads to the neoformation of a mixed layer phase formed from the sorbate species and the sorbent metal. This surface-induced precipitation mechanism is a general phenomenon that may account for the formation of secondary clays as coatings on silicates.

Key Words: **quartz; kerolite; clay minerals; EXAFS; X-ray absorption spectroscopy; adsorption; precipitation; cobalt.**

INTRODUCTION

Quartz and amorphous silica dominate many physical, chemical, and biological characteristics of subsurface environments. Silica concentrations in terrestrial waters range between 10 and 80 ppm (1), and this worldwide homeostasis is largely controlled by the solubility of quartz (11 ppm (2)) and amorphous silica (116 ppm (3)). In soils and sediments, quartz is often coated by clay minerals (Fig. 1a), but a quantitative understanding of how these coatings form is still lacking. The formation of a secondary clay on silica upon the sorption of metal cations, like Mg, Ni, and Co, has been reproduced in the laboratory and suggested to be general to many hydrolyzable cations in contact with silicates (4–6). However, in these studies it was not possible to determine the formation mechanism of the clay. The two key questions are do clay minerals precipitate homogeneously in solution or heterogeneously on the sorbent and, if heterogeneous precipitation dominates, is the sorption of cations on negatively charged quartz and silica surfaces the initial reaction step?

If sorption onto a silica substrate is the initial step in clay precipitation, then Extended X-ray Absorption Fine Structure (EXAFS) spectroscopy can be used to characterize the local atomic environment around the sorbed metal and determine clay formation mechanisms. In contrast to amorphous silica, few EXAFS studies have been performed on quartz. This is because quartz typically has a lower specific surface area than amorphous silica (~1 m^2/g vs ~100–200 m^2/g) (7) and, consequently, a lower amount of surface dangling bonds, which requires working at a much lower sorbate to sorbent mass ratio. The difficulty in analyzing a low concentration of sorbate was overcome by O'Day *et al.* (8) who succeeded in studying the structure of Co surface complexes on quartz in solutions under- and oversaturated with respect to $Co(OH)_{2(s)}$ by using fluorescence-yield EXAFS spectroscopy. Two types of complexes were inferred to be present at the quartz surface: mononuclear Co octahedra bonded to unsaturated oxygens of surface SiO_4 tetrahedra (Fig. 1b), and multinuclear $Co(OH)_{2(s)}$, which was considered to be overgrown on the quartz surface (Fig. 1b). Isolated mononuclear complexes would act as nucleation and growth sites for multinuclear complexes. This epitaxial mechanism, and the purely hydroxide nature of the cobalt overgrowth, run counter to the clay neoformation process proposed for the sorption of Co, Ni, and Mg on silica (4–6). A difference of sorption mechanism between amorphous silica and quartz is unexpected because both sorbents have

---

[1] To whom correspondence should be addressed. E-mail: manceau@obs.ujf-grenoble.fr.

0021-9797/99 $30.00

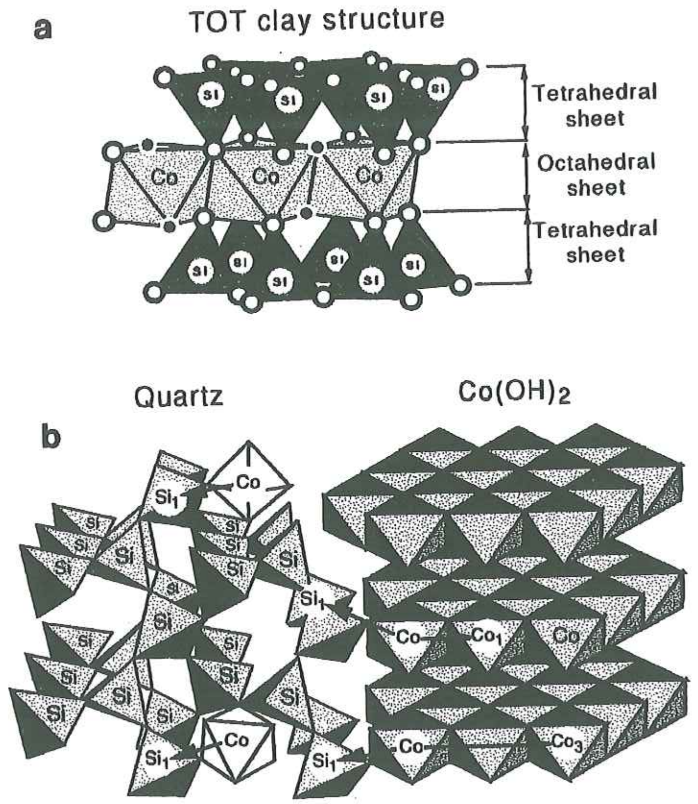

FIG. 1. (a) Polyhedral representation of a trioctahedral clay structure and (b) structural model of Co surface complexes on quartz (after (8)).

similar short-range order differing solely in the Si–O–Si bond angles, which equal 144° in αSiO_2 and range from 120° to 180° with a maximum at 144° in amorphous silica (9).

Figure 2 compares the EXAFS spectrum of Co-sorbed quartz to those of $Co(OH)_{2(s)}$ and Co/kerolite (CoKer), a 2:1 trioctahedral clay (10, 11). The Co/quartz and Co/clay spectra have a very similar shape, whereas the Co/quartz and $Co(OH)_{2(s)}$ spectra are clearly less similar. This simple comparison suggests that Co atoms are in a comparable, if not identical, structural environment in the sorbed and clay samples, which therefore prompts a closer examination of the structural model that has been proposed for the sorption mechanism of Co on quartz (Fig. 1b).

This paper has three goals. The first is to understand the incongruities in the EXAFS spectral analysis that have led to differing interpretations of the sorption mechanism of Co on amorphous silica and quartz. The second is to analyze the relative stabilities of $Co(OH)_{2(s)}$ and Co-rich layer silicates in order to determine if the formation of any of these phases is thermodynamically and mechanistically realistic. The third goal is to evaluate various sorption mechanisms in the light of the most recent EXAFS results obtained on the local structure of divalent transition metal ions in contact with the surfaces of oxides and silicates.

EXAMINATION OF THE SORPTION MODEL OF O'DAY *ET AL.* (8)

As shown in Fig. 2, the structural model proposed by O'Day *et al.* (8) for the sorption mechanism of Co^{2+} on quartz warrants reexamination. First, the short-range ordering around Co atoms obtained by O'Day *et al.* (8) from the quantitative analysis of EXAFS data will be critically discussed. Second, the plausibility of the two possible Co sorption models will be evaluated. Third, the precision of EXAFS structural parameters reported by O'Day *et al.* (8) from the least-squares fitting of experimental spectra will be reassessed. The main conclusion is that the clay-like structural model (Fig. 1a) better accounts for the experimental data than the two-site sorption model (Fig. 1b) proposed by O'Day *et al.* (8).

Discussion of Published Structural Interpretation of Co/Quartz EXAFS Spectra

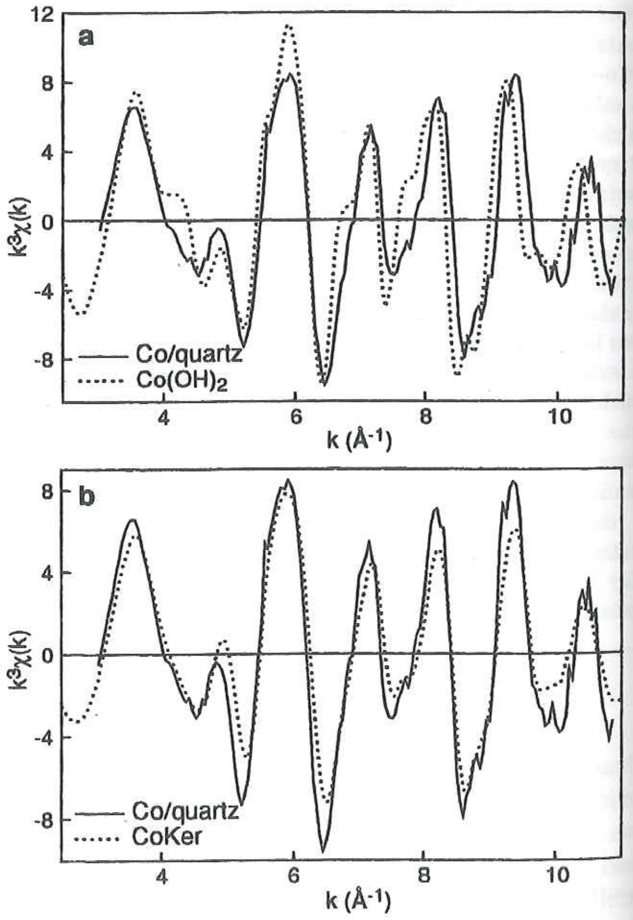

FIG. 2. k^3-weighted Co K-edge EXAFS spectrum of Co sorbed to quartz compared to $Co(OH)_{2(s)}$ (a) and Co-rich kerolite (b). The Co/quartz sample is from O'Day *et al.* (8) and corresponds to a sorption density of 9.21 $\mu mol/m^2$.

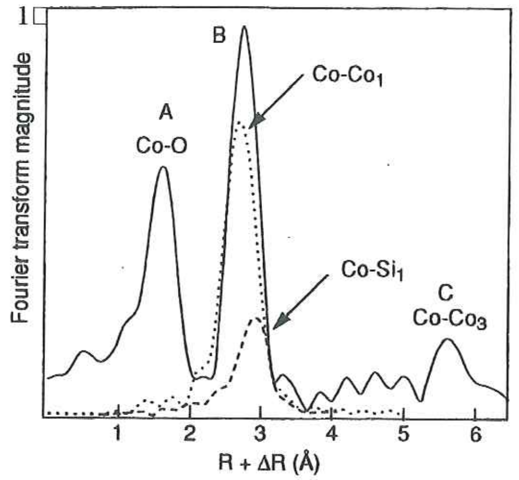

FIG. 3. Radial structure function of Co sorbed quartz at 5.21 $\mu mol/m^2$ surface coverage and Fourier transform deconvolution of the $Co–Co_1$ and $Co–Si_1$ contributions (after (8)).

The radial structure function (RSF) obtained by Fourier transforming the Co/quartz EXAFS spectrum at surface coverage of 5.21 $\mu mol/m^2$ (Fig. 3 in (8)) is shown in Fig. 3. Three peaks had been identified previously: peak A corresponding to the nearest O atoms and OH groups at 2.08 Å, peak B to the contribution from nearest cation shells, and peak C to long distance $Co–Co_3$ multiple scattering (MS) interactions at ~6.2 Å (Fig. 1b, Fig. 4). Peak B was deconvoluted into a Co_1 shell of 6 (± 15%) atoms at 3.12 (± 0.02) Å and a Si_1 shell of 1.1 to 3.1 (± 25%) atoms at 3.37–3.46 (± 0.02) Å (Table 3 in (8)). The distances and numbers of Co–Co pairs at 3.12 and 6.2 Å are characteristic of an edge-sharing layered framework and were attributed to a $Co(OH)_{2(s)}$ precipitate (Fig. 1b, Fig. 4b). These two Co–Co distances are however significantly shorter than in α/β $Co(OH)_{2(s)}$ (3.17 and 6.34 Å (12, 13)), but similar to those found in CoKer as determined by X-ray diffraction from the (060) reflection (3.10 and 6.20 Å (11)). Also, Fig. 3 shows that the $Co–Si_1$ pair has a low amplitude and, according to O'Day *et al.* (8), its existence could not be confirmed because of the proximity of the very intense Co_1 shell. Manceau *et al.* (14) showed that this situation is typical of layer silicate structures in which the nearest EXAFS contribution from the tetrahedral sheets at ~3.2–3.3 Å ($Me–Tet_1$) is dominated by an overlapping contribution from the octahedral sheet at ~3.00–3.12 Å ($Me–Oct_1$) (Fig. 4a). The $Me–Oct_1$ and $Me–Tet_1$ electronic waves add constructively (14) amplifying the second RSF peak (Fig. 3). Consequently, omitting the $Me–Tet_1$ shell contribution in sheet silicate structures during the least-squares fitting results in overestimating the number of Me–Me pairs. O'Day *et al.* (8) found that about 7 Co backscatterers (N_{Co1}) were necessary to fit the wave amplitude of the nearest cation shell contribution when the $Co–Si_1$ shell was omitted. This high amount of Co_1 neighbors is structurally unrealistic, and O'Day *et al.* (8) therefore argued for the presence of a $Co–Si_1$ contribution ($N_{Si1} = 1.1$ to $3.1 \pm 25\%$) admixed to the predominant $Co–Co_1$ contribution ($N_{Co1} = 6 \pm 15\%$) in Co-sorbed quartz. However, this argument is weak because the difference of N_{Co1} values (~7 vs 6) in the two spectral fits is within the precision range (15%).

Assessment of the Hydroxide and Clay Structural Models for Co Sorption onto Quartz

Co octahedra have the same polyhedral connectivity in the two models (Fig. 1). They are arranged in a two-dimensional

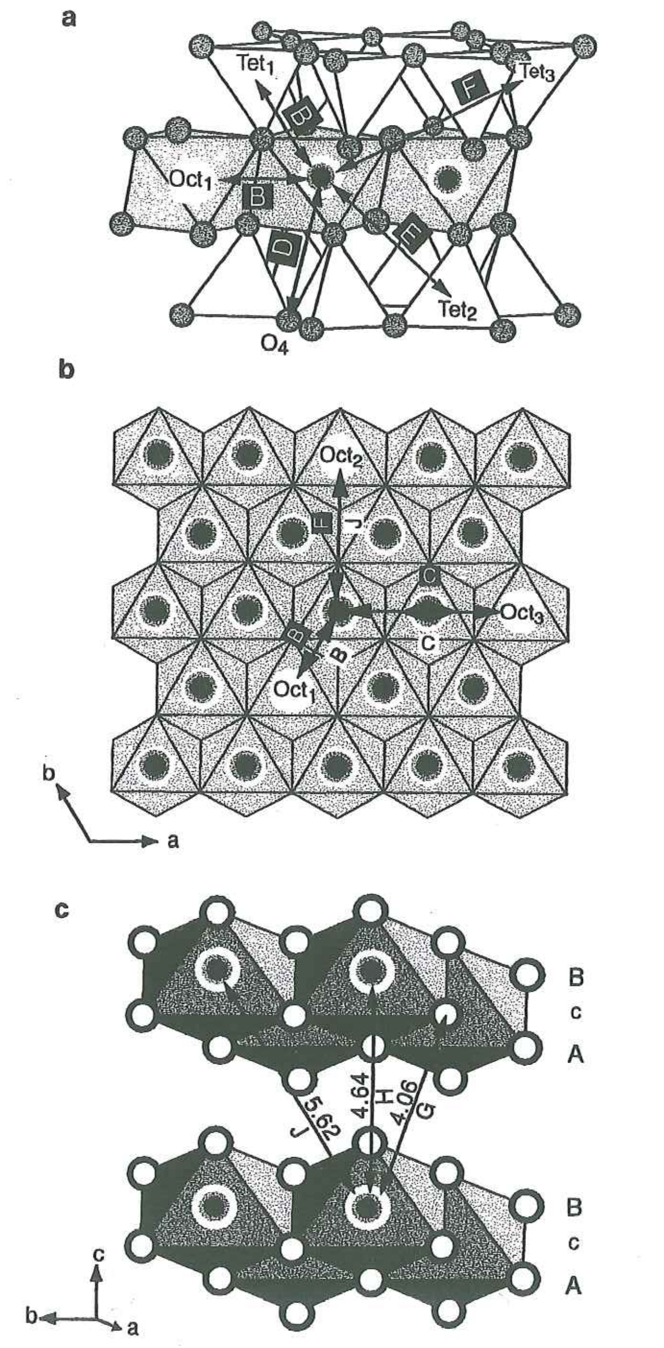

FIG. 4. Structural assignment of the successive atomic shell contributions in the radial distribution functions of kerolite and $Co(OH)_{2(s)}$. (a) Co-rich kerolite; (b) octahedral sheet of Co-rich kerolite and $Co(OH)_{2(s)}$; (c) $Co(OH)_{2(s)}$.

TABLE 1

Experimental Conditions for Co^{2+} Sorption on Quartz (After (8))

Sample	Solid/liq (m^2/L)	$[Co]_{init}$ (μM)	$[Co]_{final}$ (μM)	pH_{final}[a]	Equil. time (h)	Γ (μmol/m^2)	Γ (atoms/nm^2)	Si_{struc}[b] (μM)
A[c]	192	1900	<38	10.70	24	9.90	5.96	2483
B[c]	192	1200	<24	9.84	24	6.25	3.76	1568
C[c]	192	2000	<40	8.99	21[d]	10.81	6.50	2613
#9.21[e]	185	2000	317	7.04	42	9.21	5.48	2244
#7.4[e]	185	2000	630	6.78	54	7.41	4.46	1826
#5.21	185	1000	38	7.76	47	5.21	3.14	1280
#1.61	185	300	3	8.50	36	1.61	0.97	396
#0.77	192	150	2	8.74	24	0.77	0.46	197

Note. Pre-equilibration times were not reported by O'Day *et al.* (8).

[a] $pH_{initial}$ was assumed to be quite equal to pH_{final}.

[b] Calculated assuming a Co:Si ratio in the neoformed clay equal to 3:4.

[c] Sorption sample equilibrated with solutions oversaturated with respect to solubility reported for all stable and metastable forms of $Co(OH)_{2(s)}$.

[d] Days.

[e] Initial equilibration for 24 h with solutions oversaturated with respect to $Co(OH)_{2(s)}$ phases; pH adjusted with addition of acid to undersaturated conditions and equilibrated for the time shown.

edge-sharing sheet, and are also bridged to Si tetrahedra by their corners. However, in model 1 Co and Si atoms form a continuous clay-like structure whereas, in model 2, Co is mainly present in a pure $Co(OH)_{2(s)}$ layer structure and only partly bonded to surface SiO_4 tetrahedra of the quartz. Neither model accounts for all of the results reported by O'Day *et al.* (8), and each has its own merits and limitations. Model 2 accounts for the experimental Co–Si_1 distance of 3.37–3.46 Å, which is appreciably larger than in a clay structure (~3.3 Å (15, 16)). However, this model does not explain the reduction of the Co–Co_1 distance in sorption samples (3.12 ± 0.02 Å) compared to α/β $Co(OH)_{2(s)}$ (3.17 Å). In contrast, shortening of the Co–Co_1 distance agrees with model 1 because the presence of tetrahedral sheets in clays reduces the lateral dimension of the octahedral sheet (16). For instance, $d_{(Mg\text{–}Mg)}$ equals 3.06 Å in talc (2:1 clay (17)), 3.07–3.08 Å in antigorite and lizardite (1:1 clays (18, 19)), and 3.15 Å in $Mg(OH)_{2(s)}$ (12). The EXAFS Co–Co_1 distance in CoKer (3.12 Å) precisely corresponds to that for Co/quartz, but is 0.02 Å larger than that determined by X-ray diffraction (3.10 Å). The same difference between EXAFS and crystallographic distances was reported by Vaarkamp *et al.* (20) for Cu-Cu pairs by using theoretical phase shift functions derived from *ab initio* FEFF calculations (21) and in the present study on $Co(OH)_{2(s)}$ for which a FEFF7.02 distance of 3.19 Å was obtained vs the crystallographic distance of 3.17 Å. Consequently, use of FEFF7.02 functions results in overestimating by 0.02 Å the EXAFS Co–Co_1 distances determined for both Co/quartz and CoKer. Interestingly, the reverse was reported for Teo and Lee's *ab initio* functions (20), which yield a Co–Co_1 distance of 3.08 Å instead of 3.10 Å (10).

Model 2 (Fig. 1b) also produces anomalously high N_{Co}(6 ± 0.9) and N_{Si}(3.0 ± 0.75) values at intermediate surface coverage (Γ = 5.21 μmol/m^2, Table 1). Since Co atoms have 6 ± 0.9 Co neighbors in the $Co(OH)_2$ component and 3.0 ± 0.75 Si neighbors on the quartz surface, then the assumption of model 2 (Fig. 1b) requires that at least 85% ($N_{Co} = (6 - 0.9)/6 = 0.85$) of Co is in the $Co(OH)_{2(s)}$ and a *minimum* of 56% ($N_{Si} = (3 - 0.75)/4 = 0.56$) is complexed to four SiO_4 tetrahedra, 75% to three tetrahedra (2.25/3 = 0.75), or 112% to two tetrahedra (2.25/2 = 1.12). In all cases, the total amount of Co exceeds 100%, demonstrating the incongruity of model 2. Also, N_{Si} is low (1.1 ± 0.3, Table 3 in (8)) at the lowest surface coverage (Γ = 0.77 μmol/m^2). This result conflicts with the hypothesis that mononuclear surface complexes bonded to SiO_4 tetrahedra would form first and then provide nucleation sites for the formation and growth of $Co(OH)_{2(s)}$ multinuclear complexes (p. 2526, column 2 in (8)), because in this case N_{Si} should be maximum at low surface coverage and should decrease with increased loading.

Precision of Structural Parameters Obtained from EXAFS Spectra

The only apparent deficiency of model 1 is the $d_{(Co\text{–}Si)}$ distance, which is approximately 0.1 Å larger than expected for a clay structure (3.37–3.46 Å vs ~3.30 Å). This difference of distance contrasts with the strong spectral likeness observed in Fig. 2b, and needs to be examined in detail. Therefore, the EXAFS spectrum obtained at intermediate surface coverage (Γ = 5.21 μmol/m^2) by O'Day *et al.* (8) was carefully digitized and reanalyzed using the standard Fourier-filtering procedure (22). The Co–(Co, Si)$_1$ contribution obtained by Fourier back-transforming peak B was least-squares fitted using phase shift and amplitude functions calculated with FEFF7.02 (21, 23) and following the fitting procedure adopted by O'Day *et al.* (8).

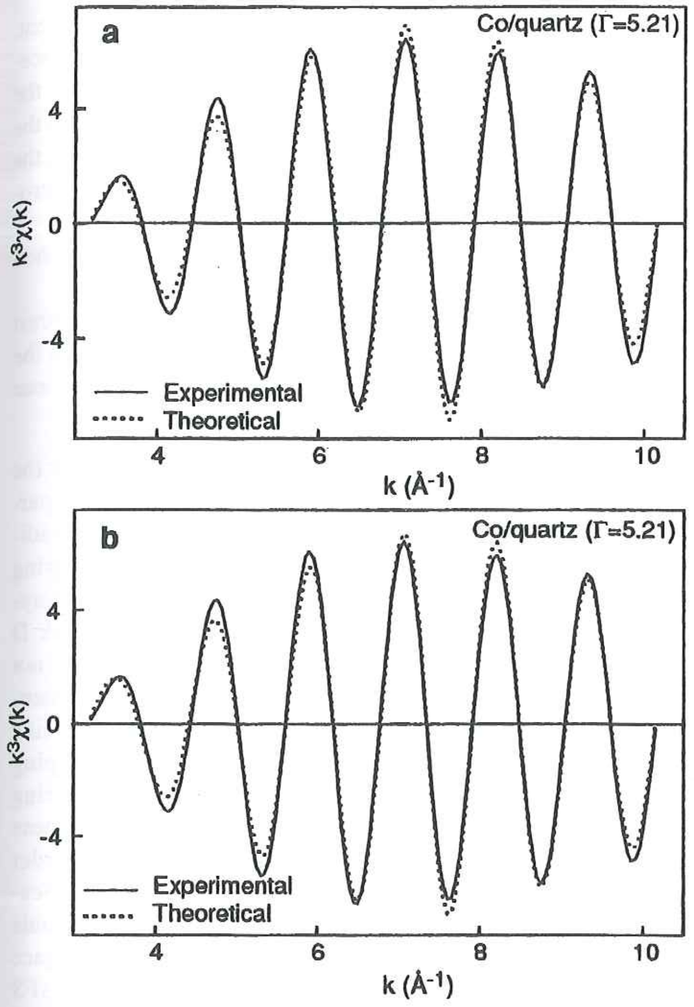

FIG. 5. Fourier filtered Co–(Co, Si)$_1$ contribution to EXAFS. (a) Two-shell fit obtained by O'Day *et al.* (8) by assuming 3 Si at 3.40 Å ($\sigma^2 = 0.005$ Å^2) and 6 Co at 3.12 Å ($\sigma^2 = 0.007$ Å^2). (b) Two-shell fit by assuming 4 Si at 3.33 Å ($\sigma^2 = 0.006$ Å^2) and 6 Co at 3.12 Å ($\sigma^2 = 0.008$ Å^2).

Figure 5a compares the Co–(Co, Si)$_1$ contribution to the theoretical spectrum obtained by assuming $N_{Si} = 3$ at $R_{Si} = 3.40$ Å ($\sigma^2 = 0.005$ Å^2), $N_{Co} = 6$ at $R_{Co} = 3.12$ Å ($\sigma^2 = 0.007$ Å^2) and a threshold energy variation (ΔE_0) of 1.6 eV as obtained by O'Day *et al.* (Table 3 in (8)). In EXAFS spectroscopy, σ^2 and N are strongly correlated, while R and ΔE_0 are moderately correlated. In two-shell fits, N and R can be slightly correlated whenever the two shells strongly overlap and one shell predominates. For this reason, O'Day *et al.* (8) chose to fix N_{Co} to be 6 and σ^2_{Si} to be 0.005 Å^2, and to vary N_{Si} and σ^2_{Co} during the spectral simulation. This strategy is arbitrary, and others may be adopted. We decided to allow σ^2 and ΔE_0 to vary and to fix N to its values in a 2:1 (i.e., $N_{Co} = 6$, $N_{Si} = 4$) and then in a 1:1 (i.e., $N_{Co} = 6$, $N_{Si} = 2$) clay structure. In the first case, structural parameters converged to $R_{Si} = 3.33$ Å (vs 3.43 Å in (8)), $\sigma^2_{Si} = 0.006$ Å^2, $R_{Co} = 3.12$ Å, $\sigma^2_{Co} = 0.008$ Å^2, and $\Delta E_0 = 3.4$ eV, and in the second to $R_{Si} = 3.34$ Å, $\sigma^2_{Si} = 0.0025$ Å^2, $R_{Co} = 3.12$ Å, $\sigma^2_{Co} = 0.008$ Å^2, and $\Delta E_0 = 5.8$ eV. The quality of the fits obtained with these new parameters (Fig. 5) is similar to that reported by O'Day *et al.* (8) as confirmed statistically by the factor of merit $R_p = \Sigma\,(k^3\chi_{exp} - k^3\chi_{th})^2/\Sigma(k^3\chi_{exp})^2$, which is equal to 5×10^{-3} for their fit and to 3×10^{-3} and 2×10^{-3} assuming a 2:1 and 1:1 clay local structure, respectively, in our analysis. The values of σ^2_{Si} and σ^2_{Co} for the 2:1 model are similar, if not identical, to values for reference clay structures (24, 25). For instance, σ^2_{Si} determined in nontronite by polarized EXAFS is equal to 0.005 Å^2 (26). The lowering of N_{Si} from 4 to 2 in the 1:1 model was compensated by a decrease in the disorder term σ^2_{Si} from 0.006 to 0.0025 Å^2. This last value is anomalously low suggesting that Co atoms are unlikely to have a pure 1:1 local structure. However, due to the low precision on N_{Si} and σ_{Si}, powder EXAFS cannot distinguish a pure 2:1 from a mixed 2:1–1:1 clay local environment.

The previous computations demonstrate that the uncertainty on R_{Si} is much higher than ±0.02 Å as stated by O'Day *et al.* (8) and is closer to the value of ±0.06 Å reported by Scheidegger *et al.* (27). The relatively poor precision on R_{Si}, and more generally on structural parameters of the Si_1 shell (R_{Si}, N_{Si}, σ_{Si}), comes from the facts that this atomic shell not only overlaps with the nearby intense Co_1 shell (Fig. 3), but also that the Co–Co_1 and Co–Si_1 electronic waves are nearly in phase over most of their wavevector range (Fig. 3 in (8)). These features destabilize structural parameters of the Si_1 shell during the fitting procedure (14, 26).

In summary, the formation of $Co(OH)_{2(s)}$ precipitate mixed with some inner-sphere mononuclear Co complexes on quartz (model 2) is not supported by EXAFS data. Rather, these data are consistent with the neoformation of a clay compound having ideally a CoKer-like structure. The uniqueness of this interpretation is assessed below.

DIFFERENTIATING CLAY AND HYDROXIDE STRUCTURES BY EXAFS

Clay Structure

In clays the contribution to EXAFS from nearest Si_1 atoms located in the tetrahedral sheet (Tet) is hidden by the predominant contribution of the octahedral sheet (Oct). Overlap between the contributions of successive atomic shells increases with distance from the central atom. Therefore, with few exceptions (25, 26), the quantitative EXAFS spectral analysis of layered clay minerals essentially has been limited to the three nearest shells (Me–O, Me–Me_1, Me–Si_1) located within ~3.3 Å. Manceau *et al.* (26, 28) recently extended this limit in polarized EXAFS (P-EXAFS) experiments on self-supporting clay films. In a P-EXAFS experiment, the contributions from out-of-plane tetrahedral cations are minimized when the X-ray polarization vector is in the *ab* plane of the layer (parallel orientation) and, conversely, the contributions from octahedral layer cations (Me) vanish when the polarization vector is aligned along the [001]* direction (normal orientation). This

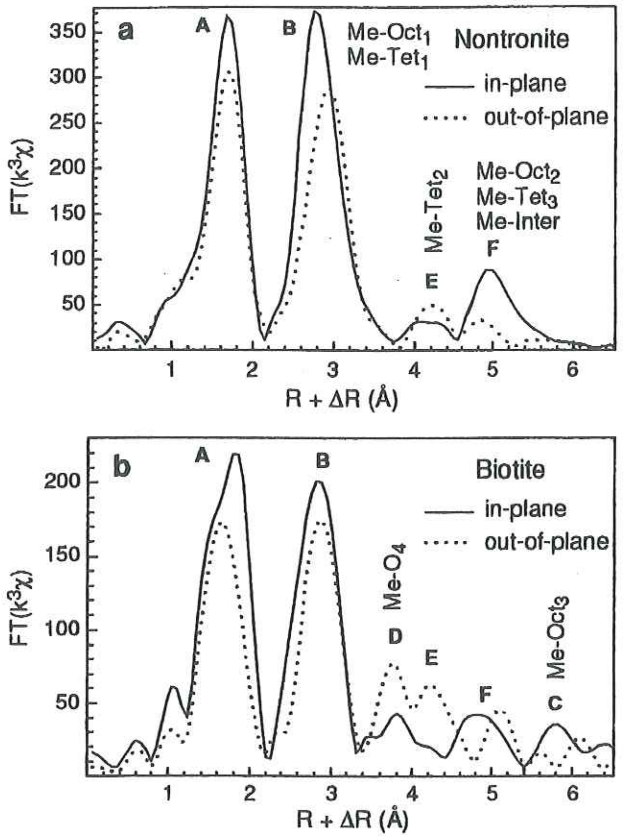

FIG. 6. (a) k^3-weighted polarized radial structure functions at the Fe K-edge for dioctahedral nontronite (a) and trioctahedral biotite (b) in the parallel (full line) and normal (dotted line) orientation.

technique was employed to analyze the nature of higher shell contributions in a trioctahedral biotite and a dioctahedral nontronite smectite (26). P-EXAFS measurements and *ab initio* FEFF7.02 calculations (21) were used to identify the structural origin of the different RSF peaks (Fig. 6). The main conclusions are as follows:

(a) Peak B corresponds to the overlapping contributions of the nearest octahedral (Oct_1) and tetrahedral (Tet_1) shells. The Me–Tet_1 component is selected in normal orientation, and the Me–Oct_1 component is greatly enhanced in the parallel orientation (Fig. 6a). This angular filtering of overlapping contributions increases the precision on N_{Tet1} and N_{Oct1}.

(b) Peak C (Fig. 6b) is located at twice the distance of peak B, and corresponds to the third Oct shell (Oct_3) at $R = 6.2$ Å ($R + \Delta R = 5.8$ Å, Fig. 4b) (8). This peak is amplified in trioctahedral structures (biotite, Fig. 6b) by a shadowing (focusing) MS effect as demonstrated by O'Day *et al.* (25). Conversely, this MS path is absent in dioctahedral structures (nontronite, Fig. 6a) because of the existence of vacancies that break the focusing of the electronic waves (26).

(c) Peak D corresponds to the contribution of the O_4 shell of the tetrahedral basal plane (Fig. 4a, Table 2). This peak is intense in trioctahedral clays (biotite) because basal oxygens are at the same z position and Oct–O_4 distances are coherent. In dioctahedral clays, the O_4 atoms undergo a vertical displacement to relieve the misfit between the octahedral sheet and the attached tetrahedral sheet (29), and this corrugation of the oxygen basal plane splits the Me–O_4 distances causing the disappearance of peak D in the experimental RSFs of nontronite (26).

(d) Peak E originates from the next-nearest tetrahedral shell (Tet_2, Fig. 4a, Table 2).

(e) Peak F originates predominantly from the next-nearest octahedral shell (Oct_2) in the parallel orientation, and from the third-nearest tetrahedral shell (Tet_3) and from interlayer cations in the normal orientation (Fig. 4, Table 2).

These results have several important consequences for the structural interpretation of spectra of layer silicates. In particular, the simultaneous presence of peaks D and E indicates that SiO_4 tetrahedra bridged to a layer of edge-sharing octahedra are not isolated but polymerized to form a clay-like tetrahedral sheet (Fig. 4a). The occurrence of peak D indicates that apical oxygens of SiO_4 units, which are not bonded to Oct cations, form a noncorrugated two-dimensional oxygen framework, i.e., a trioctahedral clay-like structure. Also, peak F contains, among several overlapping shells, the Tet_3 contribution from the ditrigonal SiO_4 ring typical of clay structures (Fig. 4a). Unfortunately, these different tetrahedral contributions are lowered in powder measurements because of the absence of angular amplification of atomic shell contributions. Therefore, the amplitude of spurious side-lobe peaks, generated by the limited k space integration interval during the Fourier transform of EXAFS spectra (22), must be minimized in order to assign the low intensity peaks in the mid-distance range of powder RSFs. This was achieved in the present study by using a Kaiser apodization function, which practically nullifies the intensity of side-lobe peaks (30, 31). For instance, the absence of Fourier transform rippling peaks is seen in Fig. 6a by the lack of features in the [3.4, 3.8 Å] $R + \Delta R$ interval at the bottom of the very intense B peak. Figure 7a shows that, under such spectral treatment, peaks D, E, F, and C are clearly identifiable in the powder RSF of CoKer. Peak C shows up more strongly than in biotite because the octahedral sheet of CoKer is made up only of strongly backscattering Co atoms, whereas in biotite it contains Fe and Mg atoms. Also, the fact that Fe–Fe and Fe–Mg electronic waves are out-of-phase (32) contributes to lessen peak C in biotite.

TABLE 2

Principal Atomic Shells Contributions around Co in $Co(OH)_{2(s)}$ and around Mg in Talc (12, 17)

Talc[a]			$Co(OH)_{2(s)}$		
Shell	*R* (Å)	RSF peak	Shell	*R* (Å)	RSF peak
6 O_1	2.05–2.08	A	6 O	2.10	A
6 Mg_1	3.05	B	6 Co_1	3.17	B
4 Si_1	3.24	B	6 O	3.80	B
2 O_2	3.35	B	6 O_1^{adj}	4.06	G
6 O_3	3.69	B	2 Co_1^{adj}	4.64	H
4 O_4	4.05	D	12 O	4.95	I
4 Si_2	4.45	E	6 O	5.15	I
6 Mg_2	5.29	F	6 Co_2	5.50	J
8 Si_3	5.40	F	12 Co_2^{adj}	5.62	J
6 Mg_3	6.11	C	6 Co_3	6.34	C

[a] In Co-rich kerolite interatomic distances are slightly larger due to the difference of ionic radii between Mg (0.72 Å) and Co (0.745 Å) (99).

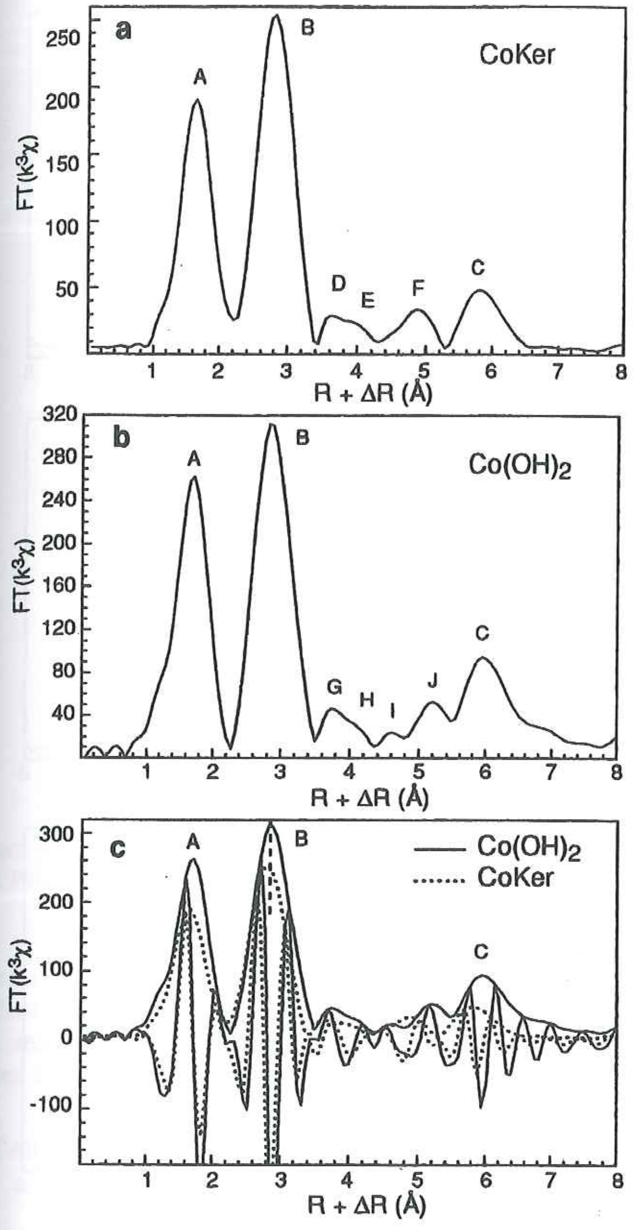

FIG. 7. k^3-weighted radial structure functions at the Co K-edge for Co-rich kerolite (a) and $Co(OH)_{2(s)}$ (b). (c) Modulus (RSF) and imaginary part of the Fourier transform for Co-rich kerolite and $Co(OH)_{2(s)}$.

Hydroxide Structure

The RSF of $Co(OH)_{2(s)}$ (Fig. 7b) is compared to CoKer in Fig. 7c. As expected from the difference of the Co–Co_1 distance in $Co(OH)_{2(s)}$ and CoKer (3.17 vs 3.10 Å), peak B is shifted to a higher distance in $Co(OH)_{2(s)}$. The higher distance peaks bear distinctive features between hydrous silicate and hydroxide frameworks. Peak C obviously arises from MS paths between Co–Co_3 pairs as in CoKer (Fig. 4b). *Ab initio* FEFF7.02 calculations showed that peaks G to J result predominantly from the single scattering (SS) contribution from nearest O (peak G) and Co (peak H) atoms of adjacent layers located at $R = 4.06$ and 4.64 Å, from layer oxygens at 4.95–5.15 Å (peak I), and from the layer Co_2 shell at 5.50 Å plus the next nearest Co shell from adjacent layers at 5.62 Å (peak J, Figs. 4b and 4c, Table 2). $Co(OH)_{2(s)}$ has a one layer close-packed hexagonal structure, and the mutual arrangement of successive layers can be described by the notation A, B, and c in which capital letters stand for unequivalent crystallographic sites occupied by OH groups, and the lowercase letter for the positions of Co (Fig. 4c). The one layer stack can be denoted . . . AcB–AcB–AcB . . .. Anions from successive layers form an empty octahedron (B–A stack) so that Co atoms are surrounded by 3 O_1^{adj} from the lower sheet (B) and 3 O_1^{adj} from the upper sheet (A) of adjacent layers (peak G). Cation sheets are instead juxtaposed vertically (. . . ccc . . .), and each Co is therefore neighbored by 2 Co_1^{adj} of adjacent layers (peak H, Fig. 4c, Table 2). Manceau *et al.* (28) first documented this capacity of EXAFS to identify atoms located in adjacent layers by P-EXAFS experiments and FEFF7.02 simulations on CoOOH self-supporting films.

Comparison of the Fourier Transforms for $Co(OH)_{2(s)}$ and CoKer

The previous analysis showed that layer hydroxide and silicate frameworks have a distinct mid-range structure. Peaks D and G both arise from oxygens at similar distances, but peak E (in CoKer) originates from Si_2 atoms at ~4.5 Å and peak H (in $Co(OH)_{2(s)}$) from Co_1^{adj} atoms at 4.64 Å, so that the Co–Si_2 and Co–Co_1^{adj} waves should have a different phase. Also, peak J in $Co(OH)_{2(s)}$ results only from Co atoms (Co_2 + Co_2^{adj}) whereas peak F in CoKer contains contributions from Co (Co_2) and Si (Tet_3) atoms (Figs. 4 and 7a, Table 2). Consequently, these two structures should and do yield a discernible signal in the [3.8, 5.4 Å] $R \pm \Delta R$ interval (Fig. 7c). The oscillating curve is the imaginary part of the FT, and the envelope of this curve is the amplitude or RSF (RSF = $[\mathrm{Im(FT)}^2 + \mathrm{Re(FT)}^2]^{1/2}$). The imaginary parts of peak A are superposed because Co–O distances are identical in the two structures (2.08–2.10 Å), while those of peaks B and C possess the same frequency but are shifted in position due to the difference of Co–Co_1 and Co–Co_3 distances in $Co(OH)_{2(s)}$ and CoKer. The two imaginary parts have a complex and very different shape in the [3.8, 5.4 Å] $R + \Delta R$ interval, thereby allowing reliable fingerprinting of hydroxide and layer silicate structures. It should be emphasized that the unique imaginary part frequency of CoKer in this mid-distance range arises directly from the contributions of the Si_2 and Si_3 shells so that it can be used to trace the existence of a two-dimensional SiO_4 corner-sharing ring typical of clay structures (Fig. 4a).

STRUCTURAL EVIDENCE FOR THE NEOFORMATION OF A Co/CLAY IN Co-SORBED QUARTZ

The Fourier transform of the full EXAFS spectrum for Co/quartz (Fig. 2) closely resembles that of the Co/clay reference over the entire $R + \Delta R$ range (Fig. 8). Specifically, the similarity in mid-range wave frequency (Fig. 8c) is compelling evidence that the local atomic environment around sorbed Co is identical to that in a layered trioctahedral clay.

The specific mid-range structure of clays in R space should be also recognizable in reciprocal k space, and it is interesting to determine what sort of peculiar feature this structure gives rise to in the full EXAFS spectrum. We performed an inverse Fourier transform (FT^{-1}) of real and imaginary parts by choosing two types of $R + \Delta R$ windows. The FT^{-1} was initially performed in the [0–10 Å] interval in order to test that our Fourier transformation code satisfies Fourier's inversion theorem, which states that the FT^{-1} restores the initial spectrum, i.e., that the $k \rightarrow R \rightarrow k$ double Fourier transformation does not lower the wave amplitude or, worse, create spurious spectral features. Fourier filtered EXAFS spectra for CoKer and Co/quartz are barely distinguishable from raw spectra (Figs. 9a and 9b). The only difference is that the recalculated spectrum for Co/quartz is less noisy because the double Fourier transformation eliminated the high-frequency part of the statistical noise in the [10–∞ Å] $R + \Delta R$ range. The FT^{-1} was then performed in the [0–3.4 Å] + [5.3–10 Å] interval. Omitting the mid-range contribution significantly modifies the shape of EXAFS spectra ($k^3\chi$) in the 4–5 $Å^{-1}$ range and also appreciably changes the amplitude of the main oscillations (Figs. 9c and 9d). The [3.4–5.3 Å] FT^{-1} was also computed (Fig. 9d) and is identical to the difference between $k^3\chi_{exp}$ and $k^3\chi$ ([0–3.4 Å] + [5.3–10 Å]) as a result of the additivity property of the Fourier transform. The amplitude of $k^3\chi$ ([3.4–5.3 Å]) is highest near $k = 4–5\ Å^{-1}$ and then decreases above this range. The k dependence of the wave amplitude indicates that this sine function has a *structural* origin because if it were noise the amplitude would have increased with k. This numerical analysis demonstrates that the spectral differences observed between $k^3\chi_{exp}$ and $k^3\chi$ ([0–3.4 Å] + [5.3–10 Å]) are significant, and it provides additional proof that the [3.4–5.3 Å] $R + \Delta R$ region contains meaningful structural information.

The spectral differences (Fig. 2a) observed between $Co(OH)_{2(s)}$ and Co-sorbed quartz can now be explained in structural terms. The spectral dissimilarities in the 4–5 $Å^{-1}$ range pertain to the distinct mid-range structures of these two compounds. In $Co(OH)_{2(s)}$ the shoulder at 4 $Å^{-1}$ decreases in amplitude and moves to higher k values when the [3.4–5.4 Å] $R + \Delta R$ contribution is eliminated (data not shown). The second major spectral difference is the higher frequency of the EXAFS signal for $Co(OH)_{2(s)}$, which stems from the larger Co–Co distances in hydroxide than in layer silicate structures (3.17 Å vs 3.10 Å and 6.34 Å vs 6.20 Å). The difference in phase is more pronounced at high k because of the higher weight of Co–Co pairs in this wavevector range.

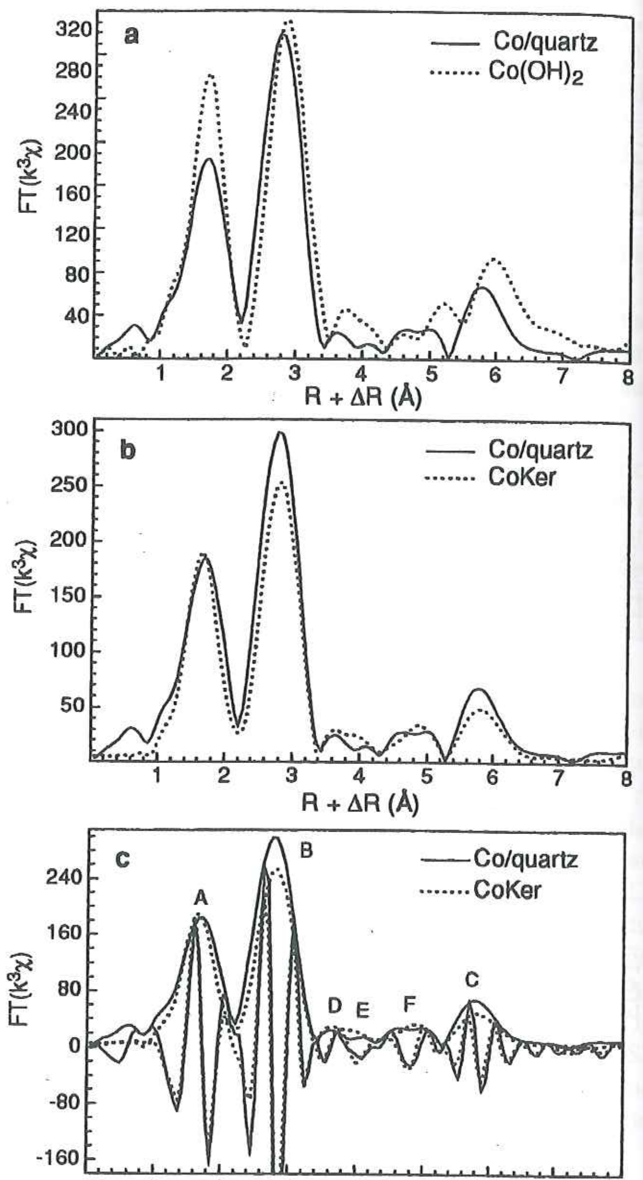

FIG. 8. k^3-weighted radial structure functions at the Co K-edge for Co/quartz compared to $Co(OH)_{2(s)}$ (a) and to Co-rich kerolite (b). (c) Modulus (RSF) and imaginary part of the Fourier transform for Co-rich kerolite and Co/quartz ($\Gamma = 9.21\ \mu mol/m^2$).

In conclusion, Co atoms polymerize in the form of an edge-sharing layer framework bridged to a two-dimensional silica framework as in 2:1 and 1:1 clay structures (Fig. 1a) when they sorb on quartz, and this occurs regardless of the surface coverage ($0.77 < \Gamma < 9.21\ \mu mol/m^2$). To corroborate this structural interpretation, chemical evidence for the preferred formation of Co clays is presented next.

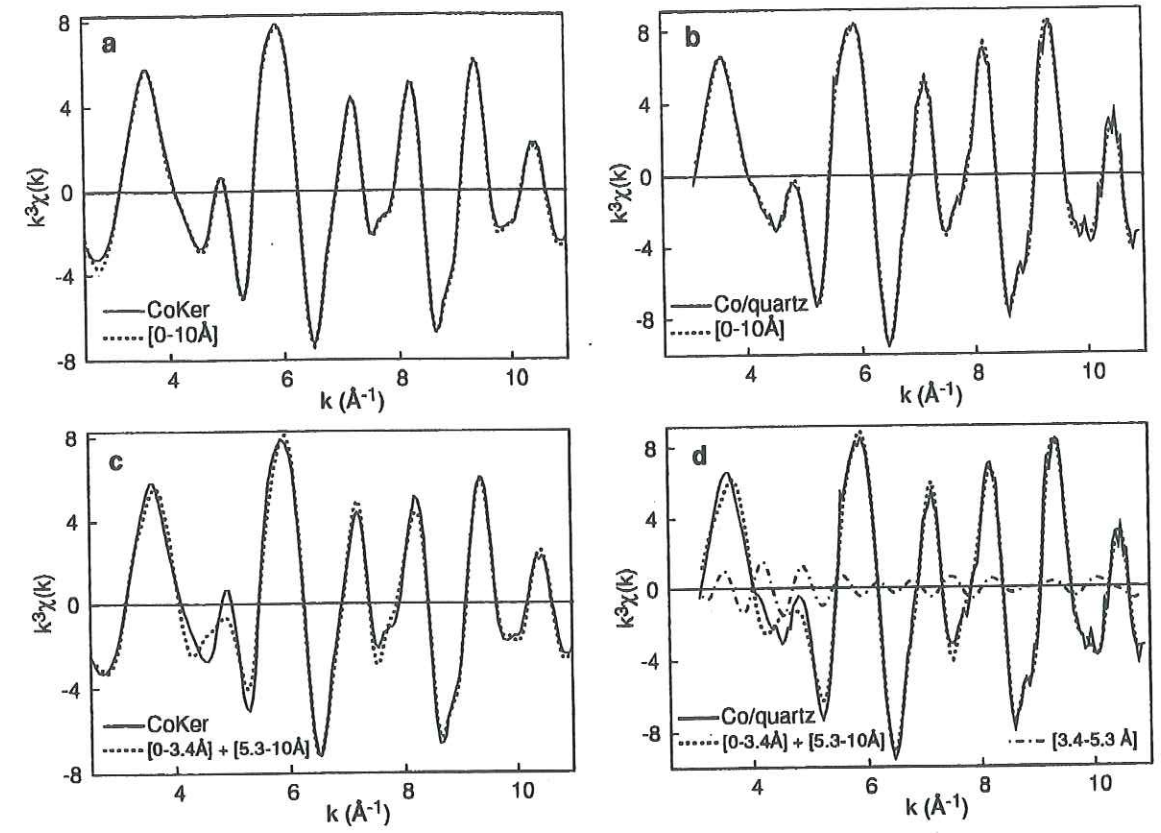

FIG. 9. Raw k^3-weighted Co K-edge EXAFS spectra for Co-rich kerolite and Co/quartz compared to Fourier filtered spectra. The $R + \Delta R$ interval of the back Fourier transform is equal to [0–10 Å] in (a) and (b) and to [0–3.4 Å] + [5.3–10 Å] in (c) and to [0–3.4 Å] + [5.3–10 Å] and [3.4–5.3 Å] in (d).

STABILITY OF Co-CONTAINING PRECIPITATES AND FORMATION MECHANISM OF Co/CLAYS

The system of Co/clays, CoKer, Co/Chrysotile (CoChrys), and Co/Stevensite (CoStev), is an analogue to the naturally occurring Mg layered silicates common in alkaline lake environments (33). For example, Khoury *et al.* (34) and Eberl *et al.* (35) discussed solid and solution evidence for formation of mixed-layer kerolite/stevensite in the Amargosa Desert, Nevada. Reports of stevensite formation on diatoms in alkaline lakes also provide evidence for nucleation of these types of clays on silica phases in nature (36). These observations are consistent with our reinterpretation of the EXAFS data. We have calculated theoretical stabilities of the Co/clays, and compared these calculated solubilities along with the measured solubility of $Co(OH)_{2(s)}$ (37) to the experimental solution compositions reported in O'Day *et al.* (8). We also performed a set of experiments to measure Si dissolution from quartz under experimental conditions similar to those of O'Day *et al.* (8) in order to better assess the stability of Co/clays. Finally, using the theoretical and experimental results we evaluate possible mechanisms of Si incorporation into a Co/clay phase.

Experimental Determination of Silica Release Rates from Quartz

Experimental methods. The experimental design was modeled after that of O'Day *et al.* (8). The quartz was from the same lot as the quartz sand used by Rimstidt and Barnes (3) (H. Barnes, personal communication). Quartz was washed in 4 N HCl ten times for a total period of 8 h at 60 ± 10°C to simulate the extensive acid washing in the published study. The quartz was rinsed 25 times in deionized water and then dried in an oven at 65°C for 2 weeks. The surface area of the quartz was 0.206 m^2/g as determined by BET N_2 adsorption using a Micromeritics surface area analyzer. $Co(NO_3)_2$, $NaNO_3$, and NaOH solutions were prepared from ACS reagent-grade salts and 18 MΩ/cm deionized water. pH was measured using a glass Ross combination electrode calibrated against buffers traceable to NIST (National Institute of Standards and Technology). pH measurements took place within 5–10 min after opening the experiments, and under a headspace of $N_2(g)$. Estimated accuracy of the pH measurements is ±0.05 pH units. Some drift in pH was observed over a measurement period of

TABLE 3

Quartz Dissolution Rates in the Presence of Co for Experiments of This Study

Exp. number	Solid/liq (m^2/L)	$[Co]_{init}$ (μM)	$[Co]_{final}$ (μM)	pH_f (pH_i)	Γ ($\mu mol/L$)	Equil. time[a] (h)	Duration[b] (h)	$[Si]_{final}$ (μM)	Si diss. rate ($mol/m^2/s$)
QCo1	39.0	664	658	6.70 (7.67)	0.154	52.27	95.20	138	1.0310^{-11}
QCo2	39.0	664	655	6.80 (7.83)	0.231	48.98	92.00	145	1.1210^{-11}
QCo3	39.0	664	630	7.18 (8.45)	0.871	43.55	86.75	140	1.1510^{-11}
QCo4	39.0	0	0	[c]	0	0	16.85	20	8.3710^{-12}
QCo5	39.0	0	0	6.85 (7.48)	0	0	92.58	137	1.0410^{-11}
QCo6	0	664	666	7.15 (7.69)	0	51.00	93.70	0	0
QCo7	39.0	664	665	[c]	0	0	40.67	51	8.9310^{-12}
QCo8[d]	39.0	664	627	6.51	0.949	94.03	143.53	198	9.8310^{-12}
QCo9[d]	38.6	1314	1283	7.28	0.803	48.37	97.97	140	1.0310^{-11}
QCo10[d]	38.6	1314	1290	6.55	0.622	94.30	143.88	186	9.310^{-12}
QCo11[d]	77.2	1314	1291	5.90	0.298	48.33	98.05	203	7.4510^{-12}
QCo12[d]	39.2	337	237	7.29	2.55	92.68	142.45	158	7.8710^{-12}
QCo13[d]	24.8	337	228	7.55	4.40	92.97	142.80	115	9.010^{-12}

[a] Time during which experiment equilibrated after addition of NaOH.

[b] Total duration of experiment, including pre-equilibration with 0.1 M $NaNO_3$ and $Co(NO_3)_2$.

[c] pH was not raised by addition of NaOH.

[d] Initial pH was not measured after addition of NaOH.

20 min. Si was measured using the molybdate blue method (38) and a Bausch and Lomb Spectronic 501 UV–visible light spectrophotometer with an uncertainty of ±3%. Si standards were prepared with a spectroscopic standard, but without the $NaNO_3$ matrix. Co was determined using inductively coupled plasma atomic emission spectroscopy (ARL 3410+) with an uncertainty of ±3%. Co standards were prepared using a spectroscopic standard and a matrix of 0.1 M $NaNO_3$.

The experiments were performed similarly in terms of an initial equilibration of quartz in 0.1 M $NaNO_3$ for 15 to 17 h, equilibration with added $Co(NO_3)_2$ for 24 h, and a final reaction period initiated by raising the solution pH using NaOH. All experiments were conducted at room temperature, 22.4 ± 0.4°C. The final period during which pH was raised varied in length from 46 to 97 h. Solid surface area to solution ratios ranged from 25 to 77 m^2/L, 13 to 41% of the values in O'Day *et al.* (8). Experiments were carried out in 50 mL plastic test tubes in which the solutions were sparged with $N_2(g)$ for 10 min prior to adding the $Co(NO_3)_2$. After addition of the $Co(NO_3)_2$, the headspace in the test tubes was flushed with $N_2(g)$ and the test-tubes were cap-sealed with Teflon tape. The test tubes were rotated 360° on a LabQuake rotator turning at approximately 8.5 revolutions/min. We did not raise solution pH significantly above the solubility curve of $Co(OH)_2$ at any Co concentration. Most experiments were maintained below $Co(OH)_2$ solubility.

Experimental results. Results are shown in Table 3. Because the surface area to solution ratio was lower in our experiments and because the pH was not raised very high, the measured drop in Co concentration was smaller than in the experiments of O'Day *et al.* (8), and in a number of cases statistically immeasurable. However, for experiments with measurable Co sorption, calculated surface coverages are similar to those reported by O'Day *et al.* (8).

The primary result is that Si concentrations rose to near or slightly above quartz solubility within the maximum reaction time of 144 h. Calculated Si dissolution rates are constant with time and average 9.5 ± 1.3 × 10^{-12} $mol/m^2/s$. There is no statistically significant dependence of the Si dissolution rate on either pH or Co concentration. For cases with measurable sorption, Co sorbed quickly upon raising solution pH and then remained at a constant concentration in solution. In all experiments, the pH of the solution decreased with time.

The dissolution rate of Si is ~7 times higher than the highest reported dissolution rates for quartz (39) at 23 to 25°C and near the highest value reported for the dissolution rate of fused silica powder at 25°C (3). This may occur because the surface is behaving as though it were amorphous silica, probably because of the extensive acid pretreatment. The pH of the solution in QCo1-3 and QCo5 after contact with 8.84 g of quartz for 41–43 h was 4.85 to 4.88 vs 5.60 in the similar experiment without quartz. The continued decrease in pH over time in experiments with quartz may be explained either by clay formation or by diffusion of residual acid outward the surface layer into the solution.

Dissolution Equilibria for Solubility of Co/Clays and Co(OH)₂

The solubilities of CoKer ($Co_3Si_4O_{10}(OH)_2$), CoChrys ($Co_3Si_2O_5(OH)_4$), and CoStev ($NaCo_{2.5}Si_4O_{10}(OH)_2$) were calculated using the free-energy approach of Tardy and co-workers (40–43) (Appendix).

To our knowledge, the solubility product (K_{CoKer}) of the CoKer dissolution reaction,

$$Co_3Si_4O_{10}(OH)_2 + 6\ H^+ + 4\ H_2O \rightarrow 3\ Co^{2+} + 4\ Si(OH)_4, \quad [1]$$

has not been determined experimentally. Our calculations lead to $\log(K_{CoKer}) = 15.1 \pm 3.7$ for poorly ordered CoKer. K_{CoKer} alternatively can be estimated by writing Eq. [1] as the sum of two reactions, the first involving the replacement of Co by Mg in the kerolite framework, and the second describing the dissolution of Mg-rich kerolite:

$$Co_3Si_4O_{10}(OH)_2 + 3\ Mg^{2+} \rightarrow Mg_3Si_4O_{10}(OH)_2 + 3\ Co^{2+} \quad [2]$$

$$Mg_3Si_4O_{10}(OH)_2 + 6\ H^+ + 4\ H_2O \rightarrow 3\ Mg^{2+} + 4\ Si(OH)_4. \quad [3]$$

Hence, K_{CoKer} can be written as the product of the Co–Mg partition constant, $K_{Co\text{-}Mg}$ (stability constant for Eq. [2]) and the solubility product of Mg-rich kerolite, K_{MgKer} (Eq. [3]). Taking $K_{Co\text{-}Mg} = 10^{-9.21}$ (44) and $K_{MgKer} = 10^{25.79}$ (45), $\log(K_{CoKer})$ equals 16.6. This value lies within the uncertainty range of the constant calculated by the method of Tardy and co-workers (15.1 ± 3.7). In the following discussion K_{CoKer} will be taken to be $10^{15.1\pm3.7}$.

Likewise, the solubility of CoChrys according to the reaction

$$Co_3Si_2O_5(OH)_4 + 6\ H^+ \rightarrow 3\ Co^{2+} + 2\ Si(OH)_4 + H_2O \quad [4]$$

was determined to be $10^{22.2}$ by the free energy method of calculation. The solubility of CoStev for the reaction

$$NaCo_{2.5}Si_4O_{10}(OH)_2 + 6\ H^+ + 4\ H_2O \rightarrow Na^+ + 2.5\ Co^{2+} + 4\ Si(OH)_4 \quad [5]$$

was determined to be $10^{19.2}$. CoStev is a likely clay phase because the Co-sorption experiments were carried out in 0.1 M $NaNO_3$ solutions. Na sorbs onto amorphous silica with a sorption edge at pHs between 6 and 7 at 25°C for 0.001 and 0.01 M solutions (46). These data suggest that in 0.1 M $NaNO_3$, Na would also sorb onto quartz and be available for incorporation into a clay structure.

The relative stability of $Co(OH)_{2(s)}$ and Co/clays during the sorption experiments can be obtained by determining the solubility (i.e., the saturation concentration) of Co with respect to the solids as a function of pH. However, the solubility of Co with respect to the Co/clays depends on the activity of both H^+ and $Si(OH)_4$. Since O'Day *et al.* (8) did not measure dissolved Si, the solubilities for the Co/clays were calculated for two cases (Fig. 10): (a) the concentration of $Si(OH)_4$ is fixed by the congruent dissolution of the Co/clays, and (b) the concentration of $Si(OH)_4$ is at saturation with respect to quartz, i.e., $[Si(OH)_4] = 183\ \mu M$ at 25°C (2), this last choice being substantiated by the high concentrations of dissolved Si measured in our own experiments. For each case, activity coefficients were calculated using the Davies equation and assuming a 0.1 M $NaNO_3$ background (47). Plots of aqueous Co concentration (Fig. 10) show that all three Co/clays have a much lower solubility than pink $Co(OH)_{2(s)}$ below pH 9. Additional calculations for various values of $[Si(OH)_4]$ showed that the solubility of Co becomes higher for CoKer than for pink $Co(OH)_{2(s)}$ only when $[Si(OH)_4] < 5\ \mu M$, which is well below the solubility of quartz.

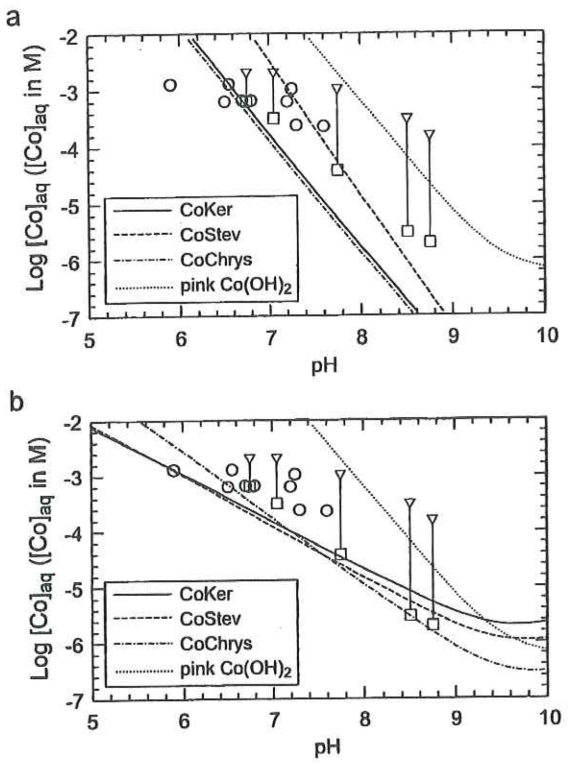

FIG. 10. Saturation concentration (M) of Co with respect to pink stable $Co(OH)_{2(s)}$ (dotted line) and to various Co/clays: Co-rich kerolite (CoKer), Co-rich stevensite (CoStev), and Co-rich chrysotile (CoChrys). (a) $[Si(OH)_4]$ = 183 μM controlled by quartz solubility at 25°C. (b) $[Si(OH)_4]$ controlled by congruent solubility of the Co/clays. Triangles and squares refer respectively to the (hypothetical) initial and final chemical conditions for the preparation of sorption samples of O'Day *et al.* (8). Open circles refer to the sorption samples obtained in this paper.

Thermochemical Evidence for the Precipitation of a Co/Clay-like Compound

The next step of this analysis consists in placing the Co sorption samples studied by O'Day *et al.* (8) in the $[Co]_{aq}$ = f(pH) equilibrium diagram. Initial sorption pH (pH_i) values are not available, but they must be greater than final pH values (pH_f, Table 1) because the sorption of Co or the formation of a Co-containing solid both result in an acidification of the supernatant. Therefore, pH_i is bounded at low pH by pH_f and we decided to choose $pH_i \approx pH_f$ for the representation of the initial chemical conditions. Samples A, B, and C of O'Day *et al.* (8) are not represented because final Co concentrations were below their detection limits. Figure 10 shows that Co was initially sorbed from solutions greatly oversaturated with respect to CoKer, and at a minimum slightly undersaturated or oversaturated with respect to $Co(OH)_{2(s)}$. This conclusion is valid even if pH_i is increased by ~0.5 to 1 unit. The *final* solutions are all undersaturated with respect to $Co(OH)_{2(s)}$ and are oversaturated or near saturation with respect to the Co/clays. This analysis of the thermodynamic stabilities of secondary Co precipitates clearly supports the interpretation of Co/clay formation determined by reassessing the EXAFS data.

Our new experimental data also indicate supersaturation or near saturation with respect to the Co/clays and undersaturation with respect to $Co(OH)_{2(s)}$ (Fig. 10). Although EXAFS spectra were not obtained for these samples and Co sorption was not universally demonstrated, the solution analyses provide support for the hypothesis that measurable Si was present in the solutions of O'Day *et al.* (8).

The solubility curves for the Co/clays in Fig. 9 were plotted for dissolved silica concentrations at equilibrium with respect to quartz. Such a high Si concentration is compatible with the fast dissolution rates observed for our acid-treated quartz. However, a number of experiments have shown that this saturation concentration is attained only after several years of reaction for clean quartz surfaces (2, 3, 48). In the next section, we discuss how such a high dissolved Si concentration relates to the formation mechanism of the clay.

Mechanism of Si Incorporation in the Co/Clay

The amount of Si required to form Co/clay in the experiments of O'Day *et al.* (8) was calculated from the Co surface excess by assuming a Co:Si ratio equal to the stoichiometric ratio in CoKer, i.e., 3:4. This amount is rather high, reaching 2244 μM for $\Gamma = 9.21\ \mu mol/m^2$ (Table 1). Si must come either from silanol groups in the quartz surface or from dissolved Si. The quantity of dissolved Si within the time scale of the sorption experiments of O'Day *et al.* (8) can be estimated either from our measured dissolution rates ($\approx 10^{-11}$ mol/m²/s) or from quartz dissolution rates measured in the absence of hydrolyzable cations. These rates range from 10^{-12} mol/m²/s at pH 7.0 to 10^{-11} mol/m²/s at pH 11 for reaction times between 50 and 300 h (49), and drop by one order of magnitude after 400 days (39). The total amount of dissolved Si for a reaction time of 42 h plus a minimum pre-equilibration time of 12 h ($\Gamma = 9.21\ \mu mol/m^2$) is thus between 36 (rate of 10^{-12} mol/m²/s) and ~380 μM, which is much less than the amount of Si needed to incorporate all of the adsorbed Co in the form of Co/clay (2244 μM for $\Gamma = 9.21\ \mu mol/m^2$). A number of hypotheses might explain this difference. The first set is related to the formation of a Co/clay coating at the quartz surface, or within an amorphous surface layer. The second set is related to the precipitation of Co/clay in solution and requires enhanced dissolution of quartz.

The apparent paradox between clay neoformation and deficit of Si released by quartz dissolution can be explained by assuming that the clay coating forms at the quartz–water interface. The harsh acid treatment at 65°C performed by O'Day *et al.* (8) likely altered and disorganized the quartz surface through protonation and hydrolysis of Si–O–Si bonds. For instance, a thick (>1000 Å) surface layer of amorphous silica formed upon leaching chain silicates at pH 2, within which reconstructed linkages of Si tetrahedra were observed by HRTEM (50). Linked Si tetrahedra also have been observed by HRTEM and XRD in the surfaces of weathered natural glasses (51). In pure water Vigil *et al.* (52) and Axelos *et al.* (53) demonstrated that the surface of silica reconstructs to a 20 Å thick siliceous gel. Therefore, sorbed Co^{2+} may diffuse into the amorphous layer and form a (Co, Si) gel which rapidly transforms into a clay phase (Fig. 1a) upon aging (44, 54). The highest experimental surface coverage reported by O'Day *et al.* (8) (9.21 μmol/m², Table 1) is also consistent with the formation of a Co/clay coating at the quartz surface stricto sensu. Indeed, the surface density of Co in a clay surface layer is equal to $6/(a \cdot b) = 6/(b^2/\sqrt{3}) = 12.01$ atoms/nm², or 20.75 μmol/m², and is thus more than double 9.21 μmol/m². Therefore, in O'Day *et al.*'s (8) experiments, the total surface of quartz grains was high enough to allow the formation of a clay surface coating, especially at the highest Co concentration. The formation of a protective Co/clay coating would passivate the quartz surface and slow its dissolution. Surface passivation by a hydrolyzable metal ion may explain the inhibition of quartz crystal growth observed by Brown and Thomas (55). It is also consistent with the observation that divalent metal cations such as Zn^{2+}, Cu^{2+}, and Be^{2+} slow dissolution rates of glass and diatoms (56–58).

The alternate hypothesis of Co/clay formation in solution requires the dissolution rate of quartz to be higher than values reported in the literature. Several distinct mechanisms may enhance dissolution. First, Co^{2+} may accelerate dissolution through direct interaction with the quartz surface. Co would sorb onto silanol surface groups and promote the detachment of these groups from the quartz surface by polarizing the chemical bonds. This adsorption-promoted dissolution mechanism was proposed by Espinose de la Caillerie *et al.* (59) for the enhanced dissolution rate of γAl_2O_3 in the presence of Ni^{2+}. They quantified the effect of Ni^{2+} by sealing γAl_2O_3 in a dialysis bag and adding Ni^{2+} outside the bag. After two weeks of reaction, they found that the total concentration of Al outside the bag amounted to 370 μM, whereas in the absence of Ni^{2+} this amount was as low as 0.74 μM. Second, rapid dissolution rates are observed in suspensions that are highly undersaturated with respect to dissolved species (49, 60–62). For example, Van Cappellen and Qiu (63) found that the dissolution rate of biogenic silica (diatoms) increased, sometimes by one order of magnitude, when the concentration of dissolved Si decreased from 20 to 5% of the saturation concentration. If the concentration of dissolved Si remains low, then the dissolution rate may remain high and provide a continuous source of Si for the growing Co/clay nuclei. Third, the quartz loads used by O'Day *et al.* (8) were unusually high, up to 240 g/L. Agitation of these suspensions inevitably would have led to abrasion of the quartz grains producing freshly broken and highly reactive surfaces. This mechanical effect may have increased the dissolution rate at the surface of quartz (3).

In summary, two distinct molecular-level mechanisms of clay neoformation, formation within the quartz–water interface and precipitation from solution, are consistent with available macroscopic and microscopic data. It is important to emphasize that in neither of these two mechanisms the solubility of quartz is attained, as true equilibrium takes several years to be reached (39). In fact, the concentration of dissolved Si is likely controlled by reactions in a multiphase system. In such a system the Si concentration is controlled neither by pure quartz nor by a pure Co/clay, but rather by the two simultaneous reactions of silica dissolution and clay formation.

DIFFERENTIATING HOMOGENEOUS FROM HETEROGENEOUS PRECIPITATION

Five uptake mechanisms that partition elements between aqueous and solid phases have been identified and characterized in the past decade using noninvasive spectroscopic and structural techniques (Fig. 11):

(a) Outer-sphere surface complexation (OSC). The sorbate ion and its hydration sphere are retained at a charged surface within the diffuse ion swarm by electrostatic interactions (64, 65).

(b) Isolated inner-sphere surface complexation (ISC). Sorbate cations or oxyanions bond separately to the surface by sharing one or several ligands (generally oxygens) with one or several cations from the sorbent (7, 66–74). Sorbed ions then may be incorporated progressively in the sorbent structure during crystal growth (75).

(c) Multinuclear surface complexation (MSC). Sorbate ions polymerize on the substrate, which acts as a structural template for the heteroepitaxial overgrowth (76, 77). The two phases may be chemically bonded as in Fig. 11a, or they may maintain contact by electrostatic interactions, hydrogen bonds, or Van der Waals forces. But in both cases, anionic frameworks of the substrate and the surface precipitate are coherently oriented (Fig. 11b). The multinuclear surface complex may form an epitaxial solid-solution (mixed-solid) if the sorbent and sorbate grow simultaneously or a mixed-layered intergrowth (78). Mixed-layering occurs in many minerals including manganese oxides, such as lithiophorite (interlayered MnO_2–$Al(OH)_{3(s)}$ (79)), and Ni-rich asbolane (interlayered MnO_2–$Ni(OH)_{2(s)}$ (80)), clay minerals such as rectorite and corrensite (81), and in the valleriite group of minerals where sulfide and brucitic layers alternate regularly (82).

(d) Homogeneous precipitation (HP). A new phase may precipitate in solution and then be deposited onto the substrate to form a surface coating (6, 50, 83, 84). The precipitated phase may incorporate species dissolved from the substrate, in which case the mechanism may be called "dissolution-induced homogeneous precipitation" (DI-HP).

(e) Lattice Diffusion (LD). The sorbate diffuses into the sorbent, filling vacancies or substituting for sorbent atoms (31, 85–88).

Differentiating these uptake or precipitation mechanisms is important because chemical species sorbed by distinct sorption phenomena generally would be remobilized by distinct chemical processes. For instance, a cation entrapped in a bulk structure eventually may be remobilized by decreasing its concentration in solution if it sorbed through a LD mechanism. But if it has been buried during crystal growth (ISC), then its remobilization necessitates the dissolution of the sorbent phase. Distinguishing these various surface processes is difficult and requires combining solution chemistry and mineral surface structural studies in their most advanced application.

The first source of complexity comes from the protocol used to sorb cations in a suspension and the interpretation of chemical results. Previous investigators (76, 84, 89) showed that the formation of highly reactive polymers and mixed hydroxides, for which thermodynamic data may be lacking, is possible. A neoformed phase may precipitate on the surface (MSC) if the energetics at the sorbent–precipitate interface are favorable or in solution if its solubility product is reached (HP). Solution chemistry alone fails at differentiating the processes because the heterogeneous and homogeneous precipitates have the same solubility (76, 84). Also, multiple rate-limited reactions may control solution compositions. In this study, it was not possible to conclude from the available data whether neoformation of Co/clay resulted from a DI-HP or MSC mechanism. However, precipitate nuclei are thought to have a lower interfacial energy on the surface than in solution and, therefore, MSC should be favored over HP (84, 90). Careful experimentation in which all chemical species are monitored and better information on the solubilities of secondary precipitates are needed.

The second source of complication comes from EXAFS spectroscopy, which cannot always be used to distinguish an adion coordinated to the surface from a species that is not and, consequently, to differentiate MSC from DI-HP phenomena. This limitation explains the lack of a definitive conclusion regarding the mechanism of Co sorption on quartz and silica (5). According to Towle *et al.* (84) the only conclusive EXAFS evidence of true MSC concerns the sorption of Cr^{3+} on hydrous ferric oxide (HFO) and goethite (76). Cr^{3+} atoms were shown to have a mixed structure representing that of the bulk sorbent

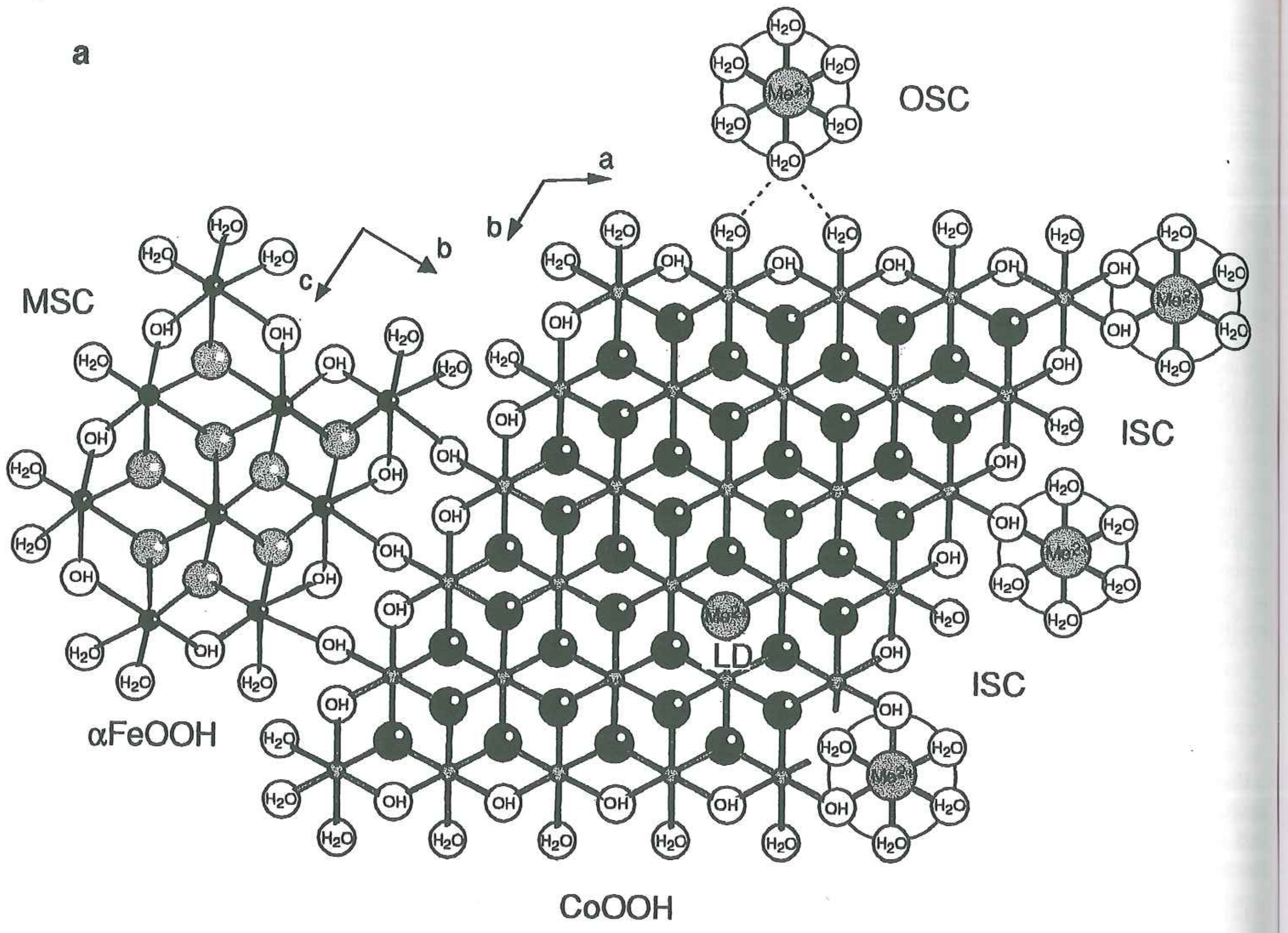

FIG. 11. Schematic representation of the different surface sorption processes. (a) Projection of the CoOOH structure in the *ab* plane. MSC, multinuclear surface complexation represented by an epitaxy of αFeOOH; ISC, mononuclear monodentate and bidentate, and binuclear bidendate inner-sphere complexation; OSC, outer-sphere surface complexation; LD, lattice diffusion. (b) Example of epitaxy without sharing of oxygens. The . . .AB–AB. . . close-packed anionic layer sequence of $Co(OH)_{2(s)}$ is coherently stacked on the . . .AB–BC–CA. . . layer sequence of CoOOH. $Co(OH)_{2(s)}$ has a 1H polytypic structure, and CoOOH a 3R. Small circles are H.

αFeOOH and a precipitate of γCrOOH local structure, even though the solution was undoubtedly undersaturated with respect to γCrOOH (76). Without such experimental evidence in any study, the designation of "*surface*" complex is unsupported.

Heteroepitaxy per se can be demonstrated by polarized EXAFS experiments on single crystal or on highly textured self-supporting films of fine grained layered minerals (28, 91). The angular dependence of the metal sorbate–metal sorbent pair contribution is given by

$$\chi_j(k, \theta) = 3 < \cos^2\theta_j > \chi^j_{\text{iso}}(k),$$

where j denotes the atomic pair, θ_j is the angle between the electric field vector (ϵ) and the sorbate–sorbent pair, and χ_{iso} is the isotropic (i.e., for a nonoriented powder) EXAFS contribution. If the sorbate complex is overgrown on the surface, then the contribution of the sorbate–sorbent pair will be modified by varying the angle between the substrate and ϵ. The orientation of the metal sorbate–metal sorbent pair with respect to the substrate can be obtained in favorable cases from the quantitative analysis of angular spectra. This technique has been used to investigate the sorption mechanism of Co on the phyllomanganate birnessite (31) and on smectitic clays (11). For the first time, direct structural evidence has been obtained for the formation of a monomeric inner-sphere surface complex on the layer edges of smectite. This technique also can be used to study multinuclear surface layers coherently stacked on the substrate, because it allows the detection of sorbent cations located on the other side of the interlayer space as shown in Fig. 4c for $Co(OH)_2$ and by Manceau *et al.* (28) for CoOOH. Unfortunately, this method cannot be applied to wet pastes and suspensions.

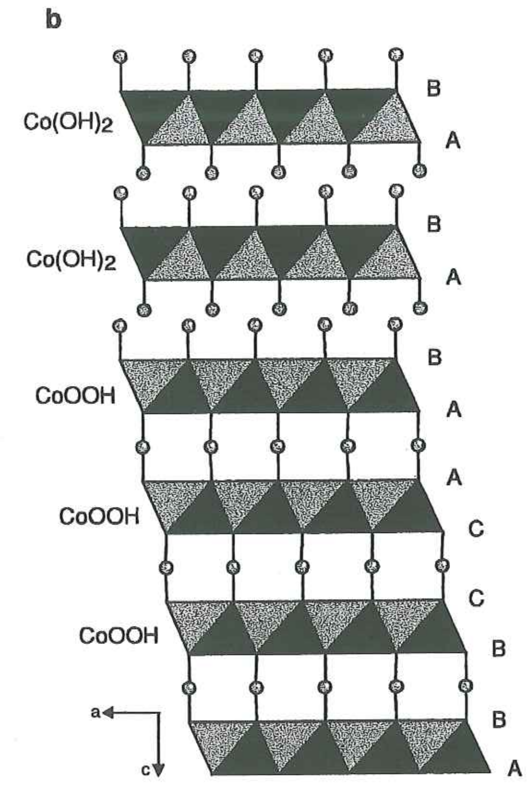

FIG. 11—*Continued*

The best way to discriminate MSC from DI-HP mechanisms involves combining time-resolved chemical and spectroscopic approaches. Knowledge of *all* dissolved species as a function of reaction time, and for different sorbate to sorbent ratios, combined with structural data on the evolution of the local environment of the sorbate species, should provide revealing information on surface processes. It should be possible to identify the threshold of surface precipitation or the mechanisms of enhanced dissolution of the substrate by a sorbate ion. Initial studies in that direction were attempted for the oxidation of Cr^{3+} by birnessite (88) and for the sorption of Ni^{2+} on pyrophyllite (92). This dual approach should lead to a better understanding of the mechanism of Co sorption on quartz and, in turn, provide invaluable information on the formation mechanisms of clays in natural systems.

APPENDIX

Calculation of the Solubility Constants

The method of (40–43) was used to calculate $\Delta_f G^0$ of three hypothetical Co-rich phyllosilicates: Co-rich kerolite (CoKer), Co-rich chrysotile (CoChrys), and Co-rich stevensite (CoStev). The parameter $\Delta O^{2-}(Me^{Z+})$ of a given metal ion is obtained from (40, 41)

$$\Delta O^{2-}(Me^{z+}) = \Delta_f G^0(MeO_{cryst}) - \Delta_f G^0(Me^{z+}_{aq}),$$

where $\Delta_f G^0$ (MeO_{cryst}) and $\Delta_f G^0$ (Me^{z+}_{aq}) are the Gibbs free energy of formation of crystalline MeO and of the aqueous Me^{Z+} ion. A linear regression relates ΔO^{2-} (Me^{z+}) to the Gibbs free energy of formation of the Me-containing clay ($\Delta_f G^{0\prime}$ (Me–clay)), formed out of its constituent oxides (43, 44)

$$\Delta_f G^{0\prime}(\text{Me-clay}) = A \cdot \Delta O^{2-}(Me^{z+}) + B.$$

The goal is to calculate the solubility products for each of the Co/clays. Common values of $\Delta_f G^0$ used in all calculations are given in Appendix Table 1.

APPENDIX TABLE 1

$\Delta_f G^0$ for Various Compounds Used in the Calculation of Co/Clay Solubilities

Compound	Phase	$\Delta_f G^0$ (kJ/mol)
$Co^{2+}(aq)^a$	Aqueous Co^{2+}	−53.6
$CoO_{ox}{}^a$	Crystalline CoO	−205.0
$Si(OH)_4{}^b$	Hydrated aqueous silicate	−1309.2
$SiO_{2\cdot ox}{}^c$	Crystalline SiO_2 (quartz)	−856.4
H_2O^c	Liquid water	−237.1
$H_2O_{ice}{}^c$	Metastable ice at 258°C	−223.8

[a] From (98) cited by (41), and from (97).
[b] From (97).
[c] From (96) used by (43).

APPENDIX TABLE 2

Chemical Data for the Calculation of the Solubility of CoKer, CoChrys, and CoStev (in kJ/mol)

Mineral	Element	ΔO^{2-} (M^{z+})	$\Delta_f G^0$ (M–Sil)^a	$\Delta_f G_{ox}$ (M–Sil)	$\Delta_f G_{ox}$ (M–Sil)$_{rec}{}^b$
CoKer	Mg^{2+}	-114.4^c	-5504.4^c	-147.8^c	−150
	Fe^{2+}	-172.3^c	-4479.0^c	-76.4^c	−69.8
	Al^{3+}	-201.13^c	-5256.7^c	-25.5^c	−29.9
	Co^{2+}	-151.3^d			−98.9
CoChrys	Mg^{2+}	-114.4^c	-4035.5^c	−167.7	−167.7
	Al^{3+}	-201.13^c	−3784.8	−42.4	−42.4
	Co^{2+}	-151.3^e			−114.4
CoStev	Mg^{2+}	-114.4^c	-5549.4^c	-316.4^c	−315.2
	Fe^{2+}	-172.3^c	-4696.3^c	-258.3^c	−255.4
	Al^{3+}	-201.13^c	-5345.2^c	-217.2^c	−225.6
	Fe^{3+}	-244.27^c	-4613.7^c	-185.4^c	−181.1
	Co^{2+}	-151.3^d			−277.1

[a] M-Sil stands for poorly ordered M-rich phyllosilicate (M = Mg, Al, Fe, Co).
[b] Recalculated from the regression line.
[c] From (43).
[d] From (98) cited by (41).
[e] From (41).

APPENDIX TABLE 3

Comparison of the Solubility Products for Mg-Rich and Co-Rich Phyllosilicates

Designation	$\log(K_{Mg})$	$\log(K_{Co})$	$\log(K_{Mg}) - \log(K_{Co})$
Kerolite	25.79[a]	15.11	10.68
Chrysotile	32.17[b]	22.21	9.96
Stevensite		19.23	
$Me(OH)_2$	16.84[c]	12.48	4.36

[a] From (45).
[b] From (95).
[c] From (37).

For CoKer (Eq. [1]), the $\Delta_f G^0$ values of the M–Sil phases (M = Fe, Mg, Al) were taken from (43) (Appendix Table 2). Chemical data for the Fe^{3+} phyllosilicate were excluded because they do not appear to be of experimental origin. For these 2:1 phyllosilicates, $A = -1.3846$ kJ/mol, and $B = -308.4$ kJ/mol (43). $\Delta_f G^0$ (CoKer) equals -4362.9 kJ/mol, and the Gibbs free energy of dissolution of CoKer: ΔG^0_{diss} (CoKer) = -86.3 kJ/mol. Thus $\log(K_{CoKer}) = 15.11$.

For CoChrys (Eq. [4]), the regression line was determined using $\Delta_f G^0$ values for halloysite ($\Delta_f G^0 = -3783.2$ kJ/mol) and chrysotile ($\Delta_f G^0 = -4037.2$ kJ/mol). $\Delta_f G^0$ (halloysite) is from heat of solution data (93). Devidal *et al.* (94) showed that the similar value for kaolinite (93) was reliable, placing greater confidence in the value for halloysite. $\Delta_f G^0$ (chrysotile) is based on experimental solubility data (95). $\Delta_f G_{ox}$ values for chrysotile and halloysite were calculated assuming: $\Delta_f G^0$ (Al_2O_3) = -1582.2 kJ/mol and $\Delta_f G^0$ (MgO) = -569.2 kJ/mol (43) (Appendix Table 2). The linear regression yields $A = -1.445$ kJ/mol and $B = -333.0$ kJ/mol. $\Delta_f G^0$ (CoChrys) calculated from data in Appendix Tables 1 and 2 equals -2889.5 kJ/mol, and ΔG^0_{diss} (CoChrys) = -126.8 kJ/mol. Thus $\log(K_{CoChrys}) = 22.21$.

The calculation for CoStev (Eq. [5]) proceeds in two steps (43). First, $\Delta_f G^0$ of K-exchanged Co/stevensite ($KCo_{2.5}Si_4O_{10}(OH)_2$) was calculated using values in Table 3 of Tardy and Duplay (43). $\Delta_f G^0$ values for the M–Sil phases (M = Fe, Mg, Al) (43) yield $A = -1.033$ and $B = -433.4$ kJ/mol (Appendix Table 2). $\Delta_f G^0$ (K–CoStev) equals -4599.6 kJ/mol. Second, the Gibbs free energy of Na–K exchange of the dehydrated part of the hydrated clay does not depend on the mineral phase at first approximation (43) and is equal to ΔG_{exch}(K-Na) = 25.2 kJ/mol (Table 5 in (43)), so that $\Delta_f G^0$ of Na–CoStev can be easily calculated and is equal to -4573.95 kJ/mol. Thus $\log(K_{CoStev}) = 19.23$.

Appendix Table 3 compares the solubilities for the Mg/ and Co/clays. Except for the three calculated values for the Co/clays, all solubilities listed are obtained from experimental data. If the thermochemical values for Co compounds (Co^{2+}, CoO. . .) of (96) or (97) (all values except Ref. 1) are used instead of those of Latimer (98), then $\Delta_f G$ (CoO) ~ -215 kJ/mol, and the equilibrium constants for all three Co/clays decrease significantly, e.g., $\log(K_{CoKer}) = 11.66$. In this case, the solution compositions of O'Day *et al.* (8) are clearly oversaturated with respect to the Co/clays. Thus, the Co/clay solubilities shown in Fig. 10 are upper limits.

ACKNOWLEDGMENTS

The authors acknowledge comments from an anonymous reviewer. K. Nagy acknowledges support from the U.S. Department of Defense, Strategic Environmental Research and Development Program, and the U.S. Department of Energy, Office of Basic Energy Sciences, Geoscience Research Program.

REFERENCES

1. Davies, S. N., and DeWiest, R. C. M., "Hydrogeology." Wiley, New York, 1966.
2. Rimstidt, J. D., *Geochim. Cosmochim. Acta* **61,** 2553 (1997).
3. Rimstidt, J. D., and Barnes, H. L., *Geochim. Cosmochim. Acta* **44,** 1683 (1980).
4. Clause, O., Kermarec, M., Bonneviot, L., Villain, F., and Che, M., *J. Amer. Chem. Soc.* **114,** 4709 (1992).
5. Charlet, L., and Manceau, A., *Geochim. Cosmochim. Acta* **58,** 2577 (1994).
6. Espinose de la Caillerie, J. B. D., Kermarec, M., and Clause, O., *J. Phys. Chem.* **99,** 17273 (1995).
7. Osthols, E., Manceau, A., Farges, F., and Charlet, L., *J. Colloid Interface Sci.* **194,** 10 (1997).
8. O'Day, P. A., Chisholm-Brause, C. J., Towle, S. N., Parks, G. A., and Brown, G. E., Jr., *Geochim. Cosmochim. Acta* **60,** 2515 (1996).
9. Mozzi, R. L., and Warren, B. E., *J. Appl. Crystallogr.* **2,** 164 (1969).
10. Manceau, A., and Decarreau, A., *Clays Clay Minerals.* **36,** 382 (1988).
11. Schlegel, M., Manceau, A., Chateigner, D., and Charlet, L., *J. Colloid Interface Sci.* **215,** 140 (1999).
12. Brindley, G. W., and Kao, C.-C., *Phys. Chem. Minerals* **10,** 187 (1984).
13. O'Day, P. A., Brown, G. E., and Parks, G. A., *J. Colloid Interface Sci.* **165,** 269 (1994).
14. Manceau, A., *Can. Mineral.* **28,** 321 (1990).
15. Bailey, S. W., "Micas." Mineralogical Society of America, Washington, DC, 1984.
16. Bailey, S. W., "Hydrous phyllosilicates." Mineralogical Society of America, Washington, DC, 1988.
17. Rayner, J. H., and Brown, G., *Clays Clay Miner.* **21,** 103 (1973).
18. Mellini, M., and Zanazzi, P. F., *Am. Mineral.* **72,** 943–948 (1987).
19. Wyckoff, R. W. G., "Crystal Structures." Interscience, New York, 1978.
20. Vaarkamp, M., Dring, I., Oldman, R. J., Stern, E. A., and Koningsberger, D. C., *Phys. Rev. B-Condensed Matter* **50,** 7872 (1994).
21. Rehr, J. J., Mustre de Leon, J., Zabinsky, S. I., and Albers, R. C., *J. Amer. Chem. Soc.* **113,** 5135 (1991).
22. Teo, B. K., "EXAFS: Basic Principles and Data Analysis." Inorganic Chemistry Concepts 9, Springer-Verlag, Berlin, 1986.
23. Mustre de Leon, J., Rehr, J. J., Zabinsky, S. I., and Albers, R. C., *Phys. Rev. B* **44,** 4146 (1991).
24. Manceau, A., and Calas, G., *Clay Miner.* **21,** 341 (1986).
25. O'Day, P. A., Rehr, J. J., Zabinsky, S. I., and Brown, G. E., Jr., *J. Amer. Chem. Soc.* **116,** 2938 (1994).
26. Manceau, A., Chateigner, D., and Gates, W. P., *Phys. Chem. Miner.* **25,** 347 (1998).
27. Scheidegger, A. M., Strawn, D. G., Lamble, G. M., and Sparks, D. L., Geochim. Cosmochim. Acta **62,** 2233 (1998).
28. Manceau, A., Schlegel, M., Chateigner, D., Lanson, B., Bartoli, C., and Gates, W. P., *in* "Synchrotron X-ray Methods in Clay Science" (D. Schulze, P. Bertsch and J. Stucki, Eds.), Vol. 9, p. 69, The Clay Minerals Society, 1999.
29. Lee, J. H.; and Guggenheim, S., *Am. Mineral.* **66,** 350 (1981).
30. Silvester, E., Manceau, A., and Drits, V. A., *Am. Mineral.* **82,** 962 (1997).
31. Manceau, A., Drits, V. A., Silvester, E., Bartoli, C., and Lanson, B., *Am. Mineral.* **82,** 1150 (1997).
32. Manceau, A., Bonnin, D., Stone, W. E. E., and Sanz, J., *Phys. Chem. Miner.* **17,** 363 (1990).
33. Jones, B. F., and Galan, E., *in* "Hydrous Phyllosilicates" (S. W. Bailey, Ed.), p. 631. Mineralogical Society of America, Washington DC, 1991.
34. Khoury, H. N., Eberl, D. D., and Jones, B. F., *Clays Clay Miner.* **30,** 327 (1982).
35. Eberl, D. D., Jones, B. F., and Khoury, H. N., *Clays Clay Miner.* **30,** 321 (1982).
36. Badaut, D., and Risacher, F., *Geochim. Cosmochim. Acta* **47,** 363 (1983).
37. Baes, C. F., and Mesmer, R. E., "The Hydrolysis of Cations." Wiley, New York, 1976.
38. Koroleff, F., *in* "Methods of Seawater Analysis" (K. Grasshoff, M. Ehrhardt and K. Kremling, Eds.), p. 174. Springer-Verlag, New York, 1983.
39. Tester, J. W., Worley, W. G., Robinson, B. A., Grigsby, C. O., and Feerer, J. L., *Geochim. Cosmochim. Acta* **11,** 2407 (1994).
40. Tardy, Y., and Garrels, R. M., *Geochim. Cosmochim. Acta* **41,** 87 (1977).
41. Tardy, Y., and Garrels, R. M., *Geochim. Cosmochim. Acta* **40,** 1051 (1976).
42. Tardy, Y., and Fritz, B., *Clay Miner.* **16,** 361 (1981).
43. Tardy, Y., and Duplay, J., *Geochim. Cosmochim. Acta* **56,** 3007 (1992).
44. Decarreau, A., *Geochim. Cosmochim. Acta* **49,** 1537 (1985).
45. Stoessel, R. K., *Geochim. Cosmochim. Acta* **52,** 365 (1988).
46. Berger, G., Cadore, E., Schott, J., and Dove, P. M., *Geochim. Cosmochim. Acta* **58,** 541 (1994).
47. Sposito, G., "Chemical Equilibria and Kinetics in Soils." Oxford Univ. Press, New York, 1994.
48. Morey, G. W., Fournier, R. O., and Rowe, J. J., *Geochim. Cosmochim. Acta* **26,** 1029 (1962).
49. Brady, P. V., and Walther, J. V., *Chem. Geol.* **82,** 253 (1990).
50. Casey, W. H., Westrich, H., Banfield, J. F., Ferruzzi, G., and Arnold, G. W., *Nature* **366,** 253 (1993).
51. Tazaki, K., Fyfe, W. S., and van der Gaast, S. J., *Clays Clay Miner.* **37,** 348 (1989).
52. Vigil, G., Xu, Z., Steinberg, S., and Israelachvili, J., *J. Colloid Interface Sci.* **165,** 367 (1994).
53. Axelos, M. A. V., Tchoubar, D., and Bottero, J. Y., *Langmuir* **5,** 1186 (1989).
54. Decarreau, A., *Bull. Mineral.* **103,** 579 (1980).
55. Brown, C. S., and Thomas, L. A., *J. Phys. Chem. Sol.* **13,** 337 (1960).
56. Hudson, G. A., and Bacon, F. R., *Ceramic Bull.* **37,** 185 (1958).
57. Lewin, J. C., *Geochim. Cosmochim. Acta* **21,** 182 (1961).
58. Weigel, V. E., *Glastechnische Berichte* **37,** 141 (1964).
59. Espinose de la Caillerie, J. B. D., Kermarec, M., and Clause, O., *J. Am. Chem. Soc.* **117,** 11471 (1995).
60. Carroll-Webb, S. A., and Walther, J. V., *Geochim. Cosmochim. Acta* **60,** 2609 (1988).
61. Van Cappellen, P., and Qiu, L., *Deep-Sea Res. II* **44,** 1129 (1997).
62. Nagy, K. L., Blum, A. E., and Lasaga, A. C., *Am. J. Sci.* **291,** 649 (1991).
63. Van Cappellen, P., and Qiu, L., *Deep-Sea Res. II* **44,** 1109 (1997).
64. Papelis, C., and Hayes, K. F., *Colloid Surf. A* **107,** 89 (1996).
65. Muller, F., Besson, G., Manceau, A., and Drits, V. A., *Phys. Chem. Miner.* **24,** 159 (1997).
66. Manceau, A., Charlet, L., Boisset, M. C., Didier, B., and Spadini, L., *Appl. Clay Sci.* **7,** 201 (1992).
67. Spadini, L., Manceau, A., Schindler, P. W., and Charlet, L., *J. Colloid Interface Sci.* **168,** 73 (1994).
68. Waite, T. D., Davis, J. A., Payne, T. E., Waychunas, G. A., and Xu, N., *Geochim. Cosmochim. Acta* **58,** 5465 (1994).
69. Manceau, A., and Charlet, L., *J. Colloid Interface Sci.* **168,** 87 (1994).
70. Persson, P., Parks, G. A., and Brown, G. E., *Langmuir* **11,** 3782 (1995).
71. Manceau, A., *Geochim. Cosmochim. Acta* **59,** 3647 (1995).
72. Sturchio, N. C., Chiarello, R. P., Cheng, L. W., Lyman, P. F., Bedzyk, M. J., Qian, Y. L., You, H. D., Yee, D., Geissbuhler, P., Sorensen, L. B., Liang, Y., and Baer, D. R., *Geochim. Cosmochim. Acta* **61,** 251 (1997).
73. Fendorf, S., Eick, M. J., Grossl, P., and Sparks, D. L., *Environ. Sci. Technol.* **31,** 315 (1997).
74. Cheng, L., Lyman, P. F., Sturchio, N. C., and Bedzyk, M. J., *Surface Sci.* **382,** 690 (1998).
75. Watson, E. B., *Geochim. Cosmochim. Acta* **60,** 5013 (1996).
76. Charlet, L., and Manceau, A., *J. Colloid Interface Sci.* **148,** 25 (1992).
77. Chiarello, R. P., and Sturchio, N. C., *Geochim. Cosmochim. Acta* **58,** 5633 (1994).
78. Chiarello, R. P., Sturchio, N. C., Grace, J. D., Geissbuhler, P., Sorensen, L. B., Cheng, L., and Xu, S., *Geochim. Cosmochim. Acta* **61,** 1467 (1997).
79. Wadsley, A. D., *Acta Crystallogr.* **5,** 676 (1952).
80. Manceau, A., Gorshkov, A. I., and Drits, V. A., *Am. Mineral.* **77,** 1144 (1992).
81. Brindley, G. W., and Brown, G., "Crystal Structures of Clay Minerals and Their X-Ray Identification," Mineralogical Society, London, 1980.
82. Organova, N. I., Drits, V. A., and Dmitrik, A. L., *Am. Mineral.* **59,** 190 (1974).
83. Scheidegger, A. M., Lamble, G. M., and Sparks, D. L., *J. Colloid Interface Sci.* **186,** 118 (1997).
84. Towle, S. N., Bargar, J. R., Brown, G. E., and Parks, G. A., *J. Colloid Interface Sci.* **187,** 62 (1997).
85. Stipp, S. L., Hochella, M. F., Parks, G. A., and Leckie, J. O., *Geochim. Cosmochim. Acta* **56,** 1941 (1992).
86. Pingitore, N. E. J. R., Lytle, F. W., Davies, B. M., Eastman, M. P., Eller, P. G., and Larson, E. M., *Geochim. Cosmochim. Acta* **56,** 1531 (1992).
87. Reeder, R. J., Lamble, G. M., Lee, J. F., and Staudt, W. J., *Geochim. Cosmochim. Acta* **58,** 5639 (1994).
88. Manceau, A., and Charlet, L., *J. Colloid Interface Sci.* **148,** 443 (1992).
89. Dzombak, D. A., and Morel, F. M. M., "Surface Complexation Modeling. Hydrous Ferric Oxide." Wiley, New York, 1990.
90. Stumm, W., "Chemistry of the Solid–Water Interface." Wiley, New York, 1992.
91. Manceau, A., Bonnin, D., Kaiser, P., and Frétigny, C., *Phys. Chem. Miner.* **16,** 180 (1988).
92. Scheidegger, A. M., Lamble, G. M., and Sparks, D. L., *J. Phys. IV* **7,** 773 (1997).
93. Barany, R., and Kelley, K. K., *U.S. Bureau of Mines Reports of Investigations* **5825,** 1 (1961).
94. Devidal, J. L., Dandurand, J. L., and Gout, R., *Geochim. Cosmochim. Acta* **60,** 553 (1996).
95. Hostetler, P. B., and Christ, C. L., *Geochim. Cosmochim. Acta* **32,** 485 (1968).
96. Robie, R. A., and Waldbaum, D. R., "Thermodynamic Properties of Minerals and Related Substances at 298.15K (25°C) and one Atmosphere (1.013 bars) Pressure and at Higher Temperatures." *US Geological Survey Bulletin,* **1259,** 1968.
97. Woods, T. L., and Garrels, R. M., "Thermodynamic Values at Low Temperature for Natural Inorganic Materials: An Uncritical Summary." Oxford Univ. Press, New York Oxford, 1987.
98. Latimer, W. M., "The Oxidation States of Elements and their Potentials in Aqueous Solutions." Prentice Hall, New York, 1952.
99. Shannon, R. D., and Prewitt, C. T., *Acta Crystallogr. B* **25,** 925 (1969).

Discussion et conclusion

Les résultats de l'adsorption du zinc à la surface de l'hectorite en présence de silice libre illustrent de manière expérimentale le continuum existant entre l'adsorption de cations, la nucléation, et la néoformation de phyllosilicates. À partir du protocole expérimental utilisé, il est possible d'étudier l'impact de facteurs tels que le pH [183, 184], la concentration de cations et de silice dissoute, et la nature de l'électrolyte, sur la cinétique de néoformation et la nature des minéraux néoformés. D'autre part, ces expériences mériteraient d'être réalisées sur de plus longues durées, par exemple afin de déterminer expérimentalement la constante de solubilité des phyllosilicates zincifères néoformés. Cette donnée thermodynamique présente un réel intérêt pour la prédiction du devenir du zinc dans le milieu naturel. Une telle étude mériterait également d'être réalisée avec le nickel, un cation présent en grandes quantités dans les phyllosilicates des profils d'altération sur roches ultrabasiques [185].

Dans nos expériences de croissance de phyllosilicates zincifères, le rapport Mg/Zn en solution a varié de 0,04 à près de 0,87, cependant Mg ne semble pas avoir été incorporé de manière significative dans le solide. Ceci est en accord avec la forte affinité de Zn par rapport à Mg pour les phyllosilicates [165]. Cette différence d'affinité pourrait être quantifiée en variant $[Mg]_{aq}$. Il serait alors intéressant de déterminer par cette approche les coefficients de sélectivité de Zn, Mg, et d'autres cations, pour les phyllosilicates, ainsi que la dépendance éventuelle de ces coefficients avec par exemple le pH et la température.

L'étude de la fixation du cobalt par le quartz est à replacer dans le contexte plus général du rôle joué par ce minéral dans la néoformation de minéraux argileux dans les milieux naturels. La présence d'encroûtements argileux à la surface des grains de quartz naturels [95] atteste de l'importance de ce processus de cristallogenèse. Pour mieux étudier la réactivité du quartz, il faudrait envisager des expériences similaires à celles réalisées avec le zinc sur l'hectorite, c'est-à-dire avec contrôle du pH tout au long de la réaction, dosage de toutes les espèces chimiques en solution, y compris Si. Par ailleurs, la présence probable d'une couche de silice amorphe à la surface des grains de quartz est un facteur important, dont il faudrait tenir compte à l'avenir [176, 177, 186].

Cinquième partie :
Application à la notion de capacité d'échange cationique dans les sols

(La capacité d'échange des sols. Structures et charges à l'interface eau-particule. Article paru dans les Comptes-Rendus de l'Académie d'Agriculture Française*)*

LA CAPACITÉ D'ÉCHANGE DES SOLS. STRUCTURES ET CHARGES À L'INTERFACE EAU/PARTICULE

THE EXCHANGE CAPACITY OF SOILS. STRUCTURES AND CHARGES AT THE PARTICLE/WATER INTERFACE

par Laurent **Charlet** (*) et Michel L. **Schlegel** (*)

(*note présentée par* Laurent **Charlet**)

RÉSUMÉ

La capacité d'échange d'un sol est une donnée empirique, dont la valeur varie selon la méthode utilisée. Les bases scientifiques des différentes méthodes sont passées en revue. Les valeurs sont interprétées en termes de différentes composantes de la densité de charge de surface d'un sol, telles qu'elles ont étés définies par **Sposito** (27). Parmi les ions associés aux particules d'un sol, on distingue ceux présents dans la double couche diffuse et ceux présents sous forme de complexes de surface. On parlera, dans ce dernier cas, de complexe hors sphère (CHS) ou de complexe de sphère interne (CSI), selon que l'ion adsorbé conserve ou non l'intégralité de sa sphère d'hydratation. Divers exemples de tels complexes sont discutés, et les groupes réactionnels avec lesquels ces complexes sont formés sont passés en revue. Il est montré que les bordures des particules de phyllosilicates sont susceptibles de jouer un grand rôle dans la chimie des sols, rôle négligé jusqu'à présent. Un cation adsorbé initialement par échange cationique peut former ensuite, en quelques heures, des CSI sur les côtés des particules d'argiles. Le temps réactionnel, utilisé dans la mesure de la capacité d'échange et fixé de façon assez arbitraire. Or elle s'avère ainsi être l'un des paramètres fondamentaux qui conditionnent les valeurs de capacité d'échange. D'une façon générale, la capacité d'échange d'un sol ne peut être appréhendée dans toute sa complexité qu'en combinant des approches microscopiques et macroscopiques. Les études de chimie aqueuse permettent de décrire et de quantifier, à l'échelle macroscopique, les réactions d'échange cationique et de complexation de surface. Les constantes thermodynamiques de ces réactions peuvent être intégrées aux codes de calcul de spéciation et permettent de prédire le devenir d'un élément, qu'il soit nutritif ou toxique. Ces calculs sont néanmoins fondés sur un choix d'écriture des réactions chimiques, choix qui est sous-tendu par l'image microscopique que l'on a du phénomène macroscopique. Cette image comprend la structure des complexes formés ou la morphologie des particules minérales et des polymères organiques. Ces données sont maintenant accessibles grâce aux méthodes spectroscopiques (résonance de spin électronique, résonance magnétique nucléaire, spectroscopie de structure fine étendue d'absorption des rayons X) et microscopiques (microscopie de force atomique des argiles, microscopie électronique par transmission des matières organiques) qui permettent l'observation des mécanismes réactionnels *in situ*, c'est-à-dire dans l'eau, et en temps réel, c'est-à-dire en intégrant la dimension temps.

Mots clés : capacité d'échange ionique, propriété physicochimique du sol, cation, adsorption.

(*) Groupe de Géochimie de l'Environnement, LGIT, Université Grenoble I - CNRS, BP 53, F-38041 Grenoble Cedex.
C.R. Acad. Agric. Fr., 1999, 85, n° 2, pp. 7-24. Séance du 10 février 1999.

SUMMARY

The cation- and anion- exchange capacity of soils (denoted respectively CEC and AEC) is an empirically defined macroscopic concept. The CEC (and AEC) values vary depending on the method used. The different methods commonly used to measure the CEC are reviewed, and the capacity hereby measured is interpreted in terms of the various soil surface charge densities as defined by ***Sposito*** *(27). Ions present at the surface of a soil particle either are located within the diffuse ion swarm, or have formed complexes with surface functional groups. In outer-sphere complexes (OSC), the ion keeps its full hydration sphere whereas in inner-sphere complexes (ISC), it shares elements from its coordination sphere with the sorbent surface. The chemical nature of the surface functional groups likely to enter the adsorbate hydration sphere is reviewed, and examples of surface complexes are discussed. For instance, as soil clay particles are typically smaller in size than reference clay particles, the clay edge functional groups may influence the soil chemistry more than what has been commonly assumed. It is shown that cations initially adsorbed by cation exchange tend to form later on ISC at the edges of these particles. The reaction time chosen to measure the CEC is therefore a critical parameter which determines the measured CEC value. The soil exchange capacity can only be fully understood by a combination of macroscopic and microscopic studies. Wet chemical studies lead to a macroscopic and quantitative description of phenomena such as cation exchange and surface complexation. These chemical equilibria and their thermodynamic constants can be included in speciation codes. The mobility and fate of major or trace elements can then be predicted. However, these computations are dependent on the way a given chemical equation is written, and this choice is often based on microscopic concepts. Information on the structure of surface complexes and on the morphology of mineral particles and organic polymers is now available, thanks to recent developments of* in situ *and real time spectroscopic (extended X-ray absorption fine structure spectroscopy, electron-spin resonance, nuclear magnetic resonance) and microscopic (atomic force microscopy, scanning electron microscopy) techniques. These techniques allow the study of sorption phenomena at the surface of organic and inorganic soil particles under water and as a function of time.*

Key words *: ion exchange capacity, soil chemicophysical properties, cations, adsorption .*

INTRODUCTION

Les ions libérés lors de l'altération des roches, de la dissolution des engrais ou de la décomposition de la matière organique (plantes, micro-organismes..) sont retenus dans le sol de façon transitoire et inversible. Ces ions peuvent repasser dans la solution du sol, permettant ainsi la croissance des végétaux. La solution du sol ne contient en effet qu'un très faible pourcentage des ions nécessaires à une saison végétative. La capacité de stockage des ions par un sol est classiquement mesurée par la capacité d'échange en anions (CEA) ou en cations (CEC), toutes les deux exprimées en mol_ckg^{-1} (1 meq/100g = 1 $cmol_ckg^{-1}$).

La capacité d'échange est donc un concept macroscopique qui recouvre une variété de mécanismes microscopiques qui se déroulent à l'interface solide/solution. Nous verrons comment les méthodes spectroscopiques développées ces dernières années permettent de mieux comprendre la structure du *solide* et des ions présents à cette interface, et comment, inversement, les méthodes développées pour la détermination de la CEC et de la CEA (ensemble de méthodes que nous présenterons synthétiquement à la fin de l'exposé et qui seront discutées plus en détail dans l'exposé de Jean-Luc **Julien**) correspondent à une approche de chimistes des *solutions* aqueuses.

Cette brève revue ne saurait être exhaustive et nous renvoyons le lecteur aux ouvrages de référence de **Bolt** (5), **Sposito** (27) et **McBride** (18) pour de plus amples analyses de la capacité d'échange et de son interprétation structurale.

1. LES COMPOSANTES DE LA CHARGE DE SURFACE

Un ion qui s'approche de la surface d'une particule, qu'elle soit minérale ou organique, peut être fixé au moins de trois façons différentes (figure 1). Dans deux cas, l'ion reste entouré de sa sphère de molécules d'eau d'hydratation : il est soit retenu à la surface par des interactions purement électrostatiques et reste localisé dans la "couche diffuse", soit retenu sur un site réactionnel de surface pour former un complexe de sphère externe, appelé aussi complexe hors sphère (CHS). Dans le troisième cas, l'ion perd certaines de ses molécules d'eau pour former une liaison chimique avec un site fonctionnel de surface. On a alors affaire à un complexe de sphère interne (CSI). Les ions adsorbés vont donc développer à la surface de la particule trois types de densité de charge de surface (26) :

- σ_{SI} est la densité de charge due aux CSI. Dans ces complexes, les ions perdent une partie des molécules d'eau d'hydratation qui les entourent en solution au profit de sites hydroxyles, sulfures, carbonates, phénols ou carboxyles liés à la surface de la particule, et avec lesquels ils forment une liaison chimique par "partage" d'atome d'oxygène ou de soufre entre la particule et la sphère de coordination de l'ion ainsi adsorbé ;
- σ_{HS} est la densité de charge due aux CHS. Dans ce cas, l'ion reste entouré de molécules d'eau d'hydratation. Il ne peut former avec la surface de la particule que des liaisons hydrogènes ou électrostatiques. Il reste cependant immobilisé au niveau du site de surface réactionnel un temps supérieur au temps qui lui est nécessaire en solution pour migrer par diffusion sur une distance égale à son propre diamètre, soit 10 picosecondes (29). Les ions ainsi adsorbés forment une "couche" d'environ 0,5 nm d'épaisseur ;
- σ_d est la densité de charge due aux ions présents dans la couche diffuse. L'épaisseur de cette couche varie, pour un électrolyte monovalent, de 1 nm à 10 nm pour une force ionique de 0,1 M à 10^{-3} M. Les ions sont complètements hydratés. Leur distribution dans l'espace est décrite par l'équation de Gouy Chapman, solution de l'équation de Poisson et de celle de Boltzmann.

Ces trois densités de charge de surface neutralisent la densité de charge intrinsèque σ_{int} localisée directement à la surface de la particule, et que l'on peut décomposer en deux contributions distinctes :

- σ_O, la densité de charge structurale de surface. C'est une charge permanente qui résulte de substitutions isomorphiques des ions par d'autres ions de charge différente au sein des particules. Elle n'existe donc que pour des particules minérales. Elle est dite permanente, car elle est indépendante du pH et de la force ionique. σ_D peut cependant varier en fonction du potentiel rédox du sol, suite à des réactions d'oxydo-réduction impliquant des cations structuraux. C'est notamment le cas lors de la réduction des ions Fe^{3+} présents dans les smectites ;

• σ_H, la densité nette de charge protonique de surface. Elle résulte de l'adsorption et de la désorption de protons au niveau de sites fonctionnels présents à la surface des phases organiques et inorganiques.

Le principe d'électroneutralité implique :

$$\sigma_O + \sigma_H + \sigma_{SI} + \sigma_{HS} + \sigma_d = 0 \quad \text{ou} \quad \sigma_O + \sigma_H = -(\sigma_{SI} + \sigma_{HS} + \sigma_d) \quad [1]$$

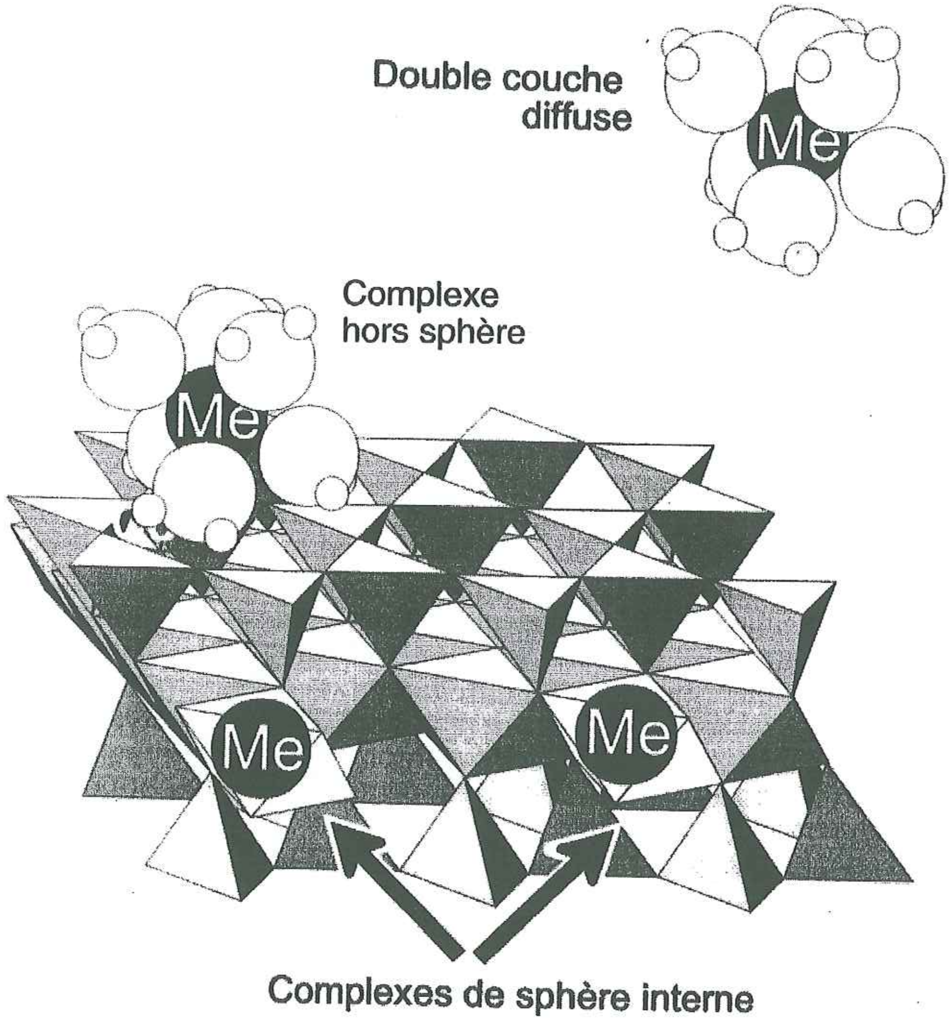

Figure 1 : Les trois mécanismes responsables de l'adsorption d'un ion métallique Me^{n+} à la surface d'une particule d'argile.
Figure 1 : Three sorption mechanisms of Me^{n+} metal ion at the clay-water interface.

Nous étudierons tout d'abord la charge intrinsèque d'un sol, σ_{int}, et sa localisation au niveau *de sites réactionnels de surface.* Nous verrons ensuite comment σ_{HS} et σ_d sont reliées à la capacité d'échange du sol, et nous montrerons enfin comment les différentes façons de mesurer cette capacité d'échange permettent d'estimer en retour les variations de σ_H en fonction du pH de la solution du sol, et donc les besoins en chaulage.

---

2. LA CHARGE INTRINSÈQUE DE SURFACE

1. La densité de charge permanente (σ_O) et sa localisation sur la face des phyllosilicates et phyllomanganates

La charge permanente est, d'une façon générale, caractéristique des sols des zones tempérées ou semi-arides. Cette charge est engendrée par des substitutions isomorphiques présentes au sein d'une structure minérale. Ces substitutions ont lieu principalement dans deux familles de minéraux à structure lamellaire : certains phyllosilicates à deux couches de tétraèdres et une couche d'octaèdres (smectites, vermiculites, illites…) et les phyllomanganates (busérite…). Dans le cas des phyllosilicates, des ions Al^{3+} présents dans la couche octaédrique sont substitués par des ions Fe^{2+} et Mg^{2+} (smectites) et des ions Si^{4+} de la couche tétraédrique par Al^{3+} (illites, vermiculites). Dans les phyllomanganates, de type birnessite, certains ions Mn^{4+} sont vacants et d'autres substitués par Mn^{2+} et Mn^{3+} (16). Dans tous les cas, la charge est délocalisée au niveau d'atomes superficiels délimitant des *cavités*, qui constituent les sites fonctionnels de ces surfaces. Elle donne lieu à une densité de charge à la surface de ces minéraux (en coulomb m^{-2}). On peut cependant estimer, une charge permanente moyenne pour tous les composants minéraux du sol (1). On aboutit ainsi à la densité de charge permanente du sol, σ_O.

Chez les phyllosilicates, en particulier, le groupe fonctionnel est la cavité siloxane ditrigonale. Cette cavité est entourée par une couronne d'atomes d'oxygène correspondant à six tétraèdres SiO_4^{4-}. Le diamètre de cette cavité est de 0,26 nm pour les smectites (27) et de 0,167 nm pour les vermiculites (34), ce qui est proche du diamètre des ions Cs^+ (0,338 nm) et K^+ (0,266 nm) déshydratés. Ceci conduit à une stéréospécificité des substrats vis-à-vis de ces ions, et donc à la stabilité (bien connue) des micas potassiques et des vermiculites potassiques, et à la "fixation" du potassium par les argiles, bien connue en agriculture.

La cavité siloxane est une base au sens de **Lewis**, c'est-à-dire une entité susceptible d'engager ses niveaux électroniques saturés en électrons pour initier une réaction chimique. Cette base est d'autant plus "molle" au sens de **Misono** (3, 27, 31) que la charge électronique est davantage délocalisée sur l'ensemble des atomes d'oxygène de la cavité siloxane. Cela est notamment le cas pour les smectites, dans lesquelles les substitutions isomorphiques sont localisées dans la couche octaédrique (27, 31). Les cations, quant à eux, forment des acides de Lewis. Ils seront d'autant plus "mous" qu'ils perdront facilement leurs molécules d'eau d'hydratation et qu'il auront une forte polarisabilité et une faible électronégativité. Étant donné que les acides mous ont tendance à s'associer aux bases molles, et les acides durs aux bases dures, les cations forment un complexe d'autant plus stable avec la cavité siloxane qu'ils sont mous. Cela explique les séries d'affinité observées pour la fixation d'ions de charge similaire sur les smectites (18) :

$$Cs^+ > Rb^+ > K^+ > Na^+ > Li^+$$

et

$$Ba^{2+} > Sr^{2+} > Ca^{2+} > Mn^{2+} > Mg^{2+}$$

Ces séries d'affinité suivent l'ordre des énergies croissantes d'hydratation. La très forte affinité des phyllosilicates (mais aussi de la matière organique) pour Ba^{2+}, Cs^+ et NH_4^+ seront des données sous-jacentes aux différentes méthodes utilisées, dans la mesure de la capacité d'échange.

Pour les illites et vermiculites, contrairement aux smectites, les substitutions isomorphiques ont lieu principalement dans la couche tétraédrique de ces phyllosilicates, c'est-à-dire beaucoup plus proche de la surface. La charge est alors localisée au niveau de trois atomes d'oxygène de surface attenants, et la cavité siloxane est moins molle. Cependant, les complexes formés avec les cations présents dans l'interfeuillet (et particulièrement avec K^+) seront d'autant plus stables que la distance entre charge positive et charge négative est faible (par exemple, suite à la déshydratation du cation). Les systèmes illitiques et vermiculitiques seront donc caractérisés par une très grande charge structurale permanente, mais peuvent n'avoir néannoins que peu de cations échangeables, car la majorité des cations adsorbés est “fixée” sous forme de CSI très stables au niveau des cavités siloxanes.

La charge permanente est pratiquement absente des sols tropicaux (sols latéritiques par exemple). Dans ces sols, les smectites, si elles existaient, ont généralement été solubilisées, et les seuls minéraux silicatés restant sont le quartz (dont la cinétique de dissolution est très lente) et la kaolinite. Dans ces sols, la densité de charge σ_{int} est due exclusivement à la densité de charge variable σ_H portée par trois composants principaux de ces sols : kaolinite, oxyhydroxydes de fer et d'aluminium et matière organique (10). C'est cette densité de charge variable que nous allons maintenant étudier.

2. La densité de charge variable (σ_H) et sa localisation sur les particules organiques et minérales

La densité de charge nette protonique de surface, σ_H, est définie par la quantité de charges par unité de surface liée à des réactions acido-basiques de protonation-déprotonation de groupes fonctionnels de surface. Ces sites réactifs, que nous dénoterons $>LH_l$, sont d'une grande variété. On les trouve à la surface de la matière organique, sous forme de sites carboxyles, phénoles et, dans une moindre mesure, de sites amines, carbonyles et sulfhydryles. Ces derniers contiennent S^{2-}, un anion qui, comme nous le verrons, est très réactif vis-à-vis des “métaux lourds”. On les trouve également à la surface d'(hydr)oxydes, de carbonates, de sulfures, et en bordure des phyllosilicates (smectites, kaolinites…). La réaction de déprotonation du groupe fonctionnel s'écrit :

$$>LH_l = >L^{-l} + l\,H^+ \qquad K^s_a \qquad [2]$$

Une réaction concurrente à la réaction 2 est la réaction d'adsorption de cations sur ces sites et de formation d'un complexe de surface. Cette adsorption s'accompagne d'une libération de protons, par exemple selon la réaction :

$$M^{m+} + >LH_l = >LM^{(m-l)} + l\,H^+ \qquad K^s_1 \qquad [3]$$

L'ampleur de cette adsorption est mesurée macroscopiquement en suivant soit la disparition de M^{m+} de la solution (on appellera alors les courbes expérimentales des “crêtes d'adsorption” ou des “isothermes d'adsorption” selon que $[M]_t$ est fixée et le pH variable, ou que le pH est fixé et $[M]_t$ est variable, soit la libération de protons (on parlera alors de courbes de titration potentiométriques). Un exemple de crêtes d'adsorption et de courbes de titration est donné dans les figures 2 et 3 dans le cas de l'adsorption de Cu^{2+}, Cd^{2+} et Al^{3+} sur la montmorillonite et sur divers oxydes.

La réaction [2] peut être vue, dans le cas où l = 1 et L = OH, comme une hydrolyse du cation par les groupements hydroxyles présent à la surface des particules. Cette hydrolyse a toujours lieu à un pH plus bas que l'hydrolyse équivalente du métal en solution (équation 4), donc $pK^s_1 < pK_1$. On montre aussi que pK^s_1 et pK_1 sont proportionnels l'un à l'autre (22).

$$M^{m+} + H_2O = MOH^{(m-l)} + H^+ \qquad K_1 \qquad [4]$$

Comme nous l'avons discuté dans le cas des phyllosilicates, la stabilité du complexe formé dépendra de la mollesse du groupe réactionnel

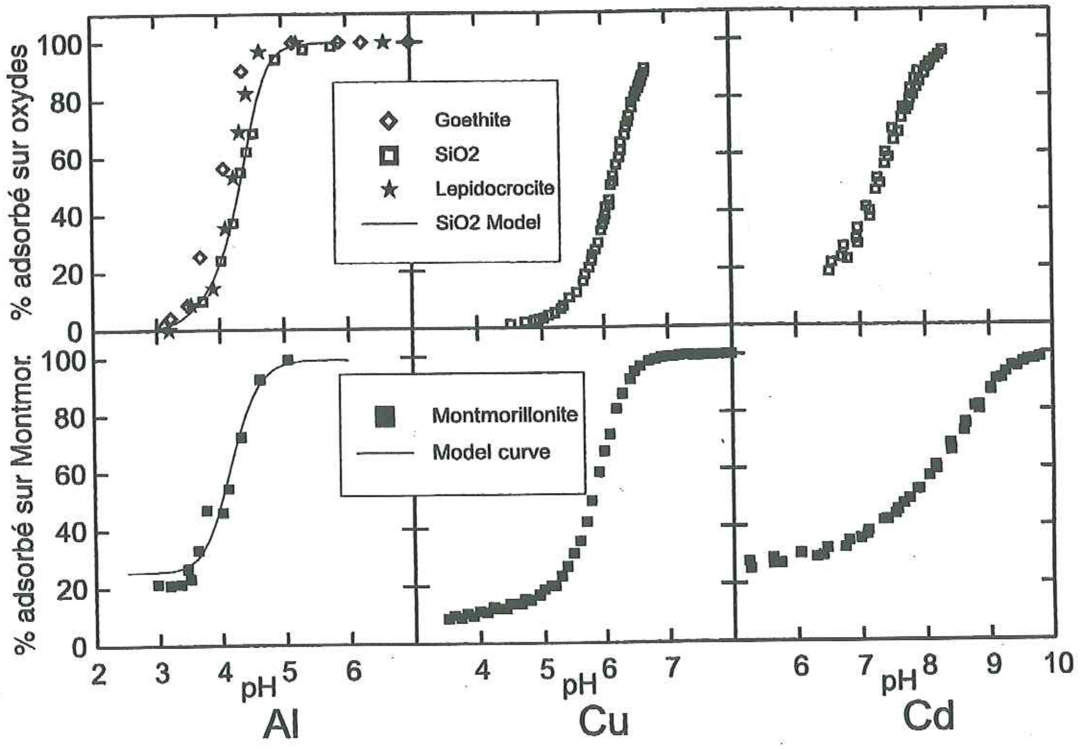

Figure 2 : **Comparaison de courbes d'adsorption de Al^{3+}, Cu^{2+} et Cd^{2+} sur les oxydes et sur la montmorillonite à force ionique élevée. La similarité de ces courbes suggère que les mécanismes d'adsorption des ions sont similaires dans les deux cas, et correspondent à la formation de complexes de sphère interne (9).**

Figure 2 : ***Comparison of Al^{3+}, Cu^{2+} and Cd^{2+} adsorption on montmorillonite and on oxides at high ionic strength. The similarity of sorption behavior suggests that in both cases sorption occurs via the formation of inner-sphere surface complexes (after (9)).***

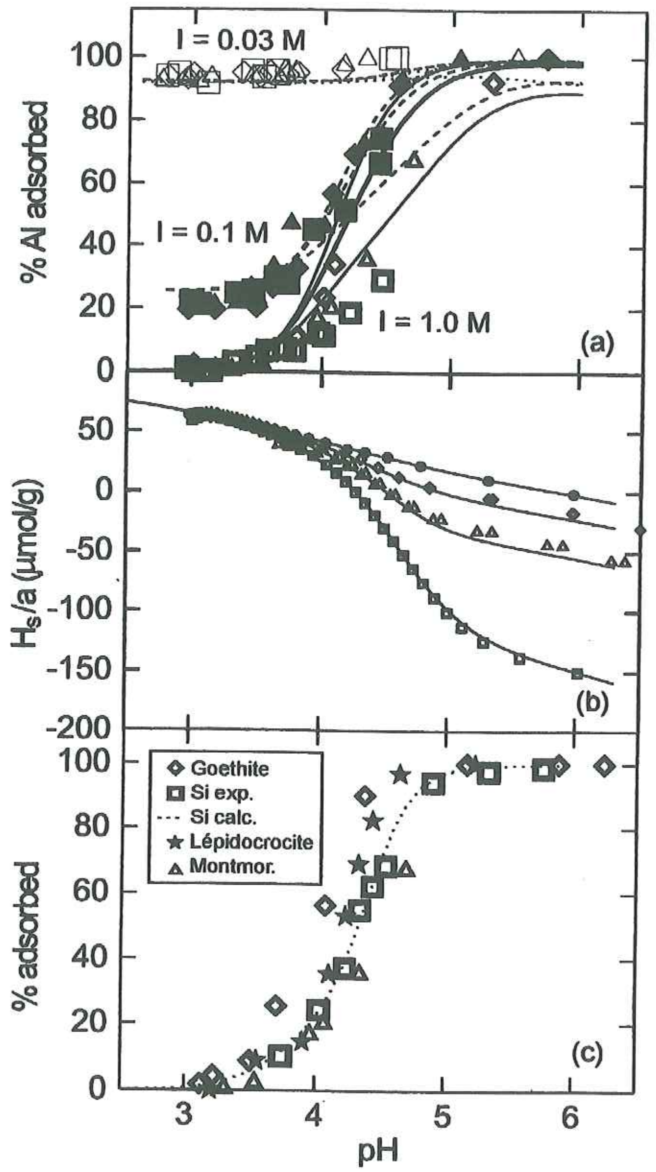

Figure 3 : Adsorption d'Al^{3+} sur la montmorillonite (a et c) et différents oxyde (b). (a et c) Adsorption sur montmorillonite en fonction du pH et de la force ionique. À faible pH, l'adsorption est fonction de la force ionique, ce qui correspond à un mécanisme d'adsorption par échange cationique. À pH élevé, l'adsorption est indépendante de la force ionique et se fait selon un mécanisme d'adsorption similaire à celui des oxydes. (a) Net excès de protons libérés en solution en présence de concentrations croissantes d'Al^{3+}. Les courbes divergent quand Al^{3+} s'adsorbe (comparer (a) et (c)). (b) Comparaison de l'adsorption de Al^{3+} sur la montmorillonite ainsi que sur des oxydes de fer (9).

***Figure 3 :** Sorption of Al^{3+} on montmorillonite (a and c) and different oxides (b). (a and c) Sorption isotherm on montmorillonite as a function of pH and ionic strength. At low pH, adsorption increases with decreasing ionic strength, suggesting the occurrence of a cation exchange mechanism. At high pH, adsorption is independent of ionic strength, and occurs via the formation of inner-sphere surface complexes. (a) Net excess of proton release as a consequence of Al^{3+} sorption. The titration curves diverge upon the onset of Al^{3+} sorption (compare (a) and (c)). (b) Comparison of sorption isotherms on montmorillonite and iron oxides (after (9)).*

(qui décroît dans l'ordre S, N, O) et de la mollesse du cation[1], qui suit, à quelques exceptions près, la série d'**Irwing-Williams** :

$$Ba < Sr < Ca < Mg < Mn < Fe < Co < (Pb <) Ni < Cu > Zn$$

Cette série est basée sur divers critères : le rayon et l'électronégativité du cation, la stabilité de complexes avec divers ligands organiques en solution (éthylène diamine, glycinate et oxalate) et la solubilité des sulfures correspondants (30). À la série originale d'**Irwing-Williams**, on a ici rajouté le plomb, fortement adsorbé par la matière organique, et intercalé ici selon l'ordre d'électronégativité croissante.

L'utilisation des équilibres (2) et (3) nécessite la connaissance de la concentration totale en groupes fonctionnels de surface (σ_{Hmax}), ainsi que celle de I, pK^s_1 et pK_1. Cette détermination est truffée d'embûches, et nous renvoyons aux monographies de **Davis** et **Kent** (11), **Sposito** (27, 28) **McBride** (18) et **James** et **Parks** (14) sur ce sujet. Nous discuterons ici un seul cas, encore peu abordé dans la littérature, à savoir la chimie de surface du côté des phyllosilicates.

Certains phyllosilicates (smectites, illites) présentent à la fois une densité de charge permanente σ_0 d'origine structurale, et une densité de charge variable σ_H localisée sur les bordures de feuillets. Les particules de phyllosilicates présentes dans les sols sont en général de plus petite taille que celles utilisées dans les études de laboratoire et qui sont censées représenter la réactivité de surface de ces matériaux (les "argiles de référence"). Par exemple, les particules d'illite, de micas ou de smectites des sols observées par microscopie électronique à transmission font environ 100 nm de long par 40 nm de large, avec des petites particules de l'ordre de 20 nm (2, 13), alors que les particules de référence ont des dimensions de l'ordre du micron. Ceci signifie que, pour les smectites des sols, le rapport entre surface des côtés et surface totale est plus élevé que celui des smectites de référence, estimé en général à 2 % (9, 33). Pour étudier la chimie de ces minéraux, nous avons donc choisi une smectite trioctaédrique, l'hectorite, dont le rapport surface des côtés sur surface totale des particules est grand, de l'ordre de 3-5 % (4, 6) (figure 4). Nous avons pu montrer, en combinant des études structurales (par spectroscopie polarisée de structure fine étendue d'absorption des rayons X ; en anglais, "*polarized EXAFS*") et des études de cinétique chimique, que l'adsorption d'un cation, Co^{2+}, se faisait en deux étapes (23, 24). Dans les premières minutes, le cation est adsorbé par échange cationique sur la face de l'hectorite ; autrement dit, il compense la charge σ_0. Dans les heures qui suivent cependant, le cation va migrer (ou se désorber et se réadsorber) pour former des CSI sur le côté de l'hectorite. L'octaèdre d'atome d'oxygène qui entoure le cation va se retrouver dans le prolongement de la couche octaédrique et partager des atomes d'oxygène avec des octaèdres de Mg et des tétraèdres de Si (figure 6). Non seulement le cation s'est déshydraté et n'est plus en position échangeable, mais de plus il est intégré au sein d'une structure de type phyllosilicate(8). La capacité de fixation de la smectite inclut alors non seulement σ_O, mais aussi σ_H. De plus, cette capacité variera en fonction du temps de réaction choisi.

---

[1] qu'on désigne habituellement sous le terme de "force d'acidité" (cf. article de J.L. **Julien**).

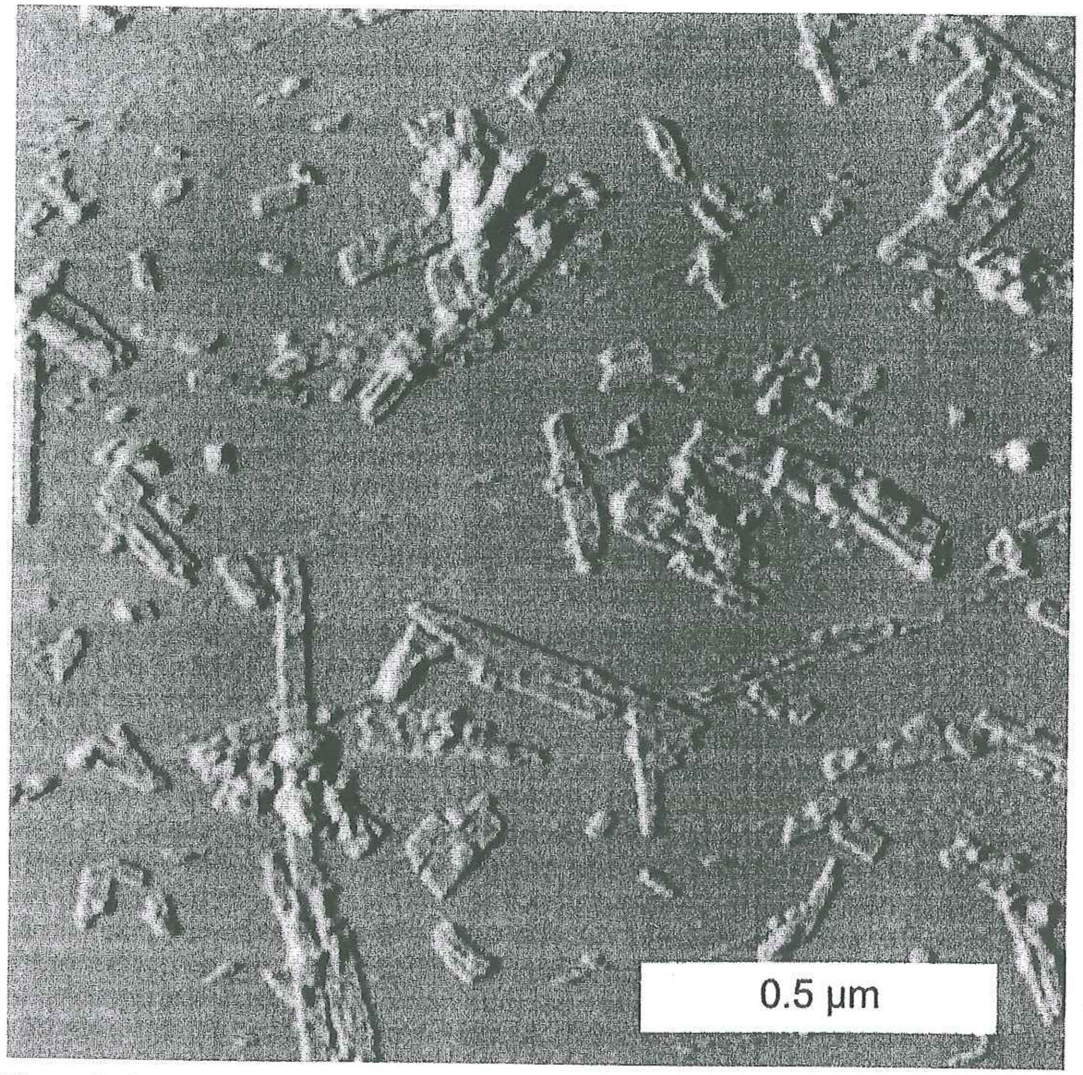

Figure 4 : **Image AFM de particules d' hectorite, une smectite trioctaédrale, attachées dans l'eau à une plaque de mica par un polymère organique (*contact mode, scan area* : 1,5 x 1,5 µm). La taille moyenne des particules est de 60 nm par 200 nm. L'épaisseur moyenne de la particule est de 20 Å, ce qui représente une maille unitaire d'hectorite plus le film organique (6).**

Figure 4 : AFM image of hectorite particles. Hectorite crystallites were attached to a mica plane with an organic polymer and data were acquired in contact mode in water. Average size of particle is 60 by 200 nm. The measured average thickness (20 Å) corresponds to the thickness of one clay platelet plus the polymer layer (after (6)).

3. La charge intrinsèque d'un sol (σ_{int}), résultat de l'équilibre entre phases organiques et inorganiques

La densité de charge intrinsèque σ_{int} a été définie précédemment par :

$$\sigma_{int} = \sigma_O + \sigma_H \quad [5]$$

Elle va donc être fonction du poids relatif des quatre composants du sol dont la charge par unité de surface est représentée schématiquement dans la figure 5 :

- les smectites (et phyllomanganates), qui déterminent σ_O,

- la matière organique (et la silice amorphe), qui tendent à imposer un point de charge net protonique nul (PCNPN, défini par $\sigma_H = 0$) très bas,
- les phyllosilicates dont la contribution à σ_H sera d'autant plus grande qu'ils seront de petite taille, c'est-à-dire que la densité de charge portée par leurs côtés sera importante,
- les oxyhydroxydes de fer et d'aluminium, qui tendent à imposer un PCNPN élevé.

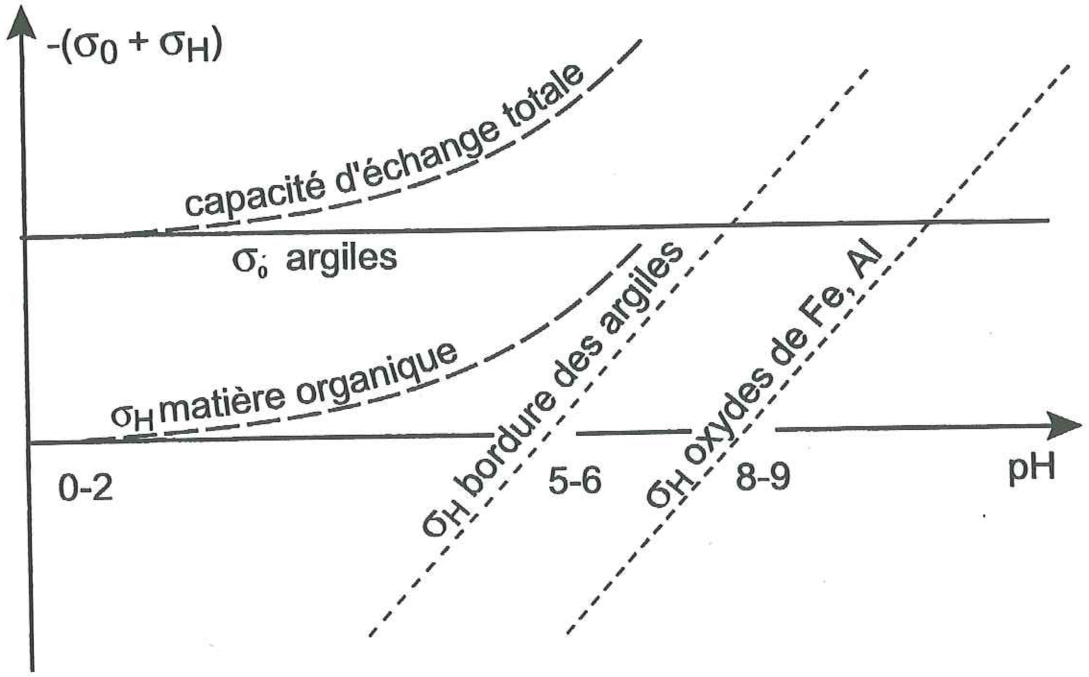

Figure 5 : **Les composantes de la densité de charge intrinsèque d'un sol. Ces composantes se subdivisent en une charge permanente σ_0 structurale, provenant des argiles, et en charges protoniques σ_H correspondant aux réactions de protonation-déprotonation à la surface des oxydes, en bordure des feuillets de phyllosilicates et associés à la matière organique.**

Figure 5 : Various components of the intrinsic charge density of a soil. The intrinsic charge is the sum of the σ_0 permanent charge of clay minerals, and of the σ_H, the net proton charge which results from protonation-unprotonation reactions of reactive groups present at the surface of organic matter (oxides and clay mineral edges).

Dans les sols tempérés comme ceux de la France, les trois premiers composants auront une influence majeure sur la chimie du sol et, comme cela sera indiqué dans les articles suivants de J. L. **Julien** et de D. **Tessier**, le point de charge nul (PCN) du sol sera situé en dessous de pH 5. L'importance de la réactivité de bordure des phyllosilicates, discutée ci-dessus, pourrait expliquer que le PCN des sols n'est proche ni de celui des oxydes de Fe ou de Mn, ni de celui de la matière organique (figure 5), mais est beaucoup plus près de celui du côté des phyllosilicates. Dans les sols tropicaux, il est légèrement plus élevé : il est typiquement entre pH 4 et 4,5, rarement plus (10, 17). Ce n'est donc pas tant le point de charge nulle que la charge intrinsèque maximale qui différencie ces deux types de sol.

3. LES IONS ADSORBÉS ET LA CAPACITÉ D'ÉCHANGE

Les différentes méthodes utilisées pour estimer la capacité d'échange cationique sont comparées dans le tableau 1. Ces méthodes enchaînent généralement au moins trois étapes fondamentales.

1. Saturation du sol par un cation. Les différents cations présents sous forme échangeable sont remplacés par un "cation saturant". La CEC est alors soit la somme de la charge des cations ainsi extraits, soit la concentration de ce "cation saturant", dont la mesure nécessite les étapes 2 et 3 décrites ci-dessous. Différents "cations saturants" ont été utilisés. Les ions NH_4^+, Ba^{2+} et Cs^+ ont une affinité très spécifique pour les phyllosilicates, soit pour des raisons de stéréospécificité vis-à-vis de la cavité ditrigonale siloxane (NH_4^+ et Cs^+), soit pour des raisons d'énergie de déshydratation (Ba^{2+} et Cs^+). Si l'affinité des deux cations monovalents pour la matière organique est bonne (7, 15), elle devrait en revanche être faible dans le cas du Ba^{2+}, comme l'indique la série d'Irwing-Williams donnée précédemment. Dans le cas des oxydes, en revanche, les ions monovalents sont en général moins adsorbés que les divalents. Il n'existe donc pas de cation saturant idéal.

2. Rinçage. Les cations non adsorbés et présents dans la solution associée au sol après centrifugation sont éliminés par rinçage à l'alcool éthylique, ou sont ramenés à une concentration connue (0,01 M dans le cas de Ba^{2+}). L'alcool est préféré à l'eau pour ne pas provoquer (i) la dispersion (et perte par centrifugation) des particules très fines au contact d'une eau de faible force ionique, (ii) la désorption du cation saturant, les cations saturants ayant peu d'affinité pour la phase liquide organique de rinçage, et (iii) la dissolution de phases solides, dont les cations une fois libérés pourraient provoquer une désorption précoce du cation saturant.

3. Extraction du cation saturant. Le cation adsorbé dans la première étape est extrait, par loi d'action de masse, en mettant le sol en présence d'un excès d'un autre cation ayant une affinité pour l'adsorbant si possible semblable au cation saturant. La CEC est alors obtenue en mesurant la concentration du cation saturant dans la solution extractante, et en l'exprimant en $mol_c\ kg^{-1}$ d'adsorbant. Dans le cas de la méthode au Ba, on extrait les ions Ba^{2+} adsorbés par loi d'action de masse en maintenant l'activité de Ba^{2+} en solution au plus bas, par précipitation avec un excès d'ions sulfates. Le sulfate de Ba précipité est ensuite dosé.

On voit que la première étape vise en général à favoriser la formation d'un CSI stable entre le cation saturant et le groupe fonctionnel de surface afin, entre autres, de désorber tous les cations "échangeables" mais aussi ceux présents en partie sous forme de CSI (K^+, Al^{3+} et ses complexes hydrolysés par exemple). Une méthode fait cependant exception : la méthode à la cobaltihexamine (20). Le complexe $Co(NH_3)_6^{3+}$, tendra soit à rester dans la couche diffuse, soit à former avec les groupes réactionnels de surface un complexe hors sphère. Il remplacera donc spécifiquement les cations qui sont à l'origine de $\sigma_{HS} + \sigma_d$ et ne remplacera en aucun cas les cations qui forment des CSI avec les sites fonctionnels de surface.

Tableau 1 : Méthodes couramment utilisées pour déterminer la capacité d'échange d'un sol. Principales étapes de la méthode et composantes de la charge de surface ainsi mesurées. *I* indique la force ionique de la solution saturante du sol.

Table 1 : Review of the various methods commonly used for the determination of soil cation exchange capacity. The successive stages and the identity of the measured soil surface charge component are given. I stands for the ionic strength of the soil solution under saturating conditions.

Méthode	Cation saturant	Rinçage	Cation déplaçant	pH	σ_{int}	Remarques
NH_4OAc (19)	NH_4^+	Alcool éthylique	Na^+ (excès)	7	$\sigma_o + (\sigma_H)_{pH\,7}$	Risques de dissolution de calcite
$BaCl_2$ (12)	Ba^{2+}	$BaCl_2$ (0,01 M)	$MgSO_4$ ($BaSO_4$ précipite)	4,8	$\sigma_o + (\sigma_H)_{pH\,4,8}$	Risques de dissolution de calcite
$Co(NH_3)_6Cl_3$ (20)	$Co(NH_3)_6^{3+}$ (I = 0,01 M)	—	—	pH et I du sol (extrait 1:5)	$CEC_{eff} = \sigma_o + \sigma_H$	Pour sols très altérés (I = 0,01 M)
NaOAc (21)	Na^+	—	Mg^{2+}	8,2	$\sigma_o + (\sigma_H)_{pH=8,2}$	Pour des sols calcaires (8,2 ≈ pH d'équilibre avec la calcite et l'atmosphère)
CsCl (1)	Cs^+	Alcool éthylique (puis séchage)	NH_4^+ (après Li^+)	7	σ_o	Pour isoler la charge permanente

La différence entre la méthode à la cobaltihexamine de **Orsini** et **Rémy** (20) et la méthode de **Metson** (19) tient aussi au pH atteint lors de la saturation initiale. Dans la première méthode, il s'agit du pH du sol et, dans la seconde, d'un pH égal à 7,0. En comparant les deux valeurs de CEC mesurées, on a une méthode simple, comme le détaille **Julien** dans son exposé, pour estimer la charge protonique de surface à compenser par chaulage, pour remonter le pH du sol du pH "naturel" à pH 7,0.

Si l'on suppose maintenant que les capacités d'échange en cations (CEC) et en anions (CEA) correspondent seulement aux ions présents à l'interface qui peuvent être facilement déplacés, c'est-à-dire aux cations dont l'adsorption est inversible sur une échelle de temps imposée par la méthode, alors la différence CEC-CEA est proportionnelle à la somme $\sigma_{HS} + \sigma_d$. En termes mathématiques,

$$\sigma_{HS} + \sigma_d = (F/S)\ (CEC - CEA) \qquad [6]$$

où F est la constante de Faraday, S est la surface spécifique d'un sol (en $m^2\ kg^{-1}$, mesurée par exemple par la méthode du BET, N_2 ou CPEG) et où CEC et CEA sont exprimées en $mol_c kg^{-1}$. L'équation 6 exprime le concept que CEC-CEA est proportionnelle à la densité de charge de surface intrinsèque, corrigée pour les charges des CSI, si de tels complexes existent :

$$\sigma_O + \sigma_H = \sigma_{int} = -\ (F/S)\ (CEC - CEA) \qquad [7]$$

On voit ici le rôle critique que jouent les ions présents dans le sol sous forme de CSI. L'hypothèse $\sigma_{SI} = 0$ est nécessaire pour passer des équations (1) et (6) à l'équation (7). Les ions présents sous forme de CSI, tels K^+ ou Cs^+ fixés sur les vermiculites, ne sont en général que partiellement désorbables sur une échelle de temps de l'ordre du jour, et limitent la validité de cette hypothèse.

4. TEMPS CARACTÉRISTIQUE ET VOLUME CARACTÉRISTIQUE

Nous venons de voir que la définition de la capacité d'échange est basée sur un *temps caractéristique*, le temps de réaction utilisé pour la mesure. La deuxième grandeur essentielle à la définition de la capacité d'échange d'un sol est la *taille caractéristique* - ou volume - de l'échantillon de terre choisi, et que l'on voudrait représentatif du sol d'un champ, d'un pédon, voire d'un bassin versant.

4. 1. Temps caractéristique

Bien que de nombreuses plantes et micro-organismes puisent leurs éléments nutritifs de la roche qu'ils altèrent, ces éléments nutritifs sont exclus des cations (ou anions) dits échangeables. Le temps caractéristique des réactions de dissolution des roches est en effet bien supérieur à celui considéré dans la mesure de la capacité d'échange, à une exception près : la dissolution de la calcite et du gypse. L'influence de cette dissolution sur les résultats de la mesure de la CEC est d'autant plus grande que le pH de l'eau utilisée pour cette mesure est plus faible. Des méthodes spécifiques, telles que les méthodes de **Rhoades** (21) et de **Orsini** et **Rémy** (20) ont donc été conçues pour mesurer la CEC au pH et à la force ionique du sol (20), ou au point d'équilibre de la calcite, de l'eau et du CO_2 atmosphérique (21) (tableau 1).

Sont donc considérés comme échangeables, tous les ions dont la cinétique de désorption peut être considérée comme rapide comparée à l'échelle de temps sur laquelle se fait le transport de ces ions vers la plante ou la nappe phréatique. Ce temps caractéristique est souvent choisi de façon arbitraire et, pour des raisons pratiques, égal à 24 h ou à des multiples de 24 h. Or, le temps caractéristique de la réaction de désorption d'un cation hydraté adsorbé par un phyllosilicate est souvent de l'ordre de la milliseconde (32). À cette cinétique rapide s'ajoute une cinétique de diffusion lente dans l'interfeuillet. Les ions rapidement adsorbés peuvent à leur tour être désorbés lorsque d'autres réactions de fixation de cations ont lieu dans le sol et n'ont pas encore atteint leur équilibre. La figure 6 illustre cela dans le cas de l'adsorption du cobalt sur l'hectorite. Après une première phase d'adsorption par échange cationique (virtuellement complète en cinq minutes), le cobalt s'adsorbe sur les bordures de l'argile et forme des CSI. Cette seconde adsorption a deux conséquences. D'une part, en système fermé, le cobalt adsorbé par échange cationique est libéré en solution pour compenser la disparition du cobalt dissous dû à la formation de CSI. D'autre part, le cobalt adsorbé sur les sites de bordure ne peut être remobilisé qu'à des échelles de temps beaucoup plus longues que celle de 24 h utilisée pour la mesure de la capacité d'échange. D'une façon générale, il faut replacer le temps au centre de la définition de la capacité d'échange, et ceci prendra toute son importance dans le futur avec le développement de modèles de transport réactif des solutés dans les sols.

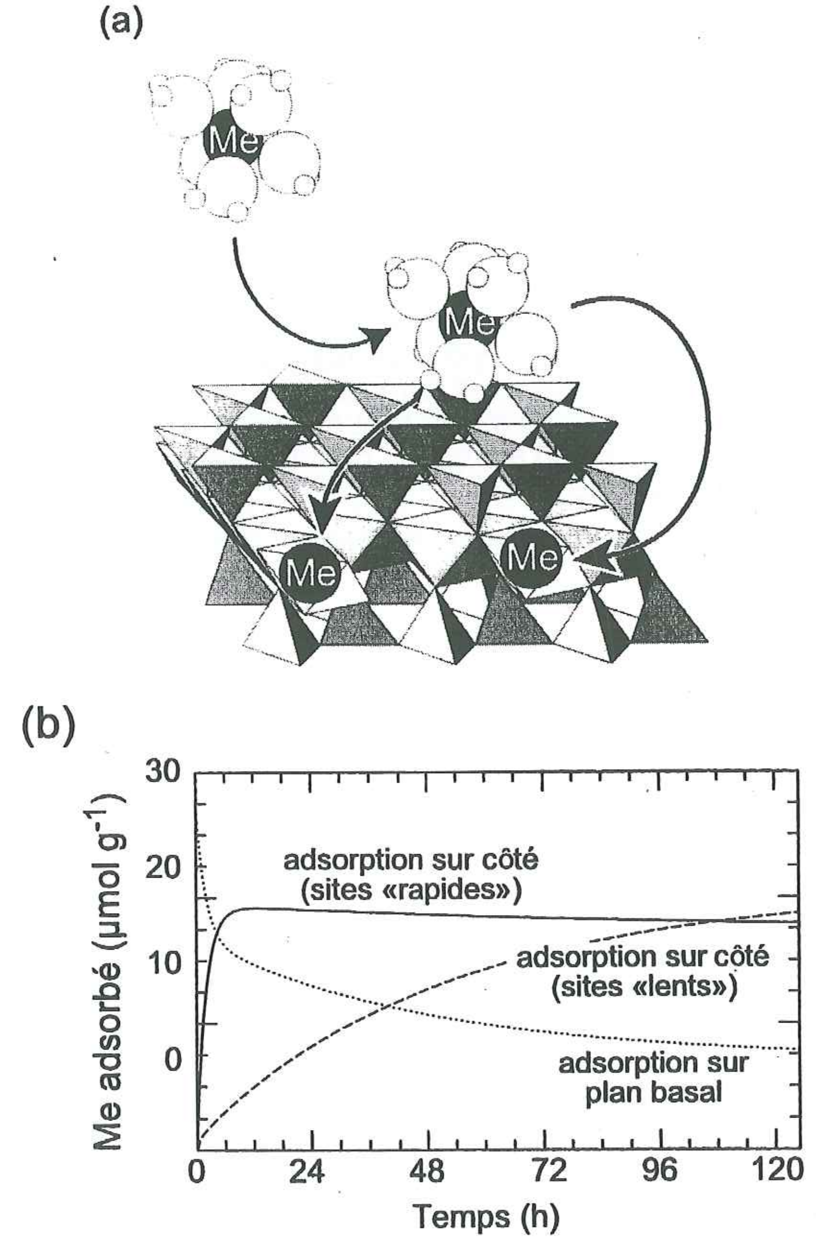

Figure 6 : Étapes cinétiques dans l'adsorption d'un cation, Me^{2+}, à la surface d'une argile, l'hectorite : (a) interprétation des données structurales (voir figure 1 pour la description des différents mécanismes) et (b) données cinétiques (le site "rapide" et le site "lent" correspondent à deux sites de surface avec lesquels le cation forme un complexe de sphère interne) (d'après 23, 24).

Figure 6 : ***Mechanism of a metal cation (Me^{2+}) sorption on hectorite. (a) Interpretation of structural results (see figure 1 for the corresponding sorption mechanisms). (b) Kinetics data. After a very fast outer-sphere complex formation, with the siloxane cavity, two types of inner-sphere surface complexes, characterized by distinct sorption kinetics, are formed (23, 24).***

2. Volume caractéristique

Autant les physiciens du sol réfléchissent depuis longtemps à la notion de changement d'échelle, autant la chimie du sol n'a encore fait que peu d'études sur l'impact du changement d'échelle sur la valeur des paramètres fondamentaux qu'elle utilise, tels que la capacité d'échange. De l'échelle de la motte de terre, on peut, tout en restant dans le même horizon pédologique, aller vers le microscopique et l'échelle atomique, et nous avons beaucoup utilisé cette approche "réductionniste" tout au long de cette revue pour comprendre les divers phénomènes qui se cachent derrière l'"échange cationique" et l'"adsorption spécifique". On peut aussi aller vers l'échelle mégascopique, c'est-à-dire celle du champ, ou du pédon. Le problème qui se pose au chimiste, contrairement à l'hydrologue, est en général l'absence d'outils pour quantifier la capacité d'échange à ces grandes échelles. Or, l'étude d' un même horizon au sein d'un lysimètre indique déjà une extrême hétérogénéité spatiale chimique (figure 7). Un protocole de prélèvement géostatistique devrait impérativement accompagner les méthodes de mesure de la CEC dans les normes à venir. On peut enfin imaginer que, dans l'avenir, des outils stochastiques prendront le relais des outils déterministes utilisés jusqu'à présent, comme cela s'est fait ces dix dernières années en physique du sol.

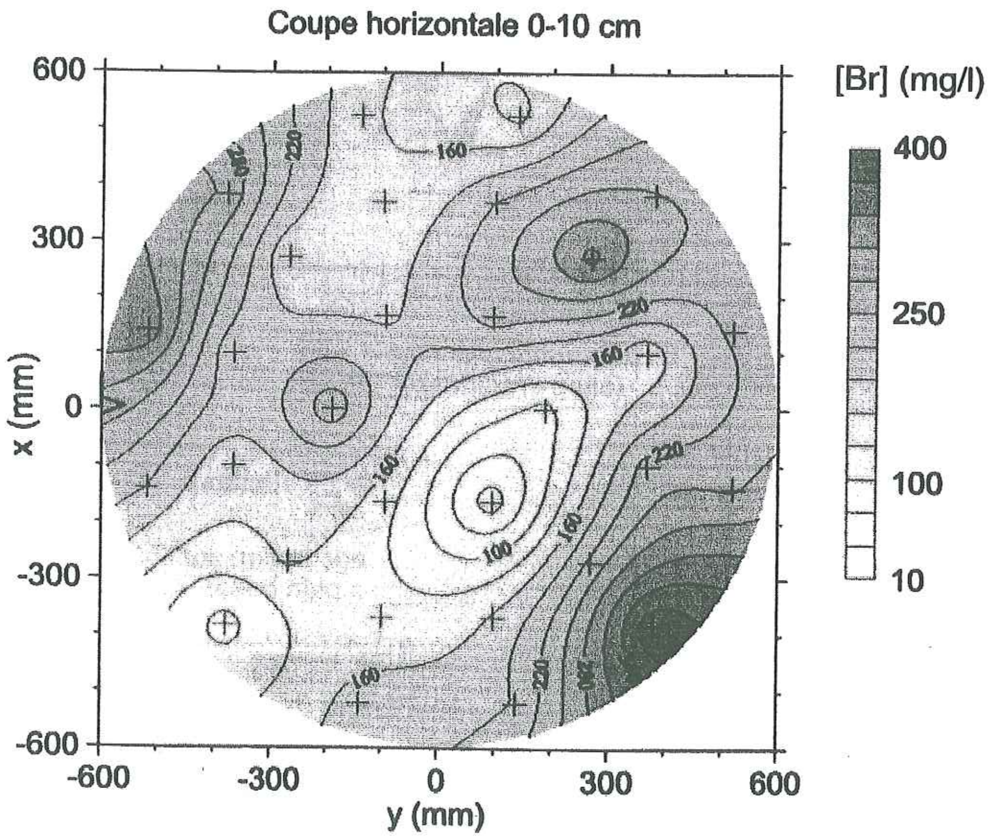

Figure 7 : **Concentration en Br^- de l'eau d'un sol contenu dans un lysimètre. Cette cartographie reflète l'hétérogénéité spatiale du transport de l'eau et de la charge de surface dans un sol (25).**

Figure 7 : ***Br- concentrations in soil water contained in a lysimeter. The observed heterogeneity reflects the heterogeneity of water movement and surface charges (after 25).***

CONCLUSIONS ET PERSPECTIVES

La capacité d'échange apparaît comme une mesure de la densité de charge intrinsèque d'un sol. Celle-ci comprend la densité de charge permanente structurale du sol, σ_0, mais aussi la densité de charge protonique σ_H. Cette dernière varie en fonction du pH et il faut la neutraliser quand on cherche à augmenter le pH par chaulage. Les méthodes de mesure de la capacité d'échange en cations au pH du sol (20) et à pH 7 (19) permettent d'estimer ce besoin en chaulage.

La capacité d'échange est basée sur le concept de cation (et d'anion) échangeable sur une échelle de temps donnée (en général 24 h). Le cas des cations adsorbés sous forme de complexes de sphère interne (CSI) est un cas très litigieux. Si ces CSI sont tous désorbés par le cation saturant utilisé dans la mesure de la capacité d'échange (Cs^+, NH_4^+, Ba^{2+}...), alors celle-ci donnera bien la valeur de la charge intrinsèque du sol ($\sigma_{in} = \sigma_0 + \sigma_H$). Cependant, la valeur obtenue pourra être supérieure à la somme des cations réellement échangeables dans les conditions qui prévalent dans le sol, où une partie des cations sont présents sous forme de CSI dont l'échangeabilité sera fonction de l'échelle de temps utilisée.

Il est essentiel de combiner, aux études chimiques classiques, des études spectroscopiques, seules capables de déterminer la nature et la structure des complexes formés à l'interface eau/particule. Ces études doivent être effectués *in situ* (en milieu aqueux) et en temps réel, afin de pouvoir suivre la cinétique des processus. Le développement récent d'une variété de méthodes spectroscopiques (spectroscopies de structure fine étendue d'absorption des rayons X, de résonance magnétique nucléaire, de résonance paramagnétique électronique) et microscopiques (microscopie de force atomique) devraient permettre dans un proche avenir de mieux affiner encore la nature des mécanismes impliqués dans un "échange" de cations ou d'anions, et donc de mieux préciser la nature de la "capacité d'échange" mesurée par les différentes méthodes proposées.

Remerciements

Nous dédicaçons cet article à la mémoire de Werner **Stumm**, dont nous apprenons la mort au moment de conclure cet article. Les concepts développés dans cet article doivent beaucoup à deux pôles de la chimie de surface, le pôle californien (G. **Sposito**) pour les sols et argiles, et le pôle suisse (W. **Stumm** et P.W. **Schindler**) pour les oxydes.

RÉFÉRENCES BIBLIOGRAPHIQUES

(1) ANDERSON S.J., SPOSITO G., 1991. – Cesium-adsorption method for measuring accessible structural surface charge. Soil Sci. Soc. Am. J., **55**, 1569-1576.
(2) AOUDJIT H., ROBERT M., ELSASS F., CURMI P., 1995. – Detailed study of smectite genesis in granitic saprolites by analytical microscopy. Clay Min., **30**, 135-147.
(3) AUBOIROUX M., MELOU F., BERGAYA F., TOURAY J.C., 1999. – Hard and soft acid-base model applied to bivalent cation selectivity on a 2:1 clay mineral. Clays Clay Min., **46**, 546-555.
(4) BICKMORE B., HOCHELLA M.F., BOSBACH D., CHARLET L., 1999. – Methods for performing atomic force microscopy imaging of clay minerals in aqueous solution. Clays and Clay Minerals (*sous presse*).
(5) BOLT G.H., 1979. – *Soil Chemistry. B: Physico-Chemical Models*, Elsevier, Amsterdam.
(6) BOSBACH D., CHARLET L., BICKMORE B., Hochella M.F.J., 1999 – The dissolution of hectorite: In-situ, real-time observations using Atomic Force Microscopy. Amer. Mineral. (*soumis*).
(7) BRITTAIN J.E., BJØRNSTAD H.E., SALBU B., OUGHTON D.H., 1992. – Winter transport of Chernobyl radionuclides from a montane catchment to an ice-covered lake. Analyst, **117**, 515-519.
(8) CHARLET L., MANCEAU A., 1994. – Evidence for the neoformation of clays upon sorption of Co(II) and Ni(II) on silicates. Geochim. Cosmochim. Acta, **58**, 2577-2782.
(9) CHARLET L., SCHINDLER P.W., SPADINI L., FURRER G., ZYSSER M., 1993 – Cation adsorption on oxides and clays: the aluminium case. Aquatic Sci., **55**, 291-303.
(10) CHARLET L., SPOSITO G., 1987 – Monovalent ion adsorption by an oxisol. Soil Sci. Soc. Am. J., **51**, 155-1160.
(11) DAVIS J.A., KENT D.B., 1990. – Surface complexation modeling in aqueous geochemistry. *In* Mineral-water interface geochemistry, M. F. J. Hochella and A. F. White, Eds., Mineralogical Society of America, Washington, 1990.
(12) GILLMAN G.P., 1979. – A proposed method for the measurement of exchange properties of highly weathered soils. Austr. J. Soil Res., **24**, 173-192.
(13) HEIL D., SPOSITO G., 1995 – Organic matter in illitic soil colloids flocculation : III. Scanning Force Microscopy, **59**, 266-269.
(14) JAMES R.O., PARKS G.A., 1982. – Characterization of aqueous colloids by their electrical double layer and intrinsic surface chemical properties. *In* Surface and colloid science, E. Matijevic, Ed., Plenum Publishing corporation, New York.
(15) MALMGREN L., JANSSON M., 1995. – The fate of Chernobyl radiocesium in the River Öre catchment, northern Sweden. Aquatic Sci., **57**, 144-160.
(16) MANCEAU A., CHARLET L., 1992 – X-ray absorption spectroscopic study of the sorption of Cr(III) at the oxide-water interface. I. Molecular mechanism of Cr(III) oxidation on Mn oxides. J. Colloid Interface Sci., **148**, 425-442.
(17) MARCANO-MARTINEZ E., Mc BRIDE M.B., 1989. – Comparison of the titration and ion adsorption methods for surface charge measurements in oxisols. Soil Sci. Soc. Am. J., **53**, 1040-1045.
(18) Mc BRIDE M.B., 1994. – *Environmental chemistry of soils*, Oxford University Press, Oxford.
(19) METSON A.J., 1956. – Methods of chemical analysis for soil survey samples. N.Z. Soil Bur. Bull., **12**.
(20) ORSINI L., REMY J.C., 1976. – Utilisation du chlorure de cobaltihexamine pour la détermination simultanée de la capacité d'échange et des bases échangeables des sols. Sci. Sol, **4**, 269-275.
(21) RHOADES J.D., 1982. – Cation exchange Capacity. In *Methods of soil analysis*, , American Society of Agronomy Publisher, New York.
(22) SCHINDLER P.W., 1991. – A solution chemist view of surface chemistry. Pure Appl. Chem., **63**, 1697-1704.
(23) SCHLEGEL M.L., CHARLET L., MANCEAU A., 1999. – Sorption of metal ions on clay minerals. II. Mechanism of Co sorption on hectorite at high and low ionic strength, and impact on the sorbent stability. J. Colloid Interface Sci. (*soumis*).
(24) SCHLEGEL M.L., MANCEAU A., CHATEIGNER D., CHARLET L., 1999. – Sorption of metal ions on clay minerals. I. Polarized EXAFS evidence for the adsorption of cobalt on the edges of hectorite particles. J. Colloid Interface Sci. (*sous presse*).
(25) SCHOEN R., GAUDET J.P., BARIAC T., 1999. – Preferential flow and solute transport in a large lysimeter, under controlled boundary conditions. J. Hydrol., **215**, 70-81.
(26) SPOSITO G., 1984. – The future of an illusion: ion activities in soil solutions. Soil Sci. Soc. Am. J., **48**, 531-536.
(27) SPOSITO G., 1984. – The surface chemistry of soils, Oxford university press: Oxford.
(28) SPOSITO G., 1986 – Sorption of trace metals by humic materials in soils and natural waters. CRC Critical Reviews in Environmental Control, **16**, 193-229.
(29) SPOSITO G. , 1992. – *In* Sampling and characterization of environmental particles, I. J. Buffle and H. P. Van Leeuwan, Eds., Lewis Publisher inc., Chelsea MI.
(30) STUMM W., MORGAN J.J., 1981. – *Aquatic chemistry*, 2 ed., John Wiley & Sons, New York.
(31) SULLIVAN P.J., 1977. – The principle of hard and soft acids and bases as applied to exchangeable cation selectivity in soils. Soil Sci., **124**, 117.
(32) TANG L., SPARKS D.L., 1993. – Cation-exchange kinetics on montmorillonite using pressure-jump relaxation. Soil Sci. Soc. Am. J., **57**, 42-46.
(33) WANNER H., ALBINSSON Y., KARNLAND O., WIELAND E., WERSIN P., CHARLET L., 1994. – The acid/base chemistry of montmorillonite. Radiochimica Acta, **66/67**, 157-162.
(34) WEISS C.A.J., KIRKPATRICK R.J., ALTANER S.P., 1990. – Geochim. Cosmochim. Acta, **54**, 1655-1669.

(accepté le 10 février 1999)

Conclusion générale

Des techniques macroscopiques (cinétique chimique) et spectroscopiques (spectroscopie EXAFS) ont été utilisées conjointement pour étudier les mécanismes d'adsorption du zinc et du cobalt sur les phyllosilicates. Les résultats obtenus dans cette étude peuvent être synthétisés comme suit.

À pH modéré (pH ≤ 6,5) et à haute force ionique, les ions Co^{2+} et Zn^{2+} sont adsorbés en bordure des feuillets de smectite, dans le prolongement de la couche octaédrique. Leur environnement cristallochimique est similaire à celui d'un cation octaédrique de la structure phyllosilicate. À pH 6,5 et basse force ionique, Co et Zn sont initialement adsorbés sur les sites d'échange cationique du feuillet, puis ils migrent progressivement vers les sites de bordure des feuillets.

À pH plus élevé (pH = 7,3), des polymères de zinc se forment à la surface des smectites. Leur taille et leur structure est fonction de la concentration en silice dissoute, $[Si]_{aq}$. À faible $[Si]_{aq}$, ces polymères sont constitués de 2-3 octaèdres de Zn et sont localisés dans la continuité de la couche octaédrique. Lorsque $[Si]_{aq}$ atteint des valeurs importantes (et réalistes pour des milieux terrestres), un phyllosilicate zincifère se forme en épitaxie dans le plan ab des feuillets d'hectorite. Bien que la cristallogenèse d'argiles par nucléation hétérogène n'ait été étudiée que pour le système Zn-hectorite, elle permet de mieux comprendre la néoformation de phyllosilicates cobaltifères à la surface du quartz.

Ce travail démontre l'importance qu'il faut accorder à l'ensemble des paramètres chimiques lors d'expériences de fixation de cations sur les phases minérales. Ces paramètres ne se limitent pas au pH, à la force ionique, et au rapport cation-substrat, mais ils englobent aussi la solubilité du substrat et la teneur de la solution en espèces dissoutes susceptibles d'influencer le processus d'adsorption. Un bon contrôle des conditions chimiques est nécessaire pour exploiter pleinement le potentiel des méthodes spectroscopiques, comme la spectroscopie EXAFS polarisée. L'identification des mécanismes de fixation des cations à l'interface minéral/solution est par ailleurs grandement facilitée par l'étude confrontée de références structurales appropriées.

Perspectives

L'utilisation conjointe de techniques macroscopiques et microscopiques présente un grand intérêt pour l'identification des mécanismes de fixation des cations à la surface des matériaux minéraux. La grande variété des résultats obtenus ouvre un champ de perspectives pour des études quantitatives approfondies des mécanismes d'adsorption de cations et de nucléation hétérogène des phyllosilicates en solution.

La démarche utilisée dans ce travail pourrait être étendue à l'étude de la réactivité de surface des phyllosilicates dioctaédriques. Dans ce but, une collaboration a été initiée avec l'équipe d'André Scheidegger à l'Institut Paul Scherrer de Zürich. Les résultats obtenus jusqu'à présent montrent que les cations adsorbés forment des hydrotalcites avec l'aluminium libéré par dissolution du substrat. Il serait intéressant d'évaluer l'impact de $[Si]_{aq}$ sur la stabilité à long terme de ces hydrotalcites, ainsi que sur l'éventuelle nucléation et croissance de phyllosilicates.

L'impact de $[Si]_{aq}$ sur la cinétique et le mécanisme de nucléation de phyllosilicates à la surface de l'hectorite a été étudié à pH 7,3. Il serait intéressant d'étendre cette étude à d'autres conditions de pH, de concentration en Si et en métal, et à des substrats variés, afin de mieux contraindre les modèles cinétiques de nucléation et de croissance des phyllosilicates. Pour ces expériences, l'hectorite s'avère un bon substrat en raison de sa grande réactivité et de sa faible stabilité qui permettent de réaliser des expériences en des temps relativement courts.

Une autre thématique intéressante concerne les mécanismes de fixation des cations sur le quartz. Le quartz est abondant dans les systèmes naturels, et les incrustations de minéraux argileux (« coatings ») à sa surface sont fréquents. Le mécanisme de formation de ces incrustations pourrait être étudié de manière approfondie sur la base des résultats obtenus sur le système cobalt/quartz. Un préliminaire à cette étude est la caractérisation structurale de l'interface quartz-solution, et notamment les conditions physico-chimiques de formation d'une couche de silice amorphe.

Enfin, un dernier axe de recherche dans la continuité de ce travail pourrait être l'étude de la synthèse de phyllosilicates *alumineux* à température ambiante. Cette synthèse s'est avérée jusqu'à présent être lente et difficile, mais l'exploration systématique des conditions de pH et de concentrations en Al et Si en solution permettrait peut-être de réaliser en laboratoire des néoformations à des taux cinétiques raisonnables. Enfin, l'emploi de cations métalliques dopants analogues à l'aluminium et dont l'environnement cristallochimique peut être caractérisé par EXAFS (ex : Ga) devrait permettre d'étudier le mécanisme structural de cette cristallogenèse.

Bibliographie

1.McCracken, R.J. (1987). Soils, soil scientists, and civilization. *Soil Sci. Soc. Am. J.*, **51**, 1395-1400.

2.Sposito, G. (1984). *The surface chemistry of soils*. Oxford University Press, Oxford.

3.Güven, N. (1988). Smectites. In *Hydrous Phyllosilicates* (S.W. Bailey, Ed.), pp 497-559. Mineralogical society of America, Washington, DC.

4.Righi, D., & Meunier, A. (1995). Origin of clays by rock weathering and soil formation. In *Origin and mineralogy of clays* (B. Velde, Ed.), pp 43-161. Springer, Berlin.

5.Wilson, M.J. (1999). The origin and formation of clay minerals in soils: past, present and future perspectives. *Clay Min.*, **34**, 7-25.

6.Millot, G. (1964). *Géologie des Argiles*. Masson, Paris.

7.Velde, B. (1995). Composition and mineralogy of clay minerals. In *Origin and mineralogy of clays* (B. Velde, Ed.), pp 15-42. Springer-Verlag, Berlin.

8.McBride, M.B. (1994). *Environmental chemistry of soils*. Oxford University Press, Oxford.

9.Laudelout, H. (1987). Cation exchange equilibria in clays. In *Chemistry of clays and clay minerals* (A.C.D. Newman, Ed.), pp 225-236. Longman scientific & technical, Harlow.

10.Harder, H. (1977). Clay mineral formation under lateritic weathering conditions. *Clay Min.*, **12**, 281-288.

11.Borchardt, G. (1995). Smectites. In *Minerals in soils environments* (J.B. Dixon, & S.B. Weed, Eds.), pp 675-728, Madison, WI.

12.Manceau, A., Boisset, M.-C., Sarret, G., Hazemann, J.-L., Mench, M., Cambier, P., & Prost, R. (1996). Direct determination of lead speciation in contaminated soils by EXAFS spectroscopy. *Environ. Sci. Technol.*, **30**, 1540-1552.

13. Manceau, A., Lanson, B., Schlegel, M.L., Hargé, j.-C., Musso, M., Hazemann, J.-L., Chateigner, D., & Lamble, G.M. (2000). Quantitative speciation Zn speciation in smelter-contaminated soils by EXAFS spectroscopy. I. . *Am. J. Sci.* (sous presse).

14. Bickmore, B., Hochella, M.F., Jr., Bosbach, D., & Charlet, L. (1999). Methods for performing atomic force microscopy imaging of clay minerals in aqueous solution. *Clays Clay Min,* **47**, 573-581.

15. Manceau, A., Drits, V.A., Silvester, E., Bartoli, C., & Lanson, B. (1997). Mechanism of Co^{2+} oxidation by the phyllomanganate buserite. *Amer. Mineral.*, **82**, 1150-1175.

16. Manceau, A., Chateigner, D., & Gates, W.P. (1998). Polarized EXAFS, distance-valence least-squares modeling (DVLS) and quantitative texture analysis approaches to the structural refinement of Garfield nontronite. *Phys. Chem. Minerals*, **25**, 347-365.

17. Sparks, D.L. (1998). Kinetics and mechanisms of chemical reactions. In *Soil physical chemistry* (D.L. Sparks, Ed.), pp 135-191. CRC press, New York.

18. Scheidegger, A.M., Strawn, D.G., Lamble, G.M., & Sparks, D.L. (1998). The kinetics of mixed Ni-Al hydroxide formation on clay and aluminium oxide minerals: a time-resolved XAFS study. *Geochim. Cosmochim. Acta*, **62**, 2233-2245.

19.Giese, R.F. (1979). Hydroxyl orientation in 2:1 phyllosilicates. *Clays Clay Min.*, **27**, 213-223.

20.Besson, G. (1980). Structure des smectites dioctaédriques. Paramètres conditionnant les fautes d'empilement des feuillets. Thèse de doctorat. Université d'Orléans, Orléans.

21.Suquet, H., Prost, R., & Pezerat, H. (1982). Étude par spectroscopie infrarouge et diffraction X des interactions eau-cation-feuillet dans les phases à 14.6, 12.2 et 10.1 Å d'une saponite-Li de synthèse. *Clay Min.*, **17**, 231-241.

22.Shannon, R.D. (1976). Revised effective ionic radii and systematic studies of interatomic distances in halides and chalcogenides. *Acta Cryst.*, **A32**, 751-767.

23.Bailey, S.W. (1980). Structures of layer silicates. In *Crystal structures of clay minerals and their X-ray identification* (G.W. Brindley, & G. Brown, Eds.), pp 1-123. Mineralogical Society, London.

24.Bailey, S.W. (1984). Crystal chemistry of the true micas. In *Micas* (S.W. Bailey, Ed.), pp 13-60. Mineralogical Society of America, Washington, DC.

25.Hazen, R.M., & Wones, D.R. (1972). The effect of cation substitution s on the physical properties of trioctahedral micas. *Amer. Mineral.*, **57**, 103-129.

26.Newman, A.C.D., & Brown, G. (1987). The chemical constitution of clays. In *Chemistry of clays and clay minerals* (A.C.D. Newman, Ed.), pp 1-128. Longman scientific & technical, Harlow.

27.Besson, G., Decarreau, A., Manceau, A., Sanz, J., & Suquet, H. (1990). Organisation interne du feuillet. In *Les atériaux argileux. Structures, propriétés, applications.* (A. Decarreau, Ed.), pp 5-162. Société française de minéralogie et de cristallographie, Paris.

28.Cases, J.-M., Bérend, I., Besson, G., François, M., Uriot, J.-P., Thomas, F., & Poirier, J.E. (1992). Mechanism of adsorption and desorption of water vapor by homoionic montmorillonites: 1. The sodium-exchanged form. *Langmuir*, **8**, 2730-2739.

29.Cases, J.-M., Bérend, I., François, M., Uriot, J.-P., Michot, L.J., & Thomas, F. (1997). Mechanism of adsorption and desorption of water vapor by homoionic montmorillonites: 3. The Mg^{2+}, Ca^{2+}, Sr^{2+} and Ba^{2+}-exchanged forms. *Clays Clay Min.*, **45**, 8-22.

30.Bérend, I., Cases, J.-M., François, M., Uriot, J.-P., Michot, L.J., Masion, A., & Thomas, F. (1995). Mechanism of adsorption and desorption of water vapor by homoionic montmorillonites: 2. The Li^+, Na^+, K^+, Rb^+ and Cs^+-exchanged forms. *Clays Clay Min.*, **43**, 324-336.

31.Suquet, H. (1990). Les différents modes d'empilement des feuillets. In *Les matériaux argileux. Structure, propriétés et applications* (A. Decarreau, Ed.), pp 173-179. Société française de minéralogie et de cristallographie, Paris.

32.Joffe, J.S., & Kolodny, L. (1938). Effect of alternate drying and wetting on the base exchange complex with special reference to the behaviour of the potassium soil. *Soil Sci. Soc. Am. Proc*, **3**, 107-111.

33.Mamy, J., & Gaultier, J.-P. (1979). Étude comparée de l'évolution des montmorillonites biioniques K-Ca de Camp-Berteaux et du Wyoming sous l'effet des cycles d'humectation et de dessication. *Clay Min.*, **14**, 181-192.

34.Besson, G., Glaeser, R., & Tchoubar, C. (1983). Le césium, révélateur de structure des smectites. *Clay Min.*, **18**, 11-19.

35.Charlet, L., & Schlegel, M.L. (1999). La capacité d'échange des sols. Structure et charges à l'interface eau-particule. *C.R. Acad. Agric. Fr.*, **85**, 7-28.

36.McBride, M.B., Pinnavaia, T.J., & Mortland, M.M. (1975). Electron spin relaxation and the mobility of manganese(II) exchange ions in smectites. *Amer. Mineral.*, **60**, 66-72.

37.McBride, M.B. (1979). Mobility and reactions of VO^{2+} on hydrated smectite surfaces. *Clays Clay Min.*, **27**, 91-96.

38.McBride, M.B. (1982). Hydrolysis and dehydration reaction reactions of exchangeable Cu^{2+} on hectorite. *Clays Clay Min.*, **30**, 200-206.

39.Weiss, C.A., Jr., Kirkpatrick, R.J., & Altaner, S.P. (1990). The structural environments of cations adsorbed onto clays: ^{133}Cs variable-temperature MAS NMR spectroscopic study of hectorite. *Geochim. Cosmochim. Acta*, **54**, 1655-1669.

40.Lambert, J.-F., Prost, R., & Smith, M.E. (1992). ^{39}K solid-state NMR studies of potassium tecto- and phyllosilicates: the *in situ* detection of hydratble K^+ in smectites. *Clays Clay Min.*, **40**, 253-261.

41.Kim, Y., Cygan, R.T., & Kirkpatrick, R.J. (1996). ^{133}Cs NMR and XPS investigation of cesium adsorbed on clay minerals and related phases. *Geochim. Cosmochim. Acta*, **60**, 1041-1052.

42.Kim, Y., & Kirkpatrick, R.J. (1997). ^{23}Na and ^{133}Cs NMR study of cation adsorption on mineral surfaces: local environment s, dynamics, and effects of mixed cations. *Geochim. Cosmochim. Acta*, **61**, 5199-5208.

43.Suquet, H., Malard, C., Copin, E., & Pezerat, H. (1981). Variation du paramètre b et de la distance basale d_{001} dans une série de saponites à charge croissante. II. État 'zéro couche'. *Clay Min.*, **16**, 181-193.

44.Ben Brahim, J., Amargan, N., Besson, G., & Tchoubar, C. (1986). Méthode diffractométrique de caractérisation des états d'hydratation des smectites: stabilité relative des couches d'eau insérées. *Clay Min.*, **21**, 111-124.

45.Boek, S.E., Coveney, P.V., & Skipper, N.T. (1995). Monte Carlo molecular modeling studies of hydrated Li-, Na-, and K-smectites: understanding the role of potassium as a clay swelling inhibitor. *J. Am. Chem. Soc.*, **117**, 12608-12617.

46.Greathouse, J., & Sposito, G. (1998). Monte Carlo and molecular dynamics studies of interlayer structure in $Li(H_2O)_3$-smectites. *J. Phys. Chem. B*, **102**, 2406-2414.

47.Skipper, N.T., Chang, F.-R.C., & Sposito, G. (1995). Monte-Carlo simulation of interlayer molecular structure in swelling clay minerals. 1. Methodology. *Clays Clay Min.*, **43**, 285-293.

48.Skipper, N.T., Sposito, G., & Chang, F.-R.C. (1995). Monte-Carlo simulation of interlayer molecular structure in swelling clay minerals. 2. Monolayer hydrates. *Clays Clay Min.*, **43**, 294-303.

49.Gaultier, J.-P., & Mamy, J. (1978). Étude des facteurs influençant l'évolution structurale de la montmorillonite K et sa réversibilité. *Clay Min.*, **13**, 139-146.

50.Prost, R. (1975) *Ann. Agron.*, **26**, 400.

51.Suquet, H., Prost, R., & Pezerat, H. (1977). Etude par spectroscopie infrarouge de l'eau adsorbée par la saponite-calcium. *Clay Min.*, **12**, 113-126.

52.Dillard, J.D., & Koppelman, M.H. (1982). X-ray photoelectron spectroscopic (XPS) surface characterization of cobalt on the surface of kaolinite. *J. Colloid Interface Sci.*, **87**, 46-55.

53.Davison, N., McWhinnie, W.R., & Hooper, A. (1991). X-ray photoelectron spectroscopic study of cobalt(II) and nickel(II) sorbed on hectorite and montmorillonite. *Clays Clay Min.*, **39**, 22-27.

54.Dent, A.J., Ramsay, J.D.F., & Swanton, S.W. (1992). An EXAFS study of uranyl ion in solution and sorbed onto silica and montmorillonite clay suspensions. *J. Colloid Interface Sci.*, **150**, 45-60.

55.Siantar, D.P., & Fripiat, J.J. (1995). Lead retention and complexation in an magnesium smectite. *J. Colloid Interface Sci.*, **169**, 400-407.

56.Papelis, C., & Hayes, K.F. (1996). Distinguishing between interlayer and external sorption sites of clay minerals using X-ray absorption spectroscopy. *Coll. Surf. A: Physicochem. Engineer. Aspects*, **107**, 89-96.

57.Muller, F., Besson, G., Manceau, A., & Drits, V.A. (1997). Distribution of isomorphous cations within octahedral sheets in montmorillonite from Camp-Berteaux. *Phys. Chem. Minerals*, **24**, 159-166.

58.Burgess, J. (1978). *Ions in Solution: Basic Principles of Chemical Interactions*. John Wiley & Sons, New York.

59.Glaeser, R., & Mering, J. (1954). Isothermes d'hydratation des montmoeillonites bi-ioniques. *Clay Min.*, **2**, 188-193.

60.Mering, J., & Glaeser, R. (1954). Sur le rôle de la valence des cations échangeables dans la montmorillonite. *Bull. Soc. Franç. Minér. Crist.*, **77**, 519-530.

61.White, G.N., & Zelazny, L.W. (1988). Analysis and implication of the edge structure of dioctaedral phylosilicates. *Clays Clay Min.*, **36**, 141-146.

62.Pauling, L. (1929). The principles determining the structure of complex ionic crystals. *J. Am. Chem. Soc.*

63.Brown, I.D., & Shannon, R.D. (1973). Empirical bond-strength-bond-length curves for oxides. *Acta Cryst.*, **A 29**, 266-282.

64.Brown, I.D. (1987). Recent developments in the bond valence model of inorganic bonding. *Phys. Chem. Minerals*, **15**, 30-34.

65.Brown, I.D., & Altermatt, D. (1985). Bond-valence parameters obtained from a systematic analysis of the Inorganic Crystal Structure Database. *Acta Cryst.*, **B41**, 244-247.

66.Brown, I.D. (1981). The bond-valence method: an empirical approach to chemical structure and bonding. In *Structure and bonding in crystals. II* (M. O'Keefe, & A. Navrotsky, Eds.), pp 1-30. Academic Press, New York.

67.Brown, I.D. (1978). Bond valences-a simple structural model for inorganic chemistry. *Chem. Soc. Rev.*, **7**, 359-376.

68.Brown, I.D. (1977). Predicting bond Lengths in inorganic solids. *Acta Cryst.*, **B 33**, 1305-1310.

69.Brown, I.D. (1976). On the geometry of O-H...O hydrogen bonds. *Acta Cryst.*, **A32**, 24-31.

70.Brown, I.D. (1992). Chemical ans steric constraints in inorganic solids. *Acta Cryst.*, **B48**, 553-572.

71.Brese, N.E., & O'Keeffe, M. (1991). Bond-valence parameters for solids. *Acta Cryst.*, **B47**, 192-197.

72.Manceau, A., & Gates, W.P. (1997). Surface structural model for ferrihydrite. *Clays Clay Min.*, **43**, 448-460.

73.Brown, I.D. (1995). Anion-anion repulsion, coordination number, and the asymmetry of hydrogen bonds. *Canad. J. Phys.*, **73**, 553-572.

74.Hiemstra, T., Van Riemsdijk, W.H., & Bolt, G.H. (1989). Multisite proton adsorption modeling at the solid/solution interface of (hydr)oxides: a new approach. I. Model description and evaluation of intrinsic reaction constants. *J. Colloid Interface Sci.*, **133**, 91-104.

75.Hiemstra, T., Venema, P., & Van Riemsdijk, W.H. (1996). Intrinsic proton affinity of reactive surface groups of metal (Hydr)oxides: the bond valence principle. *J. Colloid Interface Sci.*, **184**, 680-692.

76.Hiemstra, T., De Wit, J.C.M., & Van Riemsdijk, W.H. (1989). Multisite proton adsorption modeling at the solid/solution interface of (hydr)oxides: a new approach. II. Application to various important (hydr)oxides. *J. Colloid Interface Sci.*, **133**, 105-117.

77.Spadini, L., Manceau, A., Schindler, P.W., & Charlet, L. (1994). Structure and stability of Cd^{2+} surface complexes on ferric oxides. 1. Results from EXAFS spectroscopy. *J. Colloid Interface Sci.*, **168**, 73-86.

78.Gates, W.P., Jaunet, A.-M., Tessier, D., Cole, M.A., Wilkinson, H.T., & Stucki, J.W. (1998). Swelling and texture of iron-bearing smectites reduced by bacteria. *Clays Clay Min.*, **46**, 487-497.

79.Peigneur, P., Maes, A., & Cremers, A. (1975). heterogeneity of charge density distribution in montmorillonite as inferred from cobalt adsorption. *Clays Clay Min.*, **23**, 71-75.

80.Zachara, J.M., & McKinley, J.P. (1993). Influence of hydrolysis on the sorption of metal cations by smectites: importance of edge coordination reactions. *Aquatic Sci.*, **55**, 250-261.

81.Zachara, J.M., & Smith, S.C. (1994). Edge complexation reactions of cadmium on specimen and soil-derived smectite. *Soil Sci. Soc. Am. J.*, **58**, 762-769.

82.Zysset, M. (1992). Die protoneninduzierte Auflösung von K-Montmorillonit. Thèse de Doctorat, Université de Bern, Bern.

83.Wanner, H., Albinsson, Y., Karnland, O., Wieland, E., Wersin, P., & Charlet, L. (1994). The acid/base chemistry of montmorillonite. *Radiochim. Acta*, **66/67**, 157-162.

84.McKinley, J.P., Zachara, J.M., Smith, S.C., & Turner, G.D. (1995). The influence of uranyl hydrolysis and multiple site-binding reactions on adsorption of U(VI) to montmorillonite. *Clays Clay Min.*, **43**, 586-598.

85.Kraepiel, A.M.L., Keller, K., & Morel, F.M.M. (1999). A model for metal adsorption on montmorillonite. *J. Colloid Interface Sci.*, **210**, 43-54.

86.Charlet, L., Schindler, P.W., Spadini, L., Furrer, G., & Zysset, M. (1993). Cation adsorption on oxides and clays: the aluminium case. *Aquatic Sci.*, **55**, 291-303.

87.Stadler, M., & Schindler, P.W. (1993). Modeling of H^+ and Cu^{2+} adsorption on calcium-montmorillonite. *Clays Clay Min.*, **41**, 288-296.

88.Schindler, P.W., & Stumm, W. (1987). The surface chemistry of oxides, hydroxides and oxide minerals. In *Aquatic surface chemistry* (W. Stumm, Ed.). Wiley-Interscience, New York.

89.Sposito, G. (1983). On the surface complexation model of the oxide-aqueous solution interface. *J. Colloid Interface Sci.*, **91**, 329-340.

90.Singh, U., & Uehara, G. (1998). Electrochemistry of the double layer: Principles and applications to soils. In *Soil physical chemistry* (D.L. Sparks, Ed.), pp 1-46. CRC Press, New York.

91.Westall, J.C. (1986). Reactions at the solid-solution interface: chemical and electrostatic models. In *Geochemical processes at mineral surfaces* (J.A. Davis, & K.F. Hayes, Eds.), pp 54-78. American Chemical Socitey, Washington, DC.

92.Baeyens, B., & Bradbury, M.H. "A quantitative mechanistic description of Ni, Zn and Ca sorption on Na-montmorillonite. Part I: Physico-chemical characterisation and titration measurements," Paul Scherrer Institut, 1995.

93.Baeyens, B., & Bradbury, M.H. "A quantitative mechanistic description of Ni, Zn and Ca sorption on Na-montmorillonite. Part II: Sorption measurements," Paul Scherrer Institut, 1995.

94.Bradbury, M.H., & Baeyens, B. "A quantitative mechanistic description of Ni, Zn and Ca sorption on Na-montmorillonite. Part III: modelling," Paul Scherrer Institut, 1995.

95.Davis, J.A., Coston, J.A., Kent, D.B., & Fuller, C.C. (1998). Application of the surface complexation concept to complex mineral assemblages. *Environ. Sci. Technol.*, **32**, 2820-2828.

96.Bradbury, M.H., & Baeyens, B. (1999). Modelling the sorption of Zn and Ni on Ca-montmorillonite. *Geochim. Cosmochim. Acta*, **63**, 325-336.

97.Stumm, W., Huang, C.P., & Jenkins, S.R. (1970). Specific chemical interaction affecting the stability of dispersed systems. *Croat. Chem. Acta*, **53**, 291-312.

98.Davis, J.A., & Kent, D.B. (1990). Surface complexation modeling in aqueous geochemistry. In *Mineral-water interface geochemistry* (M.F. Hochella, Jr, & A.F. White, Eds.), pp 177-260. Mineralogical Society of America, Washington, DC.

99.Huang, C.P., & Stumm, W. (1973). Specific adsorption of cations on hydrous γ-Al_2O_3. *J. Colloid Interface Sci.*, **43**, 409-420.

100.Davis, J.A., James, R.O., & Leckie, J.O. (1978). Surface ionization and complexation at the oxide/water interface. I. Computation of electrical double layer properties in simple electrolytes. *J. Colloid Interface Sci.*, **63**, 480-499.

101.Kreit, J.F., Shainberg, I., & Herbillon, A.J. (1982). Hydrolysis and decomposition of hectorite in dilute salt solutions. *Clays Clay Min.*, **30**, 223-231.

102.Kaviratna, H., & Pinnavaia, T.J. (1994). acid hydrolysis of octahedral Mg^{2+} sites in 2:1 layered silicates - an assessment of edge attack and gallery access mechanisms. *Clays Clay Min.*, **42**, 717-723.

103.Nagy, K.L. (1995). Dissolution and precipitation kinetics of sheet silicates. In *Chemical weathering rates of silicate minerals* (A.F. White, & S.L. Brantley, Eds.), pp 173-233. Mineralogical Society of America, Washington, DC.

104.Zysset, M., & Schindler, P.W. (1996). The proton promoted dissolution kinetics of K-montmorillonite. *Geochim. Cosmochim. Acta*, **60**, 921-931.

105.Tiller, K.G. (1968). Stability of hectorite in weackly acidic conditions. I. A chemical study of the dissolution of hectorite with special reference to the release of silica. *Clay Min.*, **7**, 245-259.

106.Komadel, P., Madejova, J., Janek, M., Gates, W.P., Kirkpatrick, R.J., & Stucki, J.W. (1996). Dissolution of hectorite in inorganic acids. *Clays Clay Min.*, **44**, 228-236.

107.Bosbach, D., Charlet, L., Bickmore, B., & Hochella, M.F., Jr. (1999). The dissolution of hectorite: In-situ, real-time observations using atomic force microscopy. *Amer. Mineral.* (soumis).

108.Stumm, W., & Morgan, J.J. (1996). *Aquatic chemistry*, 3 ed. John Wiley & Sons, New York.

109.Wieland, E., Wehrli, B., & Stumm, W. (1988). The coordination chemistry of weathering: III. A generalization on the dissolution rates of minerals. *Geochim. Cosmochim. Acta*, **52**, 1969-1981.

110.Novak, I., & Cibel, B. (1978). Dissolution of smectites in hydrochloric acid: II. Dissolution rate as a function of crystallochemical composition. *Clays Clay Min.*, **26**, 341-344.

111.Egozy, Y. (1980). Adsorption of cadmium and cobalt on montmorillonite as a function of solution composition. *Clays Clay Min.*, **28**, 311-318.

112.Bloom, P.R., McBride, M.B., & Chadbourne, B. (1799). Adsorption of aluminium by a smectite: I. Surface hydrolysis during Ca^{2+}-Al^{3+} exchange. *Soil Sci. Soc. Am. J.*, **41**, 1068-1073.

113.Brigatti, M.F., Campana, G., Medici, L., & Poppi, L. (1996). The influence of layer charge on Zn^{2+} and Pb^{2+} sorption by smectites. *Clay Min.*, **31**, 477-483.

114.Charlet, L. (1994). Reactions at the mineral-water interface. In *Chemisty of aquatic systems: local and global perspectives* (G. Bidoglio, & W. Stumm, Eds.), pp 273-305, Brussels.

115.Gast, R.G. (1972). Alkali metal cation exchange on Chambers montmorillonite. *Soil Sci. Soc. Am. Proc*, **36**, 14-19.

116.Inskeep, W.P., & Baham, J. (1983). Adsorption of Cd(II) and Cu(II) by Na-montmorillonite at low surface coverage. *Soil Sci. Soc. Am. J.*, **47**, 660-665.

117.Maes, A., Stul, M.S., & Cremers, A. (1979). Layer charge-cation exchange capacity relationships in montmorillonite. *Clays Clay Min.*, **27**, 387-392.

118.Puls, R.W., & Bohn, H. (1988). Sorption of cadmium, nickel and zinc by kaolinite and montmorillonite suspensions. *Soil Sci. Soc. Am. J.*, **52**, 1289-1292.

119.Wold, J., & Pickering, W.F. (1981). Influence of electrolytes on metal ion sorption by clays. *Chem. Geol.*, **33**, 91-99.

120.Stumm, W., & Morgan, J.J. (1981). *Aquatic chemistry*, 2nd ed. John Wiley & Sons, New York.

121.Lyklema, J. (1983). Adsorption of small ions. In *Adsorption from solution at the solid-liquid interface* (G.D. Parfitt, & C.H. Rochester, Eds.). Academic Eds., London.

122.Dzombak, D.A., & Morel, F.M.M. (1990). *Surface complexation modeling*. John Wiley and sons, New York.

123.Sposito, G. (1994). *Chemical equilibria and kinetics in soils*. Oxford University Press, Oxford.

124.Galicia Flores, H.F. (1989). Adsorption of cadmium and copper by forrest humic acids and (K, H)-montmorillonite. Thèse de doctorat, université de Bern, Bern.

125.Scheidegger, A.M., & Sparks, D.L. (1996). Kinetics of the formation and the dissolution of nickel surface precipitates on pyrophyllite. *Chem. Geol.*, **132**, 157-164.

126.Zachara, J.M., Smith, S.C., Resh, C.T., & Cowan, C.E. (1993). Cadmium sorption on specimen and soil smectites in sodium and calcium electrolytes. *Soil Sci. Soc. Am. J.*, **57**, 1491-1501.

127.Degueldre, C., Ulrich, H.J., & Silby, H. (1994). Sorption of ^{241}Am onto montmorillonite, illite and hematite colloids. *Radiochimica Acta*, **65**, 173-179.

128.Tiller, K.G. (1968). Stability of hectorite in weackly acidic conditions. II. Studies of the chemical equilibrium and the calculation of free energy. *Clay Min.*, **7**, 261-270.

129.Stoessel, R.K. (1988). 25°C and 1 atm dissolution experiments of sepiolite and kerolite. *Geochim. Cosmochim. Acta*, **52**, 365-374.

130.Scheidegger, A.M., Lamble, G.M., & Sparks, D.L. (1996). Investigation of Ni adsorption on pyrophyllite: an XAFS study. *Environ. Sci. Technol.*, **30**, 548-554.

131.Scheidegger, A.M., Lamble, G.M., & Sparks, D.L. (1997). Spectroscopic evidence for the formation of mixed-cation hydroxide phases upon metal sorption on clay and aluminium oxides. *J. Colloid Interface Sci.*, **186**, 118-128.

132.Ford, R.G., Scheinost, A.C., Scheckel, K.G., & Sparks, D.L. (1999). The link between clay mineral weathering and the stabilization of Ni surface precipitates. *Environ. Sci. Technol.*, **33**, 3140-3144.

133.Kelley, W.P. (1948). *Cation exchange in soils*. Reinhold publishing corporation, New York.

134.Anderson, S.J., & Sposito, G. (1991). Cesium-adsorption method for measuring accessible structural surface charge. *Soil Sci. Soc. Am. J.*, **55**, 1569-1576.

135.Gapon, E.N. (1933). Theory of exchange adsorption in soils. *J. Gen. Chem. (U.S.S.R.)*, **3**, 144-152.

136.Vanselow, A.P. (1932). The utilization of the base-exchange reaction for the determination of activity coefficients in mixed electrolytes. *J. Am. Chem. Soc.*, **54**, 1307-1311.

137.Vanselow, A.P. (1932). Equilibria of the base-exchange reaction of bentonites, permutites, Soil colloids and zeolites. *Soil Sci.*, **33**, 95-113.

138.Sposito, G. (1981). *The thermodynamics of soil solutions*. Oxford University Press, Oxford.

139.Gaines, G.L., & Thomas, H.C. (1953). Adsorption studies on clay minerals. II. A formulation of the thermodynamics of exchange adsorption. *J. Chem. Phys.*, **21**, 714-718.

140.Rothmund, V., & Kornfeld, G. (1918). Die Basenaustauch im Permutit. *Z. Anorgan. Chem.*, **103**, 129-162.

141.Jensen, H.E., & Babcock, K.L. (1973). Cation exchange equilibria on a sandy loam. *Hilgardia*, **41**, 475-487.

142.Jensen, H.E. (1973). Potassium-calcium exchange equilibria on a montmorillonite and a kaolinite clay. I. A test on the Argersinger thermodynamic approach. *Agrochimica*, **17**, 181-201.

143.Gast, R.G. (1969). Standard free energies of exchange for alkali metal cations on Wyoming bentonite. *Soil Sci. Soc. Am. Proc*, **33**, 37-41.

144.Dzombak, D.A., & Hudson, R.J. (1995). Ion exchange: the contributions of diffuse layer sorption and surface complexation. In *Aquatic chemistry: interfacial and interspecies processes* (C.P. Huang, C.R. O'Melia, & J.J. Morgan, Eds.), pp 59-94. American chemical society, Washington, DC.

145.Westall, J.C. (1987). Adsorption mechanisms in aquatic surface chemistry. In *Aquatic surface chemistry* (W. Stumm, Ed.), pp 520. John Wiley & sons, New York.

146.Atkins, P.W. (1994). *Physical chemistry, Fifth edition*. Oxford university press, Oxford.

147.Sposito, G. (1986). Distinguishing adsorption from surface precipitation. In *Geochemical processes at mineral surfaces* (J.A. Davis, & K.F. Hayes, Eds.). American Chemical society, Washington D.C.

148.Watson, E.B. (1996). Surface enrichment and trace element uptake during crystal growth. *Geochim. Cosmochim. Acta*, **60**, 5013-5020.

149.Barrow, N.J., Brümmer, G.W., & Strauss, R. (1993). Effects of surface heterogeneity on ion adsorption by metal oxides and by soils. *Langmuir*, **9**, 2606-2611.

150.Gouhier, J. (1971). Une hectorite dans les pépérites du Puy-Chalard (Puy-de-Dome). *Bull. Groupe franç. Argiles*, **23**.

151.Walther, J.V. (1996). Relation between rates of aluminosilicate mineral dissolution, pH, temperature and surface charge. *Am. J. Sci.*, **296**, 693-728.

152.Carroll-Webb, S.A., & Walther, J.V. (1988). A surface complex reaction model for the pH-dependence of corundum and kaolinite dissolution rates. *Geochim. Cosmochim. Acta*, **52**, 2609-2623.

153.Van der Hoek, M.J., Werner, W., & Van Zuylen, P. (1986). Design, construction and test results of a slitless, high-power, high-resolution double crystal x-ray monochromator for synchrotron radiation. *Nucl. Instr. Meth. Phys. Res.*, **A246**, 190-193.

154.Van der Hoek, M.J., Werner, W., & Van Zuylen, P. (1986). Slitless double crystal monochromator for EXAFS and XANES measurements. *Nucl. Instr. Meth. Phys. Res.*, **A246**, 380-384.

155.Hazemann, J.-L., Manceau, A., Sainctavit, P., & Malgrange, C. (1992). Structure of the $\alpha Fe_xAl_{1-x}OOH$ solid solution. I. Evidence by polarized EXAFS for an epitaxial growth of hematite-like clusters in Fe-diaspore. *Phys. Chem. Minerals*, **19**, 25-38.

156.Sainctavit, P. (1989). Spectroscopie d'absorption X de chalcogénures de structures blende ou chalcopyrite et de complexes fer-soufre dans des verres silicates. Thèse Université Paris VII, Paris.

157.McBride, M.B., Pinnavaia, T.J., & Mortland, M.M. (1975). Electron spin resonance and the studies of cation orientation in restricted water layers on phyllosilicate (smectite) surfaces. *J. Phys. Chem.*, **79**, 2430-2435.

158.McBride, M.B. (1977). Mobility and orientation of charged molecules at silicate surfaces. *Clay Min.*, **12**, 273-277.

159.McBride, M.B., & Bloom, P.R. (1977). Adsorption of Aluminium by a smectite: II. An Al^{3+}-Ca^{2+} exchange model. *Soil Sci. Soc. Am. J.*, **41**, 1073-1077.

160.Chisholm-Brause, C.J., Conradson, S.D., Buscher, C.T., Eller, P.G., & Morris, D.E. (1994). Speciation of uranyl sorbed at multiple binding sites on montmorillonite. *Geochim. Cosmochim. Acta*, **58**, 3625-2631.

161.Morris, D.E., Chisholm-Brause, C.J., Barr, M.E., Conradson, S.D., & Eller, P.G. (1994). Optical spectroscopic studies of the adsorption of UO_2^{2+} species on a reference smectite. *Geochim. Cosmochim. Acta*, **58**, 3613-3623.

162.Farquhar, M.L., Charnock, J.M., England, K.E.R., & Vaughan, D.J. (1996). Adsorption of Cu(II) on the (0001) plane of mica: a REFLEXAFS and XPS study. *J. Colloid Interface Sci.*, **177**, 561-567.

163.Fürrer, G., Zysset, M., & Schindler, P.W. (1993). Weathering kinetics of montmorillonite: investigations in batch and mixed-flow reactors. In *Geochemistry of clay-pore-fluids interactions* (D.A.C. Manning, P.L. Hall, & C.R. Hughes, Eds.), pp 243-262. Chapman & Hall, London.

164.Decarreau, A. (1981). Mesure expérimentale des coefficients de partage solide/solution pour les éléments de transition A^{2+} dans les smectites magnésiennes (A= Ni, Co, Zn, Fe, Cu, Mn). *C. R. Acad. Sc. Paris*, **292**, 459-462.

165.Decarreau, A. (1985). Partitioning of divalent transition elements between octahedral sheets of trioctahedral smectites and water. *Geochim. Cosmochim. Acta*, **49**, 1537-1544.

166.Pedro, G. (1982). The conditions of formation of secondary constituents. In *Constituents and properties of soils* (M. Bonneau, & B. Souchier, Eds.). Academic Press, London.

167.Ross, C.S. (1946). Sauconite-a clay mineral of the montmorillonite group. *Amer. Mineral.*, **31**, 411-424.

168.Rivière, M., Rautureau, M., Besson, G., Steinberg, M., & Amour, M. (1985). Complémentarité des rayons X et de la microscopie électronique pour la détermination des diverses phases d'une argile zincifère. *Clay Min.*, **20**, 53-67.

169.Robarge, W.P. (1998). Precipitation/dissolution reactions in soils. In *Soil physical chemistry, second edition* (D.L. Sparks, Ed.), pp 1-46. CRC Press, New York.

170.Thompson, H.A., Parks, G.A., & Brown, G.E., Jr. (1999). Dynamic interractions of dissolution, surface adsorption, and precipitation in an aging cobalt(II)-water system. *Geochim. Cosmochim. Acta*, **63**, 1767-1779.

171.Davies, S.N., & De Wiest, R.C.M. (1966). *Hydrogeology*. John Wiley & sons, New York.

172.Rimstidt, J.D. (1997). Quartz solubility at low temperatures. *Geochim. Cosmochim. Acta*, **61**, 2553-2558.

173.Iler, R.K. (1979). *The chemistry of silica*. John Wiley & Sons, New York.

174.O'Day, P.A., Chisholm-Brause, C.J., Towle, S.N., Parks, G.A., & Brown, G.E., Jr. (1996). X-ray absorption spectroscopy of Co(II) sorption complexes on quartz (α-SiO_2) and rutile (TiO_2). *Geochim. Cosmochim. Acta*, **60**, 2515-2532.

175.Manceau, A., & Calas, G. (1986). Nickel-bearing clay minerals: II. Intracrystalline distribution of nickel: an X-ray absorption study. *Clay Min.*, **21**, 341-360.

176.Brady, P.V., & Walther, J.V. (1990). Kinetic of quartz dissolution at low temperatures. *Chem. Geol.*, **82**, 253-264.

177.Rimstidt, J.D., & Barnes, H.L. (1980). The kinetics of silica-water reactions. *Geochim. Cosmochim. Acta*, **44**, 1683-1699.

178.Towle, S.N., Bargar, J.R., Brown, G.E., Jr., & Parks, G.A. (1997). Surface precipitation of Co(II)(aq) on Al_2O_3. *J. Colloid Interface Sci.*, **187**, 62-82.

179.Charlet, L., & Manceau, A. (1994). Evidence for the neoformation of clays upon sorption of Co(II) and Ni(II) on silicates. *Geochim. Cosmochim. Acta*, **58**, 2577-2782.

180.Tardy, Y., & Garrels, R.M. (1976). Prediction of Gibbs free energies of formation-I. Relationships among Gibbs energies of formation of hydroxides, oxides, and aqueous cations. *Geochim. Cosmochim. Acta*, **40**, 1051-1056.

181.Tardy, Y., & Garrels, R.M. (1977). Prediction of Gibbs free energies of formation-II. Monovalent and divalent metal silicates. *Geochim. Cosmochim. Acta*, **41**, 87-92.

182.Tardy, Y., & Duplay, J. (1992). A method of estimating the Gibbs free energies of formation of hydrated and dehydrated clay minerals. *Geochim. Cosmochim. Acta*, **56**, 3007-3029.

183.Caillère, S., Hénin, S., & Esquevin, J. (1956). Étude expérimentale du mécanisme de la formation des antigorites nickelifères. *Bull. Soc. Franç. Minér. Crist.*, **59**, 408-420.

184.Caillère, S., Hénin, S., & Esquevin, J. (1955). Synthèse à basse température de quelques minéraux ferrifères (silicates et oxydes). *Bull. Soc. Franç. Minér. Crist.*, **58**, 227-241.

185.Brindley, G.W., & Hang, P.T. (1973). The nature of garnierite. I. Structures, chemical compositions and color characteristics. *Clay Min.*, **21**, 27-40.

186.Tester, J.W., Worley, W.G., Robinson, B.A., Grigsby, C.O., & Feerer, J.L. (1994). Correlating quartz dissolution kinetics in pure water from 25°C to 625°C. *Geochim. Cosmochim. Acta*, **58**, 2407-2420.

Thèse de doctorat de l'Université
Joseph Fourier Grenoble

Titre de l'ouvrage :

De l'adsorption du cobalt et du zinc sur l'hectorite et le quartz, à la nucléation hétérogène de phyllosilicates

Nom de l'auteur :
Michel Schlegel

Établissement :
Université Joseph Fourier

Résumé. Les approches macroscopiques (cinétique chimique) et microscopiques (spectroscopie EXAFS polarisée) ont été couplées dans le but de caractériser les mécanismes moléculaires de fixation de cations divalents (Co, Zn) sur l'hectorite, une smectite magnésienne, et sur le quartz.

À pH = 6,5, haute force ionique, et pour un rapport Zn/hectorite de ~ 50 μmol/g, une adsorption spécifique de Co et Zn a lieu. Cette adsorption n'atteint pas l'équilibre avant plusieurs heures, et coïncide avec une libération initiale accrue de protons et de Mg en solution, puis une inhibition à long terme ($t \geq 48$ h) de la cinétique de dissolution de l'hectorite. Co et Zn adsorbés forment des complexes de surface mononucléaires en continuité structurale de la couche octaédrique des feuillets d'hectorite. À basse force ionique, Co et Zn sont initialement adsorbés par échange cationique. Cette réaction atteint l'équilibre en moins de 5 min. Ces cations forment initialement des complexes de sphère externe sur les sites d'échange, puis ils migrent progressivement vers les sites de bordure des feuillets, où ils forment des complexes de surface similaires à ceux formés à haute force ionique.

Le mécanisme et l'amplitude de l'adsorption de Zn sur l'hectorite à pH 7,3, à haute force ionique et pour un rapport Zn/hectorite de 1480 μmol/g, dépend de la concentration en silice dissoute, [Si]. La quantité de Zn adsorbé est limitée pour [Si] ≈ 30-60 μmol/L, et Zn forme des polymères de petite taille (2-3 octaèdres) en continuité structurale de la couche octaédrique de l'hectorite. La quantité de Zn adsorbé est beaucoup plus importante pour [Si] ≈ 540 μmol/L ; cette adsorption est corrélée à une adsorption de Si, et correspond à la nucléation de phyllosilicates TOT zincifères en épitaxie dans le plan ab des feuillets.

Une analyse approfondie de spectres EXAFS de Co adsorbé sur le quartz révèle que cet élément polymérise sous forme de couches d'octaèdres liées à des couches de tétraèdres de Si, pour former des phyllosilicates cobaltifères. Le mécanisme de cette néoformation est discuté.

Mots clés : hectorite, quartz, cobalt, zinc, EXAFS, cinétique, adsorption, échange cationique, épitaxie, phyllosilicate